SiF'04

STRUCTURES IN FIRE
Proceedings of the Third International Workshop

Ottawa, ON, Canada
10 – 11 May 2004

Editors:
J.M. Franssen
N. Benichou
V.R. Kodur
M.A. Sultan

STRUCTURES IN FIRE

Third International Workshop

Ottawa, Ontario, Canada, May 10 & 11, 2004

Co-organized by

National Research Council of Canada
University of Liege, Belgium

Organizing Committee

Venkatesh Kodur, National Research Council Canada
Noureddine Benichou, National Research Council Canada
Mohamed Sultan, National Research Council Canada
Joe Hum, National Research Council Canada
Philippe Ladouceur, National Research Council Canada
Guylaine Lalande-Guérin, National Research Council Canada
Les Richardson, Forintek Canada Corp.
George Hadjisophocleous, Carleton University
Dave MacKinnon, Canadian Institute of Steel Construction
Richard McGrath, Cement Association of Canada

International Technical Committee:

Jean Marc Franssen, University of Liege, Belgium
Jürgen König, Trätek, Sweden
Asif Usmani, University of Edinburgh, UK
Kazunori Harada, University of Kyoto, Japan
Joël Kruppa, CTICM, France
Andy Buchanan, University of Canterbury, New Zealand
Richard Liew, National University of Singapore
Paulo Vila Real, University of Aveiro, Portugal
G. Q. Li, Tongji University, China
James Milke, University of Maryland, USA
Yngve Anderberg, Fire Safety Design, Sweden
Jim Mehaffy, Forintek Canada Corp.
Venkatesh Kodur, National Research Council Canada
Noureddine Benichou, National Research Council Canada
Mohamed Sultan, National Research Council Canada

Why this Workshop?

Some 10 or 20 years ago, the researchers that deal with the fire resistance performance of structural building elements were divided into two groups with different approaches. One group considered that the critical temperature of 540°C, where the steel loses most of its strength in steel structures or in steel reinforced bars of concrete structural building elements is the only parameter that should be used to assess the fire resistance of such building elements. The other group investigated the fire resistance performance of building elements using fire resistance standard test methods that follow either the ISO or ASTM temperature-time curve.

Other aspects were also considered by the fire science community, such as human behaviour, risk analysis, etc. This evolution led to the now widely-accepted concept of Fire Safety Engineering that deals with fire-related problems in the same manner as in other engineering fields. Growing from this, a number of specialized seminars, workshops and conferences were regularly organized. Some examples of these are:

- The ECCS Workshop on material properties at elevated temperatures, organized by ECCS Committee 3 - Fire Safety of Steel Structures, was held in Arnhem, The Netherlands in June 1986.
- The EGOLF seminar "Protection contre l'incendie des structures en acier, Harmonisation Européenne" was held in Brussels, Belgium in November 1986.
- The Abschlusskolloquium "Bauwerke unter Brandeinwerkung" was held at Technische Universität Braunschweig, Braunschweig, Germany in April 1987.
- The Structural Fire Design seminar, organized by the Eurocode fire drafting groups, was held in Luxembourg in June 1990.
- The 3rd CIB/W14 Fire Safety Engineering Workshop on Modelling was held in Rijswijk, The Netherlands in January 1993.
- The first European Symposium on Fire Science, IAFSS was held in Zurich, Switzerland in August 1995.

Although the aspects of interest in fire research were certainly narrow, the progress was spectacular.

During 1999, the idea of creating specific activities around structural fire modelling was widely being considered. To this end, two activities were created: a discussion on Structures in Fire (SiF) via the internet where different experts could exchange their views; and another via the organization of workshops where experts in the fire resistance research area presented their current research activities and received feedback from their peers.

The First SiF Workshop was held in Copenhagen in June 2000 and provided fire resistance researchers with the opportunity to meet, present papers, establish collaborations and discuss their work with their peers. The Second SiF Workshop was held in Christchurch, New Zealand in 2002 (60 participants). Following the success of these two workshops, the Fire Risk Management Program, Institute for Research in Construction of the National Research Council of Canada was selected to host the Third SiF Workshop to be held in Ottawa in May 2004.

SURVEY OF MULTI-STORY BUILDING COLLAPSES DUE TO FIRE, FIRE-RESISTANCE CAPABILITIES OF TEST LABORATORIES, AND RESEARCH NEEDS

Beitel, J. J., Senior Scientist
Iwankiw, N. R., Senior Engineer

Hughes Associates, Inc.
3610 Commerce Drive, Suite 817
Baltimore, MD 21227-1652

INTRODUCTION

There are continuing concerns about the adequacy of structural fire protection in the wake of the 9/11 tragedies in the US. As significant as these events were, they were also clearly not representative of the normal accidental impact of fire on building structures. To assess both the extent and nature of structural collapses due to fire in taller buildings, and fire testing capabilities, historical information was collected and reviewed.

The collapse survey was international in scope, and included building collapses due to fire in structures with four, or more, stories that had occurred between 1970 and 2002. Both total and partial collapses were included in the survey. Since no database exists that systematically identifies building collapses due to fire (including the NFIRS system), the survey was necessarily exploratory. A total of 22 fires were identified that caused either partial or total collapse of a multi-story structure. While this total number of fire events may appear low (average of one/year), these fire events are high consequence occurrences with respect to potential for loss of life, injuries and economic costs.

The survey of various test laboratories was performed to provide information concerning their fire-resistance testing capabilities especially with respect to test sample size, orientation and loading.

A needs assessment was developed to address the need for additional testing and/or experimental facilities to allow the performance of structural assemblies and fire resistance materials to be predicted under fire conditions within actual buildings.

This project was sponsored by the National Institute of Standards and Technology (NIST) under the direction of Dr. William Grosshandler, and the Report is available from NIST.

COLLAPSE SURVEY RESULTS

For the purposes of this NIST survey, multi-story buildings were defined as those having four or more stories. Non-building structures, such as tunnels, bridges, observation or transmission towers, were not included. Either partial or total failure of the structural framing, members, and/or connections was considered to have constituted a collapse, and it was necessary for a fire to have been the direct cause of this failure.

A total of 22 such cases were identified after extensive searches of the literature, News, and other contacts, with the Sept. 11, 2001 disasters counting as 5 of these incidents (World Trade Center-WTC 1,2, 5 and 7, and the Pentagon). The cases had occurred not just in the US and North America, but also internationally. This NIST survey data demonstrated that buildings of all types of construction and occupancies, in the US, North America, and abroad, are susceptible to fires, particularly older buildings and those that may be undergoing construction, renovations or repairs.

The NIST survey of 22 fire-induced building collapses since 1970 involved a variety of conditions, materials, locations, and buildings. Fifteen cases were from the US, 2 from Canada, and 5 from Europe, Russia and South America. The numbers of fire collapse events can be categorized by building material as follows:

- Concrete: 7 (1 in Pentagon 9/11 event)
- Structural steel: 6 (4 in 9/11 WTC events)
- Brick/masonry: 5
- Unknown: 2
- Wood: 2

Three of these events were from the 1970's, another three from the 1980's, four from the 1990's, and twelve for 2000 and beyond. This temporal distribution is skewed towards more recent occurrences, as expected, both due to the magnitude of the 9/11 events.

The fire-induced distribution by building story height was as follows:

- 4-8 stories 13
- 9-20 3
- 21 or more 6

Almost 60% of the cases are in the 4-8 stories range, with the remainder being much taller buildings. Six collapses occurred in buildings over 20 stories, and three of these were the WTC steel-framed buildings (WTC 1, 2 and 7).

At least four of these fire-induced collapses had occurred during construction or renovations of some kind, when the usual expected architectural, structural and fire protection functions were still

incomplete or temporarily disrupted, and/or potential new fire sources were introduced, such as electrical and gas line repairs, welding, and the presence of other flammable supplies and/or equipment. Partial collapses (14 events) were the most frequent occurrences, and the WTC disasters (listed as 4 separate events, with 3 full collapses) dominated the full collapse event total of 8 cases. Office and residential were the primary types of occupancy in these 22 buildings, as would be expected in multi-story construction, with the occupancy distribution being as follows:

- Office: 9
- Residential: 8
- Commercial: 3
- Combined commercial/residential: 2

The now well-known 9/ 11 events are quite thoroughly documented in the FEMA 403, (2002) and ASCE-SEI Pentagon (2003) Reports, and will not be further covered herein. Rather, several interesting and more obscure cases of fire-induced collapses will be described.

Two large department store fires in Athens, Greece in 1980 are documented in the paper by Papaioannoa, Kyriakos, 1986. These fires began at 3 AM on Dec. 19, 1980, with arson being suspected as the cause. The Katrantzos Sport Department Store was an 8-story reinforced concrete building. Its fire started at the 7th floor and rapidly spread throughout the building, due to lack of vertical or horizontal compartmentation and the absence of sprinklers. Collected evidence indicated that the fire temperatures reached 1000°C over the 2-3 hour fire duration, and the firefighters concentrated on containing the fire spread to the adjacent buildings. Upon termination of these fires, it was discovered that a major part of the 5-8th floors had collapsed. Various other floor and column failures throughout the Katrantzos Building were also observed, see Figure 1. The cause of these failures was considered to be restraint of the differential thermal expansion of the structure that overloaded its specific elements or connections.

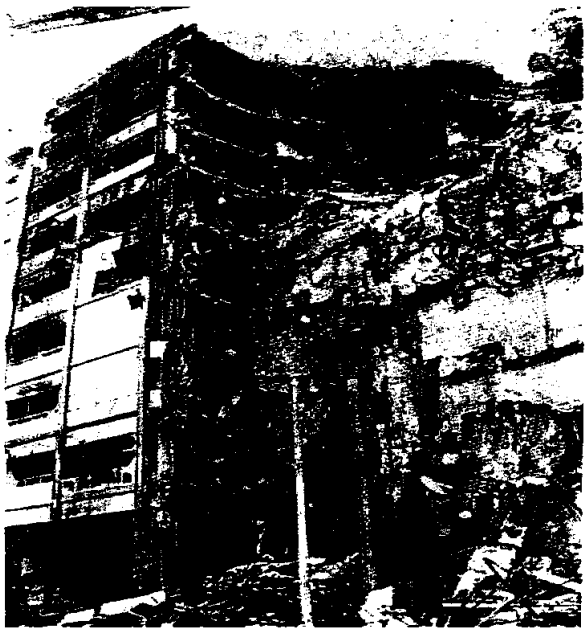

Figure 1 : Katrantzos Department Building in Athens, Greece After 1980 Fire

On May 21, 1987, Sao Paulo had one of the biggest fires in Brazil, which precipitated a substantial partial collapse of the central core of the tall CESP Building 2. (Berto, Antonio Fernando and Tomina, Jose Carlos, 1988) This was a 21-story office building, headquarters of the Sao Paulo Power Company (CESP), after whom the building was named. Buildings 1 and 2 of this office complex were both of reinforced concrete framing, with ribbed slab floors. According to this Berto and Tomina (1988) paper, these two buildings had several unique internal features and contents. Both buildings still retained their original wood forms used for pouring the concrete floor slabs, which were never removed. Low-height plywood partition walls were also used in the interiors. Approximately two hours after the beginning of the fire in CESP 2, its structural core area throughout the full building height collapsed. This collapse was attributed to the thermal expansion of the horizontal concrete T-beam frames under the elevated fire temperatures, which led to the fracture of the vertical framing elements and their connections in the middle of the building, and the consequent progressive loss of gravity load-carrying capacity. (see Figure 2)

Figure 2 : CESP 2 Core Collapse in Sao Paulo, Brazil

A fire-initiated full collapse of a textile factory occurred in Alexandria, Egypt on July 19, 2000 (BBC News, 2000). This 6-story building was built of reinforced concrete, and its fire started at about 9 AM in the storage room at the ground floor. Fire extinguishers were non-functional, and the fire spread quickly before the firefighters could arrive. An electrical short-circuit accelerated the fire spread. At about 6 PM, 9 hours after the start of the fire, when the blaze seemingly was under control and subsiding, the building suddenly collapsed, killing 27 people. Figure 3 shows a photograph of this collapse.

During the survey, it was not possible to fully access the performance of the partial or fully-collapsed buildings with respect to their performance vis-à-vis their initial building design, construction in accordance with local codes, fire exposure conditions, etc. Thus, a specific building may have performed adequately as it was designed, but suffered full or partial collapse due to issues (e.g. fire duration, exposure, etc.) that the initial building design did not contemplate.

Figure 3 : Collapsed Textile Factory in Alexandria, Egypt

LABORATORY SURVEY RESULTS

The objective of this NIST Project Task was to survey private and public facilities capable of testing structural integrity of building elements under fire conditions to establish the current global research capabilities in structural fire protection. A total of 55 fire testing laboratories were surveyed from around the world, and 29 responses were received.

In order to attain a fire resistance rating, the material, product or assembly is evaluated using existing standard fire resistance tests. The most common fire resistance standards throughout the world are:

- ASTM E119 – "Standard Test Methods for Fire Tests of Building Construction and Materials"
- NFPA 251 – "Standard Methods of Tests of Fire Endurance of Building Construction and Materials"
- UL 263 – "Fire Tests of Building Construction and Materials"
- ISO 834 – "Fire Resistance Tests – Elements of Building Construction"

All of these tests are standardized fire resistance tests that have been used for many years to test and regulate fire resistance of building elements. In general, they use similar fire exposure conditions as measured and controlled by the air temperature within the furnace. Over the years, the fire test methods have standardized many of test details, such as sample size, measurement of temperatures, loading, etc. As such, the majority of test laboratories have designed and built their current fire resistance test furnaces to meet the standard test methods.

The responding laboratories have various sized vertical and horizontal furnaces that can be used for fire resistance testing. In some cases, they also have small-scale furnaces that are used for

scoping/R&D testing even though they do not meet the requirements of the standard tests with respect to the minimum size of the samples. In most of the laboratories, full-scale furnaces that can evaluate the standard sample sizes are available.

The standard practice in fire resistance testing is to test each building element individually. For example, roofs or floors are not tested in combination with walls or columns. Thus, the roof assembly is tested as an individual element and the column or the wall is also tested as an individual item. Connections between building elements are not usually evaluated under the existing fire resistance test methods.

Full-scale vertical furnaces can typically evaluate assemblies approximately 3 m high x 3 m wide. The largest can evaluate samples 4.6 m high x 4 m wide. Most vertical furnace are shallow (e.g. 0.6 m deep or less), but several have depths up to 1.2 m to 1.5 m. Some of the test facilities can also provide expansion collars that will increase the depth of the furnace as well as the size (height & width) of the test sample.

Full-scale horizontal furnaces can evaluate construction assemblies up to approximately 4 m long x 5.5 m wide. The largest experimental furnace can accommodate a sample that is 10.5 m. long x 4 m. wide. Generally, the depth of the full-scale furnaces is approximately 1.8 m. The largest furnace described above, however, has a depth of 2.4 m. Most laboratories can build-up the sides of the horizontal furnaces such that deeper or taller specimens, such as columns, can be tested.

Fire testing combinations of structural elements can be conducted, but one must be careful with respect to the type and size of the combinations. For example, it may be possible to test a full-scale floor and a column together within some limits on the size, but most laboratories cannot test a full-scale roof and wall combination. The largest horizontal furnace may have this capability, since parts of the furnace can be closed off and thus one could build a wall inside the furnace such that it will meet a floor. Also, another lab has a medium scale furnace that can potentially expose a wall (3 m tall x 3.6 m wide) in conjunction with a floor (3.6 m wide x 4.9 m long) by removing one side wall of the furnace.

Loading of test assemblies is accomplished in various ways, depending on the orientation of the test sample. Most of the laboratories load walls using hydraulic jacks, such that the wall is in compression during the test. Columns are typically tested without applied load, since most of the testing involves the fire protection materials on the columns, and thus limiting temperatures are used rather than structural integrity. Several laboratories have the capability to test columns under axial compression load. When assembly loads are applied during a standard fire test, they are usually the *maximum* load determined from the governing design standard.

In horizontal fire testing, loading is typically limited to live loads placed on top of the test assembly. The vertical live loading is typically accomplished using water tanks or hydraulic jacks. Special loading with respect to tension, shear, etc. is not typically done. One test laboratory can perform tension loading in their small-scale horizontal furnace.

Generally, instrumentation in fire resistance testing is limited to:

- Temperatures / heat flux of exposing fire
- Temperatures on the test sample (interior and exterior)
- Deflection of the test sample
- Limited data on load history by some laboratories
- Pressure in the furnace with respect to atmosphere near the sample location

In some cases, research testing was conducted wherein load cells, or strain gauges, were used, but this is very rare. Some of the laboratories have the capability to use this instrumentation, but many experimental problems exist with their use. For example, at high temperatures, these devices may give faulty data, and can be damaged/destroyed prior to the attainment of elevated temperatures of interest.

In summary, most of the responding laboratories have the capability to perform the standard fire resistance tests with respect to size, type of exposure, loading, and measurements. In some cases, laboratories can subject samples to a variety of fire exposures, and several fairly large furnaces exist that may be used to evaluate, within some size limitations, connections or a combination of building elements. No single laboratory stands out as having all combinations of facilities such as largest size, capabilities of testing connections or combination of elements, loading, exposure conditions, etc. In general, the large commercial laboratories have greater than normal capabilities. The selection of a particular laboratory would depend on the specific objective of the test program and the test requirements. Real-scale size facilities and loading conditions and instrumentation other than those used or specified in the standard fire test methods are not readily available.

ASSESSMENT OF NEEDS

One important finding is the lack of systematically collected information about partial or total structural collapses due to fire. Generally, very little building collapse information was available, especially for events that occurred outside North America. Even in North America, there was no specific reporting of collapse via NFIRS, or other reporting system. Therefore, it is recommended that an ongoing structural damage and collapse reporting system be developed, or be incorporated into existing databases, whereby structural damage and collapse due to fires can be collected for the future. Without this information, the full scope of this problem cannot be well documented or understood.

Except for several recent research studies conducted overseas, (Bailey, 2002; Newman, et al., 2000; Bailey, 2001) current fire resistance testing is primarily limited to qualifying materials or assemblies using the standard fire resistance tests. When viewed from a whole building perspective, the standard fire testing has the following limitations:

- Tests are conducted on individual building elements of limited size.
- Tests do not evaluate the connections of one building element to another.
- Tests demonstrate the fire resistance capability based typically on limited temperature measurements and limited load carrying capability
- Other than significant deflections, no other structural measurements or data are obtained
- Tests typically use a similar but single standard fire exposure (i.e., ASTM E 119 and ISO 834)

- The test assembly is exposed from only one side, except for columns (i.e., all sides) and beams (i.e. typically 3 sides). Walls and other elements may be exposed on two sides due to flame plumes exiting windows, etc.
- Tests are typically not conducted to ultimate failure. Tests are stopped when the required rating period is attained, or when the appropriate temperature or deflection limit is observed.

This type of standardized fire resistance testing has been used for many decades. It appears that it has provided a reasonable measure of safety, since most buildings that have a significant fire do not exhibit collapse. This performance may be due to many factors, such as a limited fire spread area, so that load is transferred to elements not exposed to the fire, redundancy and/or operation of fire protection features and over-design of the structural components, their fire protection and the other fire protection features within the building. However, despite these general successes, several notable failures identified in this report have occurred. Based on this history, periodic structural failures due to fires are likely to continue to occur in the future. The lack of technical documentation and follow-up to evaluate the causes and effects of these incidents, and potentially make necessary adjustments or corrections to testing and design practice, remains a clear need.

Improved methods and tools need to be developed to provide an engineering basis for structural fire resistance. It is readily apparent that the current state-of-the-art in fire resistance testing does not address the "whole building" as a single entity. In this regard, the WTC collapses have highlighted the lack of communication between the structural engineering and the fire protection professions when designing buildings. Also, the issue of a single mode of failure (i.e., loss of some structural stability) resulting in progressive collapse has arisen, as well as the interactions of mutually dependent structural elements.

If a column is exposed to a fire, how its behavior, or failure, will affect the structural elements that it supports is generally unknown or not explicitly considered. Currently, we would test the column with protection such that the element will not exceed pre-defined critical temperatures, below which its structural integrity is assumed to be adequate. Even though the column is connected to a beam or floor, we do not evaluate the connection type, nor its protection, to assure that the connection will perform as intended. Also, if the column was to fail, the impact of this failure on the rest of the structure is usually not determined. It has always been assumed that if each individual structural element performs well by itself, then the entire framing will also perform successfully. In some cases, this may be a faulty assumption.

Overall structural performance at elevated temperatures, except for the support of a given live load or the prevention of a critical material temperature, is typically ignored in current fire resistance testing methods. In effect, an assembly or element is evaluated for its structural performance by a critical temperature or its ability to support an imposed live load. In some cases, the live load used in the test may not be the maximum design load. Other loads, or stresses, or combinations may also be imposed on a structural element during a real fire event that may need to be considered. Thus, the more detailed engineering analysis for the combination of thermal load effects on structural load-carrying performance is usually ignored in practice.

The existing fire test facilities evaluate building elements with specific size limitations, such as length of beams (3.7 m), height of columns (2.7 m), etc. In real-world applications, building

elements are often significantly larger that those tested. This raises potential scaling concerns relative to structural performance of the larger or longer span members when they are exposed to a fire. In these cases, the performance under a specific load on a smaller or shorter span member will not accurately reflect the response of a larger or longer member.

In the standardized fire tests, the measurements and data collected are minimal. To understand how structural elements behave in a fire, greatly enhanced and unique instrumentation will be required. This will include monitoring the structural members for movement, state of stress, and temperature distribution within the elements. Without this information, it will be impossible to more accurately predict the performance of the building elements or systems when exposed to a fire.

The history of fire-induced building collapses, coupled with identified concerns surrounding the limitations of existing fire resistance test methods, clearly indicate that there is a need for a more reliable structural fire protection methodology that goes beyond what is practiced today. In order to accomplish this goal of advancing our understanding and knowledge, along with enhancing the combination of fire protection and structural engineering, empirical data developed from research-based, realistic tests must be generated. These data will be necessary to provide the validation basis for future analytical models and structural fire protection design methods.

Since our concerns center on a greater understanding of the impact of fire on the building elements, on combinations of building elements, their connections to each other, more realistic loadings and on real-scale size of building elements, most of our existing test facilities may be inadequate. Newer or unique facilities will be required to appropriately address these issues. If a connection, such as a column to a beam is to be evaluated, even the existing larger furnaces will have to be substantially adapted to provide the appropriate exposure, instrumentation and loading systems. The current limitations on the size of the members that can be tested in existing furnaces remain a concern. For testing a combination of walls, exterior columns and floors, a unique test facility will have to be constructed to accommodate the required size, appropriate loading and the fire exposures needed. Even for longer, wider or taller members, a unique facility will again be required.

Currently, the path to the design, construction, and operation of a unique facility to provide the required research-based information is unclear. Future discussions within the fire protection and the structural engineering communities are required in order to begin building a consensus with respect to the path forward. Deliberations with respect to developing a comprehensive research, development and implementation program for the future must continue with a sound plan to be developed. The Fire Resistance Determination and Performance Prediction Research Needs Workshop (Grosshandler, 2002) was a significant step forward in this direction. Along with the research plan, implementation strategies with respect to identification of stakeholders, investments of time and funding must be discussed and determined. Other interested professional, code, standards, and industry organizations, such as ASCE, SFPE, AISC, NFPA, etc. have been more active recently in this regard, and a joint collaboration among all these entities, even extending beyond national boundaries, appears to hold much promise for advancements in this field.

CONCLUSIONS

Past experience and this study confirms that fire-induced partial or full collapses are essentially rare and random events, whose effects depend highly on the time, nature and circumstances of the fire occurrence. Thus, a significant fire represents a hazard to all building types, materials, and occupancies.

The results of this survey indicated that a total of 22 fire-induced collapses were identified spanning from 1970 to 2002. The 9/11 events accounted for five of these events.

Another important finding of this study was the lack of readily available, and well-documented, information on partial or total structural collapse due to fire. Unless the fire event was significant for other reasons, i.e., loss of life, very little information was available. It is recommended that a centralized database be developed, whereby structural damage and collapse can be investigated and systematically compiled in the future. The current lack of systematic information on fire-induced collapses seriously limits the profession's understanding of the scope and nature of the real structural fire protection problem.

The current capabilities and limitations of fire testing laboratories throughout the world were also surveyed and documented. In general, the test facilities are limited to evaluating the fire resistance of structural elements via standard fire tests.

The needs assessment found that a more complete understanding of structural performance of building elements when exposed to a fire is required. Structural fire protection has largely been ignored in the US as a research area in the past 25 years, and the 9-11-01 collapses have renewed interest in this area of research. It is apparent that research into structural fire protection performance will require unique test facilities to be developed. Specialized test apparatus and instrumentation for large structural assemblies, for real-scale building elements and their connections and for full- or real-scale combinations of elements will be needed to be developed. Specialized and enhanced instrumentation will also be needed and employed in future testing.

REFERENCES

ASCE-SEI (2003), *The Pentagon Building Performance Report*, ASCE, Reston, VA, January, 2003

BBC News (2000), *"Factory Fire Kills 15 in Egypt"*, World: Asia-Pacific, July 20, 2000

Bailey, C.G., (2002)"Holistic Behavior of Concrete Buildings in Fire," *Structures and Buildings*, Vol. 152, Issue 3, 2002.

Bailey, C.G., (2001) "Holistic Behavior of Concrete Buildings in Fire", pgs 199-212, *Proceedings of the Institution of Civil Engineers*, Structure and Buildings 152, Issue 3, August, 2002.

Bailey, C.G. (2001), "Steel Structures Supporting Composite Floor Slabs: Design for Fire", Building Research Establishment, 2001, BRE Digest 462.

Berto, Antonio Fernando and Tomina, Jose Carlos (1988), "Lessons From the Fire in the CESP Administration Headquarters", IPT Building Technologies, 1988, Sao Paulo, Brazil

FEMA 403 (2002), *World Trade Center Building Performance Study: Data Collection, Preliminary Observations, and Recommendations*, Federal Emergency Management Agency, Washington, DC, May, 2002

Grosshandler, W. L. (2002), Fire Resistance Determination & Performance Prediction Research Needs Workshop: Proceedings, *NISTIR* (NISTIR 6890) - September 1, 2002

Iwankiw, N. and Beitel, J. (2002), *"Analysis of Needs and Existing Capabilities for Full-Scale Fire Resistance Testing"*, Hughes Associates, Report NIST GCR 02-843, December, 2002

Newman, G.M., Robinson, J.F., and Bailey, C.G., (2000) "Fire Safe Design: A New Approach to Multi-Story Steel-Framed Buildings", Steel Construction Institute, Berkshire, UK, 2000.

Papaioannoa, Kyriakos, (1986), "The Conflagration of Two Large Department Stores in the Centre of Athens", Fire and Materials, Vol. 10, 1986, pg. 171-177, John Wiley and Sons, Ltd.

LARGE POOL FIRE EXPOSURE TO REINFORCED CONCRETE STRUCTURE

Frank STEWARD
University of New Brunswick, retired
fsteward@unb.ca

Luke MORRISON
Professional Loss Control, P. O. Box 162, Fredericton, NB E3B 4Y9, Canada
lukeplc@nb.aibn.com

Issam KFOURY
Hydro Quebec, 855 Ste Catherine St (E), Montreal, Que.
Kfoury.Issam@hydro.qc.ca

ABSTRACT

Pool fires are traditionally modeled using empirically derived equations of burning rate based on a liquid pool in an open environment. These equations are valid where air for combustion is available over the complete circumference of the pool. This paper describes a calculation method developed for determining the pool fire characteristics and resulting thermal exposure to a reinforced concrete structure located on the edge of the pool. For this physical arrangement the burning rate of the pool is influenced by the reduced air entrainment where the building blocks airflow to the pool. A computer model was developed to perform the appropriate calculations. The model results include: details of fire intensity, maximum surface temperature on the building wall, location of maximum temperature, area of wall above a specified temperature and the temperature profile in the wall at specified locations. Results of the model were used to predict likelihood of structural damage.

KEYWORDS: *reinforced concrete, pool fire, fire modeling, thermal penetration*

INTRODUCTION

This paper summarizes a study was of the thermal exposure of a large pool fire on a reinforced concrete structure at the edge of the pool. Pool fires are traditionally modeled using empirically derived equations of burning rate based on a liquid pool in an open environment. These equations are valid where air for combustion is available over the complete circumference of the pool. This paper describes a calculation method developed for determining the pool fire characteristics and resulting thermal exposure to a reinforced concrete structure located on the edge of the pool. For this physical arrangement the burning rate of the pool is influenced by the reduced air entrainment where the building blocks airflow to the pool.

BACKGROUND

The reinforced concrete structure utilized for this evaluation was cylindrical in shape measuring 42 meters high and 44 meters in outside diameter. The exterior wall of was of pre-stressed reinforced concrete construction. The wall is 1.0675 meters thick and reinforcing steel is approximately 500 mm from the exterior wall surface.

The properties of the concrete used for this study are shown in Table 1.

Table 1
Concrete Properties (Stone 1-2-4 mix)

Density (kg/m3)	2400
Thermal Conductivity (W/m°C)	1.73
Heat Capacity (kJ/kg°C)	0.88
Thickness of Wall (m)	1.0675

For the purpose of evaluating the impact of fire on the structure, only one half of the structure was considered to be exposed. This portion of the building exterior was divided into cells. Cell size for the wall was 1.157 m wide by 1.083 m high. Cell size near the roof of the structure was 1.189 m wide by 1.067 m high. Each cell was then assigned a row and column number for analysis purposes (See Figure 1).

For the purpose of this study aviation fuel (JP-5) was considered as the liquid available to form the pool and the pool was assumed to form adjacent to the structure. Details of this fuel are shown in Table 2.

Table 2
Fuel Properties

Density (kg/m3)	780
Lower Heating Value (kJ/kg)	43,150
Stoichiometeric air fuel ratio (kg/kg)	14.775
Fuel Volume (l)	94,052
Fuel Mass (kg)	73,360

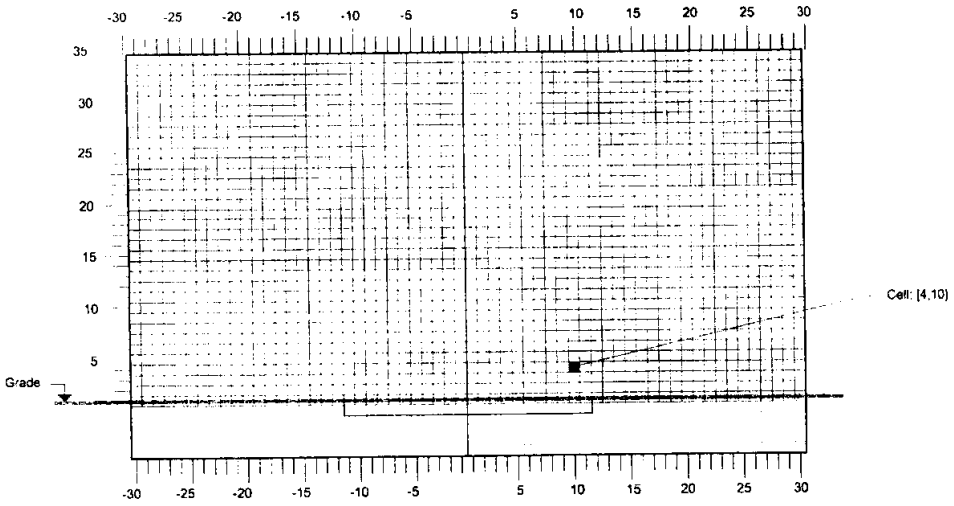

Figure 1 : Building Cell Designations

POOL FIRE MODELING

The pool fire evaluated was a liquid pool adjacent to the structure. The liquid fuel was assumed to form in the space on the side of the structure and bounded by ground contour. The resulting pool fire would have an area of 355 m^2 and the flame height from the fire would be approximately 15 m. See plan and elevation views in Figure 2.

Pool fire modeling was performed to determine the heat flux and temperature distribution on the outside surface of the structure, and in the wall, as a function of time. The calculation method was based on a combination of the theoretical principles and empirical data collected on pool fires either open or partially enclosed. The flame temperatures and surface heat fluxes calculated by the fire model are consistent with experimental data from large-scale hydrocarbon pool fires.

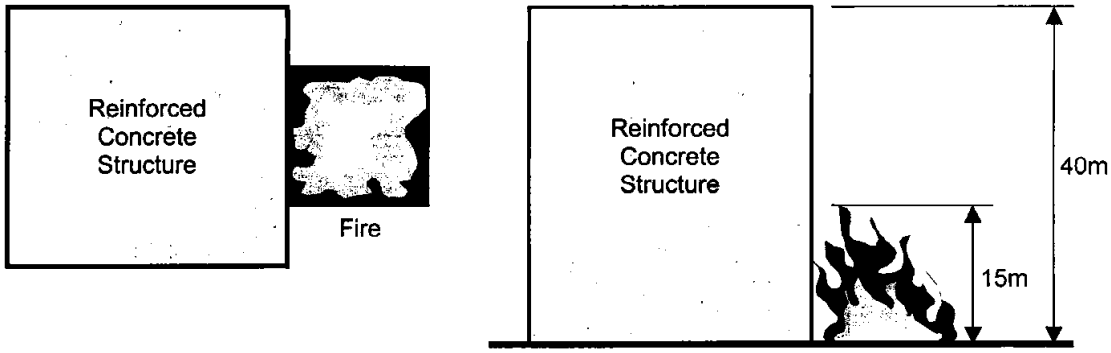

Figure 2 : Plan & Elevation Views of Pool Fire

The model follows seven basic calculation steps:

1. Input required data.
2. Conduct preliminary calculations.
3. Define air entrainment zone.
4. Calculate the flame temperature distribution within the pool fire.
5. Calculate the local flame temperature adjacent to the wall.
6. Calculate the heat flux to the wall of the building.
7. Calculate the surface temperature of the wall.
8. Calculate the temperature distribution within the wall.

The input data required for the program was of four main types, physical properties, physical constants, empirical coefficients and quantities that define the fire. A number of well-defined basic calculations were performed. Based on the area for the pool and the quantity of fuel established in Table 2 two preliminary calculations were made. The first was to calculate the depth of fuel in the pool and the second the duration of burning. The depth of fuel was calculated based on its volume divided by the spill area. The duration of burning was calculated based on an accepted regression rate for large pool fires of jet fuel of 4 mm per minute.

To determine the temperature distribution in the flame above the pool it was necessary to first determine the mixing between the fuel vapour, and surrounding air to form combustion gas. This calculation was based on a set of entrainment equations that were determined by a combination of theoretical considerations and data collected from large-scale fires.

The entrainment analysis was divided into three zones:

- Area Fire Close to Surface
- Neck Fire Region
- Fire Plume

The equations used were from Delichatsios (1) and were based on considerable data from experimenters such as Schneider and Kent (2) as described in equations 1, 2 and 3.

For fire close to the surface of the burning liquid ($z/D_f < 1.0$) then

$$m_{ent} = (W_d\ 0.086/W)\ (S + 1)/F_{rf}\ m_f\ (z/D_f)^{1/2} \quad [1]$$

For the neck fire region defined where $1.0 < z/Df < 4.0$ then

$$m_{ent} = (W_d\ 0.093/W)\ (S + 1)/F_{rf}\ m_f\ (z/D_f)^{3/2} \quad [2]$$

In the fire plume region ($z/Df > 4.0$) the mass of air entrainment is defined by

$$m_{ent} = (W_d\ 0.018/W)\ (S + 1)/F_{rf}\ m_f\ (z/D_f)^{5/2} \quad [3]$$

Where: m_{ent} = mass flux of air into the fire up to height z
W_d = empirical factor based on wind velocity
W = empirical coefficient for blocking (1.3)
S = stoichiometric ratio
F_{rf} = fire Froude number
m_f = burning rate of the fuel (kg/s)
z = vertical distance above the fuel (m)
D_f = diameter of the pool fire (m)

In each of the zones an empirical coefficient was used to account for the blocking of entrainment by the building wall. This in turn increased the flame height. A value of 1.3 was determined for the increase in flame height of fires against a wall based on data from McCaffrey (3).

Wind affects this analysis in two ways. The wind has an effect on air entrainment into the burning region of the pool fire and it will also cause flame to tilt. The increase in air entrainment was accounted for by use of an empirical factor in the equations used for each entrainment zone. This empirical factor was determined from an analysis of Mudan and Croce (11), which was based on a correlation by Thomas (12) of flame height data.

The tilt of the flame due to wind was calculated from a relationship given by Mudan and Croce (11) based on the correlations of others (12) (13) (14). This flame tilt was used to modify the boundary of the fire above the fuel source as the wind spreads the fire over the building wall surface.

For the purposes of this study a simplified equation was used to calculate flame temperature. This equation contains empirical parameters to account for less than ideal combustion and heat losses from the flame. This simplified equation is shown here as equation 4 and was calculated for each air entrainment zone.

$$T_f - T_a = f_f\ m_f\ \Delta H_f\ /\ ((m_{ent} + m_f)\ C_p)\ (X_A - X_R - X_D) \quad [4]$$

Where: T_f = temperature of flame (K)
T_a = ambient air temperature (K)
f_f = fraction of fuel burned
m_f = mass of fuel burned (kg)
ΔH_f = heat of combustion of the fuel (kJ/kg)
m_{ent} = mass flux of air into fire zone (kg/s)

C_p = heat capacity of the product gases
X_A = fractional combustion efficiency (0.9)
X_R = fraction of heat of combustion loss from flame (0.35)
X_D = fraction of heat not released due to turbulent mixing

In order for the combustion reaction to occur the fuel vapour and oxygen from the air must mix on a molecular scale. The mixing considered in the calculations was turbulent mixing, which must be followed by molecular diffusion for the heat of combustion to be released. These intermittent considerations were based on formulas given by Drysdale (7).

THERMAL IMPACT ON STRUCTURE

The previously described calculations give the temperature distribution in the fire adjacent to the building. The radiative heat flux from the fire to the surface at any position can be determined locally by the Stefan Boltzmann equation (equation 5). The values obtained by this calculation were in agreement with experimental data from pool fires (5, 6, 8, 10).

$$q_r / A = \sigma \varepsilon (T_r)^4 \qquad [5]$$

Where:
q_r = radiant heat flux (kW)
A = wall area (m2)
σ = Stefan Boltzmann constant 5.674×10^{-11} (kW/m^2 K)
ε = emissivity of the surface
T_r = temperature of the flame (K)

The surface temperature of the building at a particular point changes with time due to the local heat balance. This balance is a combination of:

1. Radiation from the fire to the wall surface,
2. Convection from the fire to the surface,
3. The removal of heat from the surface by back radiation, and
4. Conduction into the wall below the surface.

This heat balance was calculated for each defined cell of the building wall.

Also of interest to this study was the temperature penetration into the wall as a function of time. The calculation was based on a one-dimensional analysis using equation 6. The thickness of the wall was subdivided for calculation purposes and the heat penetration calculated for a cell as a function of time based on the local surface temperature.

$$T - T_a = (1\text{-erf}(c) - (e^{(b + a2)}) (1 - \text{erf}(c + a)) (T_r - T_a) \qquad [6]$$

Where:
T = Temperature at point in wall (°K)
T_a = Ambient temperature (°K)
$a = h_r/k (\alpha \tau)^{0.5}$
$b = h_r x / k$
$c = x / 2(\alpha \tau)^{0.5}$
erf = error function
h_r = heat transfer coefficient (kW/m^2 °K)

MODELING RESULTS AND CONCLUSIONS

The pool fire evaluated was 355 m^2 in area and had a heat release rate of 798 MW. The calculations showed that the flame temperature at the centerline of the pool varied with height above the pool. The resulting change of temperature with height is shown in Figure 4. It was of interest to note that the maximum temperature occurred approximately 2 m to 3 m above the pool surface.

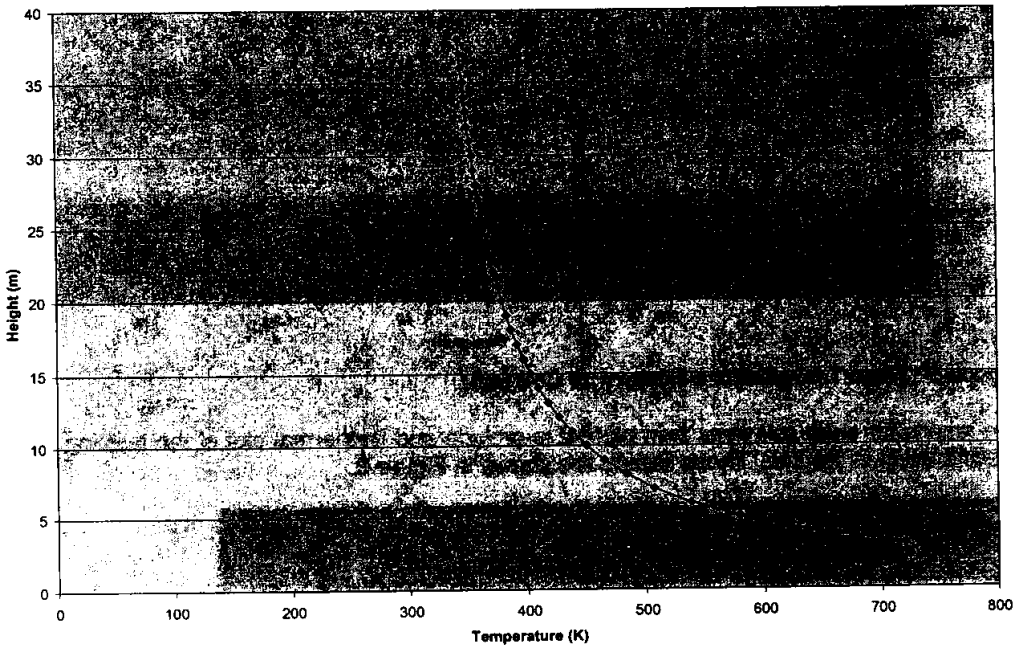

Figure 4 : Temperature Profile on Centerline of Fire

A review was made to establish the location on the building wall where thermal impact would be maximum. The location where the surface heating of the wall was maximum was found to be slightly above the pool and was consistent with flame temperature distribution above the pool. The maximum temperature was reached approximately 3 m above grade.

The model results were also reviewed to determine surface temperature history and penetration. The temperature history of the wall surface adjacent to the flaming region of the fire increased sharply in the first five to ten minutes of exposure and then heated more gradually after ten minutes. This trend can be seen in Figure 5 for Cell (4,1).

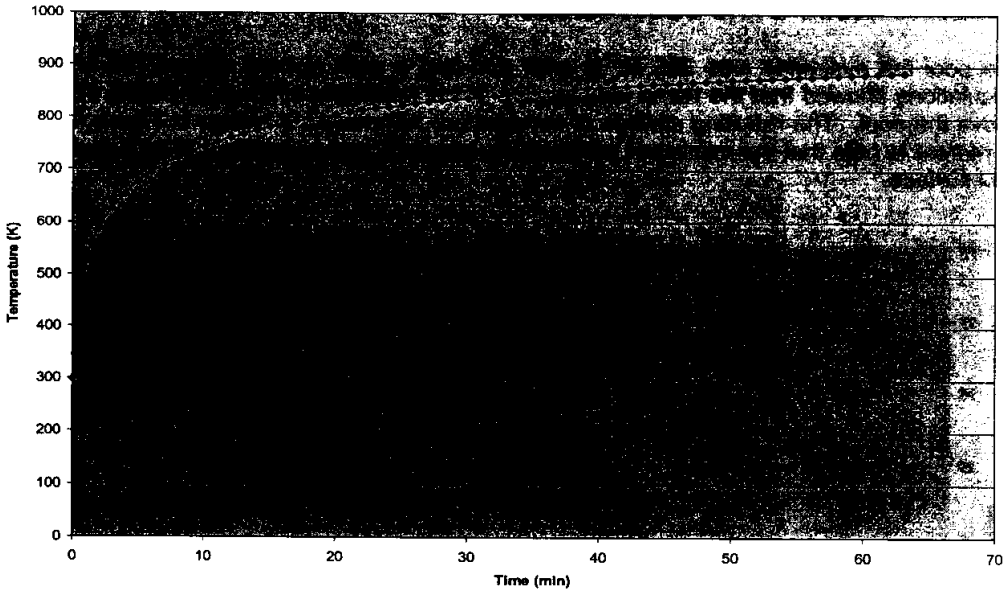

Figure 5 : Time Temperature History of Cell (4,1)

The results for each cell were then plotted to provide and isothermal plot of the building wall at specific times in the fire. These results are shown in Figure 6.

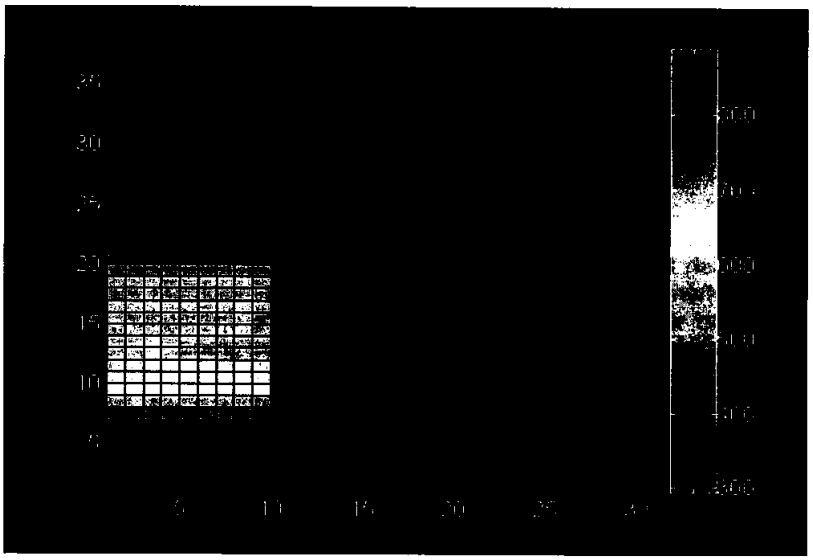

Figure 6 : Temperature Distribution at 60 Minutes – No Wind

A review of the temperature distribution accounting for wind effects is shown in Figure 7. Although the wind had the effect of heating a greater area of the building wall, the area of wall exposed to temperatures greater than 300 °C and 500 °C, was less than with no wind.

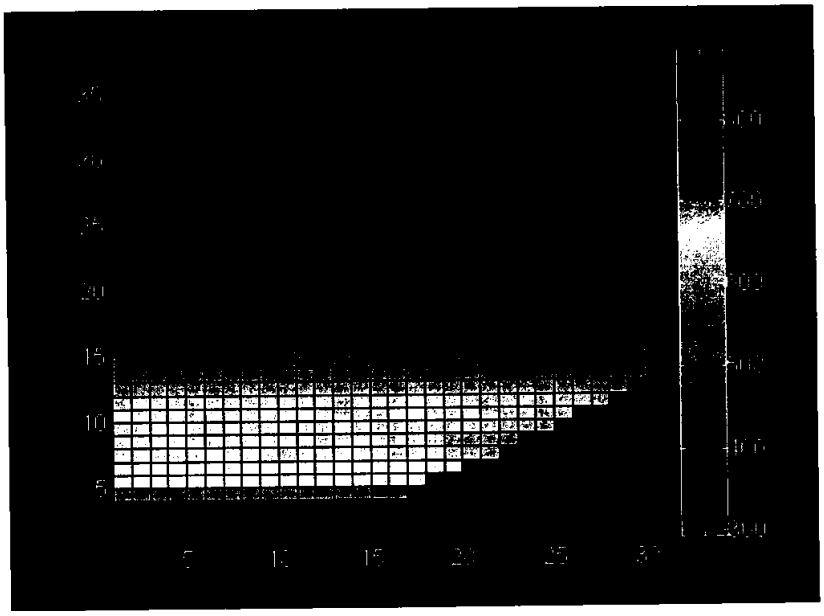

Figure 7 : Temperature Distribution at 60 Minutes - 4.17 m/s Wind

The temperature penetration into the Building wall as a function of time was also evaluated. The results of this calculation are shown in Figures 8 and 9, which presents the temperature profile in the wall at the point of maximum temperature at 10 minutes and 60 minutes respectively.

The figures show that after 10 minutes exposure there was no thermal impact 100 mm from the wall surface. After 60 minutes there was thermal penetration to nearly 200 mm. Although there was some increase in temperature nearly 200 mm into the wall a review was made to determine the depth of the concrete that would have been heated above 500 °C as this is the temperature where concrete will start to loose its compressive strength. A review of Figure 9 shows that less than 40 mm of the exterior portion of the wall was exposed to temperatures approaching this level after 60 minutes of exposure to the pool fire. Since reinforcing steel in wall is at a depth of approximately 50 mm, it was concluded to be unlikely that it would be impacted by heating.

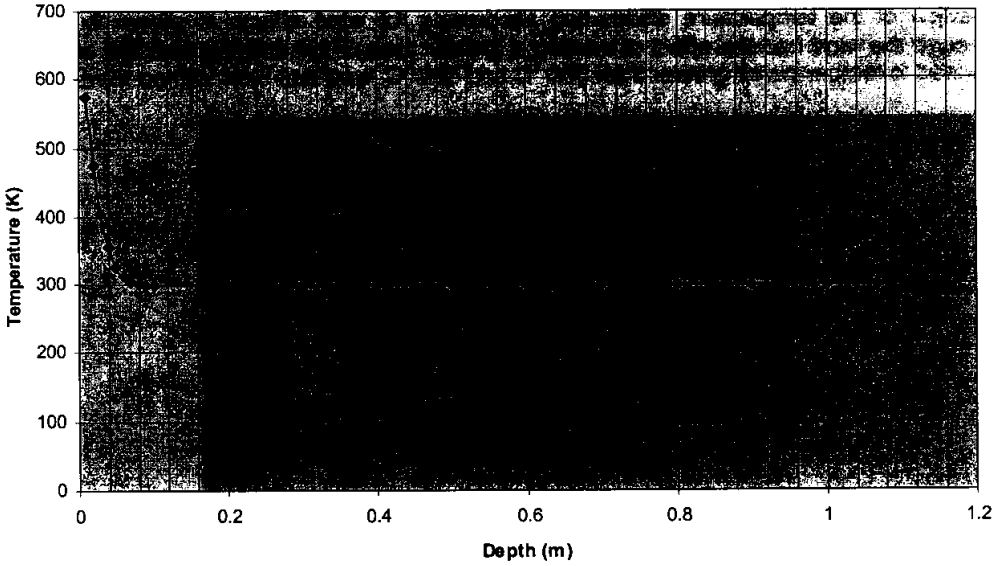

Figure 7-3 : Wall Temperature v. Depth at 10 Minutes

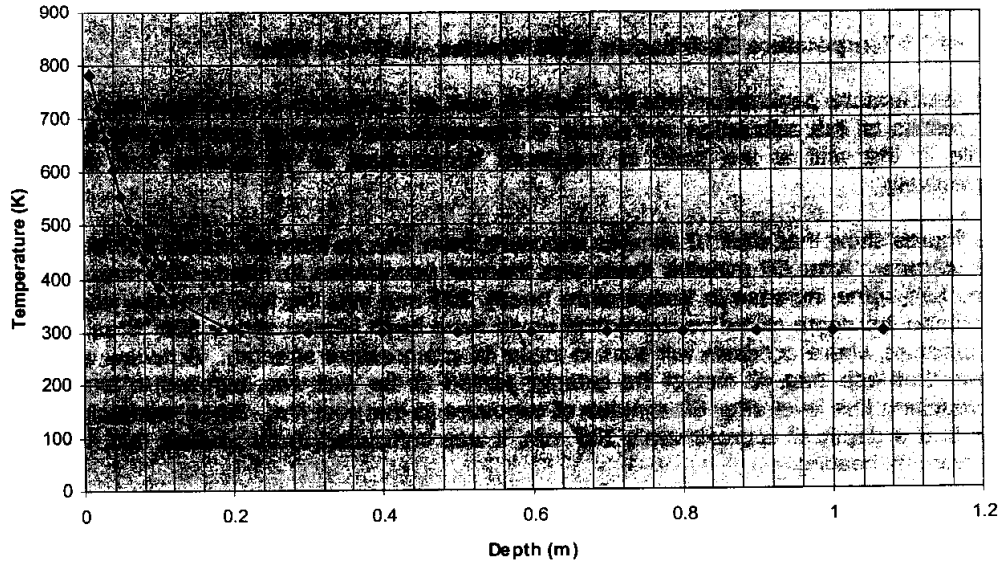

Figure 7-4 : Wall Temperature v. Depth at 60 Minutes

REFERENCES

1. Detichatsios, M.A., "Air Entrainment Into Buoyang Jet Flames and Pool Fires" SFPE Handbook of Fire Protection Engineering, 2nd Edition, Section 2, Chapter 3, pages 2, 20-31, 1995.

2. Schneider, M.E. and Kent, A., "Measurement of Gas Velocities and Temperatures in a Large Open Pool Fire", Fire Technology, 51-80 February 1989.

3. McCaffrey, B., "Flame Height" SFPE Handbook of Fire Protection Engineering, 2nd Edition, Section 2, Chapter 1, pages 2, 1-8, 1995.

4. Kartek Research, "Flame, Adiabatic Flame Temperature and Equilibrium Gas Composition", 62 Fourth Ave., Ottawa, 1991.

5. Mudan, K.S. and Croce, P.H., "Fire Hazard Calculations for Large Open Hydrocarbon Fires", SFPE Handbook of Fire Protection Engineering, 2nd Edition, Section 3, Chapter 11, pages 3, 197-240, 1995.

6. Tewarson, A, "Generation of Heat and Chemical Compounds in Fires", SFPE Handbook of Fire Protection Engineering, 2nd Edition, Section 3, Chapter 4, pages 3, 71-85, National Fire Protection Association, Queng, Mass, 1995.

7. Drysdale, D., "An Introduction to Fire Dynamics", John Wiley and Sons, Toronto, pages 122-145, 1985.

8. SFPE Task Group, "Assessing Flame Radiation to External Targets from Pool Fires", Society of Fire Protection Engineers, June 1999.

9. Heskestad, G., "Fire Plumes", SFPE Handbook of Fire Protection Engineering, 2nd Edition, Section 2, Chapter 2, pages 2, 9-19, 1995.

10. Bainbridge, B.L. and Keltner, N.R., "Heat Transfer to Large Objects in Large Pool Fires", Journal of Hazardous Materials 20, 21, 40, 1988.

11. Mudan, K.S. and Croce, P.A., "Fire Hazard Calculations for Large Open Hydrocarbon Fires", Handbook of Fire Protection Engineering, 2nd Edition, Section 3, Chapter 11, pages 3-197, 3-240.

12. Thomas, P.H., "The Size of Flames from Natural Fires", 9th International Combustion Symposium Inst., Pittsburgh, P.A., pp 844-859, 1963.

13. Welker, J.R. and Sliepcevich, C.M., "Wind Interaction Effects on Free Burning Fires" Tech Report #1441-3 to Office of Civil Defense of U.S. Bureau of Standards, 1967.

14. American Gas Association, "LNG Safety Research Program" Report IS 3-1, 1974.

15. Holman, J.P., "Heat Transfer" Fifth Edition, McGraw-Hill Book Company, 1981, page 394, 118.

16. Carslaw, H.S. and Jaeger, J.C., "Conduction of Heat in Solids", Second Edition, Oxford at the Clarendon Press, page 71.

PREDICTION OF THE THERMAL RESPONSE OF A METAL COLUMN EXPOSED TO A LOCALIZED FIRE

Daisuke Kamikawa
Graduate student, School of Science and Engineering, Waseda University, Okubo 3-4-1, Shinjuku-ku, Tokyo, 169-8555, Japan
Yuji Hasemi
Department of Architecture, Waseda University, Okubo 3-4-1, Shinjuku-ku, Tokyo, 169-8555, Japan
Takashi Wakamatsu
SW Fire Resistance Design Co, Yatabe 1073-15, Tukuba-shi, 305-0861, Japan
Koji Kagiya
National Institute for Land Infrastructure Management, Ministry of Land, Infrastructure and Transport, Tachihara 1, Tsukuba-City, Ibaraki, 302-0802, Japan

ABSTRACT

The purpose of this paper is to establish a predictive method for the temperature field of a metal column exposed to a localized fire using the Finite Elements Method.

In this report, we carried out the experiments on a steel column surrounded by fire sources to examine boundary conditions and analysis model used in FEM calculation. In the experiments, heat flux and temperature distributions along the column were measured. Then we calculated the temperature distributions of the column by FEM using the measured heat flux data. From the calculation, we speculated the convective heat transfer coefficient on the heated steel surface, thermal balance parameters, and so on. The temperature distributions along the steel column adjacent to the localized[1)] fire are calculated with speculated coefficient, and the method to calculate the temperature of member subjects exposed to a localize fire is established.

KEYWORDS:*Localized Fire, Steel Column, Heat Flux, Surface Temperature, FEM*

1. INTRODUCTION

To make a rational fire safety assessment of a column exposed to a localized fire, we have to "comprehend its heating property by assumed fire source", and "predict the thermal and dynamical response against it". About the heating property, heat flux and temperature

measurements were conducted on a square steel column adjacent to fire source[1]. The tests on the adjacent fires demonstrated a description of the heat flux profile along the column surface as a single function of the height normalized by flame height for each column-fire distance and notable decrease of surface heat flux by the increase of the column-source distance.

When we predict the thermal and dynamical response of member subjects exposed to a localized fire, we will be able to make fire safety assessments for various structural materials in various design conditions with few experiments, if we can predict the temperature field of the member by inputting these incident heat flux data into a numerical calculation model as a boundary condition. In this report, we use the Finite Elements Method. FEM is commonly used to calculate the thermal and dynamical response for common material like metal that properties at high temperature are comprehended. But, to predict the temperature field of the member by thermal calculation, we must consider some issues e.g. the determination of the convective heat transfer coefficient on the heated steel surface. On condition that a diffusion flame touches square column surface, it is difficult to solve these issues because of nonuniform distributions of heat flux and surface temperature.

In this research, measurements were conducted using a model scale facility on flame length, flame heat transfer, and temperature field of a steel column surrounded by fire sources (=surrounded condition). This configuration was chosen to represent the simplest heating property because heating properties of each column lateral are same. One of the purposes of experiments is to demonstrate the thermal response characteristics of a column exposed to a localized fire by comparing the experimental result in surrounded condition with that in adjacent condition, and another is to acquire foundational data to examine and determine the boundary conditions for the numerical calculation.

Secondly, we calculated the temperature distributions of the steel column assuming surrounded condition by FEM using the measured heat flux data. From the calculation, we speculated the convective heat transfer coefficient on the heated steel surface, thermal balance parameters, and so on. Then, the temperature distributions of the steel column in adjacent condition are calculated with speculated coefficient, and discuss the applicability of the numerical calculation.

2. CONCEPT FOR EXPERIMENTS AND CALCULATIONS

2.1 Dominant parameters on localized fire and effect of scale

The flame heating of the adjacent surface is thought to be controlled essentially by flame length L_f(m) along the member subject. And it is widely recognized that unconfined flame length L_f is controlled by positional relation between the member and fire source, and dimensionless heat release rate Q* defined as formula [1][2].

$$Q^* \equiv Q / \rho C_p T_0 g^{1/2} D^{5/2} \cdots [1]$$

Q : heat release rate [kW]
T_o : ambient temperature [K]
ρ : density of ambient air [kg/m^3]
g : gravitational acceleration(=9.8) [m/s^2]
C_p : specific heat of air [kJ/kgK]
D : characteristic fuel size [m]

The unconfined flame tips height is calculated from Q* using the semi-empirical formula[3]

$$L_f' = 3.5 Q^{*n} D \cdots [2]$$

(Q* ≥1.0 : n=2/5, Q*<1.0 : n=2/3)

Although the flame comes very close to the column surface, the similarity of flame height is thought to be consistent with this formula [2]. And the temperature distribution in flame is thought to be constant against the change of scale.

To estimate the flame heating property from experiments, we must comprehend not only the similarity of flame but the effect of scale on heat flux. The net incident heat flux on specimen surface is represented like this[4)]

$$q_{net} = h(T_{f0} - T_s) + \alpha_s(\phi_f q_r + (1-\phi_f)\sigma T_a^4) - \varepsilon_s \sigma T_s^4 \cdots [3]$$

α_s : absorptivity of specimen surface
α_g : absorptivity of heat flux gage surface
ϵ_s : emissivity of specimen surface
ϵ_g : emissivity of heat flux gage surface
ϕ_f :the configuration factor between flame and specimen
h : convective heat transfer coefficient [kW/m^{2}K]
T_a : temperature of ambient pericarp [K]
T_{f0} : temperature of air aruoud spesimen [K]
T_s : surface temperature of spesimen [K]
q_r : the flame radiant intensity [kW/m^2]
σ : Stefan-Boltzman constant (=5.67x10^{-11}) [kW/ m^{2}K^4]

Assuming that flame temperature T_f is uniform, the flame radiant intensity q_r is expressed as follows

$$q_r = \varepsilon_f \sigma T_f^4 = (1 - e^{-k\ell})\sigma T_f^4 \cdots [4]$$

ϵ_f :actual emissivity of the flame
ℓ :light path length.
k :absorption coefficient

The distribution of attenuation coefficient k is thought to be constant against the change of scale as long as fuel and combustion property are same, and the actual emissivity of the flame ϵ_f is affected by scale.

Therefore, if we apply the heat flux value measured in reduced scale experiments to real scale model, the heat flux for real scale (q_1) is expressed as follow

$$q_1 = \frac{(1 - e^{-k1\ell 1})}{(1 - e^{-k2\ell 2})} q_2 \cdots [5]$$

where subscript "1" represents "for real scale", "2" represents "for experimental scale".

2.2 Estimation of thermal balance parameters

Since heat flux gages are water-cooled type, measured heat flux value (q_g) is different from net incident heat flux (q_{net}). Assuming that the convective heat transfer coefficient differences between heat flux gage and specimen can be ignored, measured heat flux value (q_g) is expressed as

$$q_g = h(T_{f0} - T_g) + \alpha_g(\phi_f q_r + (1-\phi_f)\sigma T_a^4) - \varepsilon_g \sigma T_g^4 \cdots [6]$$

Additionally, assuming $\alpha_s=\alpha_g=\epsilon_s=\epsilon_g=1$ since $\alpha_s=\epsilon_s$, $\alpha_g=\epsilon_g$ (kirchhoff's law) and surface of the specimen and heat flux gages were covered by soot, the net incident heat flux (q_{net}) is represented as follow

$$q_{net} = q_g - h(T_s - T_g) - \sigma(T_s^4 - T_g^4) \cdots [7]$$

The second and third terms on right-hand side represent convective and radiative heat transfers from specimen (T_s [K]) to ambient atmosphere (T_g [K]). Thus, when we calculate the temperature field by inputting measured heat flux data, which includes difference caused by temperature differences between specimen and heat flux gages, temperature preset value of ambient atmosphere to calculate the convective and radiative heat transfers should be made into temperature of heat flux gages under the experiment.

3. FLAME HEATING PROPERTY OF A STEEL COLUMN SORROUNDED BY FIRE SOURCES

The heat flux and temperature measurements have been conducted on a square steel column adjacent to a fire source[1] as the commonest condition (**Figure 1**). In this research, we carried out experiments assuming a steel column surrounded by fire sources (**Figure 2**).

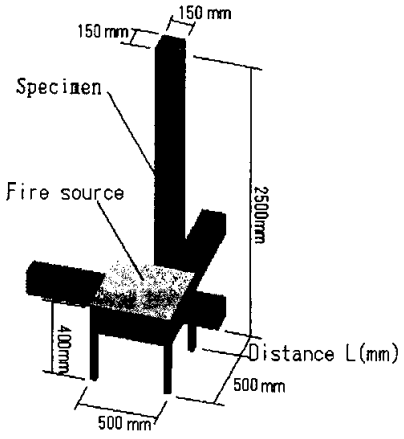

Figure 1 Experimental arrengement for Adjacent Fire Tests

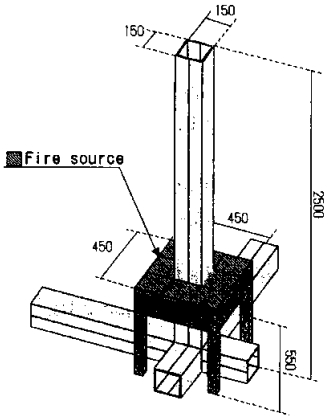

Figure 2 Experimental arrengement for Surrounding Fire Tests

3.1 General

Two 4.5mm thick, 2.50m tall and 0.15m square steel columns were prepared as the specimen; one with a line of holes for the installation of 15mm diameter Schmidt- Boelter heat flux gages(150kW/m^2 full range) and the another with 0.20mm diameter K-type thermocouples. The upper end of each column was semi-closed in order to prevent excessive pressure rise in the cavity of the column. Following previous flame heat transfer measurements on ceilings[5),6)], beams[7)] and walls[8),9)], we used the porous propane burners as fire source. Eight 0.15m square porous burners were placed around the 0.15m square column to make a 0.45m square burner-column complex, where a 0.50m square diffusion burner was used in adjusent condition.

Total heat release rate(nominal) was controlled within the range from 40.5 to 162 kW to reproduce the identical Q* with the adjacent fire configuration. **Table 1** is a summary of the experimental conditions. The reference flame height, L_f', was calculated by formula [2].

Table 1 Test Conditions (Surrounded condition)

Nominal Heat Release Rate (kW)	Q*(-)	Calculated Unconfined Flame Height, L_f'(m)	Measured Flame Height, L_f(m)
40.5	0.26	0.65	0.68
81	0.53	1.04	1.00
121.5	0.79	1.36	1.19
162	1.06	1.65	1.44

Temperature was monitored on all the external surfaces of the specimen and in the cavity after the surface temperature of the specimen had reached nearly the steady state. Incident heat flux was measured at the interval of 2 seconds for 2minutes for each heat release rate Q, and we report its average. Flame was recorded with digital video, and the average of visible flame tips height for one minute sampled at the interval of 1 second will be reported. The heat flux and the temperature measurements were conducted independently to avoid intervention between the two measurements.

These experiments do not intend to simulate any specific building nor burning object, but the sectional dimension of the specimen is around 1/3 of that of common steel component. Assuming the scaling by 1/3, according to the Froude modeling, heat release rate in these experiments is believed to correspond to a fire source of the heat release rate 15.6($3^{5/2}$) times larger than the test condition.

3.2 Experimental result

The measured heat flux data summarized against the normalized height (z/L_f) is shown in **Figure 3**. **Table 2** shows its digital data. The maximum heat flux appears within the rage of z/L_f=0~0.25 for each HRR, and each maximum value is around 45kW/m^2. The heat flux is notably weaker than for the adjacent fire configuration. This is thought to be caused by decrease of flame thickness i.e.light path length. Where there is a marked decrease of heat flux downward toward the column base in the adjusent fire configuration, there is no such decrease in the surrounding fire configuration because of the lack of air-cooling of the column by entrainment.

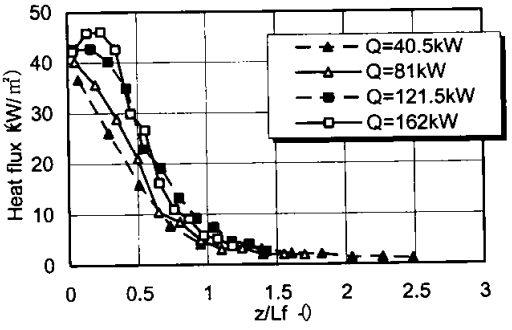

Figure 3 Heat flux distribution (surrounding fire)

Table 3 Heat flux (surrounding fire)

HRR Q(kW)		40.5	81	121.5	162
Q*(-)		0.27	0.53	0.80	1.06
Heat Flux [kW/m²]	z=0.05(m)	36.70	40.23	42.75	42.22
	0.2	26.16	35.65	42.74	45.97
	0.35	15.87	28.80	40.23	46.13
	0.5	7.72	20.90	34.90	42.63
	0.65	4.04	10.44	22.96	29.89
	0.8	3.89	8.44	19.11	26.72
	0.95	3.09	4.86	13.24	16.14
	1.1	2.17	2.99	9.22	10.89
	1.25	2.09	3.23	7.44	9.10
	1.4	1.35	2.01	4.60	5.77
	1.55	1.32	2.02	4.05	5.11
	1.7	1.14	1.83	2.64	3.68

z: Height from surface of fire source

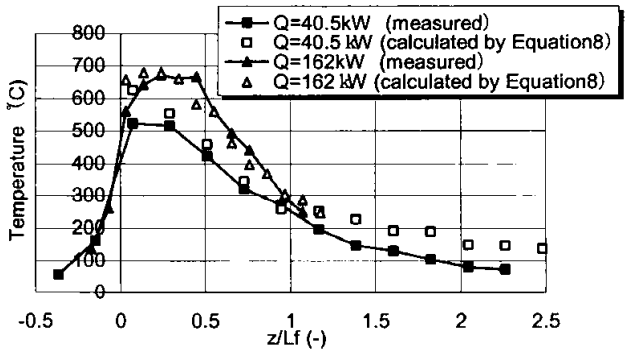

Figure 4 Temerature distribution (surrounding fire)

Vertical temperature distributions for Q=40.5kW and Q=162kW are summarized against z/L_f in **Figure 4**. The temperatures calculated from the measured heat flux assuming one-dimensional thermal conduction. The estimate of surface temperature assuming uniform heating can be calculated from

$$q = \varepsilon\sigma T_s^4 - 273.16 \cdots [8]$$

The emissivity of the column surface, ϵ, was assumed to be unity. The surface temperature of the column is generally close to the calculation using the heat flux data assuming steady uniform heating. This indicates that the high conductivity of steel no longer contributes to the relaxation of the heating of the column in the surrounding fire configuration.

4. THE CALCULATION OF THE THERMAL RESPONSE BY FEM

4.1 General of the analysis model and assumptions

The FEM code "ANSYS version 6.0" was used for calculations. In the surrounded condition, heat flux distributions on each lateral surface, which should be fed as surface load boundaries, are same. But two-dimensional calculation is not enough to describe radiative heat transfers in the cavity of the column. Therefore, we carried out the three-dimensional calculations for steady-state.

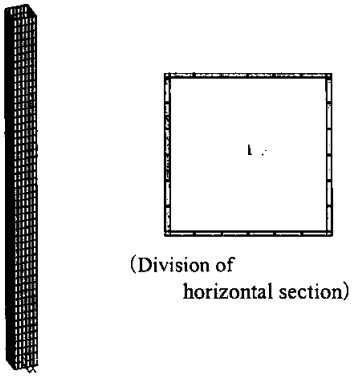

Figure 5 Computational mesh

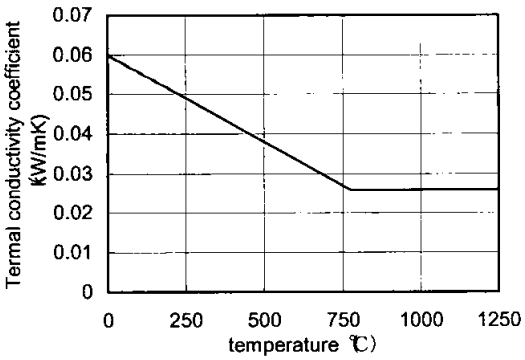

Figure 6 Temperature dependence of thermal conductivity coefficient

First, we assumed the surrounded condition. The finite element model is shown in **Figure 5**. The column model is a square steel column (150×150×4.5, h=2500(mm)), and is divided into 50 elements in the member axial direction. Since the thermal conductivity of steel is high and thickness is thin sufficiently, we divided horizontal section into 28 elements without dividing in through-thickness direction. An element that constitutes the member model has 8 nodes, and has three-dimensional heat conduction faculty. Each node has single-degree-of-freedom (temperature). We configured temperature dependence of thermal conductivity coefficient of these elements as shown in **Figure 6**[11]. We did not configured specific heat and density because these are calculations for steady-state.

Boundary to calculate convective heat transfers was configured at the external surfaces. The radiative matrix elements (matrix50) to calculate radiative heat transfers were configured at each surface. Measured heat flux distributions were configured as surface load boundaries at the external surface above the fire source surface. At the areas covered by lateral surface of burners, we configured heat flux from burner side as surface load boundaries. According to the consideration in paragraph 2, temperature preset value of ambient atmosphere for boundaries of convective and radiative heat transfer were made into temperature of heat flux gages ; 26°C.

These configurations were made upon below assumptions.

- The heat flux values between measure points are compensated according to gradient of heat flux value between these points (**Figure 7**).
- The heat flux distributions at each lateral surface are uniform in horizontal direction.
- The emissivity at heated areas is made into 1 because surfaces of these areas were covered by soot. At the other areas, the emissivity is made into 0.79 which is standard value of plain steel plate[12].
- The convective heat transfer in the cavity of the column is ignored since vertical temperature distribution of specimen and that of the air inside cavity were almost same.

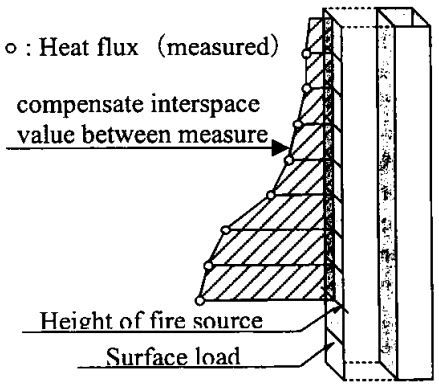

Figure 7 Configuration for sruface load using measured heat flux

4.3 Speculation of convective heat transfer coefficient

The convective heat transfer coefficient depends on temperature, components, and flow velocity of the ambient fluid and its value is not clear in condition including the flame-solid contact like above experiments. Therefore, we speculate it through comparison of the calculation and the measurement in the surrounded condition.

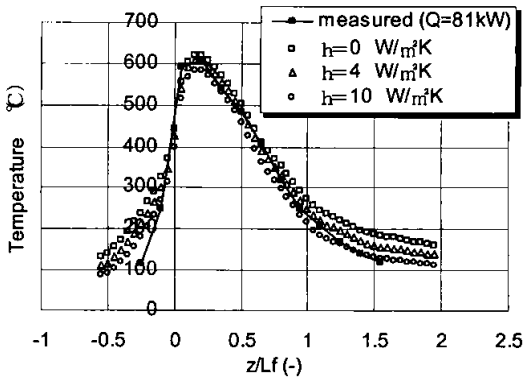

Figure 8 Relationship between calculated temperature and preset values of h (surrounding fire Q=81kW)

Figure 8 shows calculated temperature distributions at some preset values of h and measured temperature distribution for Q=81kW. The maximum temperature value is thought to be the most significant for fire safety design. In the case of h=0.004kW/m^2, the calculated maximum temperature corresponds with experimental one. Similar consideration has been made for the beam too^^, and the speculated value for the beam is h=0.01kW/m^2.

As shown in these **Figure 8**, the difference between calculated temperature and experimental one enlarges as the point comes close to column end. This difference is thought to be caused by the heat loss toward testing site floor and distribution of convective heat transfer coefficient which depends on temperature, components, and flow velocity of the ambient fluid. The convective heat transfer coefficient value speculated here is appropriate around the height where maximum temperature appears. To predict the temperature distribution more exactly, we must comprehend the distribution of convective heat transfer coefficient.

5. THE CALCULATION ASSUMING THE ADJUCENT CONDITION

Figures 9 demonstrates experimental temperature distributions and calculated one with speculated h (=0.004kW/m^2) for each HRR in surrounded condition. Each calculated maximum temperature value corresponds approximately with experimental one. The difference of maximum temperature value between experimental one and calculated one is less than 5%. Regarding whole temperature distribution, the difference is large at around z/L_f=0.5 and column end, and it is up to around 20%. Regarding the height where maximum temperature appears, the calculated one drop to a lower value than experimental one as HRR increases. Therefore, calculated temperature is lower than experimental one in the range of 0.3 <(z/L_f)<1.

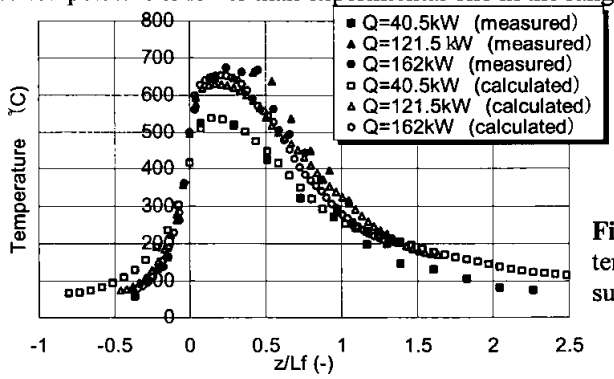

Figure 9 Measured and calculated temperature distribution for surrounding fire configuration

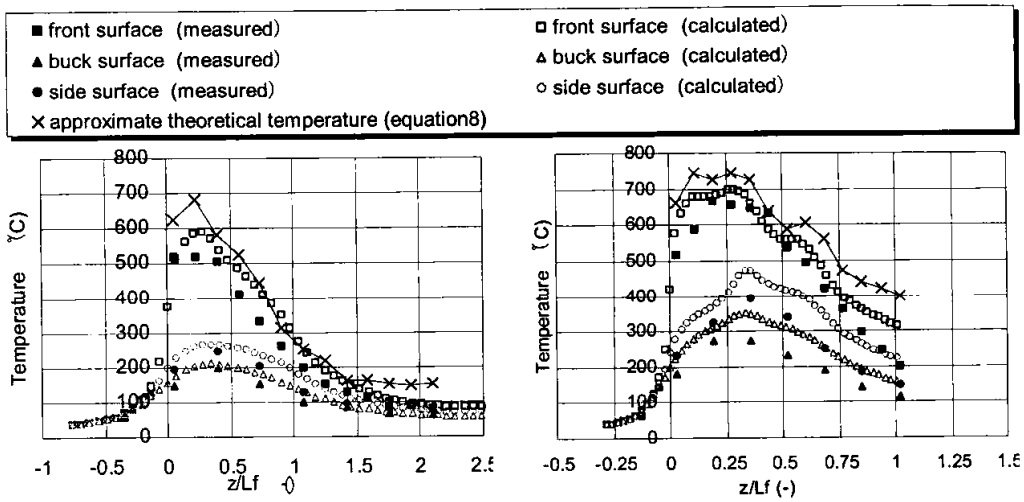

Figure 10
Measured and calculated temperature distribution for adjusent fire configuration (Q=52kW)

Figure 11
Measured and calculated temperature distribution for adjusent fire configuration (Q=255kW)

The experimental temperature distributions and calculated one with speculated h for Q=52kW and 255kW in adjacent condition are shown in **Figures 10, 11**. The theoretical temperatures calculated using the measured heat flux by equation**[3]** assuming steady uniform heating are also demonstrated in both Figures. Regarding the maximum temperature value, calculated one is higher than experimental one, and these difference is 10% for Q=52kW, 3% for Q=155kW. In all parts of the column, calculated temperature is higher than experimental one. The difference is around 15% within the high temperature rage. The assumption of "heat flux uniformity in horizontal direction" may cause these differences.

6. CONCLUSION

• The configuration to calculate the temperature field by inputting measured heat flux data was demonstrated. The temperature preset value of ambient atmosphere to calculate the convective and radiative heat transfers should be made into temperature of heat flux gages under the experiment.

•Regarding the column surrounded by or adjacent to fire source, the temperature distributions calculated by FEM with h=0.004kW/m^2 were found to be in a good agreement with the experimental result.

7. FUTURE WORK

As shown in above study, the prediction of thermal response of a square steel column exposed to a localized fire was enabled. In addition to this, if we can predict the dynamical response using above result, the fire safety assessment based on assumption of localised fire will be enabled.

Regarding the prediction of dynamical response, the characteristics owing to local heating are :

1. Since its heating is weak, even response at the steady-state temperature may fulfill the demanded capability. However, in the most case, the deformation histories will be required to verify the failure time.
2. There is large temperature gradient within the small range. Therefore, the affection of irregular deformation and strength distribution caused by temperature gradient must be considered carefully.

The calculation of structural response will be done by FEM. The computational analyze is common with the fire safety assessment. But, as mentioned above, we must consider the issues caused by temperature gradient which is not seen in usual fire safety assessment based upon uniform heating. There are few previous studies that deal with fire resistance experiments with member exposed to a localized fire.

Therefore, we are planning fire resistance experiments with square steel column exposed to a localized fire.

REFERENCES

1) Kamikawa,D., Hasemi,Y., Kagiya,K., Wakamatsu,T.: Experimental Flame Heat Transfer and Surface Temperature Correlations for A Steel Column Exposed To A Localized Fire, Proceedings of Interflam pp.443-450, 2001.
2) Cetegen.B.,Zukoski,E,E.,Kubota,T.:Entrainment and Flame Geometry of Fire Plumes,NBS-GCR-82-402, 1982
3) Hasemi,Y.,Tokunaga,T. : Flame Geometry Effects on the Plumes from Turbulent Diffusion Flames, Fire Science and Technology, Vol.4, 1984.
4) Wakamatu, T., Hasemi, Y., Yokobayasi, Y., A.V.Pchelintsev :Experimental Study on the Heating Mechanism of Steel Beam Exposed to a Localized Fier, Proceedings of Interflam '96 the Seventh Fire Science and Engineering Conference, Cambridge, pp.509-518, 1996
5) Kokkala.M.A.: Experimental Study of Heat Transfer to Ceiling from an Impinging Diffusion Flame, FIRE SAFETY SCIENCE-Proceedings of the third International Symposium, pp.261-270,1991
6) Wakamatu, T., Hasemi, Y., Yokobayasi, Y., A.V.Pchelintsev :Heating Mechanism of Building Components Exposed to a Localized Fire, Proceedings of Offshore Mechanics and Arctic Engineering '97 Yokohama, 1997
7) Hasemi.Y.: Thermal Modeling of Upward Wall Flame Spread, FIRE SAFETY SCIENCE-Proceedings of the First International Symposium, pp.87-96, 1985
8) Back.G.,Beyler.C., Dinenno.P. and Tatem.P.:Wall Incident Heat Flux Distributions Resulting from an Adjacent Fire, FIRE SAFETY SCIENCE-Proceedings of the 4th International Symposium, pp.241-252, 1994
9) Edited by Japan Institute of Construction Engineering, published by The Bulding Center of Japan : Comprehensive Fire Safety Design Method for Buildings vol.4 pp.117-151, 1988. (in Japanese)
10) Hagi, S., Murakami, S. published by Tokai University Press: Tundamentals and Practice for Convective Heat Transfer, pp.73, 1991

HEAT EXPOSURE MEASUREMENTS IN FIRE RESISTANCE WALL AND FLOOR TEST FURNACES

Mohamed A. Sultan and Noureddine Benichou
Institute for Research in Construction
National Research Council of Canada
Ottawa, Ontario, Canada K1A-0R6
mohamed.sultan@nrc-cnrc-gc.ca
noureddine.benichou@nrc-cnrc.gc.ca

ABSTRACT

This paper presents the results of 12 heat exposure tests: 6 in standard, full-scale wall and floor furnaces, and 6 in non-standard, intermediate-scale wall and floor furnaces. These tests were conducted to investigate the effect of full-scale furnace depth (wall and floor furnaces), furnace size (full-scale and intermediate-scale furnaces) and furnace orientation (intermediate-scale wall and floor furnaces) on the heat exposure.

The results showed that, the difference in heat exposure in full-scale floor and wall as well as in the intermediate-scale floor and wall furnaces is 5% and 4%, respectively. However, the heat exposure in an intermediate-scale wall and floor furnace is higher than in full-scale wall and floor furnaces by 18% and 15%, respectively.

KEYWORDS: *fire resistance, furnace, wall, floor, full-scale, intermediate-scale, heat exposure*

INTRODUCTION

Fire-rated floor and wall building systems formed with new materials and designs have been increasingly used in residential and non-residential buildings. To determine the fire resistance performance of these systems, full-scale tests are required. However, these tests are expensive and time consuming and there is a need by building designers and architects, at least in the initial design stage, to find an alternative solution. To satisfy this need, the National Research Council of Canada (NRC) has been developing simpler and less expensive tests and models to assess the fire resistance of building systems such as walls and floors. Along with these efforts, NRC has completed the construction of an intermediate-scale furnace, 1.2 m wide by 1.8 m long by 0.5 m deep, that can be used for testing loaded and unloaded wall and floor systems. However, to ensure that the intermediate-scale furnace can be used to reflect full-scale test results, it must be characterized in relation to a full-scale furnace. Heat exposure in fire resistance test furnaces is one of the critical parameters in determining the fire resistance

performance of building systems. A number of investigations of fire exposure in standard fire resistance test furnaces were carried out by Sultan et al[1] and by Cooke[2]. To characterize the heat exposure for an intermediate-scale furnace in relation to a full-scale furnace, a number of parameters need to be investigated such as the effect of full-scale furnace depth (wall and floor), furnace size (full-scale and intermediate-scale) and intermediate-scale furnace orientation (vertical or horizontal) on the heat exposure. This paper presents the results of heat exposure conducted at the NRC on 6 full-scale and 6 intermediate-scale specimens to investigate the heat exposure in an intermediate-scale and full-scale furnaces.

Comparisons of heat exposure in a full-scale and intermediate-scale fire resistance test furnace were conducted to address the effect of furnace size on the heat exposure to wall and floor surfaces. In addition, comparisons of heat exposure in full-scale and intermediate-scale for both wall and floor furnaces were conducted to address the effect of furnace depth and orientation on heat exposure. The results reported in this paper can also be used as data for the development of fire resistance models for floor and wall assemblies.

EXPERIMENTAL WORK

This experimental study was carried out at the National Research Council of Canada using full- and intermediate-scale wall and floor fire resistance furnaces. Heat exposure experiments include: 3 repeat tests using the full-scale floor furnace, 3 repeat tests using the full-scale wall furnace, 3 repeat tests using the intermediate-scale floor furnace and 3 repeat tests using the intermediate-scale wall furnace. The duration of each test was two hours and measurements were recorded every minute.

The descriptions of the heat flux sensors used to measure the fire exposure in furnaces are given below.

Heat Flux Sensor

Heat exposure to the test specimen was measured by two water-cooled Gardon Gauge heat flux sensors (see Figure 1) in the intermediate-scale furnace and by 5 water-cooled Gardon Gauge heat flux sensors in the full-scale wall and floor furnaces. These gauges are 2.5 mm diameter and 2.5 mm long copper cylinder and has a stated accuracy of 63%. The water flow temperature was maintained during the entire test within the temperature range specified by the manufacturer for the sensors.

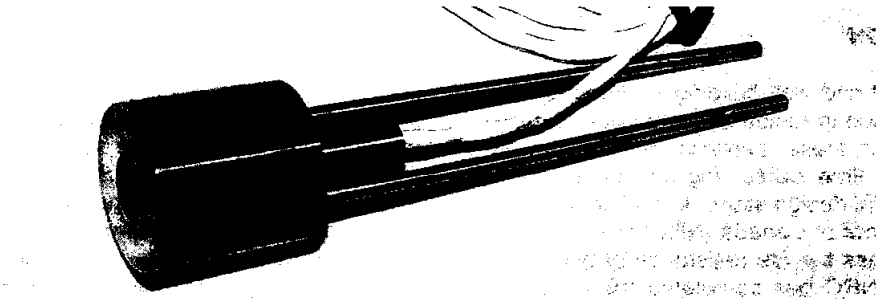

Figure 1 : Water Cooled Gardon Gauge Heat Flux Sensor

Standard Full-scale Wall and Floor Test Furnaces

Full-scale fire resistance floor furnace is approximately 4 m wide by 5 m long by 3 m deep (see Figure 2) and the wall furnace is 3.6 m wide by 3 m high by 0.5 m deep (see Figure 3). In both furnaces, the walls were made of insulated fire-brick. Thermal properties of the brick and test specimens are given in Table 1.

Tests were carried out by exposing castable refractory specimens to heat using the propane-fired horizontal and vertical furnaces. The specimens were instrumented with 2 heat flux meters in the intermediate-scale wall and floor furnaces and 5 heat flux meters in the full-scale wall and floor furnaces. These meters were installed flush to the specimen surface to measure the heat exposure in the furnaces. Each specimen was sealed at the edges against the furnace using ceramic fibre blankets. The furnace temperature was measured by 9 (20 gauge) shielded thermocouples in accordance with CAN/ULC-S101-M89[3]. The average of the 9-thermocouple temperatures was used to control the furnace. These thermocouples were located 0.3 m below the fire-exposed surface of the sample, following, as closely as possible, the CAN/ULC-S101-M89 standard time-temperature curve. This curve is similar to the ASTM E119[4] time-temperature curve.

Non-standard Intermediate-scale Wall and Floor Test Furnaces

Intermediate-scale fire resistance floor furnace is approximately 1.2 m wide by 1.8 m long by 0.5 m deep as shown in Figure 4. The furnace walls were also made of insulated fire-brick as in full-scale furnaces. The intermediate-scale furnace can be oriented vertically to become a wall furnace or oriented horizontally to become a floor furnace.

Wall and floor heat exposure tests were carried out by exposing the castable refractory specimens to heat using the propane-fired vertical or horizontal intermediate-scale furnace. The specimen was sealed at the edges against the furnace using ceramic fibre blankets. The furnace temperature was measured by 3 (20 gauge) shielded thermocouples in accordance with CAN/ULC-S101-M89. The average of the 3 thermocouple temperatures was used to control the furnace. These thermocouples were located 0.3 m below the exposed surface of the sample, following, as closely as possible, the CAN/ULC-S101-M89 standard time-temperature curve.

Full-scale Test Specimen

Test specimen used in floor furnace was a castable refractory slab, marketed as KS-4, composed of 20 rectangular slabs, 0.8 m wide by 1.2 m long by 0.15 m thick, suspended on a steel beam. The slabs were tightly butted with ceramic sheet along their perimeters to form a 4 m by 5 m unite. The properties of these slabs are given in Table 1. Five heat flux meters were installed flush with the specimen surface: one at the centre of the furnace and one at the centre of each quarter section of the furnace to measure the receiving heat exposure to the specimen surface.

Full-scale wall furnace test specimen, composed of five so-called measuring specimens, blocks of KS-4 castable refractory brick, 600 mm square by 150 mm thick, were inserted in the simulated block brick wall, one at its centre and four at the centres of its quarter sections as shown in Figure 5. One water-cooled Gardon Gauge heat flux sensor was installed flush with

the specimen surface in the centre of each measuring specimen. The location of these sensors is also shown in Figure 5.

Intermediate-scale Test Specimen

In intermediate-scale floor furnace, the test specimen was also a castable refractory slab the same as those used in the full-scale specimen and composed of one rectangular slab 0.8 m wide by 1.2 m long by 0.15 m thick. It was mounted in the centre of a concrete frame 1.2 m wide by 1.8 m long around the specimen.

Table 1 Thermal Properties of Furnace Lining and Specimen Materials

	Furnace Lining Material Fire-brick	Specimen Material Castable Refractory Slab
Thermal Conductivity ($W\ m^{-1}K^{-1}$)	1.15	0.9
Specific Heat ($J\ kg^{-1}\ K^{-1}$)	900	1000
Density ($kg\ m^{-3}$)	2600	2085

Figure 2 NRC Full-scale Floor Furnace

Figure 3 NRC Full-scale Wall Furnace

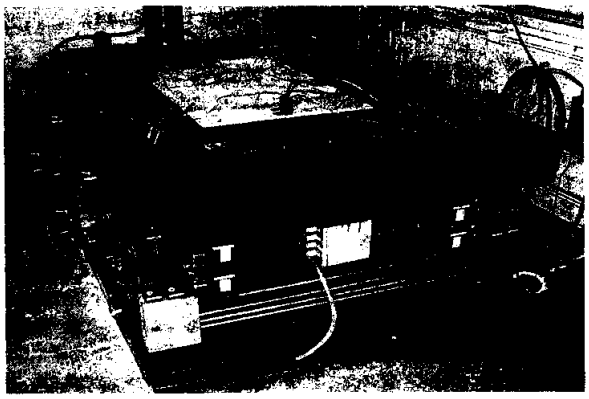

Figure 4 NRC Intermediate-scale wall and floor Furnace

Figure 5 Full-scale Wall Furnace Test Specime

RESULTS AND DISCUSSION

The effects of furnace depth (full-scale wall and floor furnaces), furnace size (full-scale and intermediate-scale and intermediate-scale orientation on the heat exposure in fire resistance test furnaces are given below.

Effect of furnace depth (full-scale wall and floor furnaces)

Results of average of heat exposure for the 3 tests using the full-scale floor furnace and the other average of 3 tests using the full-scale wall furnace are presented in Figures 6 and 7, respectively. The heat exposure increases with the increase in furnace temperature and it follows a similar trend as the furnace temperature. A comparison of the heat exposure in full-scale wall and floor furnaces of different depths is shown in Figure 10. Heat exposure in a full-scale floor furnace with a larger depth (3 m) is slightly higher (5%) than in a wall furnace with a smaller depth (0.5 m). This slight increase in heat exposure in the case of a floor furnace could be caused by the presence of a thicker hot layer gas facing the specimen fire exposed surface. This increase in heat exposure is considered insignificant.

Effect of Furnace Size (full-scale vs intermediate-scale for wall and floor furnaces)

Average heat exposure results for full-scale floor and wall furnace are shown in Figures 6 and 7, respectively. The average heat exposure results for the intermediate-scale floor and wall furnace are shown in Figures 8 and 9, respectively. Comparisons of the average heat exposure in full- and intermediate-scale floor and wall furnaces are shown in Figures 12 and 13, respectively. The results in Figure 12 indicate that, when either the full-scale or the intermediate-scale fire resistance floor furnace is heated up using the CAN/ULC-S101-89 or ASTM E119 time-temperature curve, the heat exposure in the intermediate-scale floor furnace is approximately 15% higher than in the full-scale floor furnace. Similarly, the results in Figure 13 indicate that, when either the full-scale or the intermediate-scale fire resistance wall furnace is heated up using the CAN/ULC-S101-89 or ASTM E119 time-temperature curve, the heat exposure in the intermediate-scale wall furnace is approximately 18% higher than in the full-scale wall furnace. These results suggest that the effect of furnace size on heat exposure is somewhat significant. Generally, the heat received by a test specimen in a fire resistance test furnaces is by radiation and convection. The radiative part is much greater than the convective part. In the full-scale furnaces, convective heat occurs by natural convection while, in the smaller size furnaces, it occurs by forced convection. Heat transfer by forced convection is greater than by natural convection. As the furnace size increases, the convective heat to the specimen decreases and this may explain why the heat exposure in an intermediate-scale furnace is higher than in a full-scale furnace. For a fire exposure parameter, testing an assembly in an intermediate-scale furnace will provide a conservative performance compared to a full-scale furnace.

Effect of Furnace Orientation (Vertical vs Horizontal)

The average heat exposure results for the furnace in the horizontal position and in the vertical position are shown in Figures 8 and 9, respectively. A comparison of the average heat exposure to a test specimen for the furnace in the horizontal and in the vertical position is shown in Figure 11. The results showed that, when an intermediate-scale fire resistance furnace (1.2 m wide by 1.8 m long by 0.5 m deep) is heated up using the CAN/ULC-S101-89 or

ASTM E119 time-temperature curve, the heat exposure to a test specimen in a floor furnace oriented horizontally is slightly higher (4%) than in a wall furnace oriented vertically. A similar comparison is shown in Figure 10 for a full-scale floor furnace and a wall furnace. The difference in heat exposure is considered to be insignificant.

CONCLUSIONS

This paper discussed the effect of furnace depth (full-scale), furnace size (full-scale vs. intermediate-scale) and furnace orientation (intermediate-scale) on the heat exposure in fire resistance test furnaces. Based on the results mentioned above, the following key trends can be highlighted:

1. The effect of full-scale furnace depth on the heat exposure is insignificant.
2. The heat exposure in either intermediate-scale wall or floor furnace, 1.2 wide by 1.8 m long by 0.5 m deep, is 15% and 18% higher than in the full-scale wall or floor furnace, respectively.
3. For the intermediate-scale furnace, 1.2 m wide by 1.8 long by 0.5 m deep, the effect of furnace orientation, whether vertical (wall) or horizontal (floor), on the heat exposure to the test specimen is insignificant.

ACKNOWLEDGEMENTS

The authors wish to thank Jocelyn Henrie, Yves Seguin, Roch Monette and Patrice Leroux for their help in conducting the experimental work.

REFERENCES

1. Sultan, M.A., Harmathy, T.Z. and Mehaffey, J.R., "Heat Transmission in Fire Test Furnaces", Fire and Materials, Vol. 10, No. 2, 1986.
2. Cooke, G.M.E, "Can Harmonization of Fire Resistance Furnaces be Achieved by Plate Thermometers Control?", Proceedings, 4th IAFSS, Ottawa, Canada, 1994.
3. CAN/ULS-S101-M89, "Standard Methods of Fire Endurance Tests of Building Construction and Materials", ULC, Scarborough, Ontario, Canada, 1989.
4. ASTM E119-88, "Standard Methods of Fire Tests of Building Constructions and Materials", ASTM, Philadelphia, PA, 1995.

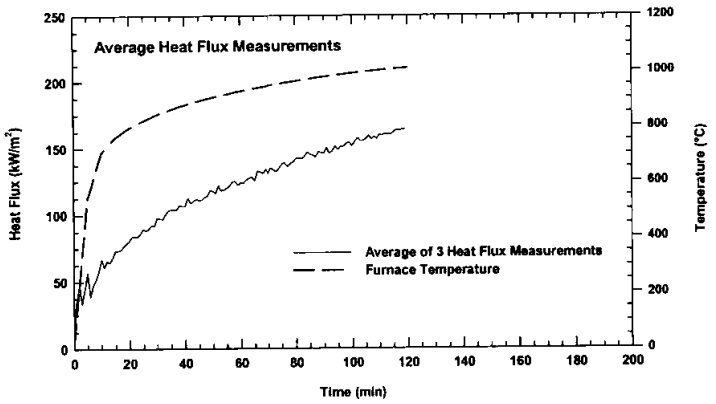

Figure 6 Heat Exposure in Full-scale Floor Furnace

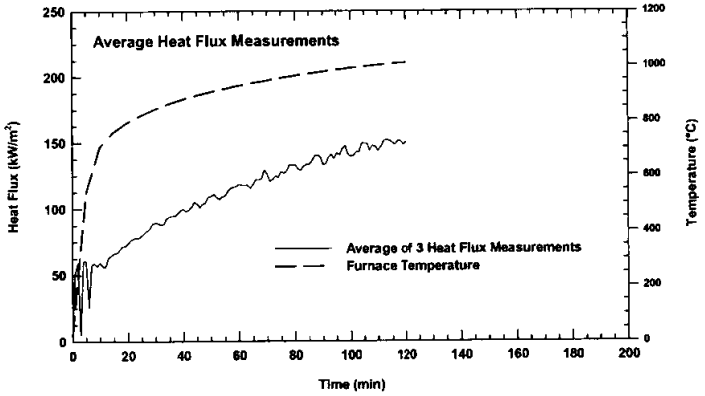

Figure 7 Heat Exposure in Full-scale wall Furnace

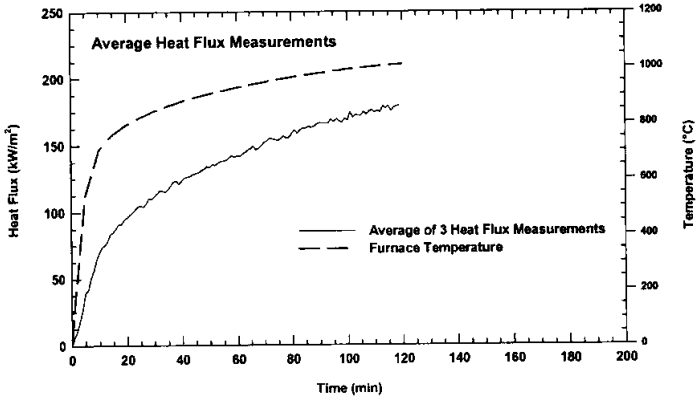

Figure 8 Heat Exposure in Intermediate-scale Floor Furnace

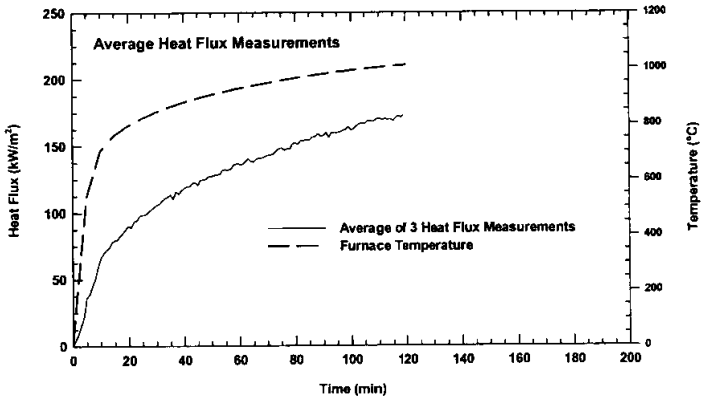

Figure 9 Heat Exposure in Intermediate-scale Wall Furnace

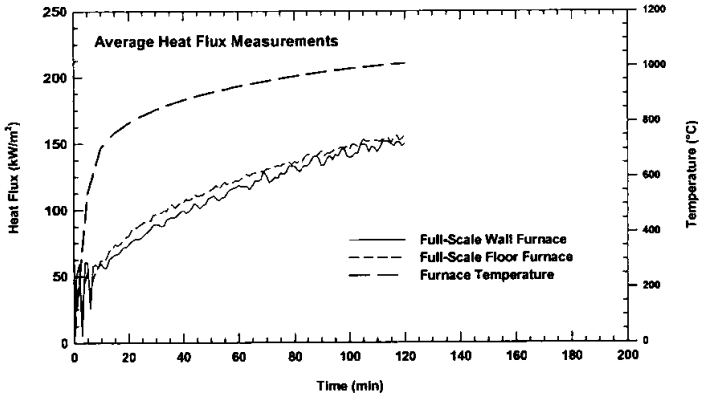

Figure 10 Comparison of Heat Exposure in Full-scale Furnaces (Floor Furnace vs Wall Furnace)

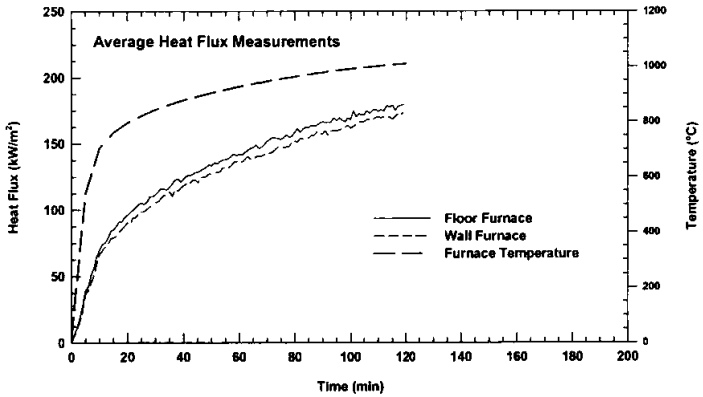

Figure 11 Comparison of Heat Exposure in Intermediate-scale Furnaces (Floor Furnace vs Wall Furnace)

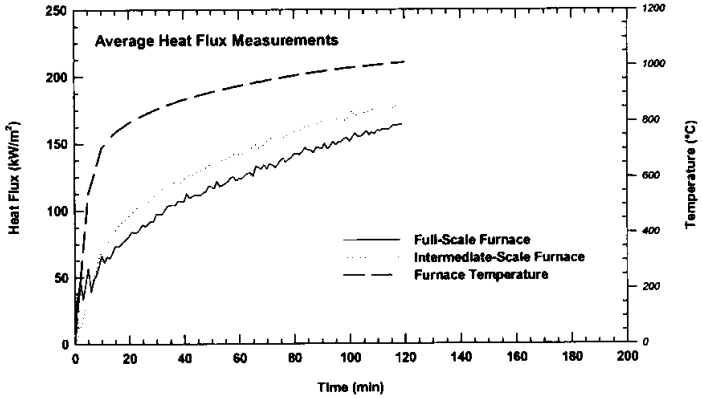

Figure 12 Comparison of Heat Exposure in Floor Furnaces (Full-scale vs Intermediate-scale)

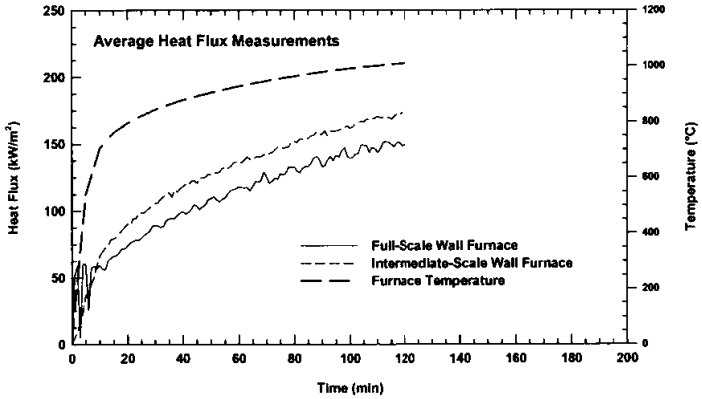

Figure 13 Comparison of Heat Exposure in Wall Furnaces (Full-scale vs Intermediate-scale)

HEAT AND MASS TRANSFER THROUGH GYPSUM PARTITIONS SUBJECTED TO FIRE EXPOSURES

Scott Kukuck and Kuldeep Prasad
Building and Fire Research Laboratory
National Institute of Standards and Technology
Gaithersburg, MD 20899-8663

ABSTRACT

The adoption of performance-based building codes for fire resistance is becoming widespread, and is expected to have a substantial impact on building design and cost as the concept evolves.. Using accepted performance methods, designs can improve safety while reducing costs. This is achieved by eliminating components that do not contribute to safety and are overly restrictive, components that were necessary under the older, prescriptive building codes. To realize these benefits, however, accurate models must exist that predict the response of building designs to fire exposures. A program has been started to improve the state of the art for structural fire modeling. The initial focus is on the most common means of reducing fire spread, i.e. the compartmentalization of a structure via gypsum wallboard partition assemblies. The ultimate goal of the project is to develop models capable of accurately predicting the various failure modes of partition assemblies. This work deals with the first part of solution to this problem by considering heat and mass transport through porous media.

Gypsum wallboard is a porous, multi-layered material whose core is composed primarily of calcium sulfate-dihydrate (CaSO4.2H2O) with small amounts of other fillers sometimes provided to enhance specific mechanical or thermal properties. When wallboard is heated, the gypsum in the core undergoes a series of dehydration reactions whereby chemically bound water is released in an endothermic process. This process absorbs a significant amount of incident thermal energy and slows the rate of heat transfer through the partition assembly, reducing the potential for the fire to spread to adjoining compartments.

A simple mass calculation shows that in its initial form, gypsum wallboard is composed of approximately 21 % by mass of hydrated water with an additional 3 % possible through adsorption. For gypsum wallboard utilized in the United States, having a density of 670 kg/m^3, this translates to nearly 161 kg/m^3 of water that must be liberated within the porous material. With a required energy of approximately 2000 kJ/kg required to evaporate water, one can easily appreciate the benefit from the large amounts of bound water. The details of the dehydration mechanism are complex and depend upon many factors, however the overall governing equation for the dehydration may be expressed as,

$$CaSO_4.2H_2O + Q \rightarrow CaSO_4 + \frac{3}{2}H_2O + \frac{1}{2}H_2O, \quad (1)$$

where supplied heat, Q, liberates the hydrated water and results in free water vapor and calcium sulfate anhydrite, $CaSO_4$. Multiple forms of the intermediate hemihydrate and final anhydrite further complicate

the details of the dehydration process and may lead to a possible third reaction, this one exothermic, where the molecular structure of the calcium sulfate reorganizes to a lower energy form [1].

In addition to the endothermic dehydration reactions, gypsum wallboard, being porous, will also adsorb water molecules along its pore surfaces. This mechanism, found by Richards et al. [2] to only weakly depend upon temperature, can provide additional water, up to approximately 3 % by mass, that must be freed from the pore surfaces. This process will also be endothermic and will thus further retard the transfer of heat across the wallboard.

There has been substantial development of models to predict the fire resistance of gypsum wallboard assemblies, achieving various levels of success. Most of these models treat the effects of moisture in an ad hoc manner [3,4] with the chemical reaction taken to occur over a finite temperature range and possessing a linear dependence upon the temperature. Heats of reaction are calculated from the enthalpies of formation and then used to modify the specific heat of the underlying substance. The entire problem is thus reduced to a simple heat transfer equation with temperature dependent material properties. Transport effects of moisture across the porous substance are neglected in these formulations.

It may be argued that the thermo-physical properties of gypsum are not dependent upon temperature. Rather they depend upon the state of the calcium sulfate n-hydrite. Further, the transport effects of the water vapor may have a dramatic effect upon the heat transfer mechanism. As chemically bound water is liberated, it migrates across the porous substance. If the vapor enters cooler areas further from the supplied heat it may recondense and release heat energy in an exothermic process. This will increase at least the initial stages of heating of unexposed wallboard. Further augmenting the heat transfer process is the thermal conductivity of any condensed phase water. With a thermal conductivity greater than that of the porous solid, the presence of condensed water will increase the conductive heat flux, and result in greater transport of thermal energy.

To determine the importance of these issues, a mathematical model for describing the thermal response of porous, hydrated materials subjected to fire exposure has been developed to simulate the response of gypsum wallboard assemblies. The model includes not only heat transfer but also incorporates mass transfer effects. Gas phase calculations allow for the convective and diffusive transport of water vapor across a porous substance, supplemented by liquid and solid phase relations. Liquid phase relations describe the adsorption / desorption of water on the porous surfaces as well as condensation / evaporation of liquid water for local relative humidities near one. Solid phase relations describe the dehydration process and utilize an Arrhenius type kinetic mechanism for the chemical reaction.

Coupled with the gas phase equations is a simplified energy equation. Due to the low thermal capacity of the gas phase compared to that of the solid and liquid phases, it is assumed that the majority of heat transfer occurs only in the solid and liquid. Energy source and sink terms are included that link the full system of equations by accounting for the energy absorption or release that occurs from the chemical reaction, adsorption / desorption, and condensation / evaporation.

The final system of nonlinear partial differential equations that governs the response of the system is expressed as,

$$\phi\frac{\partial C}{\partial t}+\nabla\cdot(C\mathbf{v})=-\frac{dL}{dt}-\frac{dS}{dt} \tag{2}$$

$$\phi\frac{\partial C_2}{\partial t}+\nabla\cdot(C_2\mathbf{v})-\nabla\cdot\left(DC\nabla\frac{C_2}{C}\right)=-\frac{dL}{dt}-\frac{dS}{dt} \tag{3}$$

$$(\rho c)_c\frac{\partial T}{\partial t}-\nabla\cdot(k_c\nabla T)=\frac{dE_L}{dt}+\frac{dE_S}{dt} \tag{4}$$

where C is the gas molar density, C_2 is the water vapor molar density, T is the temperature and $\mathbf{v}$ is the convective gas velocity. Time derivatives on the right hand side of equations (2) and (3) represent the changes in gas density due to any phase changes (L) and dehydration (S). Time derivatives on the right hand side of equation (4) represent the corresponding energy required for the phase change (E_L) and dehydration (E_S). Parameters in the above system are the porosity ϕ, the binary diffusivity for air and

water vapor D, the composite heat capacity of the solid and liquid phases $(\rho c)_c$, and the composite thermal conductivity of the solid and liquid phases k_c.

The talk will focus on the derivation and interpretation of the system of governing equations expressed in (2)-(4) as well as on the solution. The numerical techniques utilized will also be reviewed. Results obtained from the model will be compared with experimental measurements, particularly simulations corresponding to the ASTM E119 [5] test utilized in the United States for building construction and materials. Limitations and potential improvements to the model will also be discussed including experimental measurements needed to more appropriately define the thermo-physico parameters defined in the model. Finally, future avenues of development will be discussed.

References:

[1] V.S. Ramachandran, R.M. Paroli, J.J. Beaudoin and A.H. Delgado, *Handbook of Thermal Analysis of Construction Materials*. Noyes Publications, Norwich, NY (2003).

[2] R.F. Richards, D.M. Burch and W.C. Thomas, "Water Vapor Sorption Measurements of Common Building Materials," *ASHRAE Transactions*, 98, (2) (1992).

[3] H. Takeda and J.R. Mehaffey, "WALL2D: a Model for Predicting Heat Transfer through Wood-Stud Walls Exposed to Fire," *Fire and Materials*, 22, pp. 133-140 (1998).

[4] G. Thomas, "Thermal Properties of Gypsum Plasterboard at High Temperatures," *Fire and Materials*, 26, pp. 37-45 (2002).

[5] American Society o fTesting and Materials, *Standard Test Methods for Fire Tests of Building Construction and Materials*, ASTM Standard E119-00a, West Conshohocken, PA (2003).

HEAT TRANSFER ANALYSIS FOR STEEELWORK INSULATED BY INTUMESCENT PAINT EXPOSED TO STANDARD FIRE CONDITIONS

Kang Hai TAN, Zhihua WANG and Siu Kui AU
Centre of Advanced Construction Studies, School of CEE
Nanyang Technological University, Singapore
CKHTAN@ntu.edu.sg

ABSTRACT

A simplified 1D characteristic heat transfer model adopted from the Swedish approach was employed to predict the temperature response for steelwork insulated by intumescent paint. The simplification is essentially based on the "lumped capacitance" assumption, which treats the entire steel section as a lumped capacitance with uniform temperature distribution. Constant material thermal properties are assumed in the closed form formulation due to the application of Duhamel's principle with time integral.

Temperature response for steel members insulated by intumescent paint was calculated using the Swedish approach, Eurocode 3 formulation and the finite element analysis, where EC3 and FEA incorporate material nonlinearities. Computational results were compared against experimental investigations. Analysis shows that the closed form solution based on 1D analysis can be used to predict steel temperature, provided accurate thermal properties are employed. The simple numerical formulation by EC3, which incorporates time stepping and material nonlinearity, can be adopted for temperature-time analysis. EC3 predictions yield good accuracy with test results.

KEYWORDS: *heat transfer, steel, intumescent paint, lumped capacitance, standard fire, 1D analysis*

INTRODUCTION

Temperature-time analysis for insulated steelwork exposed to fire conditions is crucial in the study of structural behaviour in fire. Closed form formulations of steel temperature response have been developed in the Swedish approach, [1, 2], based on the concept of "lumped heat capacitance", where the temperature over entire steel member is assumed to be uniform. A 1D characteristic heat transfer model can be constructed based on the lumped capacitance assumption. Procedures to obtain temperature response analytically have been detailed by Carslaw and Jaeger [3], as follows. Temperature response can first be solved analytically corresponding to a stepwise temperature change at the fire interface. Duhamel's principle is then employed to integrate the step temperature response over time intervals. Melinek and Thomas [4], using Laplace transformation, have formally confirmed that the Swedish approach is suitable for the limiting case where the heat loss through convection and radiation at fire boundary is negligible. Besides, Eurocode 3 [5] provides a simple numerical equation involving time stepping to incorporate the nonlinearity of thermal properties.

However, research work on the applicability of the closed form solution for steelwork insulated by intumescent paint remains noticeably absent, primarily due to the complexity of thermal properties. This paper presents a heat transfer analysis for steelwork insulated by intumescent paint exposed to standard fire using the 1D analysis, i.e. the Swedish approach and EC3 formulation. A finite element heat transfer program incorporating material and boundary-condition nonlinearities has also been developed to predict steel temperature. Four-node quadrilateral element, Q4, was employed for all the finite element models. Results predicted by the FEA, the EC3 provision and the Swedish approach are compared with experimental data reported by PAVUS Laboratory [6]. Specimens included European steel I-sections contour-insulated with intumescent paint, and with all surfaces equally exposed to fire conditions. All tested specimens were subjected to standard ISO 834 fire curves. Test specimens and procedures were designed according to prENV 13381-4: 2001, with standard deviation within acceptable range. The computational model of contour-insulated steel I-sections subjected to ISO 834 standard fire curve is shown in Figure 1. Thermal properties of the intumescent paint were reported by FSD [7], determined using inverse finite element analysis.

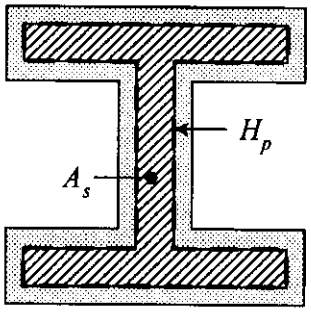

FIGURE 1: Schematics of steel I-section contour-insulated by intumescent paint

A 1D heat transfer model is shown in Figure 2, where d_i and d_s are the 1D characteristic thickness of insulation layer and steel section, respectively. For contour-insulated steel members,

d_i is assumed to be equal to the actual (physical) thickness of intumescent paint. Using the "steel section factor" of insulated steelwork provided in EC3, d_s can be expressed as

$$d_s = \frac{1}{H_p / A_s} = \frac{A_s}{H_p} \tag{1}$$

where H_p and A_s are respectively the appropriate perimeter and cross-sectional area of a steel section, and the ratio H_p / A_s is the section factor for insulated steel members given in EC3 [5].

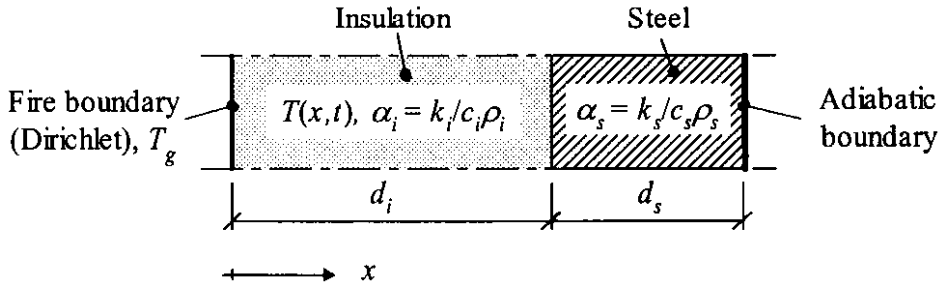

FIGURE 2: Characteristic heat transfer model for 1D analysis

CLOSED FORM SOLUTION FOR STEEL TEMPERATURE CALCULATION

Using the 1D heat transfer model in Figure 2, the temperature analysis for insulated steelwork subjected to fire is reduced to a transient conduction analysis through insulation layer. Let $T(x,t)$ (in °C) denote the temperature at time t at distance x, $0 \le x \le d_i$, from the fire interface. The governing equation in the insulation layer is

$$\alpha_i \frac{\partial^2 T(x,t)}{\partial x^2} = \frac{\partial T(x,t)}{\partial t} \tag{2}$$

where $\alpha_i = k_i / c_i \rho_i$ is the thermal diffusivity of insulation; and k_i, c_i and ρ_i are the thermal conductivity, specific heat and density of insulation, respectively.

The boundary condition at the fire interface, i.e. $x = 0$, is assumed to be

$$T(0,t) = T_g(t) \tag{3}$$

where $T_g(t)$ (in °C) is the specified fire gas temperature, which refers to the ISO 834 fire curve in this paper. It is noted that in equation 3, Dirichlet (essential) boundary condition (with specified temperature) is employed at the fire interface, i.e. the temperature of outer surface of insulation is treated to be identical to the fire gas temperature. The heat loss through surface convection and radiation is assumed to be negligibly small, which is referred as the "limiting case" by Melinek and Thomas. The significance of this surface treatment is to be discussed in the following section.

At the interface of the insulation and the steel, i.e. $x = d_i$, the boundary condition is given by

$$-k_i \frac{\partial T(d_i,t)}{\partial x} = Q_s \frac{\partial T_s(t)}{\partial t} \tag{4}$$

where $T_s(t) \equiv T(d_i,t)$ is the steel temperature; $Q_s = c_s \rho_s d_s$ is the lumped heat capacitance of steel section; and c_s and ρ_s are specific heat and density of steel, respectively.

Insulated steel member reported here are subjected to standard ISO 834 fire curve. The standard heating curve is given by Eurocode 1 [8],

$$T_g(t) = T_0 + 345 \log_{10}(8t+1) \tag{5}$$

where T_0 is the initial temperature and t is the time (in min). SBN [9] adopts an approximate expression for the standard fire curve, as a summation of exponential terms

$$T_g(t) = T_0 + \sum_{i=0}^{3} B_j \exp(-\beta_j t) \tag{6}$$

where values of constants B_j and β_j are given in Table 1.

Table 1: Constants in the exponential expression of the ISO 834 fire curve

j	0	1	2	3
B (°C)	1325	-430	-270	-625
β (h^{-1})	0	0.2	1.7	19

Using the SBN expression, an approximate solution for steel temperature response of insulated steel members subjected to ISO fire is derived based on eigenfunction analysis in the Swedish approach, as

$$T_s(t) = T_0 + \sum_{i=0}^{3} \frac{B_j}{1-\beta_j \tau} \left\{ \exp\left[-\beta_j (t-\bar{t})\right] - \exp\left[(t-\bar{t})/\tau\right] \right\} \tag{7}$$

where $\bar{t}$ is the time shift of steel temperature response, which is approximated by

$$\bar{t} = \frac{\mu \tau}{8} \tag{8}$$

with the dimensionless constant μ given by the ratio of heat capacitance of insulation to that of steel, as

$$\mu = \frac{Q_i}{Q_s} = \frac{c_i \rho_i}{c_s \rho_s} \left(\frac{H_p}{A_s} \right) d_i \tag{9}$$

And the term τ is referred as the steel thermal time constant, expressed as

$$\tau = R_i (Q_s + Q_i/3) = \frac{c_s \rho_s d_i}{(H_p/A_s) k_i} \left(1 + \frac{\mu}{3} \right) \tag{10}$$

where the subscripts s and i represent material properties of steel and insulation, respectively; and $R = d/k$ is the thermal resistance.

NONLINEAR NUMERICAL ANALYSIS: EC3 FORMULATION

For a general nonlinear case of insulated steelwork, where the material properties vary with temperature, numerical calculations are required. Approximate temperature-time derivative has been derived by Wickstrom [1] as,

$$dT_s/dt = \left(T_g - T_s\right)/\tau - \left[\exp\left(\mu/10\right)-1\right]\frac{dT_g}{dt} \tag{11}$$

The temperature-time derivative are approximated as $dT_s/dt \approx \Delta T_s/\Delta t$; $dT_g/dt \approx \Delta T_g/\Delta t$, assuming Δt is sufficiently small. Hence, an approximate expression for the increase of temperature ΔT_s in an insulated steelwork during a time increment Δt is adopted by Eurocode 3, as

$$\Delta T_s = \frac{\left(T_g - T_s\right)}{\tau}\Delta t - \left[\exp\left(\mu/10\right)-1\right]\Delta T_g \tag{12}$$

where ΔT_s and ΔT_g are the increase of steel temperature and fire gas temperature within Δt, respectively. The numerical stability of this forward difference scheme requires the time increment to be controlled such that $\Delta t \le \tau$ [1]. However, further restriction of time increment is required to obtain reasonable accuracy, e.g. $\Delta t \le 30s$ for insulated steelwork as required by Eurocode 3 [5].

In order to evaluate equation 12 numerically, discretization of the temporal interval $[0,t]$ is required, such as $\left\{t_j = j\Delta t : j = 0,1,...,N\right\}$; and the solutions are to be computed at each time step t_j. The temperature-dependent thermal properties of the insulation at a particular time instant t_j can be evaluated at an average temperature of insulation $T_m\left(t_j\right) = \left[T_g\left(t_j\right) + T_s\left(t_{j-1}\right)\right]/2$ i.e. a mean value of fire gas temperature at current time step and steel temperature at previous time step.

SIGNIFICANCE OF SURFACE HEAT LOSS

It is noted in equation 3, a simplified boundary condition is assumed at fire-insulation interface by specifying the surface temperature of insulation identical to fire gas temperature (Dirichlet boundary). Consider an alternative boundary condition by specifying the surface heat flux induced by convection and radiation at $x = 0$ (Neumann boundary) instead of equation 3, as

$$h\left[T_g\left(t\right) - T_o\left(t\right)\right] = -k_i\frac{\partial T\left(0,t\right)}{\partial x} \tag{13}$$

where h is the heat transfer coefficient of convection and radiation at the fire interface and $T_o\left(t\right)$ is the outer surface temperature of the insulation adjacent to the fire interface. Equation 13 represents a more realistic boundary condition at the fire interface for heat transfer analysis of insulated steelwork subjected to fire. When the Dirichlet boundary (equation 3 with specified

temperature) is assumed at the fire interface, as in equation 3, the heat transfer model is reduced to the limiting case with $h \to \infty$. Thus the closed form formulation in equation 7 approximates the exact solution of 1D analysis accurately if the heat loss through convection and radiation at the fire interface is negligible. To assess the significance of surface heat loss, a comparison of temperature response using the simplified Dirichlet (equation 3) and the realistic Neumann (equation 13) boundary conditions are presented in Figure 3.

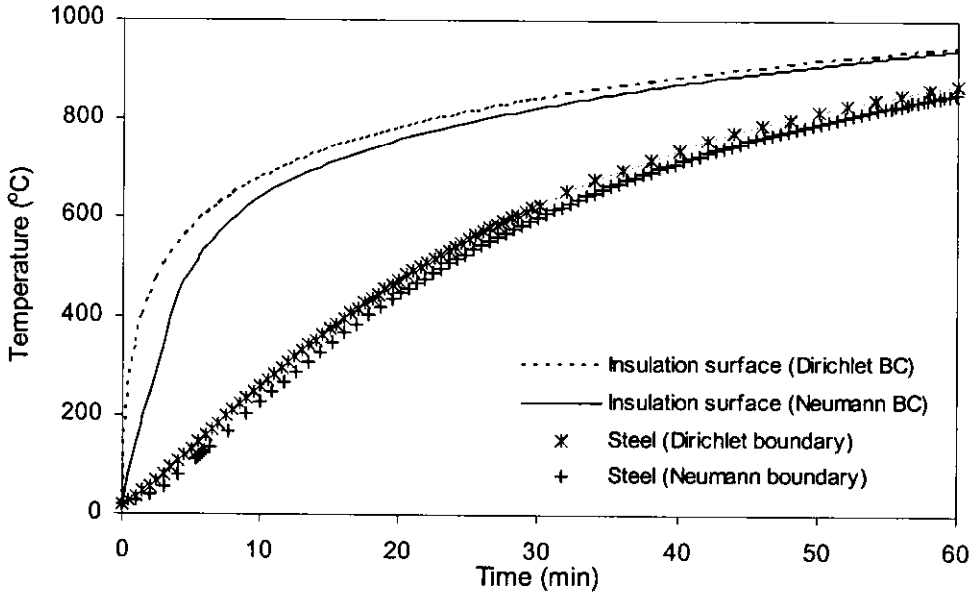

FIGURE 3: Comparison of temperature responses corresponding to Dirichlet and Neumann boundary conditions respectively

It can be seen from Figure 3 that the temperature difference at the insulation surface, using respectively Dirichlet and Neumann boundary condition, is small in magnitude and therefore negligible in analysis. An even smaller temperature difference is induced by different type of boundary conditions for steel section. Therefore, the limiting case assumption i.e. $h \to \infty$ in the closed form formulation in equation 7 is valid for temperature analysis for steelwork insulated by intumescent paint.

RESULTS AND DISCUSSIONS

A total number of 14 specimens consisting of insulated steel I-section have been analyzed. Properties for the specimens are shown in Table 2, as given in [6, 7].
The reported thermal properties of the intumescent paint, in particular, the effective thermal conductivity, are highly nonlinear and temperature-dependent. A typical thermal conductivity-versus-temperature curve is shown in Figure 4. The nonlinear thermal properties were incorporated into the FEA and the EC3 predictions of steel temperature. On the other hand, the Swedish approach (i.e. the closed form formulation in equation 7) assumes all thermal properties to be constant (independent of temperature), where $k_s = 45$ W/m/°C , $c_s\rho_s = 4.71$ MJ/m^3/°C and $c_i\rho_i = 1.0$ MJ/m^3/°C. The effective thermal conductivity used in the

Swedish approach for each specimen is listed in Table 3, which is calculated as the average constant value of thermal conductivity in the range of $[400°C, 800°C]$ corresponding to each specimen, as reported by [7].

Table 2: Properties of analyzed steel sections insulated by intumescent paint

Symbol according to prENV 13381-4: 2001	Sections profiles	Insulation thickness d_i (μm)		Section factors H_p/A_s (m^{-1})		μ	Constant k_i [W/(m°C)]
		nominal	measured	nominal	measured		
TC	HEA 300	max	1017	153	172	0.0372	0.0083
SC	HEM 280	min	323	70	75	0.0051	0.0100
SC	HEM 280	med	585	70	75	0.0093	0.0100
SC	HEB 450	max	1004	95	98	0.0208	0.0125
SC	HEB 300	min	354	116	129	0.0097	0.0083
SC	HEA 300	min	323	152	166	0.0114	0.0083
SC	HEA 300	max	1074	153	173	0.0396	0.0083
SC	HEA 200	min	333	212	231	0.0164	0.0083
SC	HEA 200	max	1034	212	238	0.0522	0.0083
SC	IPE 200	med	607	269	266	0.0342	0.0098
SC	IPE 200	max	1097	269	273	0.0638	0.0098
SC	IPE 140	med	618	335	333	0.0436	0.0098
SC	IPE 140	max	1089	335	351	0.0806	0.0098
SC	U 200×200/4	med	562	500	474	0.0563	0.0098

From these figures, it is observed that both Eurocode 3 and FEA predict the steel temperature well, when the temperature-dependent thermal conductivities of the intumescent paint as shown in Figure 4 are incorporated. As expected, the Swedish approach using constant k_i for each specimen underestimates the temperature at the earlier stage of heating, where from Fig. 4, much lower values of k_i in the earlier stage is used assuming temperature-independent. However, the Swedish approach estimates the steel temperature accurately after the steel temperature has increased above 400°C. For design purpose, the Swedish approach can be used to predict the critical temperature if it is above 400°C. Due to the simplicity and closed form of the Swedish approach, it is efficient and, in general, reliable for temperature prediction of steelwork insulated by intumescent paint. On the other hand, unlike the closed form solution provided in the Swedish approach, the Eurocode 3 provision requires time stepping and FEA

requires development of finite element code. It is also when the steel temperature increases above 400°C, all the calculation schemes converge to the experimental results.

Both Swedish approach and Eurocode 3 employ the 1D condensed heat transfer model shown in Figure 2 in virtue of the lumped capacitance assumption. The results show that the application of the 1D analysis can be extended to steelwork insulated by intumescent paint and therefore the heat transfer analysis can be significantly simplified.

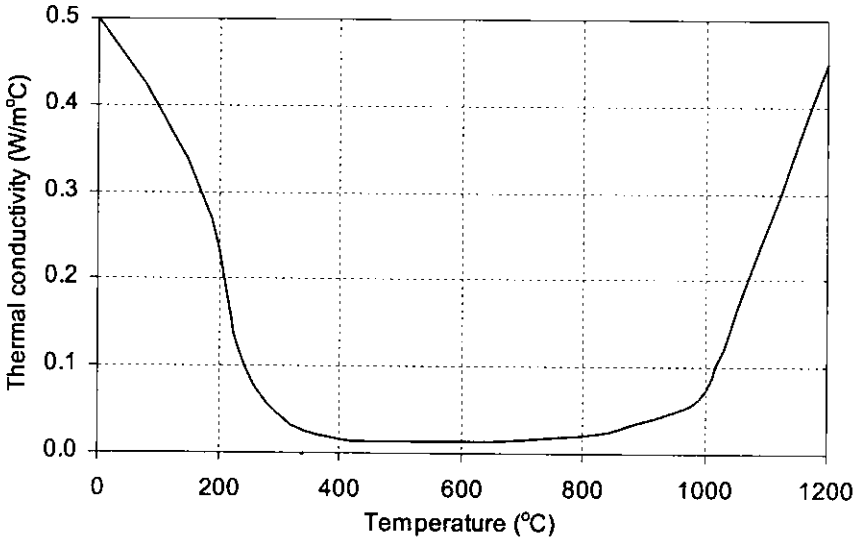

FIGURE 4: Typical effective thermal conductivity of intumescent paint (Curve D in [7])

Results of steel temperature response obtained from experimental investigation and different calculation schemes are presented in Figures 5 to 7.

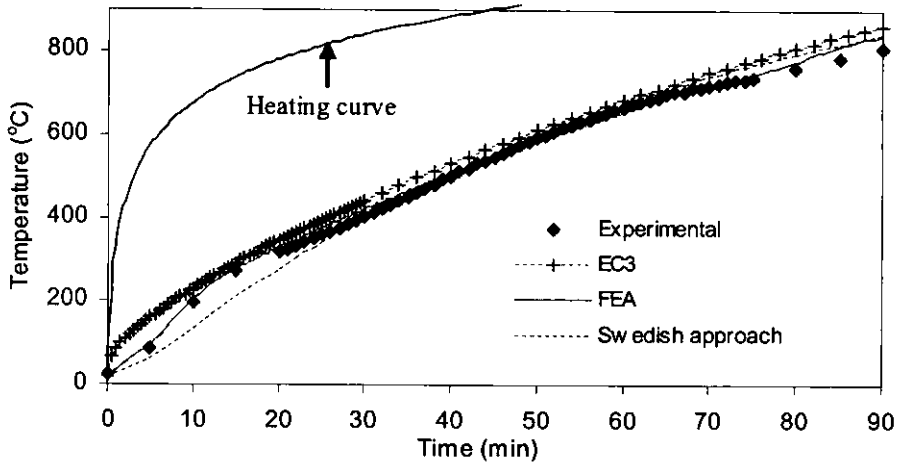

FIGURE 5: Comparison of temperature response predicted by different schemes for SC HEM 280 (min insulation)

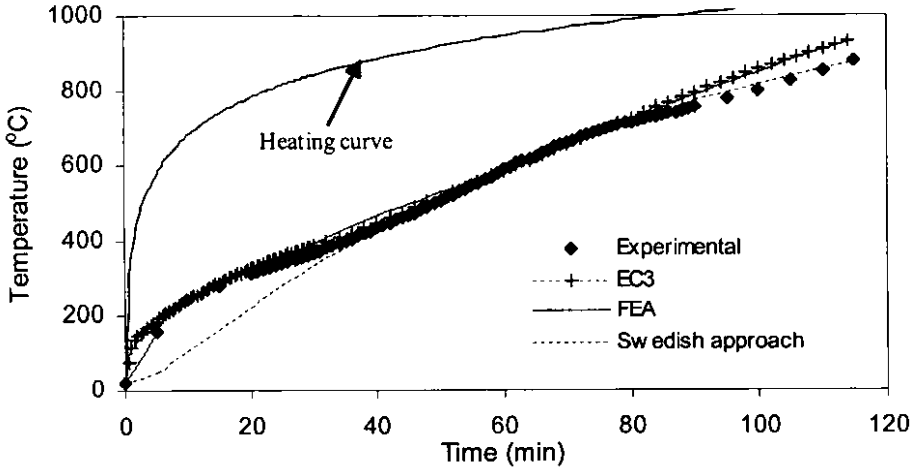

FIGURE 6: Comparison of temperature response predicted by different schemes for SC HEA 300 (max insulation)

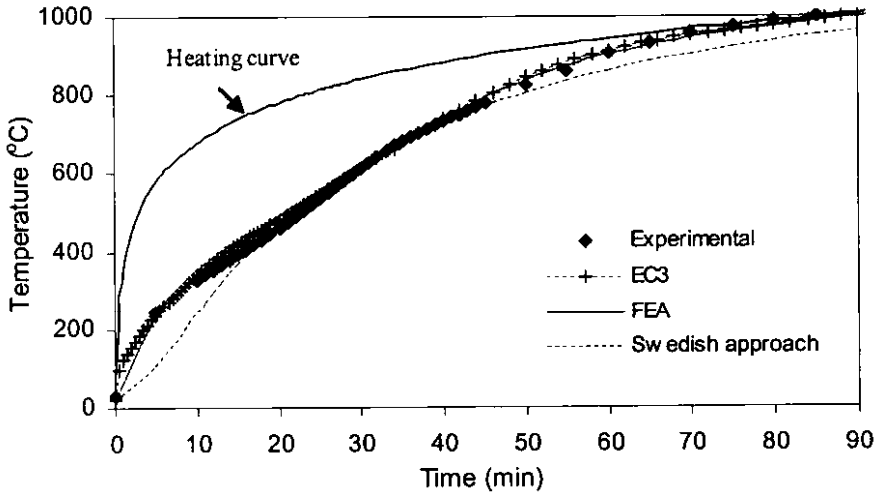

FIGURE 7: Comparison of temperature response predicted by different schemes for SC IPE 140 (med insulation)

CONCLUSIONS

In this paper, an assessment has been made for three different schemes for calculating temperature of insulated steelwork subjected to ISO fire, namely, the closed form formulation (the Swedish approach), Eurocode 3 prediction and finite element analysis. It is concluded that application of numerical calculation incorporating material nonlinearity, i.e. EC3 and FEA, yields very good results in the estimations of steel temperature when compared against experimental results. On the other hand, the Swedish approach is efficient in terms of computational cost and reliable for prediction of critical temperatures. Therefore, both EC3 and the Swedish approach employing 1D heat transfer analysis are recommended for design purpose for temperature prediction of steelwork insulated by intumescent paint in terms of time-stepping and closed form solution, respectively.

ACKNOWLEDGEMENT

The authors would like to thank Dr Claudio Pagella *and the company IRIS Vernici* for providing the experimental results on tests of intumescent paint.

REFERENCES

[1] Wickstrom U., *Temperature analysis of heavily-insulated steel structures exposed to fire*, Fire Safety Journal, Vol. 5, 281-285, 1985.

[2] Wickstrom, U., *Natural fire for design of steel and concrete structures – a Swedish approach*, Proceedings of the International Symposium on Fire Engineering for Building Structures and Safety, Melbourne, November, 1989.

[3] Carslaw, H. S. & Jaeger, J.C., *Conduction of heat in solids, second edition*, Oxford University press, New York, 1959.

[4] Melinek S. J. & Thomas P. H., *Heat flow to insulated steel*, Fire Safety Journal, Vol. 12, 1-6, 1987.

[5] ENV 1993-1-2, *Eurocode 3: Design of Steel Structures – Part 1-2: General Rules – Structural Fire Design*, CEN, Brussels, 1995.

[6] PAVUS, a.s., *Test for determining the contribution to fire resistance of steel members by applied protection of an intumescent coating system CHAR 21*, Report No. Pr-01-02.093, 2002.

[7] FSD, *Char 21 fire retardant paint on steel structures: design guide based on prENV 13381-4*, No. 02-024-RevB, Sweden, 2002.

[8] prENV 1991-1-2, *Eurocode 1: Actions on Structures – Part 1-2: General Actions – Actions on structures exposed to fire,* third draft, CEN, Brussels, 30 May 2001.

[9] SBN, *Swedish Building Code 1975*, National Board of Physical Planning and Building, 1975.

TEMPERATURE FIELD MODELING OF THE FIRST CARDINGTON TEST

Farid ALFAWAKHIRI
American Institute of Steel Construction, Chicago, IL, USA
alfawakhiri@aisc.org

Venkatesh K. R. KODUR
National Research Council Canada, Ottawa, Ontario, Canada
venkatesh.kodur@nrc.ca

George FRATER
Canadian Steel Construction Council, Toronto, Ontario, Canada
gfrater@steel.org

ABSTRACT

Results of heat transfer numerical simulations, using SAFIR program, for the composite floor beam of the first Cardington fire test in the eight-story steel-framed building are presented. For steel beam temperature predictions, the 2D mesh model was simplified by neglecting the presence of the steel deck and averaging the concrete slab thickness. This model was sufficient to yield a satisfactory match of predicted and measured temperatures in the steel beam. The predictions show that the unprotected bottom flange and web temperatures follow closely the temperature of the fire gas environment.

For temperature predictions in the ribbed concrete slab, a more detailed 2D model was generated with certain nodes to match the experimental measurement locations. Large number of SAFIR simulations was conducted to investigate the sensitivity of the output to various heat transfer parameters. The results confirm to the trends observed in earlier studies that used different software. The numerical predictions were compared with the experimental data, and the predicted temperatures in the concrete always exceeded temperatures measured in the test. Possible reasons for this over-conservativeness of predictions are briefly discussed.

KEYWORDS: *fire resistance, beam, fire test, heat transfer, steel, concrete, thermal properties.*

INTRODUCTION

Building code requirements for structural fire protection have traditionally based on the prescription of fire resistance ratings achieved in standard tests (ASTM E119). While being somewhat convenient to the regulatory process, such an approach is grossly simplified because standard test ratings do not reflect the actual time that a real structural member would endure in a real fire. Columns, beams and floors tested in specific idealized standard test conditions behave differently when forming a part of a building frame in a realistic fire scenario.

Multi-story steel framed buildings have a good fire performance record in North America and all around the world. On the other hand, there have been numerous incidents of steel framed buildings surviving severe uncontrolled long-duration fires with compete burnout of contents on several floors (Dexter and Lu 2000). This superior performance has been attributed in part to the fact that typical natural fire characteristics and actual gravity load intensities are often less severe than in standard tests. It has also been well recognized that continuity and redundancy of steel frames provide multiple alternative load paths in the heated structure to maintain its stability (Gewain and Troup 2001). Such redundant behavior is especially notable in steel framed buildings with composite reinforced concrete floor slabs. Recent six large-scale fire tests conducted in Cardington, UK, in a steel framed building with completely unprotected steel beams and steel floor units clearly demonstrated that composite steel concrete floors can survive complete burnout of office occupancy contents without any sprayed fire proofing (*Behaviour* 1999). No collapse occurred in any of the tests despite relatively large deflections of beams and floor slabs.

Following these tests numerous research initiatives in many parts of the world are underway to analyze the extensive amount of generated experimental data. These studies has already brought a better understanding of the observed phenomena that will lead to more rational fire resistance design practices (Wang and Kodur 2000). Under one such initiative a numerical analysis was carried out as part of a "collaborative steel fellowship project" between the National Research Council Canada and the Canadian Steel Construction Council. Results of heat transfer numerical simulations of the composite floor beam of the first Cardington fire test on an eight-story steel-framed building are presented in this paper.

SAFIR PROGRAM

SAFIR is a special-purpose finite element program (Franssen et al, 2000) for thermal and structural analysis of building elements and frames exposed to fire. Recently added pre- and post-processors make the program more efficient and user-friendly. SAFIR accommodates several element types and material models for various idealizations and calculation procedures. The thermal analysis generates the temperature field in construction elements. The eventual presence of insulating materials, moisture content and temperature-dependent thermal properties can be considered in the analysis. Standard or user-defined natural fire exposure can be specified. The temperature field from the thermal analysis is then used as input for the structural analysis stage, where the mechanical behavior of the heated structure is simulated. Thermal strains and large displacements are considered in the structural analysis. Various stress-strain relationships, implicitly accounting for thermal creep, are built into the program. SAFIR is a useful research tool to investigate the behavior of heated structures and conduct relevant

parametric studies. The program has been validated and used in several case studies carried out in the past (Nwosu and Kodur 1998).

THE FIRST CARDINGTON TEST

An analytical study is currently underway at NRC to process the experimental data from Cardington tests and conduct retrospective numerical simulations of these tests using SAFIR program. The overall approach taken is to use several modeling techniques and compare the predicted temperatures, deflections and strains with measured values. Outcome of sensitivity to various input parameters and material models is also studied in the process. At this stage the study is focusing on the thermal and structural simulations of the first Cardington test. This "Retrained Beam" test was carried out by heating an 8×3 m portion of a composite steel concrete floor along the supporting steel beam spanning 9 meters (Kirby 1998). Although the steel beam and the surrounding steel deck were left completely unprotected, being exposed to furnace temperatures approaching 900°C, the floor maintained its stability and integrity for the duration of the test and beyond. The mid-span deflection of the beam reached the maximum of 232 mm during the test and recovered to 113 mm once the beam cooled back to ambient temperature.

Numerous locations in the test setup were instrumented with thermocouples to obtain an accurate record of temperatures in the furnace, steel beam and the concrete slab. The records indicate insignificant scatter in the measured furnace and steel beam temperatures. Figure 2 illustrates the average temperature histories in the furnace, top flange (TF) and bottom flange (BF) of the beam.

The thermocouple measurement points across the thickness of the ribbed concrete slab are shown in Figure 4. Temperatures measurements in the concrete slab were conducted at 4 sections, as shown in Figure 5. However, only records from sections B1 and B2 were used for the purposes of this study – Figures 6 and 7 illustrate the relevant average temperature histories for thermocouple points through the depth of the flute and the rib, respectively. It should be noted that the scatter of individual temperature histories for comparable measurement points was more pronounced in the flute than in the rib. Therefore, it was judged that rib temperature histories from Figure 7 were the most suitable for comparison with numerical simulations.

NUMERICAL SIMULATIONS

For steel beam temperature predictions, the 2D mesh model was simplified by neglecting the presence of the steel deck and by averaging the concrete slab thickness to 100 mm, as shown in Figure 1. This model was sufficiently accurate to yield a satisfactory match of predicted and measured temperatures in the steel beam, as shown in Figure 2. As it could be expected, unprotected bottom flange and web temperatures closely follow the temperature of the fire gas environment. The top flange temperature is somewhat lower (by about 100°C) due to the "cooling" effect of the concrete slab. The simulated temperature histories in Figure 2 were generated with EC3 thermal steel properties, EC2 normal weight concrete thermal properties, effective emissivity coefficient of 0.8 and the convection coefficient of 25 W/m^2K for fire-exposed surfaces. For the unexposed side of the concrete slab in this simulation, the emissivity coefficient was 0.6 and the convection coefficient was 5 W/m^2K. Other simulations with

different values of thermal parameters and properties indicated that the temperature output for exposed steel beam was not very sensitive to moderate deviations from the common values above.

For temperature predictions in the ribbed concrete slab, the 2D model shown in Figure 3 was generated. Certain mesh nodes (comparative nodes) match the points of temperature measurements in the ribbed slab (Figure 4). Again, large number of simulations was conducted to investigate the sensitivity of the temperature output to thermal parameters and concrete thermal properties. Figure 8 illustrates the typical isotherm zones in the output of SAFIR simulations. In all simulations the experimental temperatures at the bottom of the slab were significantly lower than those generated by heat transfer simulation.

As an example, Figures 9 illustrates the output for slab rib temperatures based on the common thermal parameters and properties listed above and 4 % moisture content in the concrete. This simulation over-estimates the temperatures at all comparative nodes. Where the moisture content is increased to 12 %, as shown in Figure 10, good agreement of predicted and measured temperatures is observed only at the unexposed top surface of the slab. However, for other comparative nodes close to the fire, the predicted temperatures still exceed measured temperatures.

As another example, Figure 11 illustrates the output of simulations using concrete properties suggested by Lamont et al (2001) for lightweight concrete – density 1850 kg/m3, thermal conductivity 0.7 W/m K, specific heat 700 J/kg K, moisture content 5%. In this simulation, as suggested by Lamont et al, the effective emissivity coefficients of 0.7 and 0.6 were used for the fire-exposed and ambient sides, respectively; the convection coefficients were of 15 W/m^2K for fire-exposed surfaces and 10 W/m^2K on the unexposed side. Again, except for the unexposed surface point, all predicted temperatures exceed the measured temperatures.

DISCUSSION

The probable reasons to explain higher predicted temperatures are:

- The steel deck separates from the concrete slab creating a cavity that slows heat transfer. Spalling concrete particles could further fill this cavity forming an effective insulating layer.
- The model assumes uniform moisture content throughout the concrete slab. It is likely that the moisture content s higher at the bottom of the slab, because the steel deck essentially seals the concrete surface slowing the drying process.

More trivial probable causes for low experimental temperatures could also be inaccurate position of the thermocouples and thicker than specified concrete slab.

SUMMARY AND CONCLUSIONS

The paper demonstrates the application of SAFIR computer program to temperature field modeling of composite steel/concrete floors exposed to fire.
Exposed steel beam temperatures are predicted very accurately, and these predictions are not very sensitive to the choice of thermal heat transfer parameters or material thermal properties.

The use of common heat transfer parameters and EC2 thermal properties for concrete results in conservative predictions of temperatures in the slab. Traditional heat transfer simulations cannot explain the very low concrete temperatures at the bottom of the slab in this test. Possible high moisture content at the bottom of the slab or other phenomena could have been responsible for the slow development of temperatures in the slab.

REFERENCES

ASTM (1995). "Standard test methods for fire tests of building construction and materials", *E119-95a*, West Conshohochen, PA.

The behaviour of multi-storey steel framed buildings in fire (1999), British Steel Plc, Swinden Technology Center, Rotherham, UK.

Dexter, R. J., and Lu, L. (2000). "The effects of a severe fire on the steel frame of an office building", *Proceedings of the North American Steel Construction Conference*, Las Vegas, NV, May, American Institute of Steel Construction, Chicago, IL.

Gewain, R. G., and Troup E. W. J. (2001), "Restrained fire resistance ratings in structural steel buildings", *Engineering Journal*, 2nd Quarter, 78-89.

Franssen, J. M., Kodur, V.K.R., and Mason, J. (2000). *User's manual for SAFIR2001: a computer program for analysis of structures submitted to the fire*, University of Liege, Belgium.

Kirby, B. R. (1998). "The behaviour of a multi-storey steel framed building subjected to fire attack, Experimental data", Swinden Technology Center, British Steel plc., UK.

Nwosu, D., and Kodur, V. K. R. (1998). "Behaviour of steel frames under fire conditions", *Canadian Journal of Civil Engineering*, 26, 156-167.

Sanad, A. M., Rotter, J. M., Usmani, A. S., and O'Connor, M. A. (2000). "Composite beams in large buildings under fire – numerical modelling and structural behaviour", Fire Safety Journal, 35, 165-188.

Wang, Y. C., and Kodur, V. K. R. (2000). "Research toward use of unprotected steel structures", *Journal of Structural Engineering*, 126(12), 1442-1450.

Lamont, S., Usmani, A. S., and Drysdale, D. D. (2001). "Heat Transfer Analysis of Composite Slab in the Cardington Frame Fire Tests", Fire Safety Journal, 36, 815-839.

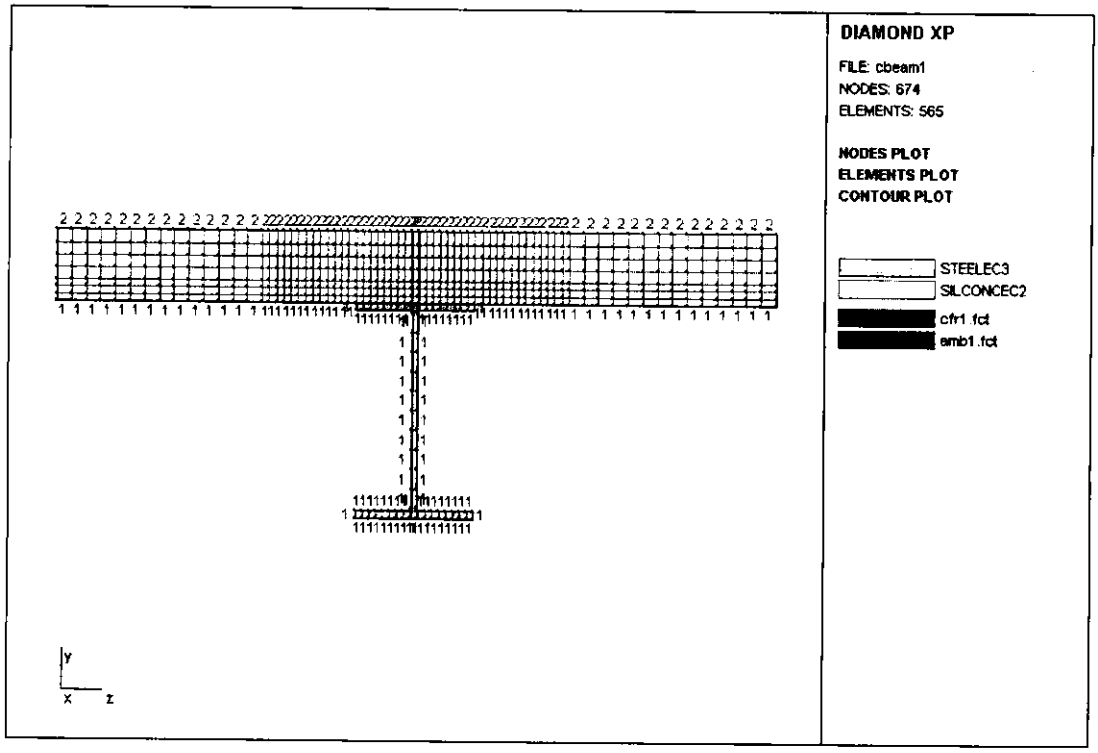

Figure 1. The simplified mesh model for temperature predictions in the steel beam.

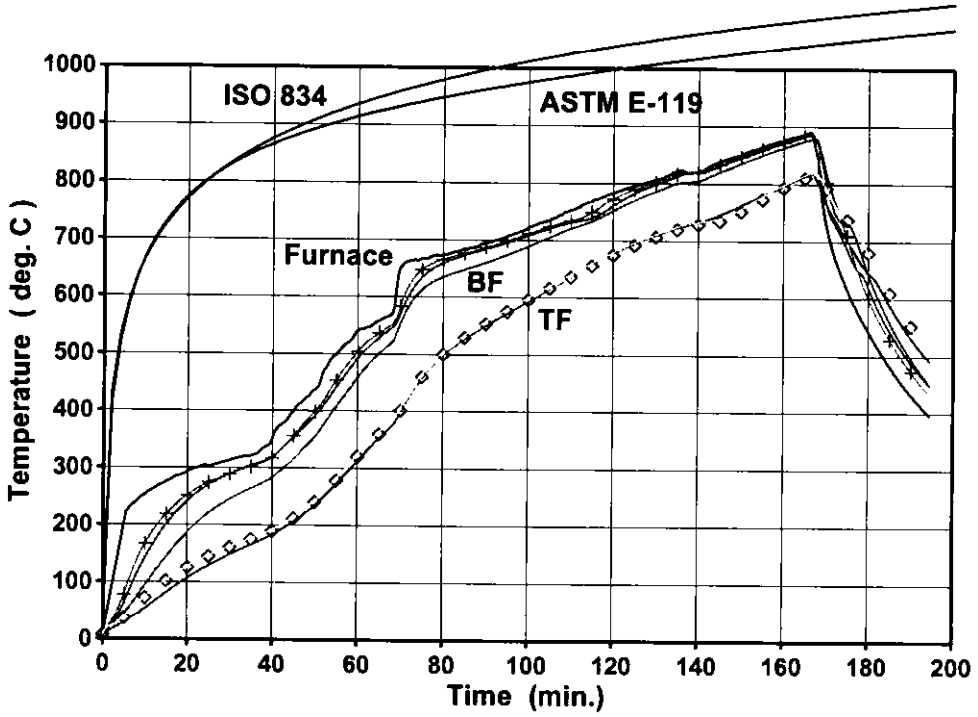

Figure 2. Comparison of predicted and measured temperatures in the steel beam.

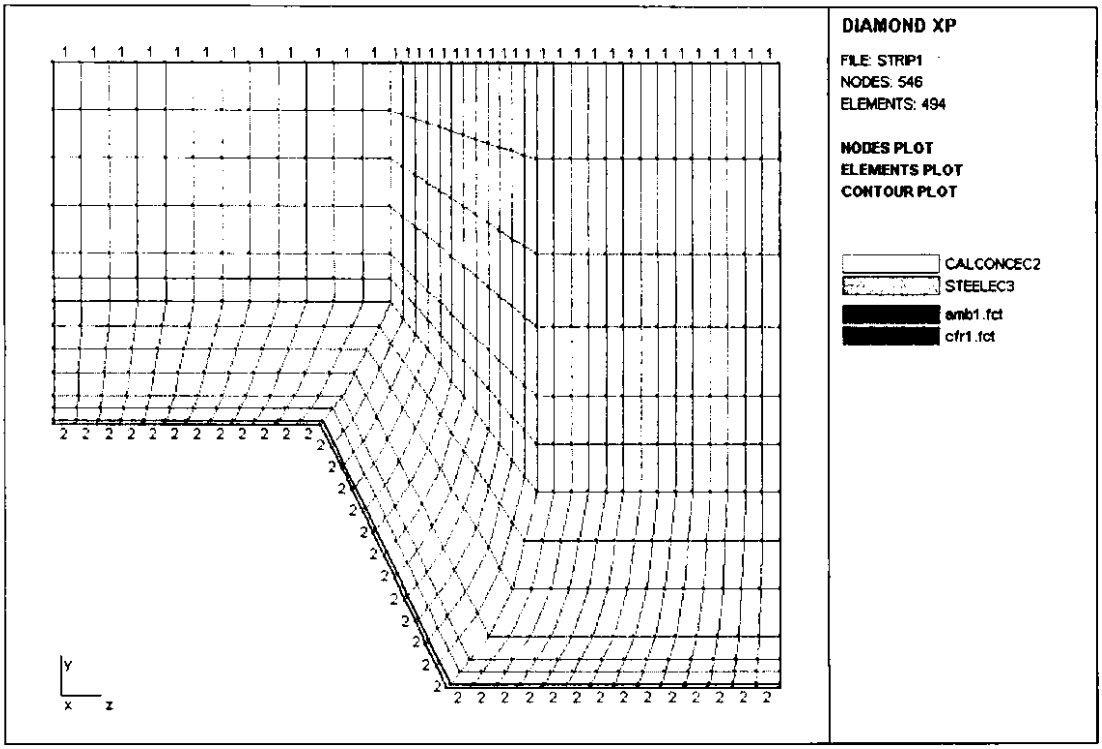

Figure 3. The mesh model for the ribbed concrete slab on fluted steel deck.

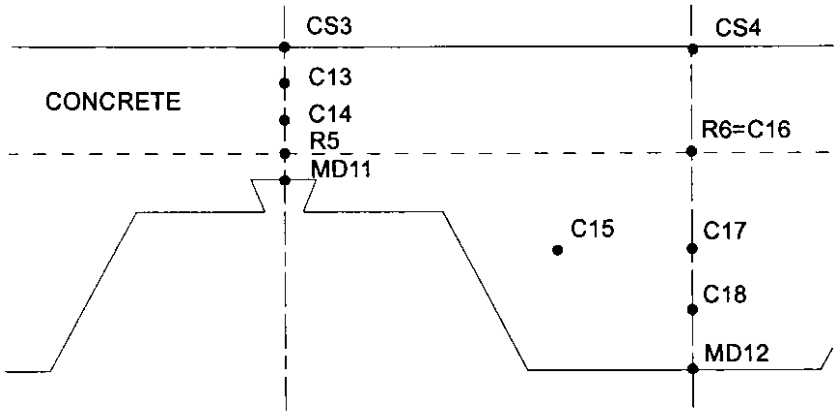

Figure 4. Temperature measurement points in the slab (locations B1 & B2)

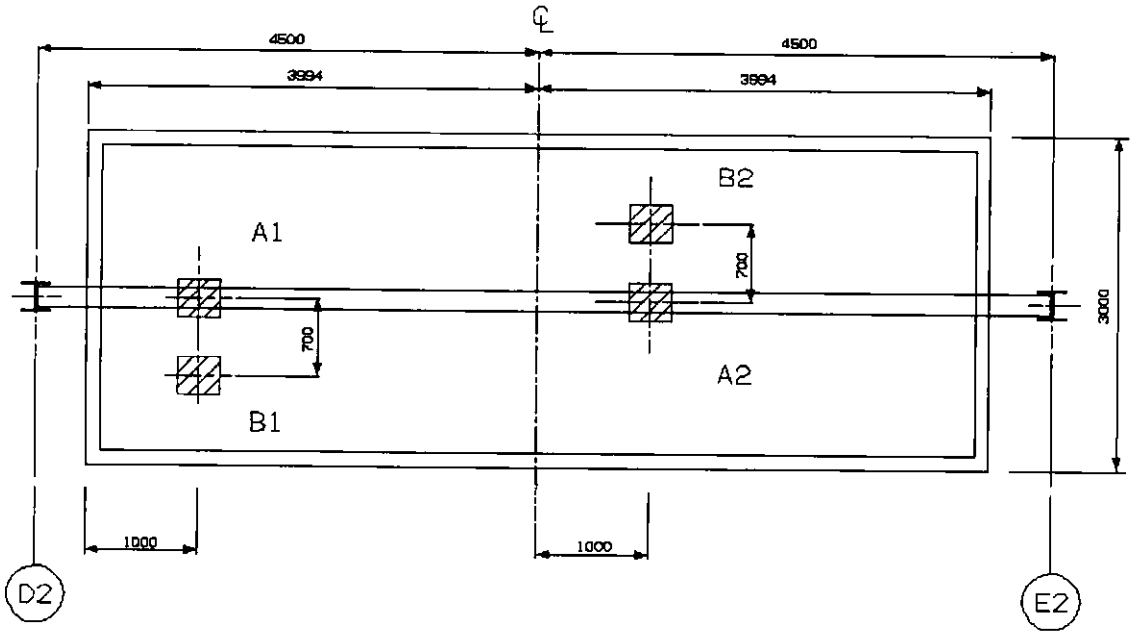

Figure 5. Temperature measurement locations B1 & B2

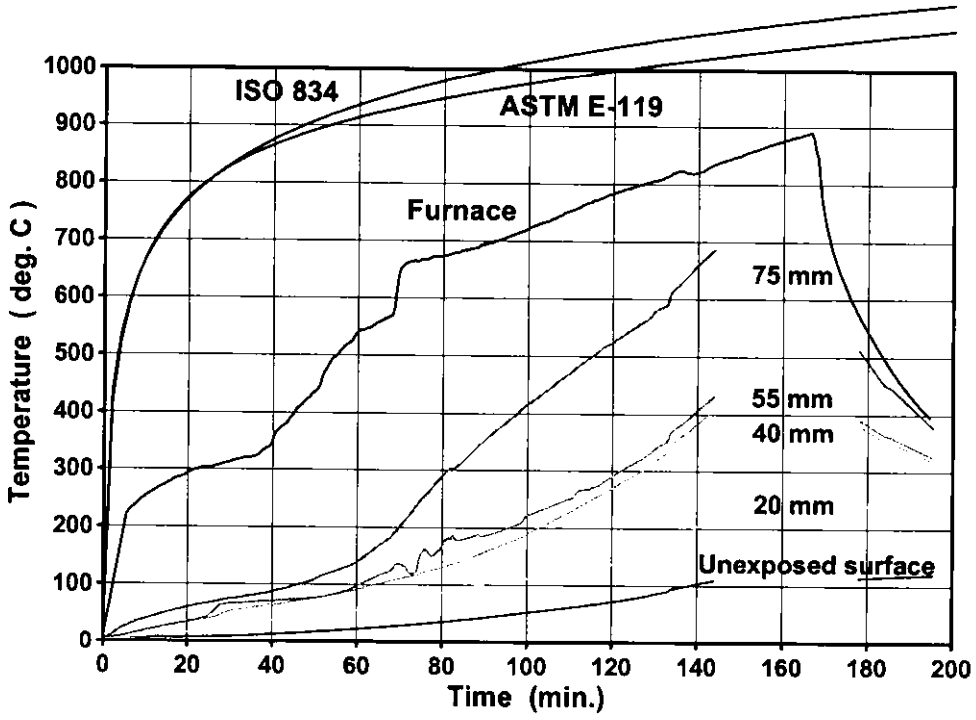

Figure 6. Temperatures measured in the fluted part of the slab (average B1 & B2)

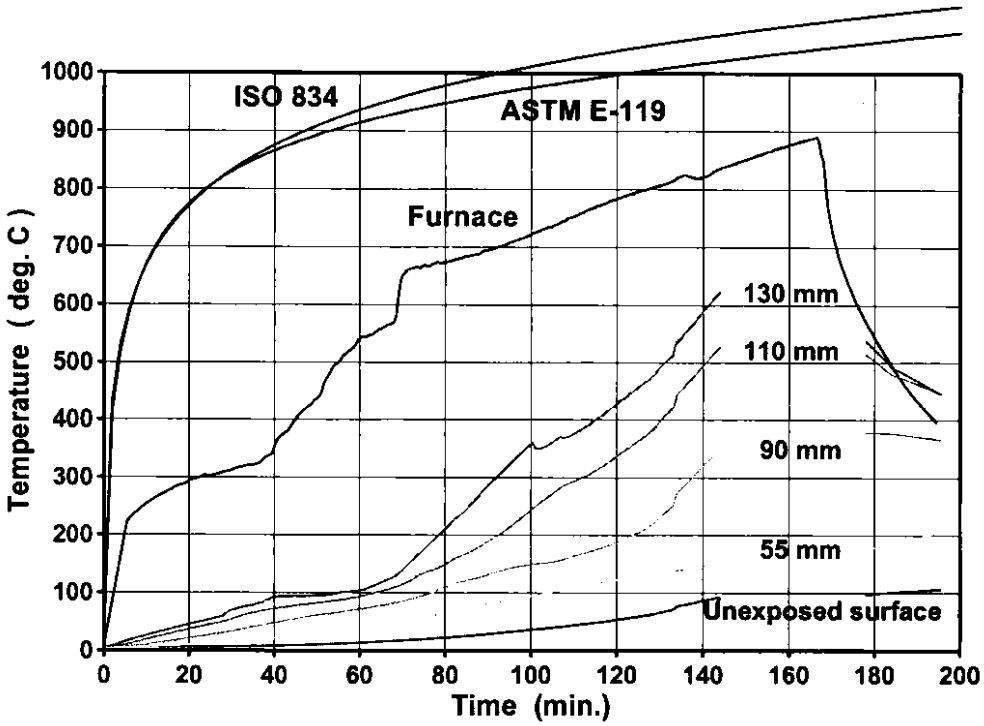

Figure 7. Temperatures measured in the slab rib (average B1 & B2)

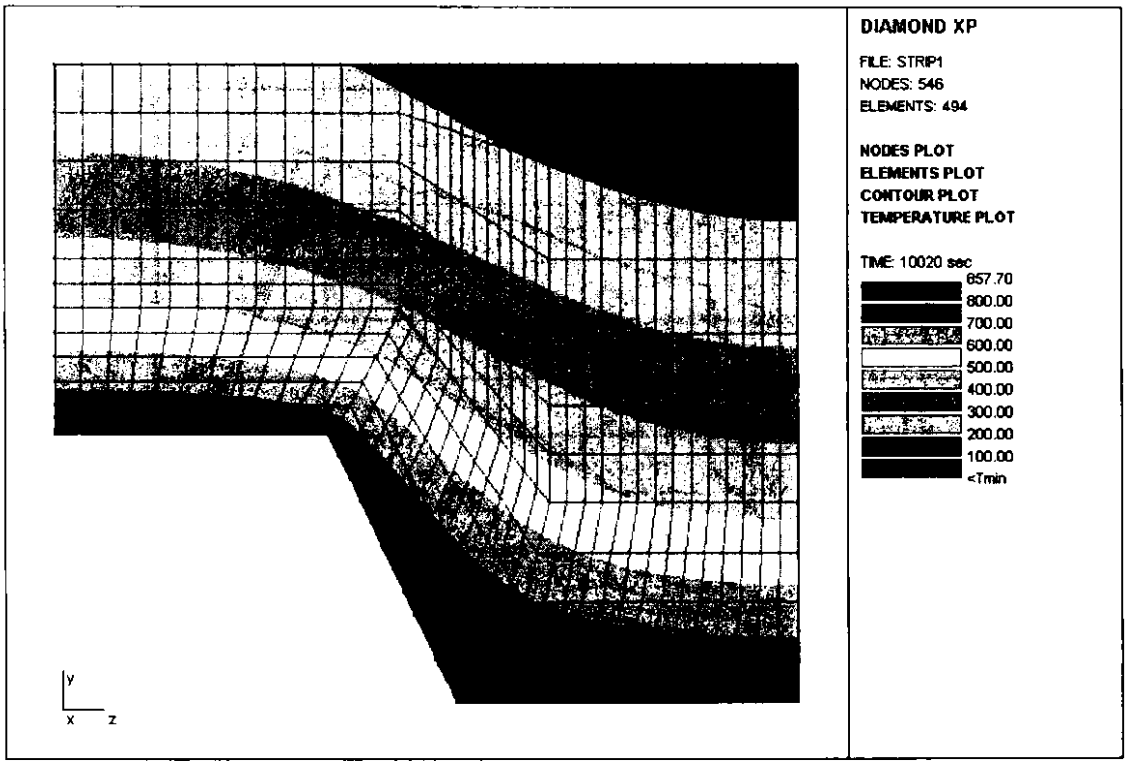

Figure 8. Typical isotherm zone output of SAFIR simulations

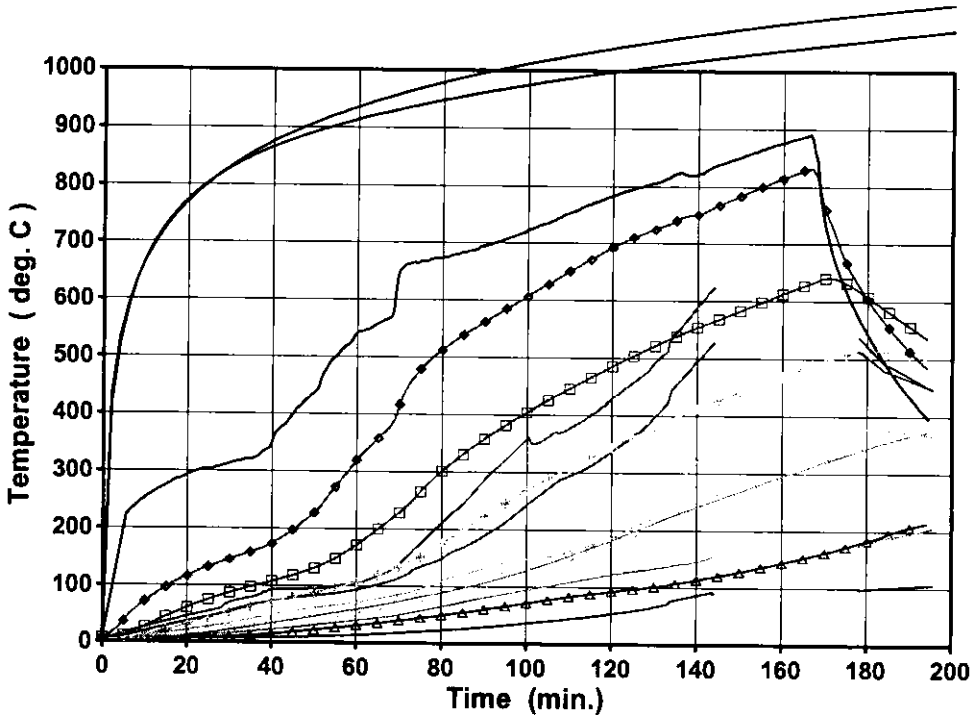

Figure 9. Temperature predictions in the slab rib compared to measured temperatures (EC2 normal weight concrete properties, 4 % moisture content)

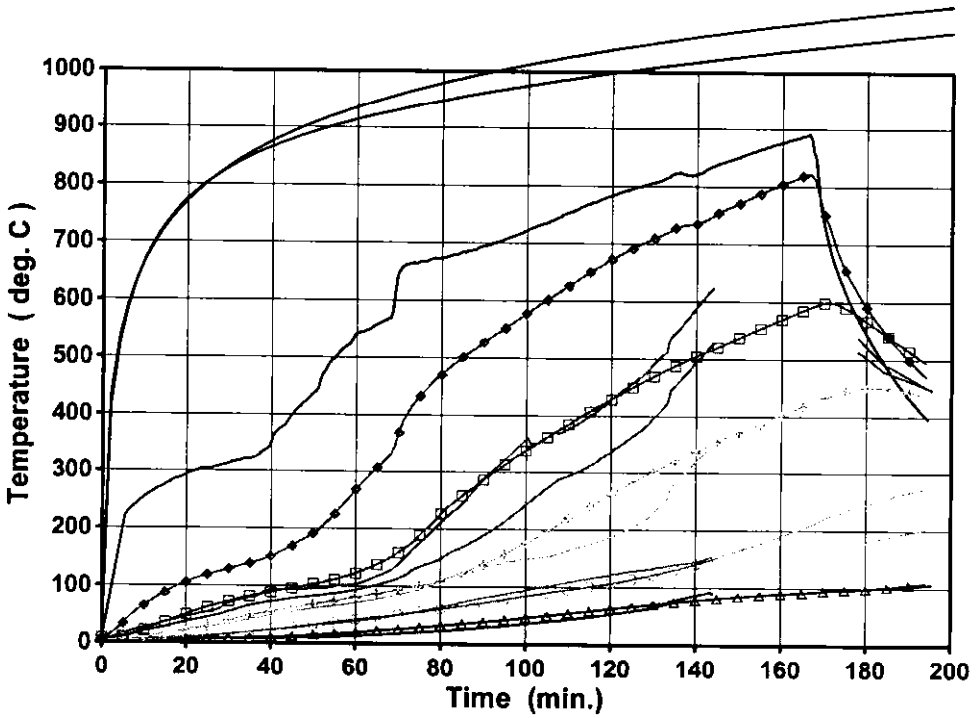

Figure 10. Temperature predictions in the slab rib compared to measured temperatures (EC2 normal weight concrete properties, 12 % moisture content)

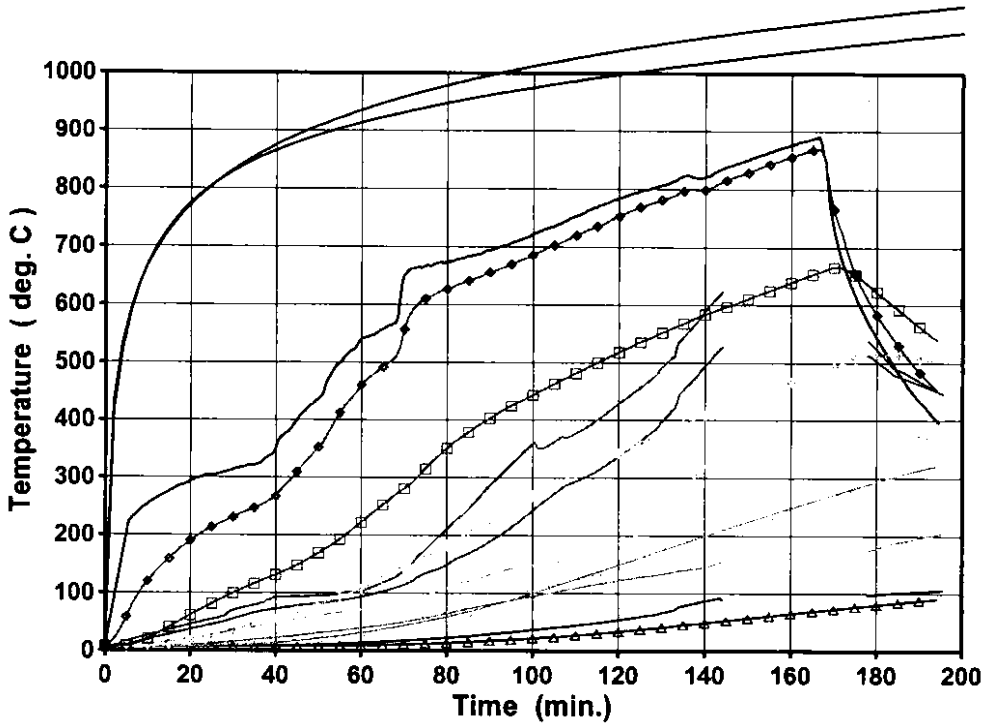

Figure 11. Temperature predictions in the slab rib compared to measured temperatures, light weight concrete properties and heat transfer parameters suggested by Lamont et al (2001)

Local buckling behaviour and strain-based effective widths of steel structures subjected to fire

Mario Fontana & Markus Knobloch
Swiss Federal Institute of Technology ETH Zurich, Institute of Structural Engineering IBK, Steel, Timber and Composite Structures, HIL D 36.1, ETH Hönggerberg, 8093 Zurich, Switzerland
mario.fontana@ethz.ch, markus.knobloch@ethz.ch

ABSTRACT

Local buckling and plastic cross sectional behaviour have a strong influence on the resistance of steel sections subjected to fire. Due to large strains required as a result of the distinct nonlinear material behaviour of steel at elevated temperatures, local buckling of steel members occurs at lower geometrical slenderness ratios in fire than for room temperature. However, large strains and plastification lead to a distinct increase of cross sectional capacity of thin-walled sections. Research indicates that the design methods for room temperature should not be adapted by changing the material properties only.

This paper presents a proposal for a structural model for steel plates in bending and compression at elevated temperatures. A strain-based formulation for effective widths considering plastic stress distribution and strain-dependent nonlinear material behaviour is developed to analyze the load-carrying capacity at elevated temperatures of steel plates supported on three or four sides.

The proposal is in good agreement with the results found using the finite-element approach. Using a finite-element program, geometrical and physical nonlinear calculations were performed. In a parametric study, the resistance of steel plates subjected on three and four sides, in bending and compression with variation of the geometrical slenderness *b/t* and steel temperature θ_a were calculated.

KEYWORDS: *fire resistance, fire engineering, steel, steel constructions, local buckling, local buckling in fire, effective widths, strain-based effective widths, plastic resistance, Eurocode*

NOTATION

Latin upper case letters	
$E_{a,\theta}$	Modulus of elasticity of steel at elevated temperature θ_a
$N_{pl_\varepsilon,\theta}$	Strain dependent plastic resistance for compression at elevated steel temperature θ_a
$M_{pl_\varepsilon,\theta}$	Strain dependent plastic resistance for bending at elevated steel temperature θ_a
Latin lower case letters	
a	Length of a plate
b	Width of a plate
t	Thickness of the plate
$b_{eff,\theta} = b_{e1,\theta} + b_{e2,\theta}$	Effective width at elevated steel temperature θ_a
$f_{p,\theta}$	Proportional limit for steel at elevated temperature θ_a
$f_{y,\theta}$	Yield strength of steel at elevated temperature θ_a
k	Plate buckling factor
$k_{E,\theta}$	Reduction factor for the slope of the linear elastic range
$k_{p,\theta}$	Reduction factor for proportional limit
$k_{y,\theta}$	Reduction factor for yield strength
Greek lower case letters	
$\alpha = a/b$	Ratio of length to width of a plate
ε	Strain, Reduction coefficient
$\varepsilon_{p,\theta}$	Strain at the proportional limit at elevated steel temperature θ_a
$\varepsilon_{y,\theta}$	Yield strain at elevated steel temperature θ_a
$\overline{\lambda}_p = \sqrt{f_y/\sigma_{cr}}$	Plate slenderness at ambient temperature
$\overline{\lambda}_{p,\theta,el}$	Plate slenderness at elevated steel temperature θ_a for elastic strains
$\overline{\lambda}_{p,\theta}$	Plate slenderness at elevated steel temperature θ_a for plastic strains
ρ_θ	Temperature dependent reduction factor for plate buckling
$\sigma_{cr,\theta}$	Temperature dependent critical buckling stress
$\sigma_\theta(\varepsilon)$	Strain dependent stress at elevated steel temperature θ_a
$\psi_\varepsilon = \frac{\varepsilon_{max}}{\varepsilon_{min}}$	Ratio between maximum and minimum strain distribution (tension positive)

INTRODUCTION

Knowledge about local buckling behaviour in the fire situation is necessary for an economic and safe use of steel structures. Steel members heat up quickly in case of fire because of their high section factors A/V and the good thermal conductivity of steel. Due to elevated temperatures in fire, the strength and stiffness of steel decreases rapidly. In addition to a good construction

practice for steel structures in fire as presented by Fontana [2] safe and economic formulas for the design of steel structures in fire are necessary.

Usually, simplified calculation formulas are used to prove the fire resistance of steel structures. Based on research results by Ranby [3] design formulas for class 4 cross sections are included in the new version of Eurocode 3 Part 1-2 [1] for example. The commonly used design method to calculate fire resistance of steel members considers uniform temperature-dependent material properties but uses the same resistance formulas as for ambient temperature design.

The decrease of the load-carrying capacity due to local buckling is usually considered using the effective widths method. This method for thin plates was developed by von Kármán [4]. The commonly used buckling curve was postulated by Winter [5].

This paper presents first the results of a parametric study of the load-carrying behaviour of steel plates at elevated temperatures in case of fire using the finite element approach. Based on these physical and geometrical nonlinear numerical calculations a novel design method will be developed in the second part. The new design method expands the well known effective widths method into plastic strain and stress distribution to calculate the load-carrying capacity of steel sections at elevated temperatures. These new strain-dependent effective widths are finally compared to the numerical results and the instructions of Eurocode 3 Part 1-2 [1].

CLASSIFICATION AND DESIGN ACCORDING TO EUROCODE 3-1-2 [1]

The cross sections are (as a simplification) often classified as for normal temperature design, although the effective yield strength $f_{y,\theta}$ at elevated temperature is reached for large, nonreversible strains $\varepsilon_{y,\theta} = 0.02$. The classification in fire design is then adjusted in comparison to ambient temperature design with a reduction factor 0.85:

$$\varepsilon = 0.85 \cdot \sqrt{\frac{235}{f_y}} \tag{1}$$

The correction value 0.85 results as a simplification from the reciprocal of the ratio between the temperature dependent reduction factors for the yield strength and the elastic modulus (table 1).

Table 1 Factors to adjust the plate slenderness at elevated temperatures (see [6] and [7])

Steel temperature θ_a	200 °C	300 °C	400 °C	500 °C	600 °C	700 °C	800 °C	≥900 °C
$\sqrt{k_{y,\theta}/k_{E,\theta}}$	1.05	1.12	1.20	1.14	1.23	1.33	1.11	0.94
$\frac{1}{\sqrt{k_{y,\theta}/k_{E,\theta}}}$	0.95	0.89	0.83	0.88	0.81	0.75	0.90	1.06

In function of the classification, the methods *elastic-elastic*, *elastic-plastic* (i.e. elastic calculation of forces and moments – plastic calculation of resistance) and *plastic-plastic* are commonly used in fire design of steel structures. The buckling resistance $N_{b,fi,t}$ and the moment resistance $M_{fi,\theta}$ is calculated with eq. (2) and (3).

$$N_{b,fi,t} = \chi_{fi} \cdot A \cdot k_{y,\theta} \cdot f_y \tag{2}$$

$$M_{fi,\theta} = k_{y,\theta} \cdot M_R \tag{3}$$

where χ_{fi} is the reduction factor for flexural buckling in the fire design situation, A is the area for class 1 to 3 sections and the effective area for class 4 sections, M_R is the plastic moment resistance of the gross cross section for normal temperature design for class 1 and 2 sections, the elastic moment resistance of the gross cross-section for normal temperature design for class 3 sections and the moment resistance calculated with the effective cross-section for class 4 sections and $k_{y,\theta}$ is the reduction factor for the yield strength of steel at temperature θ_a.

The reduction factors $k_{y,\theta}$, $k_{p,\theta}$ and $k_{E,\theta}$ to calculate the temperature dependent yield strength $f_{y,\theta}$, the proportional limit $f_{p,\theta}$, and elastic modulus $E_{a,\theta}$ for class 1 to 3 are shown in figure 1 on the left side. The effective widths method is well established for thin-walled steel structures and is also used in fire design. The effective widths take into account the decrease of the load-carrying capacity due to local buckling. The effective widths are calculated with the steel properties at room temperature and under consideration of the reduction factor ε as presented in eq. (1). The temperature dependent elastic modulus $E_{a,\theta}$ and the design stress $f_{p0.2,\theta}$ are calculated with the reduction factor for class 4 sections presented in figure 1 (right side). The yield strength is restricted to the stress according to 0.2% proof-strain. The resistance is calculated as the product of the effective widths and this plastic stress, although the effective widths are developed for elastic strains, without plastic, nonreversible strains.

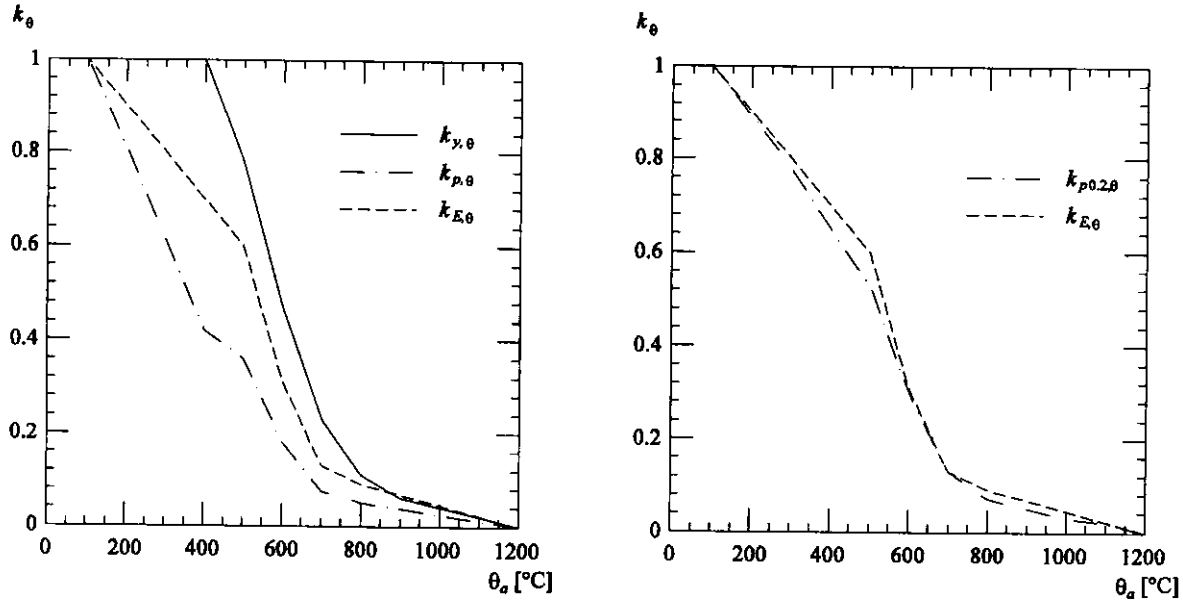

Figure 1 Reduction factors k_θ for class 1 to 3 sections (left) and class 4 sections (right) according to Eurocode 3 [1]

It is the aim of the presented research to review this procedure and to develop a new design method for steel members subjected to fire, taking into account local buckling effects. In a first step, the behaviour of steel plates supported on three and four sides with constant elevated temperatures is studied.

STRUCTURAL BEHAVIOUR OF STEEL PLATES IN BENDING AND COMPRESSION AT ELEVATED TEMPERATURES

Using the finite element program Abaqus [8] geometrical and physical nonlinear calculations were performed. In a parametric study, the internal forces $N/N_{pl,\varepsilon,\theta}$ and moments $M/M_{pl,\varepsilon,\theta}$ of steel plates supported on three and four sides, in bending and compression with variation of the geometrical slenderness b/t and steel temperature θ_a between 200 °C and 1100 °C were calculated. All plates were loaded with different strain ratios ψ_ε at the edges. The length to width ratios α and the shapes of the pre-deformation were taken from the lowest eigenvalue according to linear theory.

The following figures present examples of forces and moments considering strain dependent stresses for steel plates simply supported on three and four sides in bending and compression. The results for steel plates simply supported on four sides in compression for a steel temperature of 500 °C were presented in Fontana/Knobloch [9]. These results were extended to plates supported on three sides and plates in bending. Taking local buckling into account, the forces and moments are normalized to the corresponding plastic resistance.

$$N_{pl_\varepsilon,\theta} = \begin{cases} b \cdot t \cdot f_{p,\theta} & if\ \varepsilon \le \varepsilon_{p,\theta} \\ b \cdot t \cdot \sigma_\theta(\varepsilon) & if\ \varepsilon_{p,\theta} < \varepsilon < \varepsilon_{y,\theta} \end{cases} \tag{4}$$

$$M_{pl_\varepsilon,\theta} = \begin{cases} \frac{b^2}{4} \cdot t \cdot f_{p,\theta} & if\ \varepsilon \le \varepsilon_{p,\theta} \\ \frac{b^2}{4} \cdot t \cdot \sigma_\theta(\varepsilon) & if\ \varepsilon_{p,\theta} < \varepsilon < \varepsilon_{y,\theta} \end{cases} \tag{5}$$

The strain-dependent stresses at the elevated temperature θ_a are calculated with equations 6 to 9 (according to Eurocode 3 [1]).

$$\sigma_\theta(\varepsilon) = f_{p,\theta} - c + (b/a) \cdot \left[a^2 - (\varepsilon_{y,\theta} - \varepsilon)^2\right]^{1/2} \tag{6}$$

with

$$a^2 = (\varepsilon_{y,\theta} - \varepsilon_{p,\theta}) \cdot (\varepsilon_{y,\theta} - \varepsilon_{p,\theta} + c/E_{a,\theta}) \tag{7}$$

$$b^2 = c \cdot (\varepsilon_{y,\theta} - \varepsilon_{p,\theta}) \cdot E_{a,\theta} + c^2 \tag{8}$$

$$c = \frac{(f_{y,\theta} - f_{p,\theta})^2}{(\varepsilon_{y,\theta} - \varepsilon_{p,\theta}) \cdot E_{a,\theta} - 2(f_{y,\theta} - f_{p,\theta})} \tag{9}$$

As examples, figures 2, 4, and 5 show forces and moments in relation to the resistance calculated with the strain-dependent stresses $\sigma_\theta(\varepsilon)$ and full sectional area for steel plates simply supported on three and four sides in pure compression $\psi_\varepsilon = 1.0$ and bending $\psi_\varepsilon = -1.0$ at elevated temperatures. The figures mentioned confirm that the related load-carrying capacity decreases after exceeding the proportional limit $\varepsilon_{p,\theta}$ as known at ambient temperature. However, the maximum of the load-carrying capacity is not reached for the proportional strain $\varepsilon_{p,\theta}$ due to the nonlinear strain-stress relationship of steel at elevated temperatures. This can be seen from

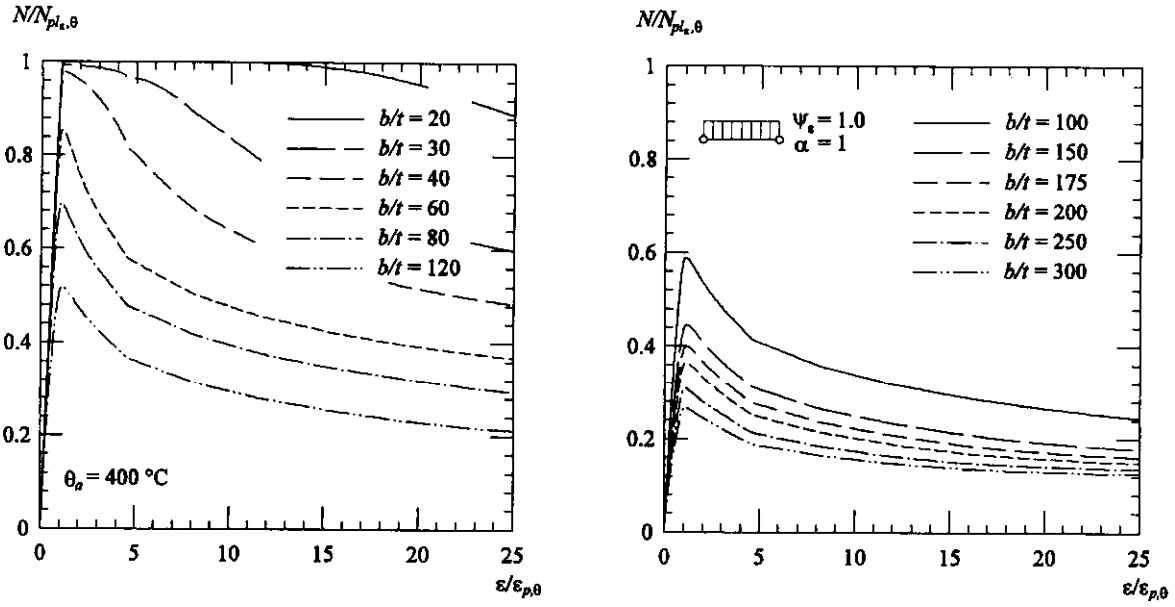

Figure 2 Relative forces for four-sided simply supported plates in compression $\psi_\varepsilon = 1.0$ at a steel temperature of 400°C

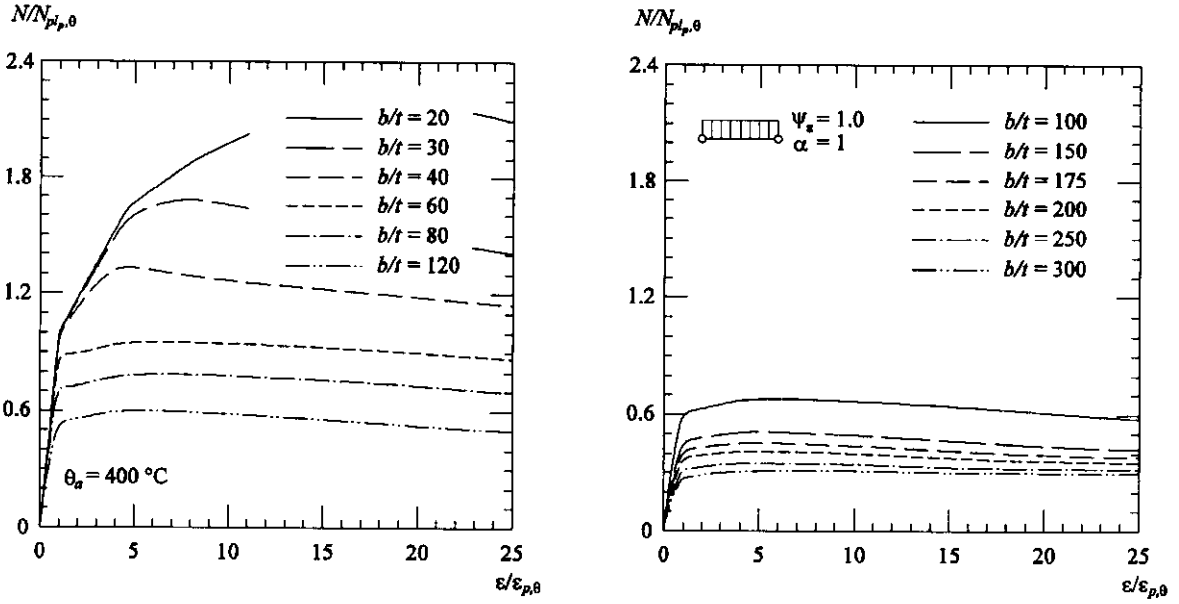

Figure 3 Forces in relation to the resistance $N_{pl,p,\theta}$ at the proportional strain $\varepsilon_{p,\theta}$ for four-sided simply supported plates in compression $\psi_\varepsilon = 1.0$ at a steel temperature of 400°C

figure 3, where the resistance is drawn in relation to the resistance $N_{pl,p,\theta}$ at the proportional strain $\varepsilon_{p,\theta}$.

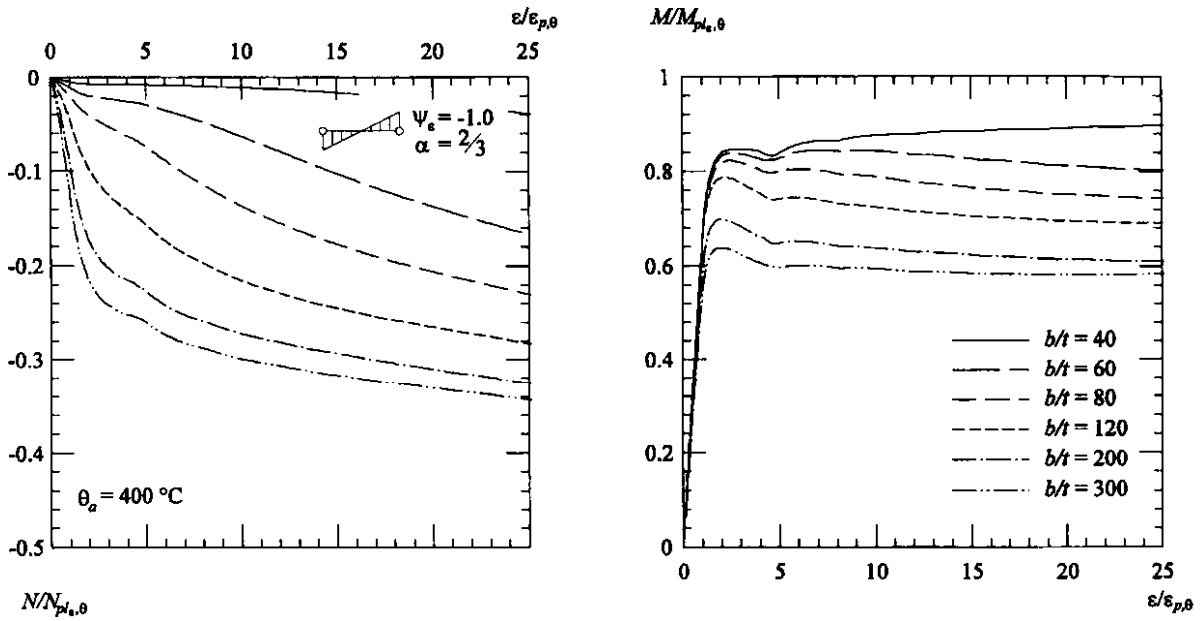

Figure 4 Relative moments and resulting tension forces for four-sided simply supported plates in bending $\psi_\varepsilon = -1.0$ at a steel temperature of 400°C

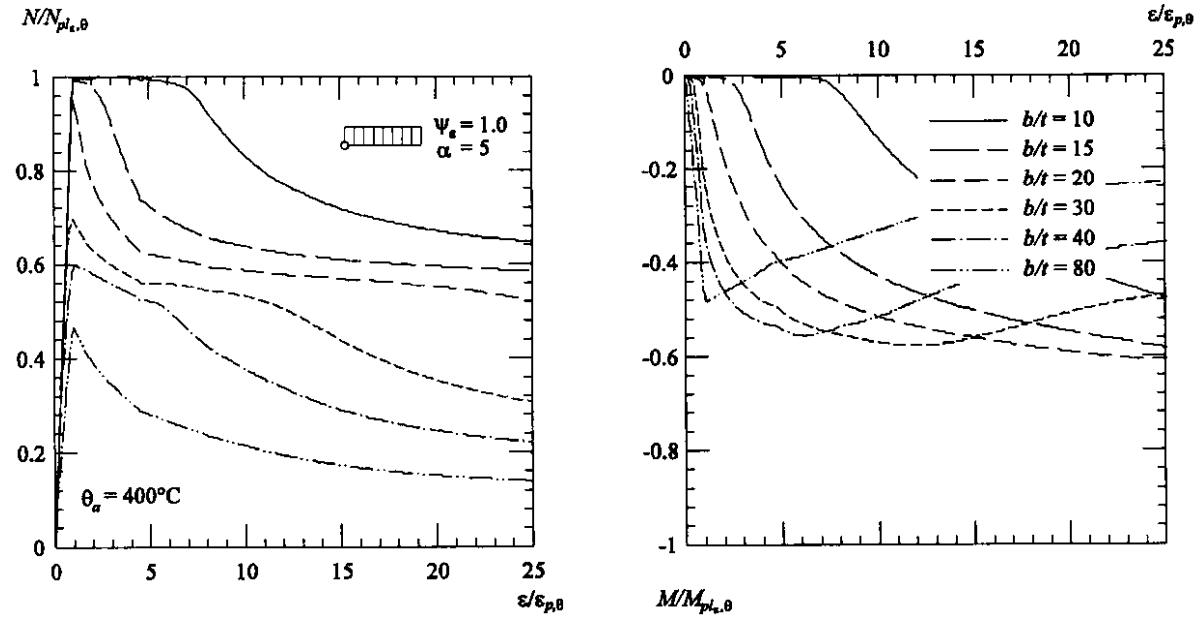

Figure 5 Relative forces and resulting moments for three-sided simply supported plates in compression $\psi_\varepsilon = 1.0$ at a steel temperature of 400°C

Figure 6 shows the relative forces and moments for steel plates simply supported on three sides with a geometrical slenderness $b/t = 20$ at different temperatures.

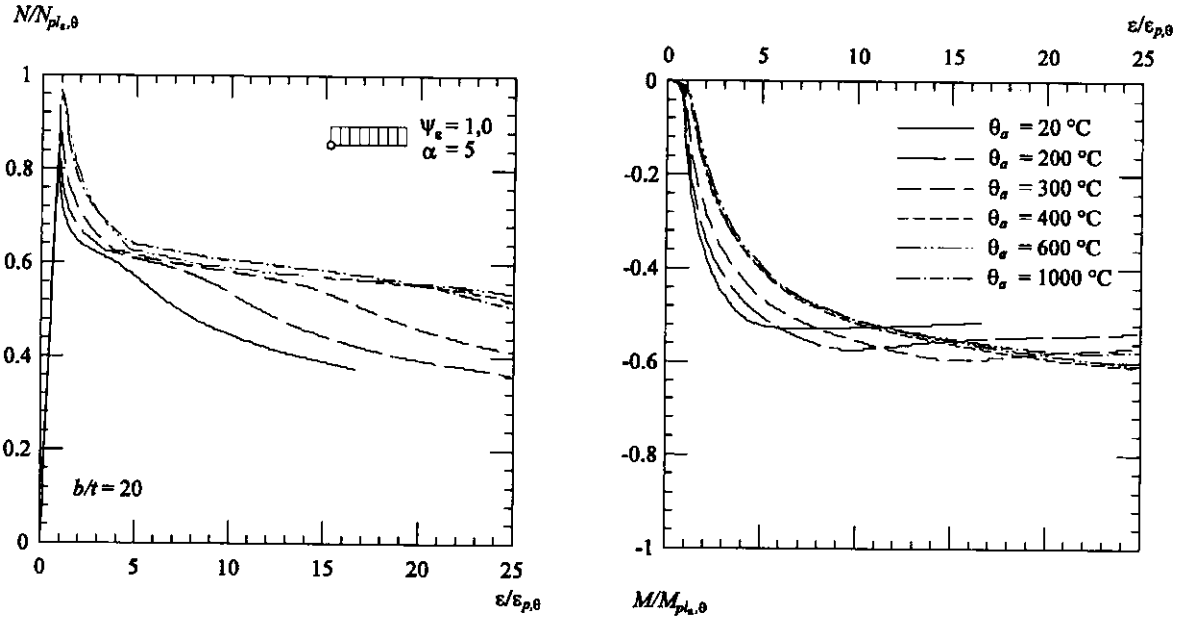

Figure 6 Relative forces and resulting moments for three-sided simply supported plates in compression $\psi_\varepsilon = 1.0$ at different temperatures

STRAIN-BASED FORMULATION FOR EFFECTIVE WIDTHS AT ELEVATED TEMPERATURES

For the design of steel structures the methods *elastic-elastic*, *elastic-plastic*, and *plastic-plastic* are commonly used. Often three cross section classes are related to these methods. Normally, a fourth class exists for thin-walled cross sections. The effective widths method takes into account the decrease of the load-carrying capacity due to local buckling for these cross-sections. This method for thin plates was developed by von Kármán [4]. He replaced the real nonlinear stress distribution in a buckled plate with a uniform stress at the effective width b' located at the boarders of the plate. Winter [5] noticed from experiments on C-sections that imperfect plates do not reach the load-carrying capacity according to the theory of von Kármán. Therefore, Winter developed the well known buckling curve (Winter-curve). The classification and the associated b/t-ratios are a result of the traditional stress-based design and are required to satisfy the different ductility requirements. In the case of fire design, a strain-based design is more efficient and precise, due to the nonlinear material behaviour. Every cross-section has ductility and can develop local buckling. Because of local buckling, the moment-curvature graph of each cross-section has a decreasing branch as can be seen at the left side of figure 7. The strain at which local buckling occurs is different. Class 4 members lose stability at small strains below the proportional strain $\varepsilon_{p,\theta}$, while class 1 members may buckle at strains much greater than yield strain ε_y at room temperature. Due to stress-based design, the whole load-deflection behaviour with the decreasing branch cannot be described. However, this would be necessary to determine ductility.

As can be seen from the stress-strain relationship in figure 7, an increase of strain has little or no effect on the corresponding stress for strains greater than the proportional strain at room temperature: $\theta_a = 20°C \rightarrow \sigma_{20°C}(\varepsilon_p) = \sigma_{20°C}(n \cdot \varepsilon_p)$. However, it leads to an important increase of

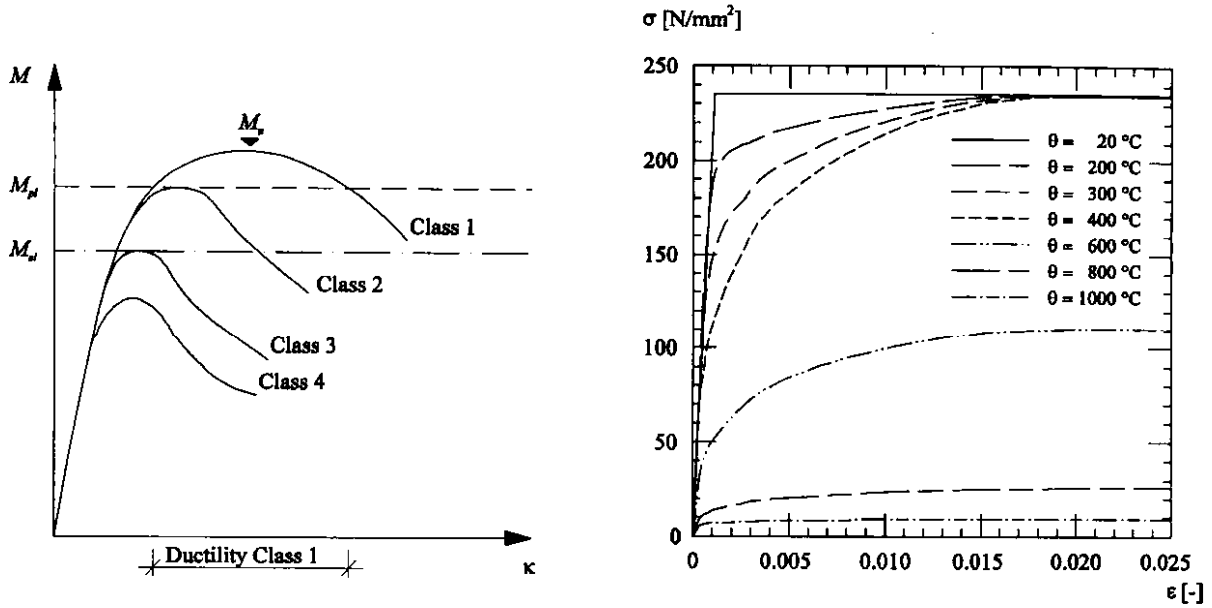

Figure 7 Moment-curvature graph at room temperature for class 1 to 4 members (left) and stress-strain relationship for steel S235 at elevated temperatures according to EC3 [1]

stress for higher temperatures: $\theta_a >> 20°C \rightarrow \sigma_\theta(\varepsilon_{p,\theta}) < \sigma_\theta(n \cdot \varepsilon_{p,\theta})$. Therefore, a limitation to reversible, elastic strains using strictly elastic design methods would lead to results well below the load-carrying capacity on the one hand side. On the other side, the effective widths established in Eurocode 1 part 1-1 [10] and part 1-3 [11] for example were developed for elastic strains without plastic, nonreversible strains. That is the reason why the method cannot be adapted for fire design directly.

The load-carrying capacity of whole cross-sections composed of several steel plates (e.g. I-sections, C-sections) are often not reached when the steel plate with the lowest buckling strain of the cross section reaches its ultimate capacity. It is e.g. possible that the load-carrying capacity still increases after buckling of the flange of an I-section in bending, due to plastification of the web. In fire conditions, four main structural effects interact for a composed steel section in bending, whose steel plates buckle after reaching the elastic limit ($\bar{\lambda}_p = 0.673$):

- Resistance decreases because of local buckling of the steel plates in bending and compression,
- Resistance increases because of plastifications in bending (see fig. 7 left),
- Resistance increases because of the temperature dependent stress-strain relationship (see fig. 7 right), and
- Resistance changes because of thermal strains.

The whole load-deflection behaviour of steel plates and cross-sections can be described using a yield line approach or a strain-based approach for the effective widths method. The use of effective widths requires the same strains at common longitudinal edges of steel plates of a composed cross-section. In contrast to fire design with nonlinear stress-strain relationship of steel at elevated temperatures, it is possible to guarantee this requirement in room temperature

design by defining a marginal strain. The strain-based effective widths have to be calculated for this marginal strain.

Design methods and standards normally apply only effective widths based on an elastic stress distribution without plastification as is shown in figure 8 (left). This method can be described as *elastic-elastic-reduced.* In this case, the marginal strain for room temperature design is equivalent to the proportional and yield strain ε_y at ambient temperature.

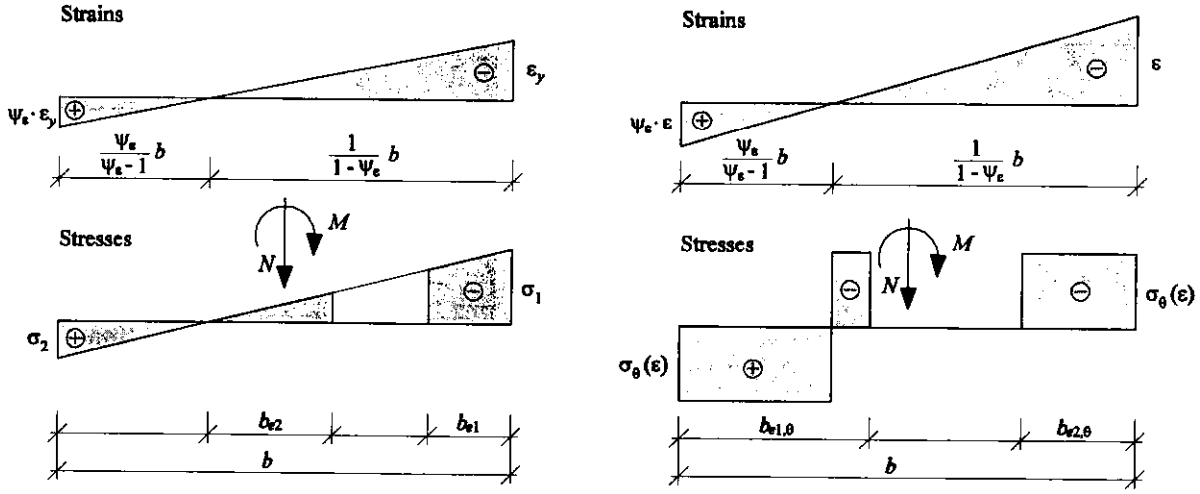

Figure 8 Effective widths based on the method *elastic-elastic* (left) and effective widths with plastic stress distribution at elevated temperatures (right)

Effective widths based on plastic strain and stress distribution are unusual, although the load-carrying capacity of steel plates is reached after plastification of some parts of the cross section in bending and compression. Further, design methods with plastic stress and strain distributions got important. Effective widths for the methods *elastic-plastic-reduced* and *plastic-plastic-reduced* must be calculated according to the increasing demand on the rotation capacity: $\varepsilon_{marginal_{EER}} < \varepsilon_{marginal_{EPR}} < \varepsilon_{marginal_{PPR}}$.

Marginal strain limitations lead to uneconomic results in fire design. Using a strain-based approach, marginal strain requirements are not necessary. The load-carrying capacity of a cross-section can be calculated by means of iterations at different strain rates.

Effective widths for steel plates supported on three and four sides in bending and compression with plastification at elevated temperatures are developed below. The structural model using beam theory and effective widths reflects to the results from the nonlinear numerical calculations based on the finite element method presented previously. For plastic strain and stress distribution as shown in figure 8 (right), the following equations were found.

$$\frac{N}{N_{pl_\varepsilon,\theta}} = \frac{b_{e1,\theta}}{b} + \frac{b_{e2,\theta}}{b} - 2 \cdot \frac{\widetilde{\psi}_\varepsilon}{\widetilde{\psi}_\varepsilon - 1} \tag{10}$$

$$\frac{M}{M_{pl_\varepsilon,\theta}} = 2 \cdot \frac{b_{e2,\theta}}{b}\left(1 - \frac{b_{e2,\theta}}{b}\right) - 2 \cdot \frac{b_{e1,\theta}}{b}\left(1 - \frac{b_{e1,\theta}}{b}\right) + 4 \cdot \frac{\widetilde{\psi}_\varepsilon}{\widetilde{\psi}_\varepsilon - 1}\left(1 - \frac{\widetilde{\psi}_\varepsilon}{\widetilde{\psi}_\varepsilon - 1}\right) \tag{11}$$

with

$$\widetilde{\psi}_\varepsilon = \begin{cases} 0 & if\ 0 \le \psi_\varepsilon \le 1 \\ \psi_\varepsilon & if\ \psi_\varepsilon < 0 \end{cases} \tag{12}$$

The effective widths $b_{e1,\theta}$ and $b_{e2,\theta}$ were calculated by solving the nonlinear system of equations (10) and (11) from the internal forces and moments found with the finite element method and as given above. The effective widths depended on the slenderness b/t, the ratio of strains ψ_ε at the edges, and steel temperature θ_a. For steel plates supported on three sides an effective width is arranged on the non-supported side to get better results as proposed by Priebe [12] for elastic effective widths at room temperature.

In the figures 9 to 11 below the effective widths $b_{eff,\theta}$ and $b_{e2,\theta}$ for three- and four-sided simply and fixed supported steel plates calculated numerically using the program Abaqus [8] are shown in dotted lines as examples. They are presented in function of the steel temperature θ_a, the plate slenderness $\bar{\lambda}_p$ at room temperature, the strain ratio ψ_ε at the edges, and the related strain $\varepsilon/\varepsilon_{p,\theta}$. Furthermore, the graphs include the temperature dependent strain-based effective widths for steel plates supported on three and four sides in bending and compression calculated with the new design approach (continuous line) presented in table 2 and 3.

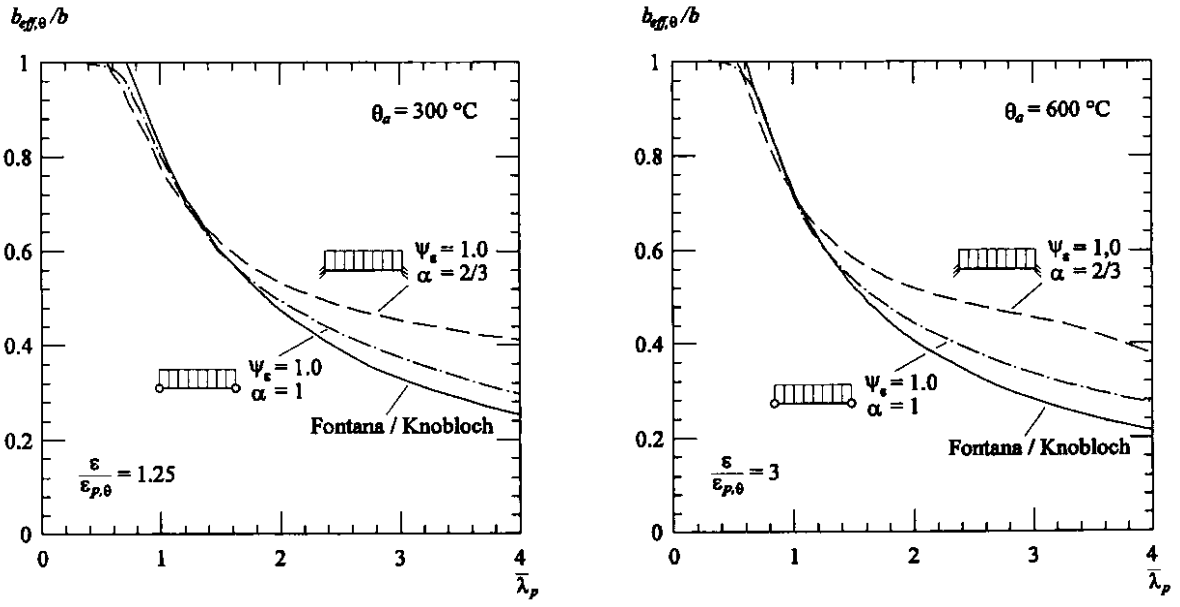

Figure 9 Effective widths for steel plates supported on four sides in compression at elevated temperatures

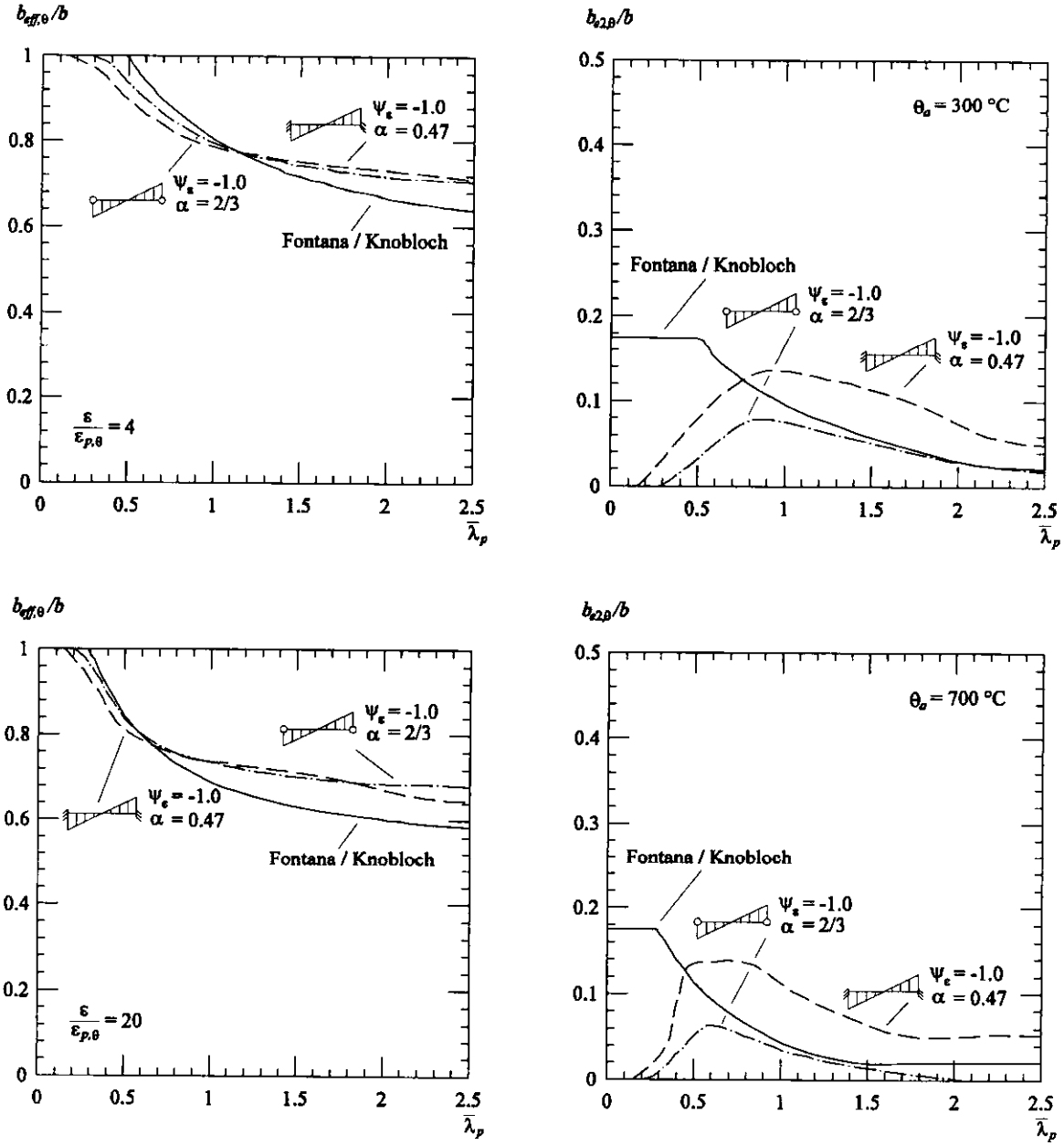

Figure 10 Effective widths for steel plates supported on four sides in bending at elevated temperatures

The new strain-based design method gives satisfactory results similar to the results from nonlinear calculations based on the finite element approach. Using Winter's formulation leads to conservative results for thin plates supported on three sides in compression. Large deformations and a basic change of the buckling mode can be accepted under fire conditions. Therefore, the load-carrying capacity does not need to be limited because of serviceability considerations included unconsciously in the Winter's formula. The use of a less conservative buckling curve for three-sided supported steel plates in fire is possible.

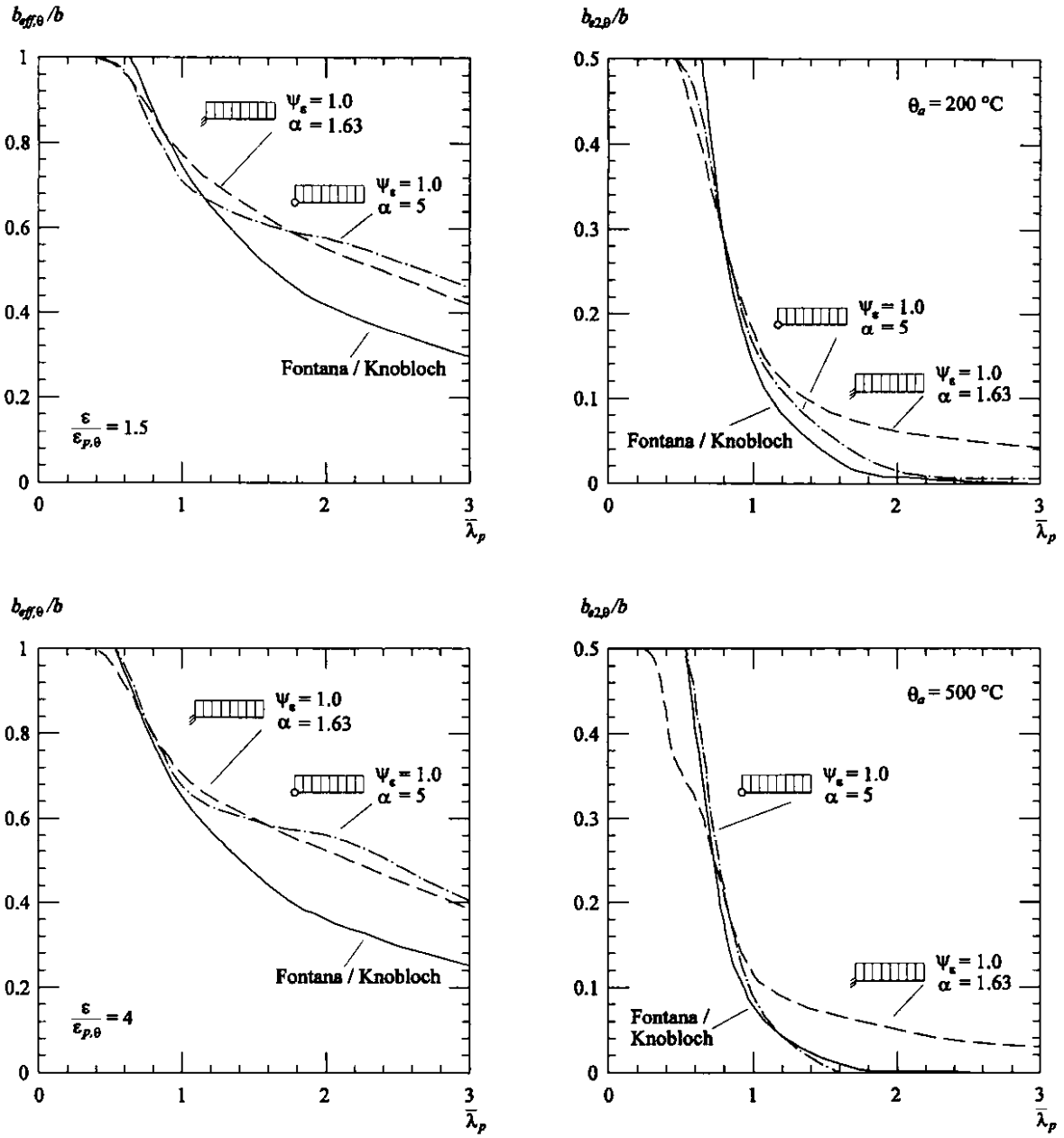

Figure 11 Effective widths for steel plates supported on three sides in compression at elevated temperatures

The well-established effective widths method is normally based on stresses within the elastic limit. Using a strain-based formulation as shown in tables 2 and 3, the method can be extended into the plastic strain range, which makes it more suitable for fire conditions with thermal strains and elevated temperatures. Strain-based formulations were postulated by Scheer/Maier [13] for an economic and realistic plastic design of steel structures.

At the top of table 2 the effective widths for four-sided supported compression elements (ψ_ε = 1.0) are specified. Below, the effective widths at elevated temperatures are given for elements in bending (ψ_ε = -1.0). The formulas for three-sided supported compression elements (ψ_ε = 1.0) are given in table 3. As mentioned above, an effective width $b_{e2,\theta}$ is arranged at the non-supported side.

Table 2 Effective widths for four-sided supported steel plates at elevated temperatures

Strain and stress distribution	Effective widths
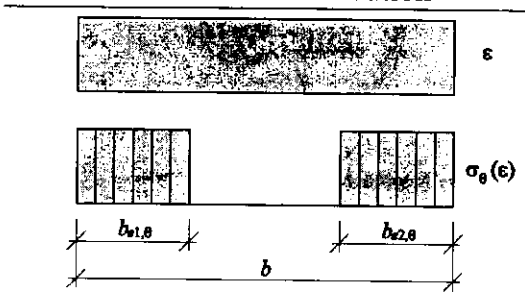	$\frac{b_{eff,\theta}}{b} = \rho_\theta$ $\frac{b_{e2,\theta}}{b} = \frac{\rho_\theta}{2}$
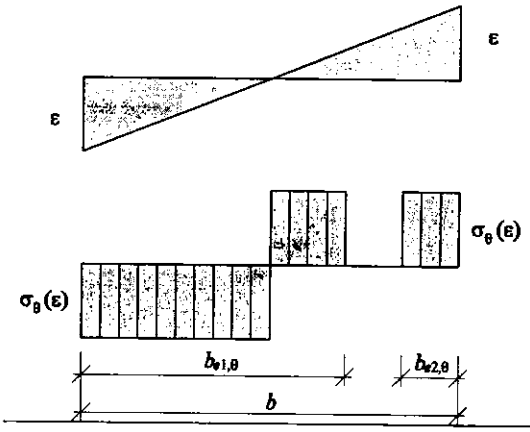	$\frac{b_{eff,\theta}}{b} = \frac{\rho_\theta - \psi_\varepsilon}{1-\psi_\varepsilon}$ $\frac{b_{e2,\theta}}{b} = \frac{\left(3-1.25\sqrt{\frac{\bar{\lambda}_{p,\theta}}{0.673}}\right)\cdot\rho_\theta}{10}$ $\bar{\lambda}_{p,\theta} \geq 0.673$ $\frac{b_{e2,\theta}}{b} \geq 0.02$

Table 3 Effective widths for three-sided supported steel plates at elevated temperatures

Strain and stress distribution	Effective widths
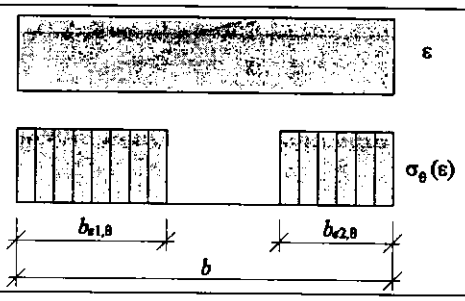	$\frac{b_{eff,\theta}}{b} = \rho_\theta$ $\frac{b_{e2,\theta}}{b} = \frac{0.173}{\bar{\lambda}_{p,\theta}^{2+\bar{\lambda}_{p,\theta}}}$

The well-known rules for the plate slenderness for elastic strains at room temperature can be used for elevated temperatures considering temperature-dependent material properties.

$$\bar{\lambda}_{p,\theta,el} = \sqrt{\frac{\varepsilon}{\varepsilon_{p,\theta}}}\cdot\bar{\lambda}_{p,\theta} = \sqrt{\frac{\varepsilon}{\varepsilon_{p,\theta}}}\cdot\sqrt{\frac{f_{p,\theta}}{\sigma_{cr,\theta}}} \qquad if\ \varepsilon \leq \varepsilon_{p,\theta} \tag{13}$$

The temperature- and strain-dependent plate slenderness for plastic strains $\varepsilon > \varepsilon_{p,\theta}$ are shown in figure 12 and presented in table 4 as an example for a steel temperature of 400°C. The temperature-dependent elastic critical buckling stress can be calculated using eq. (14).

$$\sigma_{cr,\theta} = k \cdot \frac{\pi^2 \cdot E_{a,\theta}}{12(1-\nu^2)} \cdot \left(\frac{t}{b}\right)^2 \tag{14}$$

The reduction factor ρ_θ is determined using Winter's formulation with eq. (15).

$$\rho_\theta = \frac{\bar{\lambda}_{p,\theta} - 0.22}{\bar{\lambda}_{p,\theta}^2} \tag{15}$$

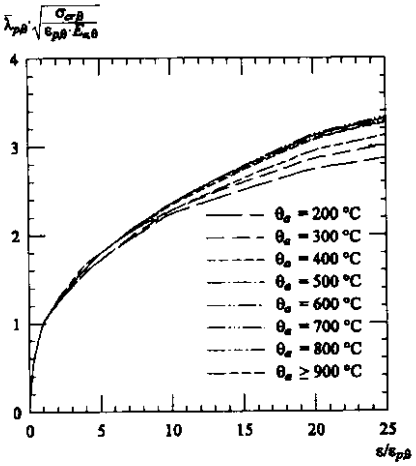

Figure 12 Slenderness at elevated temperatures

Table 4 Slenderness at a steel temperature of 400°C

Strain	Slenderness at 400 °C
$\varepsilon_{p,\theta} < \varepsilon \leq 5\varepsilon_{p,\theta}$	$\bar{\lambda}_{p,\theta} = \sqrt{\frac{\left[\varepsilon_{p,\theta} + 0.55 \cdot (\varepsilon - \varepsilon_{p,\theta})\right] \cdot E_{a,\theta}}{\sigma_{cr,\theta}}}$
$5\varepsilon_{p,\theta} < \varepsilon \leq 10\varepsilon_{p,\theta}$	$\bar{\lambda}_{p,\theta} = \sqrt{\frac{\left[3.2\varepsilon_{p,\theta} + 0.45 \cdot (\varepsilon - 5\varepsilon_{p,\theta})\right] \cdot E_{a,\theta}}{\sigma_{cr,\theta}}}$
$10\varepsilon_{p,\theta} < \varepsilon \leq 20\varepsilon_{p,\theta}$	$\bar{\lambda}_{p,\theta} = \sqrt{\frac{\left[5.45\varepsilon_{p,\theta} + 0.4 \cdot (\varepsilon - 10\varepsilon_{p,\theta})\right] \cdot E_{a,\theta}}{\sigma_{cr,\theta}}}$
$\varepsilon > 20\varepsilon_{p,\theta}$	$\bar{\lambda}_{p,\theta} = \sqrt{\frac{\left[9.57\varepsilon_{p,\theta} + 0.25 \cdot (\varepsilon - 20\varepsilon_{p,\theta})\right] \cdot E_{a,\theta}}{\sigma_{cr,\theta}}}$

COMPARISON BETWEEN THE NEW DESIGN APPROACH AND THE SIMPLIFIED FORMULATIONS ACCORDING TO EUROCODE 3 [1]

The comparison of the ultimate values of the related internal forces $N_{max}/N_{pl,\theta}$ and $M_{max}/M_{pl,\theta}$ for steel plates supported on four sides are presented in figures 13 and 14. The graphs compare the results calculated with Abaqus [8], the results calculated with the new design approach presented in table 2, and the results calculated with the effective widths according to Eurocode 3 part 1.2 (including annex E) [1]. Additionally, the results calculated with the effective widths according to Eurocode 3 considering the temperature-dependent slenderness $\bar{\lambda}_{p,\theta,EC3}$ (eq. 16) are shown.

$$\bar{\lambda}_{p,\theta,EC3} = \sqrt{\frac{k_{y,\theta}}{k_{E,\theta}}} \cdot \sqrt{\frac{f_y}{\sigma_{cr}}} \tag{16}$$

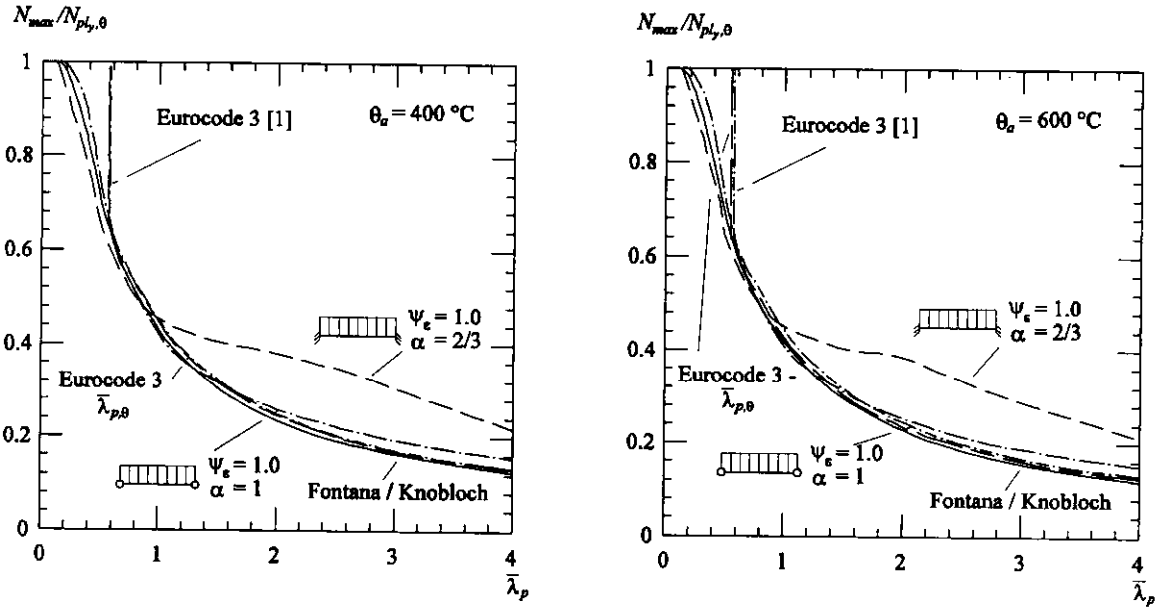

Figure 13 Temperature-dependent ultimate values of the related forces for steel plates supported on four sides in compression

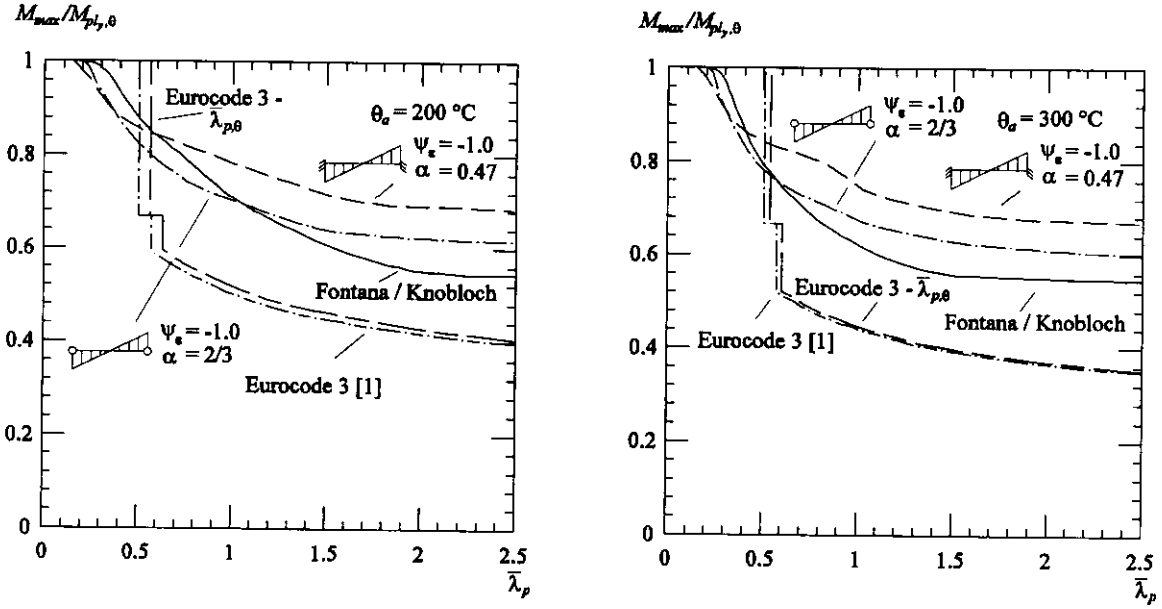

Figure 14 Temperature-dependent ultimate values of the related moments for steel plates supported on four sides in bending

The new design approach gives satisfactory results similar to the results from nonlinear calculations based on the finite element method. The effective widths calculated with Eurocode 3 [1] lead to relative forces higher than the results of the parametric study using the finite element method for steel plates $\bar{\lambda}_p \leq 0.57$ in compression ($\psi_\varepsilon = 1.0$) at elevated temperatures (fig. 13). The regulations of Eurocode 3 are unsafe for class 1 and 2 sections in compression at elevated temperatures. The strains required to obtain almost the plastic resistance lead to

buckling due to the nonlinear material behaviour. The resistance calculated according to Eurocode 3 for steel temperatures $\theta_a \leq 400°C$ and plate slenderness $\bar{\lambda}_p \leq 0.85 \cdot 0.673 = 0.572$ is not different from the fully plastic resistance at room temperature. However, the results gained from the parametric study show that there is a decrease in the ultimate load-carrying capacity for temperatures above 100 °C and slenderness $\bar{\lambda}_p > 0.3$.

Due to an elastic approach the results of Eurocode for thin steel plates (class 3 and 4) in bending are uneconomic (fig. 14). The resistance calculated with Eurocode 3 for class 1 and 2 members ($b/t \leq 0.85 \cdot 83 = 71$) in bending at steel temperatures below 400°C are not reached in the parametric study.

The strain-dependent ultimate resistance of separated steel plates (fig. 13 and 14) cannot be used directly to calculate the resistance of a cross-section composed of several plates. The ultimate resistance of all plates of a cross-section are reached together only in special cases. Generally, the different plates have different slenderness ratios, boundary conditions, and strain ratios. Therefore, they reach their ultimate capacity at different strains. Due to the requirement, that the strains of a composed section at common longitudinal edges must be the same, it is necessary that the load-carrying capacity of a composed section is calculated using an iterative procedure.

CONCLUSIONS

Local buckling and capacity resulting from plastic cross sectional behaviour have a strong influence on the resistance of all steel section classes (class 1 to 4) subjected to fire. Local buckling depends on strains primarily. In addition to the distinctly nonlinear material behaviour of steel at elevated temperatures and due to the large strains required to obtain almost full plastic resistance in fire conditions, local buckling occurs below the Winter's limit of $\bar{\lambda}_p \leq 0.673$. This paper presents a new design approach for steel sections subjected to fire and local buckling. It uses a strain-based formulation for effective widths considering a plastic stress distribution. It is applied to analyze the load-carrying capacity of steel plates supported on three or four sides at elevated temperatures. The design method is in good agreement with the results obtained using the finite element method. Comparison with numerical calculations shows that the well known design methods for room temperature should not be directly used for fire conditions without basic changes. The assumption of a plastic strain and stress distribution combined with the highly nonlinear material behaviour gives good results. A main benefit of the new design approach is that a classification of cross-sections is not absolutely necessary in fire conditions.

The ongoing research aims at determining the influence of local buckling and thermal stresses in fire conditions on the load-carrying capacity of cross-sections composed of several steel plates. Furthermore, it is the objective to develop a design method based on the strain-dependent effective widths presented in this paper considering thermal stresses and temperature gradients.

REFERENCES

[1] prEN 1993-1-2, *Eurocode 3: Design of steel structures – part 1.2: General rules Structural fire design*, Stage 49 draft, CEN, Brussels, 2003

[2] Fontana Mario, "Beispiele für richtiges Konstruieren für den Brandfall". [Good construction practice for steel structures subjected to fire], *Stahlbau* 65, pp. 60-63, 1996

[3] Ranby Anders, *Structural Fire Design of Thin Walled Steel Sections*, Licentiate Thesis, Luleå University of Technology, 1999

[4] von Kármán T., Sechler E.E., Donnell L.H., "The strength of thin plates in compression", *Transactions ASME* 54, p. 53-57, 1932

[5] Winter G., "Strength of thin steel compression flanges", *Transactions ASCE* 112, p. 527-554, 1947

[6] EKS – Technischer Ausschuss TC3 – Brandsicherheit von Stahlbauten: EKS No 89, *Feuerwiderstand von Bauteilen aus Stahl (Auf der Grundlage der ENV 1993 Teil 1-2 „Eurocode 3, Teil Brandschutz)*, 1995

[7] Fontana Mario, „Das Euronomogramm – ein praktisches Hilfsmittel zur Berechnung des Feuerwiderstandes von Bauteilen aus Stahl nach Eurocode 3", *Stahlbau* 65, pp. 57-59, 1996

[8] Abaqus, Version 6.3 and 6.4, Hibitt, Karlsson & Sorensen, Inc. 2003

[9] Fontana M., Knobloch M., „Load-carrying Behaviour of Thin-Walled Steel Sections subjected to Fire", In: *Proceedings for the Second International Conference on Structural Engineering*, Cape Town, South Africa, Accepted to be published, 2004

[10] prEN 1993-1-1, *Eurocode 3: Design of steel structures – part 1.1: General rules and rules for buildings*, Stage 49 draft, CEN, Brussels, 2003

[11] EN 1993-1-3, *Eurocode 3: Design of steel structures – part 1.3: General rules Supplementary rules for cold-formed members and sheeting*, Stage 34 draft, CEN, Brussels 2004

[12] Priebe Jürgen, *Die Methode der wirksamen Breiten und ihre Verwendung zur Berechnung der Tragfähigkeit dünnwandiger Querschnitte aus Stahl*, PhD Thesis, Dortmund, 1994

[13] Scheer J., Maier W., „Zu einer dehnungsorientierten Bemessung stählerner Stabtragwerke", In: *Festschrift H. Duddeck*, Institut für Statik, TU Braunschweig, pp. 251-270, 1980

BEHAVIOR OF WEB PANEL UNDER SHEAR AT HIGH TEMPERATURE

V. Vimonsatit
Nanyang Technological University, School of Civil and Environmental Engineering, Blk N1, #1A-37, Nanyang Avenue, Singapore 639798.
Cvanissorn@ntu.edu.sg
K. H. Tan
Nanyang Technological University, School of Civil and Environmental Engineering, Blk N1, #1A-37, Nanyang Avenue, Singapore 639798.
CKHTAN@ntu.edu.sg
Z. H. Qian
Nanyang Technological University, School of Civil and Environmental Engineering, Blk N1, #1A-37, Nanyang Avenue, Singapore 639798.
Czhqian@pmail.ntu.edu.sg

ABSTRACT

This paper presents the results from the experimental work of steel plate girders loaded primarily in shear at elevated temperature. The test girders were grouped into 5 series, that is, two series were hot-rolled steel universal column sections and the other three were fabricated sections. One girder from each series was tested under ambient temperature condition, and the other three at isothermal conditions, namely, at 400, 550, and 700°C.

The tests were to investigate the shear buckling behavior, the diagonal web tensile field action, and the development of plastic hinge mechanism in the flange plates of the girder panels. The experimental results were then compared with analytical and numerical finite element predictions. The reported test results are believed to be among the first of its kind in the field of fire resistance of steel members. The knowledge gained from both experimental and analytical works hopefully will shed some light on the joint-panel shear behavior in a steel beam-to-column connection.

KEYWORDS: *plate girder, shear strength, fire resistance of steel, shear buckling*

INTRODUCTION

The past three decades have seen the progressive development of investigations for predicting the failure load of plate girders under shear at ambient temperature. These investigations can be extended to the shear component in a steel beam-to-column connection at elevated temperature. The mechanical behavior of joint-panel shear deformation has been investigated by several researchers at ambient temperature [1] [2] [3]. However, this paper presents only the experimental behaviour of such beams at elevated temperature.

In general, to gain a better understanding of the structural performance in fire, it is necessary to conduct fire resistance tests of structure components [4]. However, in the area of plate girder research, there is still a lack of experimental work under fire conditions. This information is also useful as a few beams in the Cardington tests exhibited shear failure mode near the supports [4]. This also provides the motivation for the authors' on-going work.

An analytical model has been developed by the authors to calculate the shear strength of plate girder web panels predominantly loaded in shear at elevated temperature [5]. The model has been verified against finite element simulations. An experimental program has also been conducted by the authors to study the post-buckling capacity of the girder at elevated temperature [6]. Further experimental work on the plate girders is currently conducted to study the axial restraint effect on the plate buckling and post-buckling behavior.

Current work presents an experimental investigation of steel girders loaded primarily in shear at elevated temperature. The test girders were grouped into 5 series, namely, TG1, TG2, TG3, TG4, and TG5. The first two series were hot-rolled steel universal column sections and the other three were fabricated sections. The tests were steady-state temperature, and all the girders were free to expand during the heating stage. In the following sections, the experimental set-up will be described. The experimental results will be discussed and compared with both the analytical and finite element predictions.

TESTING METHOD

The test was intended to investigate the shear buckling behavior of plate girder web panel at elevated temperature conditions. The overall test set-up arrangement is shown in Figure. 1. Due to the furnace configuration, the test girders were simply supported onto a steel roller bearing on each end. Both supports were placed outside the furnace to avoid any damage to their function due to heating.

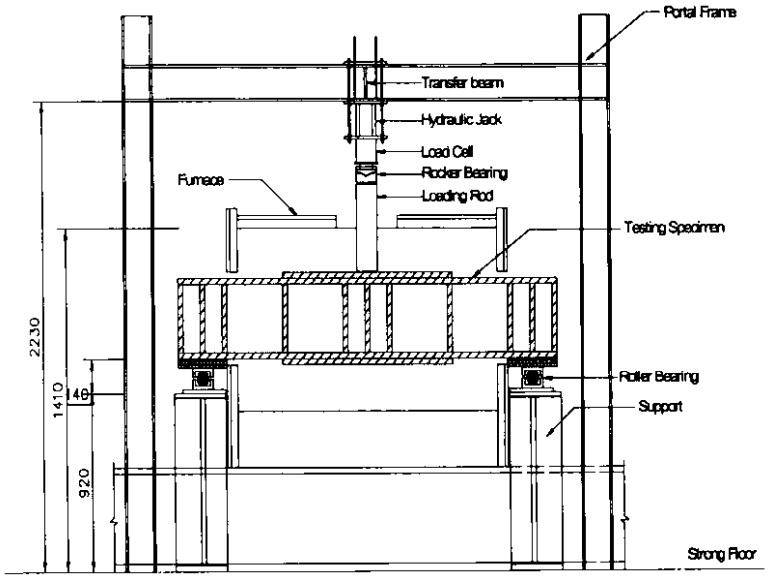

FIGURE 1 : Experimental Set-up.

Test series

In total, five series of I-shaped test girders were designed and tested, namely, TG1, TG2, TG3, TG4, and TG5. A typical configuration (TG3) is shown in Figure. 2. TG1 and TG2 were universal column sections, while TG3, TG4, and TG5 were fabricated from steel plates. The TG1 and TG2 series represented stocky plate panels with web slenderness ratio (*d/t*) of 22.8, and 22.6, respectively. TG3, TG4, and TG5 were slender plate panels, with web slenderness ratio of 152.5, 112.9, and 203.3, respectively.

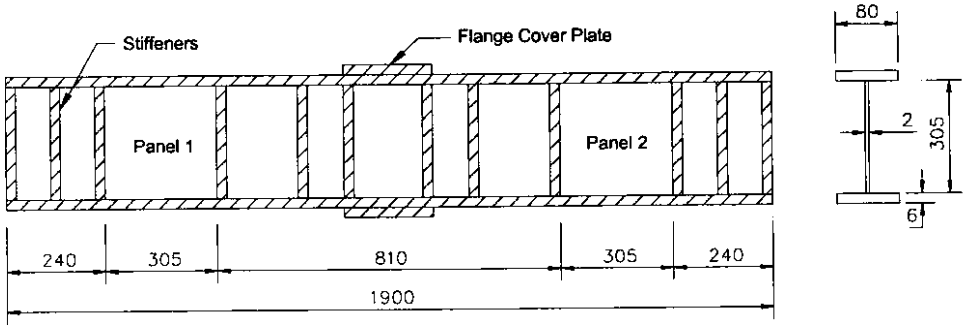

FIGURE 2 : TG3 Test Girders Configuration.

To study the web panel behavior due to shear, it was necessary to prevent the girder flexural failure which would be caused by the plastic hinge formation at mid span. Additional cover plates were welded onto the top and bottom flange plates of the test girders, as shown in Figure 2. The girders were therefore designed such that the end panels would fail primarily in shear. These panels are marked as panels 1 and 2 in TG3 girders, as seen in Figure 2.

The detailed material and geometrical descriptions of test girders are given in Table 1.

Test Panel	Web details							Flange details			
	Width b (mm)	*Depth* d (mm)	*Thickness* t (mm)	b/d	d/t	*Elastic Modulus* E (GPa)	*Yield Strength* σ_y (MPa)	*Width* b_f (mm)	*Thickness* t_f (mm)	*Elastic Modulus* E_f (GPa)	*Yield Strength* σ_{yf} (MPa)
TG1	139	139	6.1	1	22.8	197	342	152.4	6.8	207	359
TG2	181	181	8	1	22.6	205	332	203.9	12.5	213	325
TG3	305	305	2	1	152.5	200	287.8	80	6	204	274.5
TG4	305	305	2.7	1	112.9	200	232.8	80	6	204	277
TG5	305	305	1.5	1	203.3	200	332	80	6	204	277

Table 1 : Properties of Test Girders

Deformation Acquisition

Linear variable differential transducers (LVDTs) were used to measure the vertical deformations of the test panels, the mid-span deformations, and the support settlements. Typical LVDT locations for a test girder are shown in Figure. 3. Line LVDTs were used to measure the out-of-vertical-plane deformations at the center of the web panels to determine if shear buckling has occurred.

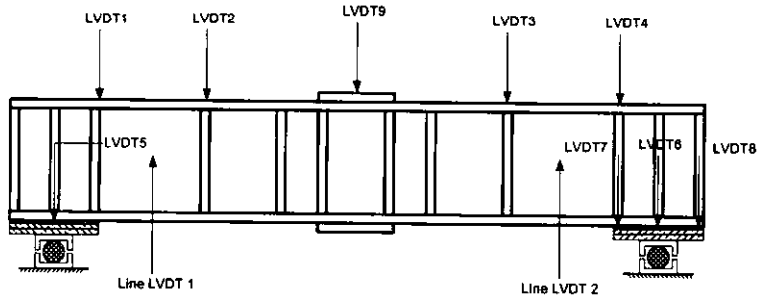

FIGURE 3 : Typical LVDT Locations.

AMBIENT TEMPERATURE TESTING

A total of 5 test girders, one from each series, were tested at ambient temperature. Loading was applied incrementally at the center of the girders. In addition to the use of LVDTs for displacement measurements, strain gages were used to measure strains at the center of the web panel, and at the top and bottom flanges of the girders, for ambient temperature. .

ELEVATED TEMPERATURE TESTING

In the present work, the steady state test method is selected as it was not possible for the electric furnace to achieve the ISO834 heating rate. To minimize heat loss, the openings at the end heating panels for the protruded specimen were heavily insulated by wool and carefully wrapped up with insulation cloth. Strain measurements had to be abandoned because normal strain gauges cannot sustain at high temperature. Thermocouples were used to monitor the specimen temperatures throughout the test.

ANALYTICAL AND FEM SIMULATIONS

In the next section, the experimental results will be presented. The results will be compared with the analytical and finite element predictions. The material stress-strain model is a bi-linear elastic-perfectly-plastic model for both analytical and FEM models. This is to provide a common comparison between the two methods. This is due to the limitation of the analytical method, which only requires elastic modulus and yield strength at a particular temperature.

The analytical method [5] for obtaining the ultimate capacity at elevated temperature is an extension of the ultimate shear capacity for calculating the shear strength of plate girder web panels at ambient temperature. The ambient temperature model was developed by Rockey and his colleagues at Cardiff University [7] [8]. Basically, the behavior of the girder web panel is assumed to undergo three distinct phases, viz., buckled, post-buckled, and collapse phase as shown in Figure. 4. Plate theory is used to predict the buckling load of the test panel with a high web slenderness ratio, and tensile field theory to predict the post-buckling capacity.

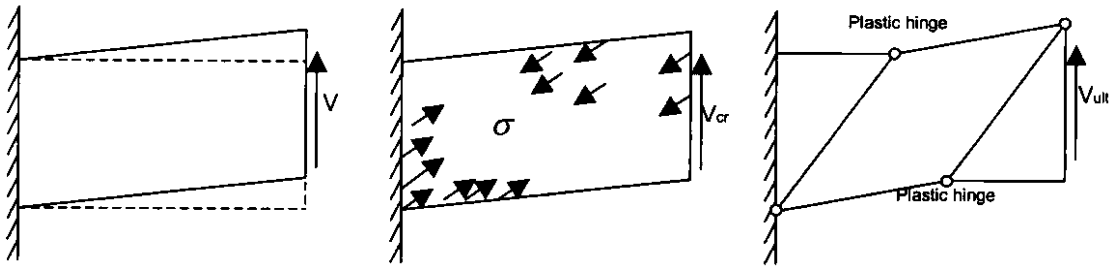

FIGURE 4 : Collapse Mechanism for Plate Girders under shear (Porter et al, 1975).

Analytical models for determining the shear strength at elevated temperature have been considered [5]. Temperature-dependent material properties are incorporated by using the respective retention ratios of the material yield strength and the elastic modulus at the elevated temperature according to Eurocode 3, Part1.2 [9].

Apart from the analytical models, simple FEM models have been developed for the analyses of the test panel under ambient and elevated temperature conditions. The FEM predictions have an

advantage over the analytical model because the panel deformations can also be obtained. Moreover, the temperature variations in the test panels could be easily incorporated into the FEM analyses. A quadratic 8-noded thick shell element was used for the discretization of both the web and the flanges of the test panel [10]. To reduce computational time and effort, the test panel was modeled as an isolated panel model to study the buckling behavior and shear strength. Furthermore, an entire beam simulation was created to verify the overall experimental set-up and to compare the experimental girder deformations with FEM analyses. The single-web FEM model was first verified by available ultimate shear test results by Rockey et al. [11].

TEST RESULTS

The purpose of the present test was to ascertain the ultimate shear strength of plate girder web panels at elevated temperatures. Material tests were carried out at ambient temperature; tensile coupons were extracted from the web and the flange plates and all the steel plate thicknesses that were used to fabricate the test girders. The results of the material yield strength and elastic modulus at ambient temperature are given in Table 1.

Ultimate shear capacity

Due to a limitation in space, the ultimate shear capacity of TG2 and TG3 test series is presented here. From the tests at different constant temperatures, the ultimate shear test results V_{test} are listed in Table 2. A comparison of the shear strength capacity from the test (V_{test}/dt), analytical (V_{anal}/dt) and FEM predictions (V_{FEM}/dt) is shown in Figure. 5. In general, the analytical results V_{anal} and FEM results V_{FEM} agree well with experimental results.

Test Girder	Temp (□)	V_{test} *(kN)*
TG2-1	20	343.8
TG2-2	400	324.3
TG2-3	550	234.6
TG2-4	700	74.2
TG3-1	20	79.85
TG3-2	400	67.63
TG3-3	565	34.34
TG3-4	690	17.15

Table 2 : Ultimate Shear Capacity of test specimen

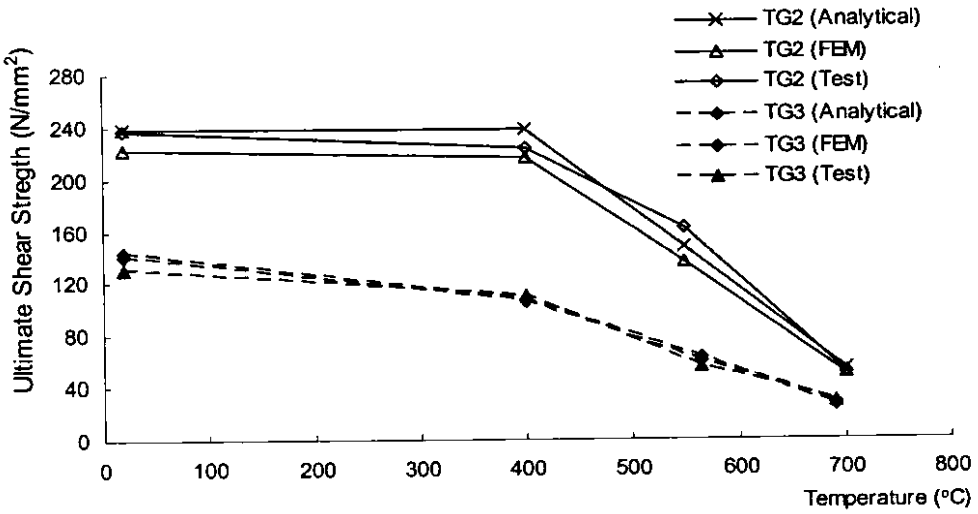

FIGURE 5 : Ultimate Shear Stress vs. Temperature for TG2-TG3 Series.

From Figure. 5, it can be seen that the deviations among the overall test results, the analytical and the FEM predictions are very small. It should also be noted that in the analytical and FEM predictions, the strength of steel at elevated temperature was taken by considering the strength retention ratio at 2% strain for TG2, and at 0.5% strain for TG3series. The strength at 0.5% strain is recommended in the British Standard [12] for the design and analysis of an element which is susceptible to buckling. This is to account for nonlinear elastic modulus on the element stability, which is much more dominant for slender test panels.

Strain results

From the ambient tests, the strains at the top and bottom flange plates and at the center of both sides of the test panels were obtained. The strains from rosette gages were used to calculate the maximum shear strain and principal strain in the web panel. A comparison between these maximum shear strains and principal strains from the test and FEM results of TG3-1 is shown in Figure. 6.

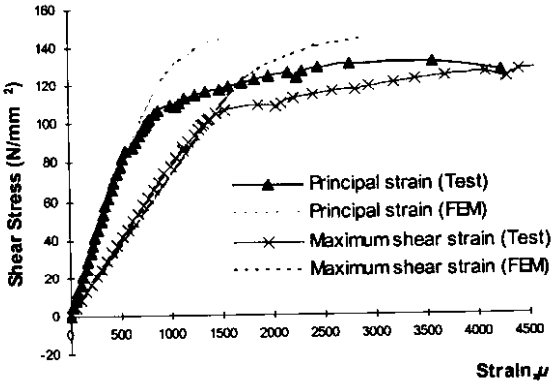

FIGURE 6 : TG3-1 web panel 1.

The shear stress values on the vertical axis are the applied shear stress, taken as $V/(dt)$, where V is the panel shear, and d and t are the web depth and thickness, respectively. From the results shown in Figure. 6, it can be seen that the FEM analyses over predict the shear strain results. This is because the elastic stress-strain model used in the FEM analysis is bilinear, consisting of elastic-perfectly-plastic type, which does not incorporate the nonlinear softening transition. As mentioned, this is to allow comparison with the same material model adopted in the analytical model.

Panel out-of-plane deformation

Test panel of TG2 have web slenderness ratios of 22.5, which is well below the 63ε limit for slender sections as defined in BS5950 Part 1 [13], where $\varepsilon = (275/\sigma_y)^{1/2}$, and σ_y is the material yield strength. The panel is considered stocky panel, and the tests showed that the panels did not buckle, the failure was due to panel yielding. As a result, there was no evidence of out-of-plane deformation in these panels.

On the other hand, the web slenderness ratio of TG3 is 152.5. This section is defined by the BS standard [13] as a slender section and its capacity would be limited by the panel plate buckling instead of yield strength. In the present tests, line LVDTs 1 and 2 (Figure. 3), were used to monitor the web buckling in the test panels.

In all the slender tests, it was found that the panel out-of-plane deformation started to occur after the loading reached a certain level. The panel deformations then increased when the load was increased further until failure. The load corresponding to the start of the panel out-of-plane deformations is taken as the buckling load. Even though the experimental buckling point is not very distinctive particularly at high temperature, it can be used to compare with the buckling loads obtained from the analytical and FEM models.

Failure mode of web panel

The stocky panel TG2 was tested at ambient, 400 °C, 550 °C, and 700°C. From the detailed failure modes [6], it was evident that the tested panels failed due to panel yielding without buckling. For the slender panel TG3, which was tested at ambient, 400 °C, 550 °C, and 700°C, the out-of-plane deformations are clearly evident.

It is also noticed from the experimental results that the buckling shapes are more visible at ambient temperature and 400°C. This is because at greater temperature, the material non-linearity is more pronounced. At 700 °C, the Eurocode material stress-strain curve does not have a distinct demarcation point between the elastic and the plastic curve. The material behaves more like rubber with continuous non-linearity.

A comparison between the experimental ultimate shear strength V_{test}, and the maximum shear strength V_{yw} ($V_{yw} = \tau_{yw} dt$) at ambient temperature of TG2 and TG3 panels was studied. Figure. 7 shows the variation of the ultimate shear strength ratio V_{test}/V_{yw} as temperature increases. In

Figure 7, the retention ratios of steel yield strength $(k_{y(T)})$ and elastic modulus $(k_{E(T)})$ at elevated temperatures according to Eurocode 3, Part1.2 [9] are also plotted with the experimental results. It can be noticed that as temperature increases the ultimate shear strength of web panel reduces following the trend of material degradation of steel. In addition, it can be observed that the slender web panel (TG3) demonstrated plate buckling failure compared to the stocky web panel (TG2) which demonstrated yielding failure.

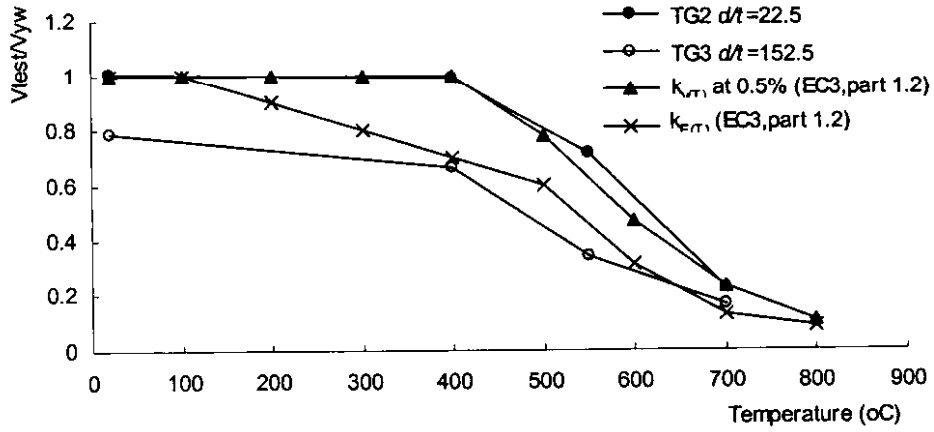

FIGURE 7: Panel Shear Stress Capacity Ratios For TG2-TG3 Series.

CONCLUSIONS

The present paper presents an experimental investigation of plate girder web panels loaded in shear under elevated temperature conditions. The test results are presented, and compared with the analytical and FEM predictions. From the study, the analytical and FEM modeling can be used as simple, alternative tools to predict the web panel shear strength.

REFERENCES

[1] Krawinkler, H., *Shear in beam-column joints in seismic design of steel frames, Engrg. J.*, AISC, 3rd Quarter, 82-91, 1978.

[2] Kato, B., Chen, W. F., and Nakao, M., *Effects of joint-panel shear deformation on frames*, J. Construct. Steel Res. 10, 269-320, 1988.

[3] Chen, W. F., and Lui, E. M., *Stability Design of Steel Frames—Chapter 6, Analysis of Semi-rigid frames*, CRC Press, Inc., USA, 275-342, 1991.

[4] Wang, Y. C., *Steel and Composite Structures, Behaviour and Design for Fire Safety*, SPON Press, London, UK, 332p, 2002.

[5] Vimonsatit, V., Tan, K. H., and Ting, S. K., *Shear strength of plate girder web panel at elevated temperature,* 2003 (*under review*).

[6] Vimonsatit, V., Tan, K. H., and Qian, Z. H., *Testing of Plate Girder Web Panel loaded in Shear at Elevated Temperature, 2004 (under review).*

[7] Porter, D. M., Rockey, K. C., and Evans, H. R., *The collapse behaviour of plate girders loaded in shear*, The Structural Engineer, 53 (8), 313-325, 1975.

[8] Rockey, K. C., Evans, H. R., and Porter, D. M., A design method for predicting the collapse behaviour of plate girders, Proc. Instn. Civ. Engrs., Part 2, 85-112, 1978.

[9] Eurocode 3, Part 1.2 *Design of steel structures: Part 1.2 General Rules, Structural Fire Design*, Draft ENV 1993-1-2, Commission of European Communities, Brussels, Belgium, 1995.

[10] MSC. Marc Mentat, *MSC. MARC User Guide Version 2001*, MSC. Software Corporation, 2001.

[11] Rocky, K. C. and Skaloud, M., *The ultimate load behaviour of plate girders loaded in shear*, The Structural Engineer, 50 (1), 29-47,1972.

[12] BS5950: Part 8, *Structural use of steelwork in building, Code of Practice for Fire Resistance Design*, British Standards Institution, 1990.

[13] BS 5950: Part 1, *Structural Use of Steelwork in Building, Code of Practice for Design in Simple and Continuous Construction*, British Standards Institution, 1990.

BEHAVIOUR OF MASONRY COMPARTMENT WALLS IN FIRE SITUATIONS

Ali. NADJAI
School of The Built Environment, Univ. of Ulster, FireSERT, Newtownabbey , Belfast, BT37 0QB, U.K., a.nadjai@ulst.ac.uk

ABSTRACT

A thermo-structural finite element model for the behaviour of masonry panels exposed to fire conditions has been developed. The model has been specifically designed to simulate the behaviour of both loaded and unloaded brickwork panels in plane stress, which are subject to various types of temperature distribution associated with typical fire situations. The current model has been evaluated using experimental results from fire tests on half and full-scale masonry walls exposed to elevated temperature on one face. Analytical and experimental results for the fire tests were basically in good agreement, indicating that reliable results can be achieved provided that accurate material properties and test boundary conditions are known, and that reliable temperature distribution data through the thickness of the wall is available.

KEYWORDS: *masonry in fire, finite element model, and experimental tests*

INTRODUCTION

In a fire situation masonry walls are predominantly subjected to heating on one face, giving rise to a thermal gradient through the thickness of the wall. If the wall is unrestrained this leads to differential thermal expansion of the material which induces thermal bowing towards the fire. The thermal displacements together with material property degradation may result in structural collapse of the wall depending on boundary conditions, magnitude of applied load and geometry of the wall.

The maintenance of structural stability of a masonry wall during the course of a building fire is necessary for the preservation of integrity, to compartmentise a fire – preventing spread to other building areas, and to mitigate against local structural collapse, facilitating in the safe evacuation of the building occupants.
At present few design codes include calculation models for the design of masonry walls for fire resistance. BS5628[1] (The Structural Design of Masonry Walls) does not include a fire resistance

design section, but Code of Practice[2] 121, pt. 1, relates minimum wall thickness to periods of maximum fire resistance in minutes. Eurocode[3] 6 pt. 10, also specifies minimum thicknesses of firewalls depending on applied load, material type and required period of fire resistance. These values are entirely dependent on results of isolated standard fire tests. The Building regulations[4] simply give times of minimum fire resistance for various building purposes, but the regulations also place emphasis on the role of masonry walls as fire separating constructions.

The importance of developing a reliable numerical model increases with the cost of associated testing, and it has been the experience that the fire testing of masonry walls is both time consuming and expensive. Presently a limited number of numerical models capable of analysing masonry wall behaviour at elevated temperature are available. This presents a clear need for the development of further numerical models in this area for the purpose of extrapolating test data and conducting extensive parametric studies. The data obtained from such studies could then assist in the compilation and development of design guides.
The finite element model presented in this paper uses internationally recognised concrete material response models and accounts for material and geometric non-linearity. The masonry composite of masonry units and mortar joints are modelled separately providing a more accurate description of the macro level behaviour between the two constituents. At present the structural model is not coupled with any temperature analysis program and relies upon temperature data recorded during fire testing when modelling experimental results.

PREVIOUS NUMERICAL MODELS

Although limited there are previous numerical models capable of predicting the behaviour of both loaded and unloaded masonry walls at elevated temperatures. Gnanakrishnan[5] et al developed a simplified plane strain finite element model, using four-noded quadrilateral isoparametric elements. The two components of the composite masonry material were modelled separately. Results obtained were considerably over conservative. This was attributed to the fact that both geometric non-linearity and cracking of the brittle material was not included in the model. The transient strain component, which is considered to be very influential in loaded materials experiencing heating for the first time, was also ignored. Dhanasekar[6] et al created a finite element model using layered thin shell elements. The model was validated against test results on an unloaded masonry wall panel and considerable agreement was achieved between analysis and experimental data. However, yet again, the transient strain component was ignored. This may lead to inaccurate results in loaded masonry wall analysis. The model also assumed a linear temperature distribution through the wall, thus ignoring the thermal stresses created by a non-linear temperature distribution.
O'Meagher and Bennetts[7] produced a computer model based on the moment-curvature method of analysis. The thermo-structural model allowed for geometric as well as material non-linearity, and is capable of predicting the thermal bowing of both reinforced and unreinforced concrete walls in plane stress. The material model employed for concrete accounted for basic creep and transient strain components. The structural program was coupled with a thermal analysis program, for the calculation of temperature distributions. The authors conducted a parametric study to investigate the influence of applied axial loading, slenderness ratio and volume of reinforcing, however, no comparisons were made with experimental results.

ASSOCIATED EXPERIMENTAL INVESTIGATIONS

Cooke[8] examined the thermal bowing of 3.0m high unloaded cantilever walls of varying thickness. Large magnitudes of thermal bowing were observed at the top of the wall, though structural collapse was not experienced. Shields[9] et al experimentally investigated the thermal bowing of a $1m^2$ ½ scale unloaded masonry panel. Thermal bowing in both vertical and horizontal directions was recorded due to vertically restrained boundary conditions.

An extensive experimental investigation was conducted by Byrne[10], where fourteen masonry wall panels were tested. The results produced conclusive findings regarding the effects of axially applied loads and slenderness ratio. Lawerence[11] et al reported on the results of 146 tests carried out by the National Building Technology Centre (NBTC Australia). Again the effects of slenderness ratio and applied load were studied along with various masonry unit material types. Many of the results obtained verified the findings of Byrne. At present, an experimental program is being carried out at Ulster by Laverty[12] on loaded ½ scale model wall panels, for the purpose of investigating the influence of applied load and slenderness ratio. The experimental data obtained from two of the tests have been used for the evaluation of the finite element model presented herein.

It is apparent from the experimental studies conducted to date that predominantly the effects of applied load and slenderness ratio were investigated. Although these factors are seen to be most influential in the case of masonry walls, the effects of other parameters such as eccentricity of load and rotational restraint merit investigation.

In order to predict reliable results using a numerical model an accurate material model must be employed. The temperature dependent material properties of concrete materials have been extensively investigated within Europe[13] and results were seen to be largely dependent on the type of aggregate used and were also influenced by mix proportion, cement type, stress conditions and age. Although a considerable scatter of results from experimental data remains evident, a few prominent mathematical material models have been developed[14, 15] and used to good effect in previous analysis

THE FINITE ELEMENT MODEL

The previous numerical models discussed above provided an important stepping stone by giving numerical insight in the problem and by highlighting the important of certain numerical features. Therefore, it was decided initially to develop a two-dimensional finite element program, which modelled a slice through the wall as a column strip. Eight noded quadrilateral isoparametric continuum elements were implemented for this purpose. The finite element model developed is capable of predicting thermal bowing under various restraints and loading conditions. The effects of both material and geometric non-linearity have been accounted for and a smeared cracking model was incorporated to simulate the brittle behaviour of a concrete type material. The inclusion of the geometric non-linearity is considered as important factor not to be neglected. The benefit of it is to accommodate the important P-Δ effects in an axially loaded wall, which can largely contribute to the structural collapse.

Material Non-Linearity

Material non-linearity was approached using the tangent modulus method. The temperature dependent parabolic stress-strain relationship for a concrete material proposed in Eurocode[13] 4 was

adopted with a linear strain-softening branch. In order to relate the uniaxial stress-strain relationship to a two dimensional continuum material, the well established biaxial failure envelope for concrete[16] was employed (Fig. 1).

The Cracking and Crushing Model

The brittle tensile nature of the masonry materials was accounted for by the inclusion of a smeared cracking model. If the maximum principle stress at any gauss point exceeded the user specified tensile failure stress then a crack was assumed to develop in a plane normal to the direction of the maximum principle stress over the associated gaussian integration area. The crack was simulated by setting the Young's modulus in the direction normal to the crack as zero. The stress in the direction normal to the crack was not set to zero immediately but reduced according to a linear crack softening relationship. The effects of crack closure were also incorporated by restoring the compressive strength of the material in the relevant direction. A certain amount of shear capacity was retained, but reduced as the crack width increases. Figure 2 illustrates the stress-strain relationship of the cracking model. Crushing of a material was modelled by reducing all strength properties and stresses in an integration area to zero when the effective biaxial strain at that particular gauss point exceeded the user specified crushing strain.

Geometric Non-linearity

It was recognised that the problem at hand contained certain aspects of geometric non-linearity. Changes in geometry due to deformation significantly influence the predicted response of a masonry wall[7]. The total langrangian descriptor was used to redefine the structural geometry, and account for the additional stresses experienced in a laterally deforming axially loaded masonry wall. Green's strain tensor was used to include higher order strain terms. With the total langrangian approach the Piola Kirchoff stress field was used and referred to the original configuration. When calculating internal nodal forces the Piola Kirchoff stresses of the undeformed area were converted to the normal Cauchy stresses of the deformed configuration. The membrane stresses, which exist in an axially loaded slender structure, may actually have a stiffening effect and have been accounted for by the inclusion of the geometric stiffness matrix.

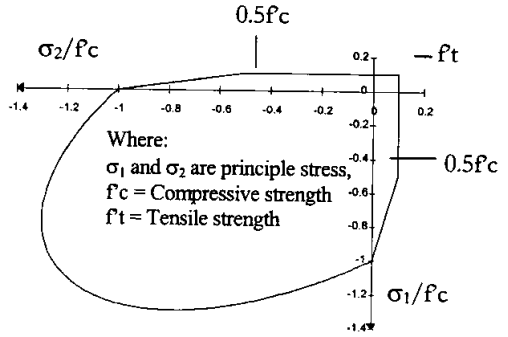

FIGURE 1: Biaxial failure surface adopted for the plane stress concrete material.

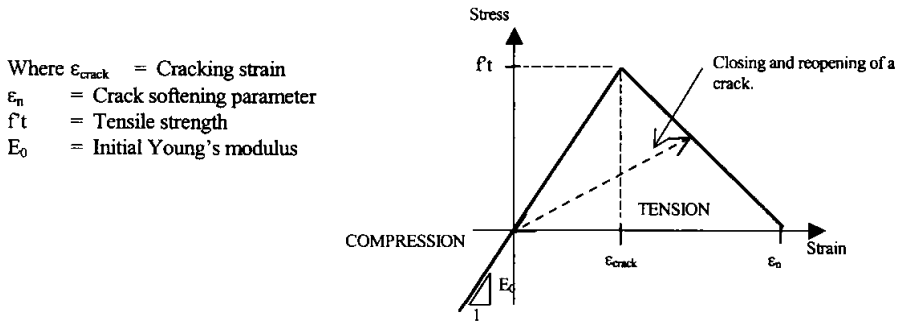

FIGURE 2 : The material cracking model adopted, with crack closing and reopening features.

Thermal Effects

The fundamental requirements when modelling the effects of elevated temperature are the inclusion of thermal expansion and material property degradation.

Thermal Expansion

The temperature distributions over the thickness of masonry walls are generally curvi-linear, giving rise to a non-linear application of thermal strains. However, due to the shear fibres in a continuum material the strain distribution may only occur linearly, and- indeed the shape functions adopted are formulated to adhere to this stipulation. Therefore the free thermal strains ε_{th}, associated with the curvi-linear temperature profile are incompatible with actual linear flexural strain distributions[17], thus at any point thermal expansion cannot occur freely and is internally restrained producing thermal stresses.

These thermal stresses are self-equilibrating both axially and rotationally and hence do not contribute to external displacements. The distribution of thermal strains through the thickness of a wall heated on one face is generally similar to that shown in Fig. 3. Assuming that there are no external loads the resulting thermal stresses will cause compression on the outer sections and tension in the centre of the wall. These tensile stresses may be of a magnitude to cause cracking in the region.

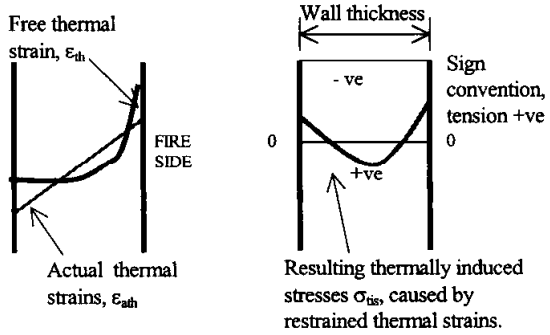

FIGURE 3 : Self-Equilibrating thermal stresses caused by non-linear temperature distribution

In the finite element idealisation temperatures were assigned to each node. The masonry panels were commonly descritised into three elements deep over the thickness of the wall (see Fig. 4) giving seven nodal points to represent the curvi-linear temperature profile, thus enabling the effects of thermally induced stresses to be calculated and accounted for.

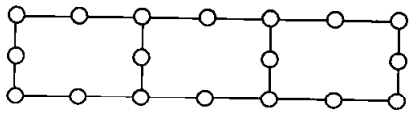

FIGURE 4. Three eight noded isoparametric elements used across the thickness of the wall.

Thermal strains ε_{th}, were defined using the fourth order polynomial thermal strain temperature dependent relationship adopted by Eurocode[13] 4. The process of obtaining thermal deformations was as follows:

1. Temperatures at the gauss points, T_{GP}, were determined from the user defined nodal temperatures, T_i, using the element shape functions, N_i.

$$T_{GP} = \{T_i\}[N_i] \tag{1}$$

2. Thermal strains, ε_{th}, were evaluated from gauss point temperatures using the ε_{th}-temperature relationship and the thermal strains were converted to stresses, σ_{th}, using the current tangent elasticity matrix, D_T,

$$\{\sigma_{th}\} = [D_T]\{\varepsilon_{th}\} \tag{2}$$

3. The equivalent thermal stresses and the strain matrix [B] were numerically integrated over the element volume to obtain equivalent thermal nodal loads, f_{th},

$$\{f_{th}\} = \int_V [B]^T \{\sigma_{th}\} dV \tag{3}$$

4 Using the current tangent stiffness matrix, K_T, and the equivalent thermal nodal loads the equilibrium equations are solved for thermal displacements, a_{th}.

$$\{a_{th}\} = [K_T]^{-1}\{f_{th}\} \tag{4}$$

For simplicity, Eqn (4) refers to thermal effects only.

5 The effect of the applied virtual nodal loads due to thermal extension, were removed when considering internal stresses by deducting the thermal and transient strain components from the total strain.

$$\{\sigma\} = [D_T](\{\varepsilon_{tot}\} - \{\varepsilon_{th}\} - \{\varepsilon_{tr}\}) \qquad (5)$$

The individual strain components in Eqn (5) are described below.

The Constitutive Strain Model for a Concrete Material

The individual components of the total strain were recognised in order to determine the stress related strain component for the calculation of internal forces. Eqn (6) describes each strain component;

$$\varepsilon_{tot} = \varepsilon_{\sigma} + \varepsilon_{th} + \varepsilon_{tr} \qquad (6)$$

Where ε_{tot} = total strain, ε_{σ} = stress related strain, ε_{tr} = transient strain, ε_{th} = thermal strain

The total strains were determined from the total displacements and considering thermal effects only the ε_{tot} component is equivalent to the ε_{th}, Fig. 3.

The transient strain component has been reported to be significant in concrete materials that were loaded and experiencing heating for the first time. This strain component has the effect of reducing and redistributing thermal strains in loaded elements, preventing excessive damage by thermally induced stresses[18]. In the present analysis the transient strain model proposed by Anderberg[15] has been employed, and is dependent on both thermal strain and stress level.

Material Property Degradation

Modification of material strength and stiffness with increase in temperature was incorporated which is particularly influential in the case of loaded masonry walls. Upon the application of temperature the material properties of compressive strength, f'_c, ultimate strain at f'_c, ε_{ult}, crushing strain, ε_{cu}, and tensile strength, f'_t, were modified for each integration area according to the temperature at the gauss point. The temperature dependent material property relationships are shown in Figs. 5 and 6.

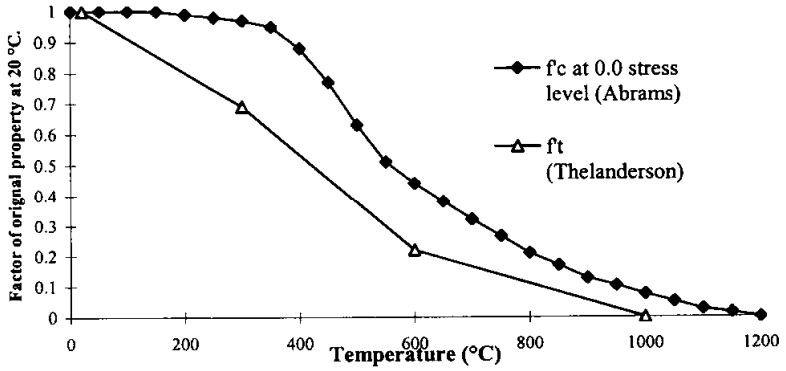

FIGURE 5 : The compressive and tensile strength relationship with temperature.

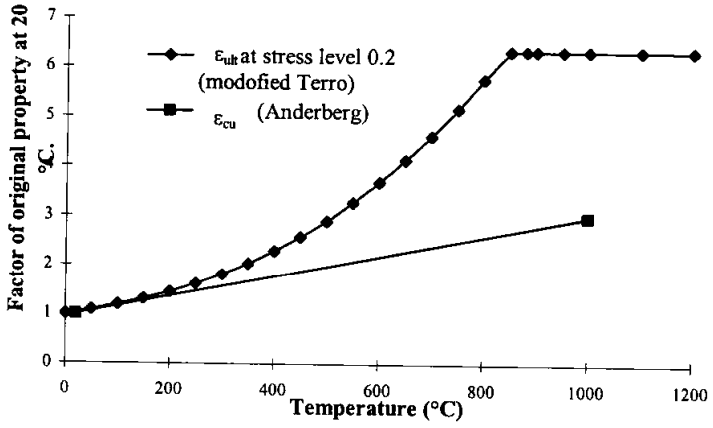

FIGURE 6. The ultimate and crushing strain relationship with temperature.

Compressive strength was not only taken as a function of temperature but also of stress level (σ/f'_{c20}), where σ is the stress in an element and f'_{c20} is the compressive strength at room temperature. Direct test results of f'_c-temperature relationships for load levels between 0.0 and 0.4, reported by Abrams[19] were used in the model. In this research a delayed reduction in compressive strength was observed in samples heated under constant load. As the load level increased the reduction in compressive strength was reduced and above a certain load level an increase in f'_c in the early stages of heating was observed.

Ultimate compressive strain was also seen to be a function of both temperature and stress level. The ε_{ult}-temperature-(σ/f'_{c20}) relationship developed by Terro[20] was used in the program. This assumed the ultimate strain to remain constant at 0.002 above stress levels of 0.2 and for $0 \leq (\sigma/f'_{c20}) \geq 0.2$ a second order interpolation function was used. The crushing strain model used by Anderberg[15] has been employed. The ε_{cu}-temperature relationship assumes a linear increase from 0.005 at room temperature to 0.015 at 1000 °C. Tensile strength modification employed a trilinear decay model based on test results reported by Thelanderson[21], with Poisson's ratio taken as being independent of temperature.

Program Solution Method

The global flow chart describing the program is shown in Fig. 7. The program solution method adopted a standard or modified non-linear Newton-Raphson iteration procedure, in which the structure firstly received an applied load, followed by successive temperature increments. The convergence criterion was based on the ratio of the normal of the internal and external forces.

VALIDATION OF THE FINITE ELEMENT MODEL

Non loaded Masonry wall

Full scale single leaf non-loaded masonry cantilever wall was carried out by the fire research station at the (BRE) Building Research Establishment[8]. The dimension of the wall was 950mm wide × 3000mm tall x 215mm thick constructed using solid common clay bricks, and were unrestrained on both verticals and top boundaries. The wall was exposed to the BS476 Pt. 20 temperature-time fire curve for a period of three hours. . The material properties employed were;

f_c = 14.0 N/mm^2 , $\alpha_l = 6.0\times10^{-6}$ (for all temperatures)
f_t = 2.0 N/mm^2 , ε_{ult} = 0.0028

Using MasSET the cross-sections of the masonry walls were descritised using a mesh of 5 elements wide and 80 elements high, with the mesh density increasing towards the fire exposed face. This resulted in 400 elements giving 1371 nodal points. The self-weight of the wall was included by taking material density and the gravity (ρg) as an applied body force on each element.

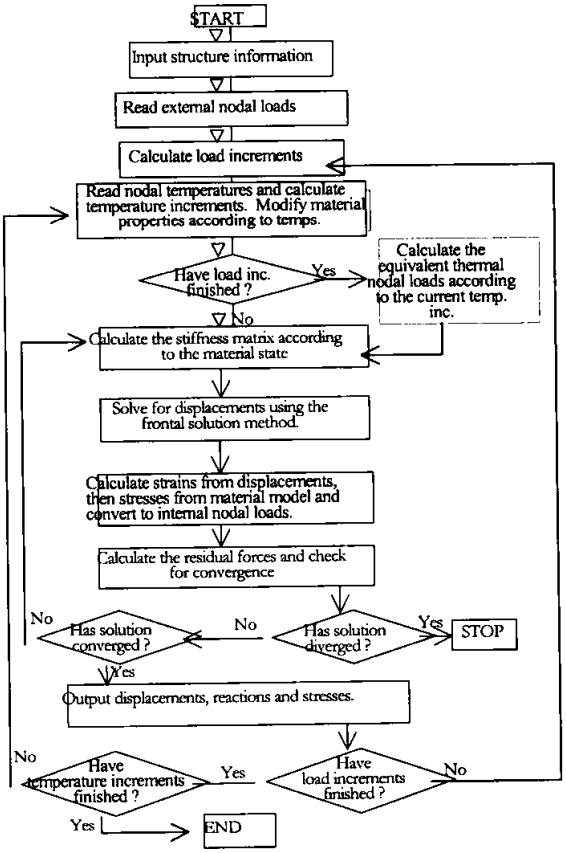

FIGURE 7 : Global flow chart of the finite element program showing solution procedure.

The temperature distribution through the thickness of the wall was taken directly from experimental thermocouple measurements. Figure 8 illustrates the top displacement-time results from MasSET and experimental investigation [8]. It can be seen that reasonable comparison between the numerical results and the experimental behaviour. The comparative success in modelling the BRE fire wall test results was attributed to by three facts. 1) The simplistic cantilever wall did not possess the previously encountered difficulties of complex boundary conditions, 2) The predominantly clay material could be accurately modelled, and 3) Since the wall was non-loaded any transient strain which may have been present in the mortar material was minimised.

Axially Loaded Masonry Wall

A full scale axially loaded masonry wall with a dimension of 3.0m × 3.0m × 90mm thick wall panel constructed of clay masonry units test was conducted by Gnanakrishnan[22]. The top and bottom boundary conditions were laterally and rotationally restrained, while the vertical edges were unrestrained with sufficient clearance for free thermal expansion. Sandwich plattens constructed of a ceramics fibre core and laminated by two steel plates, were used between the wall top and bottom boundaries and the loading plates. Their purpose was to distribute the load, but also exhibited a high degree of permanent strain allowing rotation of the top and bottom boundaries. The wall was subject to the Australian standard time-temperature curve, and an axial applied stress of $\sigma_y = 0.877$ N/mm^2.

The 3000mm high × 90mm thick wall was modelled using MasSET, and was descritised using 3 elements thick by 75 elements high. The clay masonry unit and Ordinary Portland Cement mortar joint materials were individually represented, and compressive strengths of 59.4 and 8.2 N/mm^2 as recorded by Gnanakrishnan[22], were utilised respectively. The secant coefficient of thermal expansion for both clay and mortar were measured by associated testing, and were translated to the thermal strain–temperature relationship as is shown in Fig. 9. Both relationships were implemented during analysis. Interface elements were introduced between the top and bottom boundary conditions and their loading surfaces. Sensitivity analysis to varying degrees of rotational stiffness was conducted since the behaviour of the sandwich platens was not quantifiable.

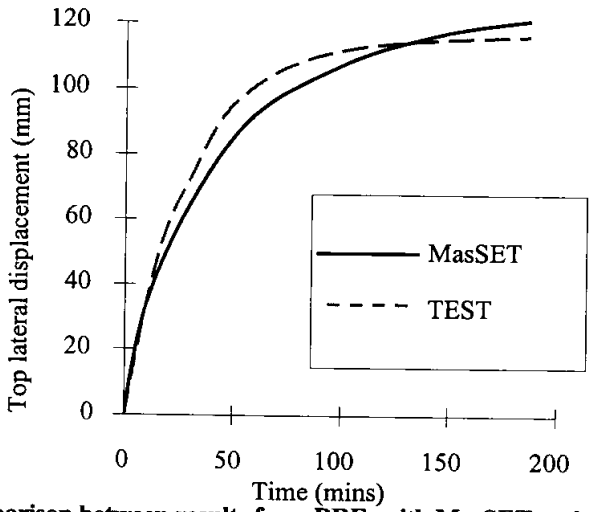

FIGURE 8 : Comparison between results from BRE, with MasSET and test.

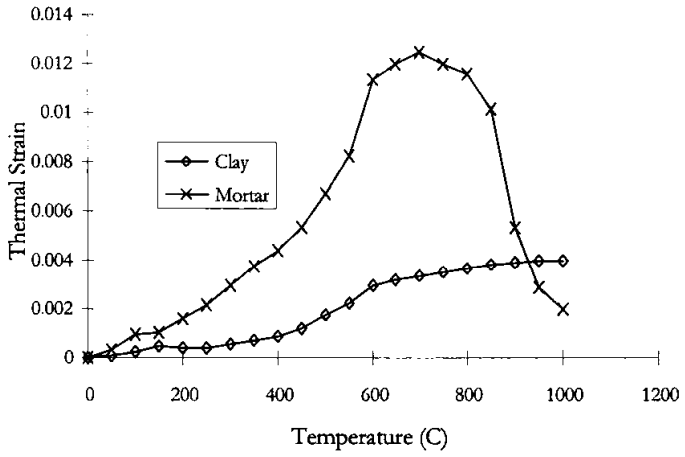

FIGURE 9. Thermal strain relationship of mortar and clay for according to Gnanakrishnan[22].

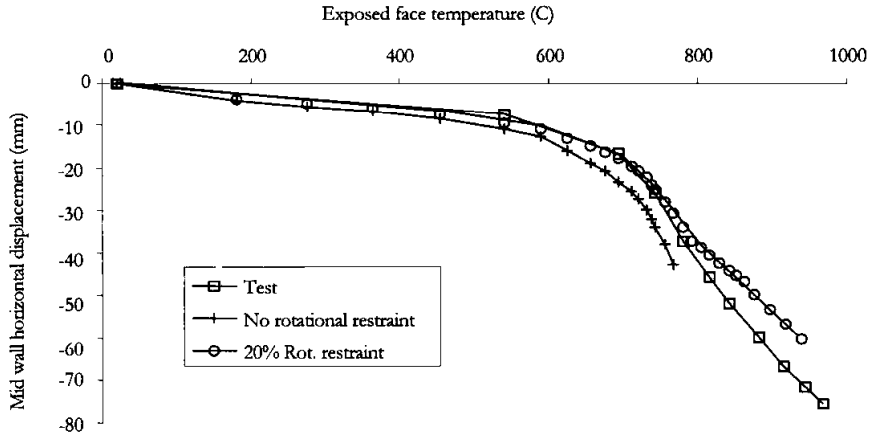

FIGURE 10. Effect of top rotational restraint on the mid wall horizontal displacements.

Relevant mechanical and thermal material properties were determined by Gnanakrishnan[22] and used directly in the numerical modelling of test results.

Figure 10 illustrates the numerical results yielded by MasSET, and clearly shows that increasing rotational stiffness produced a decrease in the extent of thermal bowing. With free rotation, failure due to buckling was experienced, and occurred prematurely in comparison to experimental results. Best overall agreement was achieved when employing 20% top and bottom rotational restraint, although numerical displacements were much smaller than experimental after 800°C. The value of rotational stiffness was assumed to be constant in the analysis: however the sandwich elements used

at the boundaries in test were reported to have a high degree of permanent strain. Given this, the value of rotational restraint may have been overestimated at higher rotations, hence resulting in decreased numerical displacements.

EXPERIMENTAL PARAMETRIC STUDY

Two half scale model walls were tested at the University of Ulster[12] (FW1 and FW2) at different levels of applied loading, 50 % and 100% of the design ultimate load. The model walls were 430 mm wide by 1330 mm high strip columns, with a thickness of 50 mm (see Fig. 11a). Masonry units consisted of concrete with a specified crushing strength of 20 N/mm^2, bedded on a 1:3 mortar mix, using Ordinary Portland Cement. The base of the walls were built on a flat steel plate and the applied axial load was distributed over the width of the panel top through a steel loading plate which was restrained against rotational movements. The vertical edges of the walls were unrestrained with sufficient space for free thermal expansion. The axial load was kept constant during all tests using an 'Enerpac' hydraulic system and was monitored using load cells. Lateral deflections were measured at support positions (top and bottom) and at midspan using LVDT's. Temperature was recorded using thermocouples arranged in two sets (5 per set) at vertical third points of the wall. At each location one thermocouple was placed in the centre of the wall, two were placed on each face and the remaining two at distances of $\frac{d}{6}$ and $\frac{5d}{6}$ into the wall measured from the wall face (see Fig. 11b).

Descritization of the Structure

The cross-section of the wall was modelled using eight noded isoparametric elements, 3 elements wide and 69 elements high, creating a mesh size of 207 elements with 766 nodes. The height of the brick unit and mortar joint used in analysis was proportionally larger than in the actual test for the purpose of reducing the problem size to save computational time. Seven nodal points over the wall thickness enabled the curve-linear temperature distribution to be simulated (see Fig. 4). The steel loading plate was also modelled and prevented numerical instabilities caused by local crushing of the top bricks. Contact elements were also introduced between the top of the wall and the loading plate and at the bottom of the wall. These elements where given zero tensile strength in the Y-direction to ensure no tensile bonding between surfaces.

Material Properties

The macro level modelling of the masonry composite enabled each constituent material to be given their individual material properties. The specified crushing strength of the masonry units was utilised. Typical values were adopted for all other properties, as given in Table 1.

Loading

Applied axial loading

FW1 - external applied axial load = 50.0kN, (2.325 N/mm^2).

FW2 - external applied axial load = 100.0kN, (4.650 N/mm^2).

Temperature loading

Temperatures were recorded during fire testing at dimensions of 0, 25.0 and 50.0mm from the unexposed face, and estimated temperature profiles were interpolated by fitting a curve-linear line through the three points recorded. Assumed temperature profiles from initial heating through to the end of the test for both walls are shown in Figs. 12 and 13.

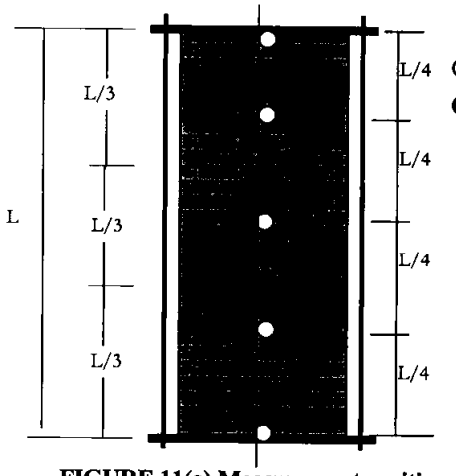

FIGURE 11(a) Measurement positions

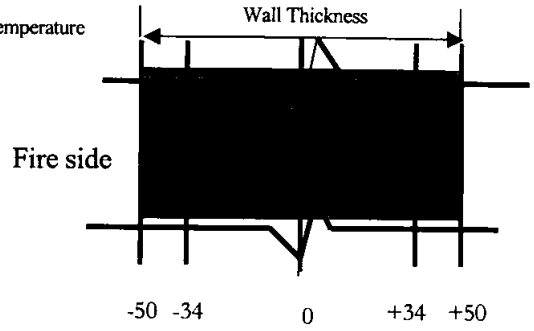

FIGURE 11(b) Position of thermocouples through wall and reference system

Table 1. Material properties of both material constituents employed in the current analysis.

Material properties at 20°C	Masonry Unit	Mortar Joint
Compressive strength, f'c, (N/mm^2)	20.0	10.0
Tensile strength, f't, (N/mm^2)	2.0	1.0
Ultimate strain	0.0023	0.004
Crushing strain	0.005	0.009
Poisson's ratio	0.17	0.20

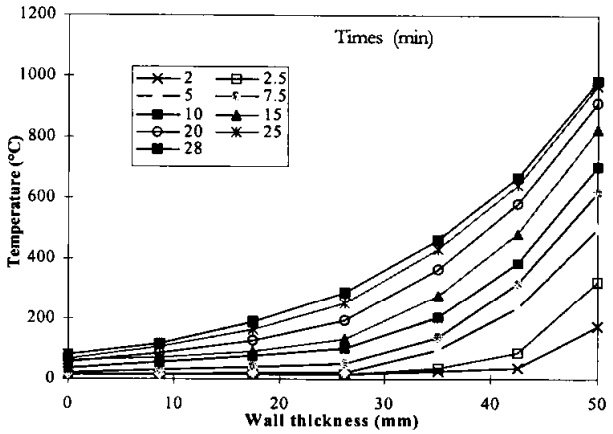

FIGURE 12 : The temperature profiles through the thickness of the wall at various time intervals up to failure for FW1.

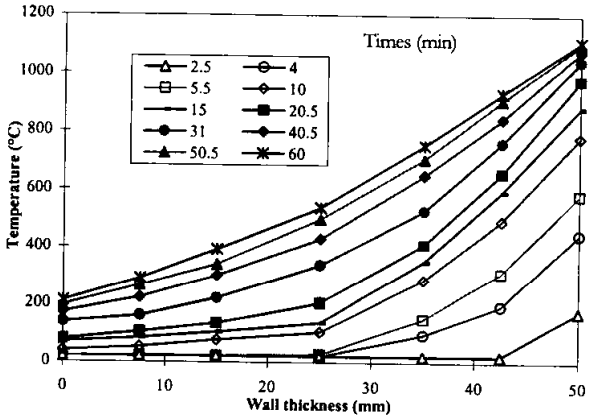

FIGURE 13 : The temperature profiles through the thickness of the wall at various time intervals up to failure for FW2.

RESULTS AND DISCUSSION

Initial analysis of the problem was conducted with complete rotational restraint applied to the steel loading plate, which resulted in almost no thermal bowing. Little lateral displacements were experienced until temperature increased and the wall started to deflect away from the fire as a result of material property degradation. It was soon realised that complete rotational restraint was unlikely the actual situation in the test rig. Rotational restraint was removed therein, where it was then observed that rotations at the top of the wall in analysis, θ_{lr}, reached a magnitude of approximately 0.02 radians prior to structural collapse. Upon examination of the test rig it was considered quite feasible that rotations of this extent may have been allowed to occur freely.

Fire Wall 1 (FW1)

The test duration for fire wall FW1 was 28 minutes, at which point complete structural collapse was experienced. During the test the wall clearly bowed towards the fire. The central deflection (Δ_{cx}) verses exposed face temperature (T_{ef}) relationship from both experiment and analysis is shown in Fig. 14. The results are in reasonable agreement, where the onset of large lateral displacements occurred at approximately 812 °C.

Several authors have reported from fire wall tests that failure due to buckling tended to occur at a central deflection of 90% the thickness of the wall[10,22] FW1 failed at a central deflection of 42.5 mm (85% wall thickness), therefore the failure mode was almost definitely one of buckling instability. The large deflections created tensile stresses on the exposed face, which produced horizontal cracking in the mortar joints followed by almost immediate structural collapse.

It was also observed during analysis that quite a pivotal event was the crushing of the mortar joint at the base of the wall on the fireside (see Fig. 15). This effectively relieved some of the rotational restraint at the bottom of the wall facilitating the onset of large displacements. This hypothesis could not be compared to experimental events, as the fireside of the wall could not be seen for obvious reasons.

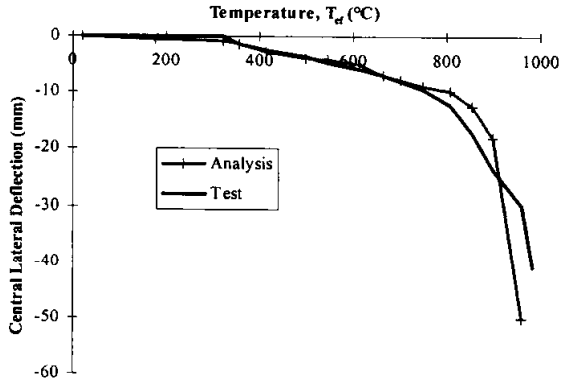

FIGURE 14. Comparison between experimental and analytical Central deflection V's Exposed face temperature for FW1.

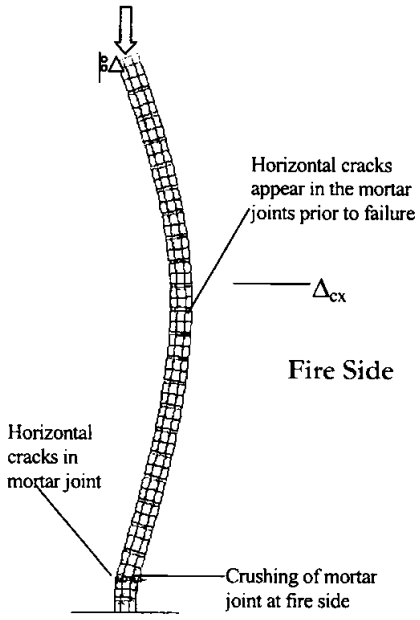

FIGURE 15. Failure mode of FW1. Deflections are magnified by a factor of 4.0.

Fire Wall 2 (FW2)

The fire resistance time of FW2 was 60.5 minutes, at which point the wall structurally collapsed in a direction away from the fire. This was in contrast with FW1, which experienced structural

collapse towards the fire. As can be seen from Fig. 16, during the initial stages of heating the central deflection of the wall bowed towards the fire as would be expected. Then at a deflection of approximately -8.5 mm and an exposed face temperature of 992°C the direction of the central deflection reversed and the wall commenced to bow away from the fire until structural collapse at a small deflection of 2.87 mm.

This phenomenon is known as reverse bowing and occurs when thermal degradation of the material properties on the exposed face dominate response, effectively creating an eccentric load towards the fire side due to the weakened material. In this test the magnitude of applied load was significantly high, prohibiting the occurrence of large thermal deformations which would promote geometric non-linearity as exhibited in FW1.

Figure 16 shows the comparison between experimental and analytical results for the central deflection of FW2. The results were in reasonable agreement up to the point of reverse bowing, where the analysis continued to deflect towards the fire, and soon reached failure by both material property degradation and lateral instability at a deflection of -22.3 mm.
The failure of the model to recover from thermal bowing towards the fire has been attributed to the earlier assumption that the loading plate at the top of the wall did not experience any rotational restraint within the limits of the tests. It was then thought to be the case that rotational restraint was present after a certain value of rotation, θ_{lim}. If in fact rotational restraint was imposed after θ_{lim} the restraining moment, M_{lr}, may well have served to limit and curtail the deflections towards the fire. Assuming rotation in the loading plate to be fixed, the wall may have continued to curve towards the fire creating the ends of the wall to tilt. This would have resulted in a redistribution of load over the top surface causing additional compressive forces on the on the exposed face of the wall, as Fig. 17 explains.

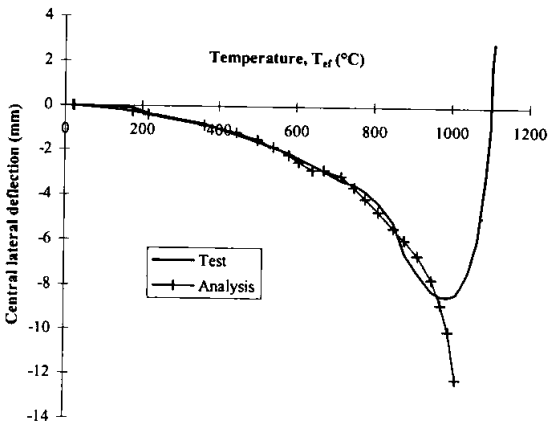

FIGURE 16 : Comparison between experimental and analytical central deflections for FW2.

Given the limiting rotation hypothesis to be correct it must be commented on why comparable results were achieved for FW1 while rotational restraint was not included. Two particular reasons arrived at were;

i) The applied loading in test FW1 was half that of FW2, thus in test FW1 the transient strain component was much smaller due to the lower load level, resulting in larger thermal deflections.

Therefore, although rotational restraint may have been present in FW1 the thermal strains were sufficient to increase lateral deflections to a point where runaway deflections occurred.

ii) The failure time of FW1 was 28 minutes indicating that the temperature in the exposed face of the wall did not have time to increase to a sufficient level to create significant material property degradation, therefore limiting the possibility of reverse bowing.

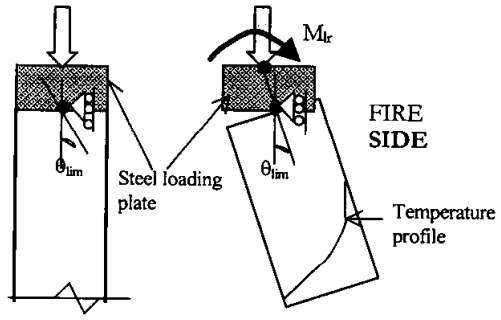

FIGURE 17 : The additional moment experienced due to rotational restraint that is present after θ_{lim} has been reached.

The investigation of the relationship between θ_{lr} and Δ_{cx} (Fig. 18) along with the θ_{lr}-T_{ef} relationship (Fig. 19) gave evidence to verify the above suggestions. Reverse bowing in FW2 occurred at a central deflection of approximately -8.0 mm, therefore the value of limiting rotation was assumed to occur at this point and was found to be 1.95 degrees, which was taken from analytical results, since the rotation of the loading plate was not measured during testing. From Fig. 18 it is apparent that the central deflection of FW1 was significantly higher than that of FW2 at the limiting rotation, which indicated that a situation of large lateral deflections was more likely to occur in FW1 than in FW2.

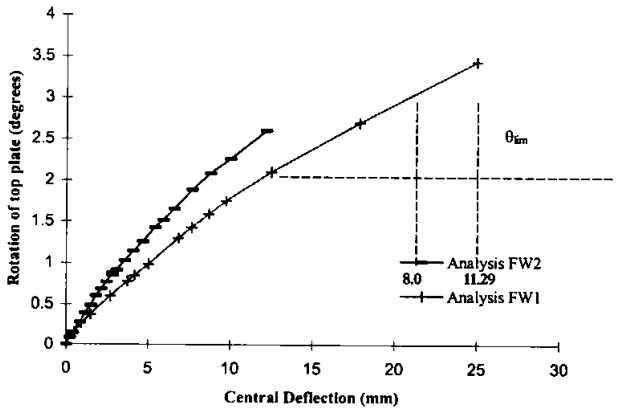

FIGURE 18. Analytical results of top rotation V's central deflection for FW1 and FW2.

Fig. 19 illustrates the exposed face temperatures in relation to rotation at the top of the wall. At the limiting rotation the temperature on the fire side of the wall was greater in FW2 than in FW1.

From the established material property degradation relationship employed it was determined that at this point the compressive strength of the material in the fire side was approximately 50 % higher in FW1 than that in FW2.
This indicated that FW1 was more capable of sustaining the additional compressive forces imposed by M_{lr}, hence limiting the possibility of reverse bowing.

The actual failure mode of FW2 was due to material property degradation, since the duration of the test was sufficient to ensure adequately high temperatures on the fire side in addition to considerable temperature sink into the wall. Structural collapse was experienced at a deflection of 2.87 mm away for the furnace and was thought to be due to crushing of the mortar joints on the fireside.

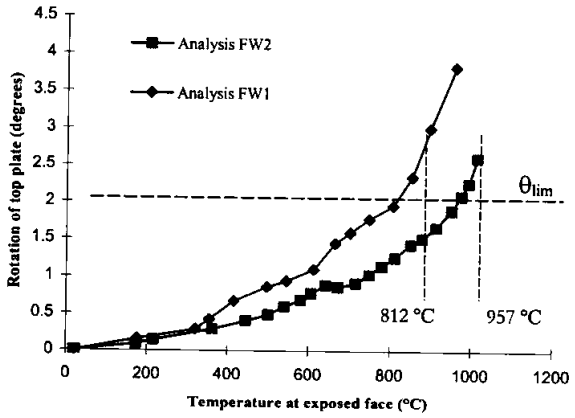

FIGURE 19 : Analytical results of top rotation V's exposed face temperature for FW1 and FW2.

CONCLUSIONS

In general the finite element model MasSET proved to be successful. Areas where experimental simulation proved difficult came as a result of undetermined experimental conditions, in particular complex boundary conditions. However where controlled rotational stiffness was present, MasSET produced close similitude.

The numerical results yielded for the fire wall test FW1 have shown good agreement with experimental data. The analytical modelling of FW2 was less successful. However, numerical and experimental results were comparable up to the point where reverse bowing was experienced during testing. The failure of the numerical model to simulate the reverse bowing in FW2 was attributed to the fact that rotational restraint of the top boundary condition was not included in the analysis. It was considered feasible that a certain amount of rotation (θ_{lim}) was allowed to occur freely, but beyond that value the rotation was at least partially restrained. In order to model test conditions accurately the M_{lr}-θ_{lr} relationship of the top boundary condition in the test rig must be determined and applied to the structure during analysis.

NOMENCLATURE

a_{th} = thermal displacements
B = stain matrix
D_T = tangent elasticity matrix
ε_{ult} = ultimate strain
f'_c = compressive strength
f'_{c20} = compressive strength at room temperature
f'_t = tensile strength
f_{th} = thermal nodal loads
K_T = tangent stiffness matrix
M_{lr} = restraint moment
N_i = shape functions
T_{ef} = exposed face temperature
T_{GP} = Temperatures at the gauss points,
T_i = nodal temperatures
Δ_{cx} = central deflection
α_l = thermal expansion coefficient
θ_{lr} = restraint rotation
θ_{lim} = limit rotation
ε_{cu} = crushing strain
ε_{tot} = total strain
ε_{σ} = stress related strain
ε_{tr} = transient strain
ε_{th} = thermal strain
σ_{th} = thermal stresses

RERERENCES

1- BS 5628, Code *of Practice for Use of Masonry, Pt 1. Structural Use of Unreinforced Masonry*, British Standards Institution, London. 1992.

1. CP 121, *Code of Practice for Walling, Pt 1: Brick and Block Masonry*, British Standards Institution, London. 1973.
2. Eurocode No.6., *Design of Masonry Structures. Pt 10: Structural Fire Design*, Commission of European Communities. 1990.
3. Building Regulations, *Technical Booklet E, Fire Safety*, Department of the Environment for Northern Ireland. June 1994.
4. Gnanakrishnan, N. & Lawther, R., *Some Aspects of the Fire Performance of Single Leaf Masonry Construction2*, International Symposium on Fire Engineering for Building Structures and Safety, Melbourne, The Institution of Engineers Australia. 89/16, 93-99. 1989.
5. Dhanasekar, M., Chandrasekaran, V. & Grubits, S.J., *A Numerical Model for the Thermal Bowing of Masonry Walls*, Tenth International Brick Masonry Conference, Canada, 1093-1102. 1994.
6. O'Meagher, A.J. & Bennetts, I.D., *Modelling of Concrete Walls in Fire*, Fire Safety Journal, 15, 315-335. 1991.
7. Cooke, G.M.E. & Morgan, P.B.E., *Thermal Bowing in Fire and how it Affects Building Design*, Building Research Establishment Information Paper.

8. Shields, T.J., O'Connor, D.J., Silcock, G.W.H. & Donegan, H.A, *Thermal Bowing of a Model Brickwork Panel*, Proceedings of 8th International Brick/Block Masonry Conference, Dublin. 2, 846-856. 1988.
9. Byrne, S.M., *Fire Resistance of Load-bearing Masonry Walls*, Fire Technology, 15 (3), 180-188. 1979.
10. Lawrence, S.J. & Gnanakrishnan, N., *The Fire Resistance of Masonry Walls - An Overview*, Fire National Structural Engineering Conference, Melbourne, 26-28 August, 431-437. 1987.
11. Laverty, D., Nadjai, A., O'Connor, D.J., *Modelling of Thermo-Strutural Response of Concrete Masonry Walls Subjected to Fire*, Journal of Applied Science, V. 10, Nbre. 1, 3-19, 2001.
12. Eurocode No.4., *Design of Composite Steel and Concrete Structures. Pt 1.2: Structural fire design (second draft)*, Commission of the European Communities. 1992.
13. Schneider, U, *Behaviour of Concrete at High Temperatures*, RILEM Committee Report. (44-PHT). 1983.
14. Anderberg, Y. & Thelandersson, S., *Stress Deformation Characteristics of Concrete at High Temperatures*, Division of Structural Mechanics and Concrete Construction, Lund Institute of Technology, (15). 1976.
15. Kupfer, H., Hilsdorf, K.H., & Rush, H., *Behaviour of Concrete under Biaxial Stresses*, Proc. ACI, 66(8), 656-666. 1969.
16. O'Connor, D.J. & Scotney, B.W., *Determination of Equivalent Thermal Response Parameters for Evaluating the Structural Response of Beams Subjected to Transient Thermal Environments*, International Journal of Mathematics, Education, Science and Technology, 26, (1), 111-130. 1995.
17. Khoury, G.A., Grainger, B.N. & Sullivan, P.J.E., *Transient Thermal Strain of Concrete: Literature Review, Conditions Within Specimen and Behaviour of Individual Constituents*, Magazine of Concrete Research. 37 (132), 131-144. 1985.
18. Abrams, Melvin S., *Compression Strength of Concrete at Temperatures to 1600F. Effect of Temperature on Concrete*, Portland Cement Association Research and Development. (SP 25-2), 33-58. 1971.
19. Terro, M.J., *Numerical Modelling of the Behaviour of Concrete Structures in Fire*, ACI Structural Journal, March-April, 183-193. 1998.
20. Thelandersson, S., *Effect of High Temperature on Tensile Strength of Concrete*, Nordisk Betong. 1972.
22. Gnanakrishnan, N., ***The Effect of end Restraint on the Stability of Masonry Walls Exposed to Fire***, National Building Technology Centre.

FIRE RESISTANCE BEHAVIOUR OF LIGHTWEIGHT-FRAMED CONSTRUCTION

Noureddine Bénichou and Mohamed A. Sultan
National Research Council of Canada, Ottawa, Ontario, Canada
noureddine.Benichou@nrc.gc.ca
mohamed.sultan@nrc.gc.ca

ABSTRACT

This paper presents the results of a number of full-scale fire resistance tests conducted in accordance with the CAN/ULC-S101 standard on wall and floor systems as part of the collaborative research program on the fire and acoustical performance of lightweight assemblies. Based on the test results, the effects of a number of design parameters on the fire resistance performance of assemblies have been investigated including: attachment of the gypsum board, insulation type, resilient channels, gypsum board thickness, number of gypsum board layers, stud arrangements, type of framing, resilient channel and framing spacing, sub-floor type and structural load. The results have shown that the main factors that affected the performance of stud wall assemblies were the type of insulation, the number of gypsum board layers, and attachment of gypsum board. The paper also describes how the information gathered from this study will be used to benefit practitioners, builders and regulators in choosing suitable assemblies for their designs. This includes, a discussion of the models that have been developed to predict the fire resistance of lightweight assemblies. Finally, the paper provides a brief summary of NRC's future research in the area of lightweight-framed construction.

KEYWORDS: behaviour, fire resistance, fire test, lightweight, models, steel, wood

INTRODUCTION

Lightweight-framed construction is widely used in up to four-storey residential buildings. This construction includes wall and floor assemblies, which are used as fire barriers in multi-family dwellings and are required to exhibit acceptable fire resistance prescribed in the National Building Code of Canada (NBC) [1]. To satisfy these requirements, designers, architects and builders can choose fire-rated assemblies from different sources such as the listed assemblies or from the Part 9 Appendix A table of the NBC. The functions of the barriers are to contain the

fire within the compartment of fire origin and to provide safety to the occupants and firefighters during evacuation and rescue operations. Aside from fire resistance, wall assemblies separating dwellings must also satisfy other requirements, including structural support, earthquake resistance and noise control between dwellings. Optimizing one factor may compromise others.

In 1990, the Sound Transmission Class (STC) between dwellings was increased from STC 45 to STC 50 in the NBC to meet public demands for better acoustic isolation. As well, construction materials and methodologies have changed over the past decade. However, with these changes, are there any concerns on the fire resistance requirements of wall and floor assemblies? To answer this question, the National Research Council of Canada (NRC), in collaboration with a number of industry and government partners, has carried out an extensive experimental program on lightweight-framed assemblies to measure the fire resistance and acoustic performance of these assemblies. The experimental studies included steel- and wood-framed wall and floor assemblies where a number of parameters have been studied, including the attachment of gypsum board to a framing or to resilient channels, types of insulation, use and location of resilient channels, gypsum board thickness, the number of gypsum board layers, stud arrangements, framing type, framing and resilient channel spacing, sub-floor type and structural load.

This paper first briefly presents the experimental studies that have been carried out on wall and floor assemblies. It then presents the effects of various parameters that influence the fire resistance performance of lightweight-framed assemblies. The paper also describes how the information gathered from this experimental program was used to: a) generate fire resistance ratings to incorporate in the National Building Code of Canada; b) develop key trends for design; and c) develop fire resistance models for designs that could provide an alternative to testing of assemblies which is both expensive and time consuming. All of this information can be useful to practitioners, builders and regulators in choosing suitable assemblies for design. In addition, a section at the end of the paper will be dedicated to providing a brief section on where NRC is going with its research in the area of lightweight-framed construction.

EXPERIMENTAL PROGRAM

To determine the effects of various parameters on the fire resistance of wood- and steel-framed assemblies, a detailed experimental study was undertaken. The experimental program consisted of full-scale fire tests on 17 walls (see Table 1) and 23 floors (see Table 2). The systems tested were replicates of assemblies commonly used in North America and listed in the NBC [1].

Typical wall or floor assemblies are constructed with materials that include:

- Wood or steel studs or joists representing the framing and spaced at 400 mm or 600 mm.
- Layers of Type X gypsum board (GB), 12.7 or 15.9-mm thick, fixed to either resilient channels (RC) or studs or joists using screws.
- Insulation within the cavities including glass fibre, rock fibre or cellulose fibre.
- Subfloor for joist assemblies attached to the framing from the top using screws or nails.

Table 1. Wall assembly parameters and fire resistance test results [3] and [4]

Wall No.	Stud			Shear Panel	Gypsum Board			Insulation Type	Resilient Channels	Load (kN)	Failure Time (min)	Failure Mode
	Type	Spacing (mm)	Rows		Type	Thickness (mm)	Exp./Unexp.					
1	SS	406	Single	No	X	12.7	1 & 2	***	***	***	65	Thermal
2	SS	406	Single	No	X	12.7	1 & 2	Glass	***	***	65	Thermal
3	SS	406	Single	No	X	12.7	1 & 2	Rock	***	***	100	Thermal
4	SS	406	Single	No	X	12.7	1 & 2	CFI[5]	***	***	62	Thermal
5	WS	406	Single	No	X	12.7	1 & 2	Glass	Yes[1]	68	51	S/F
6	WS	406	Single	No	X	12.7	1 & 2	Rock	Yes[1]	68	52	S/F
7	WS	406	Single	No	X	12.7	1 & 2	Rock	Yes[2]	68	58	S/F
8	WS	406	Single	No	X	12.7	1 & 2	CFI[6]	Yes[2]	68	56	S/F
9	SS	406	Single	No	X	12.7	1 & 2	Rock[3]	***	***	60	Thermal
10	WS	406	Single	No	X	15.9	1 & 2	Glass	Yes[1]	67	52	S/F
11	WS	406	Single	No	X	12.7	2 & 2	Glass	Yes[1]	68	79	S/F
12	WS	406	Double[4]	No	X	12.7	1 & 2	Glass	***	143	51	S/F
13	SS	406	Single	No	Reg.	12.7	2 & 2	***	***	***	63	Thermal
14	WS	406	Single	No	Reg.	12.7	2 & 2	***	***	***	65	Thermal
15	WS	406	Single	No	X	12.7	1 & 1	Glass	***	76	36	S/F
16	SS	406	Single	No	X	12.7	2 & 2	Glass	Yes[1]	78.4	56	S/F
17	SS	406	Single	No	X	12.7	2 & 2	***	Yes[1]	78.4	77	S/F

[1] On exposed side
[2] On unexposed side
[3] Loose fit (548 mm)
[4] Staggered (single plate)
[5] Cellulose wet sprayed
[6] Cellulose dry blown
Exp. = Number of GB layers on exposed side
Unexp. = Number of GB layers on unexposed side
Reg. = Regular GB
S/F – Structural Failure
*** - Null Value
CFI = Cellulose fibre insulation
SS – Steel Stud
WS- Wood Stud

Table 2. Floor Assembly Parameters and Fire Resistance Test Results [5] and [6]

Floor No.	Joist			Ceiling Finish			Sub-floor		Cavity Insulation			Resilient Channels		Load	Failure Time	Failure Type
	Type	Depth	Spacing	Type	Thick	Layers	Type	Thick	Type	Thick	Location	Orient.	Spacing			
	WJ*	(mm)	(mm)		(mm)			(mm)		(mm)			(mm)	(Pa)	(min)	
1	WJ	235	406	X	12.7	1	Ply	15.5	***	***	***	Per	406	3838	30	Flame
2	WJ	235	406	X	12.7	1	Ply	15.5	***	***	***	Per	406	3838	45	Flame
3	WJ	235	406	X	12.7	1	Ply	15.5	G1	90	B	Per	406	3838	36	Flame
4	WJ	235	406	X	12.7	1	Ply	15.5	M1	90	B	Per	406	3838	60	Flame
5	WJ	235	406	X	12.7	1	Ply	15.5	C1	93	T	Per	406	3838	59	Flame
6	WJ	235	406	X	12.7	2	Ply	15.5	***	***	***	Per	406	3838	80	Flame
7	WJ	235	406	X	12.7	2	Ply	15.5	G1	90	B	Per	406	3838	67	Flame
8	WJ	235	406	X	12.7	2	Ply	15.5	M1	90	B	Per	406	3838	72	Flame
9	WJ	235	406	X	12.7	2	Ply	15.5	C1	125	T	Per	406	3838	74	S/F
10	WIJ	240	406	X	12.7	1	Ply	15.5	***	***	***	Per	406	4605	42	S/F
11	WIJ	240	406	X	12.7	1	Ply	15.5	M1	90	B	Per	406	4653	46	S/F
12	WIJ	240	406	X	12.7	1	Ply	15.5	C1	90	T	Per	406	4654	52	Flame
13	WIJ	240	406	X	12.7	2	Ply	15.5	***	***	***	Per	406	3934	72	S/F
14	WIJ	240	406	X	12.7	2	Ply	15.5	G1	90	B	Per	406	3982	64	S/F
15	WIJ	240	406	X	12.7	2	Ply	15.5	M1	90	B	Per	406	3982	77	S/F
16	WIJ	240	610	X	12.7	2	Ply	19	G1	90	B	Per	406	290	74	S/F
17	WIJ	240	610	X	12.7	2	Ply	19	G1	90	B	Per	610	3120	65	S/F
18	SJ	203	406	X	12.7	2	Ply	15.5	***	***	***	Per	406	2950	74	S/F
19	SJ	203	406	X	12.7	2	Ply	15.5	G1	90	B	Per	406	2950	68	S/F
20	SJ	203	610	X	12.7	2	Ply	19	G1	90	B	Per	406	1799	69	S/F
21	SJ	203	406	X	12.7	2	Ply/Con	15.5/38	G1	90	B	Per	406	1915	60	S/F
22	WJ	235	406	X	12.7	2	Ply	15.5	***	***	***	Per	406	5075	69	S/F
23	WJ	235	406	X	12.7	2	Ply	15.5	G1	90	B	Per	406	5075	65	S/F

S/F – Structural Failure and Flame Penetration
Per – Perpendicular to Joists
C1 – Cellulose Fibre Insulation
WIJ – Wood-I Joist
WJ* - Screw Spacing from Gypsum Board Edges 10 mm

Ply – Plywood
T – Top
G1 – Glass Fibre Insulation
WJ- Wood Joist
X – Type X

*** - Null Value
B - Bottom
M1 – Rock Fibre Insulation
SJ- Steel Joist
Con - Concrete

The full-scale wall and floor tests were carried out by exposing one side of the assemblies to heat in a propane-fired vertical or horizontal furnace using gas fuel burners, in accordance with the CAN/ULC-S101-M89 standard [2]. The assemblies are sealed at the edges against the furnace using ceramic fibre blankets to minimize heat leakage. The furnaces can accommodate wall assemblies that are approximately 3.0 m high by 3.6 m wide and floor assemblies that are 4.8 m long by 3.9 m wide. Type K chromel-alumel thermocouples are used for measuring temperatures at a number of locations throughout an assembly. Assemblies were tested either loaded or unloaded (walls only). Loaded wall assemblies contribute to the structural load-bearing capacity of the building, while unloaded wall assemblies are used as fire barriers (partitions) and carry only their own weight. For load-bearing assemblies, the furnace has a loading device and the load is transmitted through hydraulic jacks to simulate vertical structural loads. Loads on assemblies are calculated based on the material characteristics of the assembly in accordance with CAN/ULC-S101-M89 [2]. The applied loading on the assemblies is given in Tables 1 and 2. The furnace temperature is measured by nine shielded thermocouples in accordance with CAN/ULC-S101-M89 [2]. The average of the nine-thermocouple temperatures was used to control the furnace temperature. In addition, the deflection at the unexposed surface was measured at different locations. During the tests, the furnace and assembly temperatures, deflections and the gauge pressure of the loading system were recorded at 1-minute intervals. Complete details on the construction of the wall and floor assemblies, instrumentation location and test procedures are given in references [3], [4] and [5].

The time to failure is based on failure criteria derived from CAN/ULC-S101-M89 [2], i.e.:

- Thermal failure - 140°C average temperature rise or 180°C maximum above ambient temperature on the unexposed face, or
- Integrity failure - penetration of flame and gases hot enough to ignite cotton waste, or
- Structural failure - loss of load-bearing capacity or excessive deflection of load-bearing assemblies.

DESIGN PARAMETER INVESTIGATED

The design parameters investigated include: attachment of the gypsum board, insulation type, resilient channels (RC) use and location, gypsum board (GB) thickness, number of gypsum board layers, stud arrangements, type of framing, resilient channel and framing spacing, sub-floor type and structural load. Details of the effects of all the parameters, including the graphs showing the temperature profiles in the assemblies have been reported in other references [4]' [5] and [6]. In the following sections, a summary of the effects for each parameter is provided.

Wall Assemblies

Effect of insulation use and type

Tests 1 to 4 represented the effect of the use and type of insulation in (1 & 2) non-load-bearing steel-stud assemblies (1 & 2 means 1 GB layer on the exposed side and 2 GB layers on the unexposed side). The wall with glass fibre provided the same fire resistance (FR) as the assembly without any insulation (65 min). The assembly with rock fibre provided an increase of 54% in FR (100 min) while the assembly with cellulose (wet sprayed on the exposed gypsum board (GB) surface in the cavity between studs) showed a decrease of 4% in FR (62 min) compared to a non-insulated wall. The rock fibre remains in place and protects the stud and the

GB on the unexposed side when the GB on the exposed side falls off. On the other hand, when the GB on the exposed side falls off, the cellulose fibre falls off and glass fibre melts allowing the GB on the unexposed side and the studs to be exposed to heat, resulting in earlier failure. These results indicate that an assembly with rock fibre insulation provides higher fire resistance than an assembly with either glass or cellulose fibre or with no insulation in the wall cavity.

Results from fire resistance tests 5 to 8 were used to determine the effect of insulation type on (1 & 2) load-bearing wood-stud assemblies. The fire resistance is 51 min for an assembly with glass fibre (5) and 52 min with rock fibre (6). The results show that in these assemblies, the insulation type did not affect the fire resistance, as the unprotected GB vertical joints on the fire-exposed side are the dominant factor in the FR (when RCs are used, the vertical joint is not against the vertical stud), given that these are loaded assemblies and the stud edges were being attacked with the heat after failure of the GB. When resilient channels (RCs) are on the unexposed side, the fire resistance is 58 min for an assembly with rock fibre (7) and 56 min with cellulose fibre (8), and therefore also has little or no effect in this case (failure of the fire-exposed side GB is the dominant factor).

Effect of insulation width

Results from fire resistance tests 3 and 9 can be used to determine the effect of insulation width in non-load-bearing steel-stud assemblies. The fire resistance is 60 min for an assembly with loose-fit rock fibre (9) and 100 min for an assembly with tight-fit rock fibre (3). The results show that it is important to have the insulation installed tightly between studs since a loose fit produces gaps between stud faces and the insulation leading to an earlier failure of the assembly. When rock fibre insulation was installed tightly in non-load-bearing assemblies, it provided a 60% better fire resistance than when it was loose.

Effect of resilient channels' use and location

Tests 6 and 7 were conducted to investigate the effect of the resilient channels' location on the fire resistance of load-bearing wood-stud walls. The fire resistance is 52 min for an assembly with the resilient channel on the exposed side (6) and 58 min for an assembly with the resilient channel on the unexposed side (7). The results show that the location of resilient channels plays a role in FR as the assembly with RC on the double layer side provides an increase in FR of 11%. The difference in fire resistance is caused by the presence of an unprotected vertical GB joint on the fire-exposed side in the assembly when RCs are installed (when RCs are used, the vertical joint is not against the vertical stud). With direct application to the studs, joints in the GB can be aligned with the studs.

Effect of gypsum board thickness with RCs on the exposed side

Tests 5 and 10 were conducted to investigate the effect of GB thickness on the fire resistance of (1 & 2) load-bearing wood-stud walls. The failure of the wall assembly with 12.7-mm GB (5) occurred at 51 min while in the assembly with 15.9-mm GB (10), the failure occurred at 52 min. The results show that in (1 & 2) wall assemblies with RC installed on the fire exposed side, increasing the thickness of the gypsum board layer does not improve the FR when resilient channels are present on the single-layer side. However, the fact that the fire-resistance did not improve with the increased thickness was mainly due to the ignition of the wood studs, caused by the penetration of the hot gases through the unprotected vertical gypsum board butt joints.

The gap between the studs and the gypsum board, created by the presence of the RCs, acted as a passageway through which the flames and hot gases spread freely after entering the cavity.

Effect of number of gypsum board layers with RCs on the exposed side
Tests 5 and 11 were conducted to investigate the effect of the number of GB layers in load-bearing wood-stud assemblies. The failure of a wall assembly with one layer of GB (5) occurred at 51 min, while in an assembly with two layers of GB (11), the failure occurred at 79 min. The results show that the installation of a second layer of GB on the fire-exposed side (with staggered joints) increases the FR by 55% compared to an assembly with one layer of GB on the exposed side. Having a backing to the fire-exposed GB layer adds significantly to the fire resistance, as it reduces the penetration of hot gases.

Effect of stud type
Results from fire resistance tests 13 and 14 can be used to assess the effect of stud type in (2 & 2) non-load-bearing stud assemblies. The failure in a steel-stud wall (13) occurred at 63 min while in the wood-stud wall (14), it occurred at 65 min. The type of stud used in non-load-bearing walls is insignificant for assemblies with two layers of gypsum board on each side.

Floor Assemblies
Effect of attachment of the gypsum board with RCs on the ceiling
Floor Assemblies Nos. 1 and 2 with wood joists were tested to investigate the effect of the gypsum board screw spacing (10 mm and 38 mm) from board edges with a single layer of gypsum board ceiling finish attached to resilient channels. Assembly No. 1, with screws at 10 mm, provided 30 min of fire resistance while Assembly No. 2, with screws at 38 mm, provided 45 min. These results showed that by moving the screws away from the board edges (from 10 mm to 38 mm), the fire resistance increased by 50%. This can be explained by the fact that after the water in the board was driven off and the gypsum board core became dry, the board edges started to shrink and peel away from the screw heads. The board edges peeled away from the screw heads much faster in the assembly with screws at 10 mm, as they were located much closer to the edges, than in the assembly with screws at 38 mm. Thus, the sub-floor and joist sides were fully exposed to the furnace heat much earlier in the former assembly. This accelerated the burning of the joists and sub-floor and caused the assembly with screws at 10 mm from the board edges to fail earlier.

Effect of insulation installation and type
Assemblies Nos. 2 to 5 (wood joist with 1 layer of gypsum board), Nos. 6 to 9 (wood joist with 2 layers of gypsum board), Nos. 10 to 12 (wood-I-joist with 1 layer gypsum board), Nos. 13 to 15 (wood-I-joist with 2 layers of gypsum board) and Nos. 18 and 19 (C-steel joist with 2 layers of gypsum board) were tested to investigate the effect of insulation type (glass, rock and cellulose fibre) on the fire resistance.

Floor Assemblies with Wood Joists – The results show that, for Assemblies Nos. 1 to 5, as a result of the substantial increase in board temperature (at 27 min for assemblies with either glass or rock fibre insulation and at 35 min for an assembly with cellulose fibre insulation), the board cracked and fell off, unlike the non-insulated assembly. However, in the assembly with glass fibre insulation, the fibre melted when it was exposed to furnace heat in about 2 to 3 min after

the gypsum board had fallen off; consequently, the sub-floor and joist sides were exposed to the furnace heat and the glass fibre was unable to compensate for the earlier failure of the gypsum board and provided a negative effect in the fire resistance. The rock and cellulose fibre remained in place after the gypsum board fell off and was able to compensate for the early failure of the gypsum board as well as protect the joist and sub-floor from furnace heat and thus, both rock and cellulose fibre insulation provided a positive effect on fire resistance. The fire resistance results of Assemblies Nos. 2 to 5 given in Table 2 showed that, compared to a non-insulated assembly, which provided a 45 min fire resistance, the installation of the glass fibre reduced the fire resistance by 20% while the rock and cellulose fibre increased the fire resistance by 33% and 31%, respectively.

The results show that, for Assemblies Nos. 6 to 9, as a result of the substantial increase in board temperature, the board cracked and fell off at approximately 60 min for insulated assemblies, unlike the non-insulated assembly at 75 min. In an insulated assembly with 2 layers of gypsum board, the exposure time for indirect furnace heat (conduction through the board) was much longer than in an insulated assembly with 1 layer of gypsum board. The deteriorated glass, rock and cellulose fibre insulations were unable to compensate for the earlier failure of the gypsum board and thus, all insulations provided a negative effect on fire resistance. The fire resistance results for Assemblies Nos. 6 to 9 given in Table 2 showed that, compared to a non-insulated assembly, which provided an 80 min fire resistance, the insulation reduced the fire resistance by 16% with glass fibre, by 10% with rock fibre and by 7.5% with cellulose fibre.

Floor Assemblies with Wood-I Joists - The results show that, for Assemblies Nos. 10 to 12, as a result of the substantial increase in board temperature, the board cracked and fell off. However, the rock and cellulose fibre remained in place after the gypsum board fell off and was able to compensate for the early failure of the gypsum board as well as protect the joist and sub-floor from furnace heat and thus, both rock and cellulose fibre insulation provided a positive effect on fire resistance. The fire resistance results for Assemblies Nos. 10 to 12 given in Table 2 showed that the insulation increased the fire resistance by 10% in the assembly with rock fibre and by 24% in the assembly with cellulose fibre compared to an assembly with no insulation in the floor cavity. In assemblies with wood-I-joists, the rock and cellulose fibre, like in the assembly with wood joists, provided a positive effect on fire resistance.

The results show that, for Assemblies Nos. 13 to 15, as a result of the substantial increase in board temperature, the board cracked and fell off at approximately 61 min for the assembly with glass fibre, 70 min for the assembly with rock fibre and non-insulated assembly. However, in the assembly with glass fibre insulation, the fibre melted when exposed to furnace heat in about 3 min; consequently, the sub-floor and joist sides were exposed to the furnace heat and glass fibre was unable to compensate for the earlier failure of the gypsum board and provided a negative effect in the fire resistance while the rock fibre remained in place after the gypsum board fell off and was able to compensate for the early failure of the gypsum board as well as protect the joist and sub-floor from furnace heat and thus, the rock fibre insulation provided a positive effect on fire resistance. The fire resistance results for Assemblies Nos. 13 to 15 given in Table 2, showed that the insulation reduced the fire resistance by 7% in the assembly with glass fibre and increased the fire resistance by 7% in the assembly with rock fibre compared to an assembly with no insulation.

Floor Assemblies with C-Steel Joists – The results show that, for Assemblies Nos. 18 and 19, as a result of the substantial increase in board temperature, the board cracked and fell off at approximately 62 min for the assembly with glass fibre, 71 min for the non-insulated assembly. However, in the assembly with glass fibre insulation, the fibre melted when it was exposed to furnace heat in about 3 min; consequently, the sub-floor and joist sides were exposed to the furnace heat and glass fibre was unable to compensate for the earlier failure of the gypsum board and provided a negative effect in the fire. The fire resistance results for Assemblies Nos. 18 and 19 given in Table 2, showed that the installation of glass fibre insulation in the floor cavity of the assembly with a double-layer gypsum board reduced the fire resistance by 8% compared to an assembly with no insulation in the floor cavity.

Effect of number of gypsum board layers

Floor Assemblies with Wood Joists - Floor Assemblies Nos. 1 and 6 were tested to investigate the effect of the number of gypsum board layers on the fire resistance of non-insulated wood joist assemblies. The fire resistance of these assemblies given in Table 2, showed that the assembly with a double-layer of 12.7 mm gypsum board ceiling finish provided an increase in fire resistance of 78% compared to an assembly with a single layer of 12.7 mm gypsum board.

Floor Assemblies with Wood-I Joists - Floor Assemblies Nos. 10 and 13 were tested to investigate the effect of the number of gypsum board layers on the fire resistance of non-insulated wood-I-joist assemblies. The results given in Table 2, showed that the assembly with a double-layer gypsum board ceiling finishes provided an increase in the fire resistance of 71% compared to an assembly with a single layer of 12.7 mm gypsum board.

Effect of joist spacing

Floor Assemblies with Wood-I Joists - Floor Assemblies Nos. 14 and 16 were tested to investigate the effect of joist spacing (406 mm o.c. and 610 mm o.c.) on the fire resistance of wood-I-joist floor assemblies with a double layer gypsum board ceiling finish and glass fibre insulation in the floor cavity. Assembly No. 14 (with 406 mm o.c. joist spacing) provided 64 min of fire resistance while Assembly No. 16 (with 610 mm o.c. joist spacing) provided 74 min. The assembly with the wider joist spacing provided better fire resistance due to the increase in convective cooling inside the larger floor cavities created by the joists that slightly reduced the heat build-up in the gypsum board core and insulation compared to the assembly with smaller cavities.

Floor Assemblies with C-Steel Joists - Floor Assemblies Nos. 19 and 20 were tested to investigate the effect of joist spacing (406 mm o.c. and 610 mm o.c.) on the fire resistance performance of steel joist floor assemblies with a double layer gypsum board ceiling finish and glass fibre insulation in the floor cavity. Assembly No. 20 (with 406 mm o.c. joist spacing) provided 68 min, while Assembly No. 21 (with 610 mm o.c. spacing) provided 69 min. The difference in the fire resistance is within the systematic error of the test procedure. These results showed that, unlike the case with wood-I-joist assemblies, the effect of steel joist spacing on fire resistance is insignificant. For these assemblies, the joist spacing did not play a role in the fire resistance due to the heat transfer from the steel joist edges to the web.

Effect of resilient channel spacing
Floor Assemblies 16 and 17 were tested to investigate the effects of the resilient channel spacing (406 mm o.c. and 610 mm o.c.) on the fire resistance of wood-I-joist floor assemblies with a double-layer gypsum board ceiling finish and glass fibre insulation in the floor cavity. Assembly No. 16 (with 406 mm o.c. channel spacing) provided 74 of min fire resistance while Assembly 17 (with 610 mm o.c. channel spacing) provided 65 min. The assembly with the wider resilient channel spacing provided less fire resistance due in part to the lesser number of fasteners for the gypsum board. The more screws the assembly has, the better chance for the gypsum board to remain in place and protect the frame and thus, the better the fire resistance.

Effect of sub-floor type
Assemblies 20 and 21 were conducted to investigate the effect of adding concrete topping above the plywood sub-floor. Assembly 20 with no concrete topping provided 68 min of fire resistance and Assembly 21 with concrete topping provided 60 min. Adding concrete topping reduced the heat transfer across the assembly. As a result, the gypsum board temperature was higher in the assembly with concrete topping and consequently fell off earlier than the assembly with no concrete topping.

Effect of load
Assemblies 6, 7, 22 and 23 were conducted to determine the effect of load on the fire resistance. Assemblies 6 (no insulation) and 7 (with insulation) were tested with 75% design load and Assemblies 22 (no insulation) and 23 (with insulation) were tested with 100% design load. Assembly 6 provided 80 min and Assembly 22 provided 69 min of fire resistance. Also, Assembly 7 provided 67 min and Assembly 23 provided 65 min of fire resistance. These results showed that when the load increased by 25%, the fire resistance decreased by 14% for a non-insulated assembly and by 3% in an insulated assembly.

HOW CAN WE USE THIS INFORMATION?

The information obtained from this experimental program can be used in 3 ways: a) development of listing tables for codes; b) key trends for design; c) development and validation of fire resistance models. These are explained in the following sections.

Development of Listing Tables for Codes
Fire design of wall and floor assemblies is usually carried out by reference to standard fire test results. The results of this study and a study on the acoustical performance were used as the basis for the published update Part 9 Appendix A table of the NBC [1] that included generic fire resistance ratings of hundreds of wall and floor assemblies. The list of these assemblies is on the Website (http://www.ccbfc.org/ccbfc/changes/soundfire_E.shtml). Designers can use the table for their designs, but the user can choose from any other acceptable source.

Key Trends for Design
The key design trends can be summarized in the following sections.

Wall assemblies

- Fire resistance increases considerably with an increase in the number of gypsum board layers on each side. When using multiple board layers, it is recommended to stagger joints between sheets.
- With resilient channels beneath the single gypsum board layer, increasing the thickness of the GB layer does not improve the fire resistance.
- The use of resilient channels reduces the fire resistance of stud walls, especially when fixed to a single gypsum board layer. To minimize this fire resistance reduction, resilient channels should be installed under the double gypsum board layer.
- For non-load-bearing (1&2) steel-stud walls, installing rock fibre insulation in the cavity contributes significantly to the fire resistance. To maximize the fire resistance benefits of rock fibre insulation, it is important to install the batts tightly between studs.
- For load-bearing (1&2) wood-stud walls, the cavity insulation type has no effect on fire resistance.
- For load-bearing (1&2) wood-stud walls, there is no benefit in using staggered row studs (single plate) instead of single row studs.
- The type of stud used in non-load-bearing walls has no effect on the fire resistance.

Floor assemblies

- Assemblies with screws located further away from board edges (38 mm versus 10 mm) provide higher fire resistance.
- In assemblies with wood joists and a single-layer gypsum board ceiling finish, the glass fibre reduced the fire resistance while the rock and cellulose fibre increased the fire resistance compared to a non-insulated assembly. In assemblies with a double-layer of 12.7 mm gypsum board finish, the glass, rock and cellulose fibre all reduced the fire resistance compared to a non-insulated assembly.
- For floor assemblies with wood-I-joists and a single layer of 12.7 mm gypsum board ceiling finish, the rock and cellulose fibre insulation increased the fire resistance compared to a non-insulated assembly. In assemblies with a double-layer of 12.7 mm gypsum board finish, the glass fibre reduced the fire resistance while rock fibre increased the fire resistance compared to a non-insulated assembly.
- Assemblies with two layers of 12.7 mm gypsum board with staggered joints provided a significant increase in the fire resistance compared to an assembly with one layer of 12.7 mm gypsum board.
- For wood-I joist floor assemblies with glass fibre insulation and a double-layer of 12.7 mm gypsum board, the effects of joist spacing and resilient channel spacing (406 mm o.c. and 610 mm o.c.) were significant.
- For floor assemblies with C-steel joists and a double-layer of 12.7 mm gypsum board ceiling finish, glass fibre insulation reduced the fire resistance compared to a non-insulated assembly and the effect of joist spacing (406 mm o.c. and 610 mm o.c.) was insignificant.
- Adding concrete topping to a plywood sub-floor reduced the fire resistance.
- The increase in structural load decreases fire resistance.

Development of Fire Resistance Models

Although beneficial, test methods have drawbacks, including high costs and time, limitations of specimen geometry and loading, and repeatability. To overcome these drawbacks, there is a

need to develop calculation methods for assessing the fire resistance of lightweight-frame assemblies. The calculation methods would also help in designing an experimental program, improve products manufacturing, and assist the industry in taking full advantage of the opportunities offered by performance-based codes, as these methods would facilitate a faster design process. To develop a fire resistance model for assemblies that replicate test results, the fire resistance behaviour from the experimental program must be carefully observed. In the following sections, two models for predicting the fire resistance of stud wall assemblies are presented. A third model for predicting steel-joist floor assemblies was also developed but will not be presented in this paper because of space limitation.

Wall Models

During the tests, the behaviour of wood- and steel-stud wall assemblies was observed and Figure 1 shows schematic representations of the failure modes of wood- and steel-stud wall assemblies.

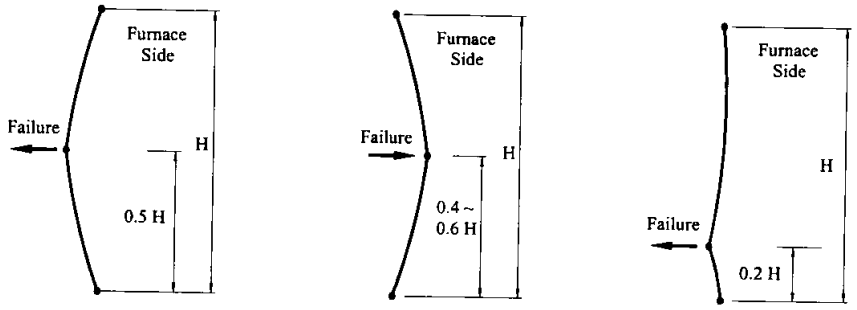

a) wood studs b) non-insulated steel studs c) insulated steel studs

Figure 1. Schematic representations of failure modes for wood- and steel-stud walls.

Description of the Wood-Stud Wall Fire Resistance Model

NRC, in collaboration with Forintek Canada Corp. (FCC), has developed an analytical model for predicting the fire resistance of wood-stud wall assemblies. The model couples a thermal response sub-model and a structural response sub-model. The thermal response sub-model, called WALL2D [7], predicts the temperature profile inside the wood-stud wall and the time to insulation failure. The thermal response is predicted using a finite difference heat transfer sub-model developed by FCC. The sub-model determines the temperature distribution in the wall as a function of time, taking into account the heat absorbed in the dehydration of gypsum and wood, and in the pyrolysis of wood, without considering mass transfer. The heat transfer, through gypsum boards and wood studs, is described using an enthalpy formulation. The sub-model assumes that heat transfer occurs mainly in the cross-section of the wall assembly and that heat flow in the vertical direction can be ignored. The finite difference mesh considers symmetry of the wall, with a mesh refinement in proximity of the wood stud and larger spacing within the gypsum board far from the wood stud. The structural fire performance of wood-frame assemblies is affected by the rate of charring, degradation of the mechanical properties of the wood at elevated temperatures and the load sustained by assemblies. To determine the structural response, a buckling load sub-model is implemented with WALL2D. The sub-model uses the temperature distribution predicted by WALL2D as an input, then calculates the deflection and

the critical elastic buckling load for a wood-stud wall. The buckling of the wood studs is restricted to the strong axis because of the lateral support by the gypsum board. The critical elastic buckling-load, assuming both ends of the studs are pinned, is:

$$P_{cr} = \frac{\pi^2 EI}{(KL)^2} \tag{1}$$

where P_{cr} is the elastic buckling-load (N), E is the modulus of elasticity of the resisting member (MPa), I is the moment of inertia (mm^4), and KL is the effective stud length (mm), with K = 1 in this case. The values of the moment of inertia and modulus of elasticity change with time. For the moment of inertia, the temperature profile and pre-set charring temperature provide an estimation of the remaining cross-section of the stud, thus allowing for calculation of the time-dependent moment of inertia. For the modulus of elasticity, the change with temperature is obtained from the literature [4]. Structural failure is assumed to occur when the load applied on the wall exceeds the buckling load. The stud's out-of-plane deflection is estimated using the theory of elasticity. The deflection of the stud, as predicted for a hinged-hinged eccentric column, can be calculated by considering the stud as a beam-column structure. The out-of-plane deflection, y, at any height x on the stud at any time, is:

$$y(x) = \frac{M_0 L^2}{8EI}\left[\frac{2\cos\left(\Psi - \frac{2\Psi}{L}x\right) - \cos(\Psi)}{\Psi^2\cos(\Psi)}\right] \quad \text{with } \Psi = \frac{\pi}{2}\sqrt{\frac{P}{P_{cr}}} \text{ and } M_0 = P(e_c - e_p) \tag{2}$$

where L is the length of the stud (mm), e_c is the eccentricity of the centroid of the resisting member (mm), and e_p is the applied load eccentricity (mm). The maximum deformation occurs at mid-height.

A fire resistance test for assembly No. 15 was used to evaluate the predictions by the fire resistance model. The predictions of time-temperature curves generated by the heat transfer have been used to calculate the reduction in load-carrying capacity of the studs and the degradation in the modulus of elasticity, which was assumed to be equal to 7000 MPa at ambient temperature. Temperatures on the unexposed sides did not reach the insulation failure criterion, as the assembly failed by structural instability at 36 min. Table 3 summarizes the model predictions and experimental results. The model predicts conservatively the onset of charring, with a difference of about 10%.

Table 3. Comparison between tests results and model predictions

Test No.	Onset of Char (min)			Insulation Failure (min)		Structural Failure (min)		
	Test	Model	Difference	Test	Model	Test	Model	Difference
15	19.0	17.0	10%	N/A	48.0	36.0	33.0	8%

Figure 2a illustrates the critical elastic buckling load versus time as predicted by the structural response sub-model. The fire resistance decreases with increasing time because the value of the modulus of elasticity decreases with time and the cross-section of the studs reduces after

charring. The intersection of the horizontal line, at the level of the applied load (8.45 kN), with the elastic buckling-curve, represents the theoretical time to structural failure of the wall. The time is 33 min for the assembly, while the time to structural failure measured experimentally is 36 min. Therefore, the model predictions are very close to the test results, with the analytical time to structural failure underestimated by 8%. The maximum mid-height deflections are also plotted versus time for both the analytical predictions and the test results (see Figure 2b). As shown in this figure, the deflection is very small in the first 30 min. After this, the model predictions and the test measurements start increasing at a faster rate. The rate of increase in the model predictions is similar to that of the test results. The rate in the model, however, starts a few minutes later. The model slightly overestimates the deflection at 33 min.

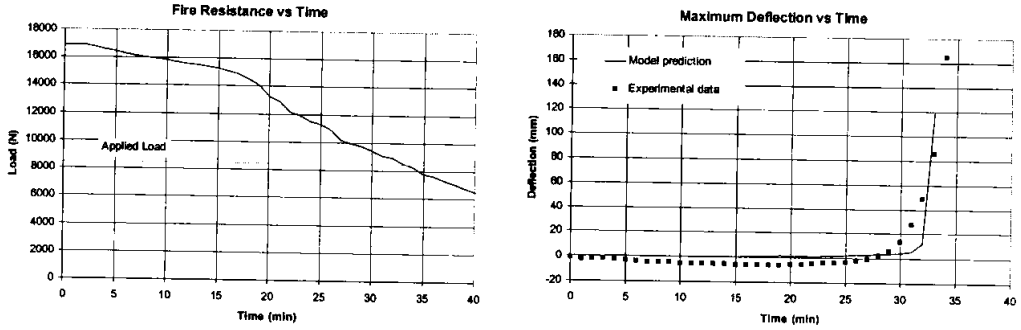

(a) (b)

Figure 2. Fire resistance determination and deflection comparisons.

Description of the Steel-Stud Wall Fire Resistance Model

As part of a joint research effort between NRC and the Canadian Steel Construction Council (CSCC), a numerical model for predicting the fire resistance of steel-stud wall assemblies was developed. The model couples a thermal response sub-model and a structural response sub-model. The thermal response sub-model, called TRACE [8], predicts the temperature history across a section of a wall assembly using a finite-difference method to solve the one-dimensional heat transfer governing equations. The model can be used to predict the temperature distribution across the assembly using any defined design fire time-temperature relationship. The structural fire performance sub-model, called STUD [8], models the stud-frame assembly as a single stud with initial imperfection, subjected to eccentric tributary load P. The model assumes: a) steel stress-strain relationships at elevated temperatures are linear up to the yield strength; b) flexural-torsional and weak axis buckling failure modes are prevented by adequate lateral restraints (bridging and blocking); c) the stud is hinged at the ends, as the load eccentricity in part models rotational end restraints; d) there is no temperature variation in the vertical direction along the stud; however, the temperature varies across the stud section from T_H at the hot flange to T_C at the cold flange. The total lateral deflection, y(x), of the stud is given by the following equation:

$$y(x) = y_1(x) + y_2(x) = (\phi\,\beta^{-2} - e)\,[\tan(0.5\beta H)\sin(\beta x) + \cos(\beta x) - 1] \quad \text{with} \quad \beta^2 = P / (E\,I^*) \quad (3)$$

where, ϕ = stress-free thermal bowing curvature, H is the height of the wall, P is the load applied in the stud, I^* = elasticity-modulus-weighted moment of inertia of the unreduced stud section

about the neutral axis parallel to flanges [8], E = steel modulus of elasticity at room temperature, $y_1(x)$ is the stress-free initial imperfection caused by thermal bowing, and $y_2(x)$ is the secondary lateral deflection caused by the vertical load, P acting with an eccentricity, e given by Equation (4) below.

$$e = (1 - K_R)\,\phi\,\beta^2 \tag{4}$$

where K_R is a reduction coefficient. The structural failure of studs can be predicted using formulas for members subjected to combined compression and bending [8], adjusted to account for the deterioration of the mechanical properties of steel at elevated temperatures. For insulated walls, a critical section near stud ends must be checked for the compressive failure of the hot flange, using the following failure criterion:

$$f_H = n_H\left(\frac{P}{A_e^*} + \frac{P\,[e - y(0.2H)]}{S_{eH}^*}\right) \geq F_{yH} \tag{5}$$

where, f_H = compressive stress at the extreme fibre of the hot flange, n_H = reduction factor for temperature T_H (given as E_{TH}/E), $F_{y\,H}$ = yield strength of steel at temperature T_H [8], A^*_e = elasticity-modulus-weighted effective stud section area in compression, and S^*_{eH} = elasticity-modulus-weighted effective stud section modulus in bending that causes compression of hot flange [8]. For non-insulated walls, a critical section at (or near) the stud mid-height must be checked for the compressive failure of the cold flange, using the following failure criterion:

$$f_C = n_C\left(\frac{P}{A_e^*} + \frac{P\,y(0.4H)}{S_{eC}^*}\right) \geq F_{yC} \tag{6}$$

where, f_C = compressive stress at the extreme fibre of the cold flange, n_C = reduction factor for temperature T_C (given as E_{TC}/E), F_{yC} = yield strength of steel at temperature T_C [8], and S^*_{eC} = elasticity-modulus-weighted effective stud section modulus in bending that causes compression of cold flange [8].

Table 4 lists predictions for Tests 16 and 17 based on measured temperature histories, and also, based on histories obtained from heat transfer simulations [8]. Predictions for non-insulated wall 17 show a reasonable agreement with test structural failure times. For insulated wall 16, predicted failure times agree well with the initiation of structural failure in central studs.

Table 4. Comparison of Predicted Failure Times with Test Results.

Assembly number	Fall-off time of gypsum board on exposed side (min)		Structural failure time in test (min.)	Initiation of failure in central studs in test (min.)	STUD predictions based on measured temperatures (min.)	STUD predictions based on simulated temperatures (min.)
	Face layer	Base layer				
16	50	in place	56	49	50	51
17	58	in place	77	N/A	77	73

Simulated mid-height lateral deflection histories for Tests 16 and 17 are presented in Figure 3. For these simulations, average HF and CF temperatures measured in the central part of wall specimens were used for T_H and T_C input, respectively. For all test simulations, the value of K_R = 0.6 proved to produce a reasonably good agreement of simulated and measured deflections until the initiation of structural failure mechanisms in central studs. More details on the validation of the model are found in other references [8].

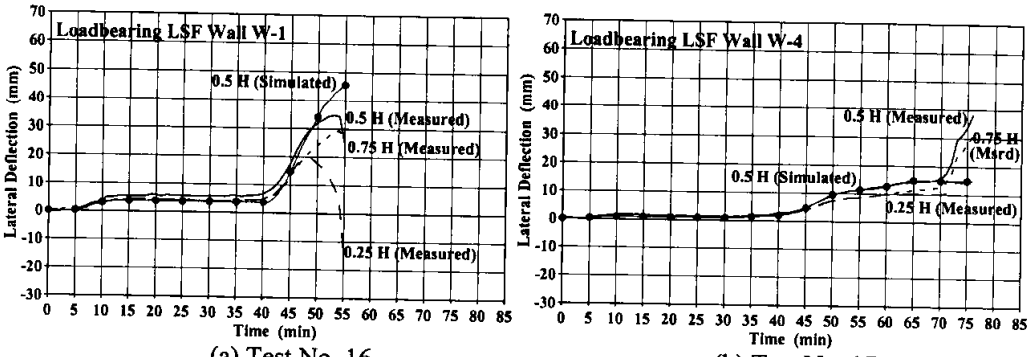

(a) Test No. 16 (b) Test No. 17

Figure 3. Measured and Simulated Histories of Lateral Deflection (H = wall height)

SUMMARY AND CONCLUSIONS

To evaluate the impact of changes in code requirements and building construction materials, an extensive experimental program has been undertaken to investigate the effects of a number of design parameters including attachment of the gypsum board, insulation type, resilient channels, gypsum board thickness, number of gypsum board layers, stud arrangements, type of framing, resilient channel and framing spacing, sub-floor type and structural load on the fire performance of wall and floor assemblies. The results have shown that the main factors that affected the performance of assemblies are the attachment of gypsum board, type of insulation, and the number of gypsum board layers. The data gathered from this study was used to produce key design trends, to propose generic ratings for possible incorporation in the appendices of the National Building Code of Canada, and to develop fire resistance models for wood and steel wall assemblies. This information is of great benefit to practitioners, builders and regulators in choosing suitable assemblies for their design.

FUTURE RESEARCH

As a next step, the models presented here will be validated against more experimental data that include exposure to both standard and non-standard fires. A new model to predict the fire resistance of wood-joist floor assemblies will be developed. Further, a sensitivity analysis on the models on different effects such as mechanical and thermal properties, length factors, and load factors, will be carried out. Furthermore, all the models will be put under the same platform so that the designers have access to all the tools from the same menu. Finally, design equations will be developed for potential incorporation in codes and standards.

ACKNOWLEDGEMENTS

This research was funded by NRC and industry partners that included the Canadian Wood Council, Canadian Home Builders Association, Canadian Sheet Steel Building Institute, Forintek Canada Corp., Owens-Corning Canada, Roxul Inc., Gypsum Manufacturers of Canada. The authors are grateful to John Latour, Patrice Leroux, Roch Monette, Jocelyn Henrie and Richard Rombough for assisting in constructing the assemblies and conducting the tests.

REFERENCES

[1] Canadian Commission on Building and Fire Codes (1995), National Building Code of Canada, Institute for Research in Construction, National Research Council of Canada, Ottawa, Canada

[2] CAN/ULC-S101-M89 (1989) Standard Methods of Fire Endurance Tests of Building Construction and Materials, Underwriters' Laboratories of Canada, Scarborough, Canada

[3] M. A. Sultan and G. D. Lougheed, Results of Fire Resistance Tests on Full-Scale Gypsum Board Wall Assemblies, Internal Report (in press), Institute for Research in Construction, National Research Council, Ottawa, Canada

[4] N. Bénichou, and M.A. Sultan, Design considerations for fire resistance performance of lightweight-framed assemblies, CSCE 2003 Annual Conference, Moncton, NB, pp. 567-1 - 567-10, 2003

[5] M.A. Sultan, Y.P. Séguin, P. Leroux, Results of Fire Resistance Tests on Full-Scale Floor Assemblies, Internal Report No. 764, Institute for Research in Construction, National Research Council of Canada, Ottawa, ON, 1998

[6] M.A. Sultan and N. Bénichou, Fire resistance performance of lightweight floor assemblies, Designing Structures for Fire Conference, Baltimore, MD, U.S.A., pp. 203-214, 2003

[7] H. Takeda and J.R. Mehaffey, WALL2D: A Model for Predicting Heat Transfer through Wood-Stud Walls Exposed to Fire," Fire and Materials, 22: 133-140, 1998

[8] F. Alfawakhiri and M.A. Sultan, Numerical modelling of steel members subjected to severe thermal loads, Fire & Materials 2001 Conference, San Francisco, U.S.A., pp. 483-494, 2001

RATIONAL TRADE-OFF BETWEEN SPRINKLERS AND REQUIRED FIRE RESISTANCE CAPACITY

Paul CLANCY Ian THOMAS
Victoria University of Technology, PO Box 14428, Melbourne City MC Victoria 8001, Australia
Paul.Clancy@vu.edu.au *Ian.Thomas@vu.edu.au*

ABSTRACT

The aim of the research was to quantify how much the required fire resistance of structures could be reduced with the use of sprinklers while maintaining the risk of collapse consistent with the risk for ambient conditions. Other safety systems were not considered. The few previous attempts at this quantification were reviewed and methodology was advanced in light of recent research in fire statistics. The method involved the determination of realistic or natural fires with the same probability of occurrence with and without sprinklers. The main variable distinguishing between fires was fire load. Other real fire variables were constant as they would be for a particular compartment in a building. It was found that sprinklers afforded a reduction in the required fire resistance much less than may be expected. The main reason for this finding is that although the probability of sprinkler failure and the incidence of fire is low, probabilities of failure for ambient structural design cases is substantially lower.

KEYWORDS: *fire resistance, sprinklers, risk, probability, consistency, real and natural fires, performance-based design.*

INTRODUCTION

There is a tendency, among fire safety engineers, to use sprinklers in lieu of passive fire protection. This use is justified by showing that occupants can evacuate safely before untenable conditions occur due to smoke or structural collapse. There has been little quantitative analysis on the reduction in risk of structural collapse due to sprinklers. After proving safe evacuation, fire safety engineers are confident in the structural stability ensured by sprinklers. The research described in this paper, is an advance on the few previous attempts to quantify this risk. The research only focussed on the trade-off between sprinklers and fire resistance. It was not intended to evaluate the impact of other safety systems, which are available, on the required fire resistance.

REVIEW

Grubits and Tung [1]

Grubits and Tung developed an efficient Monte Carlo approach (Latin Hypercube) for rationally determining a lower required level of fire resistance capacity for elements in buildings when sprinklers are installed. While their approach involved a number of variables, a simplified illustration is given in Figure 1 using the well known method of convolution applied to probability densities of fire resistance actions and capacities (FRA and FRC respectively) as functions of some measure of fire resistance x_{FR}.

The figure is not meant to be definitive. The FRA's are commonly known as fire severities. The FRC's relate to fire resistance ratings as measured in tests. In the case of a standard fire exposure [2], FRA and FRC can be clearly measured in terms of time alone – a particular time indicates a particular fire history as an action or a capacity. In this case x_{FR} could accurately be defined as time. For real fires FRA's and FRC's depend on temperature and time as ventilation, fire load and compartment size vary. The FRA and FRC are strongly correlated to the particular time when the fire has burnt-out. The correlation is not perfect since FRA and FRC also depend on fire temperature to a smaller extent. The convolution integral in equation (1) sums the incidence when FRA exceeds FRC to give the total probability of failure, p_f [3].

$$p_f = \int_{-\infty}^{\infty} F_{FRC}(x_{FR}) f_{FRA}(x_{FR}) dx_{XR} \qquad (1)$$

where F_{FRC} = cumulative probability of fire resistance capacity.
f_{FRC} = probability density, that is frequency, of fire resistance actions.

The failure probability, p_f, is related to the area of overlap between the two plots.

The convolution for the case with no sprinklers is shown in Figure 1(a). The convolution for the case with sprinklers is shown in Figure 1(b). The probability density plot for the FRA's in Figure 1(b) comprises two peaks. There is a large peak fire for the 98% of scenarios in which

sprinklers are believed to work as designed and extinguished the fire at a low value of x_{FR}. There is another small peak for the 2% of scenarios in which sprinklers failed and the fires continued for a similar duration as for the case without sprinklers. Because of the small size of the peak for sprinkler failure, the FRC plot is moved to the left to achieve the same probability of failure as for the case without sprinklers. The movement to the left represents the reduction in the required FRC due to the installation of sprinklers.

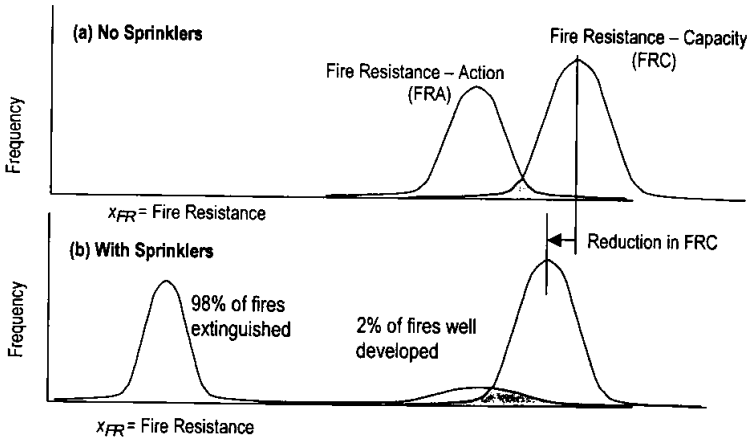

FIGURE 1. Reduction in required fire resistance capacity due to the introduction of sprinklers.

Convolution of FRA and FRC probability density functions were not actually undertaken. Instead, Monte Carlo simulations were undertaken. The predicted probability of failure was thus the number of simulations encountering failure prior to burn-out, divided by the total number of simulations. Each simulation randomly generated FRC, fire load density, floor area, compartment height, height of openings and total width of openings. The FRC was assumed to have a coefficient of variation of 0.10. Height and width of openings were assumed to randomly vary in accordance with arbitrarily chosen triangular probability distributions. All other variables were assumed to vary according to normal probability distributions.

Grubits and Tung evaluated the impact of their model for the storage compartment detailed in Table 1, except they adopted probability distributions for all variables listed. In reference to Figure 2, they deduced that sprinklers could reduce the required FRC by 60 minutes as sprinkler efficacy improved from 80% to 95%. Efficacy is the product of the reliability of the sprinkler operating, and the conditional probability that given the sprinkler operates, it actually extinguishes the fire [4]. For sprinkler efficacy improving from 95% to 96% they deduced that the required FRC reduced from 75 minutes to nil. This sudden large reduction indicates the possibility of a numerical error. Moreover, the large reductions in the required FRC have been achieved by assuming randomness in the compartment variables of size, opening width and height. Structural elements are generally not designed with random dimensions. Thus no reason is apparent for designing building elements that are framed into structural elements, as having random dimensions. Randomness increases the overlap of the FRA and FRC plots in Figure 1 and increases the calculated failure probability for the case without sprinklers which is used as the benchmark for reducing the required FRC when sprinklers are installed.

Another important factor missing from their approach is the probability of fire occurring. The level of risk among various design scenarios and load combinations should be consistent. It is not rational, for example, to say that risk from earthquakes is more tolerable than risks from fires or risks from collapse due to gravity loads alone. The probability of fire occurring affects risk and should be included in the modelling.

(Risk, of course, is the product of probability and consequences. Often probabilities are compared in evaluating consistency of risk. The comparison is valid provided that the consequences are similar.)

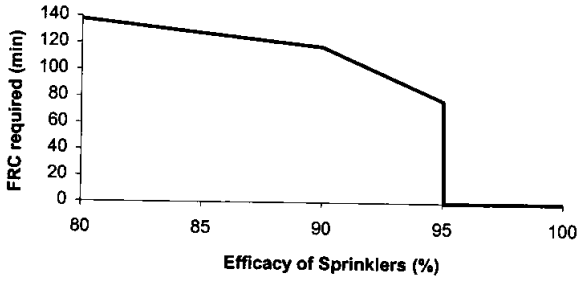

FIGURE 2. Required FRC as a function of sprinkler efficacy in case study of storage compartment.

Profil Arbed

Profil Arbed Centre de Recherches reports [5] research undertaken to improve the competitiveness of steel buildings through rational consideration of natural fires. (In this paper natural and real fires will be used virtually synonymously.) The research developed methodology for determining the required FRC as a function of natural fire variables, sprinkler performance and the performance of other fire safety systems. The fire variables included ventilation, fire load and compartment size. Other fire safety systems included egress, fire brigade intervention and occupant intervention. These other variables are beyond the scope of this paper which aims to particularly clarify the trade-off between sprinklers and required FRC. The Profil Arbed research utilised extensive fire statistics available through Europe.

Profil Arbed aimed to maintain consistency between fire risks and risks to structures in general. Assuming similar consequences, they adopted the target probability of failure, p_t , of 7.23×10^{-5} which is inherent in structural design in Europe. This probability corresponds to a safety index of 3.8.

Profil Arbed developed a Monte Carlo model for determining the safety index β_{fi} required for the fire within the context of the safety systems and risk management practices adopted. The more effective the safety systems are, the less severe the design fire need be and the lower is the

value for β_{fi} below 3.8. Application of this model was referred to as a Level 2 analysis and is represented with the equation,

$$\beta_{fi} = \phi^{-1}\left(\frac{p_t}{p_{acc}}\right) = \phi^{-1}\left(\frac{7.23\times10^{-5}}{p_{acc}}\right) \tag{2}$$

where p_{acc} = $p_1 \cdot p_2 \cdot p_3 \cdots p_i \cdots$
p_i = the failure probability of active fire safety system i.

Profil Arbed simplified and applied equation (2) in the following form to the design of individual structural elements,

$$p_{acc} = \frac{p_t}{p_{FRI} \cdot p_{sprinkler\_failure} \cdot t_{building\_lifetime} \cdot Area} \tag{3}$$

where p_{acc} = the acceptable probability of a fire exceeding the design fire, ignoring fire safety systems.
p_{FRI} = the frequency of fire starts per year per square metre of floor area; taken as $5\text{x}10^{-7}\text{m}^{-2}\text{yr}^{-1}$.
$p_{sprinkler\_failure}$ = the probability of sprinklers failing to extinguish a fire.
$t_{building\_lifetime}$ = the life of a building, typically 50 years
$Area$ = the floor area of a compartment (m^2)

After having found p_{acc} , this probability was used to determine the fire load from a normal probability distribution and a given mean and standard deviation. Fire temperatures were deduced with OZone [6] and used to design individual structural elements.

Profil Arbed also developed a simpler lower order approach for finding the fire load, $q_{f,d}$ which could be input to a real or natural fire model used in a fire engineering design. Survival of the structure exposed to the extreme fire due to this fire load assured safety measured with a safety index of 3.8. The equation for fire load, $q_{f,d}$, is,

$$q_{f,d} = q_{k,f} \cdot \gamma_{qf} \tag{4}$$

where $p_{accepted}$ = the acceptable probability of failure of a building during its lifetime. (Presumably the failure refers to an element rather than the a large portion of the building.)
= 7.23×10^{-5}
p_{FRI} = the frequency of fire starts per year per square metre of floor area.

γ_{qf} = $\gamma_{q1} \cdot \gamma_{q2} \cdot \gamma_{n1} \cdots \gamma_{ni}$

γ_{qi} = partial safety factor (analogous to load factors used in Australia) afforded by a particular fire safety system; for example, for sprinklers this factor is 0.61, which is less than 1.0 due to the benefit of sprinklers in reducing fire risks.

DESCRIPTION OF METHODOLOGY

The need for modifications to the methodology described by Profil Arbed has become apparent for at least two reasons. Firstly, using p_{acc} as a function of floor area implies that floor area can be sufficiently small to reduce the risk of fire to an acceptably small value without the use of sprinklers. Subdividing a building into many small compartments, however, does not reduce the overall risk of building fire and hence does not reduce community risk. Whatever method is used for determining risk targets for design, the total risk throughout the building must not exceed current values for a whole building. Community risk must not be increased by a performance-based design.

Secondly, the need for modification is apparent from recent research into fire statistics [4,7]. The frequency of fire starts is only weakly correlated to floor area. Fires are usually started from tools, appliances and arson. A structural element is only exposed to threatening fire if several conditions occur. A fire must start somewhere in the building. Having started, the fire must be well developed to generate sufficient heat to be a threat. It is believed that the best statistic for this condition is the incidence of spread beyond the room of fire origin. Many fires are extinguished by occupant intervention. Spread indicates failure of any such intervention and development to a stage where heat output is sufficiently developed to significantly raise temperatures in the structural element. Finally, the beam must be within the area of spread for it to be affected by fire. These conditions have been represented with the following variables:

p_{fs} = annual probability of fire starts in a building.

p_{spread} = probability of fire spread and sufficient development to threaten a structural element.

k = extent of spread as a proportion of the total building.

Statistical data is available for p_{fs} and p_{spread} [4,7]. Data for k was not readily available. A value of 0.2 was adopted.

Equation (3) was thus modified to,

$$p_{acc} = \frac{p_t}{p_{exp} \cdot t_{building\_lifetime}} \qquad (5)$$

where p_{exp} = annual probability of a structural element being exposed to fire.
= $p_{fs} \cdot p_{spread} \cdot k$

The target probability was compared with values inherent in Australian standards. Direct convolution was undertaken between arbitrary point-in-time load (G+0.25Q) and the strength limit state load (1.2G+1.5Q) in which G is the dead load and was assumed to be equal to Q which is the nominal live load. The result was 0.00432 which is considerably less than the European value of 7.23×10^{-5}. The strength limit state load used in Euro codes is 1.35G+1.5Q. It has been reported that the target safety index inherent in Australian codes was intended to be 3.5-4.0 [8]. It was decided to adopt the 7.23×10^{-5} for p_t in the research described in this paper.

The probability p_{acc} was used to obtain the fire load $q_{f,d}$ as shown in Figure 3 assuming the load was distributed normally. The literature [3,5,8] quotes several types of distributions for loads including normal, lognormal, Weibull, and Gumbel. Load has been assumed to be independent of position. This assumption and the central limit theorem indicates that the load should be normal. Weibull applies to strengths of glass or chains which are determined by the weakest part. This trait is not applicable to loads [9]. Lognormal is a construction to avoid negative values. The most important part of probability distributions in reliability analysis is the tail region between, say, the second and fourth standard deviations. Further along the tails, there is seldom the data to justify the use of the low frequencies at these extreme positions. Provided loads between the second and fourth standard deviation are positive, the normal distribution is most appropriate and has thus been adopted.

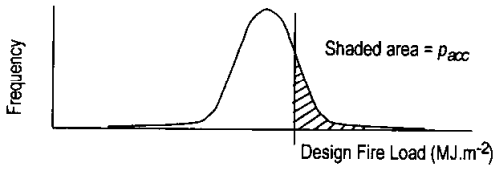

FIGURE 3. Obtaining design fire load from p_{acc}.

Having obtained the fire load, the fire temperatures were deduced with the fire zone model, Ozone [6]. A problem that appears to be common in any fire zone modelling is the selection of the heat release rate (HRR kW.m^{-2}) for the fire load. There are large inconsistencies in published values [5,10]. For example, the HRR for wood pallets stacked to a height of 0.5m is 1250 kW.m^{-2} and to a height of 3.0 m is 6000 kW.m^{-2}. Plastic bottles in cartons stacked to a height of 4.6 m have an HRR of 4320 kW.m-^{2}. It can be shown that HRR for a wood surface is approximately 75 kW.m^{-2} (assuming a char rate of 0.6 mm.min^{-1}, 500 kg.m^{-3}, net heat production of 15 MJ.kg^{-1} allowing for heats of combustion, gasification and state transition of moisture). In comparison, building fires are quoted as having HRR's mainly ranging between 250 and 500 kW.m^{-2}. It was decided to adopt values indicated for buildings. However, the large variation in HRR's remains cause for concern.

CASE STUDY

The methodology was applied to the same case study involving the storage compartment analysed by Grubits and Tung [1]. The details of the storage compartment are summarised in Table 1.

TABLE 1. Details of storage compartment for which the required FRC was determined.

Variable	Probability Distributrion	Mean	Standard Deviation
Fire load density ($MJ.m^{-2}$)	normal	1200	360
Floor area (m^2)		84	0
Height of compartment (m)		3.0	0
Height of openings (m)		1.5	0
Total width of openings (m)		9.0	0

TABLE 2. Probabilities of fire spread and exposure of structural elements in storage compartments.

Sprinklers	Passive Protection	p_{spread} [4]	$p_{fs} \cdot p_{spread}$	$p_{exp} = p_{fs} \cdot p_{spread} \cdot k$ (assuming k =0.20)	$p_{FRI} \cdot p_{sprinkler\_failure} \cdot Area$
No	No	0.60	2100×10^{-6}	402×10^{-6}	33.6×10^{-6}
No	Yes	0.45	1575×10^{-6}	315×10^{-6}	33.6×10^{-6}
Yes	Yes	0.17	$0.17 \times 0.0035 = 595 \times 10^{-6}$	119×10^{-6}	$0.4 \times 10^{-6} \times 0.02 \times 84 = 0.67 \times 10^{-6}$

Probabilities of fire spread and exposure of structural elements is summarised in Table 2. The probability of spread depends on the types of fire protection installed [4]. When sprinklers and passive protection are used the probability of spread beyond the room of fire origin is 0.17 compared with 0.60 when no protection is provided. Holborn et al [7] report a spread rate of 0.16 for storage compartments but do not distinguish between different levels of protection. The annual probability of fire starts in storage buildings, p_{fs} , is 0.0035 [7]. Assuming that, on average, when fire spreads beyond the room of origin, it covers 20% of the building the annual probability of an individual structural element is exposed ranges between 119×10^{-6} and 402×10^{-6}. Comparatively, the Profil Arbed method gives a range of 0.67×10^{-6} and 33.6×10^{-6}.

The large differences between the proposed method in this paper and the method from Profil Arbed are due to the assumption of the influence of floor area, as well as the assumed efficacy of sprinklers – 98% for Arbed compared with 83% quoted by Thomas [4] for sprinkler and passive protection. The corresponding probabilities of failure are 2% and 17% which lead to almost a ten-fold difference in risk. The large probability of 17% could well be reduced to the more widely assumed probability of 2% with building owners undertaking risk management [11] rather than relying mainly on the installation of safety systems during construction.

An HRR of 500 kW.m^{-2} was adopted as would expected to be used in fire engineering practice. The option of external flaming was adopted in the application of OZone. This option ensures that unburnt volatiles are modelled as burning and dispersing heat outside the compartment. The option involving all combustion in the compartment made little difference to the results, most likely due to the large window for this particular compartment.

TABLE 3. Fire scenarios with and without sprinklers, similar target probabilities, p_t.

	p_{acc}	$q_{f,d}$ (MJ.m^{-2})	T_{max} (°C)	t_{max} (min)
(1)No Sprinklers	$\frac{7.25\times10^{-5}}{402\times10^{-6}\times50} = 0.0036$	2167	1054	85
(2) With Sprinklers, 83% efficacy.	0.012	2012	1045	80
(3) With Sprinklers, 98% efficacy.	0.104	1653	1018	67

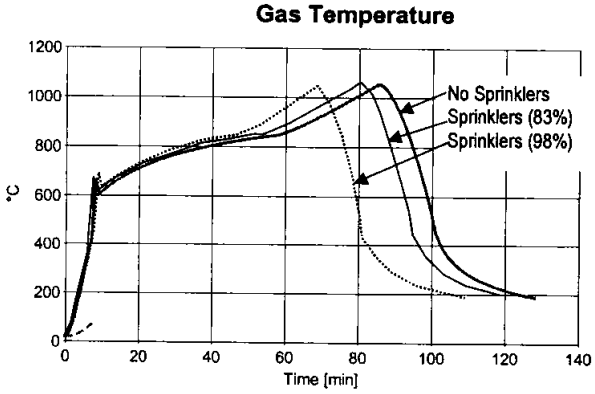

FIGURE 4. Fire temperatures predicted with Ozone for the storage compartment.

It is apparent from rows (1) and (2) in Table 3 that sprinklers reduce risk only sufficiently for an FRC reduction of 5 minutes or 6%. If sprinkler efficacy could be improved to 98%, the FRC could be reduced 18 minutes or 20%. These reductions may be less than expectations. However, the principal of consistent risk for all structural design involves the total probability of failure ,including all events in a scenario, not exceeding 7.23x10^{-5}. This is much smaller than probability of failure of sprinklers 2-17x10^{-2}. Hence supplementary fire safety systems are required to ensure consistency in risk.

However, in Australia storage rooms have 4 hour fire ratings. From thermal and structural analysis 90 minutes would be more appropriate. This period does achieve an acceptably low probability of failure which is consistent with structural design in general.

CONCLUSIONS

Methodology for determining the trade-off between sprinklers and fire resistance requirements for structures has been further developed. The trade-off is a function of the frequency of well-developed fires affecting individual structural elements, as well as sprinkler efficacy. The frequency should be determined from statistics on fire spreading rather than being directly related to floor area.

It has been shown for a case study of storage compartment that fire resistance requirements can only be reduced by a small amount, 6-20%, while maintaining the risk of collapse consistent for both fire and ambient conditions. This result is contingent on an HRR of 500kW.m^{-2}. Large variations in published values for HRR is a cause for concern. This result neglects any fire safety systems designed to maintain life safety which lies outside the scope of this research.

REFERENCES

[1] Grubits S and Tung V, *A Rational Basis for Trade-off Between Sprinklers and Fire Resistance*, International Conference on Building Fire Safety, Queensland University of Technology, 20-21 November 2003.

[2] ISO 834, Fire Resistance Tests – Elements of Building Construction. International Standards Organization, Geneva, Switzerland.

[3] Melchers RE, *Structural Reliability, Analysis and Prediction*, Ellis Horwood Limited 400pp, 1987.

[4] Thomas IR, *Effectiveness of Fire Safety Components and Systems*, Journal of Fire Protection Engineering, vol 12, No 2, pp 63-78, 2002.

[5] Schleich JB, Williams PJ, Pope RJ, Pustorino S, Kruppa J, Joyeux D, Salkin R, Fontana M, Fetz C, Kirchner U, Guibert D, Heise, Twilt L, Van Oerle J, Kindmann R, Schweppe H, Franssen J-M, Cadorin J-F and Kokkala M, *Competitive Steel Buildings Through the Natural Fire Safety Concept*, Profil Arbed Centre de Recherches, RPS Report No 32, 1999. (a)-vol 1 p 40,

[6] Cadorin JF, Pintea D and Franssen JM, *The Design Fire Tool Ozone V2.0 – Theoretical Description and Validation on Experimental Fire Tests*, University of Liege, Belgium, 2001.

[7] Holborn PG, Nolan PF, Golt J and Townsend N, *Fires in Workplace Premises: Risk Data*, Fire Safety Journal, vol 37, pp 303-327, 2002.

[8] Pham L, *Load Combinations and Probabilistic Load Models for Limit State Codes*, Civil Engineering Transactions, Institution of Engineers Australia, 1985.

[9] Hasofer M, Emeritus Professor well published in reliability, Personal Communication. 2004.

[10] Klote JH and Milke JA, Principles of Smoke Management, American Society of Heating, Refrigerating and Air-Conditioning Engineers, and Society of Fire Protection Engineer, 375pp, 2002, Table 2.2, p22.

[11] AS/NZS 4360 *Risk Management*, Australian and New Zealand Standard, 1999.

Investigation into the Impact of Fire on the Twin Towers

G.R.Flint and A.S.Usmani[1]
School of Engineering and Electronics, University of Edinburgh, Edinburgh EH9 3JN, United Kingdom

Abstract

The events of 11th September 2001 highlighted the fact that despite the considerable recent progress more needs to be done to understand the effects of fire on complex steel framed structures. It is widely acknowledged that the methods used in current design codes are not adequate to correctly account for the likely consequences of a major fire on the structure of modern buildings.

This paper reports on progress at an interim stage of a project to investigate the likely collapse mechanisms of the WTC towers. The structural frame of the towers has been modelled using the commercial finite element package ABAQUS. A half resolution 3D model has been constructed (columns and beams at 1 and 2m centres have been modelled to be 2 and 4m centres respectively). A full resolution model of one floor will eventually be used for verification.

Parametric studies are being undertaken based on the fires likely to have occurred. The structural behaviour will be investigated for a range of peak temperatures, fire duration and distribution and the effect of fire protection or lack of it. For the purposes of this paper the results presented will focus on the behaviour of a typical floor of the towers.

Keywords: composite structures in fire, finite element modelling,

1 Introduction

The tragedy that struck New York on 11th September 2001 has brought attention to the growing awareness that too little is known about the effects of fire on complex steel framed structures. Previous research at Edinburgh University and elsewhere [1–3] has highlighted some of the basic responses of structures under the effects of fire. In the area of Fire Safety Engineering it has become obvious that the current design codes have no realistic, quantitative basis for their approach to designing structures to withstand major fire events. Furthermore it is all too often expected by structural engineers that by following the relevant prescriptive codes a building will be "safe". In practice it is virtually impossible to rate the level of safety inherent in a building using current

[1]Corresponding Author: Email: asif.usmani@ed.ac.uk Fax: +44 131 6506781

methods. More exact methods using Performance Based Design and full risk assessment coupled with numerical modelling of a building can provide a much better idea of how "safe" a building is in the case of a major fire.

2 Background

The aim of this project is to utilise the latest advances in computing technology to investigate complex fire scenarios. The primary objective is to investigate the response of the World Trade Centre Twin Towers purely under fire loading. Structural damage is not being considered at this point. This project is being undertaken using the ABAQUS finite element analysis program. Previous work has verified this program against the Cardington tests [1,2] as adequate to perform such an analysis. This work moves on from this previous work by modelling a full floor rather than just part. In addition fire regimes that include cooling are to be used, although this phase is not reported here.

At this stage this project is not designed to produce a direct comparison to the response of the WTC towers. Based on previous work [9] some interesting responses have been seen that show a collapse mechanism that could occur at relatively low temperatures. In addition prior structural damage does not need to have occurred before this mechanism could start.

3 Model Description

In the interests of computational efficiency the single floor model (Figure 1) in this study has been constructed at half resolution. That is the columns and trusses have been placed at 2m and 4m rather than 1m and 2m respectively as in the original structure. The trusses have also been constructed at half resolution in terms of tie members. The sizes of the structural members in the model have therefore been increased in order to keep the original strength of the floor. The member sizes of the trusses, outer columns, spanderel beams and the details of the floor slab and its reinforcement have been taken from the FEMA report [4] and preliminary structural reports produced by Weidlinger and Arup [5,6]. The sizes of the core columns and beams have been assumed based on approximate loading data taken from the FEMA report and elsewhere.

This model was constructed using the ABAQUS FE code. Within the model all the beam, truss and column members are represented using 2-node, linear beam elements while the slab is made up of 4-node, general purpose shell elements. Large deflection theory based solvers and native material models have been used to introduce geometrical and material non-linearity. Steel and concrete properties for elevated temperatures have been extracted from Eurocodes 2 and 3 [7,8]. The concrete

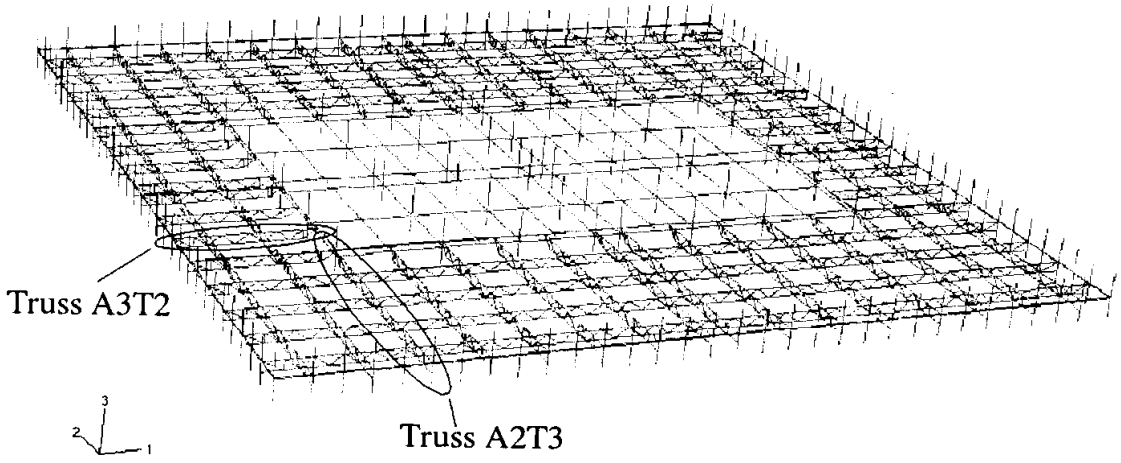

Figure 1: Full Floor Structural Mesh (slab ommitted for clarity)

has been modelled using a "damaged plasticity" based system native to the ABAQUS code. Previous work has shown this to produce reasonable results although this verification is not to be reported here.

4 Fire Input

The exact layout of fires in the WTC towers is not part of this project and so several assumptions have been made regarding them. The whole floor is assumed to be affected by the fires at the same rate. This leads to a single temperature-time curve being required for the whole compartment. At this stage the compartment temperatures are based upon a generalised exponential curve given by :

$$T(t) = T_o + (T_{max} - T_o)(1 - e^{(-at)}) \tag{1}$$

where T_{max} and T_o are the maximum and ambient compartment temperatures respectively. t represents the time over which the model is analysed and is in no way linked to the actual timing of the events on 11th september 2001. a is an arbitrary 'rate of heating' parameter and for the purposes of this paper has been taken as 0.005. Example temperature time distributions for 100mm thick floor slab may be seen below in figure 2.

The beams and trusses are assumed to have no protection and are therefore taken as being at the

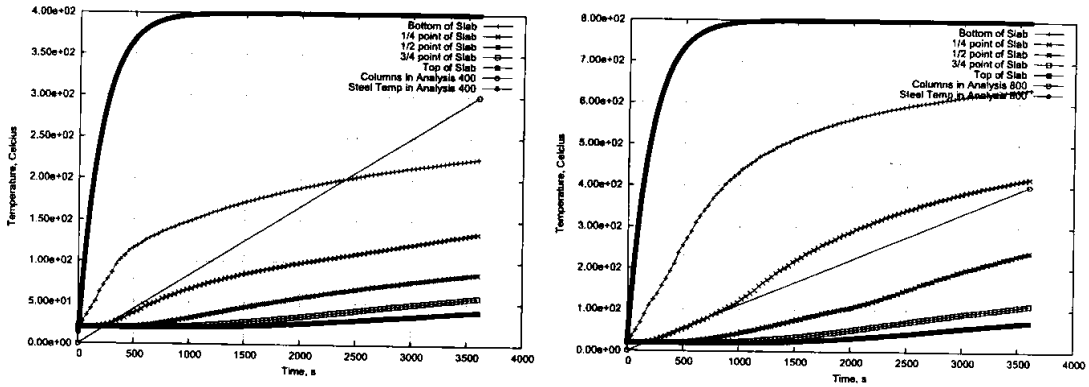

Figure 2: Temperature Time Distributions

compartment temperature. All columns are assumed to undergo more limited heating either due to greater protection or because they are in contact with the outside atmosphere.

Video footage of the event shows little external flaming which validates this last assumption. In addition the absence of a great deal of external flaming would indicate that the temperatures inside the towers will not be as high as if a fully flashed over compartment fire was occurring.

The concrete slab has a realistic temperature distribution applied through its depth rather than a mean temperature/gradient system. This is done by applying individual time-temperature curves to 5 different points through the depth of the slab (top, bottom and 1/4 points). The time temperature distributions used in this analysis were taken from a 1D heat transfer analysis.

5 Results

Due to the limitations on space only 2 different analyses of the full floor model described above are to be discussed here. They are both full floor homogenous fires one with a peak compartment/steel temperature of 400°C and the other with a peak of 800°C. The other major difference between the two analyses is that in the 400°C analysis the column temperatures are ramped up to 300°C while the columns in the 800°C analysis goes to 400°C. All results below are taken from the vicinity of 2 trusses in the model. These trusses have been marked on the floor mesh diagram above (Figure 1).

5.1 Deflections

As can be seen in Figure 3 the vertical displacements in the 400° analysis are very different to those in the 800°C one. The 800°C analysis shows rapid attainment of extremely large deflections. Final

deflections for each truss greater than span/10 and show no indication of levelling out.

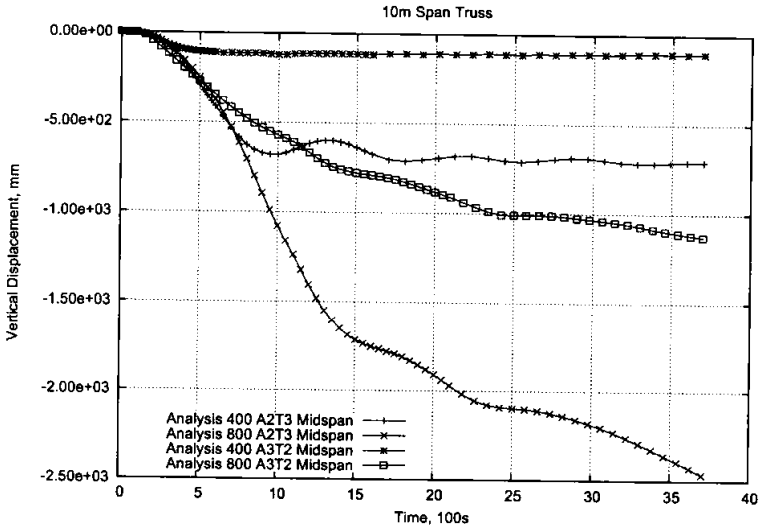

Figure 3: Truss Midspan Vertical Deflection

By contrast the deflections for the 400°C analysis, while initially increasing at the same rate, level off quite quickly and stay relatively stable for the rest of the analysis. The wobble seen in the trace for A2T3 Midspan is an interesting effect seemingly caused by the concrete slab trying to expand into the trusses when they retain significant reserves of strength. Further investigation of this phenomenon is to be undertaken. This wobble is echoed in the force plots to be described below.

The horizontal displacement of the middle of the columns is also of interest. This can be seen for the representative nodes in Figure 4. In general the responses are similar in that as the temperature increases the expansion of the floor system forces the column out. Most interestingly it is the lower temperature analysis that produces the worst case for this variable. The long span trusses obviously buckle considerably (as seen in the vertical deflection plots). This keeps the outwards movement of the columns low. The short span trusses however do not deflect to the same extent. Coupled with the relatively low temperatures and the considerable residual strength of the floor system this forces the expansion to occur in the plane of the floor. Axial force response in the truss elements verify this and are described below. Another response that is seen on a global scale is that on the long span sides the horizontal displacement of the columns are much smaller in the centre of the side and increase as you move towards the corners. On the short span sides all the outward column displacements are all roughly the same.

The high temperature analysis also shows a higher displacement on the shorter span ends of the building but not to the same scale.

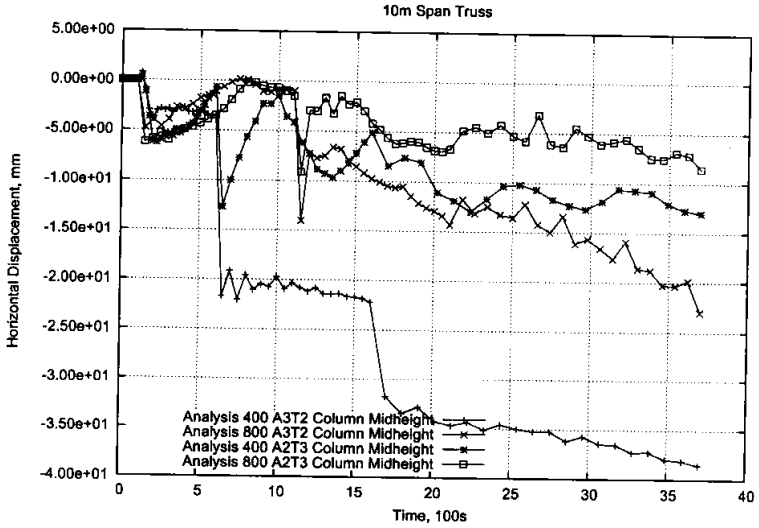

Figure 4: Horizontal Displacement at Columns (negative indicates outwards movement)

5.2 Axial Force

Figure 5 shows typical responses for long and short span trusses. In general these show expected results with all cases showing a large increase in compressive force as the steel heats up against the restraint of the concrete slab and surrounding structure. In line with the findings of previous research at about 100°C the steel buckles and the floor system begins to deflect. this leads to a large reduction in compressive axial force. The top chords of the trusses either stay in compression, indicating the truss retains its strength, or drop to near zero tensile force. This indicates that the truss has lost its strength as a truss and is being used in catenary action. The short span truss retaining its strength in this way links back well to the low midspan deflections and the relatively large horizontal displacement of the column.

The bottom chords also act in similar ways. After the floor buckles they move back into tensile action much more quickly as the composite action with the floor comes into play. In the low temperature analysis in both trusses significant tensile forces are developed. The large compressive spike at about 1400s in the long span truss (top and bottom chords) during the low temperature analysis and the resulting oscillations are obviously linked back to the "wobble" in the deflection plot. While the truss hasn't retained enough strength to withstand the floor buckling it does have enough to restrain further expansion of the slab.

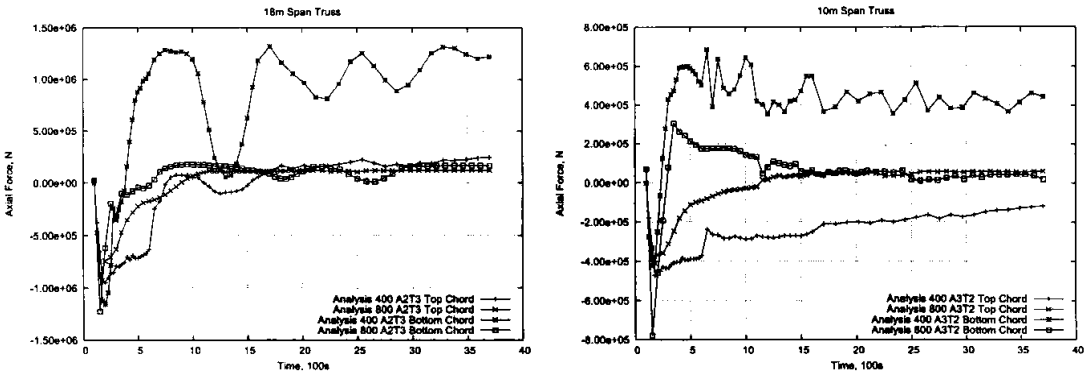

Figure 5: Truss Midspan Axial Forces

5.3 Slab Strains

Another important factor in the stability of a building under the effects of fire is the state of the reinforcement of the concrete slab. Under fire conditions because of the large displacements induced in the floor systems catenary and tensile membrane action become the primary load carrying systems. In higher temperature fires the strength of the primary and secondary steelwork can virtually be neglected which means the structural element carrying the majority of the tensile load is the slab reinforcement. Because it is embedded in concrete it is generally rather well protected and tends to stay at relatively low temperatures compared to the other steel in a building. Floor collapse is unlikely to occur until the reinforcement ruptures so keeping track of the strains at rebar level is a useful indicator. In the case of the low temperature analysis the maximum tensile strains are about 1%, well within the limits of the reinforcement. As expected this maximum occurs at the boundary of the core as the slab goes from the relatively stiff core area to the much more slender truss area. In the case of the high temperature analysis (see figure 6 below) there are areas, again mostly concentrated around the core boundary, where strains in excess of 2.5% may be found. This is the limit for normal/mild steel reinforcement and therefore could be a possible source of failure due to rupture of the floor slab.

6 Conclusions

This paper is designed to give an insight into some of the responses of the WTC towers to the effects of a large scale fire. It is not intended to be an exhaustive report on global and local phenomena. Many of the responses are in line with what was expected based on previous work done in this area.

- Heating creates large compressions until about 100°C when the floor system buckles

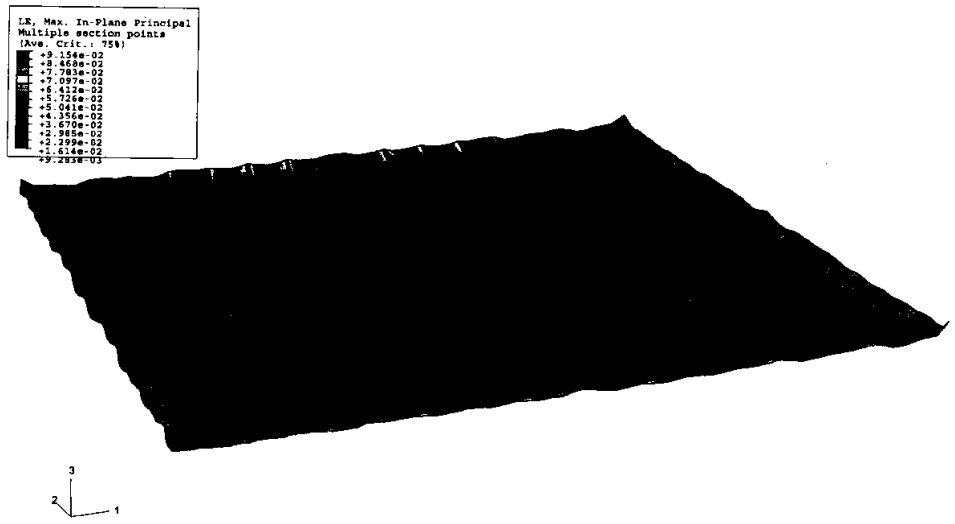

Figure 6: Final Strain at Lower Rebar Level

- Generally after buckling the steel acts primarily in tensile catenary action
- Areas of high strain in slab rebar indicate primary support points for tensile membrane action

The relatively large horizontal displacements evident in the short span columns tie in well with the theories of Usmani et al that are based on 2D models. This phenomenon will be focussed on in later analyses.

References

[1] S. Lamont, The Behaviour of Multi-storey Composite Steel Framed Structures in Response to Compartment Fires, *Edinburgh Uni PhD Thesis*, 2001

[2] M. Ghillie, The Behaviour of Steel-framed Composite Structures in Fire Conditions, *Edinburgh Uni PhD Thesis*, 2000

[3] Burgess, I.W. & Plank, R.J., 'Modelling the Fire Tests on the Cardington Full-Scale Frame', *Proc. 3rd Cardington Conference*, November 1998.

[4] Federal Emergency Management Agency, World Trade Center Building Performance Study: Data Collection, Preliminary Observations and Reccomendations, *FEMA*, May 2003

[5] M. Levy & N Abboud, World Trade Center Structural Engineering Investigation, *Weidlinger Associates*, August 2002

[6] ArupFire, World Trade Center Expert Report, *Ove Arup*, August 2002

[7] BSi, Eurocode 2, *BSi*, 1996

[8] BSi, Eurocode 3, *BSi*, 2001

[9] A.S. Usmani, Y.C. Chung & J.L. Torero, How did the WTC towers collapse : a new theory, *Fire Safety Journal* Vol.38 p501-533, June 2003

THE RESPONSE OF STEEL PERIMETER COLUMNS IN A FIRE

Maria E. Moreyra GARLOCK
Assistant Professor, Dept. of Civil and Environmental Engineering, Princeton University, Princeton, NJ 08544
mgarlock@princeton.edu

Powell DRAPER
Graduate Student, Dept. of Civil and Environmental Engineering, Princeton University, Princeton, NJ 08544
pdraper@princeton.edu

ABSTRACT

This study investigates the thermal and structural response of perimeter columns in a common steel-framed high-rise building exposed to fire. A model of a tall steel building frame is developed, which is based on a tall steel building (of common construction) that was subject to conflagration in the last decade. The progression of the fire up the building is considered in developing the time-temperature curves for the analyses. Therefore structural analyses consider that some floors are cooling down while others are heating up. The results investigate both the thermal and structural effects of the fireproofing on the structure and its individual members. Of particular interest is the stability of the perimeter columns, specifically the resulting second order, or P-Δ, effects.

KEYWORDS: *fire resistance, steel, column, stability*

INTRODUCTION

In a building, the perimeter columns are laterally supported on one side only. As the heated beams framing into the perimeter column try to expand, they push against the column and can induce large second order P-Δ moments (i.e., geometric effects) leading to instability. In addition, the reduction in strength and stiffness (i.e., material effects) that develops in the columns under high temperature further reduces the stability of a perimeter column. The P-Δ effects in particular are critical in a high-rise building where the column load P is large.

The One Meridian Plaza building in Philadelphia, Pennsylvania, USA, suffered an extensive fire in 1991 that burned for more than 18 hours and completely burned out 8 floors near the top of this 38 floor structure [1]. No structural collapse ensued and the building was dismantled in 1999. One Meridian Plaza represents a fairly common structural design for a high-rise steel building constructed around the same time as the World Trade Center. The objective of this research is to use the One Meridian Plaza structure and fire as a case study to evaluate the stability of perimeter columns in steel high rise buildings subject to a large fire. This study is not a study of the One Meridian Plaza fire event per se, but rather it uses the this structure and fire to study different scenarios that affect the performance of tall steel buildings under fire.

In this study, eleven story bays of a common structural system are modeled based on the One Meridian Plaza structure. Finite element analyses were carried out using the finite element program SAFIR, developed at the University of Liege, Belgium [2]. The modeled elements include the wide-flange perimeter columns, the gravity load carrying wide-flanged beams, and the interior columns to which those beams are connected. The analyses consider the transient action of the actual fire in developing the time temperature curves for the floors involved (i.e., it considers that some floors are cooling down while others are heating up). A parametric study is performed to evaluate the sensitivity of the structural system to the presence/absence of fireproofing on the steel beams and columns.

DESCRIPTION OF THE PROTOTYPE BUILDING AND FIRE

The Meridian Bank Building, otherwise know as the One Meridian Plaza (1MP) building, was located in the heart of downtown Philadelphia. It had 38 floors above ground, 3 underground levels, and was rectangular in shape, approximately 74 meters by 28 meters (243 feet by 92 feet). An image of the building during the fire is shown in Figure 1.

The building frame was structural steel with a slab over a metal deck. All structural steel beams and metal decks were protected with spray-on fireproofing material. The construction required 2-hour fire rated beams. The columns were protected with spray-on fireproofing as well as plaster boards. A 3-hour fire rating was required for the columns [3]. The structural system consisted of several moment frames running in each direction. Enclosed private offices were typically located along the building perimeter except along the south wall where the core was located. Most of the other space was open.

On February 23, 1991 at around 8 in the evening, a fire started on the 22nd Floor. The origin of the fire was attributed to spontaneous ignition of a pile of linseed oil-soaked rags, which were

left by a contractor [1]. Firefighting activities were hampered by a loss of electrical and emergency power, inadequate water pressure, and other issues [3]. Consequently, the fire spread all the way to the 30th floor where it was stopped by the automatic sprinkler system, which was not yet installed in the other fire-burning floors. An image of an interior space after the fire is shown in Figure 2, where very large girder deflections are evident.

Figure 1 – Exterior view of the building north face during the fire.

Figure 2 – Interior view of burned floor showing large girder deflections

DEFINING THE FIRE

The fire scenario used in the analyses is intended to represent a reasonable approximation and simplification of the 1MP fire event. Based on observations, the 1MP fire engulfed nearly the entire floor area of floors 22 through 29; that is, it was not contained in an office space/compartment. Therefore, widely-used fire time-temperature numerical models cannot be solely used to represent this fire since the scale of 1MP fire falls well outside the scale/limitations of these models. Accordingly, the fire model used in these analyses is based on a compartment fire model as well as data from large compartment tests and observations during the actual fire. The development of this model is described in more detail below.

The equations given in the Eurocode [4] were used to approximate the maximum temperature (T_{max}) reached on the floors, and the initial rate of temperature rise. These equations provide a time – temperature relationship that defines a ventilation controlled fire based on the compartment size, fuel load, ventilation openings, and compartment lining materials. For the purposes of selecting T_{max}, a compartment size equal to the area tributary to the structure being analyzed was selected (T_{max} does not vary significantly in these equations if the compartment size is increased further). In a typical office space, as was the space on fire in 1MP, the materials on the walls and ceiling would be a combination of gypsum plaster and concrete. Since the Eurocode allows the input of only one lining material, two Eurocode approximations for T_{max} were made; one for gypsum plaster lining and another for concrete lining. The resulting T_{max} equals 1145° C and 906° C for the gypsum plaster and the concrete lined

compartments, respectively. Since the actual space was a combination of both materials, it is assumed that T_{max} falls somewhere in between the two curves; therefore T_{max} was selected as 1000° C for this research.

The rate of temperature rise was selected to be similar to the concrete lined compartment where the temperature reached 725° C in 10 minutes and T_{max} in 45 minutes. Based on observations [5], the most intense part of the fire in each floor occurred during a two-hour period. The model fire (i.e., the fire time-temperature curve used in this research) was held at a constant of T_{max}, therefore, until time equaled two hours, at which time the decay period began.

The decay rate of the fire was based on observed rates in large compartment fires. Kirby et al. [6] performed large-scale compartment fires in a 23 m long by 6 m wide by 3 m high compartment. Their results show that the decay rate in these fires was significantly less than that predicted by the Eurocode equations, and a rate of about 7° C per minute was observed. Further experimental data [7] shows that the decay rate of a fire with a fully developed period of more than one hour is about 7° C per minute as well. In our study, we assumed a slower decay rate than those observed in the experiments referenced above since this fire was of a greater intensity. A decay rate of 5° C per minute was therefore selected, which results in a time-history of the fire that is consistent with the observations during the actual 1MP fire as described below.

Figure 3 shows the time-history of the floor fires used in the analyses. Each floor is subjected to the model fire described previously. The time history of the fire (i.e., the progression of the fire up the building) at 1MP was based on observations made by witnesses, which indicate that the fire was burning in as many as three floors at one time [5]. Klem [1] indicates that 5.5 hours after the fire began the fire had spread to floors 23 and 24 and was threatening floor 25. He also indicates that 11 hours after the fire began the fire was under control on floors 21 through 24, and 18.5 hours after the fire began sprinklers were activated on floor 30, which finally halted the fire's vertical progression. Beginning on Floor 22, it is assumed that the fire on each subsequent floor began 1.75 hours later. The result is a time-history that is reasonably consistent with the observations of the 1MP fire.

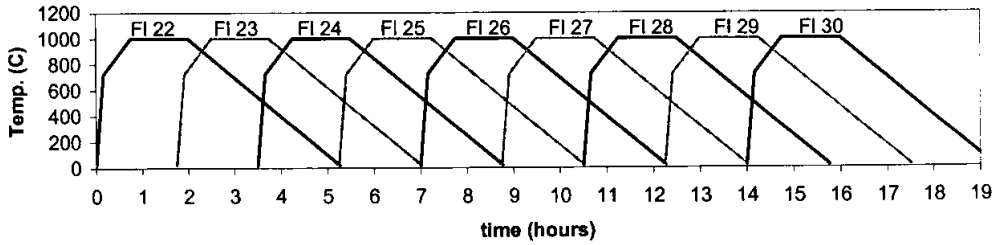

Figure 3 – Time-history of fire progression assumed in analysis

COMPUTATIONAL MODELS

A typical interior frame of steel floor beams and columns was employed as the two-dimensional model for the analysis of our prototype building. The analysis included a portion of the building from the twenty-first floor up to the thirty-second floor, thus encompassing the region affected by the fire for this segment of the building. Dimensions, member sizes, and fireproofing details of the frame were obtained from the original design drawings. The frame is shown in Figure 4. This is a portion of a moment frame (spanning in the north-south direction); therefore, the beam-column connections can transfer moment. The concrete floor slab was omitted from these analyses and it is being considered in our ongoing related research. Figure 5 shows the orientation of the beam-to-column connection, where it is seen that the column is bending about the strong axis. The computer program SAFIR [2] was employed to perform the thermal and structural analyses of the beams, columns, and frame.

Prior to the initial thermal analysis, a study was performed to determine the necessary level of element discretization or refinement. Increasing numbers of elements were used to model identical sections in successive analyses until a level of convergence was obtained with the results. The resulting level of element discretization was then employed for the thermal analysis of each member type.

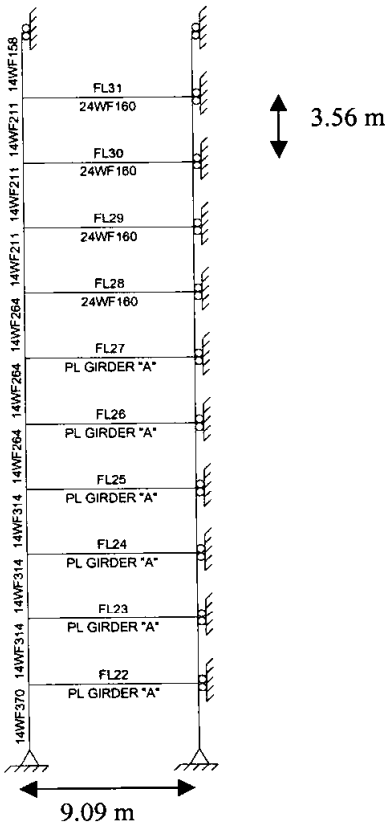

Figure 4 – 1MP Frame (elevation).

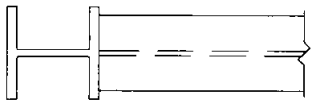

Figure 5 – Detail of frame showing orientation of beam-to-column connection (plan).

For the thermal analysis, a cross section of each particular member size of the frame (e.g., 24WF160, 14WF211, etc.) was discretized into two-dimensional solid elements and subjected to the effects of the time-temperature curve (see Figure 3). A typical finite element model for the thermal analysis of a beam section (with fire protection) is shown in Figure 6. It is seen that the web and flanges had one element through the thickness and the fireproofing had three elements through the thickness. The fireproofing's thermal conductivity and specific heat were temperature-dependent. It is also seen that the fire was defined on 3 sides since the slab protected the top flange.

For the structural analysis, the beams and columns of the frame were modeled as beam elements. As in the thermal analysis, a converging level of element refinement was used in order to ensure the validity of the results; in this case ten elements for each column and twenty elements for each beam.

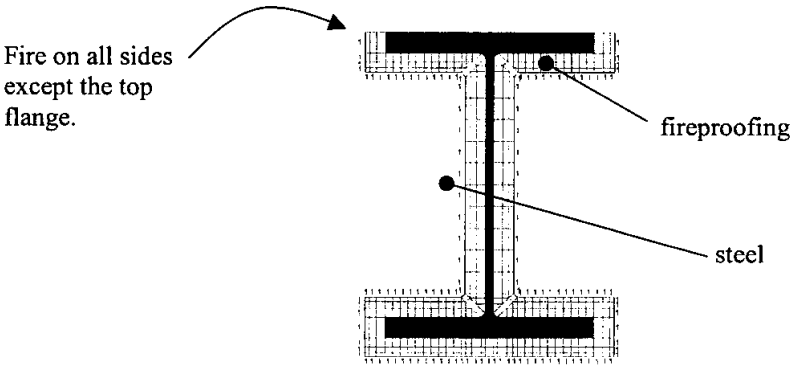

Figure 6 – Thermal finite element model of a member section

This study investigated four cases: one case in which both the beams and the columns of the frame were covered with the fire-protection material, one case in which only the beams were covered with the fire protection material, one case in which only the columns were covered with the fire protection material, and one case in which neither the beams nor columns were covered

with any fire protection material. These four cases and their denotations are summarized in Table 1.

Analysis Name	BuCu	BpCu	BuCp	BpCp
Columns	unprotected	unprotected	protected	protected
Beams	unprotected	protected	unprotected	protected

Table 1: Analysis Cases

For each case, the thermal analysis imposed the prescribed time-temperature relation on each member of the frame. This produced a time-temperature history at every node of the member's cross-section. The temperature distribution history across each section was then used in a structural analysis of the entire frame. A structural model of the frame consisting of beam elements was assembled with boundary conditions as shown in Figure 4. At the base of the bottom columns, the model was pinned. Rollers were placed at the top of the upper columns. In order to more accurately model the structural restraint and deformation of the frame, rollers were also placed at the nodes where the floor beams connect to the interior columns.

Distributed loads representing the full dead load and partial live load of the actual design loads of 1MP were imposed across the full length of each floor beam. Point loads were applied to the top of each upper column to represent the loads applied from the floors above.

The computational model has the following limitations/assumptions:

- The heat transfer analysis is two-dimensional through the cross-section. It does not account for heat transfer through the length of the member. Therefore, for example, if the fire is on Floor 22, the columns between Floors 22 and 23 are heated, but the columns in between Floors 23 and 24 remain cold until the fire begins on Floor 23.
- Similarly, it is assumed that the slab prevents heat transfer to the floor below. For example, if the fire is on Floor 22, the beams on Floor 23 are heated, but not those on Floor 22.
- It is assumed that the insulation remains intact for the duration of the fire.
- The columns in 1MP are protected with one layer of spray fireproofing and another layer of insulation. In these analyses, only the layer of spray fireproofing is considered on the columns. Future models will include the plaster layer as well.
- The structural strength provided by the slab was not accounted for.

ANALYSIS RESULTS

The time to failure for each analysis is shown in Table 2. It is noted that Analysis BpCp, which included fire protection for both the beams and columns, ran for much longer than the other analyses, yet it did not run the full length of the analysis. The reader is reminded that 1MP did not collapse, and this study is not a study of the 1MP building fire per se, but rather uses that structure and fire with fireproofing as a parameter. As mentioned previously, these analyses did not include both layers of fireproofing that were used in the 1MP columns, nor did it include the slab, which are some possibilities why the structure did not run the full length of the analysis. The analyses with the beams unprotected (BuCp, BuCu) failed in 37 minutes, mostly due to the large column deflections produced by the beams pushing out the columns as they expanded (as

will be described below). The analyses with the columns unprotected (BuCu, BpCu) ran for less than one hour, mostly due to the significant decrease in column strength and stiffness as a result of the high temperatures reached by the steel column material.

Analysis	Time to failure
BuCu	37 min.
BpCp	11 hrs 16 min.
BuCp	37 min.
BpCu	57 min.

Table 2: Time to failure for each analysis

Figures 7(a) and 7(b) show the deformation of the frame for Analyses BuCu and BpCp, respectively, at the time of failure. Figure 8 plots, for Analysis BpCp, the column deformation, Δ, as shown in Figure 7(b) for each floor in the frame, where the negative value is in the direction shown in the figures. It is seen that the maximum column deformation for Analysis BpCp was 46 mm. In Analysis BuCu the column deformation was 67 mm at the time of failure.

Figures 9(a) and 9(b) show the temperatures reached in the columns without and with fireproofing, respectively, when subject to the floor temperatures shown in Figure 3. Similarly, Figures 10(a) and 10(b) show the temperatures in the beams without and with fireproofing, respectively. The temperatures in these figures are taken at the web mid-height, which nearly represents an average temperature through the section. It is seen that if no fireproofing is used, both the beams and columns are essentially at the same temperature as the floor fire due to the relatively thin flanges and webs and the capacity of steel to conduct heat. If fireproofing is added, the temperatures are significantly less than the floor temperature as seen in Figures 9(b) and 10(b). However, the steel sections do not cool as fast as the sections without fireproofing since it is assumed that the fireproofing remains intact.

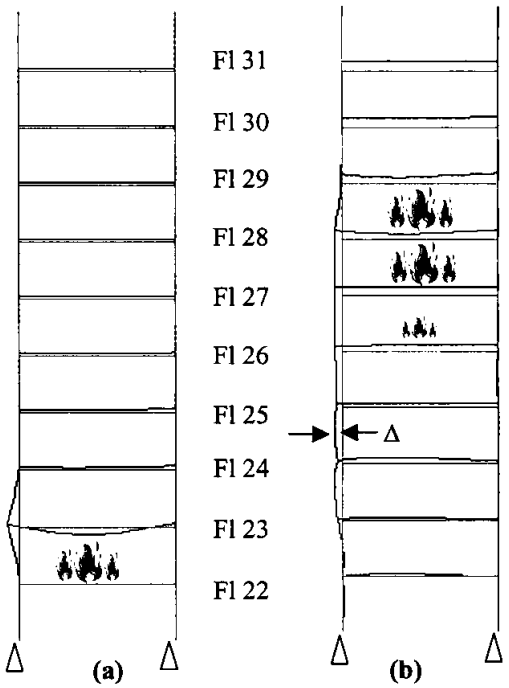

Figure 7 – Deformation of the frame for (a) Analysis BuCu and (b) Analysis BpCp, at the time of failure.

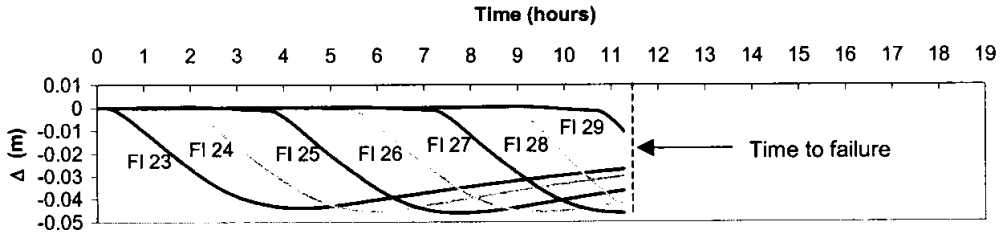

Figure 8 - Column deformation, Δ, for each floor of Analysis BpCp, where the negative value is in the direction shown in Figure 9(b).

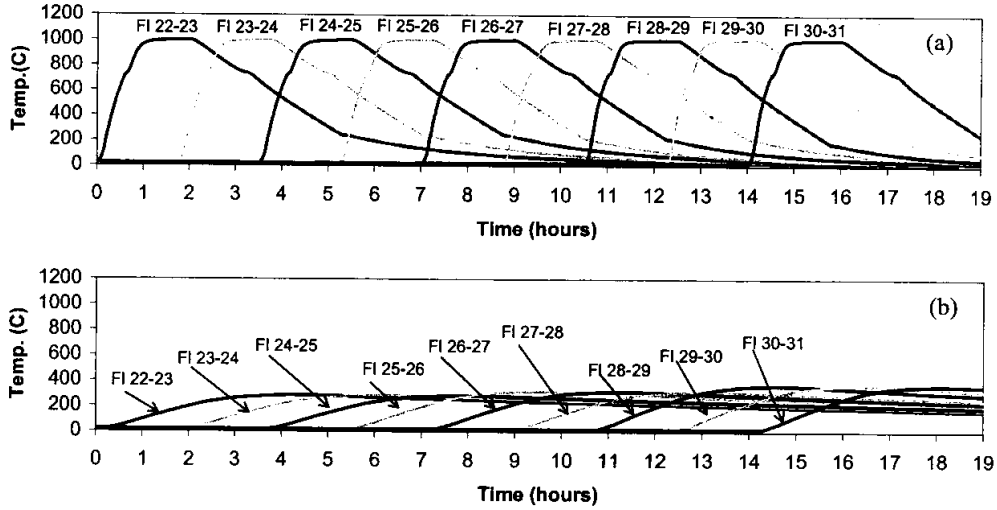

Figure 9 - Temperatures reached in the columns (a) without and (b) with fireproofing when subject to the floor temperatures shown in Figure 3

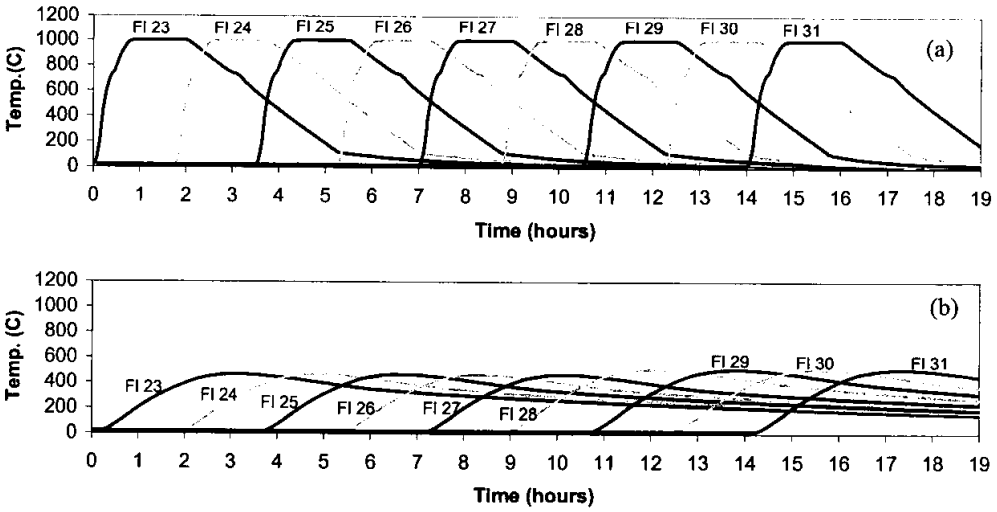

Figure 10 - Temperatures reached in the beams (a) without and (b) with fireproofing when subject to the floor temperatures shown in Figure 3

SUMMARY AND CONCLUSIONS

Analyses of a tall steel building subject to fire display the crucial role of fire protection materials in the response of the steel perimeter columns of a building. With no fireproofing, the temperatures throughout the steel section are greatly increased, which leads to an increase in displacement of the perimeter column. This, in turn, leads to a faster initiation of the failure mechanism.

The deformation of the frame as the fire progresses and the modes of failure mechanisms indicate the development and impact of secondary, P-Δ, effects within the frame. As deformation is enhanced by material effects, i.e., the reduction in the strength and stiffness of the steel under fire loads, geometric second-order effects develop, increasing the moment in the perimeter columns and exacerbating the displacement of these columns. Buckling of the floor beams under temperature loads also leads to a failure mechanism. As the floor beams become unstable, they no longer brace the perimeter columns. While the research presented in this paper does not include the slab in the analyses, we are currently developing research that will lead to conclusions on the slab's relevance to the floor beam's strength and elongation, in the context of a tall steel frame.

This study holds promise for a valid model of the full development and progression of a fire and its consequences on steel building structures. However, the results show that attention must be given to the detail of the structure, such as the slab. Examining the effects of fire on a typical high-rise building will provide useful data which could play an important role on how we treat our built environment today and design into the future.

REFERENCES

[1] Klem, Thomas J., (1991). "High-Rise Fire Claims Three Philadelphia Fire Fighters," *NFPA Journal*, September/October.

[2] Franssen J.-M., Kodur V. K. R. & Mason J., *User's Manual for SAFIR (2001). A Computer Program for Analysis of Structures Submitted to the Fire*, Univ. of Liege.

[3] Federal Emergency Management Agency (FEMA), *High-rise Office Building Fire: One Meridian Plaza, Philadelphia, Pennsylvania*, United States Fire Administration Technical Report Series.

[4] EC1 (1994). *Eurocode 1: Basis of Design and Design Actions on Structures. Part 2-2: Actions on Structures Exposed to Fire. ENV 1991-2-2.* European Committee for Standardization, Brussels, Belgium.

[5] Dexter, Robert J. and Lu, Le-Wu (2001), "The Effects of a Severe Fire on the Steel Frame of an Office Building," *Engineering Journal*, Fourth Quarter 2001, pp. 167-175.

[6] Kirby, B.R. *et al.* (1999), "Natural fires in large scale compartments," *International Journal on Engineering Performance Based-Fire Codes*, Hong Kong Polytechnic University, Construction Industry Development, Studies and Research Centre, FA.

[7] Kawagoe, K (1958), "Fire Behavior in Rooms," *Report No. 27*, Building Research Institute, Ministry of Construction, Tokyo.

IMPROVEMENT OF THE CURRENT VERSION OF THE EC3 FOR THE LATERAL-TORSIONAL BUCKLING OF UNRESTRAINED STEEL BEAMS UNDER FIRE CONDITIONS

Paulo M. M. VILA REAL, Nuno LOPES
University of Aveiro, Department of Civil Engineering, 3810-193 Aveiro, Portugal, & IDMEC Pólo FeuP
pvreal@civil.ua.pt, nuno_lopes@civil.ua.pt

Luis SIMÕES DA SILVA
University of Coimbra, Department of Civil Engineering, Polo II, Pinhal de Marrocos, 3030-290 Coimbra, Portugal
luisss@dec.uc.pt

Jean-Marc FRANSSEN
University of Liege, 1, Chemin des Chevreuils, 4000, Liège 1, Belgium
jm.franssen@ulg.ac.be

ABSTRACT

Numerical modelling of the lateral–torsional buckling of steel beams at elevated temperature has shown that the beam design curve from prEN 1993-1-2 is over-conservative for loadings other than uniform bending.

In line with the safety format of the lateral-torsional buckling code provisions for cold design, an alternative proposal for rolled sections or equivalent welded sections subjected to fire is presented in this paper, which achieves better agreement with the numerical results while maintaining safety. This proposal is based in numerical simulations that considered the influence of the loading type and the relation h/b of the beams.

KEYWORDS: *steel beam, lateral-torsional buckling, fire, Eurocode 3, numerical modelling*

INTRODUCTION

Recently, the project team in charge of the conversion of Eurocode 3 from ENV to EN status, introduced significant changes in the evaluation of the lateral-torsional buckling resistance of unrestrained beams at room temperature [1] that reduce the over-conservative approach of ENV 1993-1-1 [2] in the case of non-uniform bending.

Also recently, but for opposite reasons, Vila Real *et al* [3-5] proposed an alternative expression for the lateral-torsional buckling resistance of unrestrained beams under fire loading. This change, already adopted by the project team of part 1-2 of EC3 [6], was triggered by the identification of the unconservative nature of the previous expression [7] for the case of a simply-supported beam with fork supports under uniform bending.

In this paper a consistent safety check for the lateral-torsional buckling resistance of beams under fire loading is proposed, by adapting the newly proposed methodology for cold design to fire design.

In prEN 1993-1-1 [1] the determination of the lateral-torsional buckling of steel beams at room temperature is made taking also in consideration the relation h/b (height/base of the flange) of the profile. However, at elevated temperatures, numerical studies [8] have shown that results for the case of uniform bending are not so sensitive to this ratio, the current version of part 1-2 of Eurocode 3 not considering this parameter.

The objective of the present paper is to evaluate the influence of the relation h/b in lateral-torsional buckling of beams in case of fire, for the non-uniform bending. A parametric study is carried out, comparing the curves given by prEN 1993-1-2 [6], with the new proposals that have in consideration the influence of the type of loading [9, 10] and with the numerical results. These numerical results are assessed using the specialised finite element code SAFIR [11], which is a finite element code for geometrical and material non-linear analysis, specially developed at the University of Liege for studying structures subjected to fire.

CASE STUDY

A simply supported beam with fork supports was chosen to explore the validity of the beam safety verifications, as shown in figure 1. Regarding the bending moment variation along the member length, three values, (-1, 0 and 1), of the ψ ratio (see fig. 1) have been investigated as well as a uniformly distributed load or a mid span concentrated load. An IPE 500 (profile chosen for $h/b > 2$) and a HEA500 (profile chosen for $h/b < 2$) in steel grade S 235 were used.

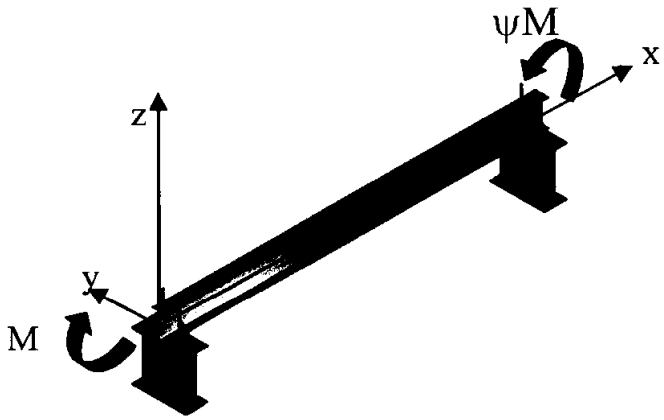

FIGURE 1 : Simply supported beam with non-uniform bending.

Uniform temperature in the cross-section has been used so that comparison between the numerical results and the eurocodes could be made. In this paper the temperatures used were 400, 500, 600 and 700 °C, deemed to adequately represent the majority of practical situations.

A lateral geometric imperfection given by the following expression was considered:

$$y(x) = \frac{l}{1000} sin\left(\frac{\pi x}{l}\right) \tag{1}$$

An initial rotation around the longitudinal axis with a maximum value of $l/1000$ rad at mid span was also introduced.

Finally, the residual stresses adopted are constant across the thickness of the web and flanges. A triangular distribution as shown in figure 2, with a maximum value of 0.3×235 MPa [12].

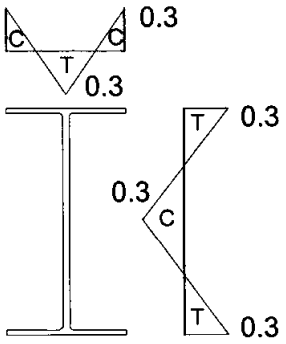

FIGURE 2 : Residual stresses: C – compression; T – tension

PARAMETRIC EVALUATION OF THE LATERAL-TORSIONAL BUCKLING CODE PROVISIONS OF EUROCODE 3

prEN 1993-1-1 Proposals at Room Temperature

At room temperature, beams with cross-sectional classes 1 and 2 subjected to major-axis bending, must generically satisfy the following relation:

$$M_{b,Rd} = \chi_{LT} W_{pl,y} \frac{f_y}{\gamma_{M1}} \tag{2}$$

where f_y denotes the yield stress of steel, γ_{M1} the appropriate partial safety factor, $W_{pl,y}$ the plastic modulus of the section about the major axis and χ_{LT} represents the reduction factor for lateral-torsional buckling and depends on the so-called non-dimensional slenderness, $\overline{\lambda}_{LT}$, given by

$$\overline{\lambda}_{LT} = \sqrt{\frac{W_{pl,y} f_y}{M_{cr}}} \tag{3}$$

where M_{cr} denotes the elastic critical moment for lateral-torsional buckling, calculated on the basis of the gross cross sectional properties and taking into account the loading conditions, the real moment distribution and the lateral restraints.

In both the ENV and prEN versions of part 1-1 of Eurocode 3, the reduction factor χ_{LT} is formally based on the Rondal-Maquoi formula, detailed derivations being found in [13]. In contrast to the ENV implementation, that presented a single option for the evaluation of the lateral-torsional buckling reduction factor χ_{LT}, summarized in Table 1, the prEN version allows two alternatives, also summarized in Table 1 and explained below, where α_{LT} denotes the imperfection factors for lateral-torsional buckling curves.

The first method described in the prEN 1993-1-1, denoted "General case" in figures 3 and 4, basically reproduces the ENV proposal with a modified level of imperfection factors, α_{LT}, and more strict conditions to neglect the LTB check, see Table 1.

	ENV 1993-1-1	**prEN 1993-1-1**	
	(5.5.3)	General Case (6.3.2.2)	Rolled sections or equivalent welded sections (6.3.2.3)
χ_{LT}	$\chi_{LT} = \dfrac{\textit{min of}\ 1}{\phi_{LT} + \sqrt{\phi_{LT}^2 - \bar{\lambda}_{LT}^2}}, 1$		$\chi_{LT} = \dfrac{\textit{min of}\ 1}{\phi_{LT} + \sqrt{\phi_{LT}^2 - \beta\bar{\lambda}_{LT}^2}}, 1, \dfrac{1}{\bar{\lambda}_{LT}^2}$
$\chi_{LT,\mathrm{mod}}$			$\chi_{LT,mod} = \dfrac{\chi_{LT}}{f}$
f		$\textit{min of}\ f = 1 - 0.5(1-k_c)\left[1 - 2(\bar{\lambda}_{LT} - 0.8)^2\right], 1$	
ϕ_{LT}	$\phi_{LT} = \frac{1}{2}\left[1 + \alpha_{LT}(\bar{\lambda}_{LT} - 0.2) + \bar{\lambda}_{LT}^2\right]$		$\phi_{LT} = \frac{1}{2}\left[1 + \alpha_{LT}(\bar{\lambda}_{LT} - \bar{\lambda}_{LT,0}) + \beta\bar{\lambda}_{LT}^2\right]$
	Dispensing Conditions		
$\bar{\lambda}_{LT}$	0.4	0.2	0.4
M_{Ed}/M_{cr}	-	0.04	0.16

Table 1 : Comparison between ENV 1993-1-1 and prEN 1993-1-1 formulae

A careful examination of the general procedure discussed above quickly reveals that the influence of the bending moment diagram on the LTB resistance of the beam only appears indirectly through the value of the elastic critical moment. This assumption is over-conservative, as can be easily seen by comparing with, for example, the Australian code of practice, or the theoretical results of Trahair [14].

The second method, denoted "Rolled Sections" in figures 3 and 4, applicable for the particular case of rolled sections or equivalent welded sections, yields greater LTB resistance, the detailed procedure for this method being also shown in Table 1. It is noted that two modifying parameters, $\bar{\lambda}_{LT,0}$ and β are introduced, that should be taken as:

$\lambda_{LT,0} = 0.4$ (maximum value)

$\beta = 0.75$ (minimum value)

and the dispensing conditions for LTB check are less strict, as shown in Table 1.

Additionally, and to address the issue of the influence of the bending moment diagram, the use of a modified reduction factor, $\chi_{LT,mod}$ (see Table 1), is allowed, that depends on the moment distribution correction factor, k_c, illustrated in Table 2 for some common loading cases. This third method is denoted "Rolled Sections / f" in figure 3 and 4.

Moment distribution	Class 1, 2, 3 sections
	k_c
 $-1 \le \psi \le 1$	$\frac{1}{1.33 - 0.33\psi}$
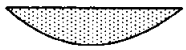	0.94
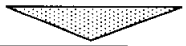	0.86

Table 2 : Correction factors k_c [1]

The imperfection factor α_{LT} depends on the buckling curve that is selected according to the relation h/b, as illustrated in Table 3 and Table 4.

Cross Section	Limits	Buckling curve
Rolled I sections	h/b ≤2	a
	h/b >2	b
Welded I sections	h/b ≤2	c
	h/b >2	d
Other cross-sections	-	d

Table 3 : Selection of lateral-torsional buckling curve for the general case

Cross Section	Limits	Buckling curve
Rolled I sections	h/b ≤2	b
	h/b >2	c
Welded I sections	h/b ≤2	c
	h/b >2	d
Other cross-sections	-	d

Table 4 : Selection of lateral-torsional buckling curve for rolled sections or equivalent welded sections

The imperfection factors for the lateral-torsional buckling are given in table 5.

Buckling curve	a	b	c	d
Imperfection factor α_{LT}	0.21	0.34	0.49	0.76

Table 5 : Imperfection factors for lateral-torsional buckling curves

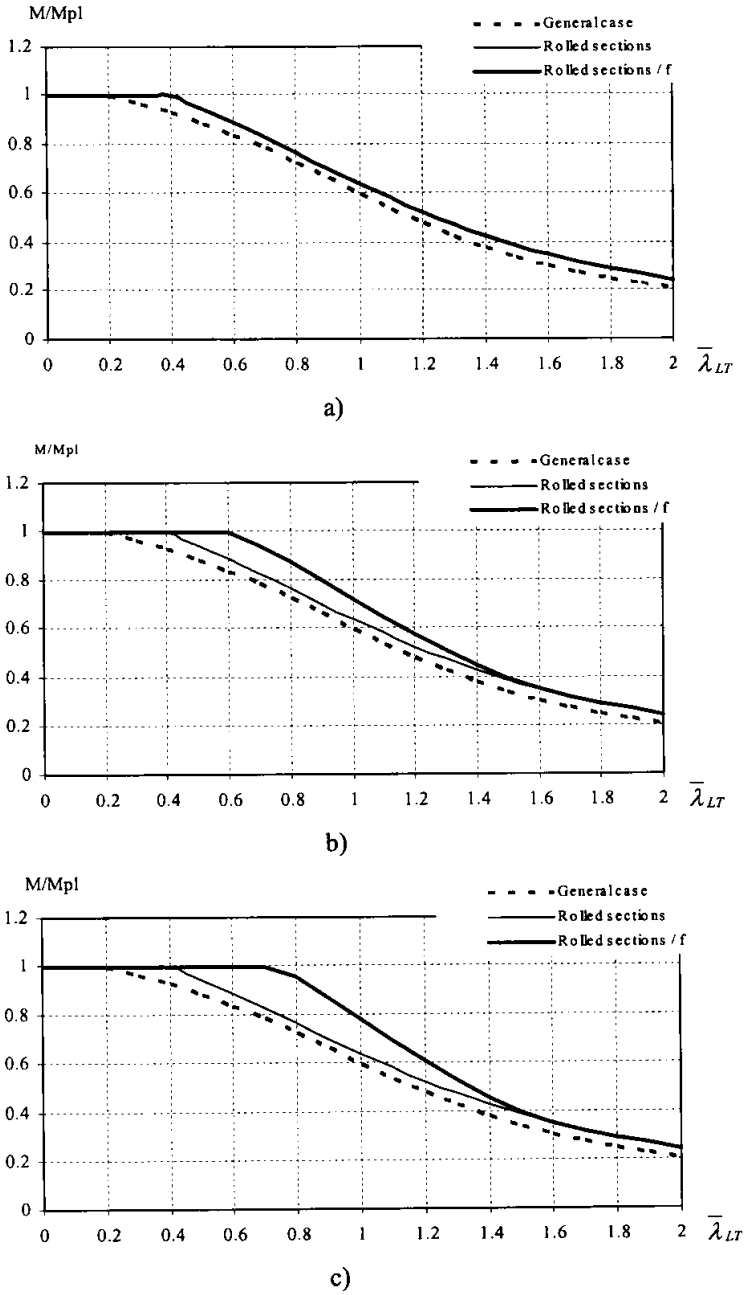

FIGURE 3 : Lateral-torsional buckling curves for the IPE 500 (h/b>2) at room temperature. a) $\psi = 1$ **; b)** $\psi = 0$ **; c)** $\psi = -1$

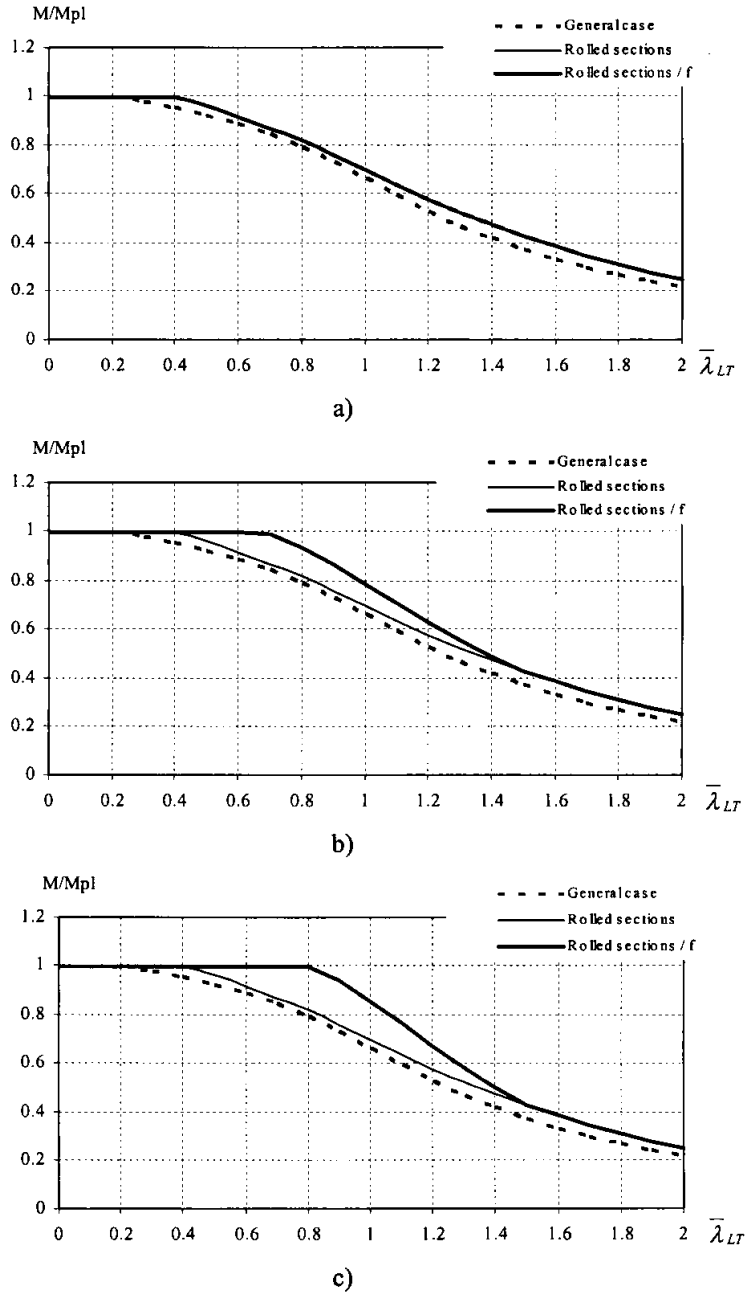

FIGURE 4 : Lateral-torsional buckling curves for the HEA 500 (h/b<2) at room temperature. a) $\psi = 1$ **; b)** $\psi = 0$ **; c)** $\psi = -1$

prEN 1993-1-2 Proposals at high temperatures

According to this proposal, the design buckling resistance moment of a laterally unrestrained beam with a class 1 or 2 cross-section type, is obtained as follows:

$$M_{b,fi,t,Rd} = \chi_{LT,fi} W_{pl,y} k_{y,\theta,com} f_y \frac{1}{\gamma_{M,fi}} \tag{4}$$

where $\chi_{LT,fi}$, is given by

$$\chi_{LT,fi} = \frac{1}{\phi_{LT,\theta,com} + \sqrt{\left[\phi_{LT,\theta,com}\right]^2 - \left[\bar{\lambda}_{LT,\theta,com}\right]^2}} \tag{5}$$

with

$$\phi_{LT,\theta,com} = \frac{1}{2}\left[1 + \alpha\bar{\lambda}_{LT,\theta,com} + \left(\bar{\lambda}_{LT,\theta,com}\right)^2\right] \tag{6}$$

The non-dimensional slenderness $\bar{\lambda}_{LT,\theta,com}$ (or $\bar{\lambda}_{LT,fi}$, if the temperature field in the cross section is uniform) is given by

$$\bar{\lambda}_{LT,\theta,com} = \bar{\lambda}_{LT,fi} = \bar{\lambda}_{LT}\sqrt{\frac{k_{y,\theta,com}}{k_{E,\theta,com}}} \tag{7}$$

The imperfection factor α, in this proposal, is a function of the steel grade and is given by

$$\alpha = 0.65\sqrt{235/f_y} \tag{8}$$

As shown in figures 5 and 6, this formulae from the prEN 1993-1-2, lead to over-conservative results when compared to numerical results for the case of non-uniform bending.

Improved Formulae at High Temperature. A new proposal

Figures 5 and 6 clearly highlight that there is scope for improvement in the evaluation of the lateral-torsional buckling resistance of beams. Based on the prEN 1993-1-1 version of the

Eurocode 3 it seems reasonable to propose, at high temperature, a second method, more accurate and less conservative that improves the results of figures 5 and 6.

Given that the main factor responsible for the over-conservative nature of the lateral-torsional buckling resistance at high temperatures was linked to the loading type, the new proposal also adopts a modified reduction factor for lateral-torsional buckling, $\chi_{LT,fi,mod}$, given by

$$\chi_{LT,fi,mod} = \frac{\chi_{LT,fi}}{f} \quad \text{but} \quad \chi_{LT,fi,mod} \leq 1 \qquad (9),$$

where f depends on the loading type.

Initially, the adequacy of part 1-1 proposals for f and k_c (see tables 1 and 2) were tested. The results, denoted as "prEN 1993-1-2 / f" in figures 5 and 6, are better and closer to the numerical values but still remain conservative. Consequently, in order to have a better approximation, taking into account the moment distribution between the lateral restraints of members, new coefficients for f and k_c were adjusted, given by the following equation

$$f = 1 - 0.5(1 - k_c) \qquad (10)$$

where k_c is a correction factor according to table 6.

As it can be seen in figures 5 and 6, this new proposal shows a very good agreement with the numerical results. These figures illustrate the results for several values of ratio ψ of case A and for the cases B and C (see table 6).

	Moment distribution	Class 1, 2, 3 sections k_c
A	 $-1 \leq \psi \leq 1$	$0.6 + 0.3\psi + 0.15\psi^2$ but $k_c \leq 1$
B	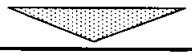	0.79
C		0.91
Note: for others bending diagrams $k_c = 1$.		

Table 6 : Correction factors k_c for the new proposal

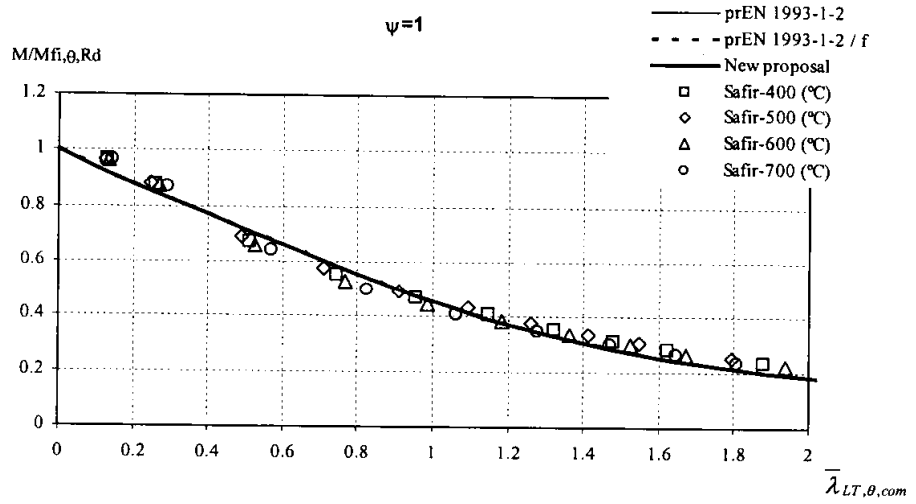
ψ=1
M/Mfi,θ,Rd
prEN 1993-1-2
prEN 1993-1-2 / f
New proposal
Safir-400 (°C)
Safir-500 (°C)
Safir-600 (°C)
Safir-700 (°C)
1.2
1
0.8
0.6
0.4
0.2
0
0
0.2
0.4
0.6
0.8
1
1.2
1.4
1.6
1.8
2
$\bar{\lambda}_{LT,\theta,com}$

a)

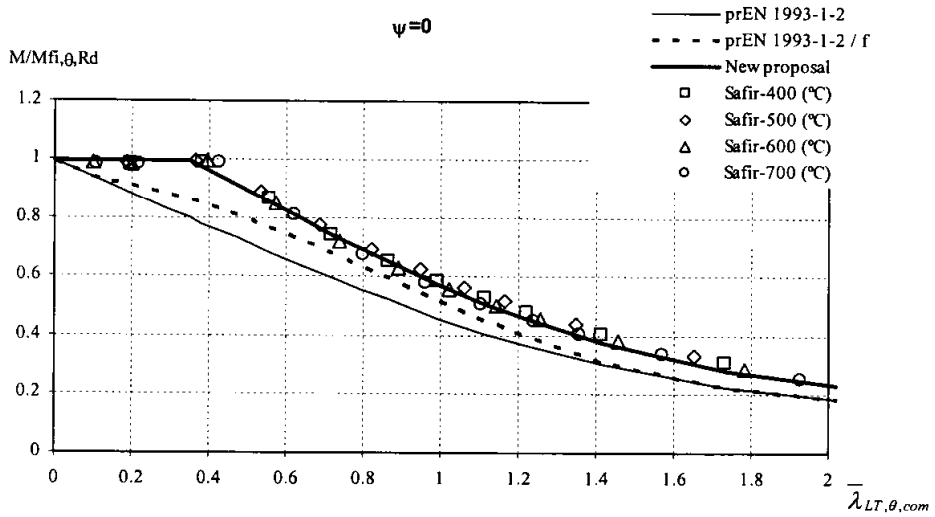
ψ=0
M/Mfi,θ,Rd
prEN 1993-1-2
prEN 1993-1-2 / f
New proposal
Safir-400 (°C)
Safir-500 (°C)
Safir-600 (°C)
Safir-700 (°C)
1.2
1
0.8
0.6
0.4
0.2
0
0
0.2
0.4
0.6
0.8
1
1.2
1.4
1.6
1.8
2
$\bar{\lambda}_{LT,\theta,com}$

b)

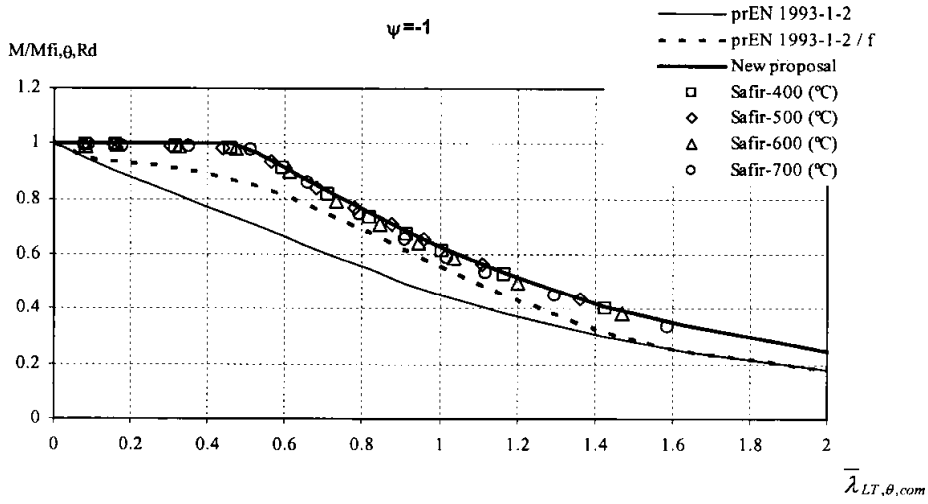
ψ=-1
M/Mfi,θ,Rd
prEN 1993-1-2
prEN 1993-1-2 / f
New proposal
Safir-400 (°C)
Safir-500 (°C)
Safir-600 (°C)
Safir-700 (°C)
1.2
1
0.8
0.6
0.4
0.2
0
0
0.2
0.4
0.6
0.8
1
1.2
1.4
1.6
1.8
2
$\overline{\lambda}_{LT,\theta,com}$

c)

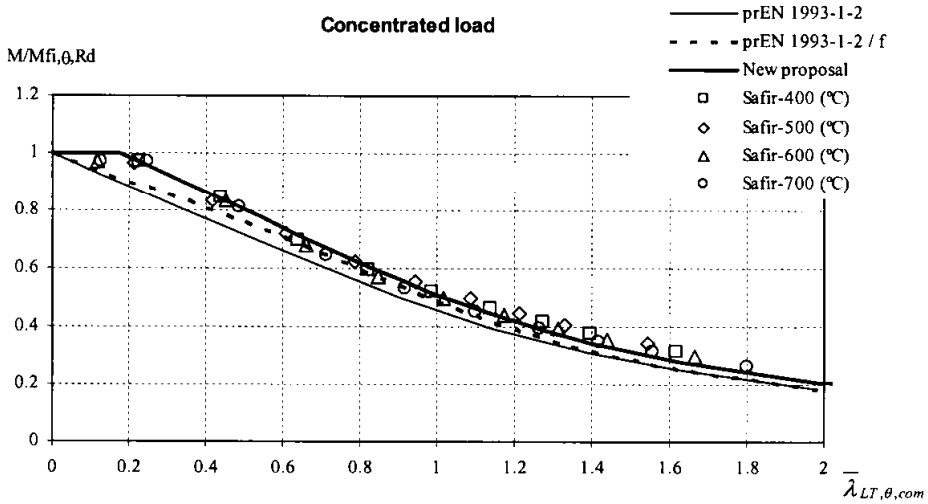
Concentrated load
M/Mfi,θ,Rd
prEN 1993-1-2
prEN 1993-1-2 / f
New proposal
Safir-400 (°C)
Safir-500 (°C)
Safir-600 (°C)
Safir-700 (°C)
1.2
1
0.8
0.6
0.4
0.2
0
0
0.2
0.4
0.6
0.8
1
1.2
1.4
1.6
1.8
2
$\overline{\lambda}_{LT,\theta,com}$

d)

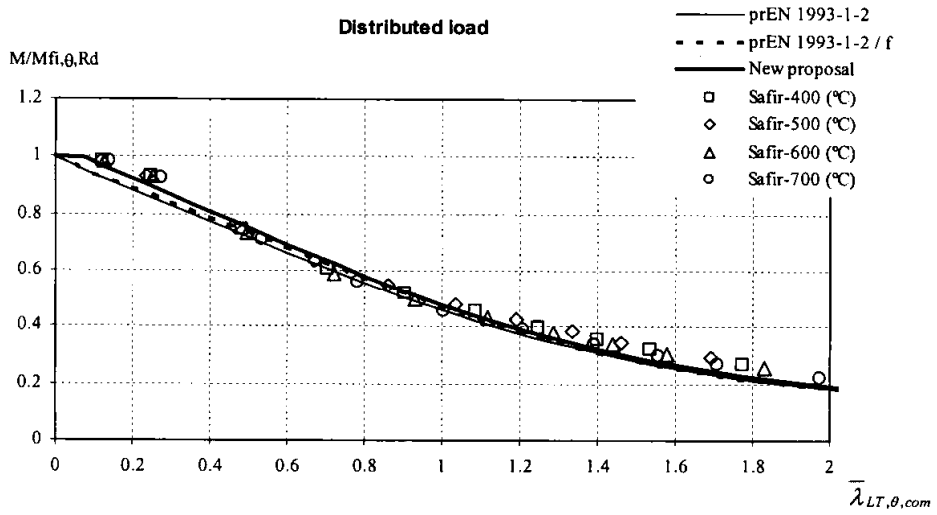

e)

FIGURE 5 : Lateral-torsional buckling curves for the IPE 500 (h/b>2). a) $\psi = 1$; b) $\psi = 0$; c) $\psi = -1$; d) Concentrated load; e) Distributed load

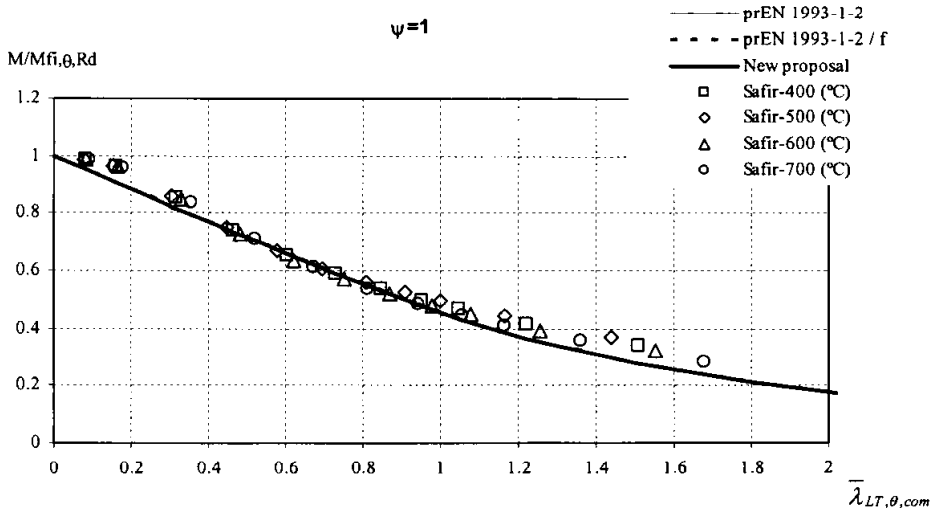

a)

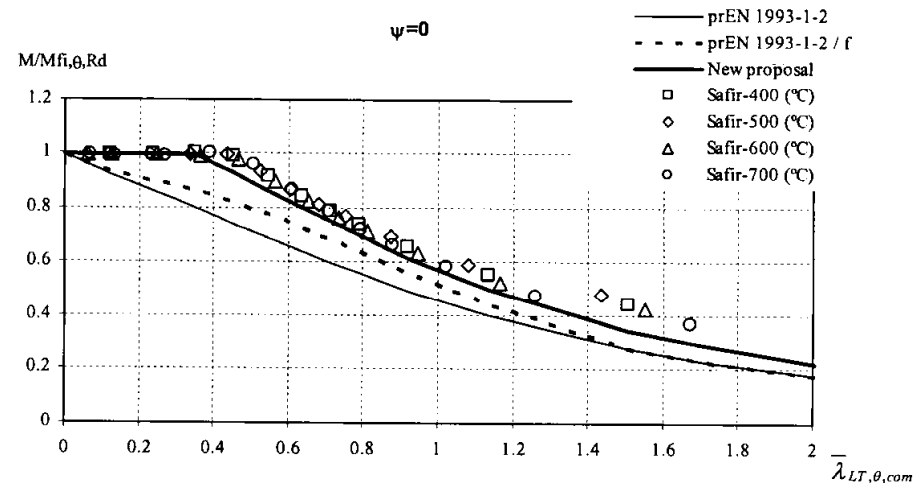
ψ=0
M/Mfi,θ,Rd
prEN 1993-1-2
prEN 1993-1-2 / f
New proposal
Safir-400 (°C)
Safir-500 (°C)
Safir-600 (°C)
Safir-700 (°C)
1.2
1
0.8
0.6
0.4
0.2
0
0
0.2
0.4
0.6
0.8
1
1.2
1.4
1.6
1.8
2
$\overline{\lambda}_{LT,\theta,com}$

b)

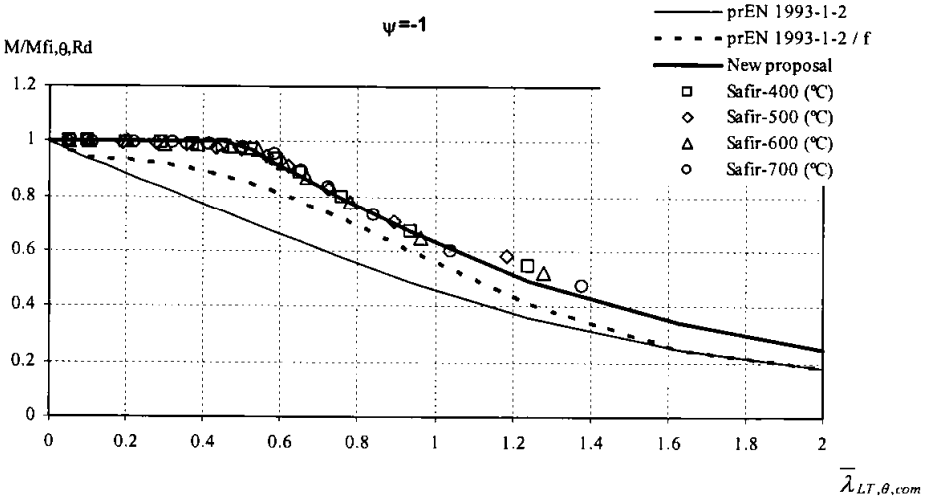
ψ=-1
M/Mfi,θ,Rd
prEN 1993-1-2
prEN 1993-1-2 / f
New proposal
Safir-400 (°C)
Safir-500 (°C)
Safir-600 (°C)
Safir-700 (°C)
1.2
1
0.8
0.6
0.4
0.2
0
0
0.2
0.4
0.6
0.8
1
1.2
1.4
1.6
1.8
2
$\overline{\lambda}_{LT,\theta,com}$

c)

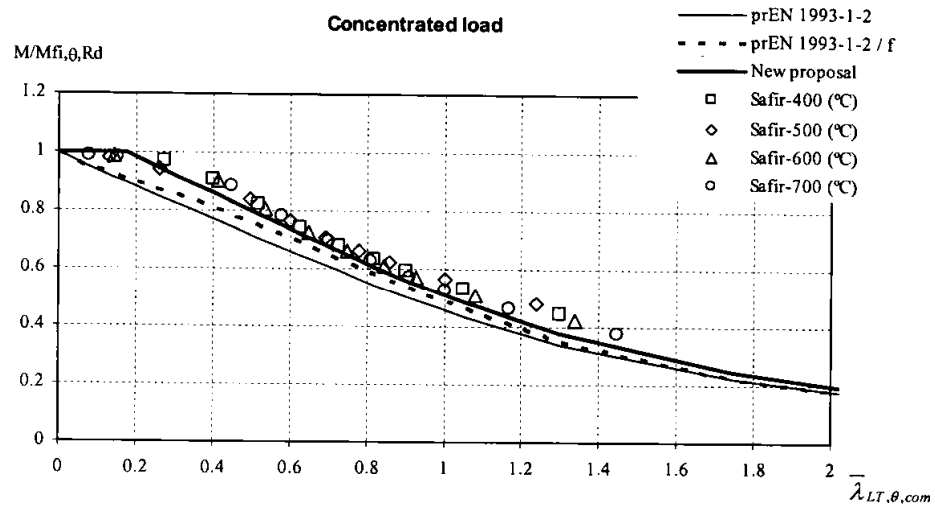

d)

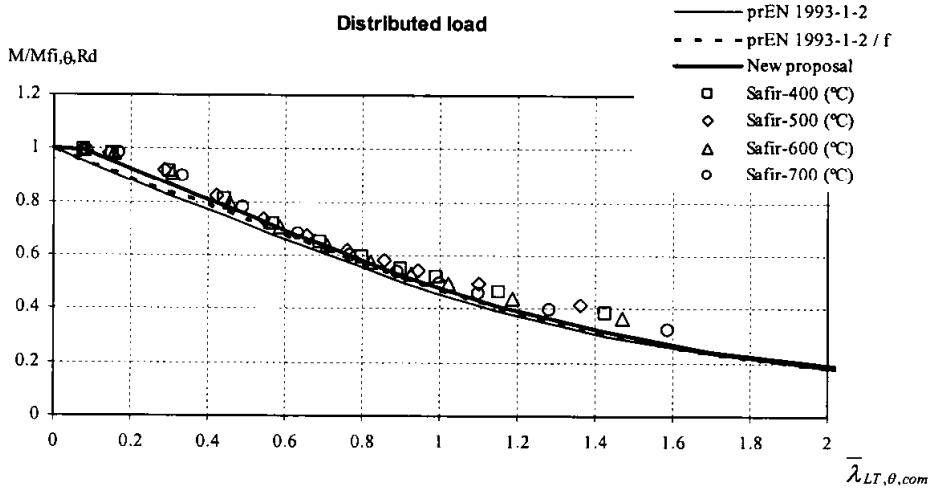

e)

FIGURE 6 : Lateral-torsional buckling curves for the HEA 500 (h/b<2). a) $\psi = 1$; b) $\psi = 0$; c) $\psi = -1$; d) Concentrated load; e) Distributed load

CONCLUSIONS

A new proposal for the lateral-torsional buckling resistance of beams under fire loading has been proposed. It was adapted from the newly proposed methodology for cold design from the

later version of prEN 1993-1-1 [1] as an alternative method for rolled sections or equivalent welded sections. The proposed method approximates more closely the numerical results of unrestrained steel beams under fire conditions, while still remaining on the safe side.

For the case h/b>2 (IPE500) the new proposal is marginally unsafe when compared with the numerical results. However, as these numerical results were obtained using the geometric imperfections and the residual stresses simultaneously with their highest value, a situation not likely to occur in a real beam [5], it seems reasonable to accept this proposal for design purposes. For h/b<2 (HEA500), the new proposal is on the safe side and approaches very accurately the numerical results.

Nevertheless, from the results presented here, it can be concluded that the influence of the relation h/b at high temperature it is not as relevant as at room temperature, so that it doesn't have to be considered in the formulae for the lateral-torsional buckling of beams.

REFERENCES

[1] prEN 1993-1-1, *Eurocode 3: Design of Steel Structures – part 1-1: General rules and rules for buildings*, Stage 49, European Committee for Standardisation, Brussels, Belgium, 2003.

[2] ENV 1993-1-1, *Eurocode 3: Design of Steel Structures – part 1-1: General rules and rules for buildings*, European Committee for Standardisation, Brussels, Belgium, 1992.

[3] Vila Real, P.M.M. and Franssen, J.-M., *Lateral buckling of steel I beams under fire conditions - Comparison between the EUROCODE 3 and the SAFIR code,* internal report No. 99/02 , Institute of Civil Engineering – Service Ponts et Charpents – of the University of Liege, 1999.

[4] Vila Real, P.M.M. and Franssen, J.-M., *Numerical Modelling of Lateral Buckling of Steel I Beams Under Fire Conditions – Comparison with Eurocode 3*, Journal of Fire Protection Engineering, Vol. 11, No. 2, , pp. 112-128, USA, 2001.

[5] Vila Real, P.M.M., Piloto, P.A.G. and Franssen, J.-M., *A New Proposal of a Simple Model for the Lateral-Torsional Buckling of Unrestrained Steel I-Beams in Case of Fire: Experimental and Numerical Validation,* Journal of Constructional Steel Research, Elsevier, Vol. 59/2, pp. 179-199, 2003.

[6] prEN 1993-1-2, *Eurocode 3: Design of Steel Structures – part 1-2: General Rules - Structural fire design*, European Committee for Standardisation, Brussels, Belgium, February 2003.

[7] ENV 1993-1-2, *Eurocode 3: Design of Steel Structures – part 1-2: General Rules - Structural fire design*, European Committee for Standardisation, Brussels, Belgium, 1995.

[8] Cazeli, R., Vila Real, P.M.M., Silva, V.P. e Piloto, P.A.G., *Análise numérica de vigas I de aço em situação de incêndio, sujeitas à flambagem lateral. Contribuição para a validação de uma proposta de revisão do Eurocode 3 – Parte 1-2*, I Congresso Internacional da Construção Metálica – I CICOM, São Paulo, Brasil, 2001.

[9] Vila Real, P.M.M., Lopes, N., Simões da Silva, L., Franssen, J.-M., *Lateral-torsional buckling of unrestrained steel beams under fire conditions: improvement of EC3 proposal*, submitted to Computers & Structures, 2003.

[10] N. Lopes, *Modelação numérica do comportamento de vigas-coluna metálicas em situação de incêndio*, (in Portuguese) MSc Thesis, University of Coimbra, Portugal, September 2003.

[11] Franssen, J.-M., *SAFIR. A Thermal/Structural Program Modeling Structures under Fire*, proceedings NASCC conference, American Institute for Steel Construction, Baltimore, April 2003.

[12] ECCS – EUROPEAN CONVENTION FOR CONSTRUCTIONAL STEELWORK, *System, Ultimate Limit State Calculation of Sway Frames With Rigid Joints*, Technical Committee 8 – Structural Stability, Technical Working Group 8.2, first edition, 1984.

[13] Maquoi R. and Rondal J., *Mise en equation des nouvelles courbes Européennes de flambement*, (in French), Construction Métallique, Vol. 1, pp. 17-29, 1978.

[14] Trahair N.S. and Bradford, M. A., *The Behaviour and Design of Steel Structures to AS 4100*; Third edition – Australian, E&FN SPON, 1998.

NEW PROPOSALS FOR THE DESIGN OF STEEL BEAM-COLUMNS UNDER FIRE CONDITIONS

Nuno LOPES, Paulo M. M. VILA REAL
University of Aveiro, Department of Civil Engineering, 3810-193 Aveiro, Portugal, & IDMEC Polo FeuP
pvreal@civil.ua.pt, nuno_lopes@civil.ua.pt

Luis SIMÕES DA SILVA
University of Coimbra, Department of Civil Engineering, Polo II, Pinhal de Marrocos, 3030-290 Coimbra, Portugal
luisss@dec.uc.pt

Paulo PILOTO
Polytechnic of Bragança, Department of Mechanical Engineering, Bragança, Portugal
ppiloto@ipb.pt

Jean-Marc FRANSSEN
University of Liege, 1, Chemin des Chevreuils, 4000, Liège 1, Belgium
jm.franssen@ulg.ac.be

ABSTRACT

The possibility of having, in parts 1-1 and 1-2 of Eurocode 3, the same approach for the design of beam-columns and for lateral-torsional buckling, was investigated by the authors in previous papers using a numerical approach, where it was concluded that those assumptions could be made.

In the present paper, a new approach for lateral-torsional buckling has been used with the formulae for the design of beam-columns at elevated temperature based on prEN 1993-1-1 combined with the formulae from prEN 1993-1-2. In both cases the results obtained are much

better than the current design expressions, when compared with those obtained in the numerical calculations.

KEYWORDS: *steel, beam-column, lateral-torsional-buckling, fire, Eurocode 3, numerical modelling*

INTRODUCTION

The final draft of part 1-1 of Eurocode 3, prEN 1993-1-1 (2003) [1], introduced several changes in the design formulae for beam-columns and unrestrained beams with lateral-torsional buckling (LTB) at room temperature. These modifications took place during the conversion of Eurocode 3 from ENV to EN status.

Two new formulae for the design of beam-columns at room temperature have been proposed in prEN 1993-1-1 (2003) [1] as the result of extensive work made by two working groups that followed different approaches, namely, a French-Belgian team and an Austrian-German one.

Under fire conditions, in prEN 1993-1-2 (2003) [2], the proposed formulae for the design of beam-columns in case of fire have not changed and are still based on ENV 1993-1-1 (1992) [3].

In order to study the possibility of having, in parts 1-1 and 1-2 of the upcoming Eurocode 3, the same approach for beam-columns, a numerical investigation was carried out, with the conclusion that it is possible to use the formulae from the part 1-1 provided that some factors are modified to consider high temperatures [4].

Significant changes, proposed in prEN 1993-1-1 (2003) [1], have been introduced in the evaluation of the lateral-torsional buckling resistance of unrestrained beams at room temperature leading to results that are still on the safe side but less conservative than those obtained using the approach prescribed in the former ENV 1993-1-1 (1992) [3] in case of non-uniform bending.

Numerical modelling of the lateral–torsional buckling of steel beams at elevated temperature has shown that the beam design curve from prEN 1993-1-2 (2003) [2] is over-conservative for bending moment diagrams other than uniform bending moment [5].

In accordance with the safety format of the lateral-torsional buckling code provisions for room temperature design, an alternative proposal for rolled sections or equivalent welded sections subjected to fire was presented by Vila Real et al [5], that addressed the issue of the influence of the loading type on the resistance of the beam, leading to better agreement with the numerical behaviour while maintaining safety.

The objective of the present paper is to evaluate the proposals made by Vila Real et al [4] in terms of a consistent safety check for the stability of beam-columns subjected to lateral-torsional buckling under fire loading, but using the new proposal for lateral-torsional buckling of unrestrained beams in case of fire [5]. This new proposal will be also used with the design formulae for beam-columns from the prEN 1993-1-2 (2003).

More specifically, using the specialised finite element code SAFIR [6], results of second-order analysis, including imperfections, for a range of lengths, levels of axial force and loading cases, are compared with the codified interaction formulae from Part 1-2 of Eurocode 3 [2] (here

denoted "prEN 1993-1-2" when the new proposal for lateral-torsional buckling [5] is not considered and "prEN 1993-1-2 / f" when this new proposal is included) and with the proposed adaptation [4] to fire loading of method 1 and method 2 in prEN 1993-1-1 (2003), henceforth denoted "EC3 Method 1, fi / f" and "EC3 Method 2, fi / f" or "EC3 Method 1, fi" and "EC3 Method 2, fi", again if the new proposal for LTB [5] is considered or not. Finally, the safety of these proposals is discussed and established.

CASE STUDY

A simply supported beam-column with fork supports has been chosen to explore the validity of the beam safety conditions, as shown in figure 1a). With respect to the bending moment variation along the member length, two values, (-1 and 0), of the ψ ratio (see fig. 1) have been investigated.

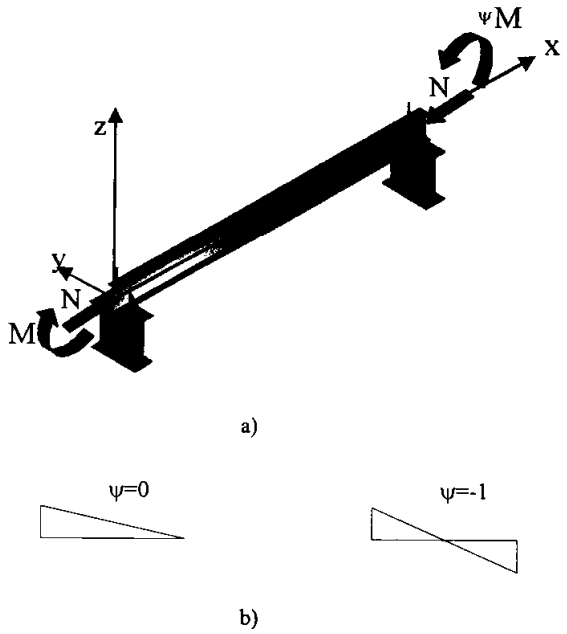

FIGURE 1 : a) Simply supported beam-column with non-uniform bending; b) Studied bending diagrams.

The case $\psi = 1$ was not studied here because this case is not affected by the new procedure for lateral-torsional buckling [5], that is, when the ψ ratio equals 1, the proposed formulae for the evaluation of the lateral-torsional buckling resistance of steel beams remains the same as those

proposed in the prEN 1993-1-2. The parametric study of beam-columns for $\psi = 1$ has already been made by Vila Real et al [4].

An IPE 220 steel section of grade S 235 has been used. Uniform temperature in the cross-section has been also used so that comparison between the numerical results and the Eurocode could be made. In this paper the temperature used was 600 °C, deemed to adequately represent the majority of practical situations.

A lateral geometric imperfection given by the following expression was considered:

$$y(x) = \frac{l}{1000} sin\left(\frac{\pi x}{l}\right) \tag{1}$$

where l is the beam length. An initial rotation around the longitudinal axis with a maximum value of $l/1000$ rad at mid span was also introduced.

The residual stresses adopted are constant across the thickness of the web and flanges. A triangular distribution as shown in figure 2, with a maximum value of 0.3×235 MPa has been used [7].

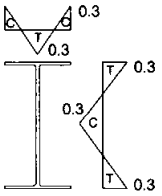

FIGURE 2 : Residual stresses: C – compression; T – tension

The lengths of the studied members were chosen so that the adimensional slenderness were smaller than 2.

IMPROVEMENT OF THE prEN 1993-1-2 PROPOSAL FOR LATERAL-TORSIONAL BUCKLING

According to the proposal of prEN 1993-1-2 [2], the lateral-torsional buckling resistance of a laterally unrestrained beam with class 1 or 2 cross-section, is obtained as follows:

$$M_{b,fi,t,Rd} = \chi_{LT,fi} W_{pl,y} k_{y,\theta,com} f_y \frac{1}{\gamma_{M,fi}} \tag{2}$$

where $\chi_{LT,fi}$ is given by

$$\chi_{LT,fi} = \frac{1}{\phi_{LT,\theta,com} + \sqrt{\left[\phi_{LT,\theta,com}\right]^2 - \left[\bar{\lambda}_{LT,\theta,com}\right]^2}} \tag{3}$$

with

$$\phi_{LT,\theta,com} = \frac{1}{2}\left[1 + \alpha\bar{\lambda}_{LT,\theta,com} + \left(\bar{\lambda}_{LT,\theta,com}\right)^2\right] \tag{4}$$

The non-dimensional slenderness $\bar{\lambda}_{LT,\theta,com}$ (or $\bar{\lambda}_{LT,fi}$, if the temperature field in the cross section is uniform) is given by

$$\bar{\lambda}_{LT,\theta,com} = \bar{\lambda}_{LT,fi} = \bar{\lambda}_{LT}\sqrt{\frac{k_{y,\theta,com}}{k_{E,\theta,com}}} \tag{5}$$

In this proposal, the imperfection factor α is a function of the steel grade and is given by:

$$\alpha = 0.65\sqrt{235/f_y} \tag{6}$$

As these formulae (from prEN 1993-1-2) lead to over conservative results when compared to numerical results for the case of non-uniform bending, Vila Real et al [5] have made a new proposal that adopts a modified reduction factor for lateral-torsional buckling, $\chi_{LT,fi,mod}$, given by

$$\chi_{LT,fi,mod} = \frac{\chi_{LT,fi}}{f} \quad \text{but} \quad \chi_{LT,fi,mod} \leq 1 \tag{7},$$

where f depends on the loading type and is given by the following equation

$$f = 1 - 0.5(1 - k_c) \tag{8}$$

where k_c is a correction factor according to table 1.

Moment distribution	Class 1, 2, 3 sections
	k_c
 $-1 \le \psi \le 1$	$0.6 + 0.3\psi + 0.15\psi^2$ but $k_c \le 1$

Table 1 : Correction factors k_c for the new proposal

INTERACTION FORMULAE FOR BEAM-COLUMNS AT HIGH TEMPERATURES

Interaction formulae proposed by prEN 1993-1-2

For fire loading, according to the new version of part 1-2 of Eurocode 3 [2], the interaction equations for beam-columns are:

$$\frac{N_{fi,Ed}}{\chi_{z,fi} A k_{y,\theta} \dfrac{f_y}{\gamma_{M,fi}}} + \frac{K_{LT} M_{y,fi,Ed}}{\chi_{LT,fi} W_{pl,y} k_{y,\theta} \dfrac{f_y}{\gamma_{M,fi}}} \le 1 \qquad (9)$$

where

$$K_{LT} = 1 - \frac{\mu_{LT} N_{fi,Ed}}{\chi_{z,fi} A k_{y,\theta} \dfrac{f_y}{\gamma_{M,fi}}} \quad \text{but} \quad K_{LT} \le 1.0 \qquad (10)$$

and

$$\mu_{LT} = 0.15 \bar{\lambda}_{z,\theta} \beta_{M,LT} - 0.15 \quad \text{but} \quad \mu \le 0.9 \qquad (11)$$

Here $\chi_{z,fi}$ is the reduction factor for flexural buckling around the zz axis, and $\chi_{LT,fi}$ is the reduction factor for lateral-torsional buckling, given by (4). These formulae for the design of beam-columns are based on the ENV 1993-1-1 (1992) [3].

To study the described methods, for each selected beam-column length and bending moment ratio ψ (0 and -1), illustrated in figures 3 and 4, the interaction equation (9) was plotted for increasing ratios of $N/N_{fi,\theta,Rd}$, together with the results of the numerical simulations for a uniform temperature of 600°C. In these figures, the results from equation (9) are denoted by "prEN 1993-1-2" whenever the new proposal for LTB is not considered and "prEN 1993-1-2 / f" otherwise.

From figures 3 and 4 it is concluded that the new proposal for LTB introduces a significant improvement in the interaction diagrams, for beam-columns with lateral-torsional buckling.

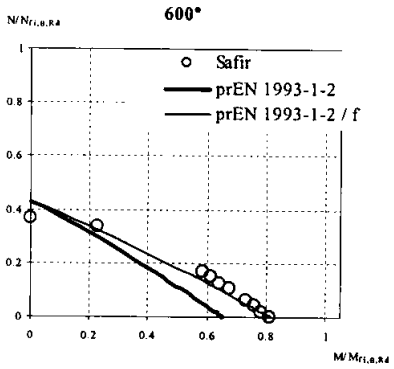

a) L=2000mm; $\bar{\lambda}_{LT,fi}$ *=0.62;* $\bar{\lambda}_{y,fi}$ *=0.29;* $\bar{\lambda}_{z,fi}$ *=1.06*

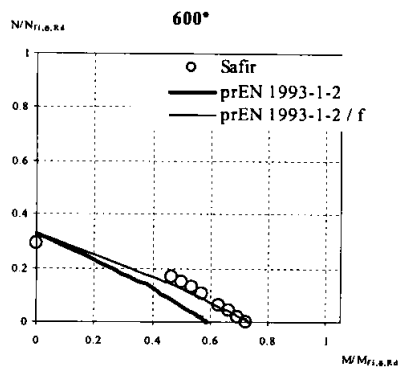

b) L=2500mm; $\bar{\lambda}_{LT,fi}$ *=0.73;* $\bar{\lambda}_{y,fi}$ *=0.36;* $\bar{\lambda}_{z,fi}$ *=1.32*

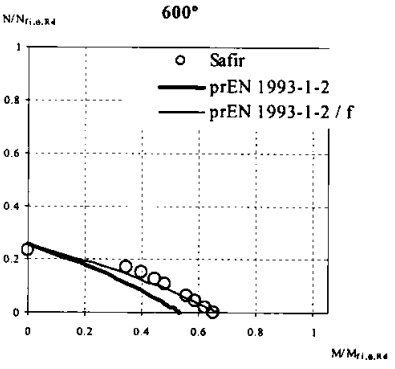

c) L=3000mm; $\bar{\lambda}_{LT,fi}$ *=0.84;* $\bar{\lambda}_{y,fi}$ *=0.43;* $\bar{\lambda}_{z,fi}$ *=1.59*

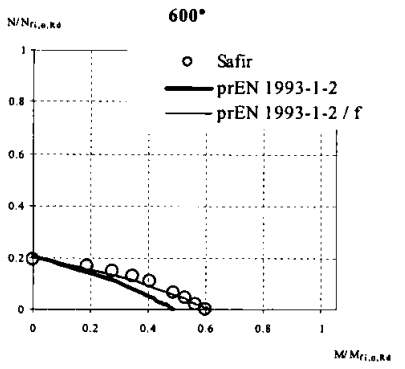

d) L=3500mm; $\bar{\lambda}_{LT,fi}$ *=0.93;* $\bar{\lambda}_{y,fi}$ *=0.50;* $\bar{\lambda}_{z,fi}$ *=1.85*

FIGURE 3 : Interaction diagrams of prEN 1993-1-2, for ψ = 0

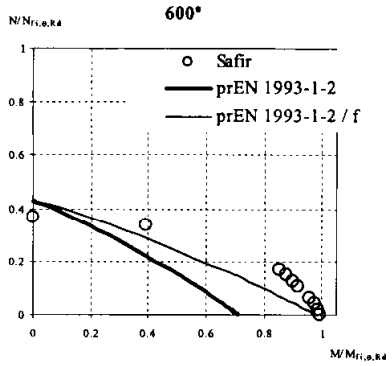

a) L=2000mm; $\bar{\lambda}_{LT,fi}$ *=0.51;* $\bar{\lambda}_{y,fi}$ *=0.29;* $\bar{\lambda}_{z,fi}$ *=1.06*

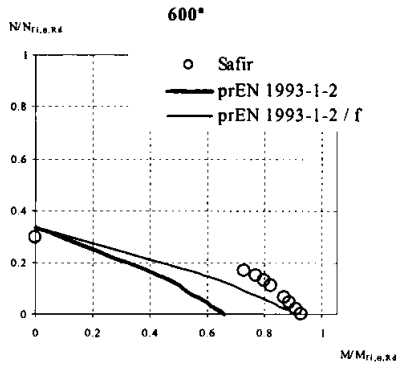

b) L=2500mm; $\bar{\lambda}_{LT,fi}$ *=0.61;* $\bar{\lambda}_{y,fi}$ *=0.36;* $\bar{\lambda}_{z,fi}$ *=1.32*

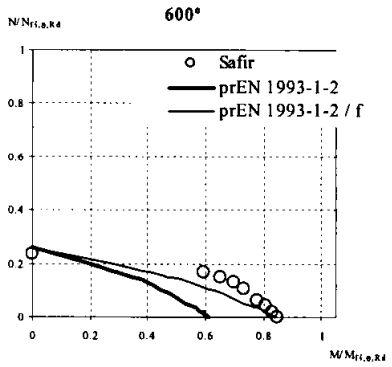

c) L=3000mm; $\bar{\lambda}_{LT,fi}$ *=0.69;* $\bar{\lambda}_{y,fi}$ *=0.43;* $\bar{\lambda}_{z,fi}$ *=1.59*

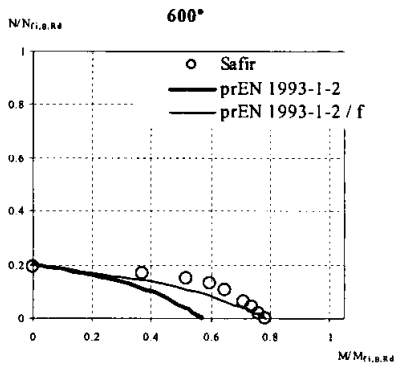

d) L=3500mm; $\bar{\lambda}_{LT,fi}$ *=0.77;* $\bar{\lambda}_{y,fi}$ *=0.50;* $\bar{\lambda}_{z,fi}$ *=1.85*

FIGURE 4 : Interaction diagrams of prEN 1993-1-2, for ψ = -1

Proposed Interaction Formulae based on prEN 1993-1-1 proposal

Vila Real et al [4] have proposed the following interaction formulae for beam-columns in case of fire:

$$\frac{N_{fi,Ed}}{\chi_{y,fi}\frac{N_{fi,Rk}}{\gamma_{M,fi}}} + k_{yy,fi}\frac{M_{y,fi,Ed}+\Delta M_{y,fi,Ed}}{\chi_{LT,fi}\frac{M_{y,fi,Rk}}{\gamma_{M,fi}}} \le 1 \qquad (12a)$$

$$\frac{N_{fi,Ed}}{\chi_{z,fi}\frac{N_{fi,Rk}}{\gamma_{M,fi}}} + k_{zy,fi}\frac{M_{y,fi,Ed}+\Delta M_{y,fi,Ed}}{\chi_{LT,fi}\frac{M_{y,fi,Rk}}{\gamma_{M,fi}}} \le 1 \qquad (12b),$$

These interaction formulae are based on the prEN 1993-1-1 provided that some factors are changed to take into consideration high temperatures. The changed factors are the yield stress, the Young modulus, and the reduction factors χ_{fi} for flexural buckling around the yy and zz axes, and $\chi_{LT,fi}$ for lateral-torsional buckling according to the proposals of prEN 1993-1-2.

The factors $k_{yy,fi}$ and $k_{zy,fi}$ are the interaction factors in case of fire that can be determined by two alternative methods ("EC3 Method 1, fi" and "EC3 Method 2, fi") described in Vila Real et al [4]. If the new proposal of Vila Real et al [5] for lateral-torsional buckling is used, two additional methods are obtained ("EC3 Method 1, fi / f" and "EC3 Method 2, fi / f") all illustrated in figures 6 to 9.

The procedure for the evaluation of the interaction factors for "EC3 Method 1, fi" is based on method 1 at room temperature, that is reported in Annex A of part 1-1 of EC3 [1] and was developed by a French-Belgian team [8] combining theoretical rules and numerical calibration to account for all the differences between the real model and the theoretical one. The specific formulae for the calculation of the interaction factors according to method 1 in case of fire are:

$$k_{yy,fi} = c_{my,fi}c_{mLT,fi}\frac{\mu_{y,\theta}}{1-\frac{N_{fi,Ed}}{N_{cr,y,fi}}}\cdot\frac{1}{c_{yy,fi}} \qquad (13)$$

$$k_{zy,fi} = c_{my,fi}c_{mLT,fi}\frac{\mu_{z,\theta}}{1-\frac{N_{fi,Ed}}{N_{cr,y,fi}}}\cdot\frac{1}{c_{zy,fi}}0.6\sqrt{\frac{w_y}{w_z}} \qquad (14),$$

where

$$c_{my,fi} = c_{my,fi,0} + \left(1-c_{my,fi,0}\right)\frac{\sqrt{\varepsilon_{y,fi}}\,a_{LT}}{1+\sqrt{\varepsilon_{y,fi}}\,a_{LT}} \qquad (15)$$

$$c_{mLT,fi} = c_{my,fi}^2 \frac{a_{LT}}{\sqrt{\left(1-\frac{N_{fi,Ed}}{N_{cr,z,fi}}\right)\left(1-\frac{N_{fi,Ed}}{N_{cr,T,fi}}\right)}} \tag{16}$$

$$\varepsilon_{y,fi} = \frac{M_{y,fi,Ed}}{N_{fi,Ed}} \cdot \frac{A}{W_{el,y}} \tag{17}$$

Duc to the non-linearity introduced by the factor ε_y the interaction curves were obtained using an iterative procedure. It was assumed that the moment of each studied beam-column could not exceed its design buckling resistance moment, $M_{b,Rd,fi}$. This justifies the vertical branch of some interaction curves of method 1.

"EC3 Method 2, fi" is related to method 2 at room temperature, which is described in Annex B of part 1-1 of EC3 [1] and results from an Austrian-German proposal [9] that attempted to simplify the verification of the stability of beam-columns, all interaction factors being obtained by means of numerical calibration. These factors are not clearly understandable from a physical point of view, but this simple formulation simplifies the verification procedure and reduces the possibility of mistakes.

The interaction factors according to method 2 in case of fire must be calculated from:

$$k_{yy,fi} = c_{my,fi}\left(1+\left(\bar{\lambda}_{y,\theta}-0.2\right)\frac{N_{fi,Ed}}{\chi_{y,fi}\frac{N_{fi,Rk}}{\gamma_{M,fi}}}\right) \le c_{my,fi}\left(1+0.8\frac{N_{fi,Ed}}{\chi_{y,fi}\frac{N_{fi,Rk}}{\gamma_{M,fi}}}\right) \tag{18}$$

$$k_{zy} = 1-\frac{0.1\bar{\lambda}_{z,\theta}}{c_{mLT}-0.25}\cdot\frac{N_{fi,Ed}}{\chi_{z,fi}\frac{N_{fi,Rk}}{\gamma_{M,fi}}} \ge 1-\frac{0.1}{c_{mLT}-0.25}\cdot\frac{N_{fi,Ed}}{\chi_{z,fi}\frac{N_{fi,Rk}}{\gamma_{M,fi}}}$$

$$\text{for } \bar{\lambda}_{z,\theta} < 0.4: \tag{19}$$

$$k_{zy} = 0.6+\bar{\lambda}_{z,\theta} \le 1-\frac{0.1\bar{\lambda}_{z,\theta}}{c_{mLT}-0.25}\cdot\frac{N_{fi,Ed}}{\chi_{z,fi}\frac{N_{fi,Rk}}{\gamma_{M,fi}}}$$

where

$$c_{mi,fi} = 0.6 + 0.4\psi_i \geq 0.4 \tag{20}$$

Figures 5 and 6 show the influence of considering or not the new proposal for LTB [5] with method 1 and method 2 adapted to elevated temperatures, for $\psi = 0$ and $\psi = -1$ respectively. It can be observed in those figures that the new proposal for LTB introduces a great improvement in the interaction diagrams for both methods.

Finally in figures 7 and 8, all the three methods studied here, considering the new proposal for the lateral-torsional buckling of beams [5] are plotted together, showing a very good agreement with the numerical results.

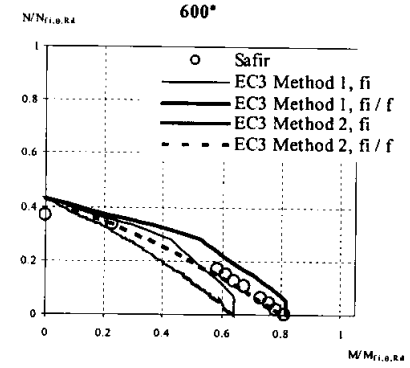

a) L=2000mm; $\bar{\lambda}_{LT,fi} = 0.62$; $\bar{\lambda}_{y,fi} = 0.29$; $\bar{\lambda}_{z,fi} = 1.06$

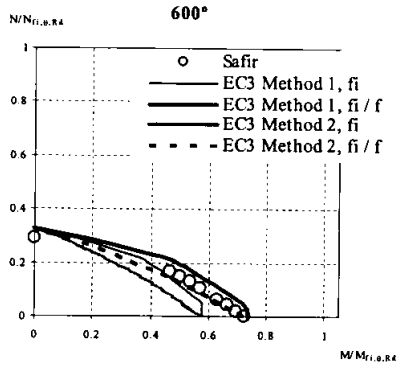

b) L=2500mm; $\bar{\lambda}_{LT,fi} = 0.73$; $\bar{\lambda}_{y,fi} = 0.36$; $\bar{\lambda}_{z,fi} = 1.32$

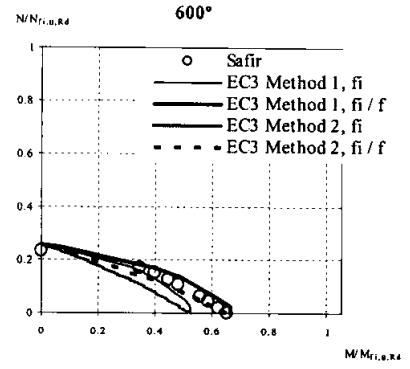

c) L=3000mm; $\bar{\lambda}_{LT,fi} = 0.84$; $\bar{\lambda}_{y,fi} = 0.43$; $\bar{\lambda}_{z,fi} = 1.59$

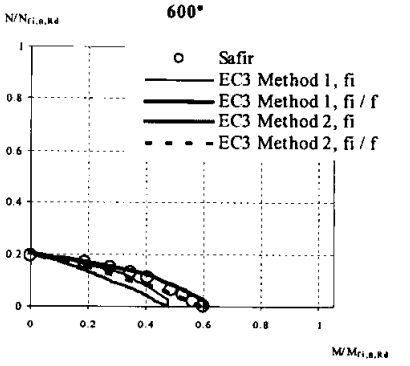

d) L=3500mm; $\bar{\lambda}_{LT,fi} = 0.93$; $\bar{\lambda}_{y,fi} = 0.50$; $\bar{\lambda}_{z,fi} = 1.85$

FIGURE 5 : Interaction diagrams of adapted prEN 1993-1-1 at 600 °C for ψ= 0

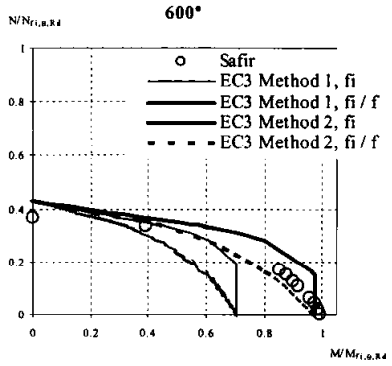

a) L=2000mm; $\bar{\lambda}_{LT,fi}$ *=0.51;* $\bar{\lambda}_{y,fi}$ *=0.29;* $\bar{\lambda}_{z,fi}$ *=1.06*

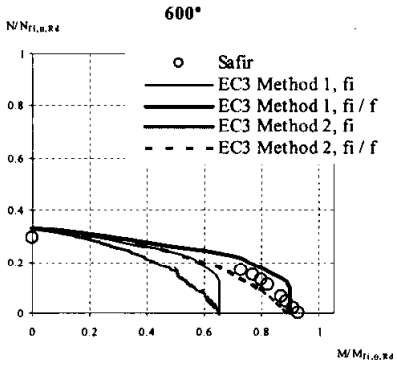

b) L=2500mm; $\bar{\lambda}_{LT,fi}$ *=0.61;* $\bar{\lambda}_{y,fi}$ *=0.36;* $\bar{\lambda}_{z,fi}$ *=1.32*

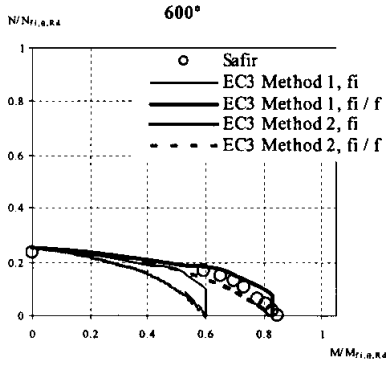

c) L=3000mm; $\bar{\lambda}_{LT,fi}$ *=0.69;* $\bar{\lambda}_{y,fi}$ *=0.43;* $\bar{\lambda}_{z,fi}$ *=1.59*

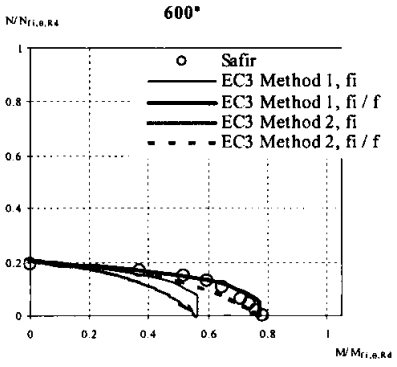

d) L=3500mm; $\bar{\lambda}_{LT,fi}$ *=0.77;* $\bar{\lambda}_{y,fi}$ *=0.50;* $\bar{\lambda}_{z,fi}$ *=1.85*

FIGURE 6 : Interaction diagrams of adapted prEN 1993-1-1 at 600 °C for ψ = -1

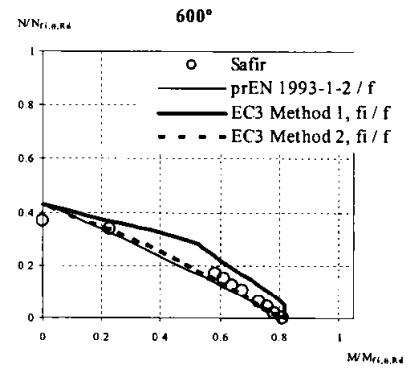

a) - L=2000mm; $\bar{\lambda}_{LT,fi}$ *=0.62;* $\bar{\lambda}_{y,fi}$ *=0.29;* $\bar{\lambda}_{z,fi}$ *=1.06*

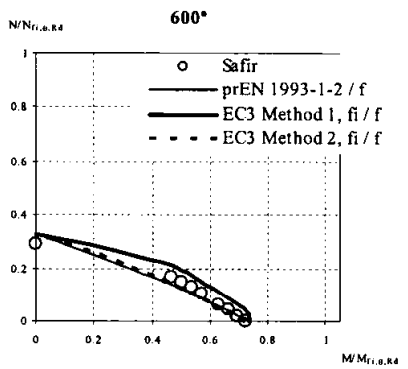

b) - L=2500mm; $\bar{\lambda}_{LT,fi}$ *=0.73;* $\bar{\lambda}_{y,fi}$ *=0.36;* $\bar{\lambda}_{z,fi}$ *=1.32*

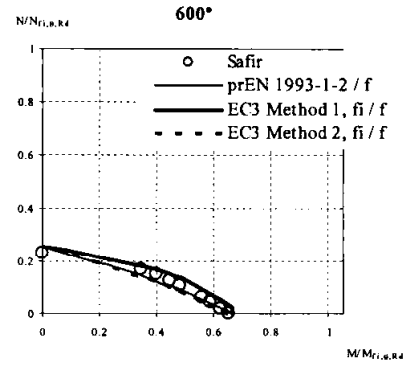

c) - L=3000mm; $\bar{\lambda}_{LT,fi}$ *=0.84;* $\bar{\lambda}_{y,fi}$ *=0.43;* $\bar{\lambda}_{z,fi}$ *=1.59*

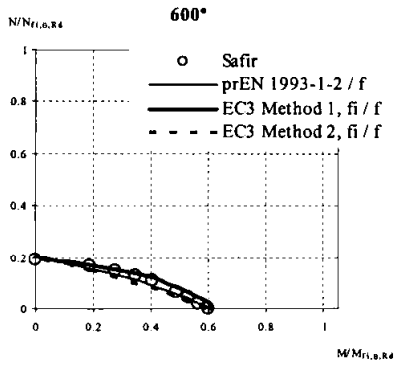

d) - L=3500mm; $\bar{\lambda}_{LT,fi}$ *=0.93;* $\bar{\lambda}_{y,fi}$ *=0.50;* $\bar{\lambda}_{z,fi}$ *=1.85*

FIGURE 7 : Interaction diagrams considering the new proposal for lateral-torsional buckling, for $\psi = 0$

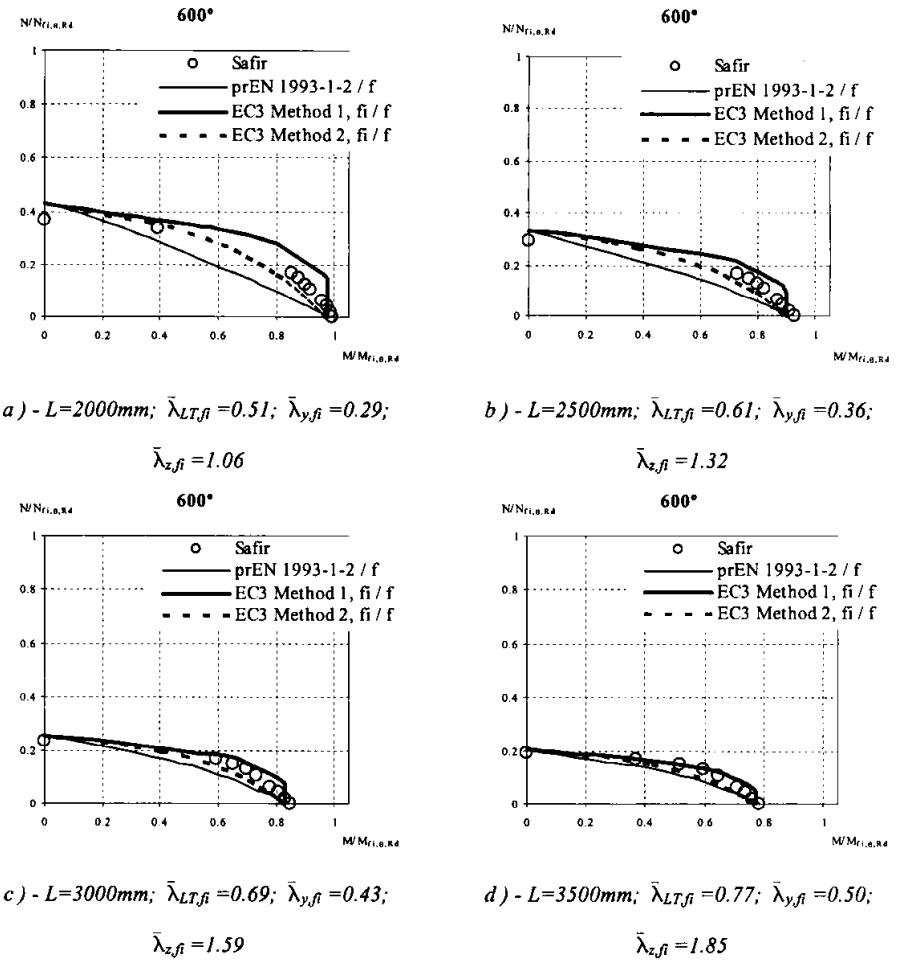

a) - L=2000mm; $\bar{\lambda}_{LT,fi}$ *=0.51;* $\bar{\lambda}_{y,fi}$ *=0.29;* $\bar{\lambda}_{z,fi}$ *=1.06*

b) - L=2500mm; $\bar{\lambda}_{LT,fi}$ *=0.61;* $\bar{\lambda}_{y,fi}$ *=0.36;* $\bar{\lambda}_{z,fi}$ *=1.32*

c) - L=3000mm; $\bar{\lambda}_{LT,fi}$ *=0.69;* $\bar{\lambda}_{y,fi}$ *=0.43;* $\bar{\lambda}_{z,fi}$ *=1.59*

d) - L=3500mm; $\bar{\lambda}_{LT,fi}$ *=0.77;* $\bar{\lambda}_{y,fi}$ *=0.50;* $\bar{\lambda}_{z,fi}$ *=1.85*

FIGURE 8 : Interaction diagrams considering the new proposal for lateral-torsional buckling, for ψ = -1

Critical temperature

The verification of the fire resistance of steel members can be made in the temperature domain, imposing that the temperature does not exceed the critical temperature during the relevant duration of fire exposure.

The critical temperature according to Eurocode 3 can be calculated with

$$\theta_{a,cr} = 39{,}19\,ln\left[\frac{1}{0{,}9674\mu_0^{3{,}833}} - 1\right] + 482 \tag{21}$$

where the degree of utilization μ_0, for members subjected to combined bending and axial compression according to the prEN 1993-1-2 is given by the following expression

$$\mu_0 = \frac{N_{fi,Ed}}{\chi_{z,fi} A \frac{f_y}{\gamma_{M,fi}}} + \frac{K_{LT} M_{y,fi,Ed}}{\chi_{LT,fi} W_{pl,y} \frac{f_y}{\gamma_{M,fi}}} \tag{22}$$

and for the proposal presented in this paper, for method 1 and method 2 given by

$$\mu_0 = \frac{N_{fi,Ed}}{\chi_{y,fi} \frac{Af_y}{\gamma_{M,fi}}} + k_{yy,fi} \frac{M_{y,fi,Ed}}{\chi_{LT,fi} \frac{W_{pl,y} f_y}{\gamma_{M,fi}}} \tag{23}$$

and

$$\mu_0 = \frac{N_{fi,Ed}}{\chi_{z,fi} \frac{Af_y}{\gamma_{M,fi}}} + k_{zy,fi} \frac{M_{y,fi,Ed}}{\chi_{LT,fi} \frac{W_{pl,y} f_y}{\gamma_{M,fi}}} \tag{24}$$

As for the buckling of axial compressed members and the lateral-torsional buckling of beams, an iterative procedure is necessary.

DESIGN EXAMPLE

Considering an isostatic unrestrained beam with an IPE 220, with 2 m of length, subjected to a bending diagram resultant of moments applied at the extremities with $\psi = -1$ and to an axial compression effort. Assuming that the beam is in steel of the grade S 235, that the moment in the extremities in fire situation, around the strong axis, is $M_{y,fi,d} = \pm 20\,\text{kN}\cdot\text{m}$ and that the axial compression is $N_{fi,d} = 100\,\text{kN}$, calculate the critical temperature in accordance with

a) The latter version of part 1-2 of Eurocode 3 (prEN 1993-1-2).

b) The latter version of part 1-2 of Eurocode 3 but introducing the factor f to determine the modified reduction factor, according to equation (7).

c) The adaptation of Method 1 at high temperatures with factor f to determine the modified reduction factor, according to equation (7).

d) The adaptation of Method 2 at high temperatures with factor f to determine the modified reduction factor, according to equation (7).

Resolution:

The following values will be needed for the resolution of the problem:

- Young's modulus $E = 210000\,\mathrm{N/mm^2}$
- Shear modulus $G = E/[2(1+\nu)]\,\mathrm{N/mm^2}$
- Poisson's ratio $\nu = 0{,}3$
- Length $\mathrm{L} = 2000\,\mathrm{mm}$
- Class of the cross-section class 1
- Area of the cross-section $A = 3337\,\mathrm{mm^2}$
- Plastic section modulus in y axis $W_{pl,y} = 285400\,\mathrm{mm^3}$
- Radius of gyration around yy $i_y = 91{,}1\,\mathrm{mm}$
- Radius of gyration around zz $i_z = 24{,}8\,\mathrm{mm}$
- Second moment of area around zz $I_z = 2049\times10^3\,\mathrm{mm^4}$
- Warping constant $I_w = 2{,}27\times10^{10}\,\mathrm{mm^6}$
- Torsion constant $I_t = 90700\,\mathrm{mm^4}$

a) The beam can undergo lateral-torsional buckling therefore the degree of utilization of the beam is calculated with the equation (22)

$$\mu_0 = \frac{N_{fi,Ed}}{\chi_{z,fi} A \dfrac{f_y}{\gamma_{M,fi}}} + \frac{K_{LT} M_{y,fi,Ed}}{\chi_{LT,fi} W_{pl,y} \dfrac{f_y}{\gamma_{M,fi}}}$$

The elastic critical moment for lateral-torsional buckling is

$$M_{cr} = C_1 \frac{\pi^2 E I_z}{L^2} \sqrt{\frac{I_w}{I_z} + \frac{L^2 G I_t}{\pi^2 E I_z}} \times 10^{-6} = 370\,\mathrm{kN\cdot m}$$

The non-dimensional slenderness takes the value

$$\bar{\lambda}_{LT} = \sqrt{W_{pl,y} f_y / M_{cr}} = 0{,}426$$

and at 20 °C

$$\bar{\lambda}_{LT,20^\circ} = \bar{\lambda}_{LT} \sqrt{k_{y,20^\circ} / k_{E,20^\circ}} = 0{,}426\sqrt{1{,}0/1{,}0} = 0{,}426$$

giving

$$\phi_{LT,20^\circ} = \frac{1}{2}\left(1 + 0{,}65 \cdot 0{,}426 + 0{,}426^2\right) = 0{,}729$$

and

$$\chi_{LT,fi} = \frac{1}{0{,}729 + \sqrt{0{,}729^2 - 0{,}426^2}} = 0{,}757$$

The slenderness at room temperature is

$$\lambda_z = \frac{l_{fi}}{i_z} = \frac{2000}{24{,}8} = 80{,}6$$

which gives

$$\overline{\lambda}_z = \frac{\lambda_z}{\lambda_1} = \frac{80{,}6}{93{,}9} = 0{,}859$$

at 20 °C

$$\overline{\lambda}_{z,20^\circ} = \overline{\lambda}_z \sqrt{k_{y,20^\circ} / k_{E,20^\circ}} = \overline{\lambda}_z = 0{,}859$$

and

$$\phi_{z,20^\circ} = \frac{1}{2}\left(1 + 0{,}65 \cdot 0{,}859 + 0{,}859^2\right) = 1{,}149$$

from the other hand

$$\mu_{LT} = 0{,}15\overline{\lambda}_{z,20^\circ}\beta_{M,LT} - 0{,}15 \le 0{,}9$$

where

$$\beta_{M,LT} = 2{,}5$$

giving

$$\mu_{LT} = 0{,}15 \cdot 0{,}859 \cdot 2{,}5 - 0{,}15 = 0{,}172$$

and

$$k_{LT} = 1 - \frac{\mu_{LT} N_{fi,Ed}}{\chi_{z,fi} A k_{y,\theta} \dfrac{f_y}{\gamma_{M,fi}}} \le 1$$

At 20 °C the reduction factor for the buckling $\chi_{z,fi}$ is

$$\chi_{z,fi} = \frac{1}{1{,}149 + \sqrt{1{,}149^2 - 0{,}859^2}} = 0{,}523$$

giving

$$k_{LT} = 1 - \frac{0{,}172 \cdot 100 \times 10^3}{0{,}523 \cdot 3337 \cdot 1{,}0 \cdot \dfrac{235}{1{,}0}} = 0{,}958$$

and the degree of utilization

$$\mu_0 = \frac{100\times10^3}{0{,}523\cdot3337\cdot235} + \frac{0{,}958\cdot20\times10^6}{0{,}757\cdot285{,}4\times10^3\cdot235} = 0{,}621$$

resulting in the following critical temperature

$$\theta_{a,cr} = 39{,}19\,ln\left(\frac{1}{0{,}9674\cdot0{,}621^{3{,}833}} - 1\right) + 482 = 548\ ^{\circ}C$$

With this critical temperature the calculation can all be repeated to obtain a new critical temperature. The iterative process must be repeated until convergence is reached, as shown in the following table:

θ [°C]	$\bar{\lambda}_{z,\theta} = \bar{\lambda}_z \cdot \sqrt{\frac{k_{y,\theta}}{k_{E,\theta}}}$	$\bar{\lambda}_{LT,\theta} = \bar{\lambda}_{LT} \cdot \sqrt{\frac{k_{y,\theta}}{k_{E,\theta}}}$	$\chi_{z,fi}$	$\chi_{LT,fi}$	k_{LT}	$\mu_0 = \frac{N_{fi,Ed}}{\chi_{z,fi} A f_y / \gamma_{M,fi}} + \frac{k_{LT} M_{y,fi,Ed}}{\chi_{LT,fi} W_{pl,y} f_y / \gamma_{M,fi}}$	$\theta_{a,cr}$ [°C]
20	0.859	0.426	0.523	0.757	0.958	0.621	548
548	1.006	0.498	0.453	0.717	0.898	0.655	539
539	1.000	0.495	0.456	0.719	0.905	0.655	539

After convergence the critical temperature is

$$\theta_{a,cr} = 539\ ^{\circ}C$$

b) Now the last version of part 1-2 of Eurocode 3 used in the previous question but with factor f considered in this paper in the equation (8) (prEN 1993-1-2 / f) will be used. The iterative process is summarized in the following table

θ [°C]	$\bar{\lambda}_{z,\theta} = \bar{\lambda}_z \cdot \sqrt{\frac{k_{y,\theta}}{k_{E,\theta}}}$	$\bar{\lambda}_{LT,\theta} = \bar{\lambda}_{LT} \cdot \sqrt{\frac{k_{y,\theta}}{k_{E,\theta}}}$	$\chi_{z,fi}$	$\chi_{LT,fi,mod} = \frac{\chi_{LT,fi}}{f}$	k_{LT}	$\mu_0 = \frac{N_{fi,Ed}}{\chi_{z,fi} A f_y / \gamma_{M,fi}} + \frac{k_{LT} M_{y,fi,Ed}}{\chi_{LT,fi} W_{pl,y} f_y / \gamma_{M,fi}}$	$\theta_{a,cr}$ [°C]
20	0.859	0.426	0.523	1.000	0.958	0.529	575
575	1.029	0.509	0.443	0.981	0.876	0.554	568
568	1.021	0.506	0.446	0.984	0.883	0.554	568

c) In this paragraph the adaptation of Method 1 at high temperatures with factor *f* to determine the modified reduction factor, according to equation (7), (EC3 Method 1, fi / f) will be used. The iterative process is summarized in the following table

θ [°C]	$\overline{\lambda}_{z,\theta}$	$\overline{\lambda}_{y,\theta}$	$\overline{\lambda}_{LT,\theta}$	$\chi_{z,\theta}$	$\chi_{y,\theta}$	$\chi_{LT,fi,mod}$	k_{yy},fi	k_{zy},fi	μ_0 = max [(23) e (24)]	$\theta_{a,cr}$ [°C]
20	0.859	0.234	0.426	0.523	0.863	1.000	0.632	0.327	0.341	644
644	1.080	0.294	0.535	0.421	0.829	0.962	0.873	0.400	0.427	610
610	1.062	0.289	0.526	0.428	0.832	0.968	0.790	0.380	0.415	614
614	1.064	0.289	0.527	0.427	0.832	0.968	0.798	0.382	0.416	614

d) In this paragraph the adaptation of Method 2 at high temperatures with factor *f* to determine the modified reduction factor, according to equation (7), (EC3 Method 2, fi / f) will be used. The iterative process is summarized in the following table

θ [°C]	$\overline{\lambda}_{z,\theta}$	$\overline{\lambda}_{y,\theta}$	$\overline{\lambda}_{LT,\theta}$	$\chi_{z,\theta}$	$\chi_{y,\theta}$	$\chi_{LT,fi,mod}$	k_{yy},fi	k_{zy},fi	μ_0 = max [(23) e (24)]	$\theta_{a,cr}$ [°C]
20	0.859	0.234	0.426	0.523	0.863	1.000	0.402	0.860	0.500	585
585	1.038	0.282	0.514	0.439	0.836	0.977	0.410	0.626	0.482	591
591	1.046	0.284	0.518	0.435	0.835	0.974	0.410	0.609	0.479	591

CONCLUSIONS

It has been shown that the proposed methods for the lateral-torsional buckling of unrestrained steel beams at high temperatures, introduce significant improvements in the design curves of beam-columns under fire conditions.

Although the new proposal based on the method 1, in some cases, is not in the safe side when compared with the numerical results all the proposals presented here are in general in very good agreement with these results. In addition, if method 1 and method 2 are adopted, this has the advantage of using the same formulae at room temperature and at elevated temperature, being in line with the procedure which used to be in usage in the Eurocodes. These aspects should be considered when the new proposal for the resistance of beam-columns has to be chosen in the next revision of the Eurocode 3.

A design example has been solved adopting methods presented in this paper, which conclude that methods 1 and 2 give higher critical temperatures.

The study presented in this paper strongly recommends the use of one of these proposals in future versions of part 1-2 of the Eurocode 3.

REFERENCES

[1] prEN 1993-1-1, *Eurocode 3: Design of Steel Structures – part 1-1: General rules and rules for buildings*, Stage 49, European Committee for Standardisation, Brussels, Belgium, 2003.

[2] prEN 1993-1-2, *Eurocode 3: Design of Steel Structures – part 1-2: General Rules - Structural fire design*, European Committee for Standardisation, Brussels, Belgium, February 2003.

[3] ENV 1993-1-1, *Eurocode 3: Design of Steel Structures – part 1-1: General rules and rules for buildings*, European Committee for Standardisation, Brussels, Belgium, 1992.

[4] Vila Real, P.M.M., Lopes, N., Simões da Silva, L., Piloto, P., Franssen, J.-M., *Towards a consistent safety format of steel beam-columns: application of the new interaction formulae for ambient temperature to elevated temperatures,* Steel & Composite Structures, an International Journal, Techno-Press vol. 3, n. 6, p.p. 383-401, 2003.

[5] Vila Real, P.M.M., Lopes, N., Simões da Silva, L., Franssen, J.-M., *Lateral-torsional buckling of unrestrained steel beams under fire conditions: improvement of EC3 proposal,* submitted to Computers & Structures, 2003.

[6] Franssen, J.-M., *"SAFIR. A Thermal/Structural Program Modeling Structures under Fire", Proc. NASCC conference, American Inst. for Steel Constr., Baltimore, April 2003.*

[7] ECCS – European Convention for Constructional Steelwork, *System, Ultimate Limit State Calculation of Sway Frames With Rigid Joints,* Technical Committee 8 – Structural Stability, Technical Working Group 8.2, first edition, 1984.

[8] Boissonnade, N.; Jaspart, J.-P.; Muzeau, J.-P. and Villette, M., *New Interaction Formulae for Beam-Columns in Eurocode 3: The French-Belgian Approach,* J. of Constructional Steel Research 60(3-5), 421-431, 2004.

[9] Greiner, R., *Background information on the beam-column interaction formulae at level 1, ECCS TC 8 Ad-hoc working group on beam-columns paper No.TC8-2001,* Technical University Graz, 19 September 2001.

A PRACTICAL APPROACH FOR PREDICTIING THE CAPACITY OF STEEL COLUMNS WITH RESTRAINS OF WALL PANELS IN FIRE

G. Q. Li, Y. Z. Wang, M. F. Li
College of Civil Engineering, Tongji Univ. CHINA
GQLi@mail.tongji.edu.cn

ABSTRACT

Steel buildings are usually enclosed by wall panels, which may be connected to the columns. The attachment of wall panels to steel columns may affect the behavior of steel columns in two aspects. Firstly, the temperature increasing of steel columns with and without wall panel attachment due to fire are different. The wall panels may slow down the velocity of temperature increasing of steel columns in fire, but cause the non-uniform distribution of temperatures over the cross-section of steel columns. Secondly, the restrains of wall panels may normally raise the capacity of steel columns, which in turn raise the capacity of steel columns in fire.

For predicting the capacity of the axially-compressed steel column with restrains of wall panels in fire, the commercial FEM program, ANSYS, is employed to conduct numerical investigations on the behavior of the steel columns subjected to fire. The effects of load ratios, the number of restrains of wall panels along the height of columns and the temperature distribution over the cross-section of columns on the critical temperatures of axially-compressed steel columns are analyzed and discussed. The torsional instability phenomena of the columns under some conditions in fire is found. Based on the numerical investigations, a practical approach for checking the fire-resistant capacity of steel columns with attachment of wall panels is presented.

KEYWORDS: *steel structure, wall panels, column, fire-resistance, finite element method*

INTRODUCTION

Wall panels are often connected to steel columns in steel buildings[1] (FIGURE1). At present, contribution of wall panels to load carrying capacity of steel columns is not normally considered in current codes for structural design. Obviously, Wall panels will provide restrain to steel columns in the plane of walls and thus the critical buckling load of a column in the wall plane is enhanced. Unfortunately, available codes give no information regarding how to consider this positive effect. In this paper, the commercial software package, ANSYS, is adopted to investigate this effect through conducting the nonlinear finite element analysis. Based on numerous parametric studies on the behavior of steel columns attached to wall panels in fire, a practical approach for predicting fire resistance of steel columns with restrains of wall panels is proposed in this paper.

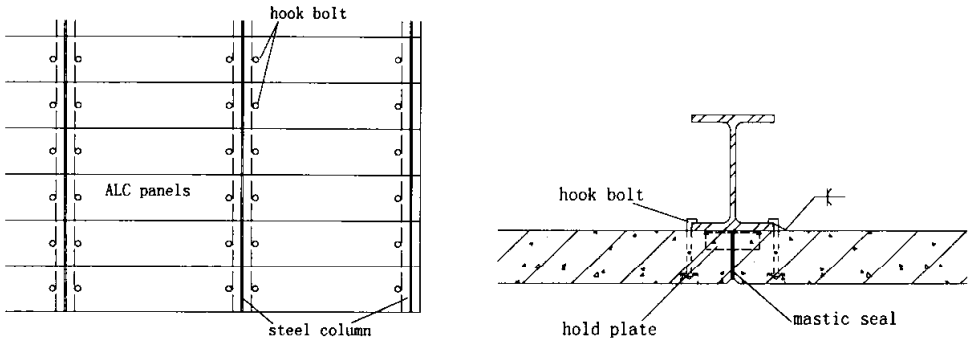

FIGURE 1 Connection of light-weight concrete wall panels and steel column

FINITE ELEMENT ANALYSIS

Finite element model

The wall panels connected to a steel column, as shown in FIGURE 1, will affect the fire resistance capacity of the steel column in two aspects. One is the temperature elevation and temperature distribution over the column section and the other is the critical load of the column. To study these two effects on the critical temperature of steel columns attached with wall panels, FEM is employed.

For the purpose of finite element analysis, the following assumptions are taken.

1) The material properties of wall panels in the direction of thickness are uniform and wall panels may be modeled by shell elements.
2) The stress and strain are uniform over the thickness of the steel column flanges and web. The steel column may be modeled by shell elements;

3) Panels are attached to the steel column by hinge connections located on one flange of the steel column.

4) The reduced yield stress and modulus of steel under high temperatures are governed by[1]:

$$\eta_T = \frac{f_{yT}}{f_y} = 1 + \frac{T_s}{767\ln(T_s/1750)} \quad 0 \le T_s \le 600°C \tag{1}$$

$$\chi_T = \frac{E_T}{E} = 1 - 17.2\times10^{-12}T_s^4 + 11.8\times10^{-9}T_s^3 - 34.5\times10^{-7}T_s^2 + 15.9\times10^{-5}T_s \quad 0 \le T_s \le 600°C \tag{2}$$

where η_T is the reduced coefficient of the yield stress of steel at elevated temperatures;

χ_T is the reduced coefficient of the elastic modulus of steel at elevated temperatures;

T_s is the temperature of steel members (℃);

f_y is the yield stress of steel at ambient temperature (MPa);

f_{yT} is the yield stress at temperature T_s (MPa);

E is the steel modulus at ambient temperature (MPa);

E_T is the steel modulus at temperature T_s (MPa).

5) The values of the strength reduced coefficient, the peak strain and the critical strain listed in Table 1[3] are used for the walls made of Autoclaved Light-weight Concrete (ALC).

With the assumptions, the finite element analysis package ANSYS is employed. The 4-node nonlinear shell element 43 in the library of ANSYS is used (FIGURE2). The modeling for finite element analysis of steel columns with restrains of wall panels is shown in FIGURE 3.

Temperature (℃)	Strength reduced coefficient of ALC	Peak strain ϵ_{pT} ($\times10^{-3}$)	Critical strain ϵ_{uT} ($\times10^{-3}$)
20	1	2.5	20.0
100	1	3.5	22.5
200	1	4.5	25.0
400	0.88	7.5	30.0
600	0.64	12.5	35.0
800	0.40	14.5	40.0
1000	0.16	15.0	45.0
1200	0	15.0	50.0

Table 1 : strength reduced coefficient of Autoclaved Lightweight Concrete

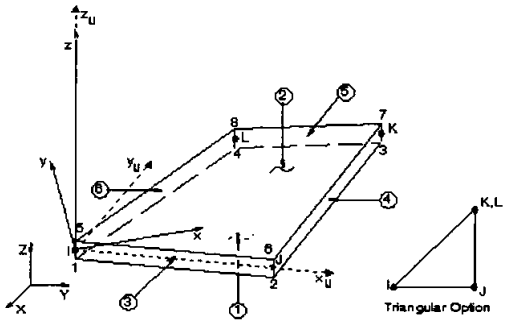

FIGUE 2 SHELL 43 element

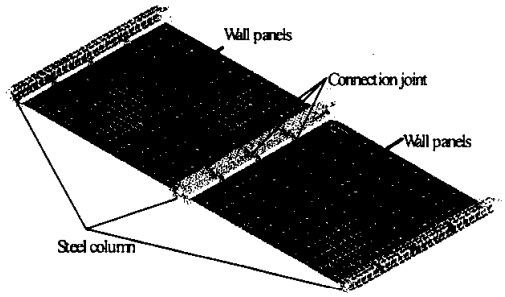

FIGUE 3 Finite element model

Validation

Eva Hedman-Petursson from Sweden conducted tests on the H-type steel column attached with panels[4], which is used to validate the finite element analysis used in this study. The sizes of the column section HEA120 and IPE200, made of S235 steel, used for the tests are shown in FIGURE 5. The critical loads obtained from tests and from FE analysis are compared in Table 2. It can been seen that the results from FE analysis agree with the results of tests quite well.

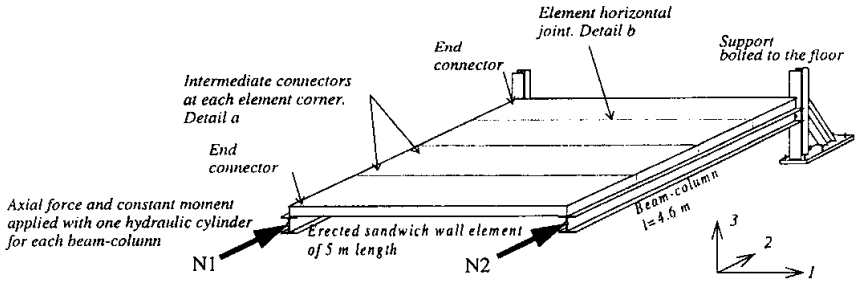

FIGUE 4 Testing model of Eva Hedman-Petursson in Sweden

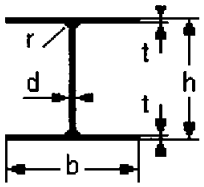

HEA120 h=114, b=120, d=5, t=8, r=12

IPE 200 h=200, b=100, d=5.6, t=8.5, r=12

FIGUE 5 **Cross-section of the steel column for the tests**

Result of Eva Hedman-petursson testing				Result from FE analysis	
column section	eccentricity	critical load	buckling mode	critical load	buckling mode
test 1 HEA 120	0	413.0kN	flexure buckling	426kN	flexure buckling
test 2 HEA 120	0.05m	223.6kN	flexure buckling	245kN	flexure buckling
test3 IPE 200	0	414.7kN	tosional buckling	430kN	tosional buckling
test4 IPE 200	0.25m	199.2kN	flexure buckling	182kN	flexure buckling

Table 2 comparison of the results from FE analysis and from tests

BUCKLING PATTERNS OF STEEL COLUMN WITH WALL PANELS IN FIRE

The material and geometrical nonlinearities are considered for studying the limit states of steel columns with wall panels in fire through FEM. The following two steps are taken in the FE analysis.

1) Axially-compressed load is applied firstly to the steel column with a definite load ratio, which is defined as the ratio of the applied load and the critical load of the column in ambient temperature.
2) Then, the steel column with wall panels is subjected to temperature elevation due to fire till buckling of the column.

For numerical studies, an example of steel columns with wall panels is taken. The cross-section of the steel columns is H200×150×10×14. The height of the columns is 3000mm and spacing of them is 4000mm. The thickness of the wall panels attached to the steel columns is 100mm. Two cases of load ratios, 0.8 and 0.3, are selected. The critical temperature, at which the column buckles, and the buckling mode of the column, obtained through FE analysis, varying with the number of connections to wall panels are listed in Table 3 and Table 4 for load ratio 0.8 and 0.3 respectively.

It can be found from Table 3 and Table 4 that with the increase of the number of connections of wall panels to columns, the effective length of the column in weak flexural direction decreases and the buckling mode of the column changes from flexural buckling in weak flexural direction to that in strong flexural direction. And torsional buckling of the column may also happen between the weak flexural buckling and strong flexural buckling.

number of connections (including that at top and bottom of the column)	critical average temperature in column (℃)	buckling mode
2	326	weak flexure
3	400	strong flexure
4	401	strong flexure
5	400	strong flexure
6	400	strong flexure
7	400	strong flexure
9	401	strong flexure
11	401	strong flexure

Table 3 FEM results under the load ratio $R = P / P_u = 0.8$

number of connections (including that at top and bottom of the column)	critical average temperature in column (□)	Buckling mode
2	600	weak flexure
3	628	weak flexure
4	645	tosion
5	659	tosion
6	667	strong flexure
7	667	strong direction flexure
9	667	strong flexure
11	667	strong flexure

Table 4 FEM results under load ratio $R = P / P_u = 0.3$

SIMIPLIFIED APPROACH

Based on the regression fit with FEM results of parametric studies, a simplified approach for assessing fire-resistant capacities of axially-compressed steel columns with wall panels is proposed as follows.

The distance between the two neighbouring connections to walls can be adopted as the effective length of the steel column with wall panels in weak flexural direction, denoted as l_{0x}, and the

effective length of the steel column in strong flexural direction, denoted as l_{0y}, can simply use the height of the column. Then the slendness ratios of the column in weak and strong flexural direction can be calculated by $\lambda_x = \frac{l_{ox}}{i_x}$, and $\lambda_y = \frac{l_{0y}}{i_y}$ respectively. The larger one of λ_x and λ_y can be adopted to calculate the fire resistance capacity of the column with wall panels with the equations as

$$\frac{N}{\varphi_T' A} \leq \eta_T \gamma_R f \tag{3}$$

where N—axially-compressed load on the steel columns in fire;

A—gross area of the column section;

η_T—reduced coefficient of steel yield strength at elevated temperatures;

γ_R—steel strength coefficient, $\gamma_R = 1.1$, and the yield strength of steel is $f_{yT} = \gamma_R f$;

f—design value of strength of steel;

φ_T'—stability coefficient of axially-compressed column considering effect of non-uniform temperature distribution; determined by

$$\varphi_T' = \beta \cdot \varphi_T \tag{4}$$

φ_T — stability coefficient of axially-compressed column at elevated temperatures, determined by

$$\varphi_T = \alpha \cdot \varphi \tag{5}$$

φ —stability coefficient of axially-compressed column at ambient temperature,

α—coefficient, listed in Table 5.

Temp (℃) / Slenderness ratio	200	300	400	500	550	570	580	600
≤50	1.00	1.00	1.00	1.00	1.00	1.00	1.00	0.96
100	1.04	1.08	1.12	1.12	1.05	1.00	0.97	0.85
150	1.08	1.14	1.21	1.21	1.11	1.00	0.94	0.74
≥200	1.10	1.17	1.25	1.25	1.13	1.00	0.93	0.68

Table 5 Coefficient α

β —coefficient calculated by

for buckling in weak flexural direction:

$$\beta_x = \begin{cases} 1-(0.267-0.267R)\cdot G & 1 \geq R \geq 0.4 \\ 1-(1.6R-0.48)\cdot G & 0.4 > R > 0.3 \\ 1.0 & 0.3 \geq R \end{cases} \tag{6}$$

for buckling in strong flexural direction:

$$\beta_y = \begin{cases} 1-(0.4-0.4R)\cdot G & 1 \geq R \geq 0.4 \\ 1-0.6\cdot R\cdot G & 0.4 > R \geq 0 \end{cases} \tag{7}$$

G—temperature gradation over the cross-section of the column (□/mm);

R—load ratio, defined as the ratio of applied load with the critical buckling load of the column at ambient temperature.

As pointed out previously, the torsional buckling may happen upon the steel columns with attachment of wall panels in fire. This buckling mode must be considered in fire-resistant design of such steel columns.

To assess the load-bearing capacity of the steel column with wall panels in torsional buckling in fire, firstly, determine the equivalent effective length of the column by[5]

$$l_{0f} = l\sqrt{\frac{1}{1+\frac{l^4 t_w^3}{4\pi^4 I_f h_w^3}}} \tag{8}$$

and determine slenderness ratio by:

$$\lambda_f = \frac{l_{0f}}{\sqrt{I_f / A_f}} \tag{9}$$

then the fire resistance capacity of the steel column with wall panels in the mode of torsional buckling can be checked by:

$$\frac{N}{\varphi_T \cdot A} \leq f_{yT} \tag{10}$$

where l_{0f} —effective length of the column for torsional buckling;

l —height of column;

t_w —thickness of web;

h_w —height of steel column web;

I_f —inertia of column flange;

N —axially-compressed load;

φ_T —stability coefficient at elevated temperatures, determined by Eq.(5) with λ_f ;

A_f —Area of bottom flange;

In summary, the fire resistance capacity of axially-compressed steel column with wall panels should be checked with considering the following two types of buckling modes:1) flexural mode in either weak or strong flexural direction; 2) torsional mode.

APPLICATION OF THE SIMPLIFIED METHOD

A simple example is used to show the application of the proposed method. The cross-section of the column, made of Q235 steel, is H200×150×10×14. The height of column is 3000 mm. The column is subjected to 656.4kN axially-compression and connected to ALC wall panels with thickness of 100mm. The distance of two neighbour connections of the column to walls is 500mm. Assuming the gradation of temperature over the cross-section of the column is G=0.373℃/mm^2, determine the critical average temperature of the column.

Solution:

Since l_{0x} =500mm, l_{0y} =3000mm and $l_{0f} = l\sqrt{\dfrac{1}{1+\dfrac{l^4 t_w^3}{4\pi^4 I_f h_w^3}}}$ =1089mm

so $\lambda_x = \dfrac{l_{ox}}{i_x}$ =13.9, $\lambda_y = \dfrac{l_{oy}}{i_y}$ =33.9, $\lambda_f = \dfrac{l_{of}}{i_f}$ =25.2

We can find out the value of λ_y is the largest, and we may presume the column will buckle in the strong flexural direction in fire. The stability coefficient of the column under ambient temperature is 0.956, and from Table 5 we have α =1. So, $\varphi_T = \alpha \cdot \varphi = 0.956$ and:

$$\beta_y = 1 - 0.4(1-R)\cdot G = 1 - 0.4(1 - \frac{656.4}{0.956 \cdot 1420}) \cdot 0.373 = 0.920,$$

hence:

$$\eta_T = \frac{N}{\varphi_T' \cdot Af_y} = \frac{N}{\beta_y \cdot \varphi_T \cdot Af_y} = \frac{656.4}{0.92 \cdot 0.956 \cdot 1420} = 0.524$$

from Eq.(1), we obtain: $T_s = 476$ □.

The critical temperature of the column obtained by FEM is $T_s = 484$ □. It can be seen that the results from FEM analysis and the simplified approach are quite close to each other.

If the temperature distribution over the cross-section of the column is assumed to be uniform, the yield stress reduction factor of the column when fails in fire can be calculated by

$\eta_T = \frac{N}{\varphi_T \cdot Af_y} = \frac{656400}{0.956 \cdot 5920 \cdot 235} = 0.48$, Then the critical temperature of the column, obtained with Eq.(1) is: $T_s = 499$ □, which is higher than the critical temperature if considering temperature gradation effect. So it is unsafe to ignore the temperature non-uniform distribution over the column cross-section.

If the restrain from wall panels is not considered, the buckling in weak flexure direction is the most dangerous case for the column in fire and the critical temperature of the column can be obtained to be $T_s = 444$ □, which is greatly lower than the real critical buckling temperature if considering restrain of effect of wall panels. So the results ignoring the restrain effect of wall panels on fire-resistance of steel columns is conservative.

CONCLUSIONS

Two meaningful findings are obtained through this study:

(1) The fire-resistance of steel columns may be under-estimated if the bracing from wall panels ignored;

(2) The fire-resistance of steel columns may be over-estimated if the non-uniform temperature distribution over the column cross-section, due to attachment of wall panels, is ignored. Though the non-uniform temperature distribution is harmful to fire resistance of steel columns, the restrain from wall panels can enhance the fire resistance of steel columns. The combined effect of temperature gradation and bracing of wall panels may fall in the positive side of increasing the fire resistance capacity of steel columns. So the less protective insulation of steel columns with attachment of wall panels is possible.

(3) Based on FEM evaluation, a practical approach for predicting the capacity of axially-compressed steel columns with restrains of wall panels is proposed.

REFERENCES

[1] Jiangsu Provincial Standard, *Detailing of ALC wall panel connections*,2002.

[2] ECCS (European Convention for Constructional Steelwork) , *European Recommendations for the Fire Safety of Steel Structures*, 1983

[3] CEN Design of Concrete Structures. Eurocode 2 Part 10: *Structure Fire Design*, April 1990.

[4] Eva Hedman-Petursson, *Column Buckling with Restrain from Sandwich Wall Panels*,9th Nordic Construction Conference.Helsinki, Finland, 18-20.

[5] G.Q.Li. H.D.Zhang. *Limit state calculation of steel frame girders with laterally restrained upper flanges subjected to local fire, Journal of Building Structures*,1997.18(4),23-29.(in chinese)

ANALYSES OF RESTRAINED STEEL BEAM SUBJECT TO RISING TEMPERATURE AND COOLING

S. X. Guo, G. Q. Li
Dept. of Civil Engineering, Tongji University
1239 Siping Road, Shanghai 200092 P. R. China

ABSTRACT

In this paper, the behaviour of restrained steel beam is investigated in temperature rising state and cooling state by finite-elements method. The effects of rigidity of axial restraint, load ratio on the beam are taken into account, and the influences of rotational restraint are investigated too. Based on the finite-elements results, a simplified method to analyze the behaviour of restrained steel beam subject to rising temperature and cooling is brought forward. By this method, the deflection, internal force and the limit state of the beam in temperature rising state and cooling state can be calculated out by hand accurately and easily.

PRECAST HOLLOW CORE SLABS IN FIRE : NUMERICAL SIMULATIONS AND EXPERIMENTAL TESTS

Jean-Claude DOTREPPE, Jean-Marc FRANSSEN
Univ. of Liege, 1, Chemin des Chevreuils, 4000, Liège 1, Belgium
Jc.dotreppe@ulg.ac.be

ABSTRACT

The design of precast prestressed hollow core slabs under normal conditions is based essentially on ultimate limit state of bending, but serviceability limit states have sometimes to be considered. Under fire conditions the design according to Eurocode 2-1.2 is also built upon ultimate limit state of bending of single structural elements, but tests have shown that premature failure due to shear near the supports can be observed. In order to examine the influence of the detailing measures usually adopted in practice with this type of element, a research study has been performed in Belgium about their shear resistance under fire conditions. Numerical simulations have been made using the computer code SAFIR developed at the University of Liège. Temperature distributions have been calculated and mechanical calculations have been performed. Various characteristics have been examined, for which several degrees of restraint have been considered. Considering practical design in buildings and the results of the numerical simulations, four fire tests have been realised. It has been clearly proved that units behave quite well in bending and in shear during standard ISO fire tests.

KEYWORDS : *slabs, precast construction, prestressed concrete, fire resistance, shear failure*

INTRODUCTION

Prestressed hollow core units are presently the most widely used type of precast floors. This success is largely due to the simple and highly efficient design and production methods, flexibility in use and structural efficiency. This type of element has no other reinforcement than the longitudinal prestressing wires or strands anchored by bond.

Under normal conditions the design is based essentially on ultimate limit state (ULS) of bending, but serviceability limit states (SLS) have sometimes to be considered. If adequate design and detailing is provided [1] research and practical experience have shown that everything is under control.

Under fire conditions, the design is also built upon ULS of bending of single structural elements. This type of approach can be found in Belgian national recommendations [2], in international recommendations [3] as well as in Eurocode 2-1.2 [4]. It is therefore recommended to provide a sufficient concrete cover in order to delay the occurrence of plastic strains in the tendons.

For shear design, there are no calculation methods available, except some rudimentary design principles. It is thus implicitly accepted that, when the shear capacity is satisfactory at normal temperature, this will also be the case under fire conditions. However tests have shown that premature failure due to shear near the supports can be observed. Despite this, little fundamental research has been carried out on the shear resistance of prestressed hollow core floors exposed to fire. Several phenomenons can explain these shear failures. At high temperatures unfavourable effects occur, such as thermal stresses leading to internal cracks, and sliding of strands bringing the anchorage zone towards the inside of the span. Fire test conditions are also determinant. They are usually realised on simply supported elements, while in practice connections exist between the various elements. The mutual interaction of the hollow core units through correctly design connections, which constitutes the basis for the stability of the floor at ambient temperature [1], plays an essential role under fire conditions.

In order to examine the influence of the detailing measures usually adopted in practice with this type of element, a research study has been performed in Belgium about their shear resistance under fire conditions. Numerical simulations have been made using the computer code SAFIR developed at the University of Liège. Thermal and mechanical calculations have been performed, and the influence of restraint on the structural behaviour has been examined. Four fire tests have also been realised with a test device conceived in such a way that detailing and restraint conditions encountered in real situations could be simulated.

This paper presents the results of this research study, with a special attention paid to the analysis of the numerical simulations.

STRUCTURAL BEHAVIOUR

Under normal conditions

The ULS of bending is generally governing, which means that failure is due to yielding of the tendons.

With the use of floors with large thicknesses and large spans, the SLS of deflection becomes sometimes prevailing. Other ULS like bursting in the transmission zone and shear are almost never decisive.

In particular shear failures can be avoided if a certain number of detailing measures are provided, which is very often the case in practice. These measures as well as the effect of restraint conditions will be presented and discussed hereafter.

Under fire conditions

The failure mode of concrete beams and slabs under fire conditions considered in various codes and recommendations [2] [3] [4] is bending. Other failure modes are not supposed to occur provided that some rudimentary design principles are encountered.

However tests have shown that shear failures are sometimes observed. In this case the critical zone is near the supports where shear is maximum. As already mentioned this type of failure does not occur under normal conditions, but the probability of exceeding the shear capacity under fire conditions is more important.

At elevated temperatures a thermal gradient appears over the cross-section due to the low thermal conductivity of concrete. As a consequence deformations occur in the slab consisting in a uniform elongation and an important curvature. However as the temperature distribution is highly non linear, self-equilibrated thermal stresses appear, and it can be shown that compression develops in the top and bottom parts of the cross-section, and tension in the central part.

These thermal stresses can be evaluated from an elastic calculation for a slab with plain cross-section and as far as no cracking occurs. For hollow core slabs these two conditions are not met. Therefore calculations become more complex and it is necessary to use general calculation methods, i.e. more advanced models such as the computer code SAFIR already mentioned.

The consequence of this phenomenon for an isolated slab on simple supports is the occurrence of quasi vertical cracks in the central part of the cross-section. The cracks appear due to the fact that there exists very little or no prestressing in the anchorage zone near the supports, and that slipping of the strands is often observed, which may shift the transmission length to the inside of the element. This cracking phenomenon decreases the shear capacity.

DESIGN PROVISIONS

Hollow core units are produced as individual elements and might be envisaged as simply supported on beams, walls or other types of transverse elements. In practical design construction, however, connections are provided between the floor units and with the other structural elements, in order to ensure mutual interaction and coherence [1]. This constitutes the basis for the stability of the floor at ambient temperature.

These connections also play a role under fire conditions, particularly on the shear capacity. The main effect due to the elevation of temperature is the development of restraint forces. Due to the thermal dilatation of the concrete, the units are not only deflecting because of the temperature difference between the top and bottom fibres, but they also undergo a longitudinal and transversal expansion. However, the latter is more or less hindered by the surrounding structure, hence mobilising additional compressive forces in the cross-section of the floor units. This can be seen as a kind of prestressing. The compressive forces mobilised by the blocking effect will decrease or even annihilate the tensile stresses in the central zone of the cross-section, and hence preserve the shear capacity of the units.

The classical design provisions and their effect under fire conditions are described hereafter.

- Reinforcing bars in cast open cores (Fig.1).

The reinforcing bars are first designed to connect the floor units with the supporting construction. The reinforcing bars should be placed in the central part of the cross-section, where the thermal stresses appear. They prevent the cracks from opening.

- Reinforcing bars in the longitudinal joints (Fig.2).

This is a variant solution of the preceding one. To transfer forces in an effective way, provisions must be taken to ensure a good anchorage of the bars in the joints. The anchorage capacity of steel bars in cracked longitudinal joints between hollow core units has been extensively studied at the Technical University of Göteborg [5].

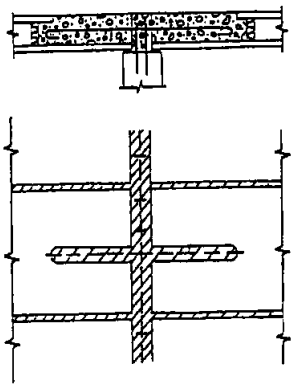

Fig. 1 : Connecting bars in open cores

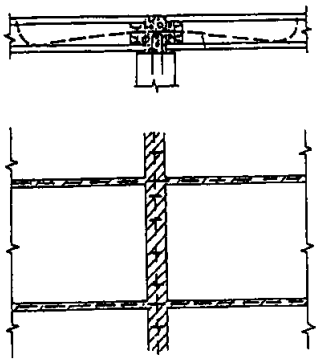

Fig. 2 : Connecting bars in longitudinal joints

- Peripheral ties (Fig.3).

Peripheral ties are playing an essential role with respect to the diaphragm action of the floor and the transversal distribution of concentrated loading. The peripheral ties are also contributing in a positive way to the preservation of the shear capacity of the units when exposed to fire. Indeed, the peripheral beam hinders directly and indirectly the expansion of the floor through the stiffness of the tie beam itself together with the supporting construction, but also through the coherence between neighbouring floor units.

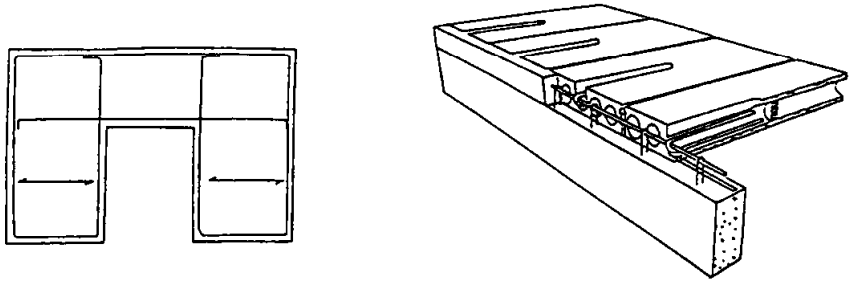

FIGURE 3 : Peripheral tie beams ensuring diaphragm action

- Restraint due to the surrounding floors and to the supporting construction.

When fire occurs in the central part of a large floor (Fig.4), the thermal expansion of the units will be highly restrained by the stiffness of the surrounding floor. This blocking effect will mobilise important compressive forces applied on the fire exposed floor units. In this case, the cracking of the central part of the cross-section will certainly not be important. The shear capacity will therefore be almost unaffected by the fire.

When fire occurs at the edge of a floor, the thermal expansion will be much less hindered. However, a certain blocking effect will also be generated through the stiffness of the supporting construction and the horizontal diaphragm action of the floor. Of course, the supporting columns should be able to take up the horizontal force, which seems quite realistic in most situations.

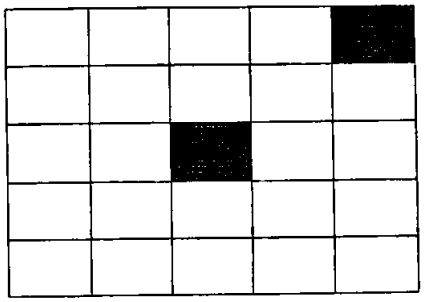

FIGURE 4 : Influence of the localisation of fire on restraint

- Reinforced topping

Constructive toppings may be used to enhance the stiffness of the floor, but also to improve the distribution of heavy concentrated loading, or to realise the horizontal diaphragm action of the floor in case of dynamic loading or large horizontal actions, like for instance in the case of earthquake. Toppings are also increasing the fire resistance of a floor, directly through the larger massivity and stiffness of the cross-section, indirectly through the impact on the coherence of the floor units. In the same way as for peripheral tie beams, the cold topping ensures that the expansion of the fire exposed units is blocked, hence enabling the functioning of the interlocking effect. However, toppings require an additional work at the building site, and constitute in this way a hindering in the context of industrialisation of the building process, aimed at by prefabrication. Despite their positive contribution to the fire resistance of floors, the foregoing shows that toppings are not absolutely needed, and that there are enough other provisions to ensure the fire resistance of precast floors.

NUMERICAL SIMULATIONS

Numerical simulations have been realised with the computer code SAFIR developed at the University of Liège to examine the behaviour of structures under fire conditions.

SAFIR is based on the finite element method with subdivision of the cross section in a mesh. It calculates the thermal gradient on the cross section of the slabs submitted to any type of fire under their bottom face, in particular here to the ISO standard temperature-time curve. This thermal calculation takes into account not only the heat transmission by conduction in the concrete itself, but also the heat transmission by radiation in the hollow cores. The evaporation of free water contained in concrete is also treated. The evolution of temperature in any point of the cross section can be evaluated.

After performing these thermal calculations, mechanical calculations can then be made taking into account the thermal elongations and the decrease of the mechanical characteristics due to the temperature variation at the centre of each mesh. As a consequence mechanical characteristics such as deflections, strains, stresses can be calculated. The materials models used in SAFIR are those proposed in Eurocode 2-1.2 [4].

The numerical simulations have been used mainly in order to prepare the experimental fire tests and to examine the importance of some effects, like for example the presence of cavities on the temperature distribution, the transverse cracking on the cross section due to thermal stresses, the influence of restraint on the deflections and on cracking. Bernoulli beam finite elements have been used for the mechanical analyses, which means that only longitudinal stresses and strains are considered.

Figure 5 presents the temperature distribution on the cross section of a SP265 floor (thickness = 265 mm) after 2 hours of ISO standard fire. In order to facilitate the discussion Fig.6 gives the temperature increase at four points of the same cross-section between 0 and 240 minutes.

SP265 floors are characterized by cavities with a large area with respect to the total area of the cross-section of the slab. As air is more insulating than concrete, one can expect that the temperature increase in concrete will be more rapid than the one occurring in a plain slab.

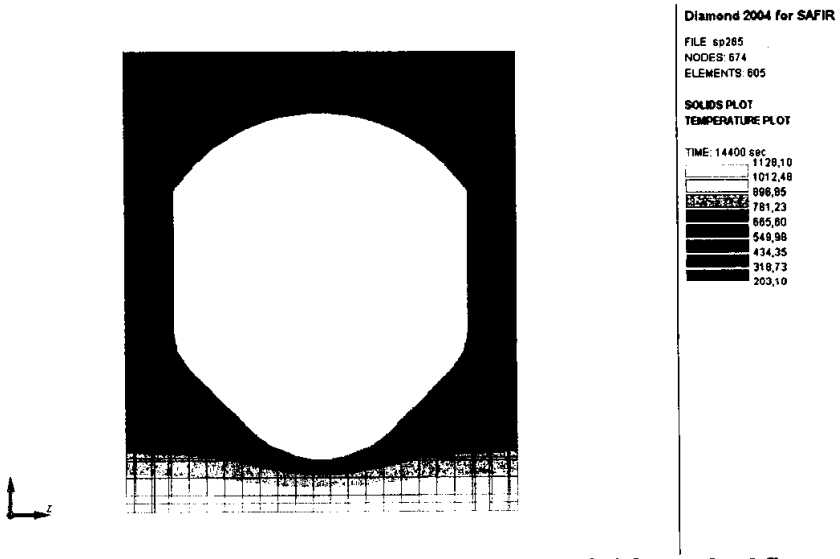

FIGURE 5 : Temperature distribution after 2 hours of ISO standard fire

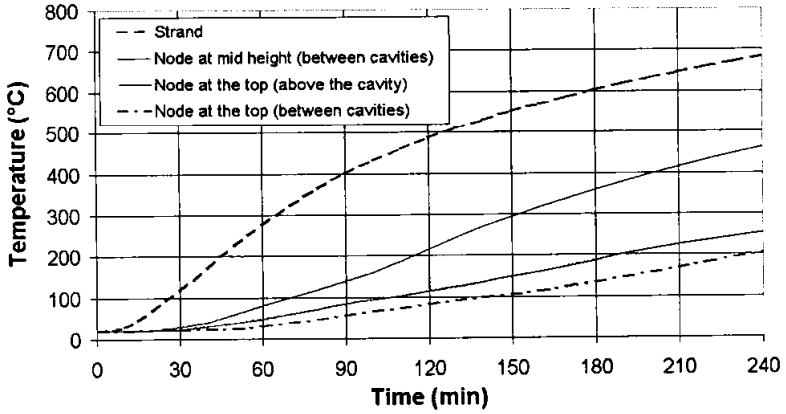

FIGURE 6 : Temperature increase at various points of the section

The presence of the cavity influences the isothermal curves as can be seen in Figure 5 ; in a plain slab they would be horizontal. This can also be observed by looking at curves 3 and 4 of Fig. 6 giving the temperature evolution at the top of the slab : the difference is equal to approximately 20°C after 60 minutes and 50°C after 240 minutes.

The most important characteristic with respect to fire endurance is the temperature increase in the tendons. In this particular case they are situated at 49 mm from the bottom of the slab. The corresponding curve of Fig. 6 has to be compared with the ones given in Eurocode 2-1.2 for plain slabs, which are not reproduced here. The difference is very small for t = 30 minutes, but reaches 70°C for t = 120 minutes. It is commonly accepted that for floors with small cavities, it can be assumed that the temperature increase in the tendons is approximately the same as for a

plain slab. In this particular case with large cavities the assumption is too much on the unsafe side, and more refined calculations like those performed here should be used.

Most numerical thermal simulations for reinforced or prestressed concrete elements do not consider the presence of steel. It can be seen in Fig. 5 that the introduction of a steel element influences slightly the isothermal curves.

In Figure 7 the deflection versus time curves at mid-span are presented for a span of 3 m. The slab is submitted to dead load and to a line load of 80 kN at mid span for a transverse length of 1200 mm, which is a little less than the value adopted in the experimental tests. Various degrees of restraint $E_{spr}A_{spr}/E_cA_c$ are considered, where E_cA_c is the axial stiffness of the slab and $E_{spr}A_{spr}$ the axial stiffness of the equivalent spring, i.e. the spring that would give the same restraint effect as the surrounding elements.

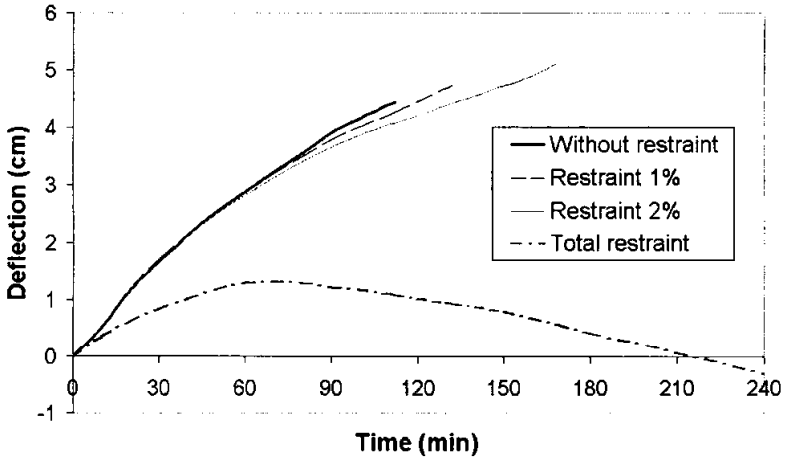

FIGURE 7 : Variation of the deflection at mid-span for various degrees of restraint

Preliminary studies not reproduced here have been made in order to find acceptable values of this degree of restraint. For a floor connected to transverse beams and four columns, this degree of restraint is less than 1 %. For a floor situated in the central part of a large building like in Fig. 4, the degree of restraint can be situated between 2 and 5 %. Therefore, in order to examine the influence of restraint on some characteristics described hereafter, degrees of restraint of 1 % and 2 % have been considered.

In view of discussing the results of Fig. 7 (where downward deflections are positive), it is interesting to examine the factors leading to a variation of the deflections.

- Decrease of the bending stiffness EI of the zones situated at the bottom.
  This produces downward deflections, but they are very limited except when yielding of the tendons starts
- Downward deflections due to the thermal gradient.
  This effect is rather important in the case of slabs, but the numerical results show that the deflections are smaller than for plain slabs

- Bending moment created by the restraint force.
  In this case it is assumed that this force is situated at the elastic centre when fire starts. Then this centre moves up due to the decrease of the axial stiffness EA of the zones situated at the bottom.
  This produces upward deflections.

Regarding the total deflections, they decrease when the degree of restraint increases, due to the latter effect, but the influence is not important for small degrees of restraint. A calculation has been made assuming a total axial restraint, which is not realistic on a practical point of view. In this case the negative bending moment created by the axial force is so important that after approximately 220 minutes, upward deflections occur.

The restraint influences also the fire resistance as can be seen in Fig. 7. The differences are rather important even for small degrees of restraint. This could be due to the decrease of tensile stress in the tendon created by the negative bending moment.

Figures 8 and 9 show the evolution of the normal stress distribution in concrete on the cross section of the slab. This section is situated at 6.7 cm from the support, i.e. at the first integration point of the first element, and it is assumed that no restraint is present.

In order to discuss this problem, it is better to consider the evolution of the stress-strain diagram of concrete in tension presented in Fig. 10. The material model adopted here is characterised by a long and smooth decreasing branch representing the progressive damage in tension.

Figure 8 considers the stress evolution between 0 and 30 minutes. For $t = 0$, the normal stresses are very small as they are calculated near the support. The evolution is then very fast, and after 5 minutes, the tensile stresses are very close to the tensile strength in a few points, while compressive stresses develop at the top and at the bottom. After 10 minutes the tensile strength is reached in many points, and the damage in tension starts, corresponding to the descending branch of the stress-strain diagram of concrete in tension. Twenty minutes later, i.e. after 30 minutes of standard fire exposure, most of the concrete situated between the cavities is either cracked or damaged in tension.

Between 30 and 90 minutes the development is much slower, as can be seen in Fig. 9. One part of the area damaged in tension becomes totally cracked. The decrease of the compressive stresses at the top and at the bottom is due to equilibrium considerations, i.e. the fact that thermal stresses are self-equilibrated.

Fig. 8 and 9 show why shear failures have been observed near the supports in many fire tests on simply supported hollow core slabs. The shear strength is mainly provided by the concrete situated between the cavities. As this concrete becomes cracked or damaged in tension due to the thermal stresses, the shear capacity is considerably reduced. The rapid evolution between 0 and 30 minutes also explains the fact that these failures occur rather quickly.

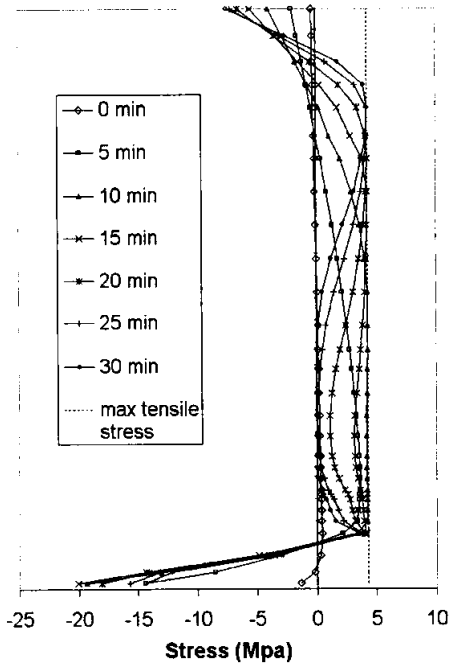

FIG. 8 : Evolution of the stress distribution on the cross section between 0 and 30 minutes

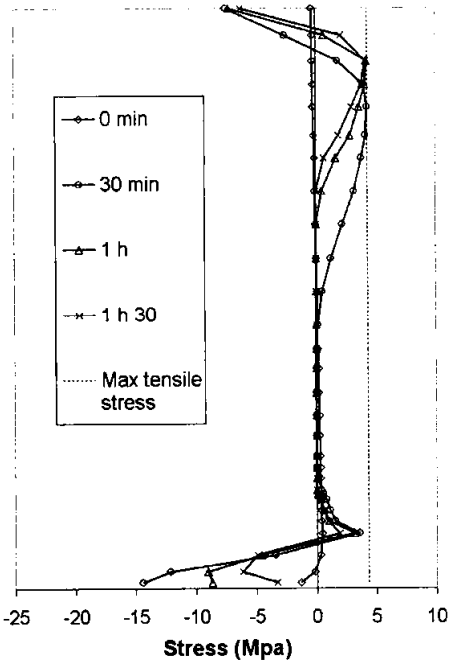

FIG. 9 : Evolution of the stress distribution on the cross-section between 0 and 90 minutes

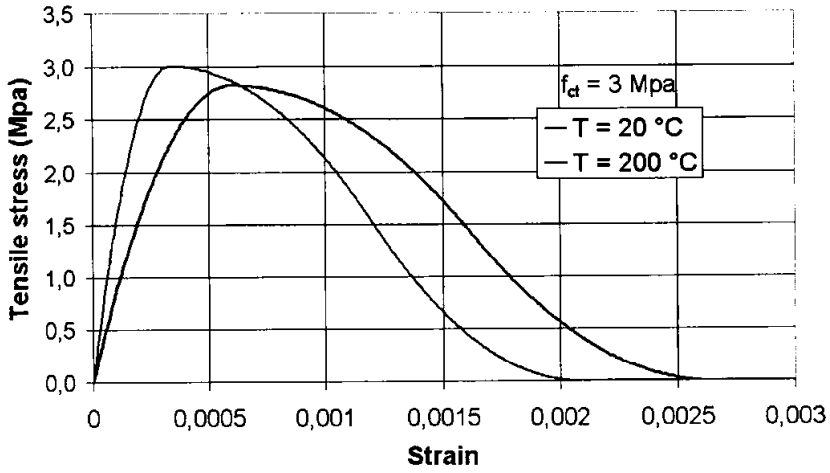

FIGURE 10 : Evolution of the stress-strain diagram of concrete in tension

Fig. 11 shows the evolution of the percentage of cracked area for various degrees of restraint. The curve without restraint can be derived from Fig. 8 and 9. The two other curves can be obtained from the same types of figures as Fig. 8 and 9 considered with the appropriate degree of restraint ; these figures are not reproduced here. Cracked area means here totally cracked, i.e the stresses being equal to zero. The cracking starts approximately after 30 minutes and develops between 30 and 60 minutes. The percentage is rather high, since approximately 30 % of the cross-section is totally cracked when no restraint is present. The influence of restraint is important, since for a small degree of restraint of 2 %, the totally cracked area goes down to approximately 22 %.

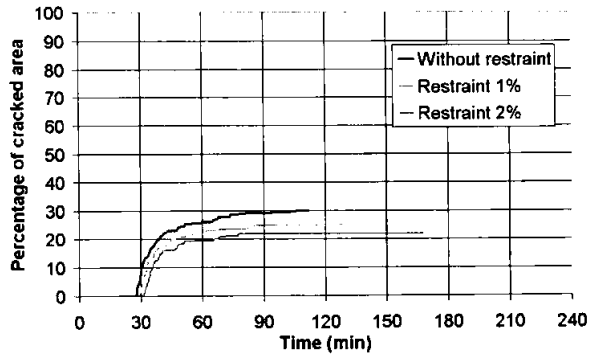

FIGURE 11 : Evolution of the percentage of cracked area for various degrees of restraint

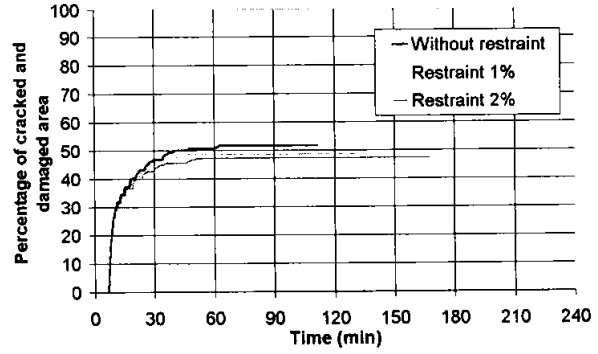

FIGURE 12 : Evolution of the percentage of cracked and damaged in tension area for various degrees of restraint

Fig. 12 shows the same type of evolution for the area that is cracked or damaged in tension. In this case the damage starts earlier, approximately after 10 minutes, and it develops between 10 and 60 minutes. The percentage is here higher, close to 50%. The influence of restraint is less important ; for a degree of restraint of 2 %, the difference is approximately equal to 6 %.

It can be concluded that restraint has a positive effect on the shear capacity of the slab, by reducing the cracked area near the supports ; the compressive force also increases shear friction and aggregate interlock in the cracks.

FIRE TESTS

The practical part of the project included 4 fire tests of approximately 2 hours at the laboratory of the University of Ghent. The dimensions of the test furnace are 6 x 3 m. The cross-sections of the elements tested are given in Figure 13.

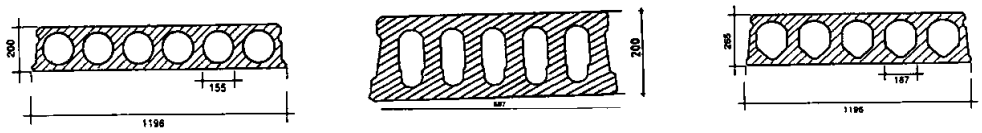

Test 1 Tests 2 and 3 Test 4

FIGURE 13 : Cross-sections of the elements tested (units : mm)

A large number of parameters have been examined in this study. Some of these were incorporated in the various experiments, so that each tested floor was different. Since the objective of the research project was to examine exclusively the shear capacity, each test included two floor spans of 3 m, supported on three beams and a floor width of 2.40 m. The load for each test was a line load of 100 kN in the middle of each of the two spans. About 40 thermocouples were cast into the hollow core units of each floor, at critical heights and at different locations in the floor. Fig. 14 shows the detailing adopted for the test No 1.

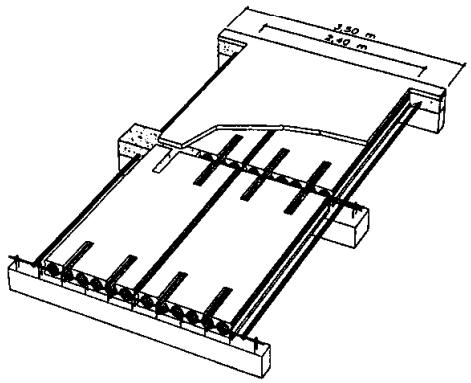

FIGURE 14 : Detailing adopted for the test No 1

During the fire tests, the following data were registered : temperature in the thermo-couples, longitudinal deformation, deformation of the lateral faces of the floors at the support, temperature and deformation of the exterior bars.

In order to simulate the effects of restraint, various detailing elements have been provided such as reinforced concrete edge beams or cold longitudinal plain steel bars at both sides of the floors, clamped at the ends in transverse reinforced concrete beams (Fig. 14). Bars of ϕ 40 mm

and ϕ 25 mm have been used. For the SP265 element, ϕ 40 mm plain steel bars provide a degree of restraint E_sA_s/E_cA_c = 4.79 %, and for ϕ 25 mm bars, this parameter is equal to 1.87 %, which is in agreement with the values discussed hereabove.

The first test was interrupted after 83 minutes because of the appearance of spalling on the horizontal face. A concentrated contact pressure most probably caused the local failure. All other tests were stopped after 120 minutes of fire exposure. At the end of each test, the loading was increased on each floor span until failure, to check the remaining capacity after the fire. The results are given in Table 1.

Test		Failure load (kN)		Failure type
		Without topping	With topping	
First test:	slab 1	178		Bending
	slab 2		(50 mm) 254	Bending
Second test:	slab 1	292		Bending
	slab 2	324		Bending
Third test :	slab 1	267		Bending
	slab 2	254		Bending
Fourth test:	slab 1	305		Bending
	slab 2		(30 mm) 305	Shear

Table 1 : Results of the 4 tests

For the floor of the first test with topping the failure load was 254 kN. The units failed in bending, from which it can be concluded that the shear capacity was higher. The other floor without topping failed at a load of 178 kN. Only the floor unit, in which local spalling appeared during the test failed. Also in this case the conclusion can be drawn that the shear capacity was not reached.

The three following tests were stopped after 120 minutes fire exposure. After that the load was increased, and all slabs failed in bending, with the exception of one, which showed a shear failure. The underside of this floor was more damaged than the one of the others, which might explain the shear failure. The damage could be explained by the high amount of restraint in the test, leading to high compressive stresses at the top and at the bottom of the slab. All failure loads are very high in comparison to the test load of 100 kN, which has to be considered as a normal loading during a fire. They prove that the hollow core units still had a large remaining resisting capacity both in bending and shear.

CONCLUSIONS

The main conclusions regarding numerical simulations that can be drawn from this research study are the following.

- The presence of cavities influences the temperature distribution on the cross-section. For slabs with large cavities, it is unsafe to assume that the temperature increase in the tendons is the same as for a plain slab.
- The total deflections decrease when the degree of restraint increases. The fire resistance corresponding to the ULS of bending increases with the degree of restraint.
- Thermal stresses due to the non linear thermal gradient are rather important. In this case, they have to be evaluated by general calculation methods. They develop mainly between 0 and 30 minutes. This explains shear failures observed in some fire tests.
- Restraint has a positive effect on the percentage of cracked area, and therefore also on the shear capacity of the slab.
- Restraint has thus a favourable effect on the ULS of bending and shear under fire conditions.

Regarding fire tests the following conclusions can be drawn.

- The detailing measures adopted have proved their efficiency.
- Restraint due to the surrounding structure has a favourable effect.
- A simple longitudinal tie reinforcement cast in opened cores or placed in the joints has already a very positive influence.
- During some tests spalling has been observed at the top or bottom face, but it has not led to premature failure of the slab and is probably due to the concentrated local pressure near the jack or to an excess of restraint in these particular tests.
- The units are keeping their high performances in bending and in shear during standard ISO fire tests. This is in agreement with the prediction of numerical simulations.
- To this end, it is necessary to provide a number of connections and tie reinforcements in the design in order to ensure a coherent flooring system.

REFERENCES

[1] FIP Commission on Prefabrication, *FIP Recommendations on Precast Prestressed Hollow Core Floors,* Thomas Telford Ltd., London, 1988.

[2] Dotreppe, et al., *Résistance au feu des structures. Principes généraux et Recommandations à l'usage des auteurs de projet,* Commission Nationale Belge de Recherche Incendie, Université de Liège et Rijksuniversiteit Gent Ed., 1983.

[3] Comité Euro-International du Béton, *Fire design of concrete structures in accordance with CEB-FIP Model Code 90,* Bulletin d'Information du C.E.B., N°208, Lausanne, 1991.

[4] Comité Européen de Normalisation, *ENV 1992-1-2. Eurocode 2 : Design of concrete structures. Part 1-2 : General rules – Structural fire design,* CEN, Bruxelles, 1995.

[5] Engström, B, *Ductility of tie connections in prestressed structures,* Chalmers Technical University, Göteborg, Sweden, 1992.

RESOLVING STEEP THERMAL GRADIENTS IN CONCRETE EXPOSED TO FIRE AND ASSESSING IMPLICATIONS FOR SPALLING PROPENSITY

Asif S Usmani
School of Engineering & Electronics, University of Edinburgh

ABSTRACT

The modelling of heat transfer in concrete and the consequent thermo-mechanical behaviour is a highly complex numerical problem. A complete resolution of this phenomenon requires a three way coupled model as illustrated in Figure 1 below.

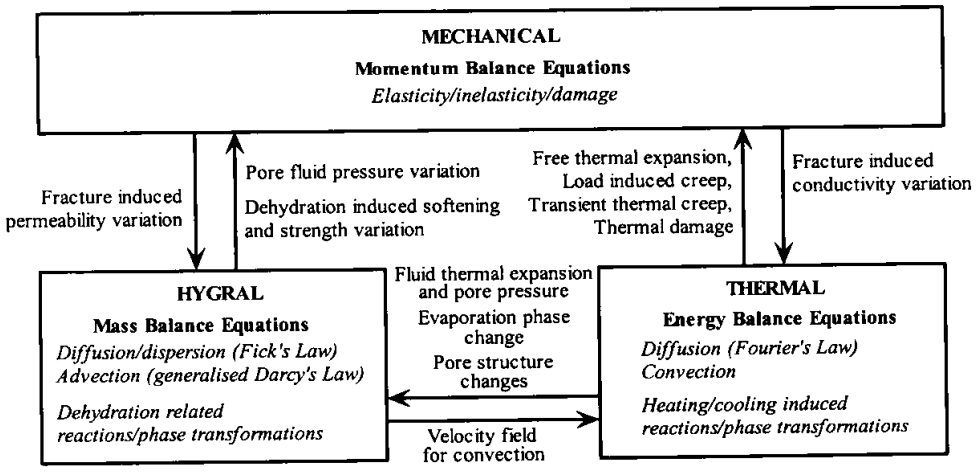

Figure 1: Schematic of all phenomena and major couplings.

This paper provides a brief review of the current status of such modelling as an introduction. The main body of the paper focuses primarily on the heat-transfer problem and uses and *h*-adaptive finite element method to investigate the steep thermal gradients normal to the fire exposed concrete surface. The results from this analysis are used to develop an understanding of the spalling phenomenon from an engineering perspective.

Resolving Steep Thermal Gradients in Concrete Exposed to Fire and Assessing Implications for Spalling Propensity

Asif S. Usmani and Allan Jowsey
School of Engineering and Electronics
University of Edinburgh

Abstract

The modelling of heat transfer in concrete and the consequent thermo-mechanical behaviour is a highly complex numerical problem. This paper provides a brief review of the current status of such modelling as an introduction. The main body of the paper focuses primarily on the heat-transfer problem and uses an *h*-adaptive finite element method to investigate the steep thermal gradients normal to the fire exposed concrete surface. The results from this analysis are used to develop an understanding of the spalling phenomenon from an engineering perspective.

1 Introduction

The response of concrete to elevated temperatures is an extremely important consideration in the design and rational integrity assessment of structural concrete that may be subjected to thermal and mechanical loading. The possible scenarios include single events, such as extreme fires in buildings (involving hydrocarbon fuels) as a result of an accident or through acts of arson and terrorism. They also include the long term effect of regular thermal loading (for example chemical plants). The nuclear industry must regularly investigate the effect of elevated temperatures on the working condition of power plants as well as conduct periodic safety-margin assessment analysis of these plants.

The Channel Tunnel fire in 1996 [1] illustrated the structural and economic consequences of a 10-hour fire that reached temperatures of 700°C. Structurally, the fire caused severe damage due to thermal spalling over a few hundred metres of the tunnel. Not only did this cause the closure of the tunnel for a significant period of time but also more immediately it hindered efforts to bring the fire under control. The incident highlighted the lack of understanding of how concrete (high performance concrete in this case) behaves under rapid thermal loading. No real consensus emerged on the exact cause of spalling [1–3] as there is a knowledge deficit with regard to the underlying processes that concrete experiences on the material level. The fire compartment parameters (geometry, ventilation and thermal properties of the boundaries) and the distribution, amount and nature of fuel determines the fire severity in buildings in terms of the time of burning and the maximum atmosphere temperatures achieved, to highs of up to 1400°C under certain conditions [4]. This may lead to concrete temperature of over 1000 °C at least in the surface layers. The main issue to be addressed in case of building and tunnel fires is the spalling of concrete. Other than the thermal environment, this depends upon the type of concrete of used (lightweight, normal weight or high strength and the type of aggregate) and any additives such as polypropylene fibres used to dissipate steam pressures (the fibre melt at 150°C providing additional pores for steam to escape). Spalling ranges from superficial damage to surface layers to explosive events leading to extensive loss of material and exposure of reinforcement. Currently there is very limited predictive capability for reliable predictions of such damage. Furthermore, accurate prediction of structural behaviour under fire depends greatly on temperature distributions in structural concrete and its mechanical response to the heating and boundary restraint conditions [5].

1.1 Physical processes describing concrete response to heating

The behaviour of concrete subjected to an aggressive environment is controlled by the history of the multi-axial stress state, temperature and moisture content. To realistically simulate structural concrete under complex loading scenarios a model must involve a coupled heat-mass transfer and mechanical analysis. The three main physical processes to be considered in such a coupled formulation are illustrated in the diagram in Figure 1.

Mechanical
Concrete is often classed as a 'low-tech' material but even under isothermal conditions it requires advanced constitutive models to describe its complex behaviour. In the tensile regime, concrete behaves in a quasi-brittle manner and experiences both loss of strength and stiffness, whereas under increasing levels of confinement the material becomes more ductile. Furthermore, concrete experiences significant time-dependent creep under sustained loading. The realistic simulation of progressive fracturing combined with these other phenomena, all within a continuum framework, presents a significant challenge and is the source of continuous research worldwide.

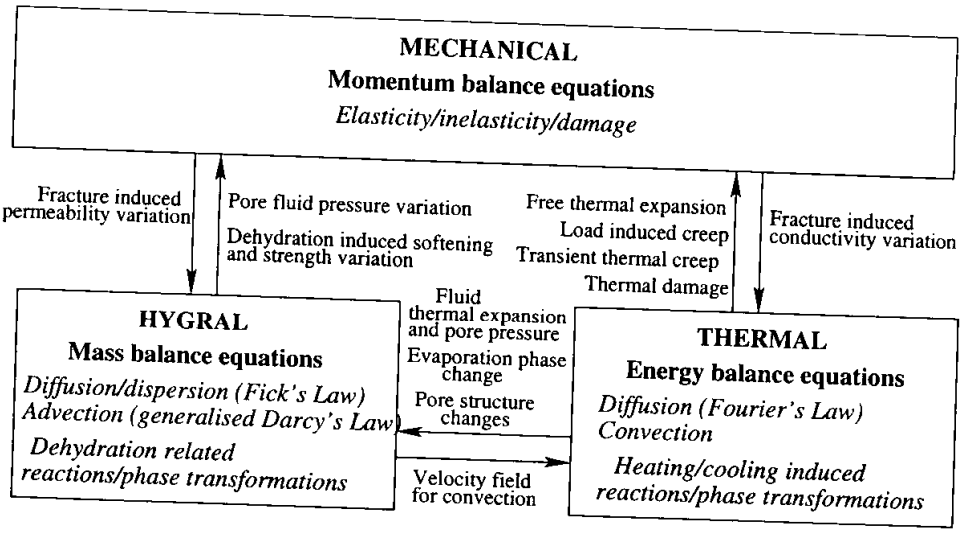

Figure 1: Physical processes describing concrete response to heating

The situation is made even more complex as a result of exposure to high temperatures such that the constitutive equations of concrete are significantly altered. When concrete is heated above 100°C, moisture is expelled and its main constituents (cement paste and aggregate) are subject to progressive dehydration leading to shrinkage and expansion respectively. This process introduces damage and micro-cracking to the cementitious matrix - thermal damage. An unloaded, unrestrained concrete specimen subject to heating generally shows free thermal expansion followed by contraction under subsequent cooling. If instead the specimen is loaded prior to transient heating, it shows a large irreversible deformation relative to the unloaded case [6–8] - this is known as transient thermal creep.

Thermal

In the modelling of multiphase media such as concrete it is tacitly assumed that local thermal equilibrium exists - in other words, all phases of the media are at the same temperature. The governing equations are related to energy balance and heat transport occurring as a result of conduction (Fourier's law) and to a lesser extent due to convection of water and gas through the porous medium. Absorption of sensible heat into heat of vaporisation of the pore water at temperatures over 100°C - due to phase change to vapour - must also be taken into account. The effect of thermal expansion and consequent rise in pressure in the pore fluid will provide for coupling of the heat transfer with mass-transfer. Heating to temperatures roughly beyond 200°C is accompanied by increasing rates of dehydration of the cement paste (microdiffusion of chemically bound moisture into the capillary pores) with an accompanying softening and pore structure changes and consequent permeability variation. Over 600°C the aggregates may begin to chemically transform with associated dilatation.

Clearly, mechanically or thermally induced damage to the bulk material will change the conductivity characteristics of the concrete leading to preferential pathways for heat transfer and possibly adverse thermal gradients. Meanwhile the rise in pressure (of the order of 1 to 4 Mpa) from vaporisation of pore moisture will contribute to the stress-strain-damage state in addition to the larger stresses induced by restrained thermal expansion.

Hygral

The governing equations for the hygral part of this complex framework are related to mass balance and consider the movement of a two-phase flow system of liquid water and a mixture of vapour and dry air. The transport mechanisms are due to advection of the different constituents as a result of pressure gradients and capillary effects (generalised Darcy's Law), diffusion of the vapour due to molecular concentration gradients (Fick's law) and evaporation and dehydration. A model for mass transfer under elevated temperatures has been presented in [9]. However this should be further extended by inclusion of temperature-dependent chemical dissolution/precipitation reactions, as well as reactions within the liquid and gas phases. Increases in temperature can lead to changes in phase and rapid heating can give rise to high pore pressure build-up. Once again damage to the bulk material will change the permeability of the concrete and therefore the convective movement of water and vapour. In the case that distinct fractures occur, there will be preferential pathways for the fluid to move. Probably one of the most important thermal-hygral couplings is with respect to dehydration of the cement paste and the subsequent effects on the mechanical properties.

1.2 Previous modelling work

Previous modelling studies have generally modelled the thermo-mechanical response of concrete by extending isothermal models to incorporate thermal dependency. In most commercial finite element codes, mechanical material properties such as strength and stiffness are simply related to temperature; although clearly such an approach does not account for the irreversible change these material properties undergo. A sophisticated, thermodynamically consistent thermo-mechanical model was presented by Stabler [10]. Temperature effects were included using a thermal damage model and the governing thermal and mechanical equations were solved in a fully coupled manner. However, hygral considerations and transient thermal creep were not included in the model. It is generally recognised that the presence of transient thermal creep is an important reason for concrete not to degrade completely when heated beyond 100°C as this effect provides a degree of relaxation [7], helping to minimise the stress gradients originating from thermal incompatibilities and temperature gradients. There are few fully coupled hygro-thermo-mechanical models proposed in the literature. A few notable exceptions include the work of Gawin [11], Grasenberger [12] and Ulm [1]. In all cases, liquid water, vapour and dry air are modelled as a single phase (with varying degrees of complexity) and none of these models include transient thermal creep. Ulm *et.al.* [1] approach the problem from a more fundamental point of view, such that they introduce an additional chemo-plastic term into their thermodynamic framework, to account for the energy dissipated due to hardening/softening during the dehydration process, rather than simply having a temperature dependent term to account for the observed phenomena of loss of strength and stiffness.

2 Thermal modelling

The authors, having recently taken on this work have begun by concentrating on the modelling of the heat transfer process initially. A 2D finite element heat transfer program HADAPT [13, 14] with h-adaptive capability is used to solve the thermal diffusion equations with time dependent convective and radiative boundary conditions (to simulate the heat input from a fire). The enthalpy method [13] is used to account for the heat lost in evaporating the pore moisture. The finite element formulation of the conduction heat transfer well known, see for example [13], however the h-adaptive process is described briefly as follows [15].

2.1 Adaptive strategy

The adaptive strategy employed generally follows the well established procedures developed by Zienkiewicz and Zhu [16]. Several distinct phases of the adaptive strategy can be described as an iterative process as follows:

1. **Preliminary analysis**
2. **Recovery** of the field variable gradients from the preliminary analysis.
3. *A posteriori* **error estimation** using the recovered gradients.
4. **Mesh refinement** based on the estimated error.
5. **Data transfer** to the refined mesh (for nonlinear/transient problems).
6. **Reanalysis** and back to step 2 if convergence not achieved.

Step 1 is essentially the same as a standard FE analysis. Theoretically it is unnecessary at this stage to worry about the element size distribution in the mesh as the adaptive procedure will automatically converge to the *optimal mesh* (where each element has approximately the *same* error). However in practice it is beneficial even at this stage to create the mesh with due care and attention to possible areas of high gradients as this will help reduce the number of cycles required for convergence to the optimal mesh. Step 5 involves the use of an appropriate interpolation scheme to transfer data for the old mesh to the new mesh with appropriate constraints ensuring conservation. Step 6 is self-explanatory. The rest of this section will deal with steps 2 to 4 (in that order).

2.2 Recovery

The gradients obtained from a standard FE analysis (such as stresses and strains in a displacement analysis) are discontinuous (C^{-1}) at element boundaries. A higher order projection of the available FE solution is used to achieve

continuous (C^0) gradients. This process is termed as *smoothing* or *recovery*. The global smoothing technique of Hinton and Campell [17] was the first, and has remained popular. A variety of gradient recovery procedures have since appeared in the FE literature which are either better [18] or more efficient or in some cases both [19].

It has been proved that the value of the field variable obtained by the finite element method is most accurate at nodal points [20], whereas its gradient is most accurate at Gauss points [21]. This is often referred to as the super-convergence phenomenon. The Gauss points have been shown to be *super-convergent* points. Based on this Zienkiewicz and Zhu introduced a local recovery procedure called *super-convergent patch recovery* [19]. In this method *smooth* nodal gradients are generated by a least square fit from super-convergent gradient values at Gauss points on a patch of elements surrounding each node. This method of recovery is more efficient and allows faster convergence towards the optimal mesh and has been used for this work.

2.3 Error estimation for scalar diffusion

The error estimator used was originally derived for heat conduction [22]. Mathematical justification of using such an estimator for hyperbolic problems may not exist, however as the estimator used is based on the scalar flux, it has proven very effective in detecting regions of high gradient. This is highly relevant to the aim of the current exercise of capturing discontinuities in advection dominated problems. It can also be argued that this error estimator is valid for use here as an indicator rather like curvatures are used in other adaptive schemes [23]. Better estimators may become available for scalar advection-diffusion equations in due course and this will be pursued in continuing this work. Brief details of the estimator are presented. Writing the diffusion equation and boundary conditions as,

$$\begin{aligned} \nabla \cdot \mathcal{D}\nabla\phi &= 0 \quad \text{in} \quad \Omega \\ \phi &= \phi_0 \quad \text{on} \quad \Gamma_\phi \\ -\mathcal{D}\nabla\phi \cdot \mathbf{n} &= \bar{J} \quad \text{on} \quad \Gamma_J \end{aligned} \tag{1}$$

Here Ω is the problem domain and $\Gamma = \Gamma_\phi + \Gamma_J$ is its boundary. $\mathcal{D}$ is a symmetric diffusivity tensor. Various other terms are self evident by the structure of the equations.

The *energy norm* for the error in diffusion problems can be defined as,

$$||e|| = \left[\int_\Omega (\nabla\phi - \nabla\hat{\phi})^T \mathcal{D}(\nabla\phi - \nabla\hat{\phi}) d\Omega\right]^{1/2} \tag{2}$$

here $\nabla\phi$ are the *exact* gradients and $\nabla\hat{\phi}$ are the calculated gradients from a previous analysis. It can be shown that [24],

$$\int_\Omega (\nabla\phi)^T \mathcal{D}\nabla\hat{\phi} d\Omega = \int_\Omega (\nabla\hat{\phi})^T \mathcal{D}\nabla\phi d\Omega = \int_\Omega (\nabla\hat{\phi})^T \mathcal{D}\nabla\hat{\phi} d\Omega \tag{3}$$

Thus, we have,

$$||e||^2 = \int_\Omega (\nabla\phi)^T \mathcal{D}\nabla\phi d\Omega - \int_\Omega (\nabla\hat{\phi})^T \mathcal{D}\nabla\hat{\phi} d\Omega \tag{4}$$

if we define,

$$\begin{aligned} ||Q||^2 &= \int_\Omega (\nabla\phi)^T \mathcal{D}\nabla\phi d\Omega \\ ||\hat{Q}||^2 &= \int_\Omega (\nabla\hat{\phi})^T \mathcal{D}\nabla\hat{\phi} d\Omega \end{aligned} \tag{5}$$

Equation (4) can be rewritten as

$$||e||^2 = ||Q||^2 - ||\hat{Q}||^2 \tag{6}$$

Such a definition allows a practical representation of the error norm in terms of a percentage error, that is

$$\eta = \frac{||e||}{||Q||} \text{x} 100\% \tag{7}$$

2.4 Mesh refinement

The first step for implementing adaptive analysis is to specify a maximum permissible error $\bar{\eta}$ that is to be achieved at the end of the analysis. After the first analysis using a preliminary coarse mesh, the square of the total error is calculated which is the sum of all individual element contributions, *i.e.*

$$||Q||^2 \approx ||\hat{Q}||^2 = \sum_{e=1}^{m} \int_{\Omega_e} (\nabla\hat{\phi})^T \mathcal{D}\nabla\hat{\phi} d\Omega_e \tag{8}$$

where m is the total number of elements. Now, the maximum permissible error for each element can be calculated by distributing $||Q||^2$ equally over all the elements,

$$||\bar{e}||_e = \bar{\eta}\left(\frac{||Q||^2}{m}\right)^{\frac{1}{2}} \tag{9}$$

where $\bar{\eta}$ is the specified maximum value. The approximate error in each element ($||e||_e$) after the first analysis, can be calculated according to Equation (2) using the smoothed values of gradients instead of the exact values. If we define a parameter ξ_e as,

$$\xi_e = \frac{||e||_e}{||\bar{e}||_e} \tag{10}$$

If $\xi_e > 1$, the size of element e must be reduced and the mesh will require refinement (for $\xi_e < 1$ element size may be increased). The predicted size of the new element is calculated from the current element size as [16],

$$\bar{h}_e = \frac{h_e}{\xi_e^{1/p}} \tag{11}$$

where $\bar{h}_e$ is the predicted element size, h_e is current element size and p is the order of the shape functions. The linear triangle element (*i.e.* with linear shape functions) is used here for which the value of p is 1. It is important to understand that the errors calculated by the error estimation procedure are obtained from a smoothed solution on the same mesh, therefore one may discover lower errors for the same problem for a coarse mesh than for a better fine mesh. The specified error ($\bar{\eta}$) is related to the scalar flux. The error in the scalar field is proportional to the square of this error ($\simeq$ 6% for $\bar{\eta}$=25%) [13]. The choice of target error seems to depend upon the order of elements used (linear, quadratic, cubic *etc.*) and the problem size and meshing constraints (*i.e.* maximum number of elements and minimum element size, as theoretically an infinite number of elements are required to model a discontinuity). It is difficult to specify a general rule for choosing the value of $\bar{\eta}$, however in the authors experience a value of 15% to 25% is suitable for linear elements and slightly lower values for quadratic elements.

In this work the mesh is completely regenerated for each adaptive cycle using a Delaunay triangulation based automatic mesh generator [13]. As the error estimator produces a scalar error norm only a uniform refinement strategy is possible. A better and more efficient procedure would be to calculate directional errors so that the refinement is applied *only* in the direction of the highest gradients (this method will also require the mesh generator to have a directional element size control). For large problems it is also more efficient to refine by *mesh movement* and/or *mesh enrichment* however there are inherent limitations to these approaches.

2.5 Example problem

Figure 2 shows a 2D idealisation of a 0.6m square reinforced concrete column exposed on all sides to a BS476 fire for 3 hours. Only an eighth of the column section is modelled taking advantage of symmetry.

Figure 3 shows two uniform meshes of 4-noded quadrilateral finite elements to analyse the column neglecting the reinforcing bar. The results from the two meshes are compared in Figure 4 showing the temperature distribution along the left edge of the model (middle of a column side to column centre). Clearly the course mesh results are not as high resolution as the fine mesh, but considering the difference in the cost of the two analyses (the fine mesh has over 200 times the number of elements in the course mesh), the course mesh results are remarkably good.

In this particular example a mesh with local refinement at the fire exposed boundary would improve the results at a very low cost. But there are two problems with this approach. Firstly the level of refinement is difficult to determine *a-priori* as it is linked to the level of the discretisation error (an estimate of this can usually be made, but only after the analysis!). Secondly, in a general non-linear time dependent problem the location of the highest thermal gradients is not often known *a-priori* to enable the analyst to generate meshes with the correct gradation before the analysis. The *h*-adaptive refinement technique based on *a-posteriori* error estimation offers a good solution to both these problems. Figure 5 shows the adaptive meshes (after five timesteps when adaptivity was switched off) for models with and without the reinforcing bar (the mesh refinement at the location of reinforcing bar is enforced not adaptive). Figure 6 shows the comparison of the results of the adaptive analysis with the fine uniform mesh analysis. It is quite evident that the results are practically identical, using a third of the number of elements used in the fine mesh. Figure 7 shows a 2D contour plot of temperatures at the end of the analyses (after the 3 hour standard fire exposure) for both meshes, with and without reinforcement. The reinforcing bar only affects temperatures locally.

In all of the analyses so far only the temperatures have been examined. In the context of spalling, the gradient of temperature perpendicular to the fire exposed surface is of greater relevance, as it is this quantity that determines

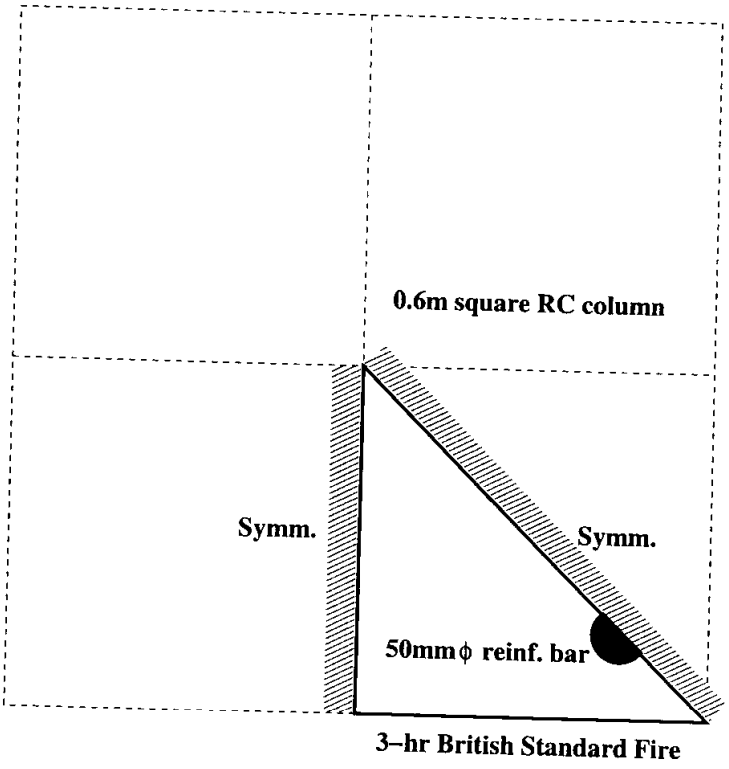

Figure 2: Idealised 2D thermal model of an RC column

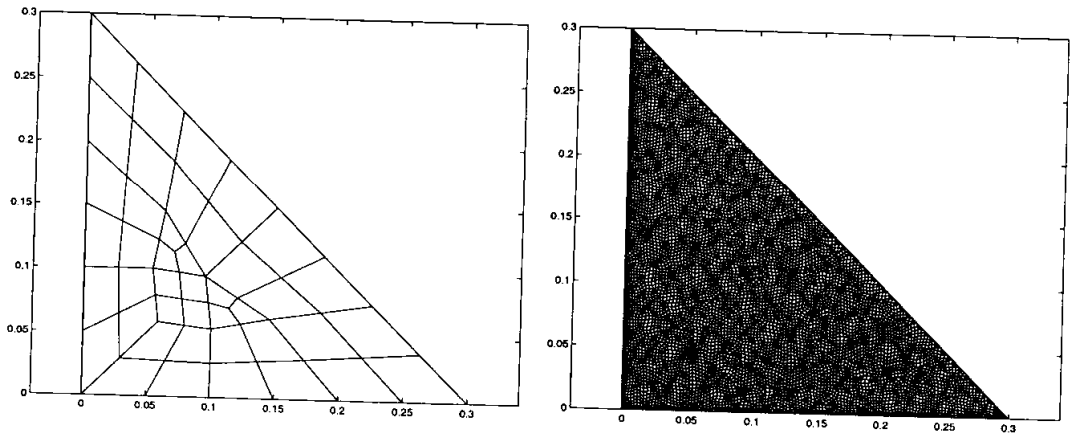

(a) 42 element mesh - mesh0

(b) 8938 element mesh - mesh3

Figure 3: Two uniform meshes used to analyse the heat transfer to column

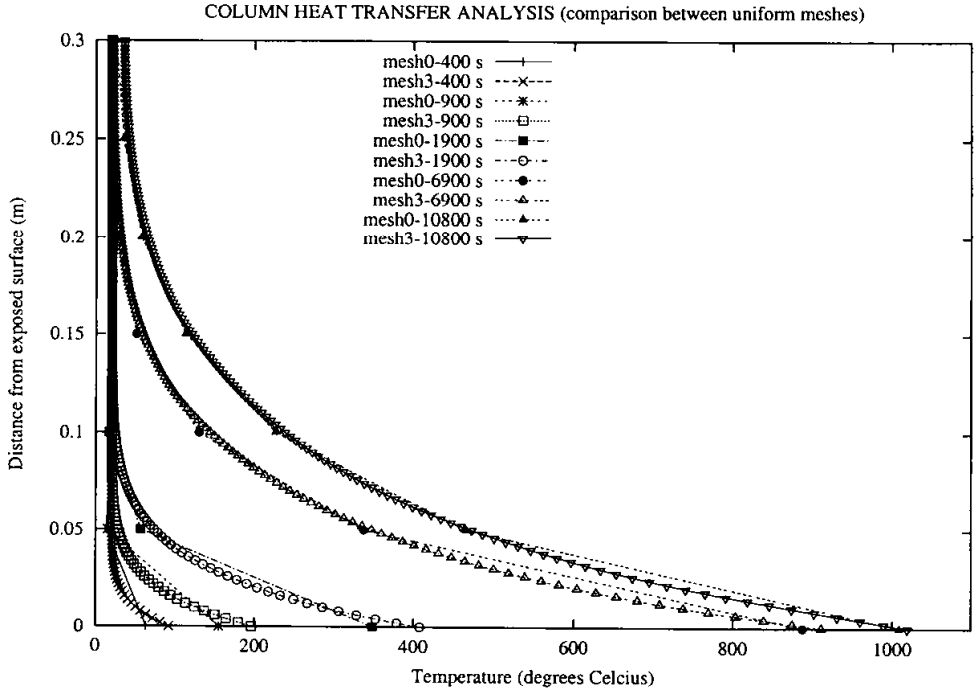

Figure 4: Comparison of results from the two uniform mesh analyses

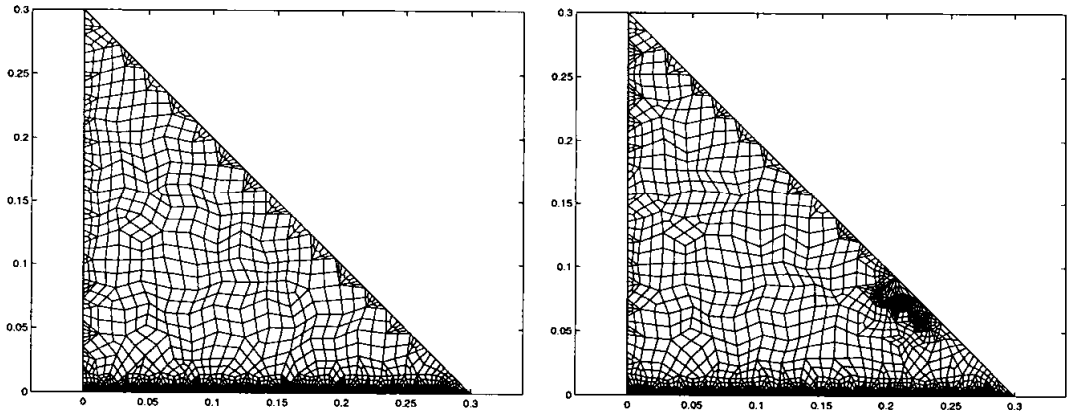

(a) Mesh without reinforcing bar - 2999 elements

(b) Mesh with reinforcing bar - 3392 elements

Figure 5: Adaptive meshes after 5 timesteps for models without and with the reinforcing bar

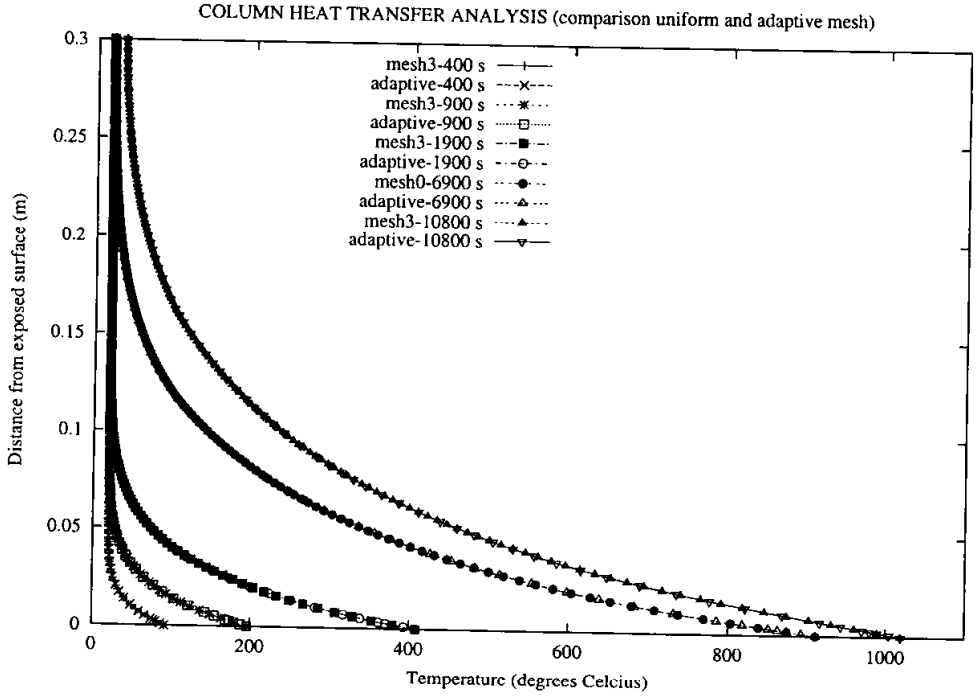

Figure 6: Comparison of results from the adaptive mesh and the fine uniform mesh analyses

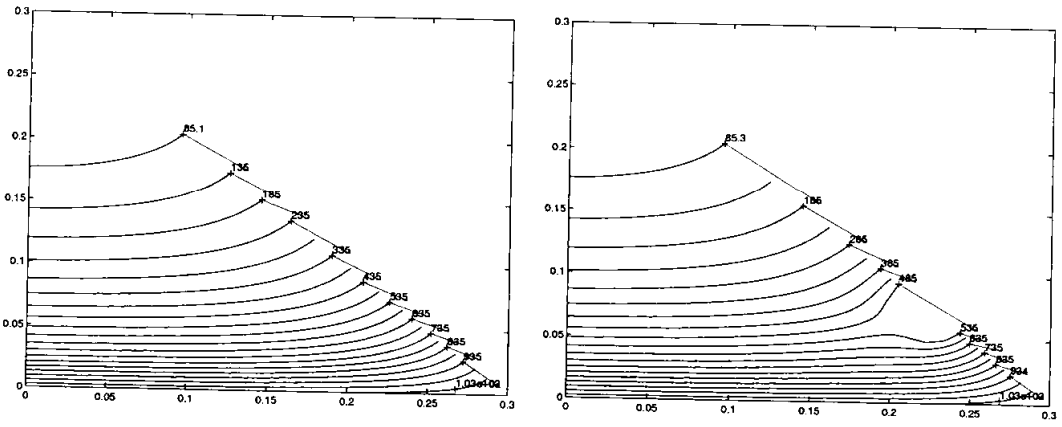

(a) Temperature distribution (without reinforcement)

(b) Temperature distribution (with reinforcement)

Figure 7: Isotherms at the end of the analysis

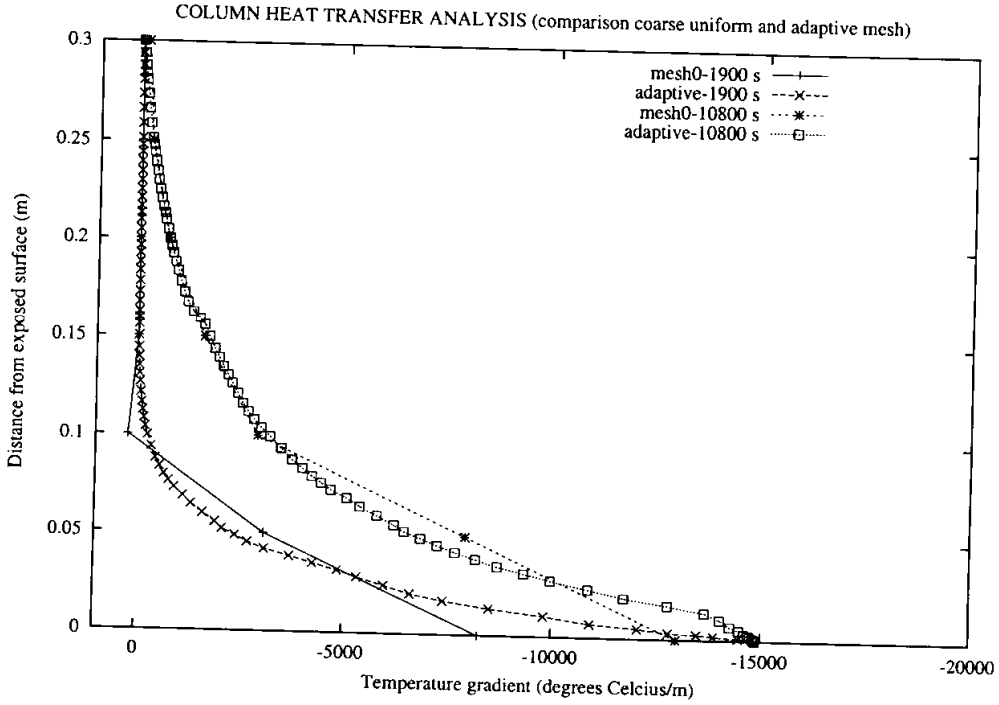

Figure 8: Temperature gradients perpendicular to the column surface

the magnitudes of thermal stresses and strains imposed on the hot surface layers of concrete. Revisiting the original analysis of the two uniform meshes and plotting the temperature gradient (using the adaptive mesh instead of the fine mesh here) along the same left hand side edge of the model, as shown in Figure 8, reveals greater differences. It is clear from the figure that the course mesh underestimates the temperature gradients despite producing relatively good temperature results seen earlier. The coarse mesh gradients are roughly half of that produced by the adaptive mesh, which would result in considerably lower stresses in the concrete. It may also be noted that these are 'recovered' smooth gradients (C^0) as described earlier, a direct calculation based on the nodal temperatures would show an even greater difference.

This effect is further exacerbated if the fire exposure is of a significantly greater severity. This is illustrated by using a Dutch RWS fire (used for designing and testing tunnels). The difference between the two fires is shown in Figure 9. Figures 10 and 11 show the temperatures and the temperature gradients achieved in the column using the two fires (using an adaptive mesh for both analyses). It can be seen that the maximum temperature gradient for the RWS fire is an order of magnitude greater than the one for the British Standard fire 6-7 minutes into the analysis but this narrows at later times as the RWS fire reaches a plateau while BS476 continues to rise.

Finally, Figures 12 and 13 show the temperatures and the temperature gradients using the coarse mesh and adaptive mesh. This analysis exposes the inadequacy of the coarse mesh quite clearly, showing poor performance in the prediction of both the temperature and gradient, thus vindicating the use of adaptive methods.

3 Implications on spalling propensity

There is an unresolved debate with respect to the primary cause of spalling as discussed earlier, with some researchers blaming the rise in pressure by evaporation of the pore moisture and others blaming the steep thermal gradients (resulting in restraint to thermal expansion to the hot external layers by the cooler internal concrete). It is not possible to answer this question without considerable further research in this area, using both experimental and computational techniques. One can however identify the possible conditions that could promote spalling. These can be listed as:

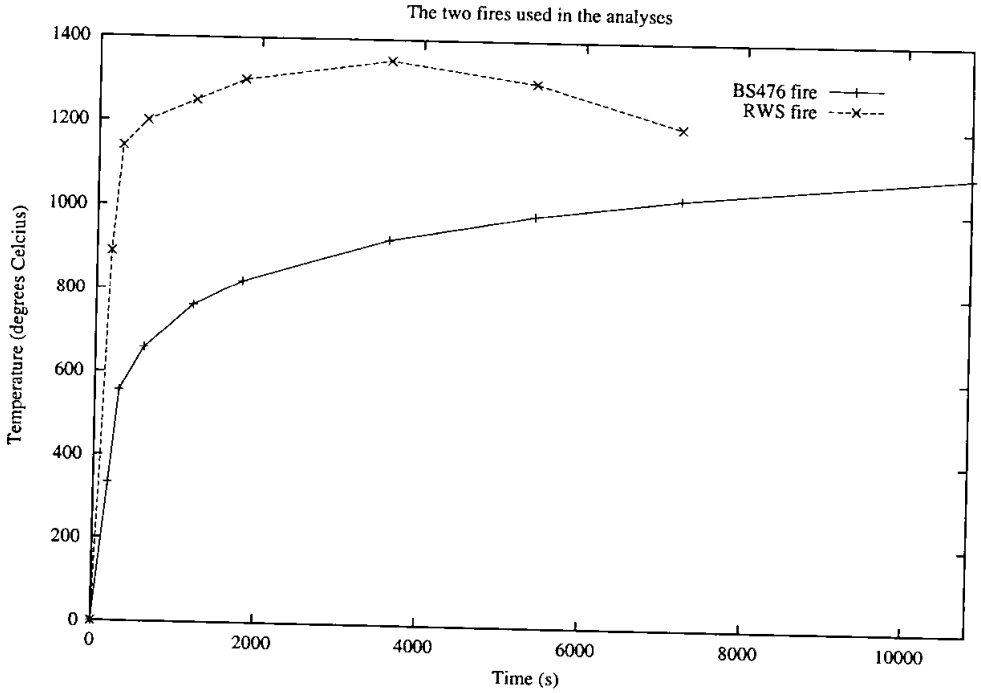

Figure 9: Comparison of the Two fires

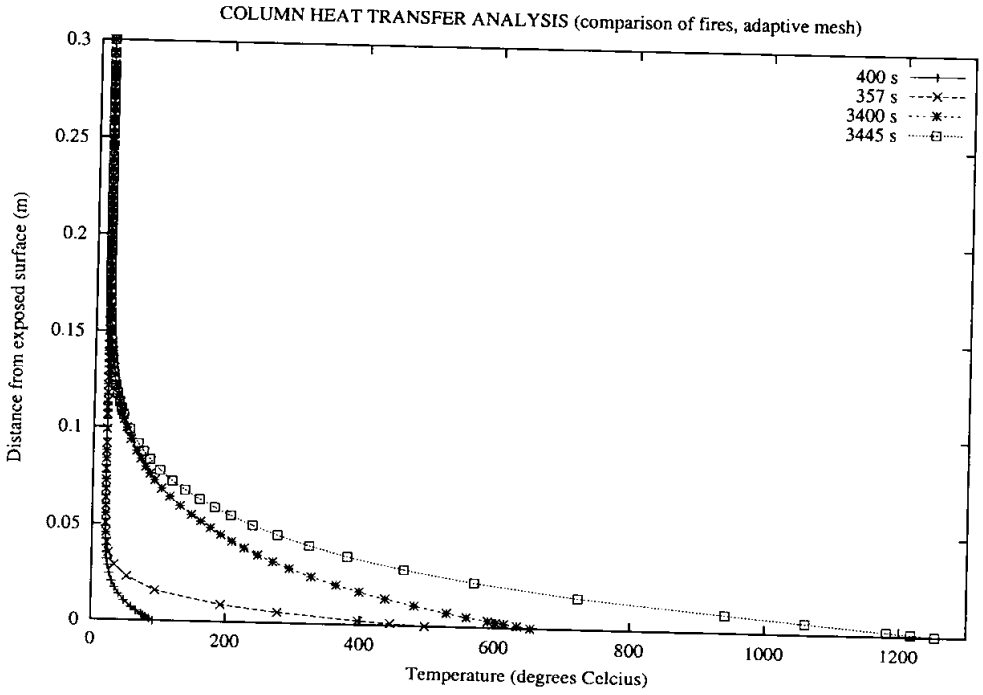

Figure 10: Comparison of the Two fires - Temperatures

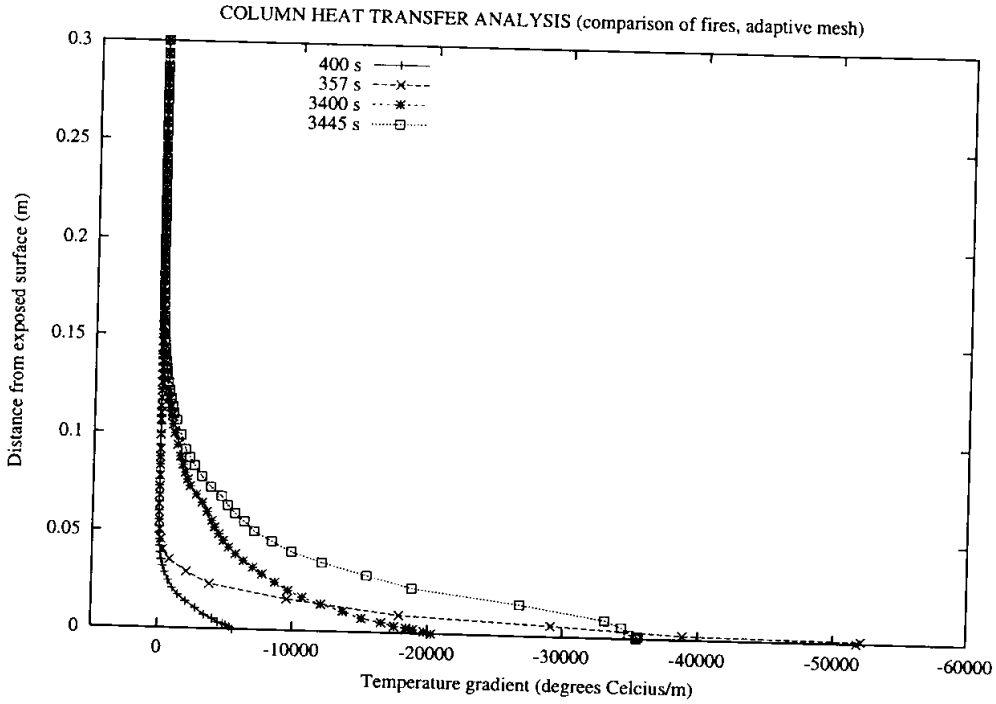

Figure 11: Comparison of the Two fires - Gradients

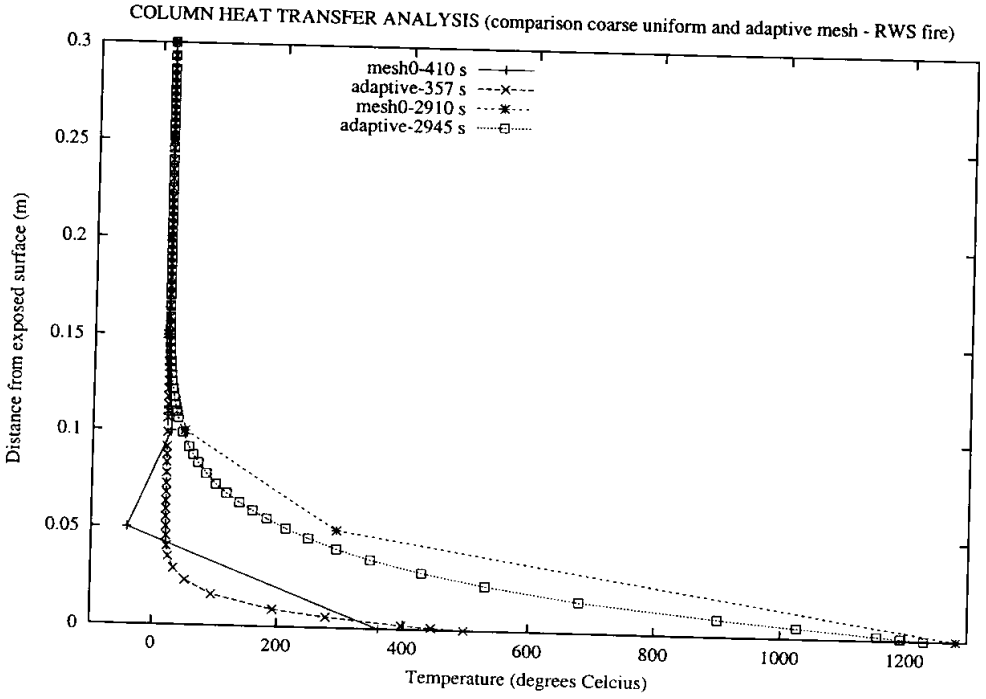

Figure 12: Temperatures in the column when exposed to an RWS fire

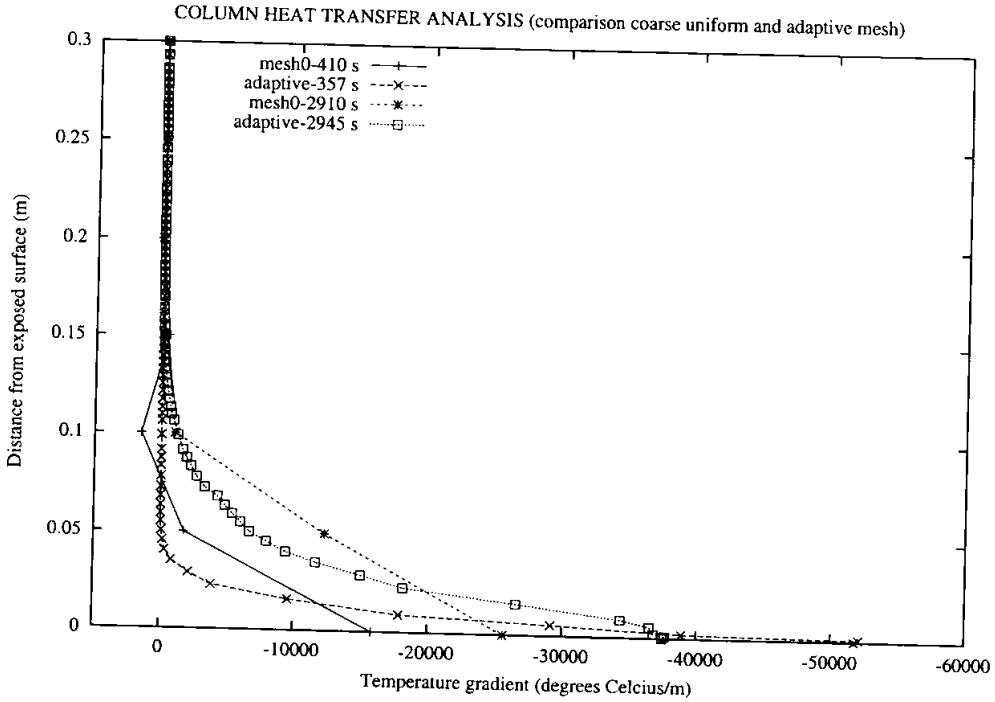

Figure 13: The gradients in the column using the RWS fire

1. *Steep thermal gradients*: The greater the thermal gradient between layers of concrete, the greater the shear stress between them, leading eventually to tensile cracking/spalling of the expanding surface layers. The exact mechanism is yet to be understood. The contributing factors to high thermal gradients are the thermal diffusivity properties of concrete (conductivity, heat capacity and density), the rate of heating (hot-fast fires will cause higher thermal gradients relative cooler slower fires). This does not necessarily mean that fast hot fires will cause greater damage. It is possible that fast hot fires may cause superficial surface damage while slower fires can cause larger deeper spalls or even explosive spalling. There is however no doubt that a high thermal gradient will increase spalling propensity, and therefore it is important to recognise that thermal analysis with a user-defined mesh (unless extremely carefully constructed) could severely under-estimate its magnitude.

2. *Level of existing load*: Clearly the larger the initial stress the quicker the heat damaged surface concrete will reach is compressive capacity through additional stresses from expansion restrained by cooler layers. Areas under high compressive stress are known to spall more readily.

3. *level of end restraint*: If the concrete member under fire attack is also restrained at its ends by a cooler stiffer part of the structure then the compressive forces could become even larger. However the property of transient thermal creep usually mitigates [7] against this, as highly stressed concrete may not expand at all because of this.

4. *Pressure of the vaporised pore water*: This is often suggested as a primary cause of spalling, measurements [25] however suggest that the pore pressure rarely rises above 1 MPa for normal concrete and 4 MPa for high strength concrete. These pressures could add significantly to the stresses caused by the thermal gradients but are unlikely to be sufficient on their own to cause spalling (*i.e.* without the aid of thermal gradients).

5. *Material damage from the combination of heating, loads, thermal gradient and restraint induced stresses and pressure*: It can be conjectured that the microstructural damage resulting from all the actions mentioned would 'integrate' to produce larger scale damage or spalling. How and in what sequence this occurs is one of the main unanswered questions in this area.

4 Conclusions

It has been demonstrated in this paper that predicting the thermal gradients in concrete using FEM requires a great deal of care is selecting the mesh. It was also shown that an *h*-adaptive technique, which is relatively simple to implement can make this task straightforward by taking it out of the hand of the analyst and estimating the discretisation error in the solution to automatically produce a satisfactory mesh.

References

[1] F.Ulm, O.Coussy, and Z.Bazant. The "Chunnel Fire". I: Chemoplastic softening in rapidly heated concrete. *Journal of Engineering Mechanics, ASCE*, 123(3):272–282, 1999.

[2] Y.Anderberg. Spalling phenomena of hpc and oc. In L.Phan *et.al.*, editor, *International workshop on fire performance of high-strength concrete, NIST Special Publication 919*. NIST, 1997.

[3] Z.Bazant. Analysis of pore pressure, thermal stresses and fracture in rapidly heated concrete. In L.Phan *et.al.*, editor, *International workshop on fire performance of high-strength concrete, NIST Special Publication 919*. NIST, 1997.

[4] D.D.Drysdale. *An Introduction to Fire Dynamics*. John Wiley and Sons, 2nd edition, 1999.

[5] A.S.Usmani, J.M.Rotter, S.Lamont, A.M.Sanad, and M.Gillie. Fundamental principles of structural behaviour under thermal effects. *Fire Safety Journal*, 36(8):721–744, 2001.

[6] U.Schneider. Concrete at high temperatures - A general review. *Fire Safety Journal*, 13:55–68, 1988.

[7] A.Khoury, B.N.Grainger, and P.J.E.Sullivan. Transient thermal strain of concrete: literature review, conditions within specimen and behaviour of individual constituents. *Magazine of Concrete Research*, 37(132):131–144, 1985.

[8] S.Thelandersson. Modelling of combined thermal and mechanical action in concrete. *Journal of Engineering Mechanics, ASCE*, 113(6):893–906, 1997.

[9] H.P.Lien and F.H.Wittmann. Coupled heat and mass transfer in concrete elements at elevated temperatures. *Nuclear Engineering and Design*, 156:109–119, 1995.

[10] J.Stabler. *Computational modelling of thermo-mechanical damage and plasticity in concrete*. University of Queensland, 2000. PhD Thesis.

[11] D.Gawin, C.Majorana, and B.Schrefler. Numerical analysis of hygro-thermic behaviour and damage of concrete at high temperature. *International Journal for the Mechanics of Cohesive-Frictional Materials*, 4:37–74, 1999.

[12] S.Grasenberger and G.Meschke. A hygral-thermal-poroplastic damage model for the durability analyses of concrete structures. In *In Proceedings of the European Congress on Computational Methods in Applied Sciences and Engineering*. ECCOMAS, 2000.

[13] H.C.Huang and A.S.Usmani. *Finite Element Analysis for Heat Transfer - Theory and Software*. Springer-Verlag, London, 1994.

[14] A.S.Usmani. *HADAPT: An h-adaptive finite element method code for scalar transport problems*. University of Edinburgh, 1994. Download from URL http://www.see.ed.ac.uk/~asif/Public/HADAPT/.

[15] A.S.Usmani. An *h*-adaptive SUPG-FEM solution of the pure advection equation. *Applied Numerical Mathematics*, 26:193–202, 1998.

[16] O.C.Zienkiewicz and J.Z.Zhu. A simple error estimator and adaptive procedure for practical engineering analysis. *International Journal for Numerical Methods in Engineering*, 24:337–357, 1987.

[17] E.Hinton and J.S.Campbell. Local and global smoothing of discontinuous finite element functions using a least squares method. *International Journal for Numerical Methods in Engineering*, 8:461–480, 1974.

[18] A.Tessler, H.R.Riggs, and S.C.Macy. A variational method for finite element stress recovery and error estimation. *Computer Methods in Applied Mechanics and Engineering*, 111:369–382, 1994.

[19] O.C.Zienkiewicz and J.Z.Zhu. The superconvergent patch recovery and *a posteriori* error estimates. Part 1: The recovery technique, Part 2: Error estimates and adaptivity. *International Journal for Numerical Methods in Engineering*, 33:1331–1382, 1992.

[20] T.J.R.Hughes. *The Finite Element Method - Linear Static and Dynamic Finite Element Analysis*. Prentice-Hall International, Inc., Englewood Cliffs, New Jersey 07632, 1987.

[21] M. Zlamal. Superconvergence and reduced integration in the finite element method. *Mathematics of Computation*, 32:663–685, 1978.

[22] R.W.Lewis, H.C.Huang, A.S.Usmani, and J.T.Cross. Finite element analysis of heat transfer and flow problems using adaptive remeshing including application to solidification. *International Journal for Numerical Methods in Engineering*, 32:767–781, 1991.

[23] R.Lohner, K.Morgan, and O.C.Zienkiewicz. Adaptive grid refinement for the compressible Euler equations. In I.Babuska, editor, *Accuracy Estimates and Adaptive Refinements in Finite Element Computations*, page 281. Wiley, New York, 1986.

[24] O.C.Zienkiewicz, Y.C.Liu, and G.C.Huang. Error estimates and convergence rates for various incompressible elements. *International Journal for Numerical Methods in Engineering*, 28:2191–2202, 1989.

[25] P.Kalifa, F.Menneteau, and D.Quenard. Spalling and pore pressure in HPC at high temperatures. *Cement and Concrete Research*, 30:1915–1927, 2000.

EFFECT OF SPECIMEN SIZE AND LOADING CONDITIONS ON SPALLING OF CONCRETE

Lars BOSTRÖM, Ulf WICKSTRÖM, Bijan ADL-ZARRABI
SP Fire Technology, Box 857, SE-501 15 Borås, Sweden
lars.bostrom@sp.se, ulf.wickstrom@sp.se, bijan.adl-zarrabi@sp.se

ABSTRACT

Different qualities of concrete have been fire tested using different geometries of the specimens as well as different load levels and load configurations. The main objective with the study was to develop a test methodology for determining the of probability of spalling and the amount of spalling of fire exposed concrete structures. A reference specimen was defined as a one-sided fire exposed slab with the dimensions 1800 x 1200 mm^2 giving an exposed area of 1500 x 1200 mm^2. A number of concrete qualities with small and great probabilities for spalling respectively, were tested using the reference specimen. These tests showed that the reference specimens worked well giving the expected test results. Small specimens were manufactured in different shapes with the same concrete as the one used in the reference tests. These small specimens were tested either at the same time as the reference specimens in the large furnace or afterwards on a small scale furnace where the fire exposed surface was 450 x 360 mm^2.

The test results clearly show the increased probability and the increased amount of spalling by using external compressive loading. The results also show that by using pre-stress through bars or wires the load can be lost due to heating of the bars/wires which results in a decreased amount of spalling.

The boundary of the specimen also affects the amount of spalling. The spalling around the edges was in all tests less than the spalling on the central parts of the exposed area. It could also be noted that the spalling not in any case continued completely through the specimen. The reason for this is probably that the water/vapour than can migrate out from the specimen.

KEYWORDS: *fire resistance, spalling, concrete, test methodology*

INTRODUCTION

Concrete is generally assumed to have a good fire resistance. Although, due to the development of new types of concrete such as high performance concrete and self-compacting concrete the characteristics of the material has changed. The changes may affect the fire resistance and especially the probability of spalling. These new concretes are much denser and therefore the permeability is lower. Hence the probability for spalling may be greater for these concretes when exposed for fire.

Spalling due to fire are generally believed to depend on the vapour pressure within the concrete and the temperature stresses or a combination thereof. When the concrete is heated to above the boiling point of water a vapour pressure will build up. The magnitude of the pressure depends on the permeability of the concrete, i.e. how easily the water or vapour can be transported within the concrete. The temperature stresses are caused by the temperature gradient within the structure when the concrete is heated.

Fire resistance tests are difficult to scale. Hence most fire resistance tests are made in full scale. Concrete is made in a wide variety of qualities and is used in many different types of applications. The costs for testing all aspects would therefore be enormous, especially if full scale tests are required. Therefore a fast and cheap small scale test would be beneficial. It is therefore crucial to find a small scale method with which experiments can be carried out giving the same results as a full scale test.

Small scale tests are currently often used for tests on concrete. However, when examining the literature the results from these tests are often contradictory. Usually it is very difficult to say whether the contradictory results are due to the actual test methodology, or to some parameter not clearly specified such as concrete recipe, moisture content etc.

In this article two different experimental studies are presented. Both studies had the objective to develop a test methodology for determining the probability of spalling and the amount of spalling. In one of these two projects conventional concretes for tunnel linings were used and in the other self-compacting concretes. The present paper will show some of the results from these investigations. A complete compilation of results can be found in a report by Boström [1].

EXPERIMENTAL STUDY

Materials and specimens

Self-compacting concretes

Specimens made according to four different self-compacting concrete recipes were manufactured. The recipes were developed by Skanska Asfalt och Betong and shown in table 1. Three different water-powder ratios, i.e. the ratio between the mass of water and the total mass of powder (cement plus filler), were used ranging from w/p = 0.30 to w/p = 0.55. Two different concretes were made with w/p = 0.40, one with addition of polypropylene fibres and one without fibres.

Table 1. Concrete recipes.

Recipe code		**w/p 0.30**	**w/p 0.40**	**w/p 0.40 fib**	**w/p 0.55**
Dry materials (kg/m^3)					
Cement	Slite (CEM I)	439.32	381.57	380.76	301.51
Limestone filler	Limus 25	126.38	118.68	119.24	77.39
Fine gravel	0-8 Sätertorp	1027.33	1016.95	899.96	941.66
Coarse gravel	8-16 Sätertorp	591.65	602.69	721.90	754.52
Plasticizer*	CemFlux Prefab	8.76	5.24	5.73	0
Plasticizer*	CemFlux PrefabS	0	0	0	3.26
Plasticizer	(% of C+F)	1.55%	1.05%	1.15%	0.86%
Fibres	Fibrin 18μm	0	0	1.0	0
Water/moisture (kg/m^3)					
Water		122.37	141.21	149.69	163.82
Dilution water		10.03	10.01	10.02	9.05
Moisture in material		43.00	46.34	37.54	37.08
w/c-ratio		0.399	0.518	0.518	0.696
w/p-ratio		0.310	0.395	0.395	0.554
Slump flow (mm)		750	700	640	630
Slump flow 500 mm (s)		4	3	4	2

* Plasticizers are given as weight in diluted form, as delivered. The moisture is included in "Moisture in material" in the table.

The compressive strength of the concrete was measured in accordance with the Swedish standard SS 13 72 10, i.e. on cubes with the dimensions 150 x 150 x 150 mm^3. Close to the day of testing were the moisture content as well as the compressive strength determined. The same specimens were used for both measurements. The moisture content was determined by weighing the specimens before and after seven days of drying in 105 °C. The measured strengths and moisture contents are shown in table 2.

Four slabs of self-compacting concrete with the dimensions 1800 x 1200 x 200 mm^3 were manufactured, one of each recipe. The slabs were pre-stressed through 13 wires with a load of 55 kN each, i.e. a total load of 715 kN. The wires were placed 35 mm from the fire exposed surface of the slabs. Hence the theoretical compressive stress, including the compressive stress due to bending of the eccentric placed wires, at the fire exposed surface was 8.8 MPa after casting.

Two beams with the dimensions 3600 x 600 x 200 mm^3 were manufactured of concrete with w/p = 0.40. One beam with fibres and one without fibres. Non-tensioned reinforcement was used in the beams, i.e. no pre-stressing was applied in the beams.

In addition to the large size specimens several small scale specimens were manufactured. Cylinders with a diameter of 150 mm and lengths 300 mm and 450 mm respectively. Small slabs with dimensions 600 x 500 x 200 mm^3 were also manufactured. The small specimens were all manufactured from all the concrete recipes. All specimens of self-compacting concrete were cured in the fire laboratory for three months before testing. In Appendix A is a list presented giving the details for all specimens in the test series.

Table 2. Concrete strength and moisture content of the self-compacting concretes.

	Compressive strength (MPa)			Moisture content (%)
	7 days	28 days	Day of fire test	Day of fire test
w/p=0.30	58.9	72.3	77.8	4.78
	61.6	72.3	78.6	4.92
	59.8	70.5	78.4	4.90
Mean	**60.1**	**71.7**	**78.3**	**4.87**
w/p=0.40 no fibres	42.9	57.1	59.4	4.95
	43.3	54.5	61.1	5.17
	43.3	54.0	59.6	5.20
Mean	**43.2**	**55.2**	**60.0**	**5.11**
w/p=0.40 with fibres	36.2	50.9	58.0	4.74
	41.1	53.6	57.9	4.83
	37.1	56.3	59.9	4.95
Mean	**38.1**	**53.6**	**58.6**	**4.84**
w/p=0.55	27.2	33.9	37.1	5.32
	27.2	33.5	36.5	5.11
	22.3	33.0	37.4	5.11
Mean	**25.6**	**33.5**	**37.0**	**5.18**

The specimens were manufactured during September 25-26, 2003. Thereafter the specimens were stored unprotected in the laboratory hall until testing in December 2003 and January 2004. The temperature in the laboratory hall was approximately 20 °C and the relative humidity 50 % during that period.

Concretes for tunnel linings

The concrete recipes used in the production of the test specimens are shown in table 3. All these concretes had the same water-cement ratio, w/c-ratio = 0.38. The w/c-ratio of the concrete including silica, concrete C and D, was defined as:

$$w/c = \frac{W}{C + 2 \cdot S}$$

where W is the amount of water, C is the amount of cement and S is the amount of silica in weight per unit volume. Two different plastisizers were used, Glenum 51 and Peramin F. In the concretes named E and F was a lime filler designated Limus 40 used. Polypropylene fibres with a diameter of 18 μm were used in concretes B, D and F.

The compressive strength of the concrete was measured in accordance with the Swedish standard SS 13 72 10 close to the day of testing, i.e. the age of the concrete deviates from the one given in the standard. The same specimens were used for determination of moisture content. The moisture content was determined through weighing the specimens before and after seven days of drying in 105 °C. The measured strengths and moisture contents are shown in table 4.

Table 3. Concrete recipes.

	Recipe A	Recipe B	Recipe C	Recipe D	Recipe E	Recipe F
Cement (kg/m^3)	420	450	405	425	445	470
Silica (kg/m^3)	-	-	25	25	-	-
0-8 mm (kg/m^3)	965	940	943	919	900	869
8-16 (kg/m^3)	174	170	170	165	144	140
16-32 (kg/m^3)	682	664	667	650	644	625
Glenum 51 (kg/m^3)	2.0	2.0	2.0	2.0	2.3	2.0
Peramin F (kg/m^3)	1.0	1.0	0.75	1.0	0.75	1.0
Limus 40 (kg/m^3)	-	-	-	-	100	100
Fibrin (kg/m^3)	-	2.0	-	2.0	-	2.0
Water (kg/m^3)	159	171	171	180	171	180

Table 4. Compressive strength and moisture content of the different concrete recipes.

	Concrete recipe					
	A	B	C	D	E	F
	Compressive strength					
Mean value (MPa)	106.9	104.7	72.9	88.1	103.2	94.2
Standard deviation (MPa)	2.5	0.7	0.8	1.4	2.1	2.7
	Moisture content					
Mean value (%)	3.7	4.2	4.0	4.9	4.2	4.8
Standard deviation (%)	0.0	0.1	0.0	0.0	0.1	0.2

Six different specimen types (geometries) were manufactured ranging from small cubes up to large slabs with concrete for tunnel linings. Large slabs with the dimensions 1800 x 1200 x 400 mm^3 as well as small slabs with the dimensions 400 x 400 x 100 mm^3 were manufactured. Columns were manufactured with the dimensions 1000 x 200 x 200 mm^3. Two different sized cylinders were made. The cylinders had a diameter of 150 mm and lengths of 300 mm and 450 mm. Finally cubes with the dimensions 150 x 150 x 150 mm^3 were manufactured for fire tests and for tests to determine compressive strength and moisture content. All specimens of concrete for tunnel linings were cured under water for three months before testing. In Appendix A is a list presented giving the details for all specimens in the test series.

In addition to the non-tensioned reinforcement, plastic tubes with an inner diameter of 28 mm were placed longitudinally in the form. Five tubes were used in each specimen, with a distance of 240 mm between the tubes. Before the testing steel bars were placed in the tubes in which a pre-stress were applied. The cover of the non-tensioned reinforcement was 50 mm.

All large slabs were fire tested under mechanical loading. The loads were applied through pre-stressing. Steel bars were placed through the plastic tubes in the specimens in the longitudinal direction. The bars passed through two specimens and thus a coupling was made between these two specimens. Between the specimens a rock wool insulation with thickness 20 mm was placed. In each pair of coupled specimens, 5 steel bars with diameter 25 mm were applied. Each steel bar was loaded in tension with a force of 200 kN. Thus the total compressive force in the

concrete was 1000 kN. In order to distribute the load over the specimen surface a 1200 mm long steel beam designated HEB 300 was placed on each side. The force applied corresponds to a compressive stress in the longitudinal direction of 2.1 MPa.

The test specimens were cast during the period March 4, 2003 to April 9, 2003. A few days after the casting, the specimens were placed in a container filled with water. The container was placed in a conditioning chamber with constant temperature of 20°C. Hence all specimens were cured under water. During the time between casting and water storage the specimens were covered with a plastic foil. All specimens were removed from the water storage one week before the fire tests. Thereafter the specimens were stored in the fire laboratory until testing which took place in mid June, 2003.

Fire tests

Two different time-temperature curves were used. In the tests on concrete for tunnel linings a specially designed time-temperature curve was adopted, see figure 1. The curve was designed to simulate a fire in the trains assumed to be used in the City tunnel in Malmö, Sweden. The curve was theoretically determined by Ingason [2]. The curve include a heating phase as well as a cooling phase.

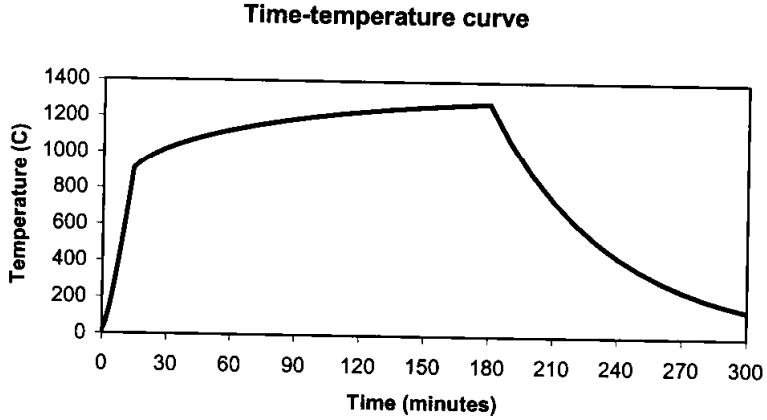

Figure 1. Specially designed time-temperature curve for the City tunnel in Malmö [2].

The full scale tests on the self-compacting concretes were performed in accordance with EN 1363-1, i.e. using the same standard time-temperature curve as defined in ISO 834. A heating phase of 60 minutes was used.

For the small scale tests made on small slabs a special small furnace was used. For all tests on the small furnace the ISO 834 curve was adopted. The furnace temperature was measured with a conventional thermocouple, i.e. not a plate thermometer as specified in EN 1363-1.

The fire exposed surface was for the large slabs 1500 x 1200 mm^2, the large beams 3000 x 600 mm^2, and for the small slabs 450 x 360 mm^2.

Measurements

Several different measurements were made on the specimens which are presented in ref. [1]. In the present article only the spalling will be covered. Two methods were used for measurement of spalling, one through weighing and one by measuring the actual depth of the scaled off material from the specimens. When measuring the spalling by weighing, the weight loss was calculated as:

$$weightloss = \left(1 - \frac{m_{after}}{m_{before}(1-u/(1+u)) - m_{fibres}}\right) \cdot 100\ \%$$

where m_{before} is the weight of the test specimen before the fire test, m_{fibres} is the weight of the polypropylene fibres, u is the initial moisture content, and m_{after} is the weight of the test specimen after the fire test. Initially the measured moisture content was used as input in the equation which caused some strange values. Negative amounts of spalling was observed in several cases. When fire testing concrete, some of the free water as well as some of the hydrate water will evaporate. Since it not has been possible to determine how much of the water in the specimens have evaporated due to the heating an estimation had to be done. Therefore the moisture content used when calculating the weight loss was not the same as the one measured on the separate cubes. The estimated amount of evaporated water was fitted in such way that the weight loss was set to zero for the specimens that did not show any visible spalling. This amount of water was then used for the other specimens in the same fire test. Since the amount of evaporated water will be different between the different specimens the calculated weight loss is not correct, but it is deemed to be a relative good estimate.

The depth of the scaled off material was measured by using a sliding calliper. A steel frame was mounted on the fire exposed face of the specimen and acted as a reference when measuring the spalling depth. The spalling was measured in a grid with a spacing of 100 mm. Due to the influence of the boundary on the spalling depth only measurements taken at least 300 mm from the boundary have been included. For the small slabs tested on the small furnace measurements were taken from 100 mm from the boundary. The results are presented as a mean spalling depth, the maximum spalling depth, and a characteristic spalling depth. The characteristic spalling depth was calculated as the upper 95 % fractile assuming a normal distribution.

TEST RESULTS

Self-compacting concretes

Tables 5-7 show the results obtained with self-compacting concrete. When calculating the weight loss of the large beams presented in table 5 the evaporated moisture was estimated to 2.8 % which gives no weight loss for specimen LS4011. For the large beams the evaporated moisture was estimated to 2.5 %.

When calculating the weight loss of the small slabs presented in table 6 the evaporated moisture was estimated to 0.5 % which gives no weight loss for specimen SS4013. It shall be noted that specimen SS3003, i.e. a small slab, has been omitted from the discussion since the test had to be shut down due to the spalled off material closed the channel of the burner. In the other tests the debris were continuously removed from the furnace. When calculating the weight loss of the

long cylinders presented in table 7 the evaporated moisture was estimated to 8.0 % which gives no weight loss for specimen LC4013.

Table 5. Test results large slabs.

Code	w/p	Fibres (kg/m^3)	Stress type	Stress level (MPa)	Fire curve	Mean spalling (mm)	Max spalling (mm)	Charact spalling (mm)	Weight loss (%)
Slabs 1800 x 1200 x 200 mm									
LS3001	0.30	0	Pre-stress, comp	8.8	Std	45	65	57	15.8
LS4001	0.40	0	Pre-stress, comp	8.8	Std	45	67	56	18.7
LS4011	0.40	1	Pre-stress, comp	8.8	Std	0	0	0	0.0
LS5501	0.55	0	Pre-stress, comp	8.8	Std	48	68	62	15.3
Beams 3600 x 600 x 200 mm									
LB4001	0.40	0	External bending	7.7	Std	8	40	21	3.1
LB4011	0.40	1	External bending	7.7	Std	0	0	0	0.0

Table 6. Test results small slabs.

Code	w/p	Fibres (kg/m^3)	Stress type	Stress level (MPa)	Fire curve	Mean spalling (mm)	Max spalling (mm)	Charact spalling (mm)	Weight loss (%)
SS3001	0.30	0	Non	0	Std	37	51	50	10.6
SS3002	0.30	0	Non	0	Std	31	52	48	9.5
SS3003	*0.30*	*0*	*External comp*	*2.5*	*Std*	*69*	*94*	*105*	*19.0*
SS3004	0.30	0	External comp	2.5	Std	102	175	186	32.1
SS4001	0.40	0	Non	0	Std	29	45	49	9.1
SS4002	0.40	0	Non	0	Std	26	36	38	7.9
SS4003	0.40	0	External comp	2.5	Std	93	167	170	27.5
SS4004	0.40	0	External comp	2.5	Std	111	180	193	32.5
SS4011	0.40	1	Non	0	Std	0	0	0	0.1
SS4012	0.40	1	Non	0	Std	0	0	0	0.1
SS4013	0.40	1	External comp	2.5	Std	0	0	0	0.0
SS4014	0.40	1	External comp	2.5	Std	0	0	0	0.1
SS5501	0.55	0	Non	0	Std	15	30	30	4.7
SS5502	0.55	0	Non	0	Std	20	34	34	5.2
SS5503	0.55	0	External comp	2.5	Std	76	125	132	26.9
SS5504	0.55	0	External comp	2.5	Std	57	113	117	16.6

Table 7. Test results long cylinders.

Code	w/p	Fibres (kg/m^3)	Stress type	Stress level (MPa)	Fire curve	Weight loss (%)
LC3001	0.30	0	Non	0	Std	1.6
LC3002	0.30	0	Non	0	Std	2.2
LC3003	0.30	0	External comp	5.3	Std	17.8
LC3004	0.30	0	External comp	5.3	Std	19.4
LC4001	0.40	0	Non	0	Std	2.1
LC4002	0.40	0	Non	0	Std	4.8
LC4003	0.40	0	External comp	5.3	Std	23.4
LC4004	0.40	0	External comp	5.3	Std	21.4
LC4011	0.40	1	Non	0	Std	1.6
LC4012	0.40	1	Non	0	Std	2.0
LC4013	0.40	1	External comp	5.3	Std	0.0
LC4014	0.40	1	External comp	5.3	Std	0.3
LC5501	0.55	0	Non	0	Std	1.6
LC5502	0.55	0	Non	0	Std	4.0
LC5503	0.55	0	External comp	5.3	Std	19.3
LC5504	0.55	0	External comp	5.3	Std	14.7

Concretes for tunnel linings

Tables 8-9 show the results from the tests of the large slabs and the small slabs. These results are the only available from the tests. A large number of small specimens were placed on the bottom of the large furnace during the fire tests. These small specimens were all covered with the spalled off debris from the large slabs, which later in the test melted. Thus it was not possible to analyse the small specimens tested at the same time as the large specimens.

When calculating the weight loss of the large beams presented in table 8 the evaporated moisture was estimated to be 2.8 % which gives no weight loss for specimen D2. When calculating the weight loss of the small slabs presented in table 9 the evaporated moisture was estimated to 2.8 % which gives no weight loss for specimen LS4011.

Table 8. Spalling of the large slabs.

Code	w/p	Fibres (kg/m^3)	Stress type	Stress level (MPa)	Fire curve	Mean spalling (mm)	Max spalling (mm)	Charact spalling (mm)	Weigh t loss (%)
A1	0.38	0	Pre-stress, comp	2.1	X2000	162	314	273	21.8
A2	0.38	0	Pre-stress, comp	2.1	X2000	127	227	213	16.9
Mean						*144*	*271*	*243*	*19.4*
B1	0.38	2	Pre-stress, comp	2.1	X2000	23	37	35	4.0
B2	0.38	2	Pre-stress, comp	2.1	X2000	8	38	28	1.8
Mean						*15*	*38*	*31*	*2.9*
C1	0.38	0	Pre-stress, comp	2.1	X2000	56	80	85	8.3
C2	0.38	0	Pre-stress, comp	2.1	X2000	61	76	78	9.7
Mean						*58*	*78*	*81*	*9.0*
D1	0.38	2	Pre-stress, comp	2.1	X2000	0	32	3	0.6
D2	0.38	2	Pre-stress, comp	2.1	X2000	0	7	2	0.0
Mean						*0*	*19*	*2*	*0.3*
E1	0.38	0	Pre-stress, comp	2.1	X2000	182	359	306	23.9
E2	0.38	0	Pre-stress, comp	2.1	X2000	84	130	116	12.5
Mean						*133*	*245*	*211*	*18.2*
F1	0.38	2	Pre-stress, comp	2.1	X2000	40	67	56	6.7
F2	0.38	2	Pre-stress, comp	2.1	X2000	33	57	54	5.0
Mean						*36*	*62*	*55*	*5.9*

Table 9. Test results small slabs.

Code	w/p	Fibres (kg/m^3)	Stress type	Stress level (MPa)	Fire curve	Mean spalling (mm)	Max spalling (mm)	Charact spalling (mm)	Weight loss (%)
A23	0.38	0	External comp	2.5	Std	18	35	27	12.5
B23	0.38	2	External comp	2.5	Std	0	0	0	0.2
C23	0.38	0	External comp	2.5	Std	13	23	19	9.4
D22	0.38	2	External comp	2.5	Std	0	0	0	2.3
D23	0.38	2	External comp	2.5	Std	0	0	0	0.3
E22	0.38	0	External comp	2.5	Std	29	48	44	18.9
E23	0.38	0	External comp	2.5	Std	19	32	29	14.4
F22	0.38	2	External comp	2.5	Std	0	0	0	0.6
F23	0.38	2	External comp	2.5	Std	0	0	0	0.0

DISCUSSION

Effect of specimen size and geometry

For specimens exposed to one face only, a very pronounced boundary effect can be seen, see figures 2-3. The spalling will show up as an "inverted pillow", i.e. the spalling takes place at the central area of the exposed surface and decreases when reaching the edges.

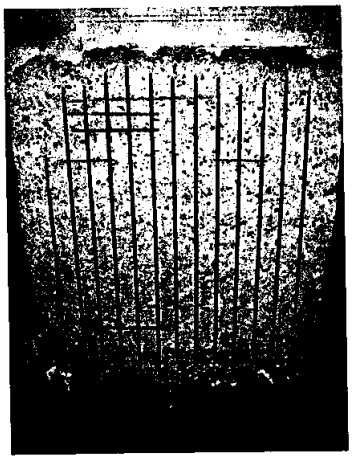

Figure 2. Large slab after test. Surface area 1800 x 1200 mm^2.

Figure 3. Small slab after test. Surface area 600 x 500 mm^2.

The small slabs were placed on the furnace supported on the outer 50 mm of the exposed face. As can be seen in figure 3 almost no spalling took place around the supporting boundary. Even if the boundary of the surface not was exposed to fire, the spalling should progress out on the sides if no boundary effects were present. It could also be noted that the spalling never passed through the specimen on the unexposed face. During the tests of the small slabs, cracks were formed on the sides as well as on the unexposed face, see figures 4-5. The spalling started after 10-15 minutes and the cracks on the sides were visible after 20-30 minutes. The cracks on the unexposed surface were observed later. A few minutes after the cracks were visible water was pouring out of them. Hence, an explanation to why the spalling never passes through the specimen is that the water and vapour easier can migrate out of the specimen when cracks have been formed.

Figure 4. Cracks on an unloaded small slab.

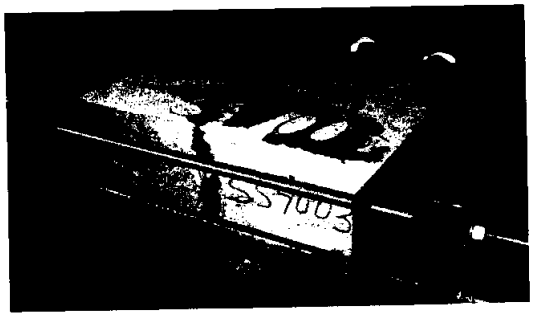

Figure 5. Cracks on a loaded small slab.

It was difficult to compare the spalling between cylinders and slabs. The cylinders had a shape of an hour-glass after the tests, which can be explained by the boundary effect discussed above. Due to the shape of the cylinders it was difficult to determine the spalling depth and therefore only weight loss was measured. For all self-compacting concretes, except the concrete including polypropylene fibers, the small slabs showed a significantly larger weight loss than the cylinders. The weight loss of the loaded cylinders were comparable with the weight loss of the large slabs. For all unloaded cylinders the weight loss was att approximately the same level, between 1.8 % to 3.8 %. The unloaded small slabs showed, as expected, a decreasing weight loss and spalling depth with increasing w/p-ratio.

When comparing the spalling between large and small slabs of tunnel concrete the weight loss was in most cases comparable. Although, the spalling depth was much smaller for the small slabs compared with the large slabs. This may also be due to boundary effects. The thickness of the small slabs was only 100 mm compared to the 400 mm thickness of the large slabs. Hence, it is more easy for the water/vapour to escape the small slabs which decreases the probability and amount of spalling.

Effect of loading conditions

Tests on both cylinders and slabs of self-compacting concrete showed a substantial effect of the loading on the amount of spalling. The load level was quite low on the small slabs, 2.5 MPa, and twice as high on the cylinders, 5.3 MPa. For the small slabs (except the concrete with fibres) the mean spalling depth was tripled by applying a small compressive load. The weight loss increased by a factor three to four by applying the compressive load. For the cylinders the weight loss increased by a factor 6 to 10 by applying the compressive load. If the greater difference on the weight loss between loaded and unloaded cylinders compared to the small slabs depend on the shape of the specimens or the higher load used on the cylinders is not possible to say. Although, a general opinion is that the probability and amount of spalling increases with increasing compressive stress.

The small slabs of self-compacting concrete spalled much more than the large. The stress level was more than three times higher in the large slabs and hence it was expected that they should spall more than the small slabs. This was not the case. Another unexpected fact was that the amount of spalling did not differ between the concrete recipes for the large slabs (expect the one with polypropylene fibres). The most probable explanation is that the concrete cover of the pre-stress wires spalled off early in the test and that thereafter the wires were heated and lost their stress and the large slabs could be considered unloaded. In other words, the large slabs spalled until the pre-stressed wires were exposed to fire after which the spalling stopped. Thus there were no difference in the amount of spalling between the different concrete recipes, and the amount of spalling of the large slabs were lower than the one for the small slabs.

CONCLUSIONS

A methodology for determination of spalling of concrete has been developed including a large scale reference specimen with a fire exposed surface of 1500 x 1200 mm^2 as well as a small scale specimen with a fire exposed surface of 450 x 360 mm^2. The latter is a fast and economic test enabling more tests for less money. It is, however, of great importance that a comparison of

the amount of spalling and the probability of spalling obtained with the small scale test is validated against the larger reference specimen.

The loading is important for the probability as well as the amount of spalling. The probability for spalling is much greater if the structure is compressed. The test results show that the compressive load shall be applied during the complete fire test in order to obtain a correct measure on the spalling. By using pre-stressing within the concrete specimens there is a probability that the compressive stress is lost during the test if the bars or wires are heated.

The amount of spalling is best measured as the depth of the spalling. Since it is more difficult to measure the spalling depth on a circular specimen, it is preferable to use specimens with a flat surface. An alternative method is to measure the spalling by the weight loss. The weight loss is, however, not recommended since it is difficult to compensate the measured weights for the loss of water during the test.

REFERENCES

[1] Boström L., *Innovative self-compacting concrete - Development of test methodology for determination of fire spalling*, SP Report 2004:06, Sweden, 2004.

[2] Ingason H., *Time-temperature curves for X2000 and the Öresund trains*, Report P003814, Borås, 2000 (in Swedish)

Appendix A - Summary of test specimens

Code	Geometry (mm)	Type of iller	w/p	Fibres (kg/m^3)	Specimens	Stress type	Stress level (MPa)	Fire curve
Self-compacting concretes								
LS3001	1800x1200x200	Lime	0.30	0	1	Pre-stress, comp	8.8	Std
LS4001	1800x1200x200	Lime	0.40	0	1	Pre-stress, comp	8.8	Std
LS4011	1800x1200x200	Lime	0.40	1	1	Pre-stress, comp	8.8	Std
LS5501	1800x1200x200	Lime	0.55	0	1	Pre-stress, comp	8.8	Std
LB4001	3600x600x200	Lime	0.40	0	1	External bending	7.7	Std
LB4011	3600x600x200	Lime	0.40	1	1	External bending	7.7	Std
SS3001-SS3002	600x500x200	Lime	0.30	0	2	Non	0	Std
SS3003-SS3004	600x500x200	Lime	0.30	0	2	External comp	2.5	Std
SS4001-SS4002	600x500x200	Lime	0.40	0	2	Non	0	Std
SS4003-SS4004	600x500x200	Lime	0.40	0	2	External comp	2.5	Std
SS4011-SS4012	600x500x200	Lime	0.40	1	2	Non	0	Std
SS4013-SS4014	600x500x200	Lime	0.40	1	2	External comp	2.5	Std
SS5501-SS5502	600x500x200	Lime	0.55	0	2	Non	0	Std
SS5503-SS5504	600x500x200	Lime	0.55	0	2	External comp	2.5	Std
LC3001-LC3002	Ø 150, l=450	Lime	0.30	0	2	Non	0	Std
LC3003-LC3004	Ø 150, l=450	Lime	0.30	0	2	External comp	5.3	Std
LC4001-LC4002	Ø 150, l=450	Lime	0.40	0	2	Non	0	Std
LC4003-LC4004	Ø 150, l=450	Lime	0.40	0	2	External comp	5.3	Std
LC4011-LC4012	Ø 150, l=450	Lime	0.40	1	2	Non	0	Std
LC4013-LC4014	Ø 150, l=450	Lime	0.40	1	2	External comp	5.3	Std
LC5501-LC5502	Ø 150, l=450	Lime	0.55	0	2	Non	0	Std
LC5503-LC5504	Ø 150, l=450	Lime	0.55	0	2	External comp	5.3	Std
Concretes for tunnel linings								
A1-A2	1800x1200x400	-	0.38	0	2	Pre-stress, comp	2.1	X2000
B1-B2	1800x1200x400	-	0.38	2	2	Pre-stress, comp	2.1	X2000
C1-C2	1800x1200x400	Silica	0.38	0	2	Pre-stress, comp	2.1	X2000
D1-D2	1800x1200x400	Silica	0.38	2	2	Pre-stress, comp	2.1	X2000
E1-E2	1800x1200x400	Lime	0.38	0	2	Pre-stress, comp	2.1	X2000
F1-F2	1800x1200x400	Lime	0.38	2	2	Pre-stress, comp	2.1	X2000
A5-A9	150x150x150	-	0.38	0	4	Non	0	X2000
B5-B9	150x150x150	-	0.38	2	4	Non	0	X2000
C5-C9	150x150x150	Silica	0.38	0	4	Non	0	X2000
D5-D9	150x150x150	Silica	0.38	2	4	Non	0	X2000
E5-E9	150x150x150	Lime	0.38	0	4	Non	0	X2000
F5-F9	150x150x150	Lime	0.38	2	4	Non	0	X2000
A10-A11	1000x200x200	-	0.38	0	2	Non	0	X2000
C10-C11	1000x200x200	Silica	0.38	0	2	Non	0	X2000
D10-D11	1000x200x200	Silica	0.38	2	2	Non	0	X2000
A12-A14	Ø 150, l=450	-	0.38	0	3	Non	0	X2000
C12-C14	Ø 150, l=450	Silica	0.38	0	3	Non	0	X2000
D12-D14	Ø 150, l=450	Silica	0.38	2	3	Non	0	X2000
A18-A20	Ø 150, l=300	-	0.38	0	3	Non, External comp	0, 2.1	X2000, spec
B18-B20	Ø 150, l=300	-	0.38	2	3	Non, External comp	0, 2.1	X2000, spec
C18-C20	Ø 150, l=300	Silica	0.38	0	3	Non, External comp	0, 2.1	X2000, spec
D18-D20	Ø 150, l=300	Silica	0.38	2	3	Non, External comp	0, 2.1	X2000, spec
E18-E20	Ø 150, l=300	Lime	0.38	0	3	Non, External comp	0, 2.1	X2000, spec
F18-F20	Ø 150, l=300	Lime	0.38	2	3	Non, External comp	0, 2.1	X2000, spec
A21-A23	400x400x100	-	0.38	0	3	Non, External comp	2.5	X2000, Std
B21-B23	400x400x100	-	0.38	2	3	Non, External comp	2.5	X2000, Std
C21-C23	400x400x100	Silica	0.38	0	3	Non, External comp	2.5	X2000, Std
D21-D23	400x400x100	Silica	0.38	2	3	Non, External comp	2.5	X2000, Std
E21-E23	400x400x100	Lime	0.38	0	3	Non, External comp	2.5	X2000, Std
F21-F23	400x400x100	Lime	0.38	2	3	Non, External comp	2.5	X2000, Std

SPALLING OF CONCRETE – AN OVERVIEW OF ONGOING RESEARCH IN THE NETHERLANDS

A.J. Breunese, TNO Building and Construction Research, the Netherlands
J.H.H. Fellinger, TNO Building and Construction Research, the Netherlands

ABSTRACT

TNO Centre for Fire Research, the Netherlands, has been involved in many research projects on the subject of spalling of concrete. Over recent years a large number of fire tests on concrete segments have been done, and from these tests a phenomenological understanding of spalling has been obtained. For the future, a more fundamental approach must be chosen to gain understanding of the mechanisms that cause spalling.
Spalling is an umbrella term, covering different damage phenomena that may occur on a concrete structure during fire. These phenomena are caused by different mechanisms: pore pressure, thermal gradient, internal thermal micro-cracking, cracking around reinforcement bars and strength loss due to chemical transitions. In different combinations of these mechanisms, possible spalling phenomena include violent spalling, progressive gradual spalling and explosive spalling.
Models have been developed that provide qualitative insight in the fundamentals of the different forms of spalling. For a quantitative prediction of spalling however, there is insufficient scientific knowledge. Further fundamental research will be carried out in the years to come.
This paper shows results of the models that are being developed, and some conclusions are drawn with regard to spalling mechanisms.

KEYWORDS: *Spalling of concrete, concrete structures, fire resistance, high temperature, spalling research*

INTRODUCTION

In recent years, spalling of concrete during fire has caused severe damage to many structures, including tunnels and car parks. Spalling of concrete is not well understood, and therefore poses a risk to human life and economy. Especially newly developed types of concrete such as HPC and SCC, Boström (2002), have shown to be sensitive to the spalling problem, which hampers the application of these new concrete types.

Although mitigating measures are at hand (insulation of the concrete by a heat-resistant coating, mix design with polypropylene fibres, etc.), the scientific knowledge on spalling is still insufficient to explain the phenomenon. Hence all measures are to be designed on the basis of largely empirical knowledge. TNO Centre for Fire Research has been actively investigating the concrete spalling phenomenon for many years, and a large number of tests have been done. From these tests a phenomenological understanding of spalling has been obtained.

It is difficult to take effective measures against spalling as long as the fundamentals (i.e. the effectiveness) of measures are not well understood. Polypropylene fibres allow for escape of moisture, and external fire protection reduces thermal gradients and absolute temperatures. However, if one doesn't know which mechanism will cause spalling in a specific case, it is hard to choose the right measure. A combination of external protection and PP-fibres might avoid all types of spalling, but taking two measures is expensive.

Although doubtful, in most building codes it is assumed that normal strength concrete does not spall during a standard (ISO-834) fire. For other curing and fire conditions, at this moment only a (duplicate) full-scale test can confirm the fire resistance of a concrete structural element.

Most of the available more fundamental spalling research focuses on only one mechanism (usually moisture pressure or thermal gradients). Instead of attributing the various spalling phenomena to one or two mechanisms, spalling of concrete should be assessed considering all known mechanisms.
Traditionally, "spalling" is an umbrella term for different types of concrete damage during fire, which makes it impossible to draw general conclusions. Instead of considering spalling of concrete as one phenomenon, each type of spalling should be considered separately, Khoury (2003).

At TNO Building and Construction Research, Centre for Fire Research, a research programme has been started, in which many aspects of spalling of concrete will be fundamentally investigated. The research includes large numbers of fire tests, that will serve as a parameter study of the spalling phenomenon. It also includes thorough theoretical study and modelling work, in which the test results will be used as validation material.

Theoretial research has so far produced interesting insights in different spalling phenomena and their underlying mechanisms. Seemingly contradictory test results may be better understood with the description of mechanisms and spalling types. The paper gives an overview of the current understanding of the spalling phenomenon, and outlines the research programme that will be under way for the next few years.

SPALLING TYPES AND MECHANISMS

The observations of spalling of concrete during fire tests cover a wide range, in random order: observation of spalling with slow (1°C/min.) or fast (250°C/min.) heating, from gradual to explosive spalling, cracking along or through aggregate grains, spalling in the beginning of the fire or after some time, stopping after some time or progressing, stopping at the reinforcement level or continuing far beyond it, and so on. In the paragraphs below the most important observed spalling phenomena are described and related to these mechanisms.

During heating, stresses develop inside the concrete cross-section. Thermal gradients and moisture pressure lead to mechanical stresses that may cause cracking as well as spalling of concrete. Figure 1 gives a schematic view of stresses in a heated concrete wall.

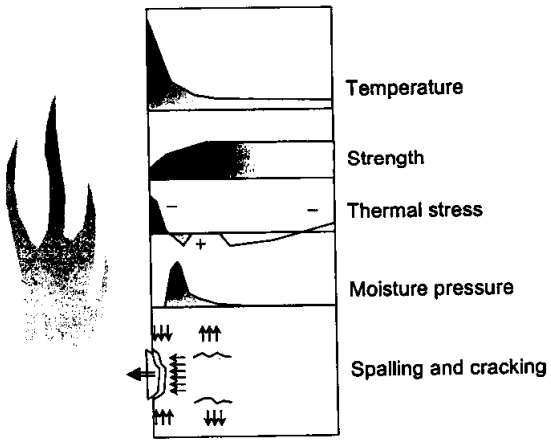

Figure 1: stresses in heated concrete

When one side of the wall is heated, a temperature distribution develops as shown in figure 1. At high temperatures, internal cracking and dehydration lead to strength loss. Due to the thermal gradient, the fire exposed surface will be in compression parallel to the surface, while the colder parts are in tension, and possibly cracked perpendicular to the surface. Depending on the amount of restraint, the back of the wall may be in compression or tension. Near the fire exposed surface, moisture will evaporate. In the colder zone, the moisture cannot escape directly and a pressure peak will develop. This pressure peak will move inward during the fire and will probably increase in size due to accumulation of moisture.
These mechanisms are widely recognised, but calculation methods have not yet advanced sufficiently for calculation of the chance, amount, speed or type of spalling in practical situations.

Often when concrete is damaged in a real fire the damage is called spalling. In many cases this is not correct; other failure mechanisms such as shear failure can also lead to severely damaged concrete. "Real" spalling can occur in different forms, each of which is caused by a specific combination of the mechanisms shown in figure 1.

Violent Spalling

Violent spalling is the separation of small or larger pieces of concrete from the cross section, during which energy is released in the form of popping off of pieces and small slices with a certain speed, and also a popping or cracking sound. This type of spalling is caused by pore pressure and thermal gradients; internal cracking on the meso-level also influences this spalling process. The surface compression during heating can increase due to lateral restraint, reinforcement, prestressing, external loading, large concrete thickness and a high heating rate.

Pore pressures are dependent on heating rate, moisture content, permeability, porosity and the presence of polypropylene fibres (artificial permeability). The typical crack pattern that is observed in tests in which violent spalling occurs, is a pattern with slices of concrete parallel to the fire exposed surface, see figure 2.

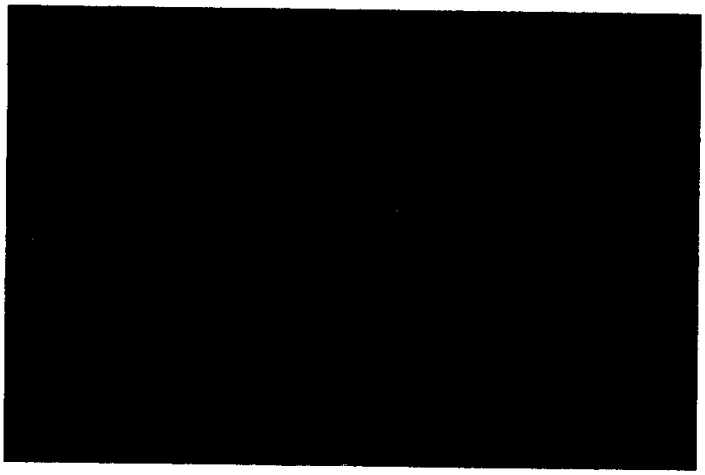

Figure 2: spalled surface after violent spalling; slices still visible in crack pattern

Progressive Gradual Spalling (Sloughing Off)

Sloughing off is the form of spalling that is caused by strength loss due to internal cracking (meso-level) and chemical deterioration of the cement paste (micro-level). This type of spalling is related to the attained temperature of the concrete (instead of heating rate). If the concrete is heated to a very high temperature the strength will be too low to carry its own weight, causing small pieces of concrete to fall down without much sound. This type of spalling is likely to occur on a slab heated from below, since gravity will pull the cracked pieces of concrete from the cross-section.

Explosive Spalling

Explosive spalling is the result of a combination of rising pore pressures and thermal gradients in the cross-section. At the front of heat penetration, an area with high pore pressure develops inside the concrete. Part of the moisture is pushed further into the colder part of the concrete due to the pressure gradient. If the heated surface is under compression due to a thermal gradient the complete heated surface may be blown away with a loud bang.

This type of spalling is especially likely to occur on structural members heated from more than one side, such as columns and beams. When high moisture levels are advancing into the concrete from all heated sides, at some point in time the moisture pressure peaks will meet in the centre of the cross-section, giving a sudden rise in pore pressure which may cause large parts of the cross-section to explode. This type of spalling can also occur after a considerable duration of the fire if the concrete surface has been protected with an insulating layer, Both (1999) or if the heating rate was low, Wong (2004). The time at which this explosion occurs is dependent on the

dimensions of the cross-section, the permeability, the heating rate and the saturation degree. It is very well possible that there is no warning that explosive spalling is going to occur; even a seemingly perfectly intact cross-section may suddenly explode, Bengtsson (1997).

MODELLING

For a fundamental understanding of the spalling problem, different models have been developed. In this paper, a meso-level thermomechanical model is presented as well as a theoretical model for calculation of the pressure in a closed pore. Both models have a limited range of applicability due to the many assumptions and simplifications, but nevertheless they provide interesting insight in spalling of concrete.

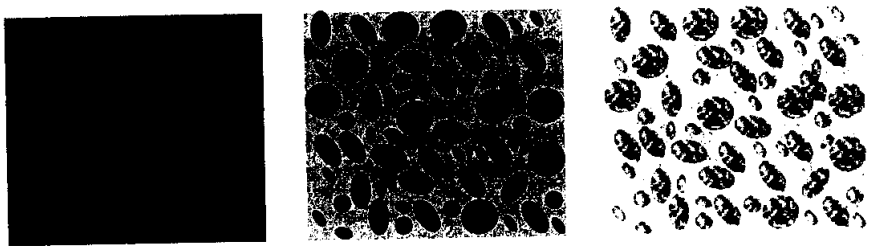

Figure 3: macro, meso and micro level

In general, concrete can be considered at three levels, see also figure 3:

- Macro-level: concrete considered as a grey homogeneous material with uniformly distributed material properties. On this level, the thermal stresses that result from the thermal gradients over the cross section must be considered, taking into account the actual geometry, support conditions and loading configuration.
- Meso-level: concrete considered as a mix of aggregate and cement paste, each with it's own material properties. On this level, the cracking due to differential thermal expansion between aggregate, mortar and reinforcement must be considered.
- Micro-level: cement paste, aggregate particles or interface layers considered as a mix of chemical constituents. On this level, the pore pressures and the degradation of mechanical properties due to chemical transitions and dehydration must be considered.

Thermomechanical behaviour

The thermomechanical model represents a vertical core inside a concrete floor slab which is heated from below. The model is 2-dimensional and near the fire exposed surface a small area has been modelled with separate behaviour of aggregate grains, cement mortar and interface zones. The circular aggregate grains are randomly positioned, and projected on a random triangular element mesh, see figure 4. At the locations of the interface zones between aggregate grain and cement mortar, small elements are created to simulate the interface zone. This produces a finite element mesh as shown in figures 4 and 5.

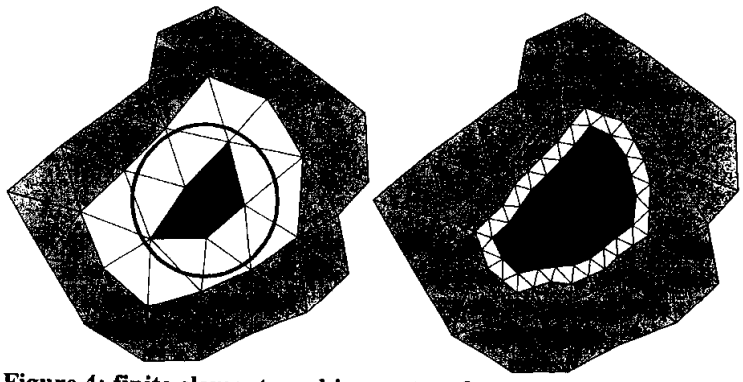

Figure 4: finite element meshing system for the meso-level model

Breunese (2001) showed that this meso-model is able to predict a realistic temperature-dependent stress-strain behaviour under tension, by calculating the crack formation on a meso-level which leads to strength loss on a macro-level. Therefore, temperature-dependent strength loss is not explicitly input in the model as a material property, but follows from the cracks that occur due to differences in thermal expansion between aggregate grains and cement mortar.

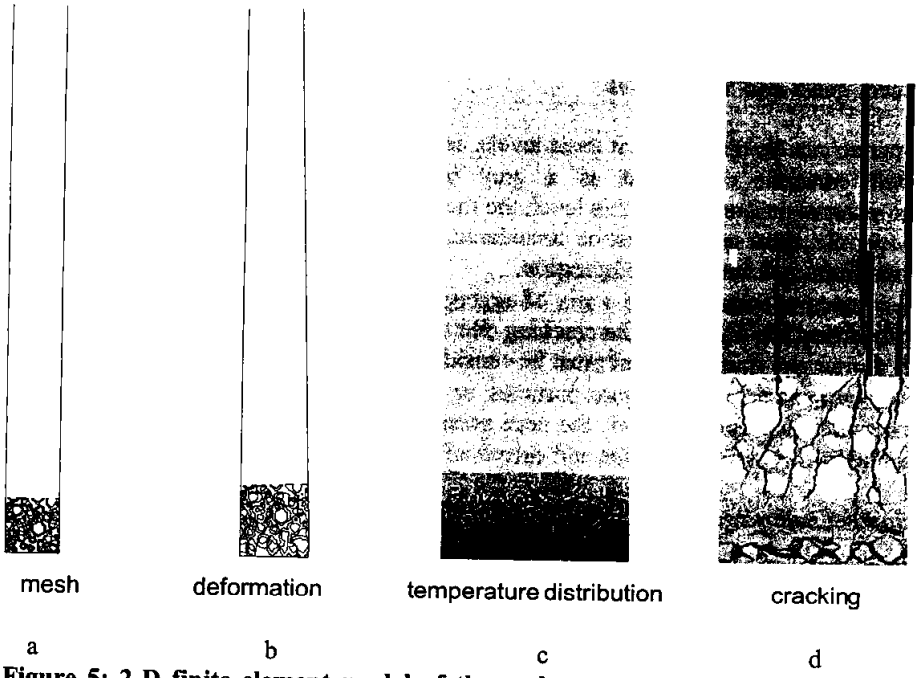

Figure 5: 2-D finite element model of thermal stresses and cracking in a concrete floor slab. The model represents a vertical core inside the slab, which is heated from below. The fire exposed area has been modelled with aggregate grains, cement mortar and interface zones separately.

Figure 5d shows a crack pattern that is often found in fire exposed concrete. In the heated area cracks develop parallel to the surface, and in the colder parts of the cross section vertical cracks occur. The cracks follow the interface zones in the particle structure.
The cracks parallel to the surface may cause the concrete surface to peel off in slices, which is observed during fire tests as the violent surface spalling type. The violent popping off of the slices however suggests an energy release that is probably caused by the combination of thermal cracking and the release of pore pressure due to moisture evaporation.

Pore pressure

The development of pore pressure can be better understood by calculation of the thermodynamic equilibrium in a pore inside the concrete. Thermodynamic equilibrium is the distribution of water over liquid and gas, depending on temperature, pressure and volume.

In a pore in real concrete, different material phases are present:

- air gas, which is present in the pores,
- capillary water, which is present in the pores in liquid and gaseous form, and gradually evaporates during heating (dependent on permeability),
- physically bound water, which is adsorbed to the pore walls, and will only start evaporating after the capillary water has evaporated, and
- chemically bound water, which is released during heating due to dehydration of the cement paste.

A simple model calculates the thermodynamic equilibrium, taking into account only air gas and capillary water in liquid and gaseous form. This model shows the dependency of pore pressure on the saturation degree and temperature.
It is assumed that as an initial condition at 20°C, a certain amount of water is present in a pore. Added to this amount of water is an amount of air, resulting in atmospheric pressure (0.1 MPa). The air is in gaseous phase, the water partly in liquid and partly in gaseous phase. For simplicity, it is assumed that the pore size is constant. Capillary pressure is only in the order of 0.1 MPa or smaller (depending on the pore radius) and therefore has been neglected. Inclusion of the capillary pressure does not influence the results significantly, which was also shown with the model.

When the pore is heated, the equilibrium between gaseous and liquid water will change, and the pressure will rise. The saturation pressure is followed until the pore is either filled entirely with liquid water or gaseous water.

While the temperature rises, the liquid water expands thermally. Therefore the available volume for the gases reduces. At the same time the saturation pressure increases which means that the allowable concentration of vapour in air increases. Below a saturation degree of 0.31 mg/mm^3, ultimately all water will evaporate and only gases are present in the pore. Above this saturation degree, eventually all water will condensate and only liquid water is present.

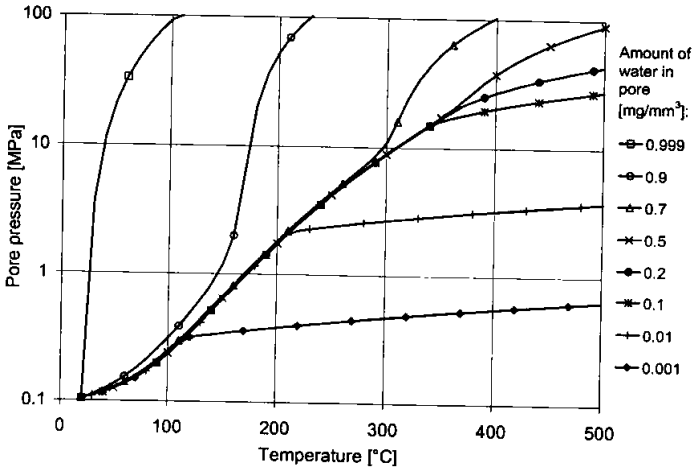

Figure 6: pore pressure dependent on temperature and saturation degree

When a pore becomes entirely filled with gases, the pressure increase with temperature is minimal, because the gas is easily compressible. On the contrary, when a pore becomes entirely filled with liquid water, the pore pressure rises rapidly due to the incompressibility of the liquid. Therefore it is concluded that in fact moisture pressure which leads to spalling is not a vapour (gaseous water) pressure but a liquid water pressure.

If the pore was almost completely filled with water initially, the pressure will rise as soon as the entire pore is filled, which is the case at a very small temperature increase already. After this the pore pressure rises dramatically, see the line for 0.999 mg/mm^3 in figure 6. On the other hand, in a pore that is almost completely filled with air and only a little bit of water, the pressure will hardly increase after all water has transferred to the gaseous phase, see the line for 0.001 mg/mm^3.

Figure 6 clearly shows why it is possible that in some cases spalling is observed at temperatures of only 100 to 200°C. Depending on the saturation degree, the pore pressure may rise to levels far beyond 10 MPa.
In the case of explosive spalling, moisture is pushed inward into the concrete, and therefore the saturation degree inside the concrete will only increase during heating. Figure 6 shows that this involves an enormous pressure rise.

It must be noted that the pore pressure cannot be directly compared to the tensile strength of concrete. Since the pore volume is only fractional compared to the total concrete volume, a high pore pressure will only lead to limited tensile stresses in the solid matrix of the concrete.
Still, pore pressures can theoretically rise to levels much higher than the tensile strength of most concrete types. When this leads to a tensile crack, the energy that was present in the compressed water is suddenly released, leading to the violent popping off of pieces of concrete or even the explosion of a complete cross-section.

Not only is the thermomechanical cracking process influenced by the development of pore pressures. At the same time, thermomechanical cracks can strongly influence moisture transport inside the concrete. The apparently random occurrence of explosive spalling can be explained

by the tensile crack that occurs in the cold zone due to a thermal gradient. When this crack occurs, the moisture is allowed to escape, and explosive spalling may be prevented. Therefore the randomness is probably related to the randomness of formation of these tensile cracks, see also Wong (2004). External restraint or compression of the concrete structure can prevent these cracks and therefore may lead to explosive spalling.

Future research

For a complete understanding, it is necessary to couple pore pressure, moisture transport and dehydration with thermomechanical behaviour, cracking and strength loss. The research that will be undertaken by TNO and other partners in the coming years will therefore focus on the micro-, meso- and macro-levels, on which all of these mechanisms act. For validation and calibration of the models a large number of tests will be carried out within different research programmes in which TNO participates. In the planned research, areas of attention are:

1. gradual progress on (coupled) modelling of moisture flow, heat flow and mechanical behaviour,
2. improvement of spalling test methods, and
3. finding relations between spalling and concrete constituents, fire type and mechanical loading.

CONCLUSIONS

Spalling of concrete is a problem that has large consequences for the economic development. Severe damage due to spalling results in possible collapse of buildings, and a long non-operational time of tunnels after a fire.
Mechanisms that cause spalling are pore pressures, thermal gradients, internal cracking, reinforcement bars and chemical transitions. Spalling is an umbrella name for different phenomena; each phenomenon is caused by a certain combination of mechanisms.

Models have been developed that provide qualitative insight in the fundamentals of the different forms of spalling. Cracking patterns and strength loss due to thermal gradients and differences in thermal expansion between aggregate grains and cement mortar can be calculated with finite element models.
The calculated crack patterns correspond very well to the ones found in fire tests, and the models show that the interaction between cracking on the meso-level due to differences in thermal expansion and on the macro-level due to thermal gradients is very important for understanding spalling of concrete.

A simple model of a closed pore gives clear indications on the possible development of pore pressure depending on saturation degree and temperature. The model shows that the pore pressure can increase orders of magnitude when all water is in liquid form, because the liquid water is relatively incompressible. Therefore the relevant pore pressure as a possible cause of spalling is in fact liquid pressure.

For a quantitative prediction of spalling, there is insufficient scientific knowledge. All mitigating measures against spalling are based upon empirical knowledge and lack a fundamental basis. To deal with the spalling problem in future, it is necessary to gain more

insight in the mechanisms that cause spalling. Only with this knowledge it is possible to understand the working of mitigating measures, enabling the designer to use the available measures effectively.

The presented models, that are currently being developed, need to be improved, coupled, validated and calibrated. Other concrete properties than just the compressive strength are needed as input for these models. Therefore, temperature-dependent material properties such as permeability and tensile strength need to be determined by testing, and large numbers of spalling tests must be done to validate and calibrate the models.
Especially the apparent randomness of spalling occurrence will be difficult to model, and a probabilistic approach may be required.

REFERENCES

Bengtsson, O. (1997). *Brandpåverkade betongbalkar med slanka tvärsnitt, Brandforsk projekt 273-941,* SP report 1997:35

Boström, L. (2002). *The performance of some self compacting concretes when exposed to fire,* SP report 2002:23

Both, C., Wolsink, G.M. and Breunese, A.J. (2003). Spalling of concrete tunnel linings in fire. *(Re)Claiming the Underground Space, proceedings of the ITA world tunnelling congress 2003,* 227-232, A.A. Balkema Publishers

Breunese, A.J. (2001). *Tensile properties of concrete during fire,* TNO report 2001-CVB-R04634

Breunese, A.J. and Fellinger, J.H.H. (2003). Tensile properties of concrete during fire, *Advances in Cement and Concrete, proceedings of a conference held at Copper Mountain, Colorado, USA,* 293-302, Engineering Conferences International

Fellinger, J.H.H. (2004). *Shear and Anchorage Behaviour of Fire Exposed Hollow Core Slabs,* dissertation, Delft University Press (to be published)

Fellinger, J.H.H. and Both, C. (1997). *Small scale fire test in determining the sensitivity to spalling of concrete samples of various mixtures subjected to RWS heating curve,* TNO report 97-CVB-R1463

Khoury, G.A. (2003). *Course on effect of heat on concrete: Spalling*, CISM, 9-13 June 2003, Udine, Italy

Wong, Y.L. (2004). Spalling of concrete under fire, *International seminar on recent developments of fire protection in structures, 19 February 2004, Hong Kong*, The Hong Kong Institute of Steel Construction

HIGH-TEMPERATURE EXPERIMENTS ON MODEL –SCALE CONCRETE SLABS AT HIGH DISPLACEMENT

Samantha J. FOSTER [1], Ian W. BURGESS and Roger J. PLANK

University of Sheffield, Mappin Street, Sheffield S1 3JD, United Kingdom
([1]s.j.foster@sheffield.ac.uk)

ABSTRACT

Large-scale fire tests in the multi-storey steel framed building at Cardington have shown large reserves of fire resistance in unprotected composite floor systems. These tests showed that the floor system does not collapse, even at very large deformations. The enhanced resistance is attributed to membrane forces which assist in maintaining the structural integrity through diaphragm action. The Building Research Establishment in the UK has since developed a new design method for composite floors in fire, based on a simplified model of the membrane action of rectangular slabs. Small-scale tests have been carried out at ambient temperature, and the experimental results compare well with the design method and are generally conservative. The experimental work has recently been extended to tests of loaded small-scale slabs at elevated temperatures. This paper presents the results from a number of such tests conducted on horizontally unrestrained slabs. The purpose of these tests is to investigate the influence of thermal curvature on the failure mechanisms of rectangular slabs, since this is not explicitly allowed for in the simplified design method. The more detailed issues being studied include the effects of reinforcement percentage and reinforcement bond strength at high temperatures on the final integrity failure due to tensile cracking. Observations from the high-temperature tests have shown that the mechanism of failure differs from that assumed in the simplified design method. The observed slab behaviour at high temperatures is that high double-curvature deflection is created quickly, and this leads to full-depth cracking across the short span of the slab, but the association with a yield-line mechanism is much less obvious. Some numerical modelling studies have accompanied the testing, and comparisons have been made with the simplified design method.

KEYWORDS: *Tensile membrane action, reinforced concrete slabs, fire performance, high temperature experiments*

INTRODUCTION

During 1995 and 1996, six localised fire tests [1] were conducted on the full-scale, eight storey, steel-framed building at the Building Research Establishment's Cardington Laboratory. These large-scale fire tests were conducted to investigate the behaviour of compartments of different sizes at various locations within the building. These tests have shown that unprotected composite floor slabs have large reserves of fire resistance. The enhanced fire resistance is attributed to membrane forces which assist in maintaining the structural integrity though diaphragm (or tensile membrane) action.

Current structural fire design codes [2] assume that a composite slab acts as a one-way spanning beam between parallel secondary beams, resisting loads through bending and shear, and as the compression flange of the composite beams themselves. Although this design method is simple, it ignores any beneficial effect deriving from tensile membrane action in the floor slabs at large displacements. This implies that the current codified design method is not addressing the true structural behaviour of the building during a fire.

Significant experimental and theoretical work [3-7] has been carried out on the behaviour of concrete floor slabs at ambient temperature when subject to large deflections. The work showed that the concrete slabs could support loads in excess of the well-known yield-line failure load. The mechanism of the enhancement was shown to be tensile membrane action, which can form within the slab irrespective of whether its boundaries are restrained or unrestrained in the horizontal sense.

Following the fire tests at Cardington a simplified design method [8] was developed based on principles taken from previous research work on tensile membrane action carried out in the late 1960s. The simple design method was a significant improvement on previous methods, which were limited to flexural behaviour. The new design method divides the floor system into square or rectangular slab panels, which are surrounded by protected support beams which usually lie on the column grid-lines. During the late stages of a fire the applied load is mainly supported by membrane action in the composite slab. One of the major assumptions in the design method is that the slab reinforcement over the protected beams fractures during the fire due to a combination of high hogging curvature and membrane tension. This assumption is conservative since, if the reinforcement were to remain intact, the induced tensile membrane forces within the slab would be much higher. A slab is assumed to be horizontally unrestrained, so that the tension field in the central region of the slab is balanced only by the compressive in-plane forces around its perimeter. This simple design method was initially limited to isotropic reinforcement, but has recently been extended to incorporate orthotropic arrangements of reinforcement [9-10]. A series of experiments was conducted by the author on horizontally unrestrained concrete slabs, with both isotropic and orthotropic reinforcement. The influence of bond was investigated by comparing the results from slabs using smooth and deformed (ribbed) reinforcing bars. The slabs were tested at ambient temperature to verify the assumptions made in the simple design method. However, it can not be assumed that the basic behaviour observed at ambient temperature will necessarily remain the same at elevated temperatures. The test series has been extended to investigate the slab and bond behaviour under elevated temperatures, in order to further understand the mechanics of the membrane action and to provide comparisons with the simple design method.

This paper presents the results from the first series of experiments on horizontally unrestrained concrete slabs with varying percentages of isotropic reinforcement, under elevated temperatures. Further tests will be carried out on orthotropic reinforcement at a later stage. The influence of bond between the reinforcement bars and concrete at elevated temperature is considered by comparing the results from slabs using smooth and deformed (ribbed) reinforcing bars.

SIMPLE DESIGN METHOD

The new equilibrium method considers a mode of failure that was observed in many ambient-temperature tests, mainly conducted on flat slabs, whose cracking pattern is illustrated in Fig. 1.

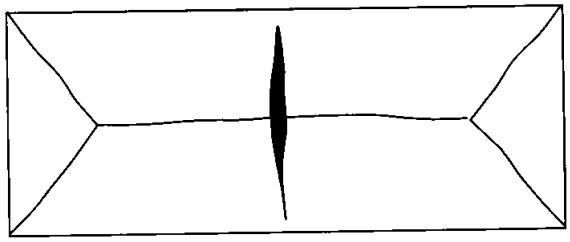

FIGURE 1: Cracking pattern observed in slabs due to tensile membrane action.

The typical model of failure in these tests, following tensile membrane action, was due to localised cracking through the full depth of the slab forming across the shorter span. This resulted in reinforcement fracture along these cracks and, although structural stability was not generally lost, the integrity of the fire compartmentation was breached.

The full derivation of the simple design method for isotropic and orthotropic reinforcement has been published [9] and will not be repeated here. The simple design method for fire conditions is based on rigid-plastic behaviour with the assumption that the mode of failure remains the same as at ambient temperature.

NUMERICAL MODELLING

Numerical studies have been carried out using the University of Sheffield software *Vulcan*. The numerical software has been developed over recent years for 3-D analysis of the structural behaviour of composite and steel-famed buildings in fire [11-12]. *Vulcan* uses the Mindlin/Reissner (thick plate) theory, and thermal expansion, cracking, geometric and material non-linearities are taken into account. Three dimensional models have been created of the model-scale slabs (Fig. 2).

The concrete elements used are quadrilateral 9-noded shell elements. The slab elements are sub-divided into 10 layers of which 8 layers represent the concrete and two layers the steel reinforcement. The reordered temperatures through the depth of the slab have been used to calculate the temperature history for each layer. The reinforcing steel bars are modelled by a smeared layer approach, the thickness of the layer being set so that its cross-sectional area is equal to the total cross-sectional area of slab reinforcement and the layer's stress properties are

set as uniaxial in the direction of the bars. Perfect bond is assumed between the reinforcing steel layers and the surrounding concrete. The Eurocode 4 part 1.2 [13] concrete material properties were used together with the concrete strengths measured on the day of the test and the yield strength of the reinforcing wire.

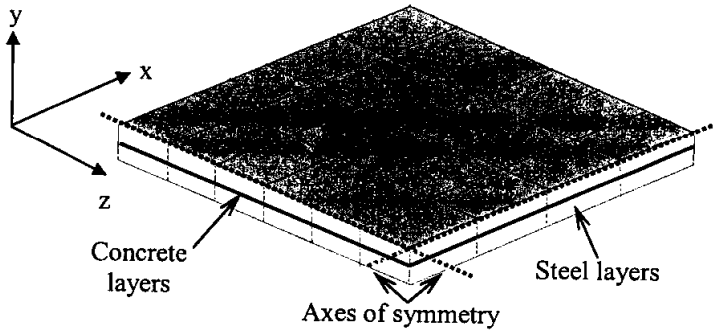

FIGURE 2 : Typical configuration of model-scale slab mesh

TEST CONFIGURATION AND INSTRUMENTATION

Two sizes of slab were tested, whose nominal dimension (in mm) were 920x620x15 and 920x620x22, with the supported area being 850x550. The actual depth of the slab varied slightly between tests, and measurements were made after each test. The test setup in these experiments is very similar to the previous tests at ambient temperature [10]. The slabs were tested in a loading rig in which constant loads were maintained at 12 points (Fig. 3).

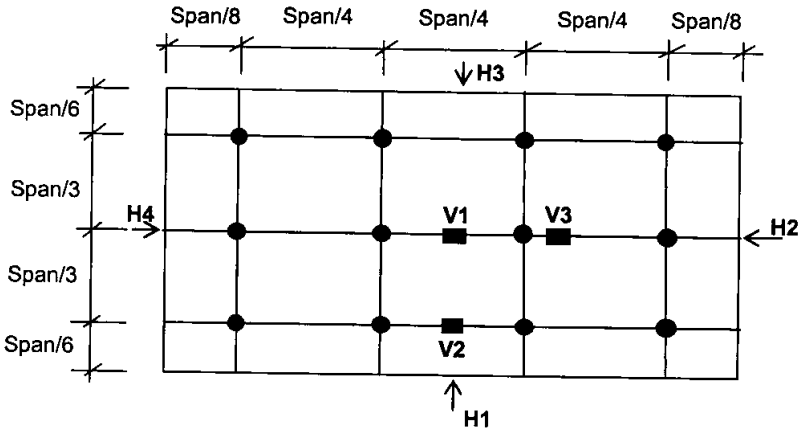

FIGURE 3 : Location of applied loading and displacement gauges

The loading frame and test set-up is shown in Fig. 4. The applied load remained vertical with the aid of ball-joints which allowed the loading system to rotate as the slab deflected. The slab was placed on a supporting frame, providing vertical support around the perimeter.

FIGURE 4 : Typical arrangement of test set-up and supporting frame

The four corners of the slab were loosely clamped to restrain vertical upward movement, but no horizontal restraint was provided at the supported edges. The heating device was constructed from a steel box lined with insulation board to increase the heating rate and protect the steel casing. Heating was generated by four electrical elements within the steel box. Fig. 5 shows the heating elements and supporting frame.

FIGURE 5 : Arrangement of heating elements

The slabs were reinforced with 0.71mm diameter smooth or deformed (ribbed) steel wire, distributed isotropically. The deformed wire was made by indenting the smooth wire using a purpose-built machine. The indentations had the effect of increased bond between the concrete and reinforcement but also reduced the reinforcement's ductility; the tested ductility for smooth wire was 20.3%, reducing to 11.4% for deformed wire. The percentage of reinforcement in any slab cross-section varied between 0.05% and 0.25%. The concrete mix was composed of gritty sand with fine aggregate ranging between 1 and 4mm, a cement-sand ratio of 1:3, and a water-cement ratio of 0.47. The measured yield strength of reinforcement and the compressive strength of concrete are shown in Table 1 in the Appendix.

The logged instrumentation included a load cell and several displacement transducers to measure both the horizontal and vertical displacements during the test (Fig. 4). The temperatures of the underside, reinforcement level and topside of the slab were measured with 12 thermocouples placed at key locations. The thermocouples measured temperatures through the depth of the slab, being placed at 4 locations, on 3 levels through the slab. Fig. 6 shows the temperature growth at these locations and levels for a typical test. The temperatures show consistency between the readings at the different positions at each of the levels through the slab.

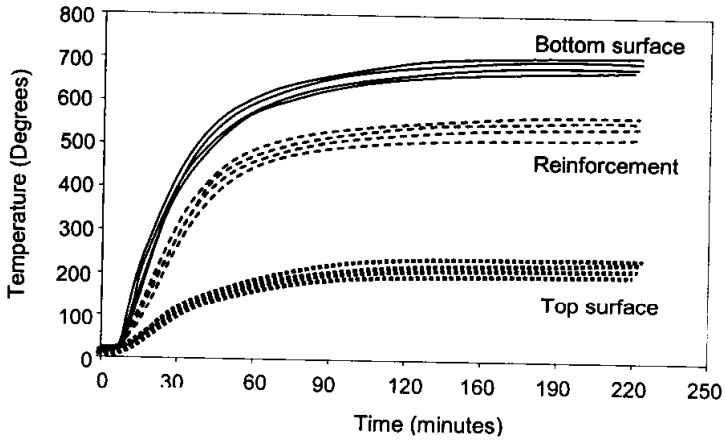

FIGURE 6 : Temperature profiles

OBSERVATIONS OF SLAB BEHAVIOUR

The slabs were subjected to the imposed load before the heating elements were switched on. They were tested in the sequence shown in Table 1. Test 1 has not been included, as it was used only to check the temperature distributions in the slab at various key locations. Test 3 was a re-test of Slab 2, which had been lightly loaded and showed little damage although it had some residual distortion. The fourteen slabs all behaved similarly. Approximately 10-15 minutes after the furnace was switched on, diagonal cracks occurred across the corners as the slab deflected into double curvature. After 20 minutes, a single transverse crack could be seen forming on the topside of the slab in its central region. Over time this crack developed outwards in the transverse short-span direction towards the long edges of the slab (Fig. 7).

FIGURE 7 : Test 7: View of the topside of slab after test.

Most of the slabs developed crack patterns resembling a yield line mechanism towards the end of the test, usually occurring after about 2 hours. The crack patterns resemble those of similar slabs tested at ambient temperature [10], except that the diagonal yield lines tended to align more in the long direction of the slab (Fig. 8(a)), giving a much shorter central yield line than usual. In Test 6, which was lightly reinforced and lightly loaded, diagonal cracking was only apparent after cooling (Fig. 8(b)). The formation of these yield lines seems to depend on the

applied load level, while the development of the initial transverse crack after the slab deflects into double curvature is associated with its thermal bowing.

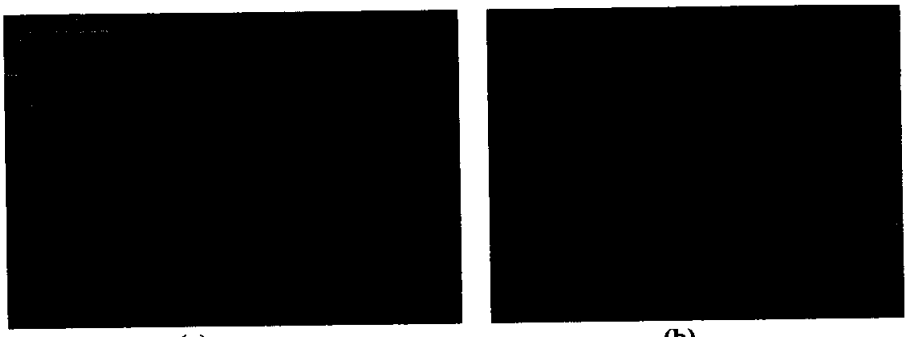

(a) (b)

FIGURE 8 : View of bottom of slab; (a) Test 9, (b) Test 6, after testing.

The bond strength between reinforcement and concrete appeared [10] to be a major contribution to the failure of the slab at ambient temperature. At elevated temperatures, the influence of bond dominates the slab failure. For comparison, Fig. 9 shows photographs taken immediately after Tests 12 and 13. These tests were identical, the slabs having the same reinforcement percentages (0.25% in any cross-section) and imposed load; the only difference being the reinforcement type. In Test 12, deformed wire was used, and it can be seen in Fig. 9 that the transverse crack has opened because the reinforcement across it has fractured. The slab in Test 13, reinforced with smooth wire, shows a transverse crack which re-closed after the test.

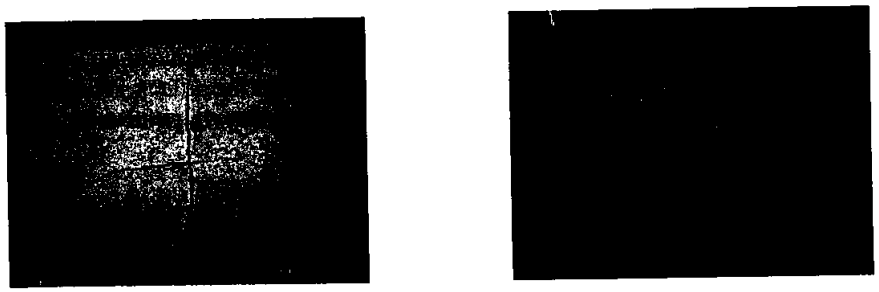

(a) (b)

FIGURE 9 : View of bottom of slab; (a) Test 12, (b) Test 13 after testing.

It was apparent that, for the slab reinforced with deformed wire, once the major tension crack had formed across the short span the reinforcement across the crack fractured. Because of the better bond achieved between the concrete and steel in this case, the straining of the reinforcement occurs over a smaller free length and fracture strains happen at quite small crack widths . In Test 12, as the transverse crack developed the reinforcing bars across the tension crack were also exposed to the high temperatures, and would fracture progressively in an "unzipping" effect more rapid than in the ambient-temperature tests [10]. This is not apparent in Test 13, in which the smooth wire has not fractured because the free lengths of wire across the tension crack can become much higher and the strains do not attain fracture levels.

DEFLECTIONS

The mid-span vertical deflections of the slabs tested so far are shown in Fig. 10. Some of these have attained deflections up to *Span/12*. The slabs show similar rates of deflection between 20°C-150°C. The slabs of depth 22mm with reinforcement placed 7.5mm from the bottom surface (Tests 9 and 11) deflections are lower than for the 15mm thick slabs. The rate of deflection for the slab reinforced with smooth wire (Test 13) can be seen to be less than for the equivalent slab using deformed wire (Test 12).

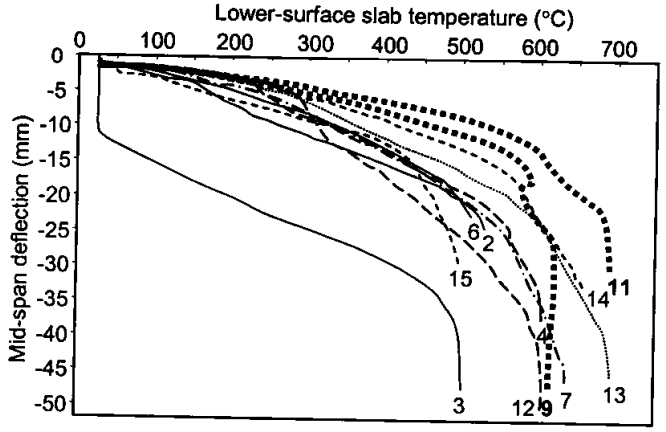

FIGURE 10: Mid-span deflections for the tested slabs (Test numbers indicated).

Some numerical modelling studies have been completed using *Vulcan*, and comparisons are presented in Fig. 11. Mesh studies were undertaken at ambient temperature in order to validate the model. The results show good correlation between test and numerical results. This seems to indicate that, even though the numerical model does not consider the effects of bond strength on reinforcement fracture, it predicts behaviour very similar to that shown in the tests. This work is currently in progress and parametric studies will be carried out.

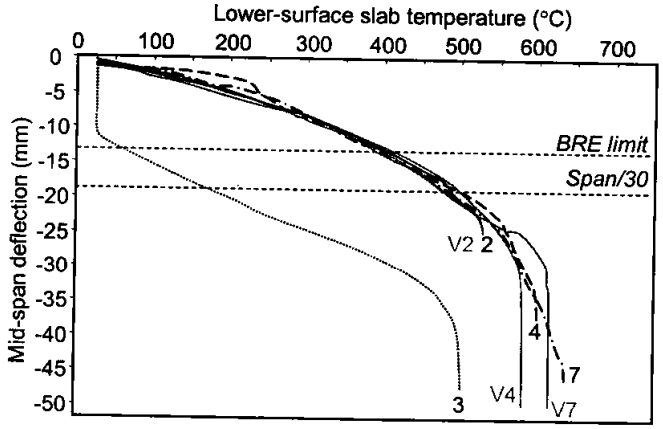

FIGURE 11 : Comparison of experimental results with numerical model *Vulcan*

The maximum displacements calculated using the BRE simple design method give results somewhat below the standard testing deflection limit of *Span/30*. At either of these deflection limits the slabs are all intact, and both limits are clearly conservative.

COMPARISONS WITH THE SIMPLE DESIGN METHOD

A reduced, high-temperature yield-line load capacity can be calculated using the reduced strengths of the reinforcing steel at elevated temperatures. The experimentally measured steel temperatures were used to assign appropriate strength reduction factors from Eurocode 3 Part 1.2 [14]. Fig. 12 plots the enhanced load ratios carried by the slabs in some of the tests in terms of the reduced yield-line capacity, showing that the slabs carried loads far greater than yield line predictions. At displacements greater than 15mm this capacity was demonstrably enhanced by tensile membrane action.

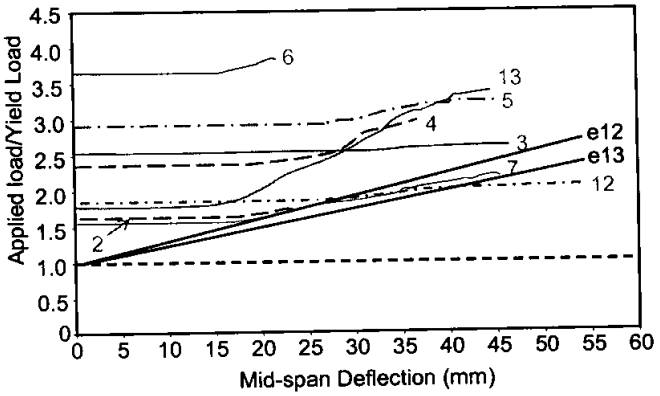

FIGURE 12: Variation of Applied load/Yield load with deflection

In order to compare Tests 12 and 13, the theoretical enhancement factors given by the BRE simple design method are plotted on Fig. 12 as lines e12 and e13 respectively. It can be seen that Test 13, which had smooth reinforcement, actually reached much higher enhancements than predicted by the BRE method. However for Test 12, using deformed reinforcement, the enhancement was close to the prediction within the permitted deflection range, but fell below it for very high deflections. Test 13 reached factors of nearly 3.5 times the yield line load compared to Test 12 which only reached 1.9.

Fig. 13 compares the load capacities calculated using the BRE design method, mapping the reinforcement temperatures onto the measured displacements in Tests 12 and 13. These tests differ only in the reinforcement type used. This illustrates again that Test 13, using smooth reinforcement, out-performs the BRE method's predictions throughout the range of deflections used. However, for Test 12 the BRE prediction increases beyond the actual load at about 27mm displacement, indicating that the deformed reinforcement is performing less well.

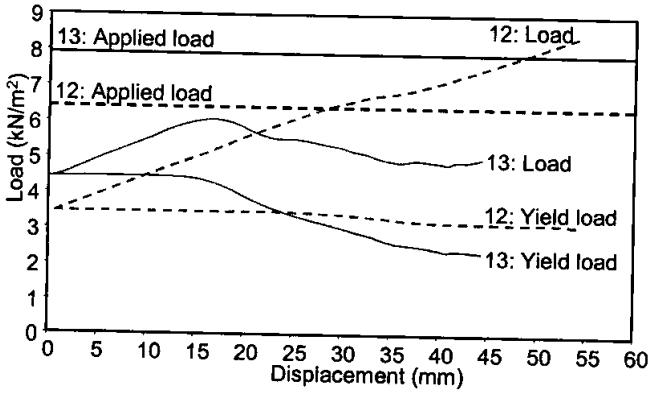

FIGURE 13: Comparison of the load and yield-line capacities for Tests 12 and 13 from the BRE design method with the actual load levels as deflections increase.

CONCLUSIONS

The paper presents the results from a number of loaded high-temperature tests conducted on horizontally unrestrained slabs. An electrical heating system and self-supporting frame have been developed to enable the slabs to be heated up to lower-surface temperatures of about 700°C. The slabs have in general performed very well and supported loads well in excess of the predicted yield line loads. Enhancements of up to 3.5 times the yield load have been achieved; this enhanced resistance being attributed to membrane forces which assist in maintaining the structural integrity through diaphragm action. The slabs reinforced with smooth bars performed better than those reinforced with deformed bars.

A major purpose of these tests was to investigate the influence of thermal curvature on the failure mechanisms of rectangular slabs. Observations from the high-temperature tests have shown that the cracking mechanism differs in some respects from that observed at ambient temperature. At ambient temperature four flat facets of the slab rotate about the edge supports and yield line cracks are formed as a low-deflection mechanism which is forced into membrane action at high deflections. At high temperatures the slab initially deflects into double curvature, generating full-depth cracking across its short span, and may later form a less distinctive yield line mechanism.

The comparisons between the numerical model *Vulcan* and the experiments have shown that *Vulcan* predicts deflections accurately, even though it does not model discrete cracking. Further studies will follow using *Vulcan* to further understand the mechanics involved in the high-temperature slab behaviour.

ACKNOWLEDGMENT

The authors gratefully acknowledge sponsorship of the first author by the Engineering and Physical Sciences Research Council of the United Kingdom, and by Arup Fire Ltd.

REFERENCES

[1] '*The behaviour of multi-storey framed buildings in fire: a European joint research programme*', British Steel Swinden Technology Centre, 1999.

[2] BS5950: *Structural use of steelwork in buildings, Part 8 : Code of practice for fire resistance design,* British Standards Institution, London, 1990.

[3] Park, R. 'Ultimate strength of rectangular concrete slabs under short-term uniform loading with edges restrained against lateral movement', *Proc. Institution of Civil Engineers, 28,* (1964) pp125-150.

[4] Sawczuk, A and Winnicki, L. 'Plastic behaviour of simply supported reinforced concrete plates at moderately large deflections', *Int. J. Solids Structures*, **1**, (1965) pp97-111.

[5] Hayes, B.,'Allowing for membrane action in the plastic analysis of rectangular reinforced concrete slabs', Magazine of Concrete Research, **20** (65), (1968) pp205-212

[6] Park, R., 'Tensile membrane behaviour of uniformly loaded rectangular reinforced concrete slabs with full restrained edges', Magazine of Concrete Research, **16** (46), (1964) pp39-44.

[7] Brotchie, J.F and Holley, M.J., *Membrane action in slabs: Cracking, deflection, and ultimate load of concrete slab systems*. Publications SP-30, American Concrete Institute, Detroit, Paper 30-16, (1971) pp345-377.

[8] Bailey, C.G., *Design of steel structures with composite slabs at the fire limit state*. BRE Final Report to the Department of the Environment, Transport and Regions, Building Research Establishment, Garston, UK, 2000.

[9] Bailey, C.G, 'Efficient arrangement of reinforcement for membrane behaviour of composite floor slabs in fire conditions'. *J. Construct. Steel Research*, **59**, (2003) pp931-949

[10] Foster, S.J., Bailey, C.G., Burgess, I.W. and Plank, R.J., ' *Experimental behaviour of concrete floor slabs at large displacements*', Research Report DCSE/03/F/2, University of Sheffield (2003), (accepted for publication: *Engineering Structures*).

[11] Huang, Z, Burgess, I.W. and Plank R.J., 'Modelling membrane action f concrete slabs in composite buildings in fire: Part I: Theoretical development'. *Journal of Structural Engineering*, ASCE, **129** (8), (2003) pp1093-1102.

[12] Huang, Z, Burgess, I.W. and Plank R.J.,' 'Modelling membrane action f concrete slabs in composite buildings in fire: Part II: Validations. *Journal of Structural Engineering*, ASCE, **129** (8), (2003) pp1103-1112.

[13] Eurocode 4, *Design of composite steel and concrete structures: Part 1.2: Structural rules, Structural fire design, prEN 1994-1-2*. European Committee for Standardisation, 2003.

[14] Eurocode 3, *Design of steel structures: Part 1.2: General rules, Structural fire design, prEN 1993-1-2*. European Committee for Standardisation, 2003.

APPENDIX

TABLE 1: Data for the high-temperature slab tests.

Test	Size (mm)	Reinf. Area (%)	t (mm)	fy (N/mm^2)	Bar Type	fc (N/mm^2)	Dx (mm)	Dy (mm)	Yield Line Capacity W_u (kN/m^2)	Imposed Load Q (kN/m^2)	Load Ratio Q/W_u
2	850x550	0.15	14	260	smooth	37	6.645	7.355	1.91	2.95	1.5
3	850x550	0.15	14	260	smooth	37	6.645	7.355	1.91	4.60	2.4
4	850x550	0.15	15	260	smooth	37	7.145	7.855	2.06	4.66	2.3
5	850x550	0.15	13	245	deformed	40	6.145	6.855	1.58	4.58	2.9
6	850x550	0.05	14	260	smooth	44	6.645	7.355	0.78	2.81	3.6
7	850x550	0.15	17	245	deformed	40	8.145	8.855	2.21	3.30	1.5
8	850x550	0.1	24	260	smooth	39	16.145	16.855	4.6	4.0	0.9
9	850x550	0.1	23	245	deformed	42	16.045	16.755	4.32	6.0	1.4
10	850x550	0.05	24	245	deformed	39	16.145	16.855	2.49	4.7	1.9
11	850x550	0.05	23	260	smooth	39	15.145	15.855	2.48	5.96	2.4
12	850x550	0.25	14.5	245	deformed	38	6.745	7.455	3.65	6.4	1.8
13	850x550	0.25	16	260	smooth	38	8.145	8.855	4.68	7.9	1.7
14	850x550	0.1	14.5	245	deformed	40	6.845	7.555	1.25	2.5	2.0
15	850x550	0.05	13.95	260	smooth	40	6.62	7.33	0.77	1.69	2.2

ASSESSMENT OF THE STRENGTH OF THE REINFORCED CONCRETE COLUMNS AT ELEVATED TEMPERATURES

Kang, Suk-Won
Senior Researcher, Daewoo E&C, Korea, sharkang@dwconst.co.kr

Lee, Ji-Woong
Researcher, Daelim Construction, Korea, Tefnet79@empal.com

Hong, Sung-Gul
Associate Professor, Seoul National University, Korea, sglhong@snu.ac.kr

ABSTRACT

A numerical method is proposed for the thermal behavior of reinforced concrete columns subjected to the fire circumstances in this study. It is assumed that the thermal capacity is determined by the P-M interaction curves of the axial force-bending moment interaction curves. P-M interaction curves are obtained by severe presumed strain distribution based on the total stresses in the section and yielding stresses of materials. Strength of the column under combined axial force and moment is estimated with the P-M interaction curves where the ratio of axial force to moment equals the value of the external load. The method considered 2nd order effect by the lateral deflection of the column at high temperature. Moment magnifier is used in order to consider the P-delta effect during the calculation of the interaction curves. The method also included the effect of restraint condition at the ends of the column.

Some applications are carried out and compared with the test results. According to the analysis results, there exists very severe nonlinear strain change with the depth measured from the fire-exposed surface, which seems to be caused by the nonlinear temperature distribution at the section. Self-equilibrating stresses are manifested during heating just to let the section remain plane after deformation. The comparisons show that the proposed method yields a good agreement with the test results and thus can give a reasonable method not only to investigate the thermal condition of the column but also to assess the residual capacity at the given state during fire circumstances.

KEYWORDS: *P-M interaction curves, elevated temperatures, P-delta effect, nonlinear temperature distribution, self-equilibrating stress, thermal condition, residual capacity*

INTRODUCTION

Concrete is inherently fire resistant and is usually treated as a fireproofing material against the loss of its resistance capacity. This inherent characteristic of the fire resistance of concrete results largely from the reduction in its thermal diffusivity and conductivity, and its gradually decreasing tendency with increasing temperature. These features give the ability to resist the transmission of heat from the fire exposed faces of the structures to the other faces with various connected members and therefore can limit the damaged zone to a comparatively shallow area in the fire-exposed region after all. Despite all these advantages of concrete, most concrete structural members or structural materials experience the deterioration at fire circumstances.

Repair, reinstatement or reinforcement could be required for the concrete structures or structural members after fire, and these can be achieved by the careful examination to the damaged parts of the concrete structural members. As a result, some investigations for the computational procedures of the basic nonlinear thermal and structural analysis on the fire response using a finite element method have been reported with the experimental tests.[1,2,3,4,5]

Recent rapid progress in the personal computer technology enables structural engineers to solve many complicated nonlinear problems by means of finite element method. However, it is still very intricate and time-consuming to analyse the behaviour of the structural members. The solution requires iteration during the calculation of stresses, strains, displacements, etc. of the section at a given temperature interval and the stiffness matrices of the system should be updated considering the temperature-dependent material properties at the corresponding temperature interval. Thus, simple analysis method for the structural behaviour at high temperature can help the fire engineers to deal with the thermal response quickly. This study aims to seek a simple numerical method to assess the fire resistance of reinforced concrete column during heating. It will be very useful for the engineers who should determine the safety or the stability of the structural members subjected to fire circumstances.

The analysis procedure of the fire response of the structural members in this study is shown Figure 1.

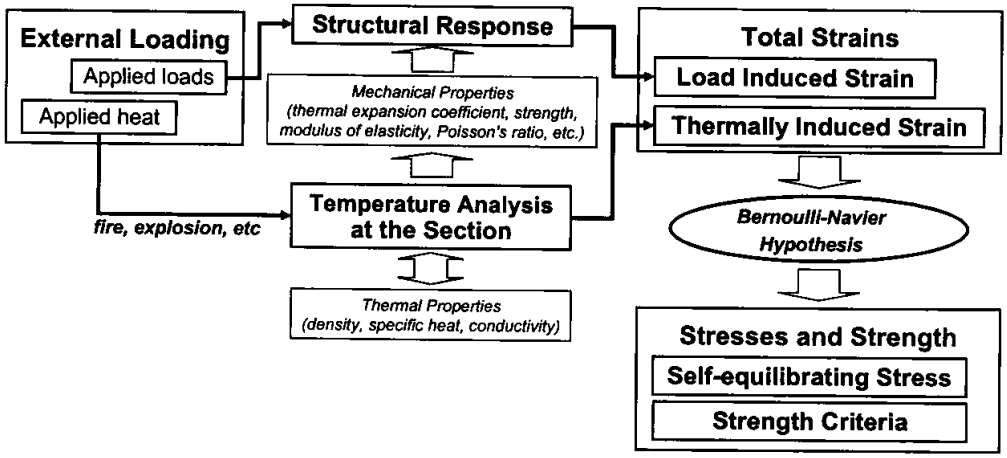

Figure 1. General procedure of thermal analysis

External loading is subdivided into two types of loads; applied load and heat. Temperature analysis was conducted for the applied heat in order to acquire the temperature information at certain structural analysis step. For the simplicity of the temperature analysis, it is assumed that the temperature and structural behaviours are uncoupled. The effects of structural response such as displacement, spalling phenomenon, or steel ratio are also ignored for the efficiency.

In the structural analysis, not only the external load condition but also the material properties at the section affected by the temperature condition, which was previously determined by the temperature analysis, were simultaneously considered during the analysis process.

The purpose of this study is to represent the numerical method for the calculation of capacity of reinforced concrete columns subjected to the elevated temperatures. The P-M interaction curves of the axial force and bending moment were drawn for the calculation of the thermal capacity of the reinforced column at elevated temperatures. From the P-M interaction curve where the ratio of axial force to moment equals the value of the external load, strength of the column under combined axial force and moment can be estimated.

The method considered 2nd order effect by the lateral deflection of the column at high temperature. Moment magnifier is used in order to consider the P-delta effect during the calculation of the interaction curves.

MATERIAL MODELS DURING HEATING

Material properties

Concrete is a composite and nonhomogeneous material, and therefore, the actual behavior at high temperature is the consequence of many simultaneously interacting factors. It is almost impossible to separate such factors into the sum of the individual variable that can be easily understood. However, the characteristics of the material properties during heating are mostly affected by the temperature and, therefore, they are assumed temperature only dependent for the efficiency of numerical analysis in this study.

It should be noted that the material properties are also subdivided into two categories following the analysis type in this study. The density, specific heat, and thermal conductivity are used in the temperature analysis and called as thermal properties in this study. Whilst, the thermal expansion coefficient, initial elastic modulus and strength are included in the mechanical properties for the successive structural analysis.

The thermal properties used for a temperature distribution analysis follow the recommendations of ASCE.[6] The mechanical properties of concrete for successive structural analysis are modeled by the simple linear regression analysis for the previous experimental results. The normalized numerical model for the mechanical properties of concrete is shown in Table 1.

As it seems reasonable to believe the steel is isotropic and homogeneous, the investigations for the thermal and mechanical characteristics of the steel at elevated temperatures have been widely executed since the early 1950's. There exists a great deal of experimental data to comprehend the thermal characteristics of steel at high temperature. So, the thermal and mechanical properties of steel at elevated temperatures are comparatively well revealed and understood. In this study, its material models followed the recommendations of ASCE.

Table 1 Normalized numerical model for the mechanical properties of concrete with temperature

Temperature (□)	Elastic modulus	Compressive strength	Strain at failure
0	1.00	1.00	1.00
20	1.00	1.00	1.00
100	0.85	1.00	1.00
200	0.70	1.00	1.25
300	0.60	1.00	1.50
400	0.50	0.80	2.00
500	0.40	0.60	2.75
600	0.30	0.40	3.50
700	0.30	0.30	4.25
800	0.30	0.20	5.00

Stress-Strain Relationships of concrete and steel during Heating

Stress-strain relationships of concrete vary with temperature. The expressions for the stress-strain relationship of concrete are highly curved and modelled following ASCE's recommendation, which is shown in Figure 2 in this study.

As the compressive strength of concrete decreases but the ductility increases with temperature, the strain value where the compressive failure occurs also move rightward in the stress-strain curve. In this study, the ratio of ultimate strain (ε_{cu}) to maximum compressive strain at failure (ε_{max}) is assumed to be constant regardless of temperature condition. Then, following equation can be derived.

$$\frac{\varepsilon_{cu}}{\varepsilon_{max}} = \frac{\varepsilon_{cu,20}}{\varepsilon_{max,20}} = 1.1381 \tag{1}$$

$$\varepsilon_{cu} = 1.1381\varepsilon_{max} = 1.1381\times\left[0.0025+\left(6.0T+0.04T^2\right)\times10^{-6}\right] \tag{2}$$

Modelling for the stress-strain curves of steel at high temperature is shown in Figure 2(b). In general, strain-hardening modulus of steel, E_T, is regarded about 10% of the modulus of elasticity at ambient temperature. It is also assumed zero when the temperature exceeds 600 Celcius.

The stress-strain curve of the reinforcing steel in this investigation is modified from the model which was developed by Becker and Bresler. The relationship can be represented by the following equations.

$$\sigma = \varepsilon_\sigma \cdot E_s \quad \text{if} \quad \varepsilon_\sigma \le \varepsilon_y$$
$$= \sigma_y + E_T(\varepsilon_\sigma - \varepsilon_y) \quad \text{if} \quad \varepsilon_\sigma \ge \varepsilon_y \tag{3}$$

where E_s, E_T, σ_y, and ε_y are the initial elastic modulus, elastic modulus at strain-hardening range, yield stress and strain, respectively.

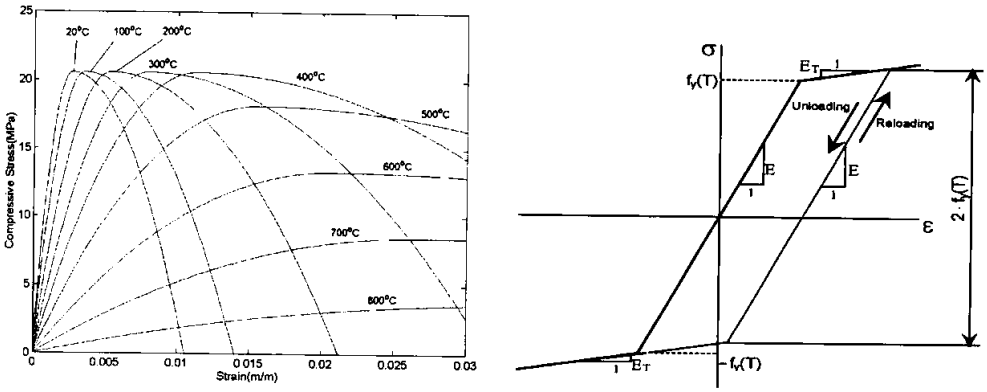

(a) Concrete **(b) Steel**

Figure 2. Stress-strain relationships at elevated temperatures

TEMPERATURE ANALYSIS

The temperature information of the elements with time is essential for the successive solution of the structural analysis. There exist three types of the heat transferring; convection, radiation, and conduction. In general, the heat flux from the fire to the structure at fire-side is mostly governed by the convection and radiation, while the heat flow inside the element is only determined by conduction.

Finite difference method (FDM) is used for the calculation of temperature distribution at the section in this study. FDM has several advantages in that it is quite simple and easy to adapt for a rectangular section. In order to solve the non-steady state heat transfer problem such as fire test, implicit equation was used for the efficiency. This method has the tendency to oscillate during the iteration depending on the heat transfer coefficient. However, this can be solved by adjusting the time interval.

NUMERICAL SOLUTION DURING HEATING

P-M interaction curves during heating

It is possible but very difficult to derive and use the equation for the calculation of the capacity of the column under combined axial force and moment. Thus, it is quite natural to assume the strain distribution corresponding to those applied axial force and moment for the assessment of the strength of the column as in Figure 3.

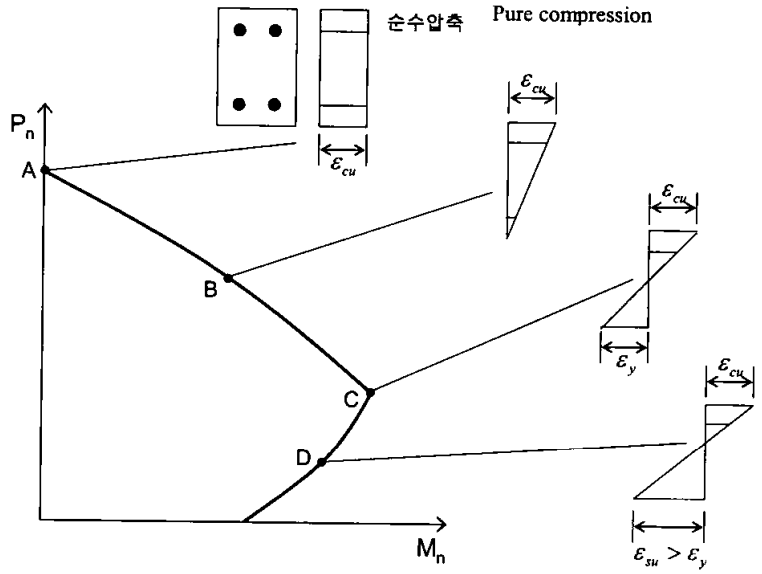

Figure 3. Strain distribution at failure for the column

If the section failure is assumed to occur when the ultimate strain of concrete reaches 0.003, the location of centre line of the section and the strain of the reinforcing steel can be calculated from the strain distribution at the section. Then, the compressive stress of concrete and the tensile stresses of the steels are determined. Through this way of calculation, the stresses over the section are summed up to be the axial force at the section and to be the moment if the length from the centre line is considered.

At elevated temperature condition, as assumed earlier the section should remain plane after heating and loading, the nonlinear strain distribution caused by the nonlinear temperature distribution leads to the additional stress at the section as shown in Figure 4.

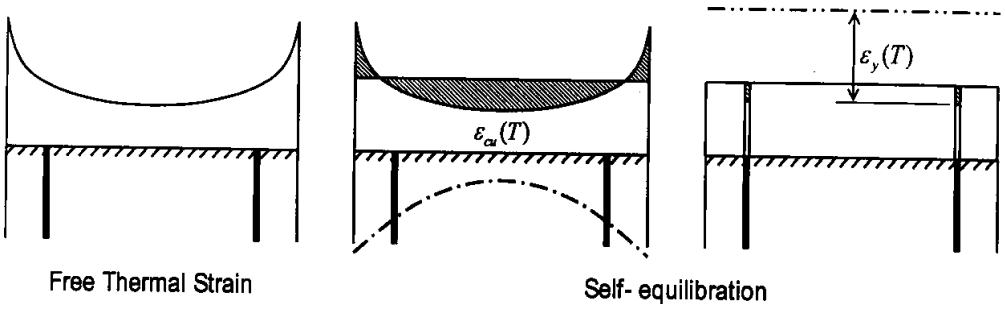

Figure 4. Self-equilibrating state at the section during heating

When the self-equilibrating stress is induced with no external loadings, the sum of the self-equilibrating stress should be zero over the section. Then following equations could be obtained.

$$P = \sum \sigma_{se} dA = 0 \tag{4}$$

$$M = \sum \sigma_{se} l_x dA = 0 \tag{5}$$

where l_y is the distance from the center line of the section. From the equilibrium condition at the section, the ultimate strains of concrete and steel can be written as follows.

$$\varepsilon'_{cu} = \varepsilon_{cu} + (\varepsilon_{se} - \varepsilon_T) \tag{6}$$

$$\varepsilon'_y = \varepsilon_{se} - (\varepsilon_{se} - \varepsilon_T) \tag{7}$$

where ε'_{cu}, ε'_y, ε_{se} and ε_T are the ultimate strains of concrete and steel, self-equilibrating strain, and total strain at the section, respectively. For the numerical solution, the equations (4) and (5) can be re-written with discrete formulation as follows.

$$P = \sum_{i=1}^{n} \sigma(T_i, \varepsilon_i) dA \tag{8}$$

$$M = \sum_{i=1}^{n} \sigma(T_i, \varepsilon_i) l_x dA \tag{9}$$

The above equations cannot be exactly solved directly due to their discrete form and mainly due to the nonlinear strain distribution corresponding temperature distribution at the section as shown in Figure 4. According to author's previous study, the equations can be solved with an implicit method and, thus, iterative procedures are required.

The implicit iteration procedure is repeated until the total stress at the section is zero according to the planeity condition after deformation, which is represented in the equation (4). However, the iteration is stopped when the sum of the stress is the smallest due to the discretization of the section.

It also should be noted that only the uniaxial behavior through the longitudinal axis of the member is assumed to be available for the calculations of the internal forces at a given discretized element. The effect of multiaxial behavior was not taken into account.

Moment magnifier

In ACI 318 code, moment magnifier is introduced in order to consider the effect of the additional moment at the ends of the member.[7] The moment is caused by the lateral deflection of the member. In this study, the additional moment created by this P-delta effect during heating is considered. The assessed moment considering the P-delta effect can be described as follows.

$$M_c = \delta_{ns} \cdot M_2 \tag{10}$$

where δ_{ns} is the moment magnifier and defined by the following equation.

$$\delta_{ns} = \frac{C_m}{1 - P_u / 0.75 P_c} \geq 1.0 \tag{11}$$

where

$$C_m = 0.6 + 0.4 \frac{M_1}{M_2} \geq 0.4 \tag{12}$$

$$P_c = \frac{\pi^2 EI}{(kl_u)^2} \tag{13}$$

and

$$EI = \frac{0.2 E_c I_g + E_s I_{se}}{1 + \beta_d} \tag{14}$$

where E_c and E_s are the modulus of elasticity of concrete and steel, respectively. They have taken into account the effect of the temperature change. β_d is the coefficient for the creep effect. However, it is not considered in this study. I_g is the second moment of inertias ignoring the steel. I_{se} is that of steel to the centroid of the concrete section and it can be obtained from the following relation.

$$I_{se} = C\rho_t \gamma^2 I_g \tag{15}$$

where C is the constant due to the steel reinforcement, and assumed to be 3 in this study, ρ_t is the reinforcement ratio, and γ is the ratio of the distance between the centres of the steel to the width of the column. The application is restricted to the pin-connected member for the comparison with the experimental results.

APPLICATIONS

Standard fire test for the reinforced concrete columns were carried out in order to prove the validity of the proposed method and their results were compared to the numerical analyses results. The geometry of the specimen is shown in Figure 5. The length of the specimen is 3.36 m from end to end. Cover thickness is 4 cm. Average yield strength of the reinforcing steel is approximately 390 MPa. Compressive strength of concrete is approximately 21 MPa.

Three types of loadings of 372.4 kN, 637.0 kN, and 911.4 kN were applied to the members. They are 24%, 42%, and 60% of the maximum strength of the columns. In order to generate the moment to the member, loading point was eccentric to the centre of the section. The applied loading was kept almost constant during fire test. ISO standard fire was used for the fire test. Support conditions at both ends were set as hinges to rotate freely.

Temperature analysis on the section was carried out as 2 dimensional heat conduction problem with the boundaries of convection and radiation. Uniform heating is assumed through the longitudinal axis of the member during fire test. In the analysis, the contribution of the reinforcing steel was ignored considering that the reinforcement ratio is so small and that the temperature drop at the interface between concrete and steel offsets the high conductivity of the steel. The results of the temperature analysis are shown in Figure 6. MATLAB software is used for the analysis. Nonlinear temperature distribution at the section can be seen in the figure.

As mentioned earlier, it is assumed that the temperature condition and structural behavior at the section are not coupled. The change of the structural behavior during heating could be obtained simply considering the temperature change.

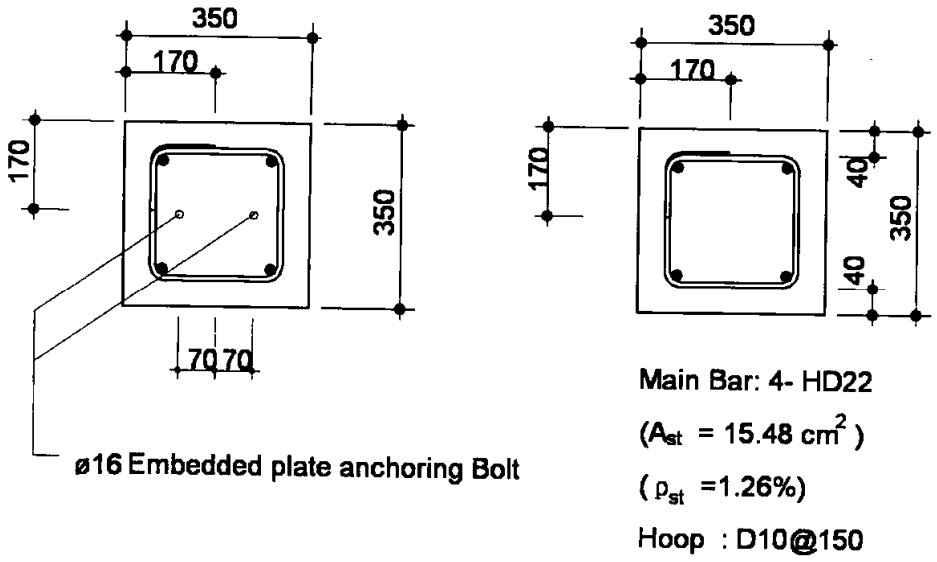

Figure 5. Section of the specimen

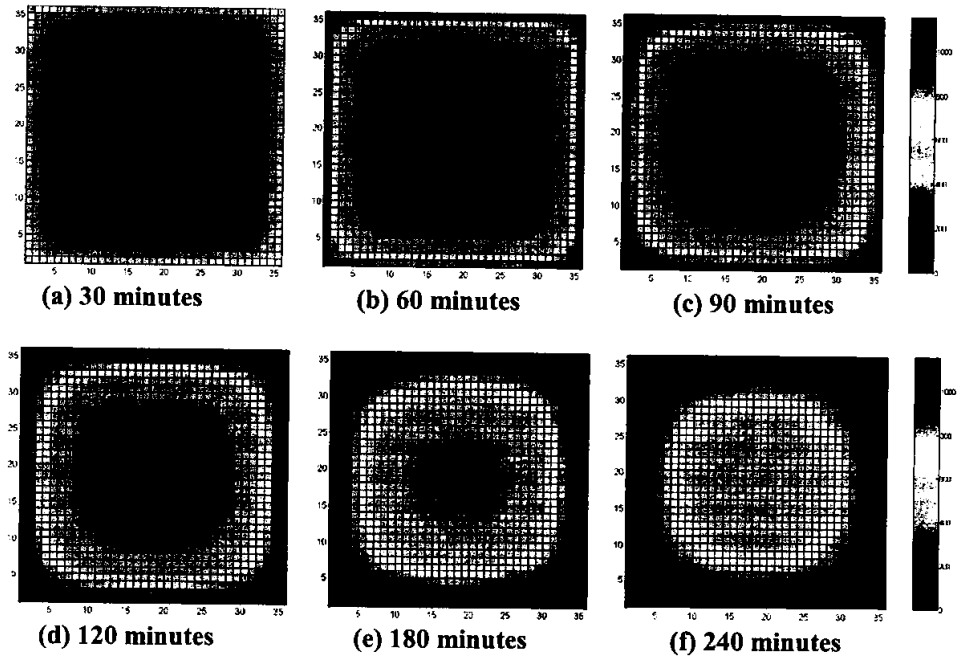

Figure 6. Temperature distribution at the section

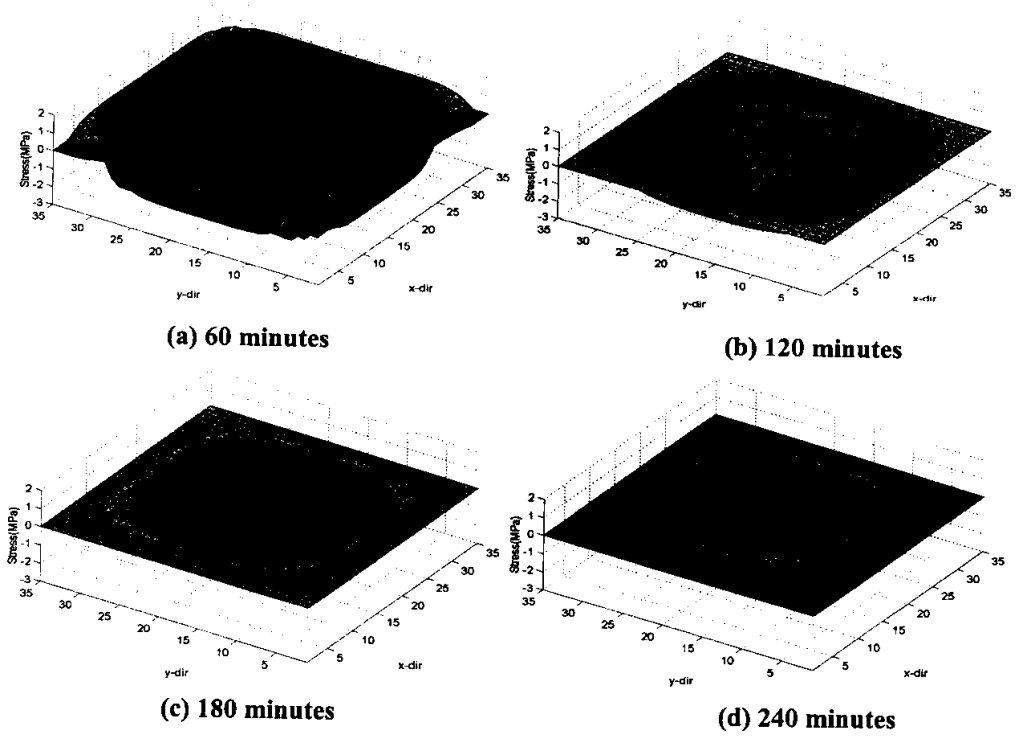

(a) 60 minutes **(b) 120 minutes**

(c) 180 minutes **(d) 240 minutes**

Figure 7. Self-equilibrating stress during fire test

From the temperature information over the section, the strains and stresses are calculated. Considering the planeity condition, the resulting self-equilibrating stress is derived. It can be seen in Figure 7.

Figure 8 is the P-M interaction curves of the tested member during heating. It shows that the interaction curves shrinks with temperature. The marked point represents the combined loaded state at ambient environment. According to this graph, the thermal capacity of the member is about 210 minutes. Table 2 & 3 are the calculated axial forces and moments at the failure conditions, respectively.

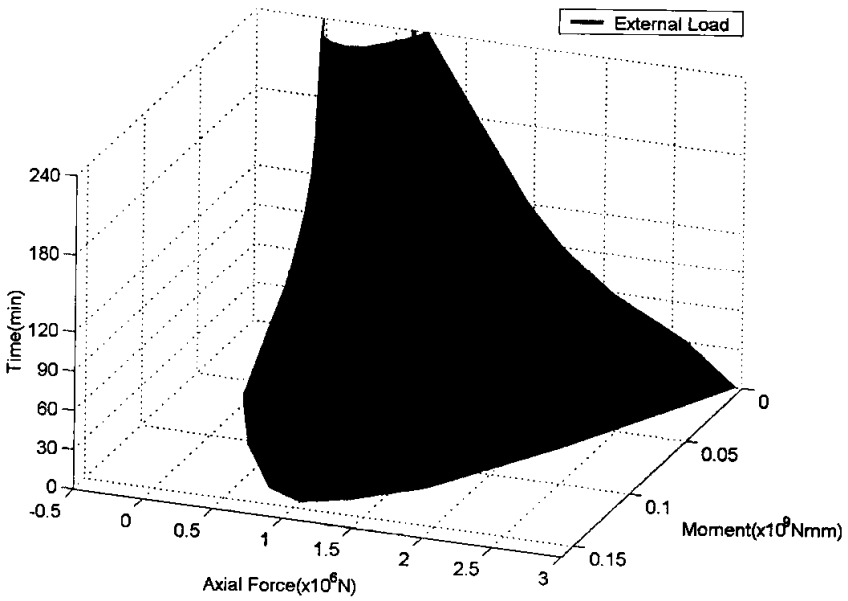

Figure 8. P-M interaction curves during fire test

Table 2 Calculated axial force during fire test [x10^3 kN]

Heating time (min)	Pure compressive failure	Compressive failure		Balanced failure	Tensile failure		Pure tensile failure
0	2.95	2.27	1.69	1.01	0.73	-0.06	-0.37
30	2.60	1.51	1.33	1.06	0.92	0.55	-0.27
60	2.06	1.20	1.07	0.86	0.77	0.49	-0.19
90	1.71	1.04	0.95	0.78	0.70	0.45	-0.13
120	1.46	0.92	0.86	0.72	0.65	0.41	-0.09
180	1.09	0.92	0.80	0.60	0.49	0.19	-0.04
240	0.73	0.65	0.59	0.44	0.35	0.09	-0.01

Table 3 Calculated moment during fire test [kN-m]

Heating time (min)	Pure compressive failure	Compressive failure		Balanced failure	Tensile failure		Pure tensile failure
0	0	69.0	117.8	144.1	136.1	63.2	0
30	0	100.7	112.4	128.9	130.8	119.1	0

60	0	75.7	83.9	97.3	99.3	93.6	0
90	0	60.1	66.2	77.1	79.2	75.5	0
120	0	48.7	52.8	61.4	63.4	60.6	0
180	0	18.3	26.3	37.3	39.6	0.0322	0
240	0	7.5	11.5	19.3	21.4	0.0152	0

The two lines in Figure 8 are the cases of with and without eccentricity while loading during the test. The eccentricity is 3.5 cm. The column with non-eccentricity loading has no cross point with the interaction curve and thus can be considered to have the fire capacity of almost 4 hours. The one with 3.5 cm eccentricity has more than 3 hour fire capacity.

The fire test reveals that the failures of non-eccentricity and eccentricity specimens occurred at less than 4 hours and at less than 3 hours, respectively. The tested fire capacities are approximately 87.5% and 70% of the calculated ones. The loss of the section caused by spalling phenomenon seemed to affect the earlier failure of the specimen. As the tested specimen were fabricated only a few months before the test. There is the possibility of effect of moisture. The eccentricity also seemed to affect spalling because the eccentricity can cause additional compressive force and spalling more.

CONCLUSION

This study presented a simple analysis method for the assessment of the capacity of a reinforced concrete column at fire circumstances. The nonlinear temperature distribution at the section causes a nonlinear strain distribution, and the resulting self-equilibrating stress.

An application of the proposed method shows relative good agreement with experimental results. A more reliable temperature-dependent material model, a more reliable temperature analysis, and a comprehension of the effects of the failure of the material during heating will also improve the reliability of the analysis method.

The self-equilibrating stresses have the tendency of increase until 120 minutes of the fire test and decrease after 120 minutes. This is mainly because the concrete elements near surface have no more bearing stresses at more than 900 Celcius and the boundary that distinguish the compressive and tensile area moves inward.

The member under compression can be affected much by the spalling and thus the study on the phenomenon can help the understanding of the fire behaviour.

REFERENCES

1. Kang S. W. and Hong S. G., "Behavior of Concrete Members at Elevated Temperatures Considering Inelastic Deformation," Journal of Fire Technology, Vol. 39, January 2003, pp.9-22
2. Kang S. W. and Hong S. G., "Material Model and Thermal Response Analysis of Concrete at Elevated Temperatures," Journal of the Korea Concrete Institute, Vol. 13, No. 3, June 2001, pp. 268-276
3. Huang Z. and Plattern A. "Nonlinear Finite Element Analysis of Planar Reinforced Concrete Members Subjected to Fires," ACI Structural Journal, V. 94, No. 3, May-June 1997, pp. 272-282
4. Heinfling G., Reynouard J. M., Merabet O., and Dubal C., "Computational Modeling of the Mechanical Effects of Pore Pressures in Concrete at High Temperatures," Proceedings of the Euro-C Conference on Computational Modeling of Concrete Structures, 1998, pp. 539-548
5. England G. L. and Khoylou N., "Modeling of Moisture Behavior in Normal and High Performance Concretes at Elevated Temperatures," Proceedings of the 4th Weimar Workshop on High Performance Concrete: Material Properties and Design, 1995, pp. 53-68
6. American Society of Civil Engineers, Structural Fire Protection, ASCE Manuals and Reports on Engineering Practice No. 78
7. American Concrete Institute, Building Code Requirements for Structural Concrete

DIRECT ANALYSIS OF STEEL FRAMES SUBJECTED TO EXPLOSION AND FIRE

J Y Richard Liew
Department of Civil Engineering, National University of Singapore,
Blk E1A, 1 Engineering Drive 2, Singapore 117576
cveljy@nus.edu.sg

ABSTRACT

This paper presents a mixed element approach for analyzing steel frame structures subjected to a localized explosion and followed by fire. Critical members that are subjected to direct action of explosion and fire are modeled using shell elements. Non-critical members that are away from the affected area are modeled using beam elements. The proposed approach is computational efficient for modeling large-scale structures and accurate enough to capture detailed behavior of member yielding and instability associated with the effects of blast and fires. Section classification may change from static load to blast load because of the enhanced yield strength due to high strain rate. The beam element approach is found to over-predict the overall resistance of steel frame structures if local deformation of cross section occurred after the blast loads. Detailed finite element modeling of critical frame members is necessary to improve the accuracy of predicting the ultimate resistance of structures. The influence of blast loads on the fire resistance of a multi-story steel frame is studied.

KEYWORDS: *Blast; Explosion; Fire; Shear Failure; Local buckling; Plasticity; Steel frames; Transient analysis.*

INTRODUCTION

In recent decades, significant amount of work has been carried out to assess the resistance of structures under fire. Simplified method has been proposed by Kruppa(1997) to calculate the fire resistance of a beam based on the plastic mechanism method, considering the reduction of material strength at elevated temperature. Janss and Minne (1981) used the column buckling

curves with reduced yield strength and elastic modulus at elevated temperature to study the load carrying capacity of columns in fire. Wong (2001) developed the plastic analysis method for fire resistance analysis of simple framed structures. Liew, et, al. (1998) and Chan and Chan (2001) proposed the use of plastic hinge methods for large displacement analysis of semi-rigid steel frames at elevated temperature. Ma and Liew (2004) proposed a two-surface yield hinge model for analyzing large scale structures in fire. The method considers inelastic redistribution of forces from fire affected members to adjacent members. Anderberg (1988), Saab and Nethercot (1991), Huang, et al. (2000) adopted the finite element approach for modeling steel subassembly frames subjected to fire. All these methods vary in their applicability and degree of sophistication; however, they cannot be applied to situations in which the fire is a direct consequence of an explosion, which can influence the fire resistance of the structure.

The response of structures under the combined actions of explosion and fire has become a major safety concern in building design in recent years. The short duration of explosion loading implies that the material is strain-rates dependent. On the other hand, fire loading is associated with elevated temperatures which cause thermal strains and lead to significant deterioration in the material properties of steel. Izzuddin, et, al. (2000) proposed an integrated analysis method using beam element for explosion and fire analysis of steel structures. Their method allows the elastic elements to be refined and re-meshed to account for elastio-plastic effects in the members. Liew and Chen (2004) proposed an inelastic transient analysis using beam and fiber elements to study the effect of explosion-induced deformations on frame stability and the subsequent effect of fire on the overall resistance of the structure.

To model a large scale framework, it is convenient and economical to use higher-order beam element, which often requires only one element per member, to be sufficiently accurate for modeling the nonlinear inelastic behavior of 3-D frame structures (Chan and Gu 2000, Liew et al. 2000). However, under blast loading, the strength of steel increases due to the high strain-rate effect, and the member cross-sections are vulnerable to local buckling, which cannot be predicted by the beam element approach. In addition, the beam element approach adopts the assumption of plane section remaining plane after deformation and hence the plasticity deformation due to high shear cannot be modeled correctly. Their uses could over-predict the explosion resistance of steel frame structures.

In a coupled analysis, high-strain rate caused by an explosion, softening of materials due to fire and dynamic and thermal responses of structure are all interrelated in a time domain. A fully integrated analysis of fluid dynamics, heat transfer and structural equilibrium equations can provide more accurate prediction of structural response, but ir requires the use of huge computational resources and are very costly to implement. In the present work, the structure is analyzed under predefined explosion and fire loads. Although full coupled analyses are not adopted at present, the current work forms the basis for further studies in which the explosion and fire analyses may be coupled. In this paper, a mixed element approach, implemented using ABAQUS, is adopted to achieve a realistic modeling of the overall framework subjected to localized explosion and fire. Beam element is used to model frame members that are not directly subjected to explosion and fire, and shell element for critical frame members directly subjected to explosion and fire. The proposed approach is found to be accurate enough to capture detailed behavior of local buckling of cross section and member instability associated with blast and fire loads. The influence of blast loads on the fire resistance of a multi-story steel frame is studied.

NUMERICAL MODELLING OF FRAMES UNDER EXPLOSION AND FIRE

Load Sequences and Solution Strategy

Analysis of frames under explosion and followed by fire generally consist of three load sequences as shown in Fig. 1. In the first load sequence, gravity loads which include self weight of the frame and permanent loads applied on frame are increased linearly till the full values over a time period t_1. In the second load sequence, explosion loads are applied on the frame according to predefined blast overpressure varying within time t_1 and t_2. In the third load sequence, temperature in the frame members caused by fire is increased with predefined curves from time t_2 till the end of the fire or the failure of the frame.

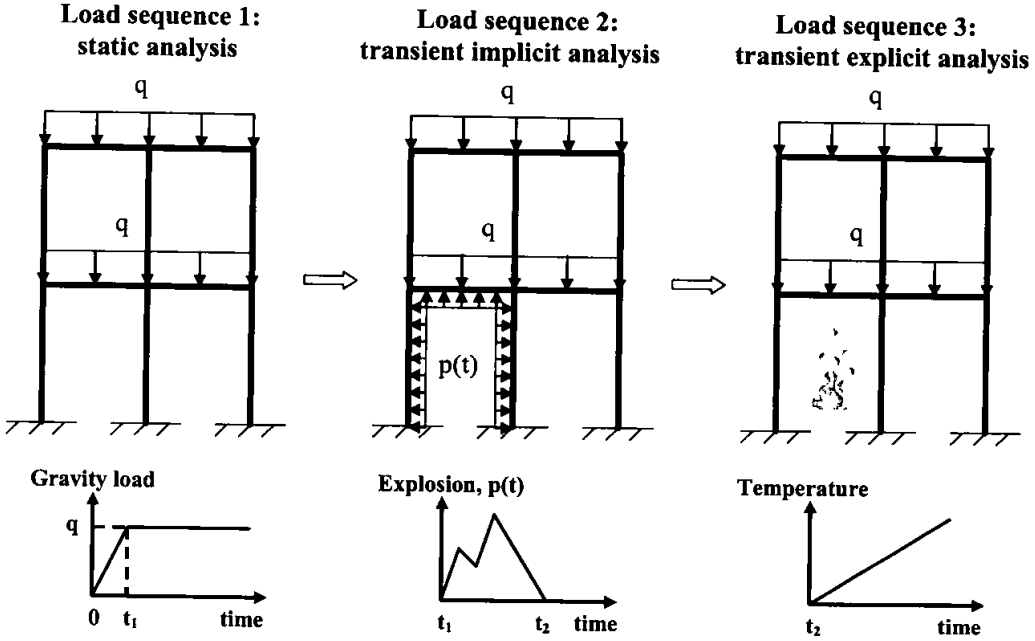

Fig. 1. Load sequences in explosion and fire analysis

Static analysis is used to analyze the frame under gravity load in the first load sequence. In the second load sequence, transient implicit analysis is performed to analyze the frame under explosion. Implicit analysis is suitable for analyzing problems that are mildly nonlinear and where the nonlinearities are smooth. Plastic deformation is a smooth nonlinearity. A converged solution satisfying the dynamic equilibrium can be obtained by implicit analysis within very little iteration steps to obtain solutions for problems with smooth nonlinearity. For the explosion analysis, the damping effect can be ignored because in most situations damping has very little effect on the fundamental response peak. In the inelastic analysis, the energy dissipated through plastic deformation is significantly greater than that dissipated by structural

damping. It is conservative to ignore the damping term in the explosion analysis (Yandzio and Gough, 1999)

The third load sequence is a quasi-static process because temperature rise, as a result of a fire, occur in a much longer duration than that of the explosion. Frame subjected to fire exhibits a highly nonlinear post-buckling behavior with significant material degradation. Transient explicit analysis is particularly effective for solving the highly nonlinear quasi-static problem. Explicit analysis uses elements with diagonal mass matrices and requires a small time increment size for the solution to be stable. The time increment depends solely on the highest natural frequencies of the model and is independent of the type and duration of loading. Simulations take a large number of increments, but the computational cost per increment is relatively small. Since the analysis of frame under fire is a long-time quasi-static solution, it is computationally more efficient that the solution be accelerated in shortest time period and at the same time the inertial forces are still insignificant. The time period can be selected to be greater than 100/f, in which f is dominant vibration frequency of the frame.

Mixed Element Technique

To achieve a realistic modelling of the overall framework subjected to localized explosion and fire, a mixed element technique is used to model the frame. As shown in Fig. 2, frame member 'A' which is not directly subjected to explosion and fire is modeled using beam element. Frame members 'B' and 'C' are modelled as 4-node doubly curved shell elements to capture local buckling and yielding due to high shear under the direct action of blast load. Centroid 'b' of end section of member 'B' and centroid 'c' of member 'C' are offset from end 'a' of member 'A' for defining temperatures varying according to different history in the three members. Distances between nodes 'a' and c', and nodes 'a' and 'b' are selected to be 1/100 length of members 'B' and C', respectively. Displacements and rotations of nodes on the end section of members 'B' and C' are kinematically controlled by those of the centroids 'b' and 'c', respectively, as indicated as the dash lines in Fig. 2. Then displacements and rotations of centroids 'b' and 'c' are kinematically controlled by end 'a' to achieve rigid connections between members 'A' and 'B', and 'A' and 'C'. By using the kinematic coupling technique, rigid joints can be modeled without explicitly detailed modeling of all the joint components. It is further assumed that connections do not fail under explosion and fire. However, the member end forces obtained from the analysis may be used to check the robustness and resistance of the joint components to ensure the validity of the rigid frame analysis.

Strain Rate Effect on Mechanical Properties

The mechanical properties of steel are affected noticeably by the rate at which strain takes place. If the mechanical properties under static loading are considered as a basis, the effects of increasing strain rate can be illustrated in Fig. 3. The yield stress increase substantially to a dynamic yield stress value. The elastic modulus generally remains insensitive to the loading rate. The ultimate tensile strength increases slightly, however the percentage increase is less than that for the yield stress; and the elongation at rupture either remains unchanged or is slightly reduced due to the increased strain rate. In the present formulation, the rate-dependent plasticity is based on the following model:

$$\dot{\varepsilon}^{pl} = \gamma \left(\frac{\sigma_y'}{\sigma_y} - 1 \right)^{1/m} \tag{1}$$

where σ_y' is the yield stress considering strain rate effect, $\dot{\varepsilon}^{pl}$ is the equivalent plastic strain rate, γ is the viscosity parameter, m is the strain rate hardening parameter, and σ_y is the static yield strength. When $\dot{\varepsilon}^{pl}$ tends to zero under very slow loading rate or γ tends to ∞, the solution converges to the static (rate-independent) solution. The suggested values for mild steel are $\gamma = 40\,\text{sec}^{-1}$ and $m = 0.2$ (Izzuddin and Fang, 1997).

After explosion is over, the frame is under the action of fire, and the rate-dependent effect will be ignored because material properties of steel will deteriorate at elevated temperature. The rate-dependent effect of steel can be suppressed by defining parameters $\gamma = 400\,\text{sec}^{-1}$ and $1/m = 1.0$ at elevated temperatures.

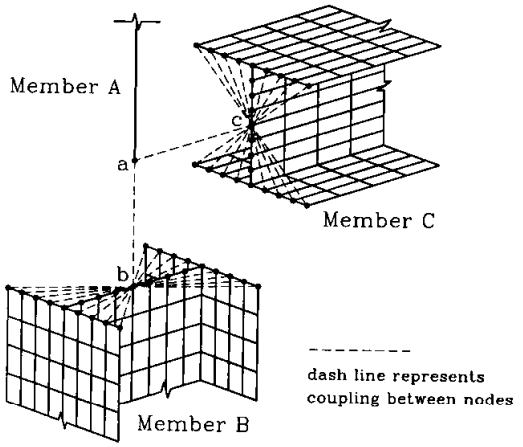

Fig. 2. Linking of beam element and shell elements

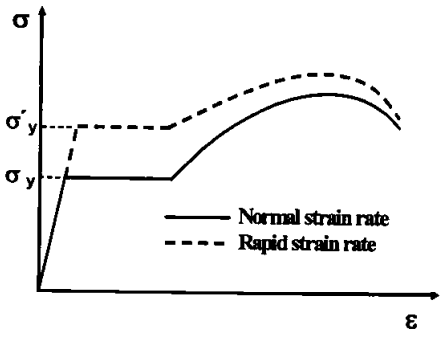

Fig. 3. Rate-dependent stress-strain relationship of mild steel

Temperature Effects on Mechanical properties

Since fire is considered to be an accidental event, large plastic strains are therefore allowed in design. Hence, an effective yield stress is adopted, which is attainable when the strain is considerably larger than the elastic limit at ambient temperatures. ECN (2001) adopts a yield strain ε_y of 2% to define the effective yield strength. The temperature dependences of the proportional limit, the effective yield strength as well as the elastic modulus are shown in Fig. 4. In the numerical formulation, the total strain in the material should be decomposed into the elastic and plastic strain components. The plastic strain is obtained by subtracting the elastic strain, defined as the value of stress divided by the Young's modulus, from the value of total strain. von Mises yield criterion is used to extrapolate a yield surface in 3D principle stress space. The plasticity model is characterized by an associated flow rule with isotropic hardening.

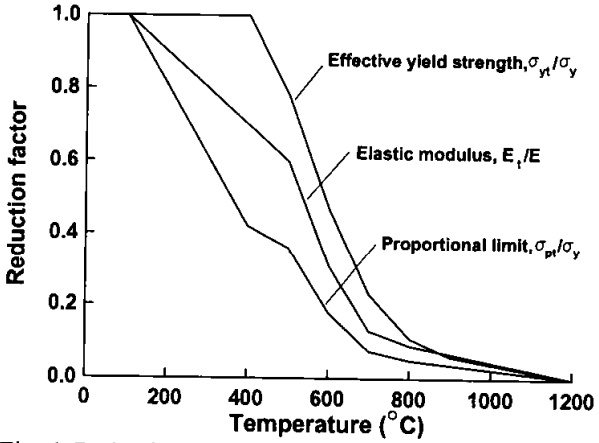

Fig. 4. Reduction factors for E_t, σ_{pt} and σ_{yt} of steel at elevated temperatures

THREE STOREY BUILDING FRAME

Fig. 5 shows a three-storey steel frame under the action of explosion and fire in the first floor side compartment. A uniformly distributed gravity load q = 75kN/m is applied on the frame as initial loads. The explosion load is represented by a uniformly distributed overpressure $p(t) = p_0\bar{p}(t)$ (Fig. 5b), in which p_0 is intensity that can be changed, and $\bar{p}(t)$ defined in Fig. 5d. The elevated temperatures due to fire are modelled as a temperature parameter, T, monotonically increased from 20°C. The steel temperature for the members in the fire compartment is given in Fig. 5c in terms of temperature parameter T. The temperature distribution is taken to be uniform over the member length and linear over the cross-section depth. Material properties at room temperature are E = 210,000N/mm^2 and σ_y=399N/mm^2. A bilinear elastic-plastic model with strain rate parameters $\gamma = 40\,\text{sec}^{-1}$ and $1/m = 5.0$ is used to model the rate-dependent effect under explosion. The EC3 stress-strain relationship of steel at elevated temperature is used to model the structure under fire.

Liew and Chen (2004) modeled the frame using the beam elements and obtained the blast resistance of the frame as p_{max} =310kN/m. Izzuddin et al. (2000) adopted an adaptive beam element approach and predicted p_{max} =333kN/m. In the present study, mixed element approach is used to model the frame. The compartment under explosion and fire is modeled using 4-node shell elements as shown in Fig. 7, and the members in other compartments are modeled using beam elements with 10 elements per member. Kinematic coupling technique between beam element and shell elements is enforced as illustrated in Fig. 2.

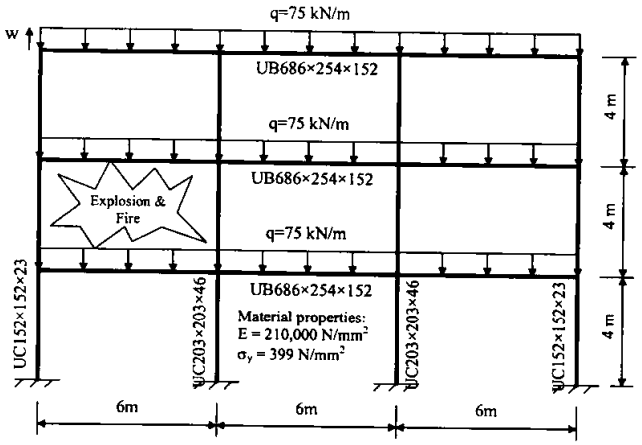

(a) Geometric configuration and loading

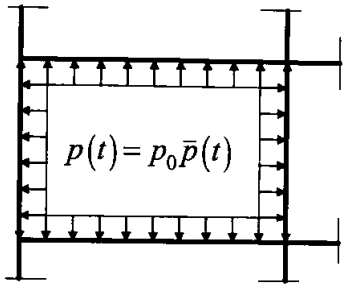

(b) Compartment blast load

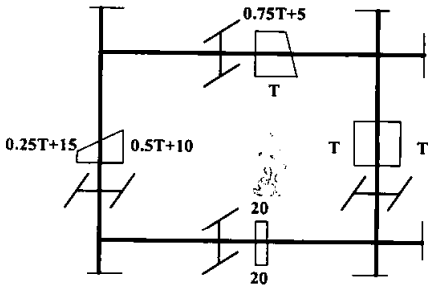

(c) Compartment blast load

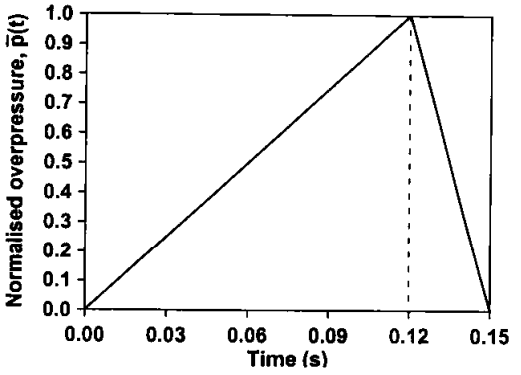

(d) Normalized overpressure $\bar{p}(t)$ over time

Fig. 5. Geometric configuration and loading of 3-storey steel frame

Transient implicit analyses are carried out on the frame under blast with different values of intensity p_0. The blast resistance is found to be p_{max} =120kN/m as shown in Fig. 6. The beam element approach used by Liew and Chen (2004) and Izzuddin et al. (2000) over-predict the blast resistance by 158% and 178% respectively. The collapse mode of the frame under explosion is shown in Fig. 7. Failure of the side column triggers the collapse of the frame. Local buckling occurs in the middle and end regions of the side column, which cannot be modelled by the beam element approach.

The critical temperature of the frame under fire alone is predicted to be T_{max} =870°C based on the beam element approach by Liew and Chen (2004), and T_{max} =894°C by Izzuddin et al. (2000). In the proposed mixed element approach, the critical temperature is predicted to be T_{max} =634°C, which is 27% lower than that predicted by Liew and Chen (2004). The corresponding relations of temperature parameter versus the vertical displacement at the left top

edge are shown in Fig. 8. When the temperature parameter reaches T=564°C, the internal column buckles (Fig. 9) and the frame displaces downward suddenly.

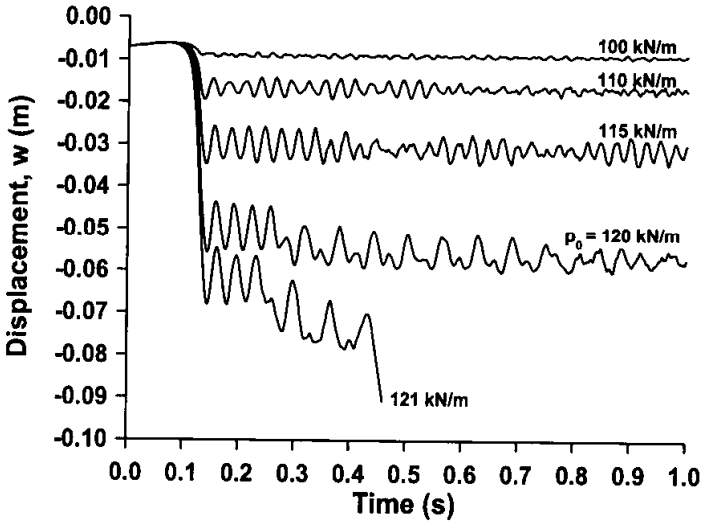

Fig. 6 Responses of frame subjected to blast with different intensities p_o

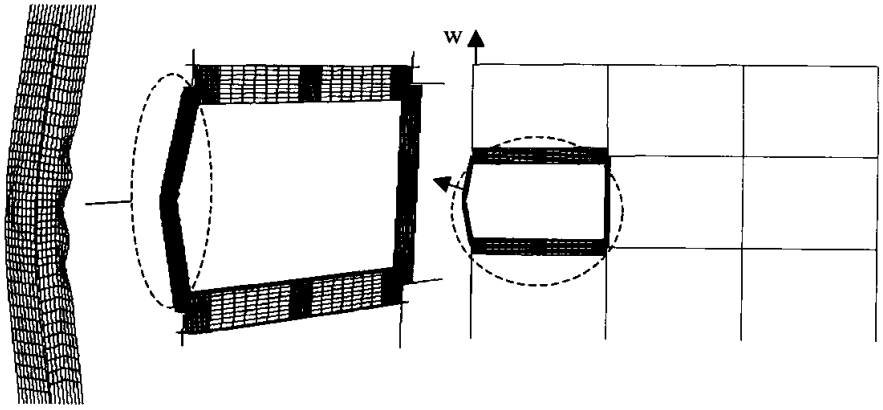

Fig. 7. Collapse mode of frame under blast with $p_0 = 121\ kN/m$

After the internal column has buckled, the redistributing the loads to the side columns. side column buckles, and the frame torsional buckling and local buckling (see assigned for this frame. The out-of-plane imperfections caused by truncation errors in frame still has adequate fire resistance by When temperature reaches T=634°C, the collapses in a coupled mode of lateral- Fig. 10). Out-of-plane imperfections are not lateral buckling is triggered by lateral the numerical solution.

A series of transient implicit analyses are carried out on the frame subjected to blast with different intensity, p_0. After the blast load is applied, transient explicit analyses are carried out

on the frame subjected to fire. Responses of frame under explosion and followed by fire are shown in Fig. 11. Interaction curves between fire resistance and explosion load is plotted in Fig. 12. When p_0 is less than 90 kN/m, the internal column buckles earlier than the side column under fire. When p_0 reaches 90 kN/m, the side column suffers permanent deformation and inelastic effects caused by fire. Both columns tend to buckle at the similar temperature. Deformed shape of frame under blast with $p_0 = 100\ kN/m$ and followed by fire is shown in Fig. 13. When the blast intensity p_0 is less than $0.7\ p_{max}$, the fire resistance is reduced by not more than 10%. Only at higher explosion load ($p_0 > 0.7\ p_{max}$), the fire resistance of the frame is significantly reduced.

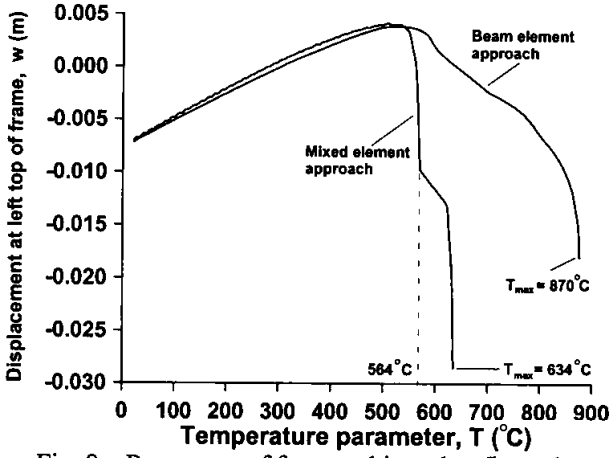

Fig. 8. Responses of frame subjected to fire only

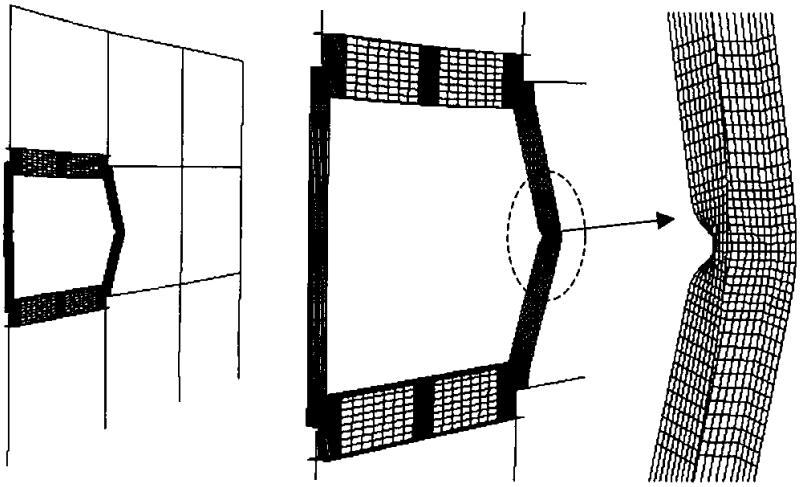

Fig. 9. Deformed shape of frame at T=564°C

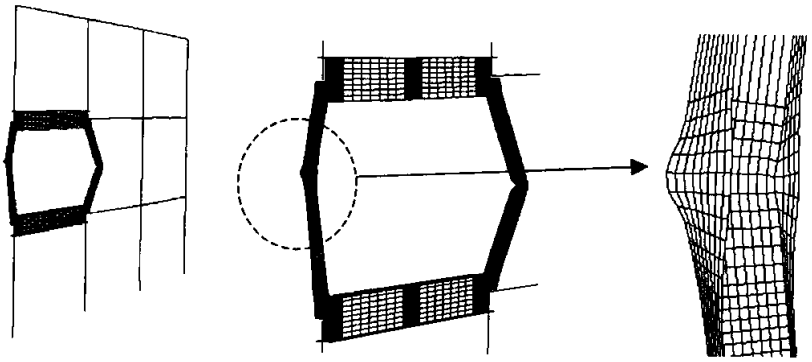

Fig. 10. Deformed shape of frame at T=634°C

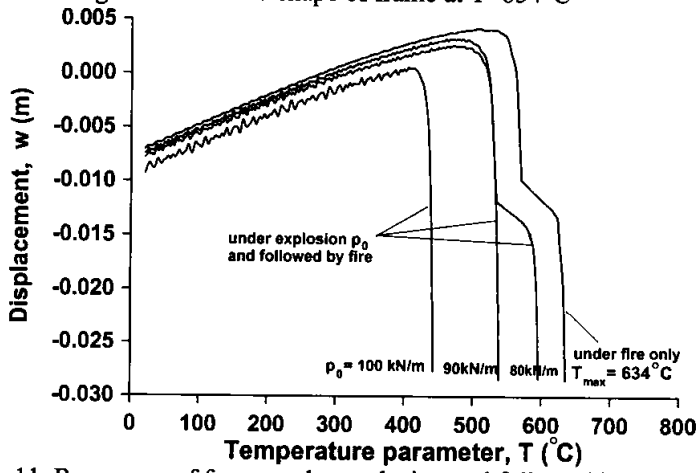

Fig. 11. Responses of frame under explosion and followed by fire

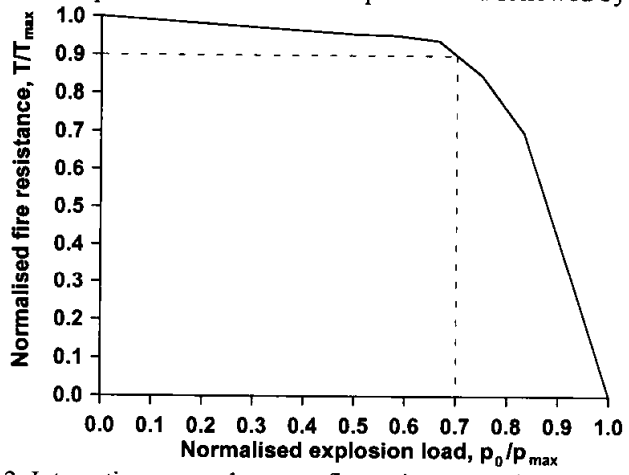

Fig. 12. Interaction curves between fire resistance and explosion load

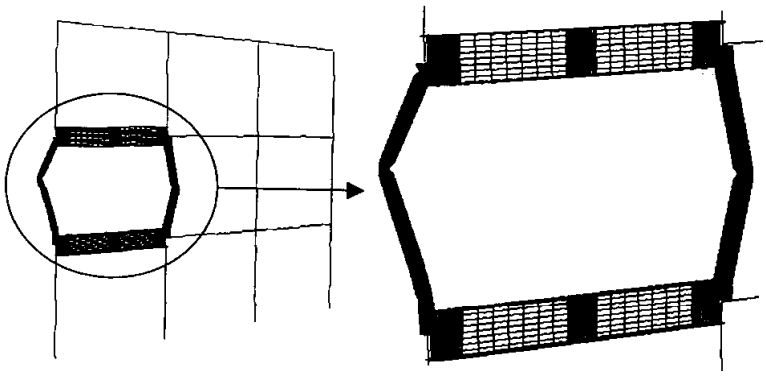

Fig. 13. Collapse mode of frame under blast with $p_0 = 90\ kN/m$ and followed by fire

CONCLUSIONS

This paper presents a numerical approach for the analysis of steel frame structures subjected to explosion and fire. Although frame members can be efficiently modeled using beam elements, their application are limited to compact sections subjected to load effects that do not result in local buckling, significant shear yielding and lateral-torsional buckling. For steel frames under the direct influence of explosion, the steel strength increases due to high strain-rate. The tendency for plate buckling in member cross section increases significantly. Possibility of shear failure may occur at critical members in the building subjected to high due to high blast loads. These phenomena cannot be predicted by the conventional beam element approach.

A mixed element approach is proposed to achieve both realistic and computationally efficient modeling of the overall framework subjected to localized explosion and fire. The proposed approach adopts the use of beam element for frame members not directly subjected to explosion and fire, and shell element for frame members exposed directly to blast and fire. Kinematic coupling is used to link beam elements and shell elements. The proposed approach can capture the detailed behavioral effects associated with high-strain rate and elevated temperature.

Numerical analyses are carried out on a three-storey steel frame subjected to an explosion and followed by a fire. Member permanent displacements, local buckling and shear yielding caused by explosion reduced the fire resistance of the frame. The fire resistance of the frame was reduced by 10% after the explosion with blast intensity $p_0 = 0.7\, p_{max}$. This was attributed to the stability interaction between columns and the overall frame system. The side column was identified as the weakest component in the frame system because of local buckling occurred after the blast. This triggered the side sway collapse of the frame when it was later exposed to fire. Further research work is needed to study the vulnerability and survivability of various framing systems exposed to blast and fire loads in order to develop an effective strategy to protect building structures against willful attacks.

REFERENCES

Anderberg, Y. (1998), Modelling steel behaviour. *Fire Safety J.*, 13, 17-26.

Saab H. A. and Nethercot, D. A. (1991), Modelling steel frame behaviour under fire conditions. *Eng. Struct.*, 13(4), 371-382.

Chan, S. L., and Gu, J. X. (2000), Exact tangent stiffness for imperfect beam-column members, *J. Struct. Engrg.*, ASCE, 126(9), 1094-1102.

Chan, S. L and Chan, B. H. M. (2001), Refined plastic hinge analysis of steel frames under fire. *J. Steel and Composite Struct.*, 1(1),111-130.

Chen, H and Liew, J. Y. R. (2002). *Explosion and fire analysis of steel frames.* In Proceedings of the Second International Conference on Structural Stability and Dynamics, December 16-18, Singapore.

ECS (2001). *Eurocode 3 Design of steel structures: Part 1.2: General rules, Structural fire design*, ENV 1993-1-2, European Committee for Standardisation, Brussels.

Huang, Z. H, Burgess, I. W. and Plank, R. J. (2000). Three-dimensional analysis of composite steel-framed buildings in fire, *J Struct. Eng., ASCE*, 126(3), 389-397.

Izzuddin, B. A. and Fang, Q. (1997), Rate-sensitive analysis of framed structures. Part I: model formulation and verification, *Struct Eng & Mech*, 5, 221-237.

Izzuddin, B. A, Song, L, Elnashi, A. S, and Dowling, P. J. (2000), An integrated adaptive environment for fire and explosion analysis of steel frames – Part II: verification and application, *J Construct Steel Res.*, 53, 87-111.

Janss, J and Minne, R. (1981), Buckling of steel columns in fire conditions. *Fire Safety J.*, 4, 227-235.

Kruppa, J. (1979), Collapse temperature of steel structures, *J Struct. Div.*, ASCE,105(ST9), 1769-1788.

Liew, J.Y. R, Tang, L. K, Holmaas, T. and Choo, Y. S. (1998), Advanced analysis for the assessment of steel frames in fire, *J. Construct. Steel Res.*,47(1-2),19-45.

Liew, J. Y. R., Chen, H, Shanmugam, N. E., and Chen, W. F. (2000). Improved nonlinear plastic hinge analysis of space frame structures, *Engrg. Struct.*, 22, 1324-1338.

Liew, J. Y. R. and Chen, H. (2004), Explosion and fire analysis of steel frames using fiber element approach, *J. Structural Engineering*, ASCE, July Issue, In Press.

Ma, K. Y. and Liew, J. Y. R. (2004), Nonlinear plastic hinge analysis of three dimensional steel frames in fire, *J. Structural Engineering*, ASCE, July Issue, In Press.

Perzyna, P. (1968), Fundamental problems in viscoplasticity, *Advances in Applied Mech.*, 9, 313-377.

Wong, M. B. (2001), Elastic and plastic methods for numerical modelling of steel structures subject to fire, *J Construct Steel Res.*,57(1),1-14.

Yandzio, E and Gough, M. (1999), *Protection of buildings against explosions*, The Steel Construction Institute, U.K.

DYNAMIC ANALYSIS USED TO COPE WITH PARTIAL AND TEMPORARY FAILURES

Jean-Marc FRANSSEN & Frédéric GENS
Univ. of Liege, 1, Chemin des Chevreuils, 4000, Liège 1, Belgium,
jm.franssen@ulg.ac.be

ABSTRACT

The step by step numerical analysis of structures submitted to fire is usually performed by a succession of static analyses taking into account the modifications of the temperatures in the structure from one time step to the other. As a consequence, the analysis cannot be pursued beyond any moment in the fire when the stiffness matrix is not positively defined. This happens normally when the load bearing capacity of the structure has decreased to the level of the effects of actions, in which case the last converged point is the "true" fire resistance time. In some cases, for reasons linked either to the geometric non-linearity or to the material behaviour, it may happen that only a part of the structure is in an unstable position. With the traditional algorithm, the simulation cannot be performed any further, but it does not mean that the load bearing capacity of the whole structure has been lost; a "numerical" failure time is observed.

This paper explains the problem and reviews some of the techniques that have been used in order to cope with this problem. None of these methods has proved to be totally satisfactory.

The paper presents the dynamic algorithm that has been recently implemented in the software SAFIR. Because the acceleration terms are now considered, the implicit integration on time of the system of equations is not in jeopardy even if the stiffness matrix is not positively defined.

The basic theory as well as some validation and demonstration examples are presented. It is shown how the simulation time can be extended way beyond the moments of partial and temporary collapse. As an additional benefit of the method, even when the "true" fire resistance time is reached, the simulation can be performed for substantially larger displacements, which gives a much better insight into the failure mode and allows, for example, to demonstrate that the failure of the part of the structure that is subjected to fire does not lead to the progressive collapse of the rest of the structure that is not subjected to the fire.

KEYWORDS: *finite element; dynamic analysis; fire resistance; partial failure*

INTRODUCTION

The step by step numerical analysis of structures submitted to fire is traditionally performed by a succession of subsequent static analyses of the structure taking into account the modifications of the temperature field in the structure from one time step to the other, see for example [1 to 8]. Figure 1 shows a schematic algorithm that explains the usual procedure for a simple structure with a behaviour that can be characterised by one displacement and one force and that is characterised by a single temperature.

The load is first applied at ambient temperature, noted T0 on the figure. If the load level in case of fire is sufficiently high to generate a non linear behaviour of the structure, the load may be applied in several increments. On Figure 1, two successive time steps have been used in order to apply the load in two increments. For each step, one initial is first found corresponding to the incremental load, and one iteration is then performed in order to treat the out of balance force that appears because of the non linear behaviour. It can be seen on the Figure that the obtained solution is not exactly converged, but the remaining out of balance force can be taken into account in the subsequent step so that they don't accumulate.

When the applied load is equal to the design load for the fire case, it is usually kept constant and the temperature in the structure is increase in an incremental manner. Figure 1 illustrates the out of balance force that occurs because of the degradation of the mechanical properties of the structure during the first temperature increase, from time step 2 to time step 3. This out of balance force leads to a new incremental displacement.

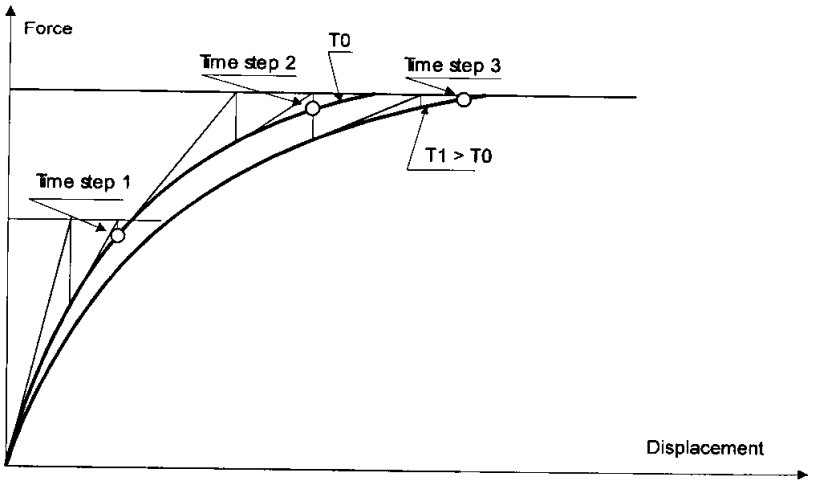

FIGURE 1 : schematic algorithm for a static analysis

If the loads at all degrees of freedom of the structure are noted $\{F\}$ and if the corresponding displacements that have to be determined are noted $\{u\}$, then Equation 1 is used to determine the incremental displacements.

$$\{\Delta F\} = [K]\{\Delta u\} \quad (1)$$

where $[K]$ is the stiffness matrix of the structure,

$\{\Delta F\}$ represents either the increment of external applied forces or the out of balance forces.

On Figure 1, the stiffness matrix is represented by the slope of the curve at each point.

In a simple structure, the evolution of the situation toward failure is depicted by Figure 2 where the last converged time step is time N° 4. For any higher temperature, the behaviour of the structure has degraded to such an extend that it is not possible to find a point on the curve 5 that satisfies the equilibrium. In other words, from point 4, it is possible to increase the displacements of the structure without any increase of the load. The structure is unstable. Mathematically, this corresponds in Equation 1 by the fact that the stiffness matrix is not anymore positive defined.

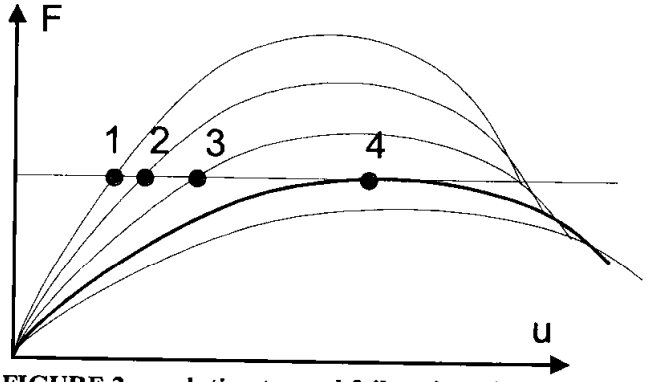

FIGURE 2 : evolution toward failure in a simple structure

For some more complex structures yet, the behaviour may be more complex. On Figure 3 for example, point 3 seems to be the last possible converged point because the structure is unstable for any higher displacement (or for any higher temperature) whereas it can be observed that another point of equilibrium exist at temperature T4, but for a significantly larger displacement.

Such a response of the structure can be generated either by material or by geometrical instabilities. In some cases, the instability affects the complete structures. This can be the case, for example, for a concrete beam on 3 supports when the negative bending moment on the central support leads to a severe cracking in the section. In this case, we would call it a temporary failure because, if the software is able to cope with this phenomena and find the other position of equilibrium corresponding to larger displacements of the beam, the simulation can be run for a longer duration after this instant when instability occurs.

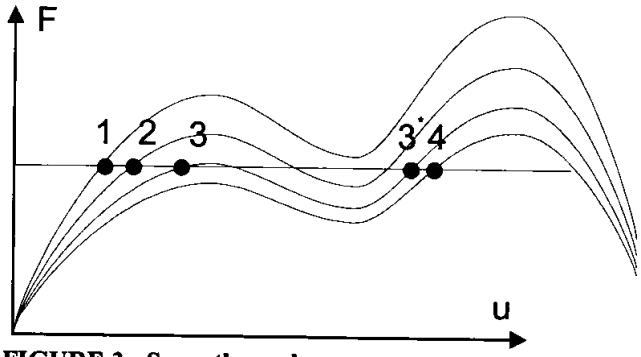

FIGURE 3 : Snap-through

In some other cases, the instability affects only one part of the structure. This can be the case, for example, for a member under compression in a statically indeterminate structure. The buckling of this single element may put the algorithm in jeopardy, whereas the rest of the structure might be able to survive for a longer duration, even if this element is completely removed. In this case, we would call it a local failure.

VARIOUS ATTEMPTS TO SOLVE THE PROBLEM

Reducing the time step to very small values has no effect on the problem mentioned here because, even if it is approached by very small time steps, there is a moment when the structure is unstable and it appears that the software is totally unable to perform any simulation beyond that moment. On the contrary, it may happen that an artificially or inadvertently chosen larger time step would allow the software to "jump", for example, from point 2 to point 4 on Figure 3. This is by no means a reliable solution as success is far from being guaranteed.

It is tempting to modify the material constitutive models in order to delete the unstable characteristics. The uniaxial relationship of steel proposed by Eurocode 3 [9], for example, has an horizontal plateau with no stiffness for a mechanical strain extending from 2% to 15%. A very small slope here can help bring some, if small, stiffness in the structure that may help somehow. It is even more tempting to disregard the descending branch that is present in this steel model from 15% to 20% and to replace it by a infinitely long plateau. Apart from the fact that these solutions yield to the presentation of results that are falsely labelled as "Eurocode model", they are not general either because they are specific to some materials and by no means solve the cases when the instability is caused by geometric reasons.

It is possible to consider the true stress-strain relationship when evaluating the out of balance forces, but using a modified stiffness when calculating the stiffness matrix. For example, the descending branch of the concrete model [10] can be considered exactly when evaluating the stresses, but a zero stiffness is considered instead of the true negative value when evaluating the stiffness matrix. This is not incorrect because only the out of balance forces have to be evaluated exactly for the non linear process to converge. In fact, an approached value of the stiffness

matrix is used leading to a modified Newton-Raphson convergence algorithm instead of the true Newton-Raphson algorithm that was implied on Figures 1, 2 and 3. On these curves, the linear branch leaving any out of equilibrium point does not need to be exactly tangent to the curve at that point in order to reach convergence. Convergence with an approximated stiffness matrix may require a larger number of iterations. The same shortcomings exist here: success is not guaranteed, the solution is specific to some specific materials and geometrical instabilities are not addressed.

Another family of solutions are the so called Risk types or arc-length methods. The first author has previously implemented such a method [11] in his code SAFIR [12]. After a traditional procedure, when an unstable situation is approached, for example point 3 on Figure 3, the temperature is kept constant and this method is activated to travel on the curve from point 3 to the other point of equilibrium, point 3^* on the figure, this supposed to occur in the same time step. The principle of these methods is that the applied loads are multiplied by a scalar load multiplier, which constitutes a new unknown to the problem, and a new constraint equation is added, expressing the fact that each obtained point is at a given distance (the arc length) from the previous point in the hyper space that contains all the loads and displacements. This method has some merits such as the fact that it is not material dependent, does not require any modification of the recommended material models and can treat geometrical instabilities as well. Some successes have been obtained with this method but time has shown that it can also fail in many cases so that it can not be considered as sufficiently general. Furthermore, it may not be without any consequences to unload than reload the total structure that has an inelastic response, when only one part of it is creating the problem. For example, if a steel diagonal at the upper floor of a complex building is entering into buckling, is it really innocuous to numerically unload then reload the heavily loaded concrete columns that may be present at the first floor.

THE DYNAMIC APPROACH

The idea is to model the behaviour of the structure as a dynamic process with the objective that acceleration term will counterbalance the negative stiffness during the unstable states of the structure. Equation 2 is the basic equation for a dynamic analysis if the behaviour of the structure is linear.

$$\{F\} = [K]\{u\} + [C]\{\dot{u}\} + [M]\{\ddot{u}\} \tag{2}$$

where $[C]$ is the damping matrix,

$[M]$ is the mass matrix,

$\{\dot{u}\}, \{\ddot{u}\}$ are the velocity and acceleration at the nodes, to be determined as well as the displacements.

The Newmark method has been used for the time integration; at any time, the velocity and acceleration (both unknown) are evaluated as the function of the displacement at that time (also unknown) and of the displacement, velocity and acceleration at the previously converged time

step, see equations 3 and 4 in which suffix 0 is related to the previously converged time step and suffix 1 is related to the new time step.

$$\{\dot{u}_1\} = \frac{\delta}{\alpha \Delta t}(\{u_1\}-\{u_0\})+\left(1-\frac{\delta}{\alpha}\right)\{\dot{u}_0\}+\Delta t\left(1-\frac{\delta}{2\alpha}\right)\{\ddot{u}_0\} \tag{3}$$

$$\{\ddot{u}_1\} = \frac{\delta}{\alpha \Delta t^2}(\{u_1\}-\{u_0\})+\frac{1}{\alpha \Delta t}\{\dot{u}_0\}+\left(1-\frac{1}{2\alpha}\right)\{\ddot{u}_0\} \tag{4}$$

where α and δ are the Newmark parameters, usually chosen as ¼ and ½ respectively,

Δt is the time step from t_0 to t_1.

Equations 3 and 4 allow to transform equation 2 in a system that contains the sole unknown $\{u_1\}$, see equation 5.

$$\{F_1\}+\{A_0\} = [K^*]\{u_1\} \tag{5}$$

$$\text{with} \quad [K^*]=[K]+\frac{\delta}{\alpha \Delta t}[C]+\frac{1}{\alpha \Delta t^2}[M] \tag{6}$$

and

$$\{A_0\}=\left[\frac{\delta}{\alpha \Delta t}\{u_0\}+\left(\frac{\delta}{\alpha}-1\right)\{\dot{u}_0\}+\left(\frac{\delta}{2\alpha}-1\right)\{\ddot{u}_0\}\right][C]+\left[\frac{1}{\alpha \Delta t^2}\{u_0\}+\frac{1}{\alpha \Delta t}\{\dot{u}_0\}+\left(\frac{1}{2\alpha}-1\right)\{\ddot{u}_0\}\right][M] \tag{7}$$

For a structure with a non linear behaviour, equation 5 is slightly modified into equation 8.

$$\{F_1\}+\{A_0\}-\{F_0\}-\{A_{-1}\} = [K^*]\{\Delta u_1\} \tag{8}$$

In SAFIR, the contribution to the mass matrix coming from the finite elements has been diagonalised in order to limit memory allocation requirements. The shell finite element has only the terms corresponding to displacements in the mass matrix. For the 3D beam finite element, the 2 masses in rotation around the axes that are perpendicular to the longitudinal axis are given the same value as the mass in rotation along the longitudinal axis. This approximation is justified by the fact that several finite elements are anyway used to model one beam member. It allows not to rotate the mass matrix from the local to the global system of coordinates. Nodal masses can also be added by the user, either for displacement or for rotation types degrees of freedoms.

For the damping matrix, one common solution is the Rayleigh damping where the damping matrix is a linear combination of the stiffness and the mass matrix, with the coefficients of the combination being calculated as a function of the critical damping and of the first two eigen frequencies of the structure. This has not been used here because, when the stiffness matrix becomes negative, the damping matrix can also become negative and the system becomes unstable (it is possible to use the initial elastic stiffness matrix instead of the updated tangent stiffness matrix, but this adds additional storage requirement). The determination of the eigen

modes also requires that the mass matrix does not contain any null term and this can also be a problem in some cases, especially when some degrees of freedom are not cinematic quantities.

This is why a numerical damping has been introduced. Practically speaking, the critical damping is taken as 0 (which means that no damping matrix is calculated) and the Newmark parameters are modified. In SAFIR they have been chosen as $\delta = 0.80$ and $\alpha = 0.45$. It has to be kept in mind that the aim is not the precise modelling of dynamic effects where a precise determination of the accelerations and of the damping is required as would be the case, for example, in a design of a building against seismic actions.

An automatic adaptation of the time step during the analysis has been implemented, based on the number of iterations required for obtaining convergence. If convergence is not obtained, the software automatically comes back to the previously converged point and tries again with a reduced time step. The required CPU time may be longer than for static analyses, but the time required for each time step is not significantly increased. A longer CPU time is mainly required when very small time steps have to be used.

EXAMPLES AND CASE STUDIES

Heated Diagonal

The first example is academic but illustrates quite well the possibility to cope with the local failure, here the buckling of a diagonal, see Figure 4. The steel frame made of HEA100 sections for the columns and IPE140 for the beam is submitted to a horizontal load (3000 N). The frame is able to withstand this load, but a pinned diagonal (HEA100) bracing has nevertheless been introduced in order to limit the horizontal displacement.

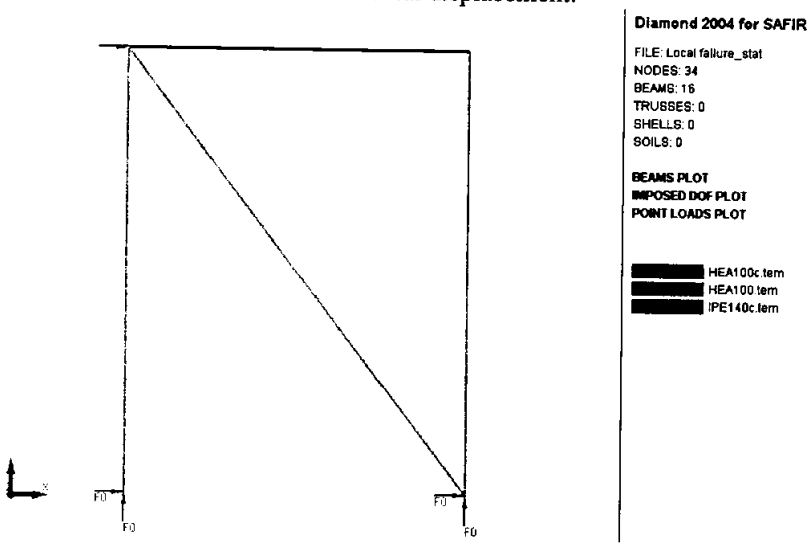

FIGURE 4 : buckling of a diagonal

The diagonal is the sole member to be heated by the ISO fire. It thus tends to elongate but the members of the frame prevent this movement. The compression in the diagonal increases while its mechanical properties decrease and buckling occurs after 3300 seconds. Figure 5 shows the evolution of the horizontal displacement at the top of the diagonal, with a first movement to the left due to thermal elongation, a progressive stabilisation, the sudden buckling with some oscillations visible only on the zoom at the right, and a final stabilisation for a displacement to the right equal to 103 mm, exactly the value that can be calculated for the frame without any bracing, a situation that the remaining structure can survive indefinitely, whatever the temperature of the diagonal.

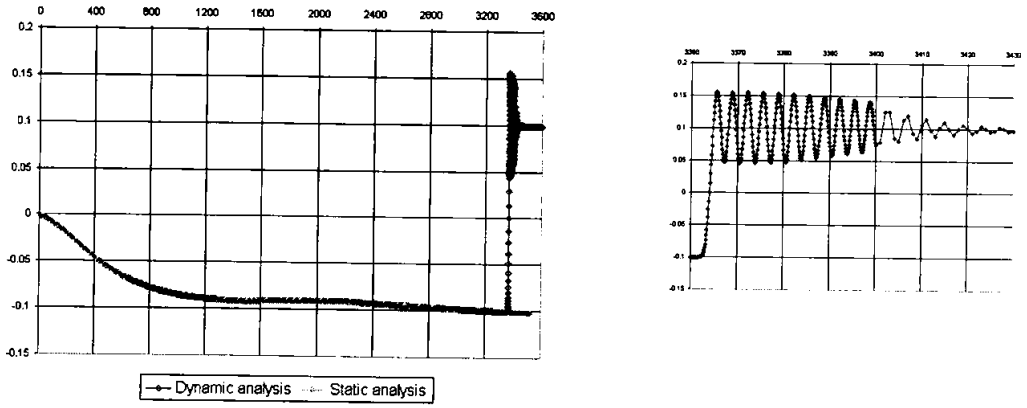

FIGURE 5 : horizontal displacement

Figure 6 shows the increase of axial load in the diagonal until buckling and, after buckling, the decrease toward a nearly zero value of this force. The structure truly lives on as if the buckled diagonal was not there. No need to say that a traditional static algorithm is unable to cope with this local buckling and the analysis stops irremediably at 3500 seconds.

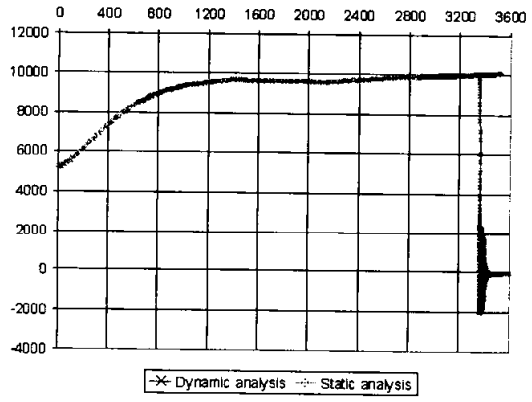

FIGURE 6 : evolution of the axial force in the diagonal

Double portal frame

Figure 7 shows a double bay one storey steel portal frame, the left part of it only is heated (ISO fire with a constant temperature on the section). This example has been treated with 3D beam finite elements but the out of plane displacements will not be shown here.

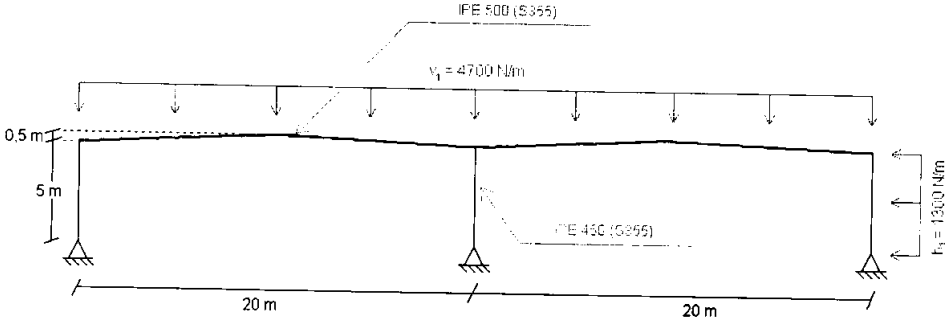

FIGURE 7 : double steel portal frame

A static analysis yields a fire resistance of 1593.5 seconds, whereas the dynamic analysis yields 1590.5 seconds. The 3 seconds are of course not significant in terms of fire resistance. More interesting is the fact that the dynamic analysis can show much larger displacements of the structure into failure. Figure 8, for example, shows the displacements at failure with a horizontal displacement of the heated column equal to 2.70 meters toward the inside, which demonstrates that failure of the heated frame is indeed toward the inside of the building whereas, for the static analysis, the top of the column was still displaced toward the outside when the software stopped (but moving fast toward the inside). The beam vertical displacement of some 5.50 meters brings it laying on the floor, which helps demonstrate that the unheated part of the building is not affected even by the total collapse of the heated part (the static analysis stopped for a vertical deflection in the order of 0.30 meters).

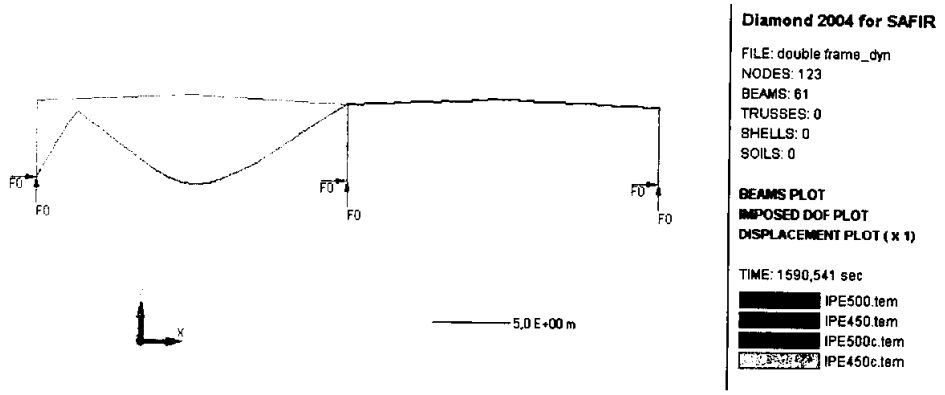

FIGURE 8 : displacements at failure

Series of parallel frames

Figure 9 shows the deflected shape at failure of a series of steel portal frame, submitted to a local fire. Failure time with the static analysis is 769 seconds, caused by buckling in one purlin. A dynamic analysis, on the other hand, shows that the heated frame is stable until 1257 seconds although, in this case, failure of the heated frame seems to produce failure of some of the parallel frames.

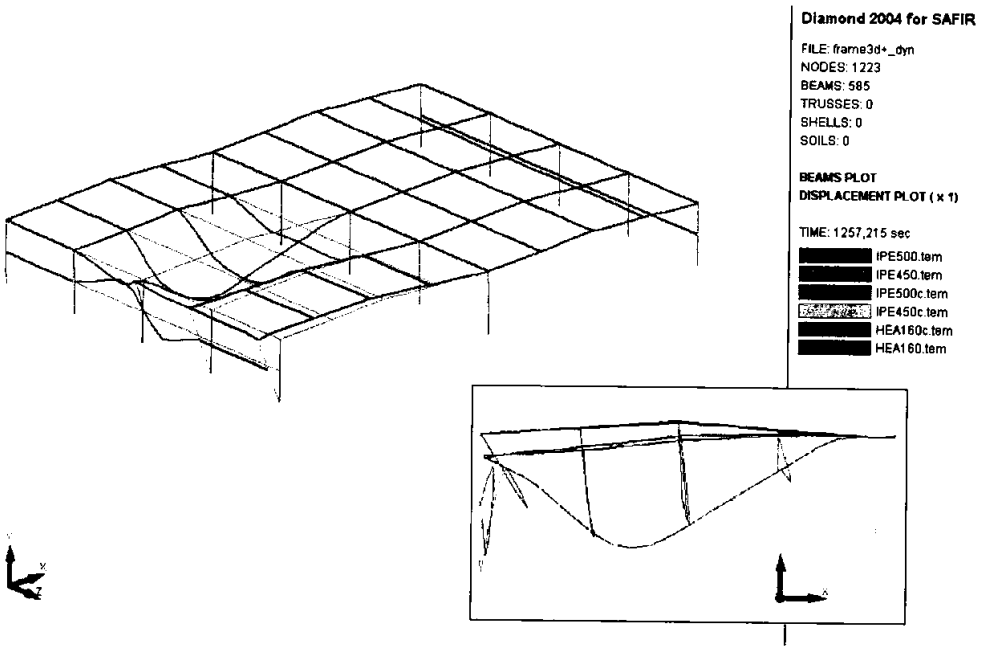

FIGURE 9 : one frame and some purlins heated

Continuous concrete beam

Figure 10 shows the deflection at failure (amplified by a factor 5) of a continuous longitudinally restraint reinforced concrete beam subjected to the ISO fire. The plastic hinges that have developed on some intermediate supports are clearly visible here.

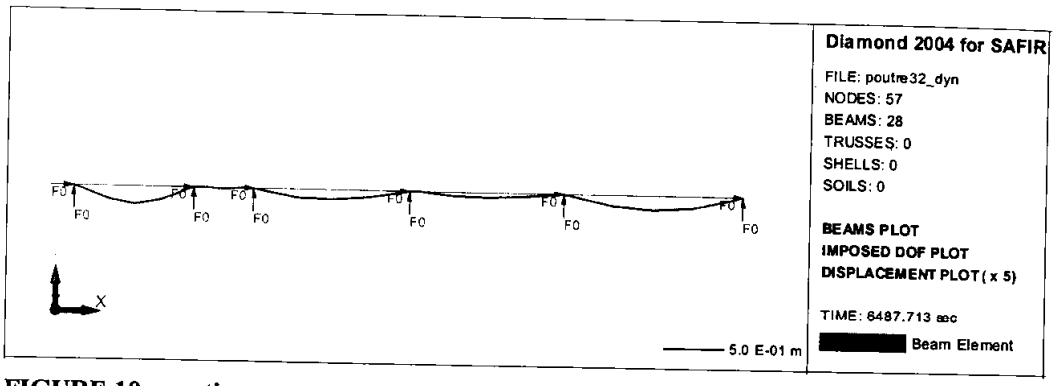

FIGURE 10 : continuous concrete beam (courtesy CSTB, Paris)

Figure 11 shows the evolution of the bending moments at the 4 intermediate supports (thin lines) and in the centre of the 5 spans (thick lines). The sudden variation of the moments that occur at 43, 50 and 67 minutes is due to the crushing of concrete in compression at one support or another. Such rapid variations cannot be accommodated by a static analysis that incorrectly yields 43 minutes as the fire resistance time.

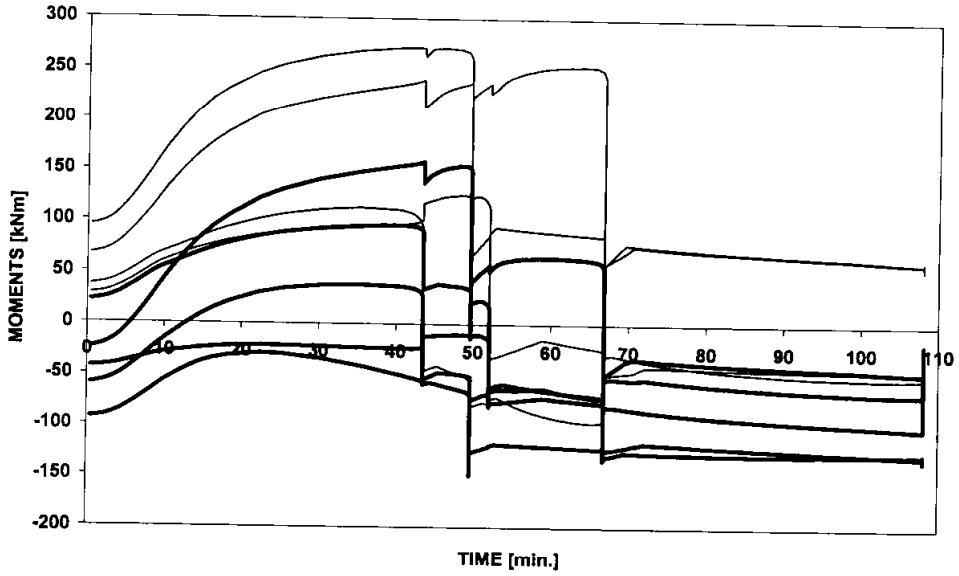

FIGURE 11 : evolution of the bending moments

Two examples with shell finite elements

Figure 12 shows the deflected shape at failure (amplified by a factor of 20) of an 87 by 28 m² reinforced concrete flat slab supported at concentrated points. This slab is analysed at room temperature in order to determine the ultimate load bearing capacity in bending. A static analysis could not cope with the high level of load redistribution when plasticity occurs, mainly in the regions near the supports.

Figure 13 shows the deflected shape of a heated short cellular steel beam at failure. Whereas the static analysis stops at 856 seconds, the dynamic algorithm was able to run until 862 seconds. Again, the failure time is nearly the same, but the final displacements are much larger in the dynamic analysis. Indeed, in the static analysis, the final displacements of the structure are nearly invisible without an amplification factor. More amazing is also the fact that, whereas the geometry and the loading are nearly symmetric (the initial out of straightness of the beam is not), the dynamic algorithm was able to run until the moment when failure is clearly localised at one of the two supports.

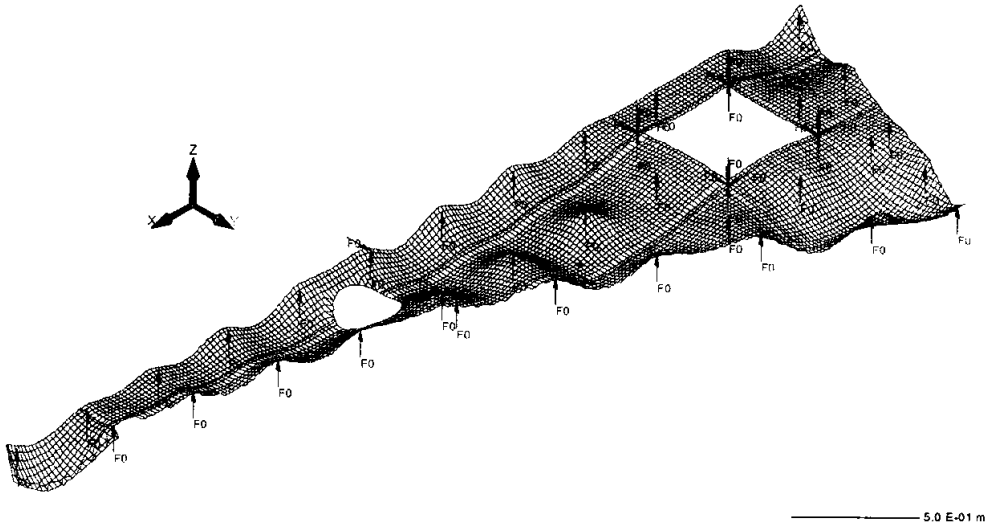

FIGURE 12 : flat concrete slab at room temperature (courtesy BATISERF, Grenoble)

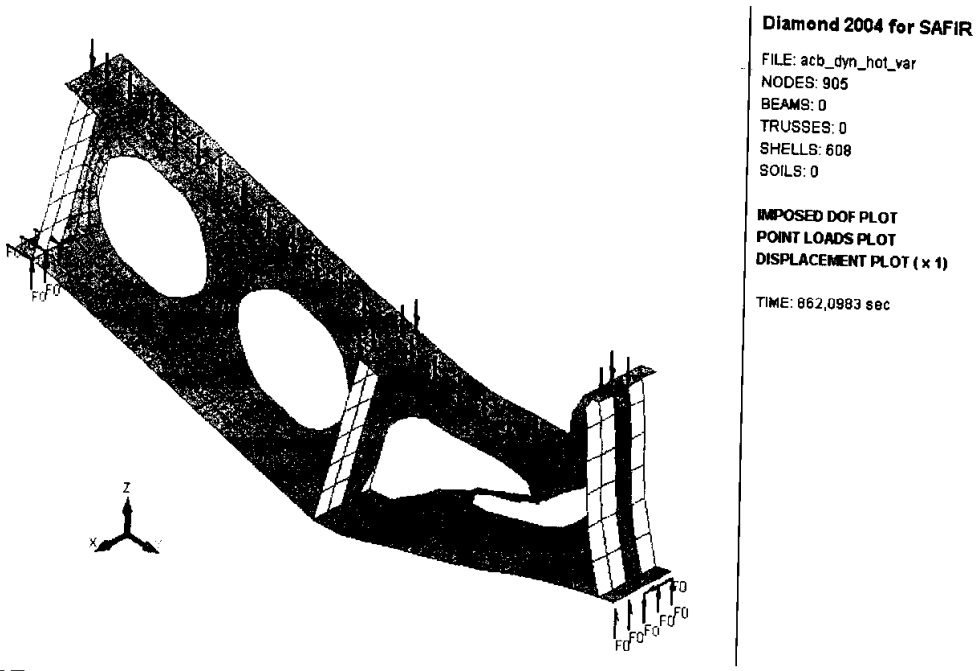

FIGURE 13 : heated short cellular steel beam

CONCLUSIONS

An algorithm has been implemented in the software SAFIR that allows considered acceleration terms in the analysis of structures subjected to fire. This algorithm has been verified for truss, beam and shell finite elements, at room temperature as well as for fire conditions.

It allows the simulation to run beyond these moments when the stiffness matrix is temporarily or locally not positive. Local failures and temporary unstable states can thus be accommodated. Even for structures without any local failure or temporary unstable states, this algorithm allows to pursue the simulation for much larger displacements than with a succession of static analyses. This gives a much deeper understand of the failure mode and allows, in certain cases, to judge on the possibility of progressive collapse.

This algorithm is not particularly expansive in terms of CPU time, except when very small time steps have to be used which, owing to an automatic adaptation of the time step, is normally the case only at the very end of the simulation or near the instants when the structure is unstable.

ACKNOWLEDGEMENT

The development in the code SAFIR presented here have been made at the University of Liege acting as a subcontractor for ARBED-Research, ARCELOR group, within the frame of the European research grant (ECSC Research 7210 PR 378).

REFERENCES

[1] Quast, U., Hass R. & Rudolph K., *STABA-F: Berechnung des Tag-und Verformungsverhaltens von einachsig gespannten Bauteilen unter Feuerangriff*, T. U. Braunschweig, 1984.

[2] Franssen, J.-M., *Etude du comportement au feu des structures mixtes acier béton*, Ph. D. thesis,, Collection de la F.S.A., N°111, Univ. de Liège, 1987.

[3] Zhao, B., *Modélisation numérique des poutres et portiques mixtes acier-béton avec glissements et grands déplacements : résistance à l'incendie*, Ph. D. thesis, INSA, Rennes, 1994.

[4] Kaneko, H. *Etude par la méthode des éléments finis du comportement mécanique d'éléments plaques en acier soumis à l'incendie*. Construction Métallique, C.T.I.C.M., **1**, 37-50, 1990.

[5] Becker, J. Bizri, H. & Bresler B., *Fires-R.C.. A computer program for the fire response of structures - Reinforced concrete*, Report UCB FRG 74-3, Univ. of California, Berkeley, 1974.

[6] Huang, Z., Burgess, I.W. & Plank, R.J., *Modelling Membrane Action of Concrete Slabs in Composite Buildings in Fire. Part I: Theoretical Development*, Journal of Struct Engineering, ASCE, 129 (8), (2003) 1093-1102

[7] Forsen, N. E., *A theoretical study on the fire resistance of concrete structures*, The Norwegian Inst. of Technology, Trondheim, 1982.

[8] Anderberg Y., *Fire-exposed hyperstatic Concrete Structures - An Experimental and Theoretical Study*, Lund Institute of Technology, 1976.

[9] ENV 1993-1-2, *Eurocode 3 : Design of steel structures. Part 1.2 : General rules. Structural fire design*, CEN, Brussels, may 1995.

[10] ENV 1992-1-2, *Eurocode 2: Design of concrete structures - Part 1-2: General rules - Structural fire design*, CEN, Brussels, November 1995.

[11] Franssen, J.-M., *Failure temperature of a System Comprising a Restrained Column Submitted to Fire*, Fire Safety Journal, Vol 34 (2000), 191-207

[12] Franssen, J.-M., *SAFIR – A thermal/Structural Program Modelling Structures Under Fire*, Engng Journal, AISC, accepted for publication, 2004.

ADVANCED MODELING OF COMPOSITE FRAMES SUBJECTED TO COMPARTMENT FIRE

H X Yu and J Y Richard Liew*
Department of Civil Engineering, National University of Singapore,
Blk E1A, 1 Engineering Drive 2, Singapore 117576
*cveljy@nus.edu.sg

ABSTRACT

Numerical modelling of composite action between concrete slab and steel beam is presented and two basic modelling schemes using beam and shell elements are discussed. These two schemes are verified against results from fire tests on simply-supported steel-concrete composite beams. Using an adaptive meshing approach in which, beam element is used for non-fire exposed structural members and mixed beam and shell model used for fire-exposed members, a very efficient representation of the composite frame can be built for analysis of its response subjected to compartment fire. Application to a 2D composite frame demonstrated that this adaptive modelling method was able to give an accurate prediction of the composite frame behaviour in fire.

KEYWORDS: *advanced analysis; composite frame; fire; numerical modelling*

INTRODUCTION

Composite constructions with steel beam and concrete slab system with or without metal-decking are widely used for its superior performance in terms of load and fire resistances. Their behaviour at normal temperature has been widely studied since 1950's covering every aspect such as the section stress distribution, slip and uplift, failure mode, shear connector behaviour, computational models, etc. Their fire resistance was firstly observed in standard fire tests on individual members. Later, with the wide recognition that the response of individual members in fire was the consequence of wide-ranging interactions between the heated member and the

surrounding members in a structure, full-scale fire tests were performed on an eight-storey typical composite framed structure in Cardington. During this long testing period, numerical modeling was on-going to gain further understanding on behaviour of restrained composite beams in fire because full-scale fire tests are too expensive to be undertaken in a regular manner. However, due to some difficulties such as the constitutive relationship of concrete material in the post cracking range, modeling of composite beams has not been easy. It is part of the objectives of this paper to review different modeling methods, to compare and contrast their advantages and disadvantages, and to understand their limitations in term of modeling different materials at elevated temperature.

In recent years, a number of researchers have been involved in numerical modeling of composite beams and composite frames. Sanad et al. (2000) used the general commercial program ABAQUS to analyze the end restrained composite beam tested in the Cardington full scale model. The steel members were modeled using 2-node beam element. The orthotropic slab was represented by a grillage. In each direction, the slab was modeled using a beam element. "Rigid-link" was used to connect steel beam and concrete slab. The major drawback of their analysis is that they adopt a stress resultant/ general strain representation of the slab section behaviour. Thus, the section stress distribution and the concrete cracking condition cannot be modeled exactly. Also, by adopting this "general beam section" behaviour, the interaction between the section forces and moments cannot be included. Eighazouli and Izzuddin (2000) performed a numerical modelling of the same structure using the in-house developed program ADAPTIC. Their modelling scheme is a simplified version of the grillage modelling. The concrete slab is represented by one line of beam elements in directions parallel and perpendicular to the beam. The two lines intersecting with each other at the middle of the beam span to model the 3D behaviour of the concrete slab. Huang (1999) developed a specialised finite element code, known as VULCAN, to model composite framed structure. Steel beam is modelled by 2-node line element and concrete slab is modelled by layered shell element. Special element is used to model the slip behaviour of shear connector and to model partial shear connection between the common nodes joining the steel beam and the concrete slab.

Most of the numerical work put emphasis on 3D behaviour of the slab system and only the structural subassembly is modelled within the 3D representation of the floor slab system. On the other hand, local buckling behaviour of the steel sections, although has been observed in many real fires [SCI, 1991; Newman et al. 2000], is not considered in the model. In this paper, two modelling methods will be introduced to model the 2-D behaviour of composite beams. One is a beam-beam model, in which both the steel section and the concrete slab is modelled with beam elements. The other is beam-shell model, in which, the concrete slab is modelled with beam elements, whilst the beam section is modelled with layered shell elements to capture the local buckling behaviour. A combined use of these two models is adopted for the analysis of composite frames subjected to compartment fire.

MODELLING SCHEMES

Beam-beam Model

This is the most widely used and most efficient method in which both concrete slab and steel beam are modeled by 2-node beam element. The numerical models presented by Sanad et al. (2000) and Eighazouli and Izzuddin (2000) belong to this category while Huang (1999) uses

shell element to model the 3D slab behaviour. When full composite behaviour is assumed, "rigid beam" can be used to connect the corresponding nodes of the concrete slab and steel beam as shown in Fig. 1. To consider the partial shear connection, "slip-spring" elements are introduced to connect the beam node and concrete node at the contact surface as shown in Fig. 1. Nonlinear shear-slip relationship of the connectors can be specified based on tests carried out on shear connectors.

Beam-Shell Model

The beam model cannot capture the behavioral effect associated with local buckling or lateral-torsional buckling. Based on test observation on composite beams restrained or partially restrained at both ends, significant compression force could be induced in the steel member, and local buckling or lateral-torsional buckling could occur. To capture this behaviour, the beam model is refined with the steel section modeled by shell elements as shown in Fig. 2. Similarly, "rigid beam" can be used to achieve a full composite behaviour, or the reference surface of the concrete slab can be shifted to the contact surface to have a detailed modeling of the partial composite behaviour.

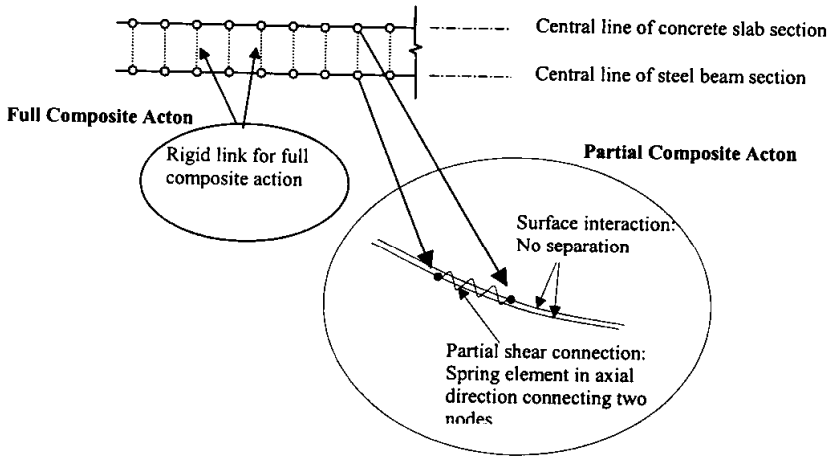

FIGURE 1: Modeling of composite beam with beam elements

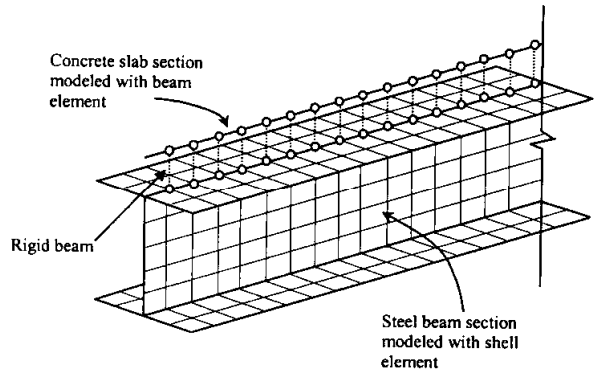

FIGURE 2: Modeling of composite beam with beam and shell elements

VERIFICATION STUDY

Verification against test results

Modeling of the fire tests on composite beam is difficult in many ways. Firstly, the temperature distribution in the member is very hard to be represented correctly. Secondly, material properties at elevated temperatures are not as well defined as at normal temperature. Besides, properties of the shear connectors at elevated temperatures were rarely studied. The British standard tests (Wainman and Kirby, 1987) are chosen for verification because of their relatively idealized test conditions. The two tests simulated-Test 15 and Test 16- are simply supported composite beams with an effective span of 4.53 m. Solid concrete slab of 130mm thick x 642mm wide is attached to the beam of 254 x 146 UB 43 with 32 shear connectors. The moment applied is about 30% of the bending capacity at normal temperature for Test 15 and 56% for Test 16.

Property of shear connectors at elevated temperature

Little attention has been paid to the behaviour of shear connectors at fire condition except of some general knowledge that the temperature of shear connectors will be lower than the corresponding steel flange temperature and they tend to be relatively stronger than the two components they connect. Mechanical properties of shear connectors are difficult to define in a fire situation not only because of the lack of the test data on the properties of shear connectors at elevated temperatures, but it is because the temperature of the shear connector is not easy to quantify. According to the test observation from Newman and Lawson (1991), the shear connector base temperature is about 110 to 130 $^{\circ}C$ lower than the corresponding flange temperature, and the temperature gradient along the height of the connector can be varied from 1700 to 3000 $^{\circ}C/m$. In the present study, the strength degradation model for shear connector proposed by Zhao and Kruppa (1996) is adopted. In the numerical modeling, 19mm diameter headed studs are used, whose characteristic strength in Grade 30 concrete, according to BS5950: Part 3, is 87kN. The corresponding force-slip deformation relationship at elevated temperature is shown in Fig. 3. The calculated shear connection degree for these two beams is 98.8%, it may be assumed that this beam is designed to be fully composite.

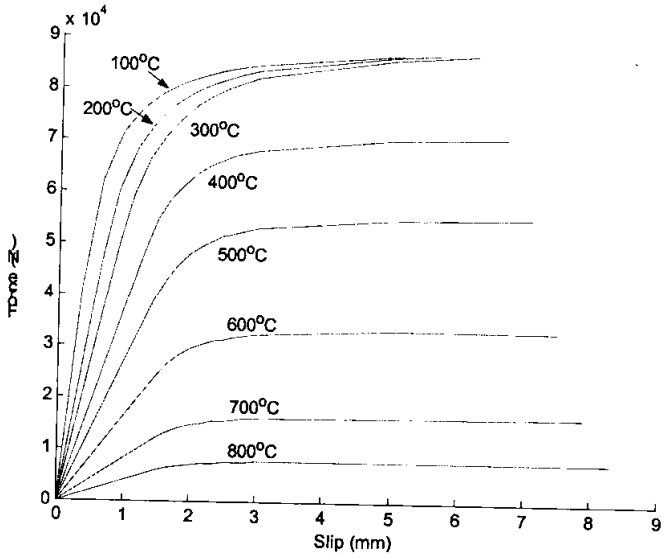

FIGURE 3: The force-slip relationship of the shear connectors at elevated temperature (Zhao and Kruppa, 1996)

Heat transfer analysis

Temperatures are measured at the upper flange, lower flange and mid-height of the web of the steel section during the tests. Heat transfer analysis is performed to calculate the temperature distribution over the whole section. The calculated temperature is firstly verified against the test results for the three temperature development curves for the upper flange, lower flange and mid-web plates. Then, the calculated temperature distribution is fed into the structural analysis program to determine the response of the composite beam.

In theory, the temperature distribution for Test 15 and Test 16 should be the same because both the section size and the fire exposure are the same. The temperature developments from the numerical heat transfer analysis are compared to the test measurements in Fig. 4. The calculated temperature distribution is very close to the test result of Test 15 and somewhat far away from Test 16. Comparison of the two test results show that the temperature of Test 16 is obviously higher than Test 15 at t = 3 minutes. After that, the temperature for the web and lower flange gradually approaches Test 15. However, the temperature of the upper flange keeps about 80 $^{\circ}C$ higher throughout the burning. The calculated temperature along the thickness of the concrete slab is compared to the temperature distribution recommended by EC 4 (CEN, 2002) for flat concrete slab. It can be seen from the comparison in Fig. 5 that the calculated concrete slab temperature is reasonable. The maximum temperature at the exposed side of the slab predicted by the numerical model is lower than the EC 4 value because of the shielding effect of the steel section.

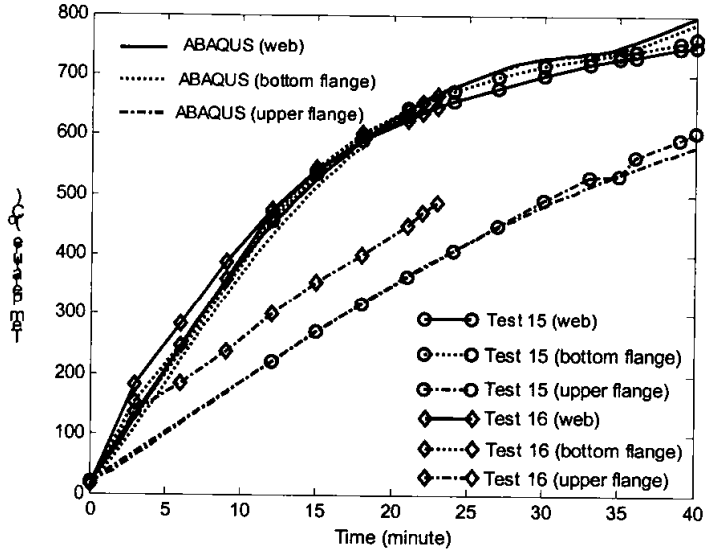

FIGURE 4: Comparison of the steel section temperature distribution

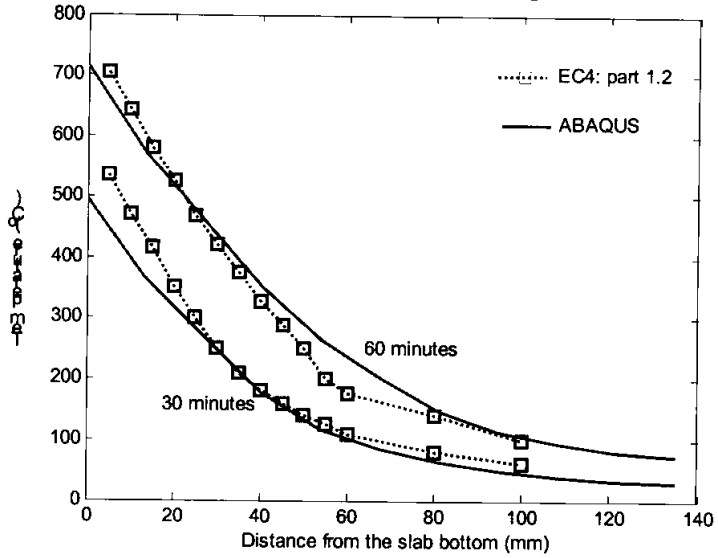

FIGURE 5: Comparison of the calculated concrete temperature to the listed data in EC4 (CEN, 2002)

The deflections measured from the tests and the numerical models are presented in Fig. 6 and Fig. 7 for Test 15 and Test 16 respectively. It can be observed that for these two tests, the deflection curve predicted by the two numerical models are almost identical. This is because local buckling is not as issue for these tests and beam-beam model gives the same result as beam-shell model. It is also observed from Test 15 that the two numerical models give good prediction to the test result. However, in Test 16, the predicted deflection is about 15mm higher

in the initial heating phase and it becomes closer to the test result near failure. This is attributed to the difference in temperature distribution. It can be seen from Fig. 4 that the upper flange temperature of Test 16 is about $80\,^{\circ}C$ higher than the predicted temperature, which helps to reduce the thermal bowing deflection in the initial phase and slightly increase the limiting temperature at failure.

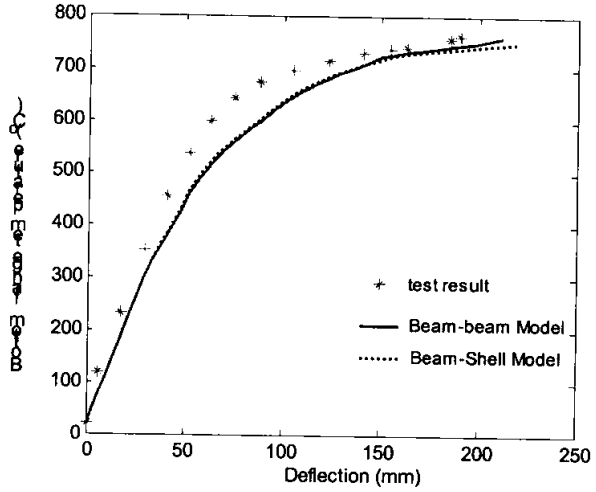

FIGURE 6: Comparison of the deflection given by numerical analysis and test 15

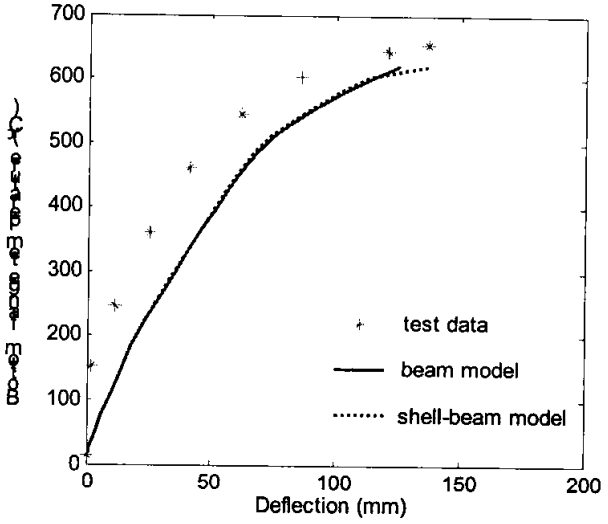

FIGURE 7: Comparison of the deflection given by numerical analysis and test 16

Verification against SCI Tests on Protected Composite Beams

Newman and Lawson (1991) perform a series of tests on fire protected composite beams with profiled steel decking. The tested composite beam spans 4.5 m with maximum bending moment 161.3 kNm at the mid span. Four fire protection schemes are tested (see the inserts of Figs. 8a-d)

and their effects are compared. The steel section used is 305 x 102 UB 33 Grade 43. Open trapezoidal deck of 60mm deep is used to support a concrete slab of 125 mm deep. Normal weight Grade 30 concrete is used. Shear connectors of 19mm diameter are placed along the span at 300 mm center spacing to provide 37% partial shear connection.

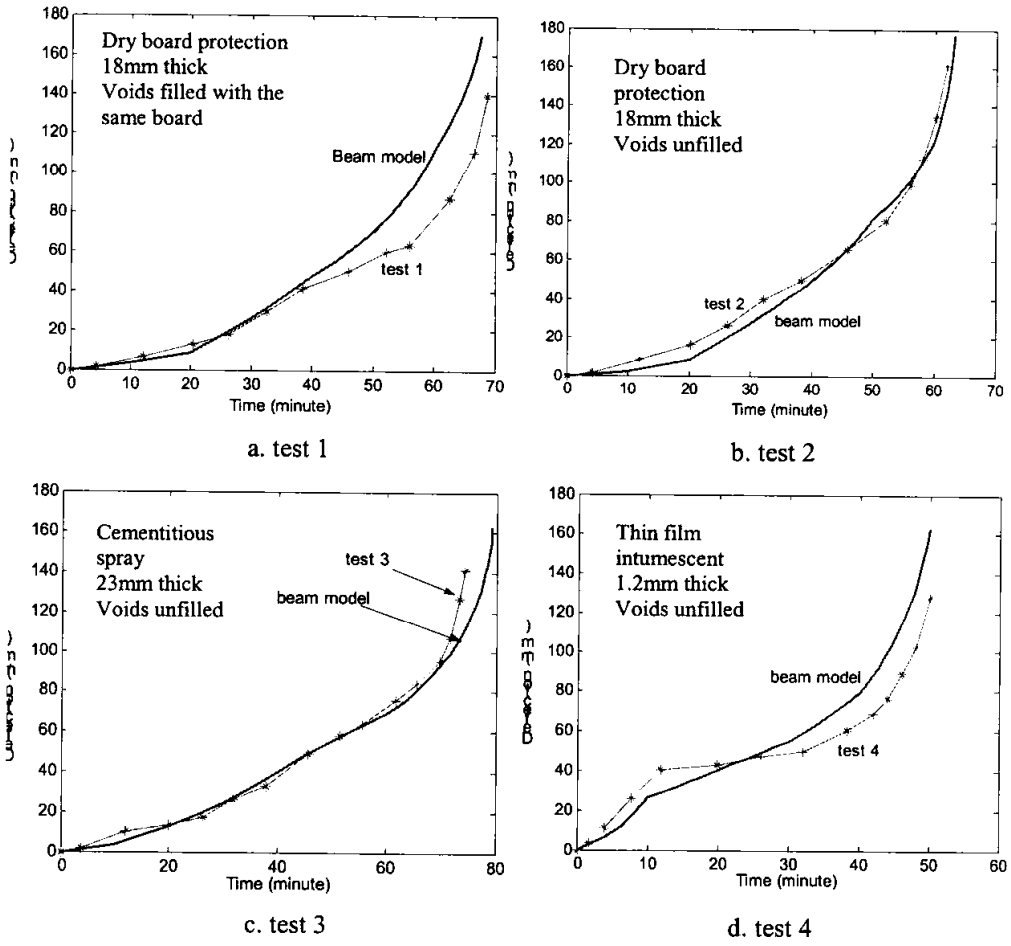

FIGURE 8: Comparison of the test results and beam model calculation results

Since the beam section is compact and local buckling is not expected, the beam-beam model is used to analyze the four tests. The "slip-spring model" illustrated in Fig. 1 is thus adopted to model the partial shear connection. The steel decking is not explicitly considered since it is not effective when exposed to fire. However, the serrated shape of the concrete slab is modeled approximately by rectangular blocks. Beam elements of 125 mm deep and 185 mm deep are used alternatively to represent the void and trough of the concrete slab. The reference axes of both the slab and beam section are shifted to the contact surface. The upper flange and lower flange temperatures are taken directly from the fire test results at the void and trough positions. Except for Test 4 where the web temperature is significantly higher than both the flanges, the

steel section temperature may be linearly interpolated between the temperatures of the two flanges. The concrete temperature is extrapolated from the upper beam flange temperature.

The calculated deflections against the test measurements are shown in Fig. 8. Due to the different fire protection applied, the temperature distributions across the depth of these four beams are rather irregular. Linear or parabolic simplifications have to be used in the numerical modeling. Also, the temperature distribution is extrapolated from the upper flange temperature. Taking into account all these factors as well as the uncertainties in shear connector properties, it should be deemed that the proposed model gives a generally good estimation of the test results. Newman and Lawson (1991) also performed the numerical modeling with another program BFIRE. These two simulated results show similar trends compared to the test results. For example in Test 4, at around 25 minutes, the predicted deflection coincides with the test curve. Before that, the calculated deflection is higher than the test result and after that the calculated deflection is lower than the test result. Similar behaviour can be observed for other cases. These demonstrated that the error between the test result and calculated results are mainly because of the inaccuracy in determining the input parameters such as material properties or temperature distribution instead of the mathematical model.

8-STORY STEEL BUILDING SUBJECTED TO COMPARTMENT FIRE

A programme of fire tests was carried out in the UK at the Building Research Establishment's Cardington Laboratory. The tests were carried out on an eight-storey composite steel-framed building that had been designed and constructed as a typical multi-storey office building (Newman et al. 2000). A typical bay of this building, as shown in Fig. 9, is selected for numerical analysis. The fire compartment includes the whole level 4. Although the fire test was unable to be exactly reproduced, the numerical model is constructed to be as close to the fire test as possible so that the analysis result can be compared to the fire test result and the accuracy of the numerical analysis can be verified. Due to symmetry of the building, only half of the frame is modeled. The steel beams at level 4, which are directly exposed to fire, are modeled with beam-shell model while the steel members that are not affected by fire are modeled using beam model. The top part of the column that is connected to the fire exposed beams including the connection is modeled with shell elements as shown in Figs. 10 and 11a. A fully rigid connection between the end of steel beam and the column flange is assumed. However, the concrete slab is not connected to the column side.

In the first study, the top part of the column above the suspended ceiling is left unprotected as performed in the test. The numerical analysis result shows that the frame fails due to the squashing of the unprotected column top. The failure mode is shown in Fig. 11a against the test observation in Fig. 11b. Although the numerical analysis is unable to reach the extent of extreme deformation, it has correctly captured the deformed mode. From test observation, the column squashing begins at approximately $670\,^{\circ}C$. Fig. 12 shows the downward movement of the column top against the fire temperature. The column squashing occurs at about $677\,^{\circ}C$, which is close to the test result. The numerical analysis also shows that when the column is unprotected, both the interior and exterior beams remain straight. Upon the time of column failure, the maximum deflection reached is only 180mm, far away from failure.

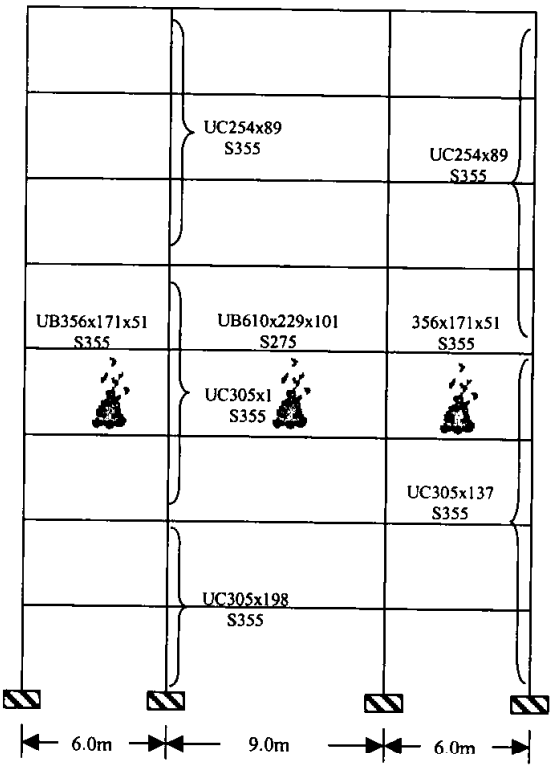

FIGURE 9: The 2D frame setup

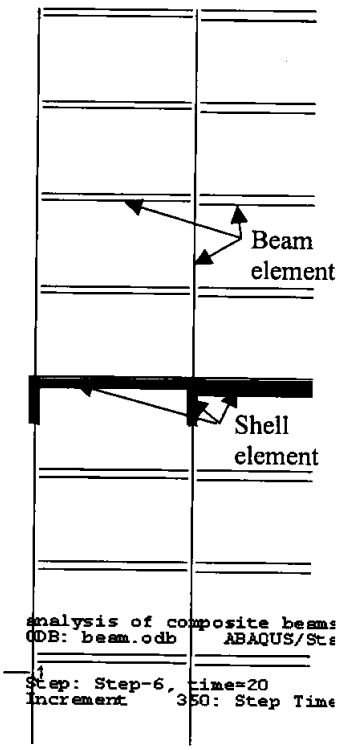

FIGURE 10: The numerical model for half-frame

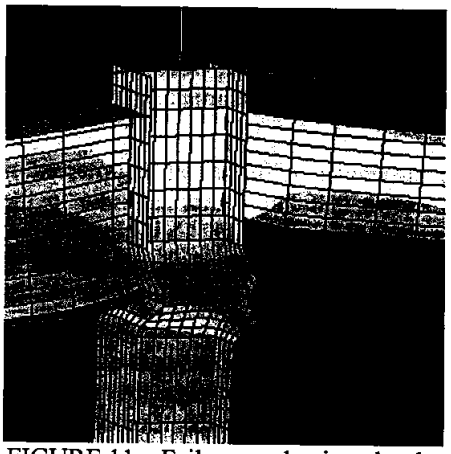

FIGURE 11a: Failure mode given by the numerical analysis

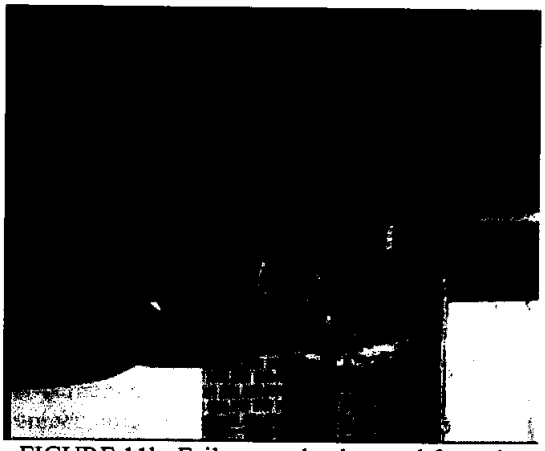

FIGURE 11b: Failure mode observed from the fire test

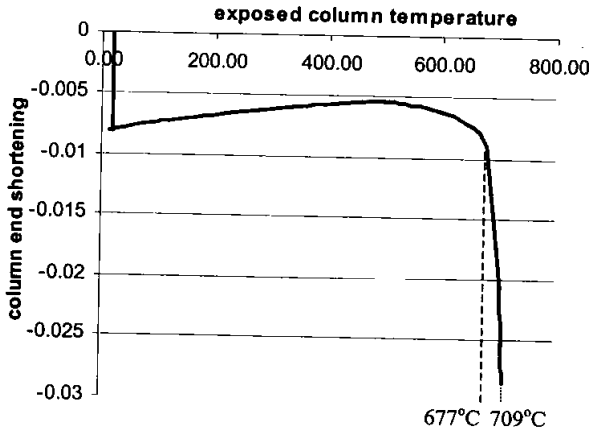

FIGURE 12: The downward movement of the column top

In the second study, the column is fully protected. The failure mode is shown in Fig. 13a. The web of the interior beam deforms in shear buckling mode near the support. Over the whole span, the lower flange of the interior beam is distorted. This implies that significant compression force has been exerted on the steel beam section. After the occurrence of local buckling, the deflection rate of the composite beam increases rapidly. The column remains almost undeformed and the frame finally fails due to the large deflection of the composite beam. Fig. 13b shows the deformed shape of the beam to column connection from test, in which the column is fully protected. It can be seen that the column remains intact after the fire and the steel beam section is deformed in a way similar to the numerical analysis results.

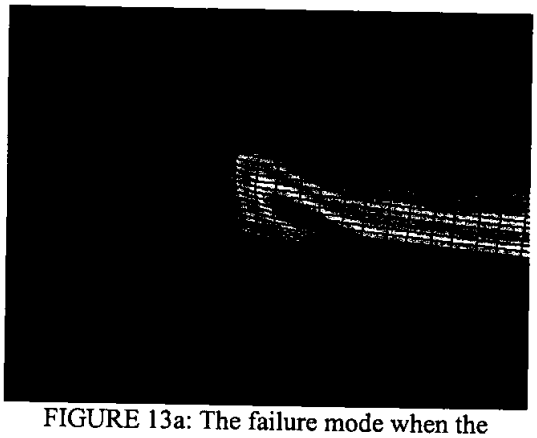

FIGURE 13a: The failure mode when the column is fully protected

FIGURE 13b: Local buckling of beams observed from fire test

These two analyses demonstrated that the proposed adaptive modeling approach is able to simulate the behaviour of composite frames in a very efficient way. Fire exposed structural members are modeled with shell elements to capture the local failure behaviour. Beam elements

are used to construct the structural framework and provide appropriate interaction with the fire exposed structural members.

CONCLUSION

Numerical analysis is essential to gain better understanding of the structural behavior in fire. It has been used for direct design of structures considering the realistic restraining and boundary effects of adjacent members. Past numerical study of composite structures has been limited to structural sub-assembly. In this paper, two methods to model the behaviour of composite beams in fire have been introduced and verified against individual beam tests. An adaptive modeling approach is proposed for study of the whole frame behaviour when subjected to compartment fire. In the adaptive approach, fire exposed members are modeled with shell elements to correctly represent its section profile and to capture possible local failure. Frame members outside the fire affected zone may be modeled by beam elements. Application of this approach to an eight-story steel building shows that it is able to accurately capture the response of a typical composite frame subjected to a compartment fire.

REFERENCES

[1] Sanad A.M, Rotter I.M, Usmani A.S, O'Connor M.A. (2000) Composite Beams in Large Buildings under Fire-Numerical Modelling and Structural Behaviour, Fire Safety Journal, 35, pp.165-188.

[2] Newman G.M, Lawson R.M. (1991) Fire Resistance of Composite Beams, Technical Report No 109, the Steel Construction Institute.

[3] Wainman D.E. and Kirby B.R. (1987) Compendium of UK Standard Fire Test Data Unprotected Structural Steel, British Steel Corporation and Swinden Laboratories, Rotherham, Report RS/RSC/s10328/1/87/B.

[4] ZHAO Bin & KRUPPA Joel (1996) Experimental and Numerical Investigation of Fire Behaviour of Steel and Concrete Composite Beams, Composite construction in steel and concrete III : proceedings of an Engineering Foundation conference, Swabian Conference Center, Irsee, Germany, June 9-14, pp. 129-142.

[5] Eighazouli A.Y., Izzuddin B.A. (2000) Response of Idealized Composite Beam-slab Systems under Fire Conditions, Journal of Constructional Steel Research, v56, pp. 199-224.

[6] Newman G.M. Robinson J.T. Bailey C.G. (2000) Fire Safety Design: A New Approach to Multi-Storey Steel-Framed Buildings, the Steel Construction Institute.

[7] SCI. Structural Fire Engineering- Investigation of Broadgate Phase 8 Fire, Steel Construction Institute, Ascot, Berkshire, 1991.

[8] Huang Zhaohui, Burgess Ian W., Plank Roger J. (1999) The influence of shear connectors on the behaviour of composite steel-framed buildings in fire, Journal of Constructional Steel Research, 51, pp. 219-237.

3D MODELLING OF BEAM-COLUMNS WITH GENERAL CROSS-SECTIONS IN FIRE

Zhaohui HUANG [1], Ian W. BURGESS and Roger J. PLANK

Department of Civil & Structural Engineering, University of Sheffield, S1 3JD, UK
([1]z.huang@sheffield.ac.uk)

ABSTRACT

A non-linear finite element, developed for three-dimensional modelling of beam-column elements of general cross-sections in fire conditions, is described. The procedure is based on general formulations proposed by Bathe, with further development to make it suitable for the analysis of steel, reinforced concrete and composite framed structures under the influence of fire. Because of the changes in material properties and the large deflections experienced in fire, both geometric and material non-linearities are taken into account in this formulation. The cross-section of the beam-column is divided into a matrix of segments, and each segment may have different material, temperature and mechanical properties. The more complicated aspects of structural behaviour in fire conditions, such as thermal expansion, cracking or crushing of concrete, and progressive change of the constitutive properties of materials with temperature, are modelled. Since it is possible to offset their nodes by pre-determined distances the elements can easily be combined with shell or plate elements to model composite floor systems in fire. One high-deflection numerical example using linear elastic material is presented to demonstrate the accuracy at high deflections of the elements. A full-scale standard fire test on a composite slim-floor beam has been modelled to show the capabilities of the element. The influences of catenary action on the behaviour of the tested beam are also investigated using different support conditions.

KEYWORDS: *geometrical non-linearity; beam-column element; segmentation; structural fire behaviour; composite structures*

INTRODUCTION

The behaviour of structures exposed to fire is usually described in terms of the concept of fire resistance, which is the period of time under exposure to a standard fire time-temperature curve at which some form of limiting behaviour occurs. Current design codes for steel framed and composite structures [1, 2] allow designers to treat fire as one of the basic design limit states, taking account of:

- Non-uniform heating due to partial protection, which may be inherent in the framing system or specially applied,
- The level of loading at the fire limit state, using partial safety factors lower than those used for ultimate limit states, because of the relative improbability of such accidental conditions,
- Realistic stress-strain characteristics of steel at elevated temperatures.

These approaches can greatly reduce the amount of fire protection required, compared with traditional prescriptive approaches, and in some cases show that no applied protection is needed. Their main limitation is that they are based on the behaviour under test of isolated simply supported members, usually heated according to the standard ISO834 time-temperature curve [3]. In real buildings structural elements form part of a continuous assembly, and building fires often remain localised, with the fire-affected region of the structure receiving significant restraint from cooler areas surrounding it. The real behaviour of these structural elements can therefore be very different from that indicated by standard furnace tests.

In 1995-96 six large fire tests were carried out on a full-scale composite building at the BRE Fire Research Laboratory at Cardington [4]. The tests made it clear that unprotected steel members could have significantly greater fire resistance within real multi-storey buildings than when tested as isolated members. This was undoubtedly due to interaction between the heated members within the fire compartment, the concrete floor slabs and the adjacent steel frame structure. If such interactions are to be used to advantage by designers in specifying fire protection strategies as part of an integrated limit state design process, then this can not practically be based on testing because of the extremely high costs which are implied. It is therefore becoming increasingly important that software models be developed to enable the behaviour of such structures under fire conditions to be predicted with sufficient accuracy.

The specialised finite element program *Vulcan* has been progressively developed over the past decade [5-8] at the University of Sheffield for three-dimensional modelling of the structural behaviour of composite and steel-framed buildings in fire. In this program steel beam-columns have previously been represented by two-noded one-dimensional line elements in which each node has 8 degrees of freedom in local coordinates, which transform into 11 degrees of freedom in global coordinates [5]. Apart from the usual three translational and three rotational degrees of freedom, five extra degrees of freedom are present, representing three derivatives of displacement ("strains"), plus twisting and warping degrees of freedom. Although these elements have proved extremely accurate up to and beyond the deflection levels which are practically acceptable in building structures in fire conditions, there are some major disadvantages to using this approach:

- Due to the presence of the five unconventional degrees of freedom at each node the processing time is increased considerably compared to analysis using the normal six degrees of freedom;
- It is necessary always to apply constraints to some of the nodal degrees of freedom, even when no external boundary conditions exist;
- There are some logical difficulties in setting nodal constraint conditions for sloping members. Different specification of these constraints for such members can influence the results of the analyses quite significantly, especially when displacements are large [9].

The main objective of this work was to develop a more robust non-linear element for three-dimensional modelling of general beam-column elements of structures in fire conditions.

NON-LINEAR PROCEDURE

Using the general continuum mechanics equations for large-displacement non-linear analysis, the calculation of the non-linear beam element matrices represents a direct extension of the linear (small displacement) formulation. The calculations are performed as in the evaluation of the matrices of the elements with the conventional six displacement degrees of freedom only. The formulation of the element matrices for large-displacement, large-rotation behaviour of a beam with rectangular cross-sectional area is considered first. Using segmentation of the element cross-section as shown in Fig. 1, and allowing some segments to be "void" (with zero mechanical strength and stiffness), different shapes of cross-section can be modelled easily.

The reference axis for a beam-column element, on which the nodes are located, can be placed inside or outside the cross-section of the element. Each node of the element has three translational and three rotational degrees of freedom, in both local and global coordinates. The main assumptions of the model can be summarised as follows:

- Plane sections originally normal to the reference axis remain plane and undistorted under deformation, but are not necessarily normal to this axis. It is assumed that there is no slip between segments.

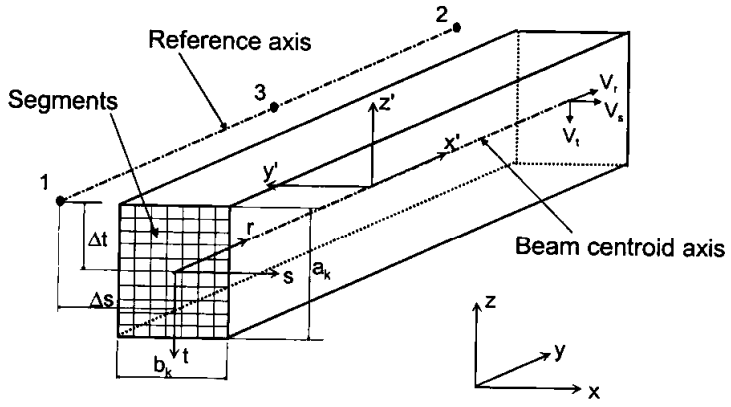

FIGURE 1: Three-dimensional three-noded beam element configuration.

- The displacements and rotations of the element can be arbitrarily large but the element strains are still assumed to be small, which means that the cross-sectional area does not change. This is an appropriate assumption for most geometrically non-linear analyses of beam-type structures [10].
- Each segment within the cross-section can have a different temperature, but this is uniform along the element. The initial material properties of each segment may be different, and the stress-strain relationships may change independently for each segment.
- For each segment only the longitudinal stress and two shear stresses are non-zero.

Using the natural coordinates *r, s, t*, shown in Fig. 1, the Cartesian coordinates of a point in an element with *N* node points at time t are given (see Fig. 1) by

$$
\begin{aligned}
{}^{t}x(r,s,t) &= \sum_{k=1}^{N} h_k\, {}^{t}x^k + \sum_{k=1}^{N}\left(\frac{t\,a_k}{2}+\Delta t^k\right) h_k\, {}^{t}V_{tx}^k + \sum_{k=1}^{N}\left(\frac{s\,b_k}{2}+\Delta s^k\right) h_k\, {}^{t}V_{sx}^k \\
{}^{t}y(r,s,t) &= \sum_{k=1}^{N} h_k\, {}^{t}y^k + \sum_{k=1}^{N}\left(\frac{t\,a_k}{2}+\Delta t^k\right) h_k\, {}^{t}V_{ty}^k + \sum_{k=1}^{N}\left(\frac{s\,b_k}{2}+\Delta s^k\right) h_k\, {}^{t}V_{sy}^k \qquad (1) \\
{}^{t}z(r,s,t) &= \sum_{k=1}^{N} h_k\, {}^{t}z^k + \sum_{k=1}^{N}\left(\frac{t\,a_k}{2}+\Delta t^k\right) h_k\, {}^{t}V_{tz}^k + \sum_{k=1}^{N}\left(\frac{s\,b_k}{2}+\Delta s^k\right) h_k\, {}^{t}V_{sz}^k
\end{aligned}
$$

in which

$h_k(r)$	= the interpolation functions,
x, y, z	= global Cartesian coordinates,
${}^{t}x, {}^{t}y, {}^{t}z$	= global Cartesian coordinates of any point in the element at time t,
${}^{t}x^k, {}^{t}y^k, {}^{t}z^k$	= global Cartesian coordinates of nodal point k at time t,
a_k, b_k	= cross-sectional dimensions of the beam at nodal point k,
$\Delta t^k, \Delta s^k$	= offsets of reference axis from the central of the cross-section at nodal point k in t and s directions,
${}^{t}V_{tx}^k$, ${}^{t}V_{ty}^k$, ${}^{t}V_{tz}^k$	= components of unit vector ${}^{t}\mathbf{V}_t^k$ in direction t at nodal point k,
${}^{t}V_{sx}^k$, ${}^{t}V_{sy}^k$, ${}^{t}V_{sz}^k$	= components of unit vector ${}^{t}\mathbf{V}_s^k$ in direction s at nodal point k,

Using Equation (1) the expressions for the total displacements (u, v, w) and their incremental components $(\Delta u, \Delta v, \Delta w)$, in terms of the nodal point values and changes in the direction cosines of the nodal point vectors, can be written as:

$$
\begin{aligned}
{}^{t}u(r,s,t) &= \sum_{k=1}^{N} h_k\, {}^{t}u^k + \sum_{k=1}^{N}\left(\frac{t\,a_k}{2}+\Delta t^k\right) h_k\left({}^{t}V_{tx}^k - {}^{0}V_{tx}^k\right) + \sum_{k-1}^{N}\left(\frac{s\,b_k}{2}+\Delta s^k\right) h_k\left({}^{t}V_{sx}^k - {}^{0}V_{sx}^k\right) \\
{}^{t}v(r,s,t) &= \sum_{k=1}^{N} h_k\, {}^{t}v^k + \sum_{k=1}^{N}\left(\frac{t\,a_k}{2}+\Delta t^k\right) h_k\left({}^{t}V_{ty}^k - {}^{0}V_{ty}^k\right) + \sum_{k=1}^{N}\left(\frac{s\,b_k}{2}+\Delta s^k\right) h_k\left({}^{t}V_{sy}^k - {}^{0}V_{sy}^k\right) \qquad (2) \\
{}^{t}w(r,s,t) &= \sum_{k=1}^{N} h_k\, {}^{t}w^k + \sum_{k=1}^{N}\left(\frac{t\,a_k}{2}+\Delta t^k\right) h_k\left({}^{t}V_{tz}^k - {}^{0}V_{tz}^k\right) + \sum_{k=1}^{N}\left(\frac{s\,b_k}{2}+\Delta s^k\right) h_k\left({}^{t}V_{sz}^k - {}^{0}V_{sz}^k\right)
\end{aligned}
$$

and

$$\begin{aligned}
\Delta u(r,s,t) &= \sum_{k=1}^{N} h_k \Delta u^k + \sum_{k=1}^{N} \left(\frac{t a_k}{2} + \Delta t^k \right) h_k V_{tx}^k + \sum_{k=1}^{N} \left(\frac{s b_k}{2} + \Delta s^k \right) h_k V_{sx}^k \\
\Delta v(r,s,t) &= \sum_{k=1}^{N} h_k \Delta v^k + \sum_{k=1}^{N} \left(\frac{t a_k}{2} + \Delta t^k \right) h_k V_{ty}^k + \sum_{k=1}^{N} \left(\frac{s b_k}{2} + \Delta s^k \right) h_k V_{sy}^k \\
\Delta w(r,s,t) &= \sum_{k=1}^{N} h_k \Delta w^k + \sum_{k=1}^{N} \left(\frac{t a_k}{2} + \Delta t^k \right) h_k V_{tz}^k + \sum_{k=1}^{N} \left(\frac{s b_k}{2} + \Delta s^k \right) h_k V_{sz}^k
\end{aligned} \tag{3}$$

in which

$$\begin{cases} V_{tx}^k = {}^{t+\Delta t}V_{tx}^k - {}^{t}V_{tx}^k \\ V_{ty}^k = {}^{t+\Delta t}V_{ty}^k - {}^{t}V_{ty}^k \\ V_{tz}^k = {}^{t+\Delta t}V_{tz}^k - {}^{t}V_{tz}^k \end{cases}$$
$$\begin{cases} V_{sx}^k = {}^{t+\Delta t}V_{sx}^k - {}^{t}V_{sx}^k \\ V_{sy}^k = {}^{t+\Delta t}V_{sy}^k - {}^{t}V_{sy}^k \\ V_{sz}^k = {}^{t+\Delta t}V_{sz}^k - {}^{t}V_{sz}^k \end{cases} \tag{4}$$

The relationship given in Equation (2) is directly employed to evaluate the total displacements and total strains (hence also the total stresses) and holds for any magnitude of the displacement components. The relationship of Equation (3) is used in the linearisation of the Principle of Virtual Work, and needs to express the components of the changes in the direction cosines V_t^k and V_s^k in terms of the nodal rotation degrees of freedom. Depending on the size of the incremental step, the actual rotations corresponding to the vectors V_t^k, V_s^k may be large, and therefore cannot be represented by vector component rotations about the Cartesian axes. However, the objective here is to express the continuum linear and non-linear strain increments by finite element degrees of freedom and corresponding interpolations, so as to achieve a full linearisation of the Principle of Virtual Work. The vector of nodal rotational degrees of freedom θ_k can be defined using the components measured about the Cartesian axes, sing the second-order approximations [11],

$$\begin{cases} V_t^k = \theta_k \times {}^{t}V_t^k + \frac{1}{2}\theta_k \times \left(\theta_k \times {}^{t}V_t^k \right) \\ V_s^k = \theta_k \times {}^{t}V_s^k + \frac{1}{2}\theta_k \times \left(\theta_k \times {}^{t}V_s^k \right) \end{cases} \tag{5}$$

where,

$$\theta_k \times {}^{t}V_t^k = \begin{Bmatrix} \theta_y^k \, {}^{t}V_{tz}^k - \theta_z^k \, {}^{t}V_{ty}^k \\ \theta_z^k \, {}^{t}V_{tx}^k - \theta_x^k \, {}^{t}V_{tz}^k \\ \theta_x^k \, {}^{t}V_{ty}^k - \theta_y^k \, {}^{t}V_{tx}^k \end{Bmatrix} \tag{6}$$

and

$$\theta_k \times {}^{t}\mathbf{V}_s^k = \begin{Bmatrix} \theta_y^k\ {}^{t}V_{sz}^k - \theta_z^k\ {}^{t}V_{sy}^k \\ \theta_z^k\ {}^{t}V_{sx}^k - \theta_x^k\ {}^{t}V_{sz}^k \\ \theta_x^k\ {}^{t}V_{sy}^k - \theta_y^k\ {}^{t}V_{sx}^k \end{Bmatrix} \tag{7}$$

The only purpose of using θ_k is to evaluate (approximations to) the new direction vectors; θ_k is discarded thereafter.

Equations (1) to (5) are the basic interpolations and expressions which are used to establish the strain-displacement interpolation matrices for geometrically non-linear analysis. In this study a Total Lagrangian (TL) formulation is adopted. The details of constructing for element stiffness matrix and internal force vector can be found in Reference [12].

CONSTITUTIVE MODELLING AND PROPERTIES OF MATERIALS

The stress-strain relationships of concrete and steel at elevated temperatures specified by Eurocode 4 [13] are adopted for this study (see Fig. 2).

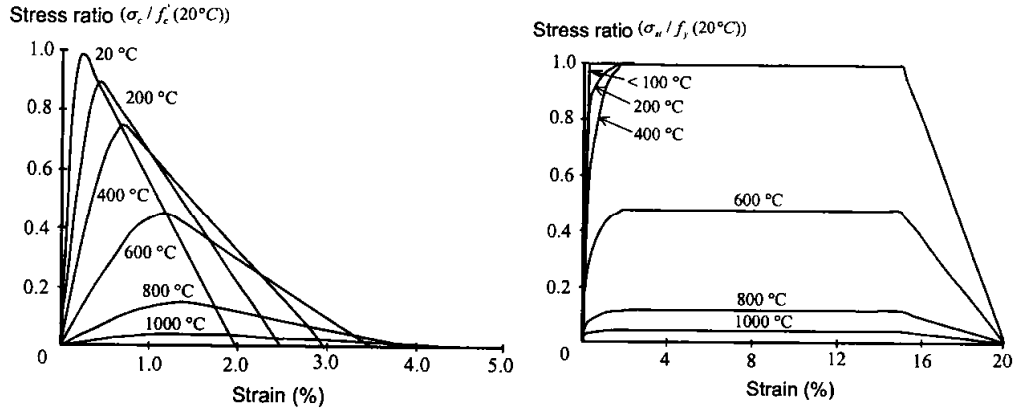

FIGURE 2: Stress-strain relationships of concrete and steel at elevated temperature: (a) Concrete in compression; (b) Steel.

The uniaxial tensile and compressive strengths of concrete are assumed to be related by $f_t'=0.3321\sqrt{f_c'}$ MPa [14]. Hence the concrete tensile strength f_t' changes with temperature. It is assumed that concrete exhibits linear elastic behaviour up to its ultimate tensile capacity. Beyond this point the concrete cracks and the tensile stress decreases gradually with increasing tensile strain, rather than dropping to zero abruptly as would occur in a perfectly brittle material. The constitutive matrix D'_c of a cracked concrete segment becomes

$$\mathbf{D}_c' = \begin{bmatrix} 0 & 0 & 0 \\ 0 & \mu G_c & 0 \\ 0 & 0 & \mu G_c \end{bmatrix} \tag{8}$$

where G_c is the shear modulus of concrete and μ is the shear retention factor for which $0<\mu \leq 1.0$. After crushing, the concrete is assumed to lose all strength and stiffness.

The model described above has been incorporated within *Vulcan* in order to model the structural behaviour of steel, reinforced concrete and composite buildings in fire conditions. The total loading or temperature rise for which the response of the structure is to be traced is divided into a number of steps. It is assumed that changes in the loads or temperatures occur only at the beginning or end of a step. During any step the external loads and temperatures in the segments of all elements are assumed to remain constant.

ILLUSTRATIVE STUDIES

A simple example study is now presented in order to illustrate the capabilities of the new beam-column element. The objective is to show the considerable improvement in accuracy given by the new formulation at very high deflections. This is followed by a comparison against the record from a full-scale fire test on a composite beam [15].

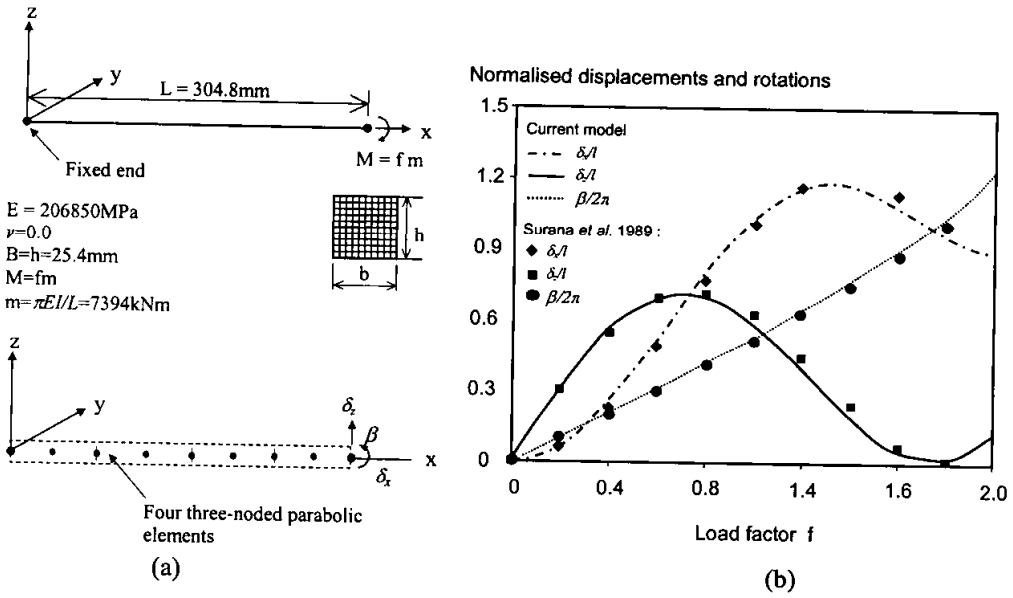

FIGURE 3: Cantilever beam subjected to a concentrated end moment: (a) Cantilever beam and its finite element model; (b) Load-deflection behaviour.

A cantilever beam of square cross-section composed of uniform linear-elastic material, subjected to a concentrated end moment M, as shown in Fig. 3(a), was analysed. In this analysis the cross-section of the beam was divided into 100 segments. Fig. 3(b) shows a plot of horizontal and vertical end-displacements δ_x, δ_y and end-rotation θ versus the load factor f, together with the results from Surana and Sorem [16]. There is very good agreement between

the current model and these results, showing the capability of this formulation to deal with displacements well beyond the range encountered in real structural fire engineering examples.
A full-scale ISO384 standard fire test on a "*Slimflor*" beam (see Fig. 4(a)), which had been tested at Warrington Fire Research Centre in 1996 [15], was modelled using the new beam element. The test specimen consisted of a simply supported composite 280ASB100 asymmetric beam with normal-weight concrete cast onto deep-deck profiled sheeting with an A142 mesh. The span of the beam was 4.5m and four hydraulic rams were used to apply a total load of 338kN (84.6kN each), to the test assembly. The load was applied directly to the upper flange of the steel section at positions corresponding to the 1/8, 3/8, 5/8 and 7/8 points of the supported span. The self-weight of the beam was 4.81kN/m. Fig. 4(a) provides details of the specimens. The yield strength of the steel at ambient temperature was measured as 402MPa and this was used in the analysis. Because no test data were available on the compressive strength of the concrete or the yield strength of reinforcement these were respectively assumed at room temperature to be 25MPa and 460MPa in the modelling.

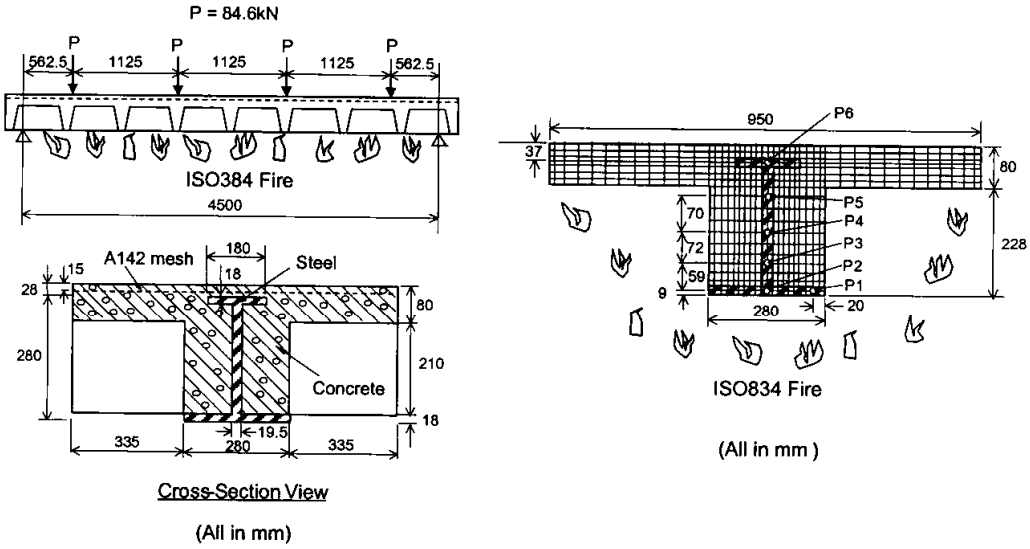

FIGURE 4: A full-scale ISO384 standard fire test on a "*Slimflor*" beam: (a) Details of the *Slimflor* beam tested; (b) The element segmentation mesh adopted.

A large number of thermocouples were employed to measure the temperatures within the steelwork and concrete during the test. However, from the test data it is quite difficult to specify reasonably the temperatures of all the segments within the cross-section of the composite beam. The first step of the analysis was therefore to perform a thermal analysis on the structure. *Vulcan* has recently been extended by one of the authors to include a two-dimensional non-linear finite element procedure to predict the temperature distributions within the cross-sections of structural member subject to given fire time-temperature regimes. This is largely based on previous work [17] by the first author. The thermal properties of the steel and concrete are assumed to change with temperature, and the influence of moisture initially held within the

concrete and protection materials is taken into account in their properties. The finite element mesh used to calculate the temperature distribution in the beam cross-section is shown in Fig. 4(b). In this analysis the thermal properties given in Eurocode 4 for concrete and steel were adopted. The predicted temperatures at various positions on the steelwork cross-section are compared with the test results in Fig. 5, and show good agreement.

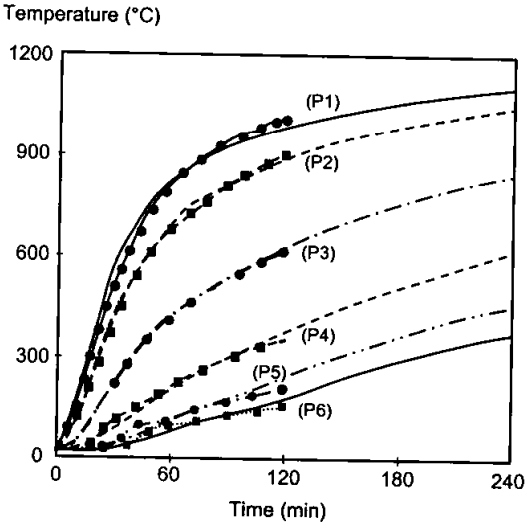

FIGURE 5: Comparison of predicted and measured [15] temperatures at several positions of steelwork of the cross-section of the *Slimflor* beam.

The predicted temperatures were used as input to perform structural analysis for the test beam in this study. The mesh used in thermal analysis was also used for the segmentation of the cross-section of the composite beam. Hence, in the structural analysis the cross-section of the beam was divided into 380 steel or concrete segments and the slab was divided into 9 layers which included 7 concrete and 2 reinforcing steel layers. The predicted central deflection of the beam for this test is plotted against time in Fig. 6, together with test results. It is evident that the analytical predictions are in very good agreement with test results. The test was stopped before 120 min but the prediction is capable of extending the "test" to 240 min, albeit with very large deflection. From both the test and computer modelling it is clear that the concrete in the *Slimflor* system provides very effective insulation to the steel beam (see Fig. 5). The temperatures within the top half of the steel beam cross-section remain below 400°C at 120 minutes into the test. The temperature of the top flange is less than 200°C. This gives a considerable enhancement to the fire resistance of the structure.

In order to investigate the influences of catenary action on the behaviour of the tested beam an axial spring has been introduced to represent the column stiffness at one support of the beam. Two different stiffnesses have been considered. To represent a fully braced frame a very large value (10^{10} N/mm) is assumed, whilst for an unbraced frame stiffnesses were calculated assuming a column size of 305x305x198UC, calculated for a 10-storey building according to BS5950 Part 1 [18]. Assuming that the height of a storey is 4m then the equivalent spring stiffnesses are 5,630 N/mm for the column minor axes. Fig. 7 compares the deflections at the

mid-span of the test beam for these different end support conditions. Also shown are the deflections for a simply supported condition, which provides no axial restraint, demonstrating that catenary action has a significant influence.

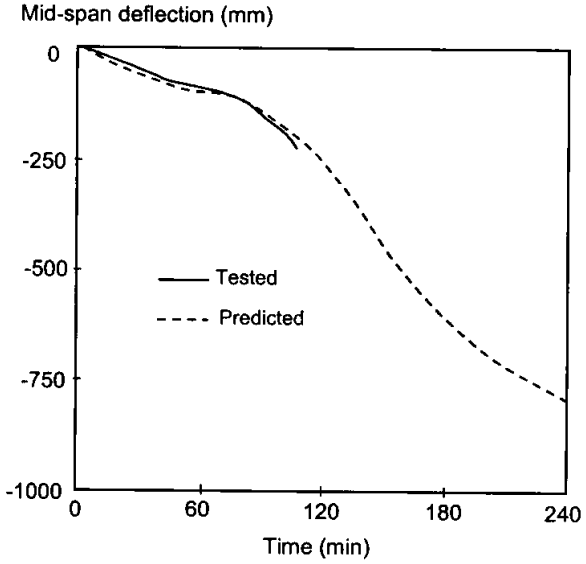

FIGURE 6: Comparison of predicted and measured [15] deflections at mid-span of the *Slimflor* beam.

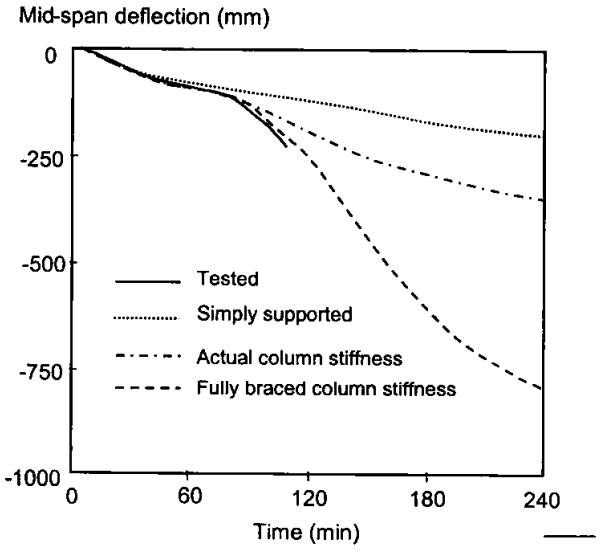

FIGURE 7: Predicted deflections at mid-span of the tested beam for different end support conditions.

CONCLUSIONS

The model proposed in this paper is based on the formulations proposed by Bathe [10], but including further developments to enable the analysis of steel, reinforced concrete and composite beam-column framed structures subject to fire. In this formulation both geometric and material non-linearities have been taken into account. The cross-section of the beam-column element is divided into a number of segments, of which each can have different material, temperature and mechanical properties. The more complicated aspects of structural behaviour in fire conditions, such as thermal expansion, cracking or crushing of concrete, yielding of steel and change of material properties with temperature are modelled. In this study a Total Lagrangian approach has been adopted throughout, in which displacements are referred to the original configuration and small strains are assumed. Since the elements possess an offset capability, these elements can also be used, with shell or plate elements, for modelling of composite buildings in fire. One simple numerical example using linear elastic material has been presented to demonstrate the capability and the accuracy of the elements. It is evident that the proposed model produces logical results when the effects of geometric non-linearity are considered, even at unrealistically high deflections. Finally, a full-scale standard fire test on a *Slimflor* beam has been modelled to show the element's capabilities in modelling situations in which both steel and concrete are key structural components, and there is non-uniform heating by fire. It is evident that the non-linear procedure proposed in this paper is very suitable for modelling such situations in fire conditions. In the current model each node of the elements has six degree of freedom, three translational and three rotational in both local and global coordinates, and hence there is a considerable saving of processing time compared to the previous *Vulcan* beam-column formulation [5]. Since a proper geometric transformation is now possible between the local and global degrees of freedom, the previous difficulty in modelling of sloping members no longer exists.

ACKNOWLEDGMENT

The authors gratefully acknowledge the financial support of the Engineering and Physical Sciences Research Council of Great Britain, under Grant number GR/M99194.

REFERENCES

[1] British Standards Institution, *BS5950: Structural Use of Steelwork in Buildings: Part 8: Code of Practice for Fire Resistant Design*, BSI, London, 1990.

[2] European Committee for Standardisation, *Eurocode 3, Design of Steel Structures, Part 1.2: Structural Fire Design (Draft)*, Commission of the European Communities, Brussels, 1993.

[3] International Organisation for Standardisation, *ISO 834: Fire Resistance Tests - Elements of Building Construction*, 1985.

[4] Swinden Technology Centre , *The Behaviour of Multi-Storey Steel-Framed Buildings in Fire: A European Joint Research Programme*, British Steel plc, Rotherham, UK, 1999.

[5] Najjar S.R., Burgess I.W., A non-linear analysis for three-dimensional steel frames in fire conditions, *Engineering Structures*, 18(1), 1996, pp. 77-89.

[6] Bailey C.G., Burgess I.W. and Plank R.J., Computer simulation of a full-scale structural fire test, *The Structural Engineer,* 74 (6), 1996, pp. 93-100.

[7] Huang Z., Burgess I.W. and Plank R.J., Modelling membrane action of concrete slabs in composite buildings in fire. Part I: Theoretical development, *Journal of Structural Engineering,* ASCE, 129(8), 2003, pp.1093-1102.

[8] Huang Z., Burgess I.W. and Plank R.J., Modelling membrane action of concrete slabs in composite buildings in fire. Part II: Validations, *Journal of Structural Engineering,* ASCE, 129(8), 2003, pp. 1103-1112.

[9] Wong S.Y.,), *The structural response of industrial portal frame structures in fire*, PhD Thesis, University of Sheffield, 2001.

[10] Bathe K.J., *Finite element procedures in engineering analysis*, Prentice-Hall Inc., New Jersey, 1982.

[11] Bathe K.J., *Finite element procedures*, Prentice-Hall Inc., New Jersey, 1996.

[12] Huang Z., Burgess I.W. and Plank R.J., *A non-linear beam-column element for 3D modelling of general cross-sections in fire,* Research Report DCSE/03/F/1, Department of Civil & Structural Engineering, University of Sheffield, 2003.

[13] European Committee for Standardisation *Eurocode 4, Design of Composite Steel and Concrete Structures, Part 1.2: Structural Fire Design (Draft)*, Commission of the European Communities, Brussels, 1992.

[14] American Society of Civil Engineers, *Finite element analysis of reinforced concrete*, New York, 1982.

[15] Wainman D.E. and Martin D.M., *Preliminary assessment of the data arising from a standard fire resistance test performed on a Slimflor beam at the Warrington Fire Research Centre on 14th February, 1996*, Technical Note, SL/HED/TN/S2440/4/96/D, British Steel plc, Swinden Technology Centre, UK, 1996.

[16] Surana K. and Sorem R., Geometrically non-linear formulation for three dimensional curved beam elements with large rotations, *International Journal for Numerical Methods in Engineering*, 28, 1989, pp. 43-73.

[17] Huang Z., Platten A. and Roberts J., Non-linear finite element model to predict temperature histories within reinforced concrete in fires, *Building and Environment*, 31(2), 1996, pp. 109-118.

[18] British Standards Institution, *BS5950: Structural Use of Steelwork in Buildings: Part 1: Code of Practice for Design: rolled and welded sections*, London, 2000.

MEMBRANE ACTION OF COMPOSITE FLOOR SYSTEMS IN FIRE

Colin BAILEY
Manchester Centre for Civil & Construction Engineering, PO Box 88, Manchester, M60 1QD, UK
Colin.Bailey@umist.ac.uk

ABSTRACT

A simple performance-based fire design method for composite floor slabs, supported by a grillage of steel beams, has been developed following the full-scale fire tests on the Cardington steel-framed building. The method, which is currently being used by designers on new projects, utilises membrane action within the floor slab. The use of membrane action allows a significant proportion of the steel beams within a given floorplate can be left unprotected for any given fire scenario.

Due to limited research and understanding, a number of assumptions, which are thought to be conservative, have been adopted within the design method. These assumptions, and the estimated impact on the design method, are discussed in this paper. Also discussed is one of the latest advances of the design method where the method has been extended to incorporate the membrane action of the slab and beam system acting compositely, whereas the previous design method only considered the membrane action of the composite slab. In addition, the new method also includes the effect of the membrane action of the slab due to the variation in the deflected form, which is assumed to follow the changing yield-line patterns as the slab/beam system is heated in a fire. Previously, the membrane action of the composite slab was based on the lower-bound yield-line pattern assuming the slab and supporting beams acted independently. Comparison with the previous design approach shows that the simplifications, of ignoring the variation in the deflected form, and ignoring the contribution of the unprotected steel beams to the membrane load-carrying capacity of the system, were conservative.

KEYWORDS:
Composite floors, membrane action, steel beams, fire protection.

NOTATION.

a aspect ratio (L / l).
b parameter defining magnitude of membrane force.
d_l effective depth of reinforcement.
e enhancement of yield-line load due to membrane action.
e_{sys} enhancement of the slab-beam system due to membrane action
e_{1m} enhancement of element 1 due to membrane forces.
e_{2m} enhancement of element 2 due to membrane forces.
e_{1b} enhancement of element 1 due to bending action.
e_{2b} enhancement of element 2 due to bending action.
g_o parameter defining the compressive stress block in flexural action.
k parameter defining magnitude of membrane force.
KT_0 force in steel per unit width in the shorter span.
L largest span of rectangular slab.
l shortest span of rectangular slab.
m moment capacity of the floor slab.
M_{fi} moment capacity of steel beam at elevated temperatures.
M_0 moment of resistance when no membrane force is present.
M_{1m} moment about support due to membrane forces for element 1.
M_{2m} moment about support due to membrane forces for element 2.
n parameter defining yield-line (refer Figure 8).
S in-plane shear at yield-line.
T_b tensile capacity of steel beam at elevated temperatures
T_0 force in steel per unit width in the longer span.
w deflection of yield line.
$w_{p\theta}$ load-carrying capacity of composite floor and grillage of beams at temperature θ.
w_p moment capacity of the slab/beam system.
φ angle defining yield line pattern (refer Figure 8).
x dimension defining the yield-line pattern.

INTRODUCTION

Following the fire tests[1,2] conducted on the Cardington steel-framed building, a number of researchers[3-6] highlighted the behaviour of membrane action in the composite floor slab as the primary reason why collapse did not occur, even though steel downstand beams were totally unprotected and fire temperatures reached values in excess of 1000°C. Application of the lessons from Cardington, together with membrane tests conducted at ambient temperature, led to the publication in 2000[4,7,8] of a simple design method that can easily be used by practicing designers. Unlike Cardington, where most steel beams were left unprotected within the fire compartments, the design method generally requires 40-50% of the beams within a given floor plate to be protected. A practical example of the use of the design method is shown in Figure 1.

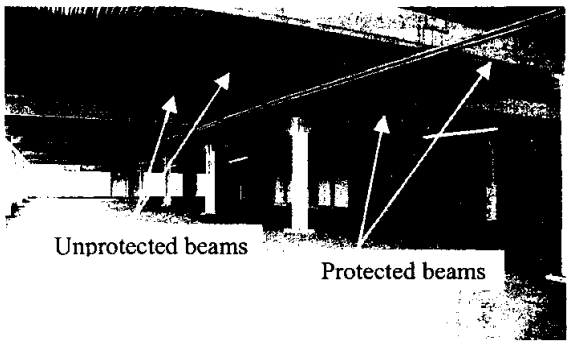

FIGURE 1: Example showing unprotected and protected beams by using membrane action of the composite floor slab.

This paper presents a quick overview of membrane action and how it is applied within the design method. Particular attention is made to the assumptions adopted in the derivation where more fundamental research is required. A recent advancement to the originally published design method, to include catenary action of the steel beams, is discussed.

MEMBRANE ACTION OF ISOLATED CONCRETE SLABS

When vertical load is applied to a square or rectangular concrete slab membrane action will occur. The type, magnitude and final failure mode of membrane action will depend on the horizontal restraint around the slab's perimeter. If the slab has full horizontal restraint then at small displacements the applied vertical load is supported by compressive membrane action. If the slab is heated the magnitude of compressive membrane action will be significantly increased due to the restraint of thermal expansion. Provided the vertical displacement remains small (typically 0.4 to 0.5 times the slab's depth) then the slab can support the vertical load by compressive membrane action. If the slab exceeds this deflection 'instability' occurs with the load-carrying capacity being drastically reduced. Provided this 'instability' is not too violent the slab goes into tensile membrane action with the reinforcement carrying the vertical load by acting as a kind of tensile net. With tensile membrane action an increase in vertical deflection is beneficial, with the load-carrying capacity increasing with increase in deflection. The mode of failure for a horizontally restrained slab is fracture of the reinforcement at the mid-span of the boundaries of the slab. With the loss of horizontal restraint overall collapse can be avoided, albeit with a decrease in the slab's load-carrying capacity, provided the slab's boundaries are vertically supported.

Membrane action will occur in horizontally unrestrained slabs provided the slab boundaries have, and maintain, vertical support. The slab supports the load by tensile membrane action occurring in the central region of the slab and compressive membrane action forming a supporting 'ring' around the perimeter of the slab. This behaviour is analogous to a bicycle wheel: the spokes representing tensile membrane action and the wheel rim representing compressive membrane action. A horizontally unrestrained concrete slab will support less vertical load compared to an equivalently reinforced restrained slab since less tensile membrane action is mobilised in the unrestrained slab. The mode of failure for a lightly reinforced

unrestrained slab is fracture across the shorter span in a rectangular slab or fracture across either span in a square slab. The qualitative load-displacement response of restrained and unrestrained concrete slabs is shown in Figure 2.

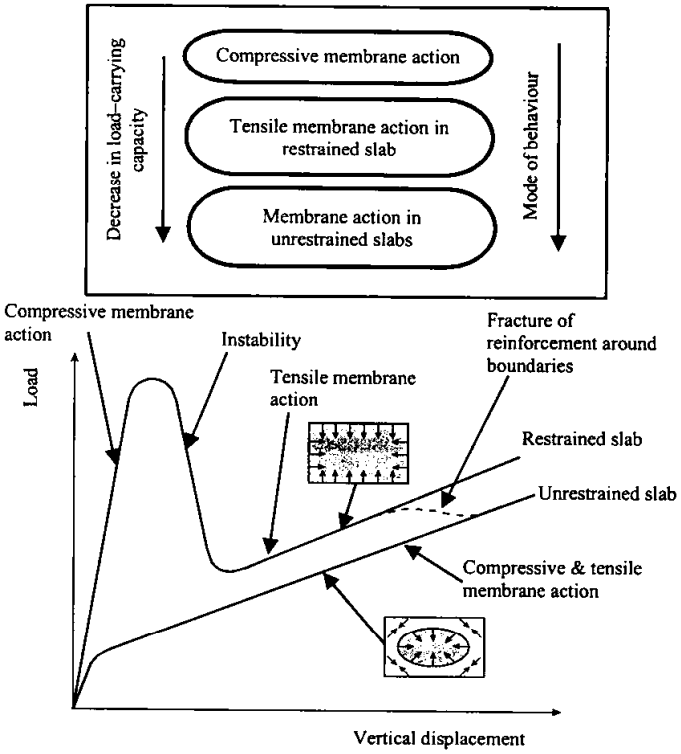

FIGURE 2: Qualitative load-displacement responses of restrained and unrestrained concrete slabs

MEMBRANE ACTION OF FLOOR PLATES

Following the Cardington fire tests it was suggested that the floor 'hung' off the columns as a kind of tensile 'net'. Apart from the localised problems around columns it is difficult to see how this mode of behaviour could occur. The mode of behaviour suggested is similar to that of flat slabs at large displacements. Previous experimental research work[9,10] has been conducted on flat slabs, which showed that compressive membrane action can occur at low displacements with an increase in load capacity above the classic yield-line load. The few flat slabs which have been tested to destruction, and have not failed by punching shear, have shown that tensile membrane effects are small, with the ultimate load-carrying capacity being close to that calculated using the normal yield-line theory. The reason why tensile membrane action is not possible in flat slabs is due to the fracture modes (Figure 3), which have been observed from tests. These are rectangular modes of fracture, which do not permit any substantial tensile membrane action to develop at large displacements.

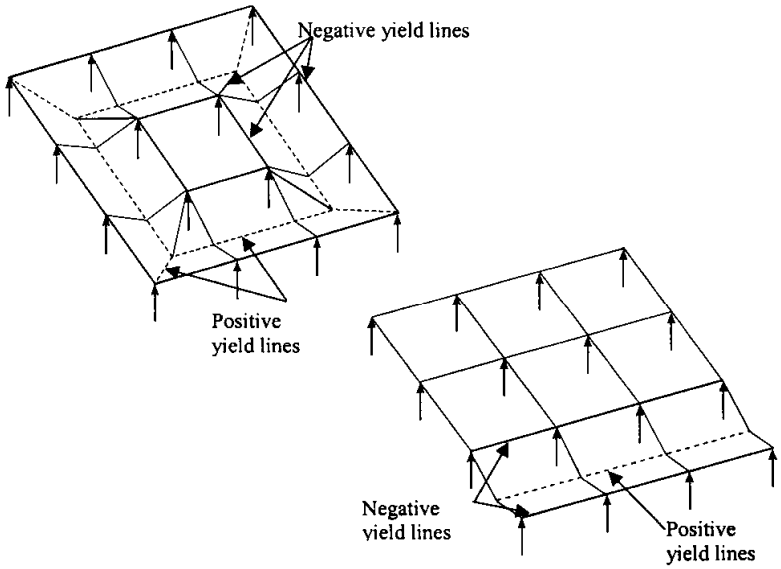

FIGURE 3: Fracture patterns of flat slabs

Considering the fundamental principles of membrane action, described previously, the floor plate consisting of a composite floor slab and supporting grillage of steel beams needs to be designed to ensure membrane action occurs. For example, if the floor plate shown in Figure 4, which consists of a slab supported by a grillage of beams and columns, is loaded with a continually increasing uniform vertical load, two modes of flexural failure are possible. If the design of the beams is such that plastic hinges form, as shown in Figure 4b, a mechanism comprising yield-lines across the whole floor plate will occur with the floor plate effectively folding along the yield-lines, which is similar to one of the fracture patterns of the flat slab shown in Figure 3. Membrane action cannot be mobilised in the mechanism shown in Figure 4b since restraint against lateral movement is not available, although catenary action of the beams could occur if the external columns are designed to resist the resulting horizontal forces.

If the beams within the floor-plate are designed such that no plastic hinges form, the ultimate flexural resistance will be governed by the individual slab panel behaviour (Figure 4c). For this flexural mechanism, provided that each panel is vertically supported around its perimeter, membrane action can occur in the slab irrespective of whether horizontal restraint around the edge of each panel is provided or not. If membrane action is included in the design, the supporting beams around the perimeter of the panels must be able to support the vertical load without plastic hinges forming. If plastic hinges form after membrane action develops in the slab, the mechanism of individual slab behaviour shown in Figure 4c will change to the mechanism shown in Figure 4b with structural collapse occurring unless the grillage of beams can support the load in catenary action, with adequate lateral restraint provided from the external columns.

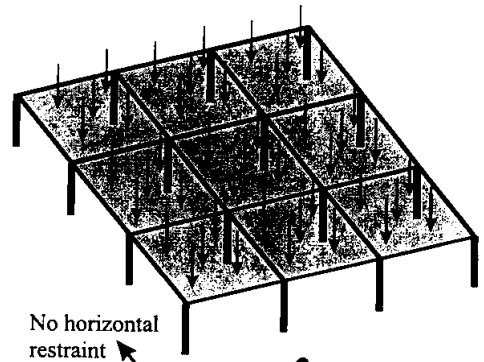

Figure 4a
Floor plate subjected to increasing vertical load.

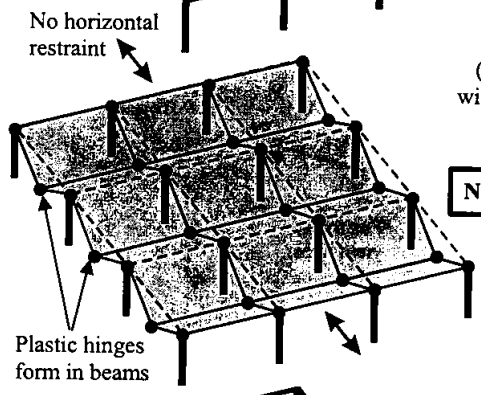

Figure 4b
Beam and panel failure (Plastic hinges form in beams with slab yield lines 'attracted' to plastic hinges)

No membrane action can develop

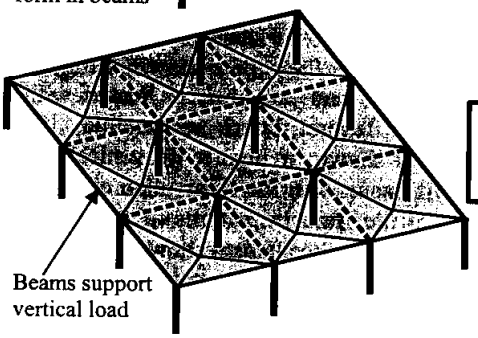

Figure 4c
Slab panel failure (No plastic hinges form in the beams, yield-line mechanisms form in individual slab panels)

Membrane action can develop provided plastic hinges do not form in the beams

FIGURE 4: Modes of behaviour of a floor plate under increasing vertical load.

The same principle of ensuring membrane action develops within a floor plate under increasing vertical load can be applied in the fire design of composite floor slabs supported by a grillage of steel beams. In a fire the vertical load remains constant and the resistance of the floor slab and supporting grillage of steel beams reduces due to the fire. By dividing the floor plate into a number of square or rectangular panels it will be possible to apply protection to the steel beams forming the perimeter of the slab panels and leave the steel beams within the panels unprotected. An example where the principle of using membrane action in the slab to reduce the need for fire protection is shown in Figure 5

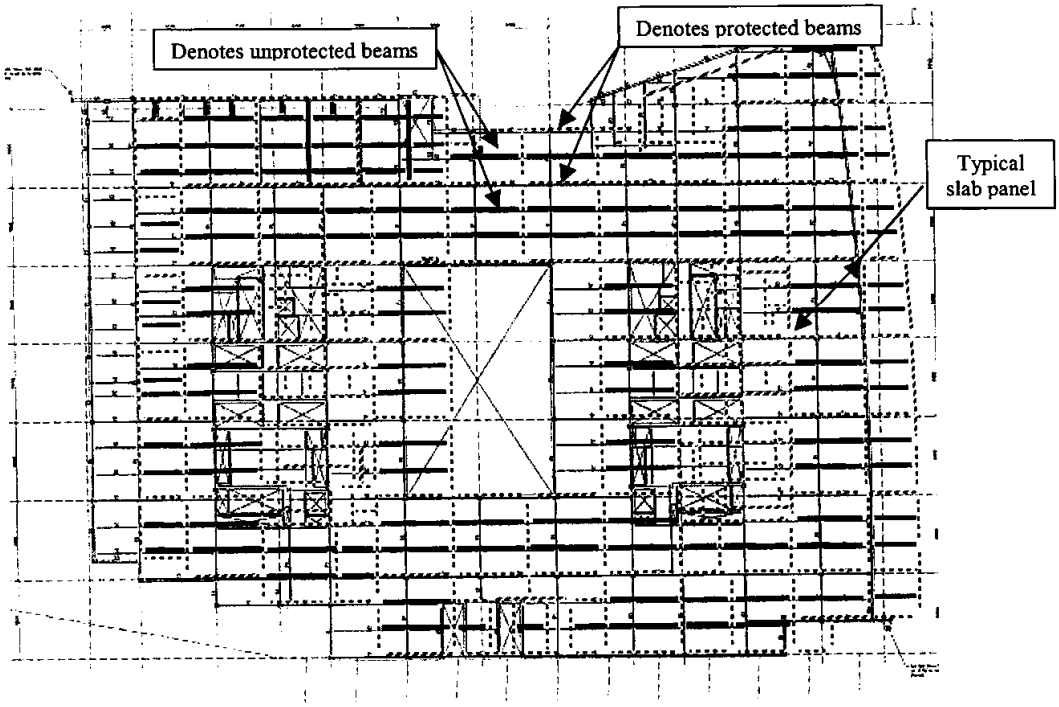

FIGURE 5: Floorplate with protected and unprotected beams

DESIGN METHOD ASSUMPTIONS

The design method, published in 2000[4,7,8], adopted a number of conservative assumptions, which included:

1. Ignoring the effects of thermal restraint.
2. Fracture of the reinforcement over protected beams.
3. Ignoring the contribution of the steel deck.
4. Transfer of load onto protected beams based on yield-line patterns.
5. Membrane action based on a low-bound yield-line pattern.
6. Ignoring catenary action of the steel beams.

It is well known that the effect of restraint to thermal expansion is very important. In the early stages of the fire induced compressive stresses into the composite slab, due to restrained thermal expansion, will significantly increase the compressive membrane action in the slab with a resulting increase in load-carrying capacity. As previously discussed compressive membrane action throughout the slab only occurs at small displacements. The vertical deflection of the floor system will increase as the fire grows due to thermal curvature and possible buckling of the slab due to the increasing compressive stresses caused by the restraint to thermal expansion. Once the slab exceeds a vertical displacement of 0.4 to 0.5 times its depth, tensile membrane action will occur within the slab. Since the aim of the proposed design method is to predict the

ultimate capacity of the slab ignoring the beneficial effects of restrained thermal expansion, during the early stages of the fire, seems a reasonable conservative assumption.

The question of whether the reinforcement fractures over the protected beams has become very topical, with some researchers assuming that the reinforcement remains intact. As discussed previously, and shown qualitative in Figure 2, if the slabs are horizontally restrained (by the reinforcement remaining continuous over the support) the load capacity of the slab is significantly higher than an equivalent slab with no horizontal restraint since greater tensile membrane action is mobilised. In the case where the edge of a slab panel coincides with the edge of a building or service duct the horizontal restraint is nominal.

The Author has taken a pragmatic, and conservative, approach to the question of fracture of reinforcement over protected beams. It is assumed that the large hogging moments that will occur over the vertical support, provided by the protected beams, together with the tensile membrane forces in the floor slab, will generally lead to fracture of the reinforcement during the early stages of the fire. By assuming that the slab panels within the floor plate (refer Figure 5) are horizontally unrestrained the panels will support the vertical load by tensile membrane action in the central plan area of the slab and compressive membrane action around the perimeter of the slab. The conservative assumption of unrestrained slabs simplifies the design since the slab panels are treated the same irrespective of their location with the floor plate. However, more research work is required to investigate reinforcement fracture over protected beams. If reinforcement continuity can be maintained, perhaps by the addition of more localised reinforcement, the design load capacity of the slab will increase.

Although at high temperature, the contribution of the deck to the slab's load-carrying capacity can be significant due to its large area. However, investigation[11,12] of fire damaged buildings, which incorporated a composite slab, has shown that the steel deck has debonded from the concrete in a number of areas due to the release of steam from the concrete. This observation led to the assumption in the design method of ignoring the contribution, to the load-carrying capacity, from the steel deck. It is however, of interest to note that the latest EN version[13] of Eurocode 4 Part 1.2 now allows the inclusion of the steel deck when calculating the capacity of a composite floor slab in fire, thus ignoring the observations from real fires. In reality the contribution from the steel deck lies between the assumption that it retains its full bond and the assumption that it completely losses its bond. Further research work is required to investigate the bond between the steel deck and concrete during a fire.

By utilising membrane action in the composite slab, to allow a number of beams to be left unprotected, the vertical applied load on the protected beams will change in a fire situation compared to that assumed at ambient temperature. For example, if the structural layout shown in Figure 6 is considered, the design method assumes, conservatively, that the load on the protected beams is calculated based on the triangular and trapezoidal loaded areas of the supported slab, defined by the yield-line pattern. This will result in higher loads on beams (1) and lower loads on beams (2), compared with the assumption of loaded tributary areas typically adopted at ambient temperature. However, it is known[14] that if the steel beams (1) are designed assuming a trapezoidal load, this loading pattern assumes that the beams are infinitely stiff compared to the slab. However, as the stiffness of the beams decreases, compared to the stiffness of the slab, the load distribution on the beams will be such that greater load is applied at the end of the beams, compared to the centre of the beams. This load distribution will reduce the beam's moment compared to the loading pattern assumed in Figure 6a. If the mechanics of

membrane action in the slab are also considered (Figure 6b) the applied load on the beams will also tend towards the ends of the beams, suggesting that the load distribution on the protected beams shown in Figure 6a is conservative. Lack of fundamental research was such that no definitive guidance could be given with confidence within the existing design method and the conservative load distribution on the supporting beams, shown in Figure 6a, was adopted.

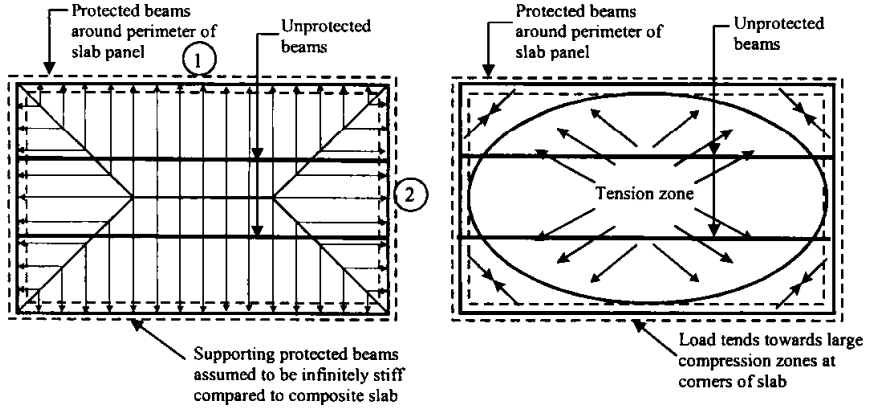

FIGURE 6: (a) Assumed load distribution with infinitely stiff supporting beams. (b) Postulated load distribution due to membrane action in the slab.

The assumptions, relating to yield line patterns and catenary action of the steel beams, have recently been addressed resulting in an extension to the design method, which is discussed below.

EXTENSION OF THE PREVIOUS DESIGN METHOD TO INCLUDE VARYING YIELD-LINE PATTERNS AND CATENARY ACTION OF THE STEEL BEAMS.

An underlying assumption adopted when estimating the membrane action of the composite slab is that the deflected shape of the slab follows the yield-line pattern with rigid plates assumed between yield-lines. This seems a reasonable assumption since the aim of the design method is to predict the capacity of the slab at failure (i.e. plastic design with change of geometry) and no attempt is made to predict the load capacity in the early stages of a fire where the significant effects of restrained thermal expansion and thermal curvature will govern. The previous design method based the magnitude of the membrane action on a lower-bound yield-line pattern ignoring the contribution of the supporting beams. The effects of varying yield-line patterns are discussed below.

Consider the behaviour of a rectangular composite floor slab vertically supported around its edges with one unprotected beam, as shown in Figure 7. At ambient temperature the applied static load is assumed to be supported by the composite floor slab spanning one-way on to the grillage of beams (Mode (i) in Figure 7). During a fire the unprotected beams and floor slab begin to lose strength and stiffness. The unprotected beam will continue to lose strength with a plastic hinge forming at mid-span. A fan-type of yield-line pattern will occur in the slab, redirecting load away from the unprotected beam towards the vertical supports (Mode (ii) in

Figure 7). As the beam continues to lose strength the yield-line pattern forms a 'cross' (Mode (iii) in Figure 7). With continuing loss of strength of the unprotected beam, a 'travelling hinge' will form as more of the load is carried by the slab, until finally no load can be carried by the unprotected beam and the slab supports the full load by the classic 'back-of-an-envelop' yield-line pattern (Mode (iv) in Figure 7). For each of the yield-line patterns described, membrane action will occur as the slab deflects vertically.

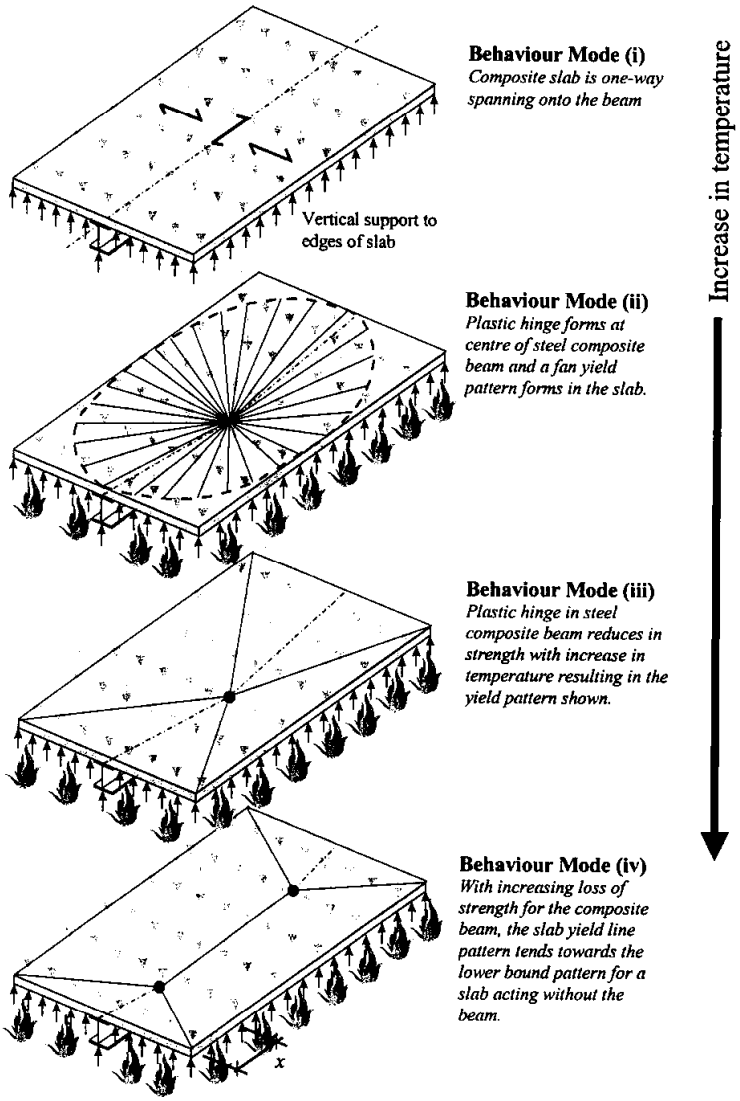

FIGURE 7: Behaviour of slab and beam system under increasing temperature

As explained the yield-line pattern is dependent on the strength of the beam which is continually changing. For example, consider Mode (iii) and (iv) in Figure 7. The behaviour changes from Mode (iii) to Mode (iv) by a 'travelling hinge' forming as shown in Figure 8.

By using the principles of virtual work the flexural load-carrying capacity of the slab/beam system, for the yield-line patterns shown in Figure 8, is given by;

$$w_p = \frac{1}{\left(\frac{Ll}{2} - \frac{xl}{3}\right)}\left[\left(\frac{2l}{x} + \frac{4L}{l}\right)m + \frac{2M_{fi}}{x}\right] \tag{1}$$

By using the equilibrium method the shape of the yield-line pattern in Figure 8 can be determined by calculating the value of 'x' given by,

$$x = \frac{-\left(\frac{w_p l^2}{6L}\right) + \sqrt{\left(\frac{w_p l^2}{6L}\right)^2 - 4\left(\frac{w_p}{6}\right)\left(\frac{-w_p l^2}{8} - \frac{M_{fi}}{l}\right)}}{2\left(\frac{w_p}{6}\right)} \tag{2}$$

If we take the fire test[1] conducted by the Building Research Establishment (BRE) on the 9m × 6m corner bay, which corresponds to the behaviour shown in Figures 7 and 8, we have w_p= 4.9kN/m^2, m=4.2kNm, L = 9m and l = 6m.

Substituting these values into Equation (1), putting x = 4.5m (relating to Mode (iii) in Figure 7) and rearranging, leads to M_{fi} = 55.6 kNm. This means that Mode (iii) cannot occur until the strength of the unprotected beam reduces to 55.6 kNm. The unprotected beam in the BRE corner fire test[1] was a 305×165×30UB which, when acting as a composite beam (assuming measured properties), had a moment capacity of 428 kNm. The load level of the beam, defined as the capacity of the beam at the fire limit state divided by the capacity of the beam at ambient temperature, is related to the temperature of the steel beam as shown in Table 1 using the principles in EC4-1-2[13]. For a bending moment of 55.6kNm, where x = 4.5m, the load level is 0.129, giving a temperature of 792°C (Table 1). Therefore, for the BRE corner fire test, Mode (iii) does not occur until the steel temperature reaches 792°C. Above this temperature 'travelling hinges' form (Figure 8) with the mode of behaviour tending towards Mode (iv) up to a steel temperature of 1200°C where the slab will support the full load in membrane action.

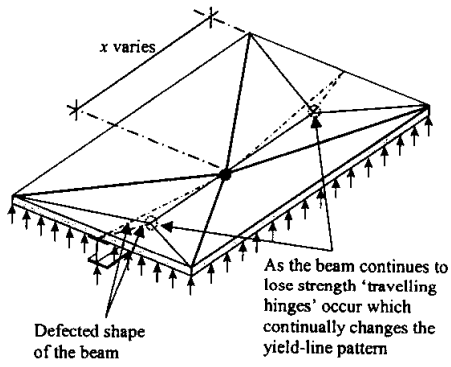

FIGURE 8: 'Travelling hinge' continually changing yield-line pattern under increasing temperature.

Load Level	0.7	0.6	0.5	0.4	0.3	0.2	0.1	0.08	0.06	0.04	0.02	0.01
Critical Temp (°C)	526	558	590	629	671	725	820	860	900	1000	1100	1150

TABLE 1: Failure temperatures for composite beams[4]

Using Equations (1) and (2) the flexural load-capacity of the slab and beam system can be calculated for varying values of M_{fi}. In addition the steel temperature can be estimated for a given value of M_{fi} based on the load level and the basic principles in EC4-1-2[13]. For the BRE test, the moment capacity of the composite floor slab (m) was taken[4] as 4.2 kNm based on measured properties and ignoring the contribution from the steel deck, which is assumed to debond from the concrete during the fire. The values of 'x' defining the yield-line pattern, the flexural load capacity of the slab and beam system, the load level of the composite beam and the temperature of the steel beam are shown in Table 2 for varying values of M_{fi}.

Moment capacity of steel beam (M_{fi}) kNm	'x' m	Flexural load capacity of beam and slab system (w_p) kN/m^2	Load Level of composite beam	Temperature of steel beam (°C)
55.4	4.50	3.39	0.129	792
50	4.40	3.26	0.117	804
40	4.25	3.02	0.09	840
30	4.08	2.77	0.07	880
20	3.92	2.52	0.047	965
15	3.83	2.39	0.035	1025
10	3.75	2.26	0.023	1085
5	3.65	2.11	0.012	1140
0	3.56	1.98	0.0	1200

TABLE 2: Flexural load capacity of beam and slab system for given steel beam temperatures for the BRE corner fire test.

It can be seen that the flexural strength of the slab and unprotected steel beam cannot support the applied static load of 4.9kN/m^2, indicating that membrane action of the slab and beam system needs to occur. Extending the Author's original method, to include the membrane action of the beam and slab system, the load carrying capacity is given by;

$$w_{p\theta} = e_{sys}\left[\left(\frac{\textit{Internal work done by the composite slab in bending}}{\textit{External work done by the floor system per unit load}}\right) + \left(\frac{\textit{Internal work done by the beam(s) in bending}}{\textit{External work done by the floor system per unit load}}\right)\right] \quad (3)$$

where e_{sys} is the enhancement applied to the composite slab and beam system to take into account membrane action. The enhancement factor is derived below based on basic equilibrium principles. Equation (3) assumes full connection between the beam and slab so that all tensile forces generated in the steel beam can be transferred, via the shear studs, to the slab. It is worth noting that Equation (3) assumes that the tensile force in the steel beam is balanced by the compressive membrane force acting around the slab's perimeter. Therefore provided vertical support is maintained around the slab's perimeter no reliance is made on the end connections to resist the tensile forces generated in the unprotected beam

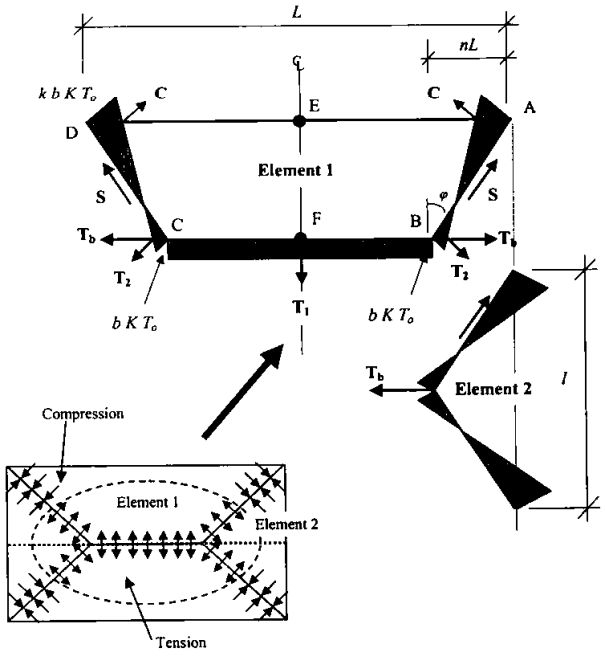

FIGURE 9: In-plane forces of slab and beam system

The membrane action of the slab/beam system can be derived by following the basic approach used by the Author for the previous design method[4,15,16] with revision to some parts of the derivation to allow the geometrical effect of the beam acting in pure tension (catenary action) to be taken into account. Parts of the derivation that are unaffected by the inclusion of the tensile capacity of the beam are not repeated here and the reader is directed towards References 4, 15 and 16.

The in-plane forces are shown in Figure 9, where nL varies to represent Mode (iii) and the translation to Mode (iv) in Figures 7 and 8. Considering the in plane forces, the values of 'k' and 'b' defining the in-plane stress in the concrete slab can be calculated from basic equilibrium and by taking moments about position 'E', assuming fracture of reinforcement along line EF (as observed from tests).

These values are given by[15]:

$$k = \frac{4na^2(1-2n)}{4n^2a^2+1} + 1 \tag{4}$$

and

$$b = \frac{1.1l^2}{8(A+B+C-D)} \tag{5}$$

where

$$A = \frac{l}{2}\left(\frac{1}{l+k}\right)\left[\frac{l^2}{8n} - \frac{\left(L/2 - nL\right)}{nL}\left((nL)^2 + \frac{l^2}{4}\right) - \frac{l}{3}\left(\frac{1}{l+k}\right)\left((nL)^2 + \frac{l^2}{4}\right)\right]$$

$$B = \frac{l}{2}\left(\frac{k^2}{l+k}\right)\left[\frac{nL^2}{2} - \frac{k}{3(l+k)}\left((nL)^2 + \frac{l^2}{4}\right)\right]$$

$$C = \frac{l^2}{16n}(k-1)$$

$$D = \left(\frac{L}{2} - nL\right)\left(\frac{L}{4} - \frac{nL}{2}\right)$$

The load-carrying capacity of the slab/beam system is estimated by considering the membrane forces in the slab and tensile force in the beam. For ease of presentation the load-carrying capacity due to membrane effects is divided by the yield-line load of the slab/beam system to derive an enhancement (e_{sys}), as shown in Equation (3).

An enhancement factor is calculated for elements 1 and 2 shown in Figure 9, with the contribution of vertical and in-plane shear along the yield-lines initially ignored. The loads determined by considering elements 1 and 2 will generally be unequal and an average value, considering the contribution of shear forces (as suggested by Hayes[17]) can be calculated.

For element 1 the enhancement for membrane action is given by[15]:

$$e_{1m} = \frac{M_{1m}}{M_0 L} = \frac{4b}{3+(g_0)}\left(\frac{w}{d_1}\right)\left((1-2n)+\frac{n(3k+2)-nk^3}{3(1+k)^2}\right) \tag{6}$$

For element 2 the tensile force of the beam needs to be included, with the enhancement given by,

$$e_{2m} = \frac{M_{2m}}{M_0 l + M_{fi}} = \left[T_0 lbw\left(\frac{2+3k-k^3}{6(1+k)^2}\right)+T_b w\right] \quad \frac{1}{T_0 d_1\left(3+g_0/4\right)l + M_{fi}} \tag{7}$$

The effect of the membrane force on the bending moment will result in an enhancement factor for element 1 of [15]:

$$e_{1b} = \frac{M}{M_0 L} = 2n\left[1+\frac{\alpha b}{2}(k-1)-\frac{\beta b^2}{3}(k^2-k+1)\right]+(1-2n)(1-\alpha b-\beta b^2) \tag{8}$$

and similarly for element 2[15]:

$$e_{2b} = \frac{M}{M_0 l} = 1+\frac{\alpha bK}{2}(k-1)-\frac{\beta b^2 K}{3}(k^2-k+1) \tag{9}$$

The net enhancement for the slab/beam system is obtained by combining these effects for each element, i.e.

$$e_1 = e_{1m} + e_{1b} \tag{10}$$
$$e_2 = e_{2m} + e_{2b}$$

Typically e_1 and e_2 are not equal. Hayes[17] suggests that if the difference can be explained by the effects of vertical shear or in-plane shear, then the overall enhancement may be shown to be given by,

$$e_{sys} = e_1 - \frac{e_1 - e_2}{1+2a^2} \tag{11}$$

The above method is an extension of the previous design method[4,15,16] since it now removes the simplifications mentioned previously. With reference to Figure 8 the new method now considers the actual yield-line pattern between Modes (iii) and (iv) taking into account the 'travelling hinges' as the unprotected beam increases in temperature. The membrane action of the slab relating to the deflected shape of the slab, which is assumed to be defined by the yield-line pattern that is continually changing, plus the tensile (catenary) capacity of the unprotected beam is embedded within the method.

The previous developed design method showed excellent correlation[4] against the full-scale fire tests at Cardington. Therefore the new method was compared against both the Author's previous design method and the BRE corner fire test to assess the impact of extending the design method.

COMPARISON WITH THE BRE CORNER FIRE TEST AND THE EXISTING DESIGN METHOD

As previously explained the modes of behaviour shown in Figures 7 and 8 relate to the BRE corner fire test, which consisted of heating a 9m × 6m bay of the steel-framed Cardington Building. For full details of the test method and results, the reader is directed towards Reference 1. Table 2 shows the estimated flexural strength of the slab/beam system for the fire test. It can be seen that at elevated temperatures the system cannot support the applied static load of 4.9kN/m^2 by flexural action and membrane action of the system needs to be considered.

Using Equations (3) to (11), the required displacement to support an applied load of 4.9kN/m^2 is estimated for the unprotected steel beam temperatures shown in Table 2. The vertical displacement estimated from the equations shown above is compared against the Author's existing design method[4] ,and test results, as shown in Figure 10.

Since both the new and existing design methods are plastic design with change of geometry a failure envelope is predicted. The accuracy of the method is assessed by the test results converging towards the predicted envelope. As discussed in Reference 4 the existing design method provided excellent predictions. Figure 10 shows the prediction using the existing design method, the new design method derived in this paper, and the test results. It can be seen that higher temperatures are obtainable for a given vertical displacement by considering the membrane action of the slab, together with the tensile strength of the beam, corresponding to the actual yield-line deformation of the slab as it continually changes with increasing temperature.

Figure 9 shows that the simplifications in the existing design method of ignoring catenary action of the steel beams and basing the membrane action of the slab on the lowest yield-line mechanism is conservative. At displacements below 130mm there is no significant difference between the new and existing design methods, since the vertical displacements are too small to allow significant mobilisation of catenary action in the unprotected steel beam. At 1200°C the two design methods converge to the same prediction due to the unprotected steel beam having zero strength and the load being totally carried by the composite slab in membrane action.

As expected the simplifications in the previous design method lead to conservative results, as well as having the advantage of being easy to implement by practising designers. The use of the new design method discussed in this paper cannot be readily presented as a 'hand calculation' and has to be used as a specification for a simple computer model.

CONCLUSIONS

At large vertical displacements membrane action of a floor slab, if designed correctly, can significantly increase the load-carrying capacity above that estimated assuming flexural behaviour. A performance-based fire design method incorporating membrane action of composite floor slabs, which was published in 2000, has been discussed with particular attention to the assumptions made and highlighting the areas where more research is needed.

A recent extension to the design method has been discussed which allows an estimate of the membrane capacity of the slab and beam system. This extension is a significant improvement on the previous method where only the membrane action of the slab was considered. The new method retains the assumption of the deflected shape of the slab following yield-line patterns.

However, in the previous method the membrane capacity of the slab was based on the deflected shape assuming a lower-bound yield-line pattern, which is only valid if the slab and beam(s) within the defined slab panel act independently, or the beams are subjected to temperatures above 1200°C, where they have zero strength. In the new method the deflected shape and the resulting membrane action is assumed to continually change as the slab/beam system is heated.

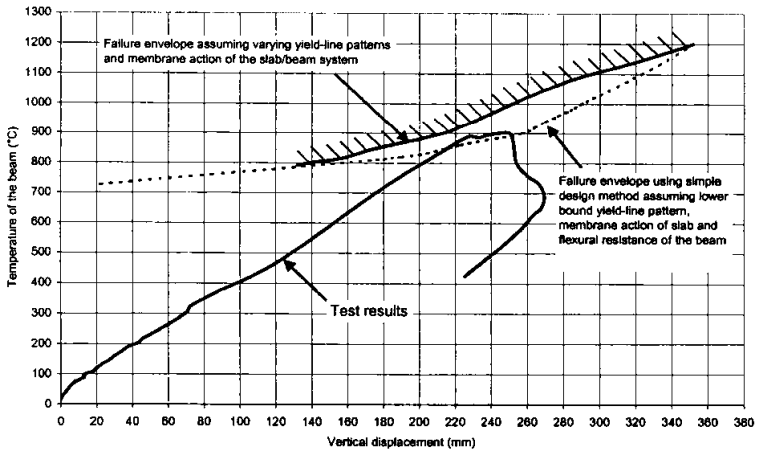

FIGURE 10: Comparison between the test results and the new and existing design methods for the BRE corner fire test

One important assumption in the derivation of the new design method, presented in this paper, is that the tensile force generated in the beam is transferred to the supporting composite slab by shear connectors and is resisted by the compressive membrane force generated around the slab's perimeter. No horizontal restraint is assumed to the perimeter of the slab or to the ends of the unprotected beams. Therefore provided vertical support is maintained around the slab's perimeter no reliance is made on either the continuity of reinforcement or the tensile capacity of the steel connections. This is considered to be a conservative assumption. If horizontal restraint around the slab's perimeter and axial restraint to beams can be guaranteed then additional tensile membrane action can be mobilised in the slab which will increase the slab's load-bearing capacity.

Comparison of the new and previous design methods shows that ignoring the contribution of the tensile strength of the beam to the membrane action of the slab/beam floor system, and basing the membrane action of the floor slab on a deflected lower-bound yield-line pattern, was conservative. The new design method also showed good correlation with the BRE corner fire test conducted on the Cardington steel-framed building.

Using the design method will allow a significant number of steel beams within the floor-plate to be left unprotected. If a board, spray or intumescent coating is adopted then significant cost savings in terms of material and fixing/application time can be achieved. Also the disadvantages, of fixing–time and increasing the buildings dead-weight, associated with encasing steel beams in concrete are significantly reduced by just protecting beams forming the perimeter of the defined slab panels within the floor-plate. Although the specification of

concrete encasement on a proportion of the beams within the floorplate will be more costly, compared to protecting the same beams with a spray, board or intumescent coating, a more robust structure against impact damage can be achieved.

REFERENCES

1. Bailey, C. G., Lennon, T. and Moore, D. B., The behaviour of full-scale steel framed buildings subjected to compartment fires, *The Structural Engineer*, Vol. 77, No. 8, April 1999. pp. 15-21.
2. O'Conner M.A, Kirby B.R and Martin D.M. Behaviour of a multi-storey composite steel framed building in fire. *The Structural Engineer* Vol. 81 No. 2 January 2003 pp 27-36.
3. Wang Y.C. *Tensile membrane action in slabs and its application to the Cardington fire tests*. Fire, Static and Dynamic Tests of Building Structures. Proceedings of the Second Cardington Conference, England 12-14 March 1996. pp 55-67.
4. Bailey C.G. and Moore D.B. The structural behaviour of steel frames with composite floorslabs subject to fire: Part 1: Theory. *The Structural Engineer* Vol. 78 No. 11 June 2000 pp. 19 – 27.
5. Huang Z., Burgess, I.W and Plank R.J., Modelling of six full-scale fire tests on a composite building. *The Structural Engineer* Vol. 80 No. 19 2002 pp. 30 – 37.
6. Gillie M., Usmani A.S. and Rotter J.M. A structural analysis of the Cardington British Steel Corner Test. *Journal of Constructional Steel Research* **58** (2002) pp 427-442.
7. Newman G.M., Robinson J,T. and Bailey C.G., *Fire Safe design: A New Approach to Multi-Storey Steel-Framed Buildings.* SCI Publication P288. The Steel Construction Institute, Ascot. 2000. ISBN 1 85942 120 2.
8. Bailey C.G. Steel structures supporting composite floor slabs: design for fire. BRE Digest 462. December 2001. ISBN 1 86081 527 8.
9. Hatcher D, S, Sozen M. A., and Chester S.P., Test of a reinforced concrete flat slab. Journal of the Structural Division, Proceedings of the American Society of Civil Engineers. ST6 June 1969. pp 1051-1072.
10. Blakey F.A., Australian experiments with flat plates. Jour. of American Concrete Institute. April 1963. pp. 515-525.
11. Structural fire engineering: investigation of Broadgate phase 8 fire' Ascot, Steel Construction Institute, 1991
12. Fire Damage Structural Survey Report to Churchill Plaza, Churchill Way, Basingstoke. Amos Broome Associates PLC. Confidential Report. June 1991.
13. Pr EN1994-1-2. Eurocode 4. Design of composite steel and concrete structures. Part 1.2. General rules. Structural fire design. Final Draft European Committee for Standardization, Brussels.
14. Wood R.H. *Studies in Composite Construction – Part II. The interaction of Floors and Beams in Multi-Storey Buildings.* National Building Studies. Research paper No. 22. HMSO. 1955
15. Bailey C.G. Membrane action of unrestrained lightly reinforced concrete slabs at large displacements. *Engineering Structures*. 23 (2001) pp. 470-483.
16. Bailey C.G. Efficient arrangement of reinforcement for membrane behaviour of composite floor slabs in fire conditions. *Journal of Constructional Steel Research* 59 (2003) pp 931-949.
17. Hayes B. Allowing for membrane action in the plastic analysis of rectangular reinforced concrete slabs. *Magazine of Concrete Research* Vol. 20 No. 65 Dec 1968. pp 205-212.

ANALYSIS AND DESIGN OF REINFORCED CONCRETE SLABS EXPOSED TO FIRES

Linus LIM, Andy BUCHANAN, and Peter MOSS
Department of Civil Engineering, University of Canterbury, Christchurch, New Zealand

ABSTRACT

This paper gives an overview of recent analytical modelling of reinforced concrete slabs in fire conditions, verified by limited experimental testing. The resulting understanding of slab behaviour allows some new design recommendations to be made.

The analysis described in this paper includes both one-way and two-way concrete slabs, with various conditions of support and restraint at the edges. The thermal and structural analyses of the slabs were carried out using the SAFIR finite element program, using different types of elements for two-dimensional and three-dimensional behaviour. The analyses accounted for large displacements and non-linear thermal and mechanical properties of the materials at elevated temperatures.

The analyses showed that the fire behaviour of axially restrained reinforced concrete slabs is very sensitive to their support conditions, particularly the height of the horizontal thrust force and the axial restraint stiffness.

Experimental fire testing on simply supported, two-way reinforced concrete slabs showed that the slabs were able to support the loads for three hours of fire exposure without collapse, despite suffering significant deflections and loss of flexural strength. The time to failure was much greater than would be predicted by calculations using yield-line theory. The finite element predictions of the tested slabs showed good agreement with the limited test results. The analyses show that, in many cases, tensile membrane action can provide additional load-bearing capacity as the strengths of the materials drop at elevated temperatures and deflections increase due to prolonged fire exposure.

KEYWORDS: *axial restraint, finite element analysis, fire resistance, reinforced concrete slabs, tensile membrane action*

INTRODUCTION

This paper presents a summary of a study by Lim [1] into the fire resistance of reinforced concrete and composite steel-concrete slabs. The main objectives of this research were to investigate the effect of compressive axial restraint and tensile membrane action on the fire behaviour of reinforced concrete slabs. The scope of this study covers one-way reinforced concrete flat slabs and two-way reinforced concrete flat slabs and composite steel-concrete slabs. The experimental part of the study only investigated two-way slab behaviour.

The main findings of the research are presented here along with design recommendations for fire resistance of concrete slabs. The details of the experimental fire tests and computer modelling results in the study are not presented here.

COMPRESSIVE AXIAL RESTRAINT

Objective

The main objective of studying compressive axial restraint on one-way slabs was to investigate the effect of various parameters such as the axial restraint stiffness and the location of the horizontal reaction force at the supports. The slabs that were analysed focussed primarily on precast concrete slabs which are normally constructed as one-way systems without flexural continuity at the end supports. Continuous slabs with axial restraint were also analysed.

The impetus for carrying out this study is because previous studies looking at the effects of axial restraint on concrete slabs were limited and had not considered parameters such as different positions of the horizontal reaction force.

Background

The first studies on the influence of compressive axial restraint on the fire resistance of reinforced concrete floor systems was carried out through fire tests on precast concrete slabs by the Portland Cement Association (PCA) in the 1960s [2 - 4]. Based on these tests, the effect of axial restraint is generally accepted as being beneficial for the performance of flexural elements under fire conditions. However, analytical studies by Anderberg et al [5] and experimental tests by Cooke [6] did not show the same beneficial effects of axial restraint and slabs may be susceptible to failure by buckling. The PCA fire tests showed that the fire behaviour of axially restrained slabs is sensitive to their support conditions, in particular the location of the horizontal reaction force [7].

A step-by-step hand method was developed by the Prestressed Concrete Institute [8], based on the PCA fire tests, to determine the thrust force required to prevent collapse of a floor system during a fire, and the required stiffness of the surrounding structure to provide that thrust force.

Some design codes such as ASTM E119 [9] and the *Fire Resistance Directory* [10] provide both restrained and unrestrained fire resistance ratings for various types of concrete floor systems in order to account for some axial restraint which may occur in many real structures. Restrained

ratings of floor systems are generally higher than unrestrained ratings as it is assumed that any amount of axial restraint will improve the fire resistance of reinforced concrete slabs.

Method of analysis

The analysis in this study was carried out with a non-linear finite element program, SAFIR [11]. The analysis consists of carrying out a thermal analysis to determine the temperatures of the slab, followed by a structural analysis to determine the structural response due to the elevated temperatures.

The finite element analysis with SAFIR takes into account of the large displacements and non-linear thermal and mechanical properties at elevated temperatures. The thermal and mechanical properties of the reinforcing steel and concrete are based on those prescribed in the Eurocode [12]. In the SAFIR analysis, the possible effects of shear failure or concrete spalling on the slab behaviour were not considered.

The reinforced concrete slab that was analysed is 200mm thick, spanning 5m between its end supports. The slab is reinforced with 16mm bars, at 125mm centres and had 25mm concrete cover to the reinforcement. The concrete was modelled with a compressive strength of 30MPa. In the computer analysis, the slab was exposed to the ISO 834 standard fire for up to four hours while supporting a uniformly distributed load of 6.9kPa. The different support conditions that were studied are described in the following sections.

Support conditions of slab

Pin-Supported Precast Slabs with Fixed Line of Thrust

Pin-supported precast concrete slabs with fixed line of thrust were analysed for the condition where the end supports are able to provide axial restraint, and the height of the line of thrust is fixed by the end detail throughout the fire exposure, such as those shown in Figure 1a, b, and c. The slabs were modelled with full axial restraint, which may occur in an interior bay of a multi-bay building that is heated by an isolated and confined fire. Separate analyses were conducted for different positions of line of thrust at the end supports, ranging from 25mm below the exposed face to 125mm into the depth of the slab (25mm above the slab mid-depth). The effects of different levels of axial restraint stiffness on the slab's fire behaviour were also studied. The axial restraint stiffnesses that were studied ranged from zero restraint (simply supported) to full axial restraint (pin-pin condition).

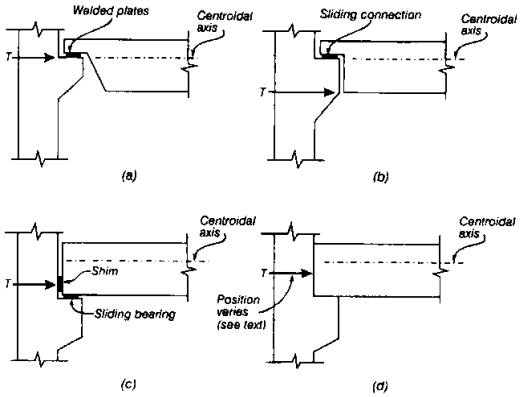

FIGURE 1: Location of line of thrust for different support conditions [7].

Pin-Supported Slabs with Moveable Line of Thrust

Pin-supported slabs with moveable line of thrust were also modelled to simulate precast concrete slabs where the end supports are cast into the surrounding construction as shown in Figure 2. In this case the height of the line of thrust is not fixed and can move up or down during the fire exposure. This is similar to the support detail shown in Figure 1d, except that there is additional reinforcing in the concrete topping which can provide limited flexural and tensile capacity if needed.

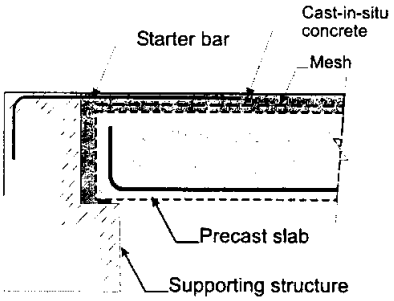

FIGURE 2: A typical support detail for precast concrete slabs with ends cast into surrounding construction [13].

Rotationally Restrained Slabs

Continuous slabs with rotationally restrained end supports were also modelled with different levels of axial restraint stiffnesses and different amounts of curtailment of the negative reinforcing steel at the end supports. Previous analytical studies and experimental tests on continuous slabs with rotationally restrained supports carried out by Anderberg [14] had not considered the effects of axial restraint on their behaviour.

Observations of SAFIR finite element analyses

General Discussion

The general findings of the analyses of restrained one-way slabs are as follows:

(i) The behaviour of one-way reinforced slabs under fire conditions is very sensitive to their end support conditions and the axial restraint stiffness.

(ii) The behaviour of a slab under compressive restraint is not easy to quantify and model, even with a sophisticated finite element program.

(iii) Computer modelling to predict the fire behaviour of restrained reinforced concrete floor systems for design purposes is difficult due to the poor information about the actual boundary conditions in real construction, such as the expected level of axial restraint stiffness and the likely height of the axial restraint force, which may change in location during fire exposure.

(iv) Tensile behaviour in catenary action becomes very important as one-way slabs approach the point of failure.

Pin-Supported Slabs

The main findings of the analyses of one-way, pin-supported slabs are as follows:

(i) For pin-supported slabs, compressive restraint is beneficial only if the line of thrust is located well below the centroidal axis of the slab at the supports, and remains below the centroidal axis in the span of the slab throughout the fire exposure (Figure 3). In this situation, the compressive thrust force, T, increases the flexural strength of the slab and prevents large deflections. Compressive restraint is most beneficial if the axial restraint stiffness of the surrounding structure is high, i.e.: when the total maximum permissible expansion is less than 0.001L (where L is the length of the slab) and the axial restraint stiffness is greater than 40% of the axial stiffness of the heated slab.

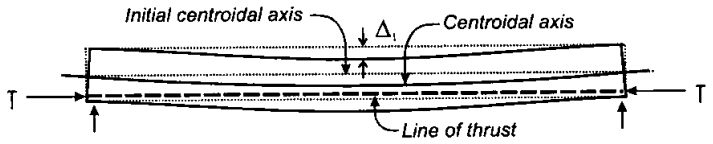

FIGURE 3: Midspan centroidal axis above line of thrust.

(ii) If the line of thrust at the supports is located below but close to the centroidal axis, compressive axial restraint produces poor behaviour in pin-supported slabs because the centroidal axis is likely to drop below the line of thrust. When this happens, the compressive restraint force becomes detrimental to the slab behaviour as it increases the vertical deflections and the applied positive moments at midspan, decreasing the time to a plastic hinge forming in the slab.

(iii) If during fire exposure, the centroidal axis of a restrained slab drops below the line of thrust (Figure 4), either due to the line of thrust moving upwards or the slab deflecting downwards, the compressive axial restraint force, T, would produce a detrimental effect on the slab as it increases the deflections and the applied positive moments at midspan, decreasing the time to a plastic hinge forming in the slab. This causes the slab to deform into catenary mode with axial tensile forces in the slab. If the tensile forces cannot be resisted at the supports of the slab, the analyses showed that the slab would fail, thus resulting in significantly lower fire resistance than would be expected from code recommended values. Slabs with high axial restraint and with their line of thrust located close to the centroidal axis have poor behaviour because the centroidal axis is likely to drop below the line of thrust.

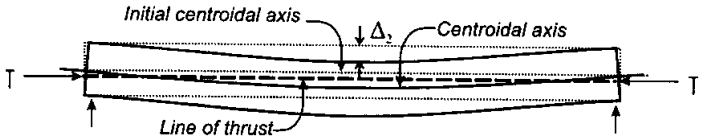

FIGURE 4: Midspan centroidal axis below line of thrust.

(iv) In pin-supported slabs which have their end supports cast into the surrounding construction (as shown in Figure 1d or Figure 2) the line of thrust moves from the heated face towards the unheated side due to the progressive depletion of the strength and stiffness of the concrete and reinforcing steel at the heated face. The position of the line of thrust during a fire also depends on the axial restraint stiffness and the stiffness of the slab itself.

Continuous slabs

The main findings of the analyses of one-way, continuous slabs are as follows:

(i) Continuous slabs with rotational restraint at both end supports have excellent behaviour and significantly higher fire resistance than pin-supported slabs. Their better performance in fires is attributed to their ability to redistribute the applied bending moments.

(ii) The position of the line of thrust in continuous slabs moves upwards from the exposed face of the slab during fire exposure, similar to the behaviour of pin-supported slabs with their end supports cast into the surrounding construction, described earlier.

(iii) Analyses on the effects of curtailment of negative reinforcement in continuous slabs showed that the slabs exhibit excellent behaviour when the negative top steel is curtailed according to code recommendations. More severe curtailment of the negative reinforcement results in large slab deflections and a decrease in the ability of the slabs to redistribute the applied moments.

Design of one-way reinforced concrete slabs for fire resistance

Based on this research, the design of one-way reinforced concrete slabs for fire resistance should be based on a hierarchical approach, as shown below. This hierarchy can be applied to reinforced concrete or precast concrete slabs.

(i) Most reinforced concrete slabs have sufficient generic fire resistance to meet prescriptive code requirements without any additional fire protection. Generic fire resistance ratings can be achieved by providing minimum member thickness and concrete cover to reinforcement as specified in tabulated requirements. All reinforced concrete and precast concrete slabs should be designed with some reinforcing anchored into the supports, to prevent catastrophic collapse if the slabs deform into catenary mode.

(ii) If the generic ratings do not provide sufficient structural fire resistance, simple hand calculation methods can be used to determine flexural strength of simply supported slabs during fire exposure. These simple hand methods, based on first principles of structural behaviour, can be found in other references [8, 15, 16, 17]. Slabs can be treated as simply supported and unrestrained if the axial restraint stiffness is less than 1% of the axial stiffness of the heated slab and the maximum permissible expansion of the slab is greater than 0.005L (where L is the length of the slab).

(iii) If the calculations for simply supported slabs do not provide sufficient fire resistance, the fire resistance can be greatly increased by designing the slabs as continuous over the supports. The negative reinforcement in the top of the slab should not be severely curtailed in order to allow redistribution of moments in the slab. Curtailment according to code recommendations for ambient temperatures is usually satisfactory. The top bars over the supports must be able to withstand high strains due to the large rotations which can occur during a fire, so ductile reinforcing bars should be used rather than welded mesh.

(iv) If flexural continuity cannot be provided, the fire resistance of the slabs can be increased by designing the slabs as two-way slabs if the geometry is suitable (Refer to the subsequent sections of this paper).

(v) Only if the simple calculation methods do not provide sufficient fire resistance and the support conditions do not allow flexural continuity or two-way action to be achieved, then compressive axial restraint can be used to increase the fire resistance. The following details must be applied:

- The supports must be detailed to keep the line of thrust at the supports well below the centroidal axis of the slab. Situations where the line of thrust is located close to or above the centroidal axis must be avoided (e.g.: flange mounted double tees with webs cut away).
- Top reinforcement must be placed in the slab to accommodate the negative moments which develop when restraint takes effect.
- The axial restraint stiffness of the supporting structure should be at least 50% of the axial stiffness of the heated slab.
- The slenderness ratios of the slab must not exceed the normal limits recommended by design codes, to minimize the risk of buckling under high axial restraint forces.

TENSILE MEMBRANE ACTION

The study into tensile membrane action was carried out for unrestrained two-way reinforced concrete and composite steel-concrete slabs under fire conditions. The study was conducted with experimental fire tests and 3D finite element analyses.

Background

The impetus for carrying out this study into tensile membrane action of two-way slabs was based on the increasing trend for floor systems in multi-storey buildings to be constructed from reinforced concrete slabs supported by unprotected steel beams. Fire tests at Cardington Large Building Test Facility [18, 19] and the fire in the Broadgate Development [19] in the UK have shown that the slabs can continue to support their loads after the steel beams reach very high temperatures and suffer large deflections.

Following the Cardington tests, significant amount of analytical work has been carried out by many researchers [20 - 26] to better understand the behaviour of steel framed structures in fire and tensile membrane action in composite slabs.

In the Cardington experiments, the fire tests were complex and involved a lot of different structural phenomenon. This study was carried out to analyse a smaller, isolated structure, free from interactions with the surrounding structure, in order to concentrate on the phenomenon in question. A simple hand method has been developed by Bailey [27] to predict the fire resistance of concrete slabs with tensile membrane action. However, there is no published fire resistance data to verify this method.

Experimental fire tests

Six slabs comprising three reinforced concrete flat slabs with different amounts and types of reinforcing steel and three proprietary composite steel-concrete slabs were tested. The slabs measured 3.3 m by 4.3 m and their thicknesses ranged from 90 mm to 130 mm. The slabs were simply supported on four sides above the furnace and were horizontally unrestrained. The slabs were heated on the underside with the ISO standard fire, while loaded with a uniformly distributed live load of 3.0kPa. The concrete used was siliceous aggregate concrete and had a specified compressive strength of 30MPa.

The objectives of the fire tests were to:

(i) Understand the behaviour of two-way concrete slabs at elevated temperatures, in a controlled furnace test.

(ii) Investigate the influence of tensile membrane action on the structural fire resistance of the slabs.

(iii) Verify the SAFIR finite element program for further analyses of other slab configurations.

The experimental fire tests of two-way slabs showed that:

(i) The slabs supported the applied loads for the entire duration of the fire without collapse despite suffering large deflections (Figure 5).

FIGURE 5: Extent of deformation of one of the tested slabs.

(ii) The tests illustrated the significant influence of tensile membrane action on the structural stability of the floor slabs under fire conditions, by resisting loads significantly in excess of their predicted yield line loads.

(iii) The tests showed that the amount of reinforcement and the spacing of the reinforcing bars in the slab are important for maintaining the integrity of the slabs. Slabs with light reinforcement and large bar spacings (three times the slab thickness) suffered large, full-depth cracks. Slabs with smaller bar spacings (up to two times the slab thickness) and more heavily reinforced suffered superficial cracking.

(iv) The high temperatures apparently increased the ductility of the cold-drawn reinforcing steel and enabled the steel to resist high tensile strains without rupture. The fire tests showed that when heated, the cold-drawn bottom reinforcing mesh became sufficiently ductile to permit large deflections.

(v) Under prolonged fire exposure, holes can form in the steel decking of composite slabs, due to oxidisation, potentially causing integrity failure.

Finite element analysis of two-way slabs

The SAFIR finite element program was used to model the behaviour of the tested slabs. The modelling was carried out to verify the program with the results of the fire tests, before further analysing other slab geometries and configurations.

The analyses of the slabs were carried out using concrete shell finite elements. A temperature dependent, biaxial concrete model was used in the shell element to model the 3D reinforced concrete slabs. The analysis takes into account crushing and cracking of the concrete and yielding of the reinforcing steel. To model the orthotropic behaviour of the composite slabs, 3D beam elements were used to represent the ribs and joists.

Similarly with the 2D analysis of the one-way slabs, a thermal analysis had to be carried out prior to the structural analysis to determine the temperatures in the slabs. The thermal and mechanical properties of the concrete and steel were based on the Eurocode [12, 28].

Modelling results of tested slabs

The main findings of the finite element analyses of the tested slabs are as follows:

(i) The results generally showed agreement with the experimental fire tests. Figure 6 shows the predicted deflections of one of the tested slabs after 3 hours exposure to the standard fire SAFIR.

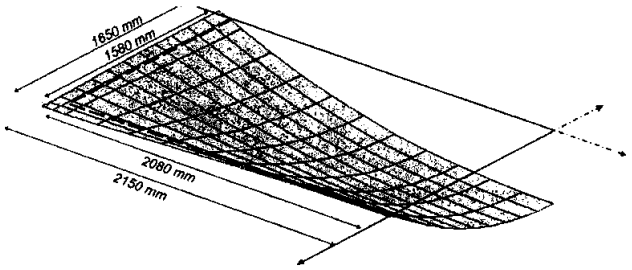

FIGURE 6: Deflected shape of the slab at 3 hours (deflections magnified 1.5 times).

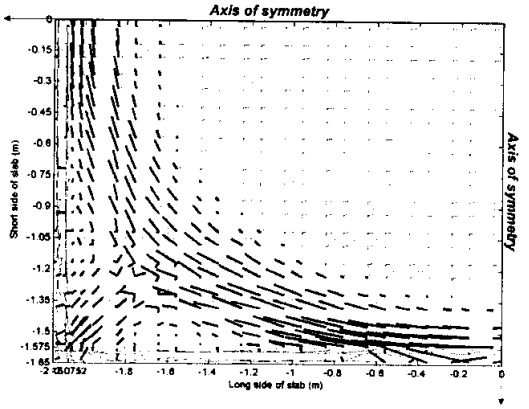

FIGURE 7: Principal tractions in one of the tested flat slabs after 3 hours fire exposure.

(ii) The deflection predictions of the slabs with light reinforcement were sensitive to the concrete tensile strength.

(iii) The analyses showed that during the initial stages of the fire, the membrane forces in the slab were very small as the loads were resisted by bending action. As the fire progressed, significant in-plane forces formed in the slab due to tensile membrane action developing

in the slab. Figure 7 shows the in-plane tractions of the deflected slab of Figure 6. The tractions comprise a tensile field in the centre (Light lines) of the slab surrounded by a compression ring at the edges (Dark lines).

(iv) The analyses showed that the behaviour of composite slabs with steel decking is difficult to predict accurately because the numerical analysis did not consider slippage and debonding of the steel decking from the concrete slab.

Modelling of slabs with different geometries and supports

In this study, the SAFIR program was used to predict the behaviour of concrete slabs of other geometries and with different types of support conditions. The purpose of this was to determine whether any of the intermediate supporting steel beams need to be fire-protected, and if so, how far apart those beams can be. Another way of posing this question is to ask how big the "fire design area" of the slab can be, compared with the "cold design area".

Figure 8 compares the midspan deflections of slabs with different sizes and aspect ratios exposed to the ISO standard fire. The analysis is based on one of the tested slabs, with 100mm thickness, 200mm^2/m of reinforcing steel and 30MPa concrete. All of the slabs are simply supported along their four edges, the supports representing fire-protected beams. The intermediate beams in the slabs are assumed to be unprotected and do not contribute to the fire behaviour of the slabs. Figure 8 shows that the ability of two-way slabs to mobilise tensile membrane action for fire resistance is dependent on their aspect ratio. As the aspect ratio of the slab increases, the fire behaviour approaches that of a one-way slab due to decreasing tensile membrane enhancement.

The analyses also showed that tensile membrane enhancement in two-way slabs cannot develop if one or more supporting beams deflect excessively. Figure 8 shows that a slab with stiff vertical supports on only three sides has substantially lower fire resistance compared with one supported on all four sides. To have good fire resistance, two-way slabs require stiff vertical beam supports on all four edges so that the slabs can deform into double curvature in order to develop tensile membrane action.

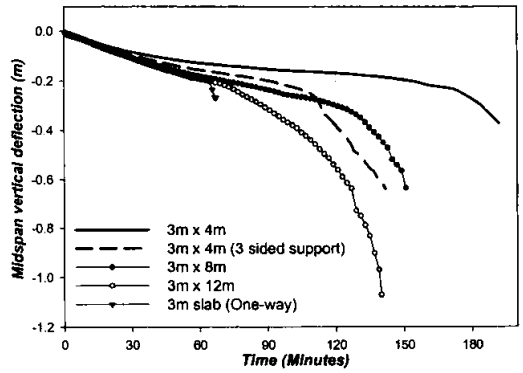

FIGURE 8: Midspan deflections of slabs with different edge supports and aspect ratios.

For a slab supported on a system of primary and secondary steel beams with widely spaced protected columns, the area of concrete slab required to be supported by tensile membrane action will grow as the fire spreads and as the number of fire-affected steel beams increases. In order to develop tensile membrane action the slab must retain some support on all four edges so that it can deform in double curvature, hence the perimeter support beams of the "fire design area" should be adequately fire-protected.

Figure 9 shows a graph of deflections versus time for a slab designed for 3×3m, as the "fire design area" grows to 9m × 9m. The SAFIR analysis showed that the size of the "fire design area" can be up to three or more times the size of the "cold design area" with the slab still having a fire resistance in excess of one hour (more than sufficient for complete burnout of most typical office occupancies). As the size of the slab increases, the fire resistance decreases and the mid-span deflections greatly increase, but tensile membrane action can be maintained provided that there is still support on all four edges.

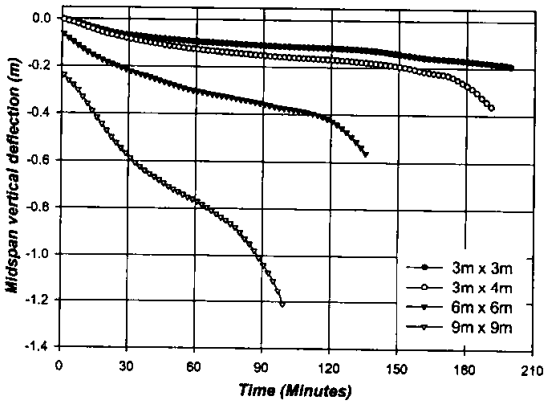

FIGURE 9: Midspan deflections of slabs with different fire design areas.

If the protected columns are more closely spaced than the "fire design area" described above, and the steel beams are all unprotected, the fire behaviour of the floor system will be different because the slab will need to behave more like a two-way flat-slab supported only on columns. This type of behaviour, observed at Cardington, is beyond the scope of this study, but a preliminary analysis shows that such slabs will have considerable fire resistance provided that they deform in double curvature, allowing them to develop tensile membrane action.

Recommendations for design and construction of two-way slabs

Recommendations for design and construction of two-way slabs, based on the experimental fire tests and finite element analyses of the slabs conducted in this study, are as follows:

(i) Two-way slabs with supports on all four edges and no axial restraint have excellent fire resistance provided there is sufficient reinforcing to develop tensile membrane action for the duration of the fire.

(ii) To mobilise tensile membrane action in two-way slabs for fire resistance, the slabs are required to deform into double curvature. The aspect ratio (L_y/L_x) of the slabs on the stiff vertical edge supports should be less than 2.5. If the slabs are supported such that they will have high aspect ratios ($L_y/L_x > 2.5$), they should be designed as one-way slabs.

(iii) Either hot-rolled reinforcing bars or cold-drawn mesh may be used as the bottom reinforcement for two-way slabs. The steel content in typical slabs should be at least 300mm^2/m and the bar spacing not greater than two times the slab thickness. The cover to the reinforcement should be based on current code recommendations.

(iv) The top layer of reinforcing in a fire-exposed slab will not reach high temperatures, so non-ductile steel such as welded wire mesh could fracture over the supports when subjected to large plastic strains as large rotations occur. Therefore, ductile reinforcing bars should be used rather than welded mesh for the top bars over the supports. This is not a strength problem if the bottom reinforcing can resist the tensile membrane action, but it could lead to large cracks and potential integrity failure of the slab near the supports.

(v) The beam-column connections must be designed with ductile connections capable of resisting high tension forces if the beams which support the slab are expected to deform into catenary mode.

CONCLUSIONS

This research project was conducted to investigate the behaviour of reinforced concrete slabs under fire conditions. The main objectives of this research were to investigate the influence of compressive axial restraint and tensile membrane action on the behaviour of reinforced concrete slabs subjected to fire conditions. The study on compressive axial restraint was performed on one-way slabs with 2D finite element analyses using the SAFIR program. The investigation on tensile membrane action was performed on simply supported, two-way slabs without horizontal axial restraint. The study was performed with experimental fire tests and 3D finite element analyses using SAFIR.

Recommendations for the design of one-way and two-way reinforced concrete slabs for fire resistance are provided in this paper.

RECOMMENDATIONS FOR FUTURE RESEARCH

The following areas should be investigated in future research projects:

(i) The effect of different slenderness ratios in fire-exposed slabs with compressive axial restraint.

(ii) 2-D finite element analyses of fire-exposed double tee and hollow-core slabs with compressive axial restraint.

(iii) The effect of 3-D actions on the fire behaviour of one-way slabs.

(iv) The behaviour of one-way and two-way slabs with unsymmetrical distributed loads or point loads.

(v) Two way flat slabs supported on columns with no beams.

ACKNOWLEDGEMENTS

The first author gratefully acknowledges the support and funding provided by the Civil Engineering Department of the University of Canterbury, BHP New Zealand Steel Limited, BRANZ (Building Research Association of New Zealand) and HERA (Heavy Engineering Research Association of New Zealand). The support of Professor Jean-Marc Franssen from the University of Liege with the use of the SAFIR program is gratefully acknowledged.

REFERENCES

1. Lim, L (2003). Membrane action in fire exposed concrete floor systems. Ph.D. thesis, University of Canterbury, New Zealand.
2. Selvaggio, S.L. and Carlson, C.C. (1963) Effect of restraint on fire resistance of prestressed concrete, American Society for Testing and Materials, STP 344, pp. 1-25. Reprinted as PCA Research Department Bulletin 164.
3. Issen, L.A., Gustaferro, A.H. and Carlson, C.C. (1970) Fire tests of concrete members; An improved method for estimating thermal restraint forces. *Fire Test Performance, ASTM, STP 464,* American Society for Testing and Materials, pp. 153-185.
4. Lin, T.D. and Abrams, M.S. (1983) 'Simulation of realistic thermal restraint during fire tests of floors and roofs'. In: *Fire Safety of Concrete Structures*. Ed: M.S. Abrams. Publication SP-80. American Concrete Institute, Detroit.
5. Anderberg, Y. and Forsen, N.E. (1982) Fire Resistance of Concrete Structures, Division of Structural Mechanics and Concrete Construction, Lund Institute of Technology, Lund, Sweden.
6. Cooke G.M.E. (1993) Results of tests on end-restrained reinforced concrete floor strips exposed to standard fires. Report prepared for the Construction Directorate of the Department of the Environment. Fire Research Station, Hertfordshire, U.K.
7. Carlson, C.C., Selvaggio, S.L. and Gustaferro, A.H. (1965) A review of studies of the effects of restraint on the fire resistance of prestressed concrete. *Proc. Symposium on Fire Resistance of Prestressed Concrete, Germany.* International Federation for Prestressing (F.I.P.) Germany. Reprinted as PCA Research Department Bulletin 206.
8. Gustaferro, A. and Martin, L.D. (1988) *Design for Fire Resistance of Precast Prestressed Concrete, Second Edition.* Prestressed Concrete Institute, Illinois, USA.
9. ASTM (1999) Standard test methods for fire tests of building construction and materials, E119-98. American Society for Testing and Materials. Philadelphia, U.S.A.
10. UL (1999). *Fire Resistance Directory*, Underwriters Laboratories Inc., USA.
11. Franssen, J.M. (2003) SAFIR: A Thermal/Structural Program Modelling Structures under Fire, Proc. NASCC 2003, A.I.S.C. Inc., Baltimore, April 2-4.
12. EC2 (1995). Eurocode 2: Design of concrete structures. ENV 1992: Part1-2: General rules-Structural fire design, European Committee for Standardization, Brussels.

13. NZCS-NZNSEE (1999) *Guidelines for the use of structural precast concrete in buildings, Second Edition.* Centre for Advanced Engineering, University of Canterbury, Christchurch, New Zealand.
14. Anderberg, Y. (1978) 'Fire-exposed hyperstatic concrete structures: An experimental and theoretical study'. In: *Analytical design of fire exposed concrete structure Bulletin 65.* Lund Institute of Technology, Lund, Sweden.
15. CRSI (1980) *Reinforced Concrete Fire Resistance.* Concrete Reinforcing Steel Institute, Chicago, USA.
16. Buchanan, A.H. (2001) *Structural Design for Fire Safety.* John Wiley & Sons, Ltd. U.K.
17. Fleischmann, C. and Buchanan, A. (2002) 'Analytical methods for determining fire resistance of concrete members'. In: *The SFPE Handbook of Fire Protection Engineering, Third Edition.* Ed: P.J. DiNenno. National Fire Protection Association, Massachusetts. pp. 4-239 to 4-256.
18. Bailey, C.G., Lennon, T. and Moore, D.B. (1999) The behaviour of full-scale steel-framed buildings subjected to compartment fires. *The Structural Engineer.* Vol. 77 No. 8. pp. 15-21.
19. Newman, G.M., Robinson, J.T. and Bailey, C.G. (2000) *Fire Safe Design: A New Approach to Multi-Story Steel-Framed Buildings.* The Steel Construction Institute, Berkshire, U.K.
20. Gillie, M., Usmani, A., Rotter, M. and O'Connor, M. (2001) Modelling of heated composite floor slabs with reference to the Cardington experiments. *Fire Safety Journal* Vol. 36. No. 8 pp 745-767.
21. Huang, Z., Burgess, I.W. and Plank, R.J. (1999) Three-dimensional modelling of two full-scale fire tests on a composite building. *Proceedings of the Institution of Civil Engineers Structures and Buildings.* Vol. 134 pp. 243-255.
22. Huang, Z., Burgess, I.W. and Plank, R.J. (2000) Non-linear modelling of three full-scale structural fire tests. *Proc. of the First International Symposium of Structures in Fire. (Copenhagen, Denmark)* pp. 53-70.
23. Huang, Z., Burgess, I.W. and Plank, R.J. (2001) Non-linear structural modelling of a fire test subject to high restraint. *Fire Safety Journal.* Vol. 36 No. 8 pp 795-814.
24. Huang, Z., Burgess, I.W. and Plank, R.J. (2004) Fire resistance of composite floors subject to compartment fires. *Journal of Constructional Steel Research.* Vol. 60 No. 2 pp 339-360.
25. Lamont, S., Usmani, A.S. and Drysdale, D.D. (2001) Fire protection of steel beams in composite framed structures. *Proc. Interflam Conference 2001 (Edinburgh, U.K.)* pp. 407-418.
26. O'Callaghan, D.J. and O'Connor, M.A. (2000) Comparison of finite element models of composite steel framed buildings behaviour in fire. *Proc. of the First International Symposium of Structures in Fire. (Copenhagen, Denmark)* pp. 41-52.
27. Bailey, C.G. (2001) Membrane action of unrestrained lightly reinforced concrete slabs at large displacements. *Engineering Structures.* Vol. 23. No. 5. pp. 470-483.
28. EC3 (1995). Eurocode 3: *Design of steel structures. ENV 1993 Part1-2: General rules-Structural fire design*, European Committee for Standardization, Brussels.

BEHAVIOUR OF STRUCTURAL SYSTEMS EXPOSED TO NATURAL FIRES CONSIDERING THE FAILURE OF SUBSTRUCTURES AND REPAIR

Dietmar HOSSER and Jochen ZEHFUSS
Institute of Building Materials, Concrete Structures and Fire Protection (iBMB)
Technical University of Braunschweig, Germany
j.zehfuss@tu-bs.de

ABSTRACT

On the basis of a given design fire, temperature-time curves of natural fires in multi-storey buildings are determined depending on the actually existing boundary conditions. The temperature-time curves of natural fires are formulated with simplified equations as so-called real fire curves and are validated using comparison calculations as well as experimental data. A fire safety design that considers the actual boundary conditions has to take into account the load-bearing and deformation behaviour of structural elements embedded in the entire structure. To activate load-bearing reserves in structural systems of multi-storey steel and composite structures, the possibility of load redistribution from fire-exposed elements to non fire-exposed elements has to be taken into account. By numeric simulations on the basis of a validated computer model it is shown, how steel and composite structural systems can be optimised to reduce the forces caused by the axial and flexural restraint in case of a fire. It is also depicted that for different fire scenarios and boundary conditions unprotected structural steel members can be used if they are embedded in an entire structure and some rules of structural detailing are observed. For structural restoration and repair after a fire building systems with prefabricated floor slabs offer advantages. Steel girders and floor slabs of a module-like structural system can be removed in the damaged area without endangering the stability of the remaining structure.

KEYWORDS: *fire safety design, design fire, multi-storey buildings, load redistribution*

INTRODUCTION

Enabling an economic and aesthetical construction, module-like steel-composite constructions offer large advantages. A common problem of those structures is the "traditional" fire safety design which often leads to an increase of cost due to the requirement of fire prevention materials that reduce the aesthetic advantages as well. Utilising the advantages of the construction, the fire safety design has to be carried out by a performance-based method which is risk-oriented and takes into account the actually existing boundary conditions. On the basis of a given design fire the realistic development of the fire is considered. On the other hand the structural system has to be optimised for activating the load-bearing reserves. Hence the ability of load redistributions in the overall structure has to be utilised.

DESIGN FIRE

The basis of a performance-based fire safety design is a realistic fire scenario which is given by a design fire. It pays respect to the relevant boundary conditions (fire load, ventilation, geometry of fire compartment). Generally the design fire is defined as a rate of heat release, which can be used as input to fire simulation models for calculating important fire effects (e. g. temperatures and mass flow). In this way the design fire can be described physically more clearly than with temperature-time-curves [1]. The rate of heat release $\dot{Q}(t)$ results to:

$$\dot{Q}(t) = \dot{m}(t) \cdot \chi \cdot H_{net} \tag{1}$$

with $\dot{m}(t)$ mass burning rate [kg/s]

t time [s]

χ combustion efficiency [-]

H_{net} net calorific value [J/kg]

For the description of the rate of heat release in the growing phase of a fire the quadratic approach (t^2-approach) is internationally accepted [2]. The maximum of the rate of heat release is determined either by the ventilation conditions or by the fire load. One distinguishes between ventilation- or fuel-controlled fires. In the case of a ventilation-controlled fire, according to EN 1991-1-2 annex E the maximum rate of heat release can be defined as:

$$\dot{Q}_v = 0.1 \cdot A_w \sqrt{h_w} \cdot \chi \cdot H_{net}, \tag{2}$$

with A_w area of ventilation openings [m^2],

h_w averaged height of ventilation openings [m].

If the fire load mainly consists of wooden furnishings (net calorific value H_{net}= 17,3 MJ/kg, combustion efficiency $\chi = 0{,}7$), (2) transfers to (3):

$$\dot{Q}_v = 1.21 \cdot A_w \sqrt{h_w} \text{ [MW]}. \tag{3}$$

In the case of a fuel-controlled fire the maximum rate of heat release can be defined as:

$$\dot{Q}_f = 0.250 \cdot A_f \,[\mathrm{MW}] \tag{4}$$

if the rate of heat release per unit floor area of wooden furnishings is assumed to be $\dot{Q}_{f,A} = 250$ kW/m² [2]. The burning area A_f [m²] is limited by the compartment area [1]. The quadratic slope of the rate of heat release turns into a constant course after achieving the maximum

$$\dot{Q}_{\max} = \mathrm{MIN}\left\{\dot{Q}_{\max,v} \; ; \; \dot{Q}_{\max,f}\right\}. \tag{5}$$

If 70% of the whole fire load is consumed, the rate of heat release decreases linearly, until the fire load is completely burnt (***Fig. 1***).

REAL FIRE CURVES

Fig. 1 illustrates the qualitative shapes of the rate of heat release and the upper layer temperature computed with CFAST [3]. Both curves can be characterised by three distinctive points at the times t_1, t_2, t_3, where the slope of the curves is changing. From the beginning of the fire until time t_1 the rate of heat release rises quadratically and the upper layer temperature increases fast. At t_1 the maximum of the rate of heat release is achieved, until t_2 it remains constant. After t_1 the upper layer temperature enhances moderately. As 70% of the fire load is consumed at t_2 the rate of heat release drops off linearly. Achieving its maximum at t_2 hence the upper layer temperature declines. At t_3 the total fire load is burnt and the rate of heat release decreases to 0. At this time the upper layer temperature-time curve bends and it declines more slowly than before (Fig. 1). Considering the lapse of the rate of heat release, the times t_1, t_2, t_3 can be determined. In order to be able to describe the run of the upper layer temperature-time-curve completely, the associated temperatures T_1, T_2 and T_3 have to be considered.

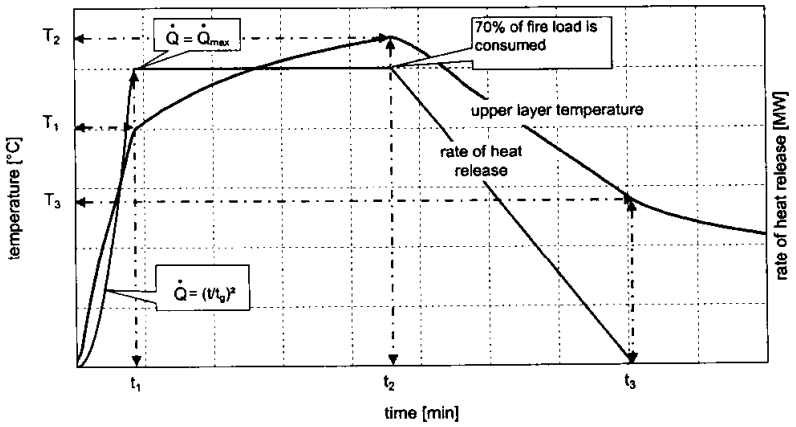

Fig. 1 Qualitative run of the rate of heat release and the upper layer temperature

For the temperature development of fuel-controlled fires the released heat of the fire source is the outstanding influencing factor, apart from the heat loss out of the fire compartment openings and enclosures [4]. Performing a regression analysis for the upper layer temperatures T_1, T_2 and T_3 (according to the definition in Fig. 1) of fuel-controlled fires the following functions can be determined for a fire load density of q = 1300 MJ/m² [5]:

$T_1 = 24000\,k + 20$ [°C] for $k \leq 0{,}04$ and $T_1 = 980$ °C for $k > 0{,}04$ (6)

$T_2 = 33000\,k + 20$ [°C] for $k \leq 0{,}04$ and $T_2 = 1340$ °C for $k > 0{,}04$ (7)

$T_3 = 16000\,k + 20$ [°C] for $k \leq 0{,}04$ and $T_3 = 660$ °C for $k > 0{,}04$ (8)

with

$$k = \left(\frac{\dot{Q}^2}{A_w \sqrt{h_w} \cdot A_T \cdot b} \right)^{1/3} \quad (9)$$

whereby $\dot{Q}$ [MW] is the maximum of the rate of heat release, A_w [m²] the area of the ventilation openings, h_w [m] the average height of the ventilation openings, A_T [m²] the enclosure surface without openings and b [J/(m²s^{0,5}K)] the average thermal property of the enclosure.

For the temperature development of ventilation-controlled fires the opening factor O is predominant, apart from the thermal property of the enclosure [6]. A regression analysis for the upper layer temperatures T_1, T_2 and T_3 of ventilation-controlled fires provides the following functions for a fire load density of q = 1300 MJ/m² [5]:

$T_1 = -8{,}75 \cdot 1/O - 0{,}1\,b + 1175$ [°C] (10)

$T_2 = (0{,}004\,b - 17) \cdot 1/O - 0{,}4\,b + 2175$ [°C] ≤ 1340 °C (11)

$T_3 = -5{,}0 \cdot 1/O - 0{,}16\,b + 1060$ [°C] (12)

with: $O = A_w \sqrt{h_w} / A_t$ and A_t : Enclosure surface including openings [m²].

For a complete mathematical description of the real fire curves, apart from the knowledge of the times t_1, t_2, t_3 and the associated temperatures T_1, T_2, T_3, the functional run between these points has to be ascertained. The run of the curve can be described within three sections (Fig. 2). In section 1 ($0 \leq t \leq t_1$), in the fire growth phase, the temperature rises quadratically:

$T = \frac{(T_1 - T_0)}{t_1^2} \cdot t^2 + T_0$ with t, t_1 [min] and T, T_0, T_1 [°C] (13)

The more moderate slope within section 2 ($t_1 < t \leq t_2$) can be described with a root function:

$T = (T_2 - T_1) \cdot \sqrt{(t - t_1)/(t_2 - t_1)} + T_1$ with t, t_1, t_2 [min] and T, T_1, T_2 [°C] (14)

likewise the decrease of temperature within section 3 ($t > t_2$):

$$T = (T_3 - T_2) \cdot \sqrt{(t - t_2)/(t_3 - t_2)} + T_2 \text{ with } t,\ t_2, t_3 \text{ [min] and } T,\ T_2,\ T_3 \text{ [°C]}. \quad (15)$$

On the basis of the real fire curve for q = 1300 MJ/m², real fire curves for any fire load densities $q_x \leq$1300 MJ/m² can be determined easily (***Fig. 2*** with q_x = 500 MJ/m² for instance). The time $t_{2,x}$, where the maximum temperature $T_{2,x}$ appears, depends on the fire load and can be ascertained directly from the approach of the rate of heat release. Inserting in Eq. (14) with $t = t_{2,x}$ the associated temperature $T_{2,x}$ can be calculated. The temperatures $T_{3,x}$ at $t_{3,x}$ of different fire load densities q_x run a logarithmic function with ($t = 0/T_0$) und (t_3/T_3):

$$T_{3,x} = T_3 / (\log_{10}(t_3 + 1)) \cdot \log_{10}(t + 1). \quad (16)$$

The decay period of the real fire curve can be obtained inserting in Eq. (16):

$$T = (T_{3,x} - T_{2,x}) \cdot \sqrt{(t - t_{2,x})/(t_{3,x} - t_{2,x})} + T_{2,x}. \quad (17)$$

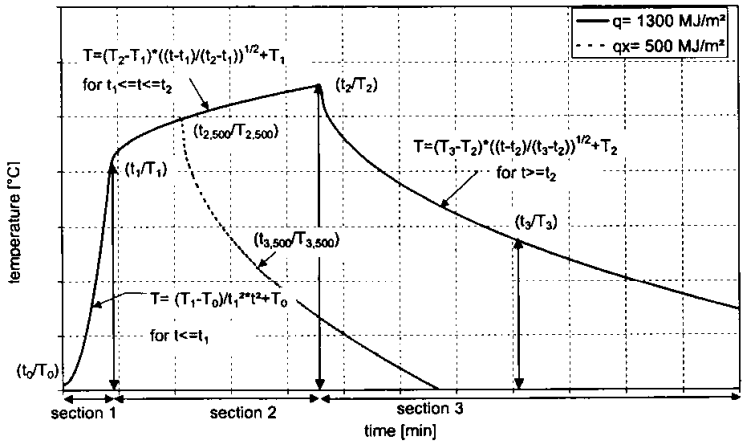

Fig. 2 Mathematical description of the real fire curves in 3 sections

The real fire curves provide an easy to handle method for the structural engineer in practice who is not familiar with the use of heat balance models taking into account the thermal action of a natural fire for the design of multi-storey residential and office buildings. The real fire curves are validated in three steps by means of a wide range of comparative calculations with different zone models and CFD models, comparative simulations of published fire tests of different fire research stations and performing a natural room fire test with ordinary office room furnishings [1, 5]. The validation reveals that the real fire curves fit well to the recorded test temperature-time curves and are able to grasp the process of temperature not less than zone models.

The parametric temperature-time curves published in EN 1991-1-2 annex A in some cases provide an unrealistic temperature increase and decrease. For fuel-controlled fires in residential and office buildings with a medium fire growth rate the maximum temperature occurs uniformly after 20 minutes so there is no temporal connection with the rate of heat release of EN 1991-1-2 annex E. ***Fig. 3*** shows the parametric temperature-time curve according to EN 1991-1-2

compared to the recorded average temperature-time curve of the $NFSC_2$ fire test No. 2 at BRE [7], governed by fuel-controlled conditions. The comparison illustrates the deficiencies of the parametric temperature-time curves respecting the maximum temperature, temperature increase and decrease. More obvious is the discrepancy between the temporal course of the parametric temperature-time curve and rate of heat release. The rate of heat release achieves its maximum after 30 minutes and declines after 43 minutes. The run of the parametric temperature-time curve and rate of heat release neither match with each other nor are they temporally congruent.

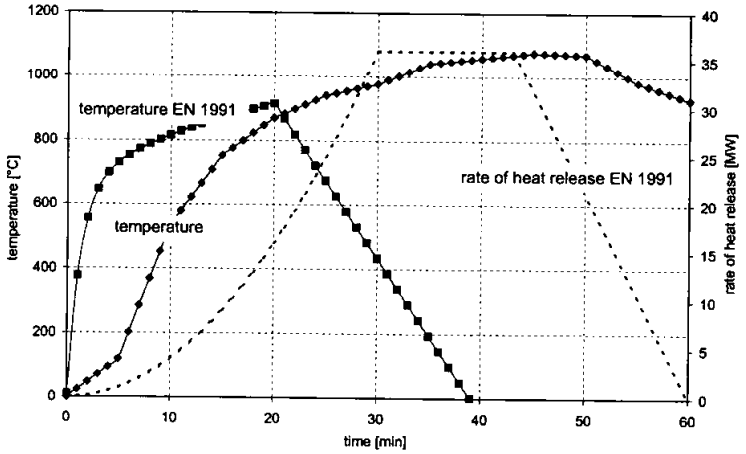

Fig. 3 Temperature-time curve and rate of heat release according to EN 1991-1-2

OPTIMISED MODULAR SYSTEM

Multi-storey office buildings are often constructed of so-called modular systems. Ensuring an easy and fast erection girders and columns of those systems are pin-jointed. The steel framework contains columns which are connected to the primary beams in the principal structural direction. In transverse direction secondary girders, over which the floor slab is spanning in the principal structural direction, are connected to the columns and primary girders. The secondary girders are tied positively by shear connectors to the floor slabs consisting of prefabricated reinforced concrete elements. Thus they can be designed as a steel-composite girder with an effective width which is maximum the distance between the secondary girders. The secondary girders are pin-jointed to the columns resp. primary girders. The girder-to-column joints consists of fin plate connections.

CONNECTIONS

The advantage of the fin plate connection lies in the fast an easy assembly. Due to the minor section modulus of the welding connection between fin plate and column, nearly no moment is transferred by the connection. In case of a fire the bolted connection between girder and fin plate can be stressed by large shear forces which can lead to failure of the bolts or the plate. An optimisation of the fin plate connection can be attained by the arrangement of bolts in so-called

slotted holes (***Fig. 4***). Due to the connection of the slotted holes a normal force hinge is formed. During a fire the expansion of the girder causes a displacement of the bolts in the slotted holes, whereby the friction is overcome. In the cooling phase due to the shrinking of the girder the bolts can be displaced in the contrary direction and so high tensile forces in the connection are avoided.

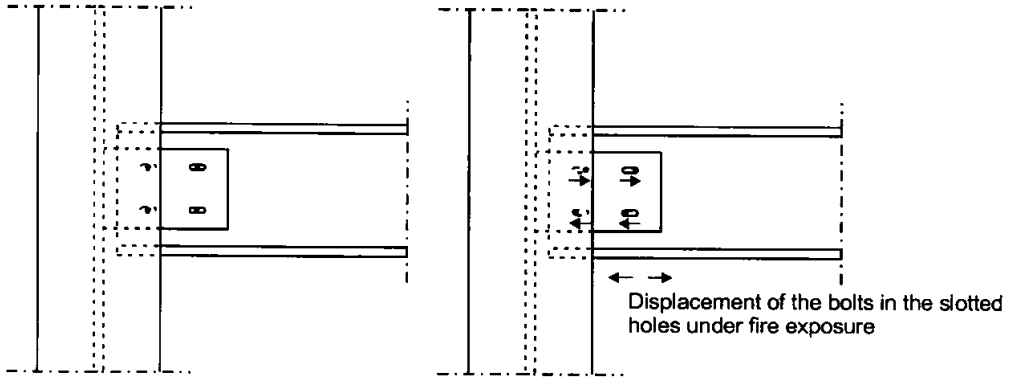

Fig. 4 Fin plate connection with bolts in slotted holes at normal temperature (left) and in case of a fire (right)

Fin plate connections with slotted holes enable a movement of the bolts in the hole after overcoming the frictional forces which are caused by the pre-stressing of the bolts. The enhancing deformation in vertical direction of the girder at midspan leads to deformations of the fin plate (***Fig. 4***). Hence the bolts in the bottom holes are displaced in external and the bolts in the top holes in internal direction. Thus the deformation of the connection with slotted holes is similar to a pinned connection whereas the fin plate without slotted holes conducts to higher axial deformations and tends to buckling.

The results of the numerical simulations reveal that the fin plate connection with slotted holes have the most favourable properties in case of a fire because of the reduction of the restraint forces and horizontal deformations. During the erection of the structure the horizontal instability has to be considered. This instability originates in the slotted holes which act as a normal force hinge.

BOUNDARY CONDITIONS

In [5] a FE-model is presented and validated with which the load and deformation behaviour of multi-storey steel structures can be simulated using the FE code ANSYS [8] and taking into account the constructive design of modular systems. *Fig. 5* gives an overview of the structural system of the steel framework consisting of columns, primary girders in the letter axes and secondary girders in the number axes. The floor slab of prefabricated reinforced concrete elements which is tied positively to the girders spans above the secondary girders. The steel sections of the secondary girders consist of IPE 220 - profiles (yield stress 355 N/mm²). The

ambient concrete strength of the floor slabs (h= 12 cm) is assumed to 30 N/mm², the yield stress of the reinforcing web is 500 N/mm².

The primary girders in axes C and F consist of IPE 300 - profiles (yield stress 355 N/mm²), in axes 1, 4 and 7 they are connected to the internal columns (HEB 260, yield stress 355 N/mm²). In the external axes A and H the loads of the secondary girders are transferred to the external columns which consist of HEB 140 - profiles (yield stress 355 N/mm²). The connections of the secondary girders to columns and primary girders are formed by fin plates with slotted holes. The connections of the primary girders to the columns are made by end-plate connections. The structure is braced by wind posts.

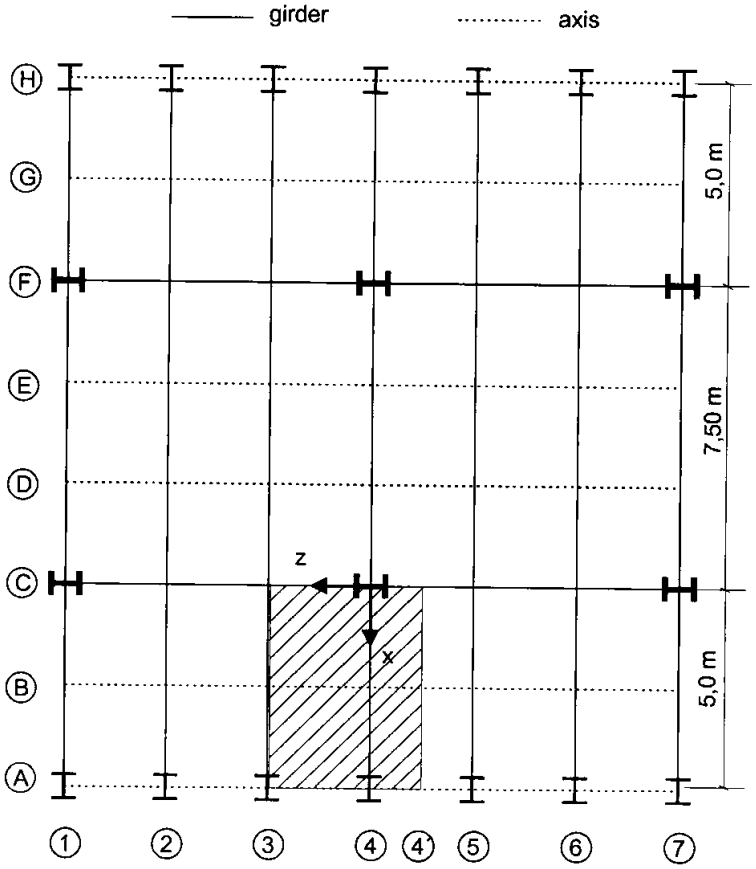

Fig. 5 Plan view with fire scenario

Due to the results of the Cardington experiments [9] columns, primary girders and the external secondary girder in axis 1 as well as all the connections are protected for a fire resistance time of 60 minutes. The secondary girders are unprotected. A distributed loading of 7.5 kN/m², corresponding to the existing dead and live load is applied to the slab. By numerical simulation

of different fire scenarios (location and spread of the fire) the load and deformation behaviour is investigated systematically. In the following the simulation-results of the fire scenario "office room" are presented [5]. The office room is located between the axes A and C and is separated to the adjacent rooms by partition walls in axis 3 and in axis 4' (*Fig. 5*).

FIRE SAFETY DESIGN

The temperature-time curve of the natural fire is computed by a real fire curve with a fire load density of $q_x = 511$ MJ/m² and a ventilation opening with $A_w = 5.0$ m² and $h_w = 2.0$ m². The average thermal property of the enclosure is assumed to $b = 2000\ \mathrm{J/(m \cdot \sqrt{s} \cdot K)}$, the floor area of the room measures $A_f = 18.75$ m². The partition walls have a sufficient fire resistance, so that the fire is limited to the office room. An intervention of the fire brigade is not taken into account. The steel temperatures increase to 900 °C after 28 minutes before decreasing. On the opposite side of the slab the maximum temperature is 67 °C after 60 minutes at the end of the simulation (***Fig. 6***).

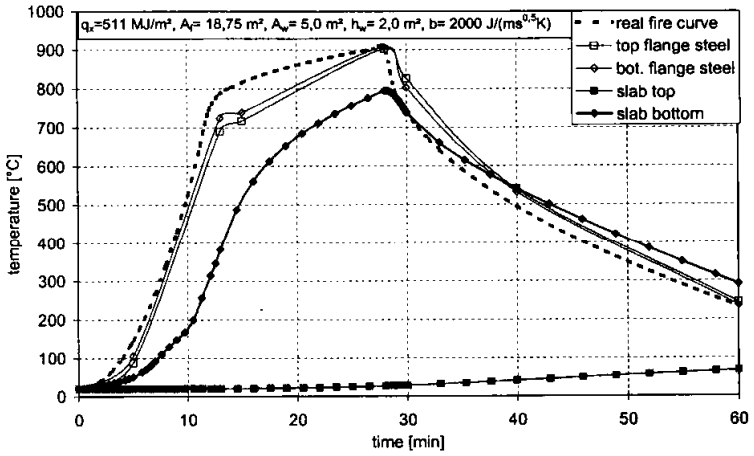

Fig. 6 Temperature-time curve of the real fire, the fire-exposed steel section and the floor slab

STRESSES AND INTERNAL FORCES

Fig. 7 depicts the stress in the bottom and top flange of the fire-exposed girders in axis 3 and 4 at midspan. The development of the stress during the heating phase of the steel section can be marked by three characteristic points (P1, P2, P3).

At P1 (appr. after 12 min) the stress in the bottom flange at midspan achieves the proportional limit of compression and the cross-section starts yielding.

At P2 (appr. after 21 min) the bottom flange at midspan is in tension again.

At P3 (appr. after 27 min) the stress in the bottom flange at midspan exceeds the proportional limit of tension and the cross-section starts yielding.

In the following decay phase due to the shrinkage in the steel section high tensile stresses occur. They are higher in the top flange than in the bottom flange because of the hotter slab which constrains the shrinkage of the top flange. For the simulation of the decay phase the same material properties are used as for the heating phase. Thus the computed results in the decay phase can only be interpreted qualitatively because the material properties of concrete in particular are not completely reversible [10].

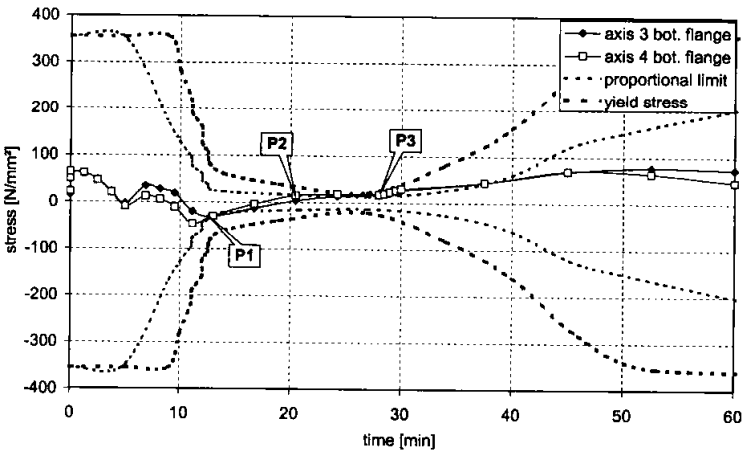

Fig. 7 **Stress in the bottom flange of the fire-exposed secondary girders in axis 3/A-C and 4/A-C at midspan**

Fig. 8 and ***Fig. 9*** illustrate the development of the internal forces at midspan of the fire-exposed secondary girders in axis 3/A-C and 4/A-C as well as the adjacent secondary girders in axis 2/A-C and 5/A-C. Due to the restraint of the cold surrounding structure substantial axial forces and moments of restraint occur which achieve its maximum after 12 minutes (P1). After 28th min the pure steel sections of the fire-exposed secondary girders nearly cannot sustain any loads so that the slab has to carry the entire load. Due to load redistribution to the adjacent secondary girders the moments at midspan increase twice of the moments at normal temperature. As a result of the horizontal deformation in external direction, reactive tensile forces in the adjacent secondary girders are activated. High tensile forces occur because of the endeavour of shrinkage during the decay phase in the steel section of the secondary girders in axis 3 and 4 (***Fig. 9***).

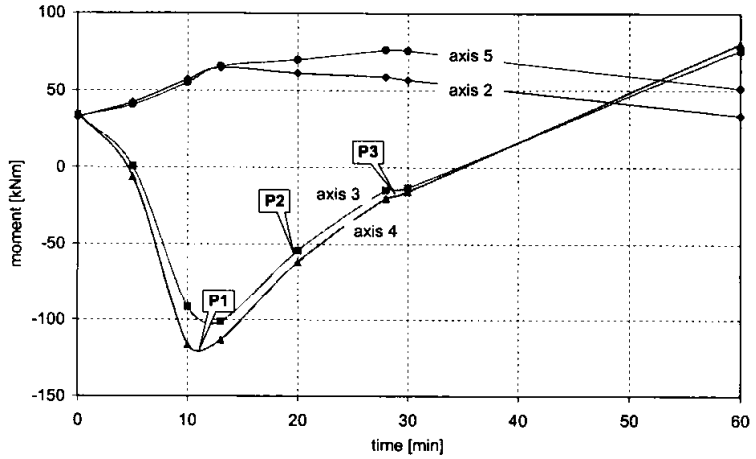

Fig. 8 Moment at midspan in the composite section of the secondary girders in axis 2/A-C till 5/A-C

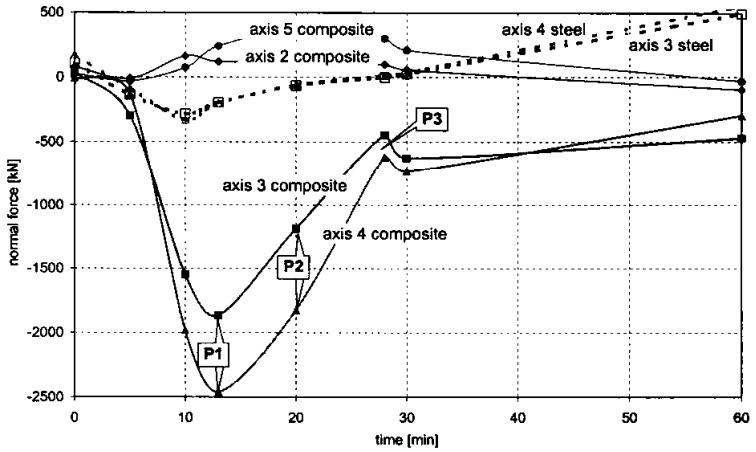

Fig. 9 Normal forces at midspan of secondary girders in the composite section in axis 2/A-C till 5/A-C and pure steel section axis 3/A-C and 4/A-C

DEFORMATIONS

In ***Fig. 10*** the vertical deformation of the secondary girders in axis 1/A-C till 7/A-C is depicted. The numerical simulation shows that assuming a realistic fire in an office room the secondary girders can be performed without encasement of the steel section. The vertical deformation remains with $u_y = 115$ mm obviously less than the critical deformation of $u_{crit} = 1 / 20 = 250$ mm [11]. The vertical deformation of the adjacent secondary girders in axis 2 and 5 increases only a little, whereas the deformation in axis 2 is slightly bigger because of the weaker system in the edge of the structure. The vertical deformation of the secondary girders in axis 6 and 7 is not influenced by the examined fire in the office room.

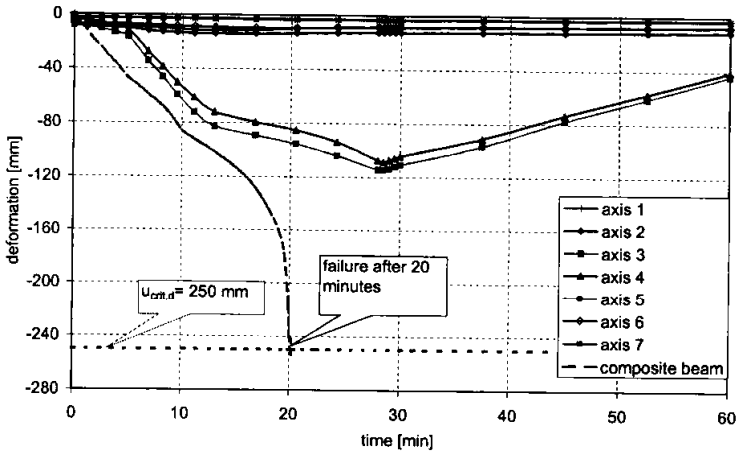

Fig. 10 Comparison between the vertical deformation of the secondary girders in an overall structure exposed to a localised real fire and a composite beam exposed to ISO 834 fire

EVALUATION OF THE RESULTS

To demonstrate the advantages of an exact fire safety design, which considers a realistic design fire and load redistributions, for comparison purpose the load and deformation behaviour of a statically determinate composite beam exposed to standard fire (ISO 834) is simulated. The composite beam fails after 20 minutes by achieving the critical deformation of $u_{crit} = 250$ mm and passing the critical deformation velocity defined by the Ryan-Robertson criteria (***Fig. 10***). This example shows that a fire safety design that assumes a standard fire (ISO 834) and considers single components by neglecting the ability of load redistribution conducts a crude underestimation of the fire resistance. This becomes obvious when compared to a realistic simulation of a girder embedded in the overall structure which is exposed to a real fire. Comparison calculations have shown that, contrary to the standard fire design, a reduction of fire protection materials of columns is feasible when carrying out a risk-oriented fire safety design as described in this paper [5].

REPAIR

When common structural steels were heated up to temperatures around 700 °C-750 °C they maintain their original material properties after cooling. Especially for elevated temperatures after the cooling hardening and embrittlement of the steel has to be taken into account as well as large plastic deformations which occur due to the high thermal exposures. The structural system presented here offers big advantages in case of a fire damage. The girders are designed as single-span girders with bolted connections. The floor slabs consist of prefabricated reinforced concrete elements. The joints between the elements are cast by mortar providing a continuous slab. The deformed steel girders can be simply disconnected by loosing the bolted connections. In the region where spalling occurred and where the concrete is damaged by elevated temperatures so that there is a risk for corrosion of the reinforcement the slabs will be rebuilt.

Due to the module-like structure the secondary girders and floor slabs in the damaged area can be removed without endangering the stability of the remaining structure. The stiffening of the remaining structure has to be ensured and in case of need it has to be maintained by temporal measures as bracings for instance. The damaged components can be sawed if required and removed out of the building through the windows which are usually damaged in case of a fire anyway. The internal columns only have a slight deformation due to their encasement and the restraint of the surrounding structure so that usually there is no need of restoration. In case of a localised fire in particular it has to be checked if the external columns have suffered plastic deformations. Hence they have to be replaced or enforced by additional plates, subsequently encasement with concrete (converting in a composite column) or even by load transfer to adjacent columns over cross members.

CONCLUSION

The ability of a girder to take over the loads of girders which elude theirs is only ensured when the load taking girder is not heated itself. The heated girders suffer a reduction of stiffness so that they carry fewer loads. Consequently the load carrying girder has to be outside the room from where the fire occurs. That requires a local limitation of the fire. Otherwise the girder has to be protected by e. g. encasements or intumescent coatings. The local limitation of a fire in a compartment of a multi-storey building is possible by light partition walls which prevent an unresisted fire spread. Comparing to ISO 834 standard fire during a natural fire unprotected steel components are usually heated to critical temperatures with slight retardation of a few minutes. The advantage of considering a realistic development of the fire for unprotected steel components results from the successive fire spread and from the break with the scenario of a fully developed fire in the entire compartment resp. storey. An appropriate utilisation of the reserves of the structural system requires adequate construction of the connections, the capability of the floor slab for load redistribution as well as the limitation of the fire in the compartment. Building systems with prefabricated floor slabs offer advantages for structural repair and restoration after a fire. Steel girders and floor slabs of a module-like structural system can be removed in the damaged area without endangering the stability of the remaining structure.

REFERENCES

[1] Hosser D., Zehfuß J., *Fire Safety Design of Multi-Storey Buildings for Natural Fires,* ISFSS 2003, International Symposium on Fire Safety of Steel Structures, Cologne, 11.-12. September 2003.

[2] Schleich J. B. et al., *Competitive Steel Buildings through Natural Fire Safety Concept* : Draft Final Report : CEC Agreement 7210-SA/125, 1999.

[3] Portier R. W., Reneke P. A., Jones W. W., Peacock R. D.: *A User's Guide for CFAST,* Version 1.6. NISTR4985, National Institute of Standards and Technology. Building and Fire Research Laboratory, Gaithersburg, Maryland, USA, 1992.

[4] McCaffrey B. J., Quintierre J. G., Harkleroad M. F., *Estimating room fire temperatures and the likelihood of flashover using fire test data correlations,* Fire Technology 17 (1981) 98-119.

[5] Zehfuß J., *Risikogerechte Bemessung von Tragsystemen mehrgeschossiger Gebäude in Stahlbauweise für natürliche Brandbeanspruchung*, dem Fachbereich Bauingenieurwesen der TU Braunschweig eingereichte Dissertation, 2004.

[6] Law M., *A basis for the design of fire protection of building structures,* The Structural Engineer 61 (1983) 25-33.

[7] Schleich J. B. et al.: *Natural Fire Safety Concept Full Scale Tests, Implementation in the Eurocodes and Development of an userfriendly design tool.* Technical report No. 6 Period from 01.01.2000 - 30.06.2000. CEC Agreement 7210-PA/PB/PC/PD/PE/PF/PR-060. Esch / Alzette, 2000.

[8] ANSYS Rev. 7.1. Swanson Analysis Systems, Inc., Houston, USA. 2003.

[9] Bailey C et al., *The Behaviour Of Multi-Storey Steel Framed Buildings In Fire,* A European Joint Resesearch Programme. Swinden: Technology Centre, 1998.

[10] Diederichs U. et al., *Hochtemperaturverhalten von Festbeton.* Sonderforschungsbereich 148 Brandverhalten von Bauteilen, Teilprojekt B3, Arbeitsbericht 1984-1986, Teil II. Braunschweig: Technische Universität, 1987.

[11] Twilt L., *Structural Fire Safety Design of Multi Storey Framed Buildings under Natural Fires.* ISFSS 2003, International Symposium on Fire Safety of Steel Structures, Cologne, 11.- 12. September 2003.

NUMERICAL AND ANALYTICAL STUDIES OF JOINT COMPONENT BEHAVIOUR IN FIRE

Florian M. BLOCK[1], Ian W. BURGESS and J. Buick DAVISON

University of Sheffield, Mappin Street, Sheffield S1 3JD, United Kingdom
([1]cip02fmb@sheffield.ac.uk)

ABSTRACT

Full-scale fire tests have clearly shown that joints in composite steel-frame buildings have a considerable effect on the survival time of the structure, due to their ability to transfer forces from hot parts of the structure to cooler zones. Realistic modelling of joints in global analysis could be of great importance in structural fire design calculations, which can either be used to give confidence about safety margins or to help to reduce the cost of fire protection strategies. A versatile approach for predicting the high temperature behaviour of joints is the "Component Method", in which a joint is considered as an assembly of a number of individual basic components, allowing a large number of possible variables in a beam-to-column joint to be considered simultaneously. This method provides a practical analytical approach to joint modelling under the simultaneous effects of loading, thermal degradation of materials and forces due to restraint of thermal expansion, all of which occur concurrently in a building fire. This paper describes the main findings from an ongoing study of the column web compression zone in fire, including the effect of superstructure loading. A range of column sections has been analysed at different temperatures and axial load ratios under transverse loading using *ANSYS*. From this study a temperature-dependent reduction factor for the transverse resistance of the column web and a simplified analytical approach have been developed to predict the force-displacement behaviour of the compression zone. The results have been compared with high temperature experiments and generally good correlation has been found. The test setup for a further series of bi-axial high temperature compression experiments is described.

KEYWORDS: *Structural fire engineering, steel joints, component method, compression zone, axial load, high temperature experiments*

INTRODUCTION

In the past 20 years considerable progress has been made in the parallel research fields of the behaviour of semi-rigid steelwork connections and structural fire engineering of steel-framed buildings. Bringing these themes together it should be possible to develop safe and economic design methods for the fire-resistance of steel frames, using the semi-rigid nature of their connections in fire. Because of the large number of possible variables in the detailed design of a semi-rigid beam-to-column connection, a versatile approach for calculating the rotational stiffness and load capacity of connections was developed in the European research project COST Action C1, and its results have been introduced into the draft Eurocode EC3 Part 1.8 [1]. The original feature of this "Component Method" is to consider any joint as a set of individual basic components. In the particular case of Fig. 1, which illustrates an external beam-to-column joint using an extended end-plate connection subject to moment, the joint is divided into the three major zones (tension, shear and compression), and then each zone is divided into the relevant components.

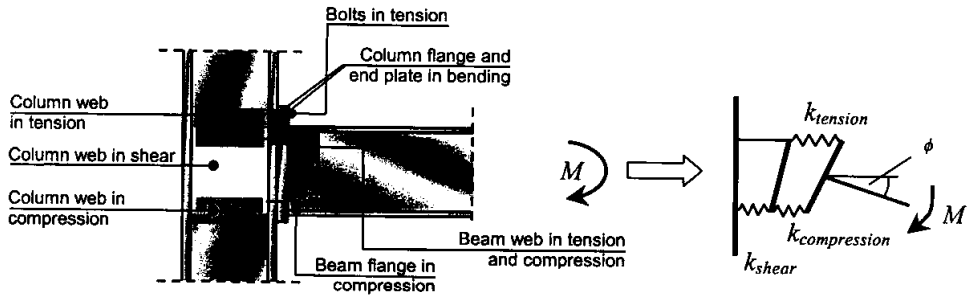

FIGURE 1 : Components of a beam-to-column joint and a simple spring model (EC3)

For each component the stiffness and maximum load is computed and assembled to form a spring model, which gives the rotational behaviour of the whole connection. Recent research [2] has shown that the compression zone in the column web is the critical component from the three zones in the connection if rotational capacity is needed, due to its limited ductility. In composite connections this zone becomes more critical because of the stronger tension zone produced by continuing slab reinforcement.

In a building fire the compression zone becomes even more critical because of restraint to the thermal expansion of the steel beams, which causes large compressive forces in the column web. Full-scale fire tests and accidental fires have clearly shown that joints have a considerable effect on the survival time of the structure because they may occur at interfaces at which forces from a hot part of the structure react against cooler zones. Considering this, realistic modelling of joints in global analysis could be of great importance in structural fire design calculations, which can either be used to give confidence about safety margins or to help to reduce the cost of fire protection strategies.

EXISTING DESIGN APPROACHES FOR THE COMPRESSION ZONE

This paper concentrates on the compression zone in the column web. To find the resistance of the compression zone at elevated temperatures, it is logical to use a proven approach for ambient

temperatures and to apply the well-established strength reduction factors adopted in EC3 Part 1.2 [3] to it to simulate fire conditions. In order to find the most accurate equation for the ultimate load at ambient temperature, different design approaches have been compared with the results of 64 tests on the compression zone in column webs of European and British rolled sections conducted by Aribert [4], Spyrou [5] and Kühnemund [2]. Most of the design approaches are conservative and give erratic correlation with the ultimate loads found in the experiments. The majority of the reported tests were conducted with two opposed transverse loads introduced through the flanges, but the co-existent axial force present in a real column has been neglected. Only Kühnemund considered the influence of the axial force in the column. A statistical comparison of the approaches has been conducted by the author [6] and it was found that the approach of Lagerqvist and Johansson [7] yielded the most accurate results with a reasonable margin of safety. This approach was used to predict the opposed patch-load tests at elevated temperatures conducted at the University of Sheffield by Spyrou [5] and good agreement was found.

In order to describe joint behaviour realistically a full force-displacement curve for each component is needed, therefore an empirical equation for the displacement at the peak load of the compression zone has been developed based on a parametric study of finite element models and test results. To describe the path up to the peak load the classical Ramberg-Osgood equation was modified. An example of the correlation between the analytical model and high-temperature test results is shown in Fig. 2 below.

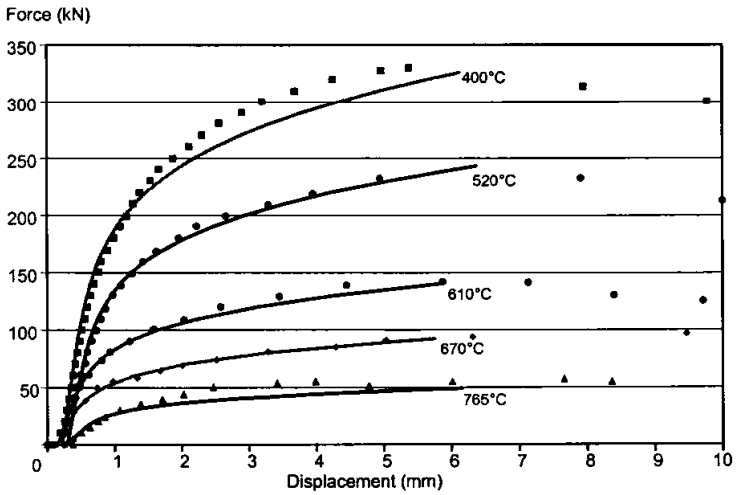

FIGURE 2 : F-δ curves of a UC 203x203x46 from tests and the new approach

From Fig. 2 it can be seen that the new approach predicts the test results very accurately. Similar good correlation was found in other experiments. The displacement at ultimate load is predicted conservatively at very high temperatures. However, the analytical model does not at present consider the influence of axial load in the column, and the current work aims to predict this influence at elevated temperatures.

THE INFLUENCE OF AXIAL LOADING ON THE COMPRESSION ZONE

Experimental research projects at different European research centres on full joint assemblies and single components have shown that the ductility as well as the ultimate resistance force of the compression zone is reduced by the presence of axial-stress in the column. Probably the first attempt to quantify the effects was made by Zoetemeijer [8] in 1975. Together with an effective-width approach for the yield load of the compression zone under opposed patch loading he developed from tests a transverse resistance reduction factor k_{wc} for cases where the longitudinal stress in the column web is larger than 50% of its yield stress. The factor k_{wc} can be calculated from

$$k_{wc} = 1.25 - 0.5\frac{\sigma_{com,Ed}}{f_{y,wc}} \tag{1}$$

where $\sigma_{com,Ed}$ is the longitudinal stress in the column web and $f_{y,wc}$ is the yield stress of the column web. This equation has been adopted in EC3 Part 1.8 and is calibrated for the effective width approach. Ahmed and Nethercot [9] applied the von Mises yield theory to the problem and concluded that no reduction factor is needed for bi-axial compression in the column web. Bailey and Moore [10] differentiated between yielding and buckling failure modes, and used the von Mises yield theory with an imperfection factor and elastic stability equations respectively to develop reduction factors for the maximum capacity of the column web. The reduction factor for yielding failure is given in Table 1, in which σ_N is the normal stress in the web and f_y the yield stress of the web.

σ_N / f_y	$k_{wc,yield}$
≤0.7	1.0
0.8	0.95
0.9	0.85
1.0	0.7

Table 1 : Reduction factor according to Bailey and Moore for yielding mode.

For buckling problems they recommend the use of

$$k_{wc,buck} = \left(1 - \frac{F_{axial}}{F_{cr(axial)}}\right) \tag{2}$$

where F_{axial} represents the axial force in the column and $F_{cr(axial)}$ its load carrying capacity. Kühnemund [2] used a different reduction factor to account for the effects of axial stresses. This factor had first been derived by Djubek and Skaloud [11] in the context of reduction of the transverse load capacity due to bending stresses in plate girders as

$$k_N = \sqrt{1 - \left(\frac{\sigma_N}{f_y}\right)^2} \tag{3}$$

These three equations are shown in Fig. 3 below.

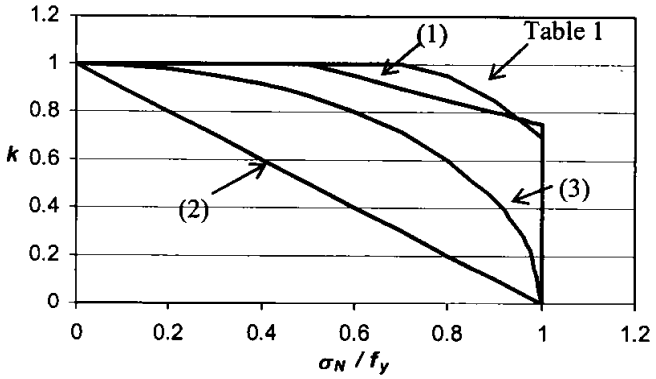

FIGURE 3 : Axial load reduction factors

FINITE ELEMENT STUDY

In order to investigate whether one of the existing reduction factors can be used to account for the effect of axial stress in the column at elevated temperatures some finite element studies have been conducted on three different British Universal Column (UC) sections, of sizes UC152x152x37, UC203x203x46 and UC305x305x167. A range of temperatures from 20°C to 650°C, and axial stress levels from 0% to 80% of the yield stress at the relevant temperatures, have been investigated. The sections have been chosen to cover a range of web slenderness, with d/t values from 22.3 to 10.4. A mixed 2D - 3D shell model was used, in which the flanges of the column section were very thick shell elements in-line with the web, so it was possible to model the spread of stress through the flanges into the web, using shell elements to model the stability and out-of-plane bending effects in the web.

In contrast to a model employing solid elements, the chosen way of modelling is very economic in terms of computing time and hard disk space, because in a solid model the thickness of the web needs to be divided into a large number of elements to enable buckling to be modelled adequately. This was shown by Tryland *et al.* [12]; the stress distribution in the web of the hybrid model was compared with a solid element model and little difference could be found. Rolled sections are never perfectly straight and therefore an imperfection in the web (according to the first eigenvalue shape) has been introduced as

$$y = \sin\left(\frac{n_1 \pi}{l} x\right) \sin\left(\frac{n_2 \pi}{h} z\right) \frac{d}{500} \qquad (4)$$

where n_1 and n_2 are the half-waves in the x and z directions respectively; h and l are the distance between the root radii and the length of the model. A picture of a typical model is shown in Fig. 4, in which the amplitude of the imperfection is scaled by a factor of 10 to make the shape more visible. The thicknesses of shell elements are shown and the root radius approximation can be seen.

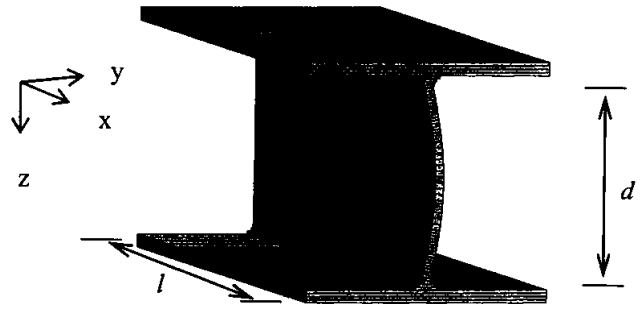

FIGURE 4 : Typical mesh and imperfection of the compression zone

In the cases where axial load is included it is introduced at the end of the section, and the boundary at the centre of the transverse load patch has restraint conditions appropriate to an axis of symmetry. To guarantee a uniform distribution of the axial load across the section the nodes on which the forces are applied are coupled in the loading direction. The material used in the models is S275 steel with a Young's modulus of 205000 N/mm^2, a yield stress of 275 N/mm^2 and an ultimate strength of 455 N/mm^2. To include the effect of elevated temperature in the analysis, a uniform temperature distribution through the cross-section has been assumed and the stress-strain curve for steel according to the recommendations in EC3 Part 1.2 has been used.
At ambient temperature the model for the stress-strain curve including strain hardening published by Zheng *et al.* [13] has been used. The tangent modulus of the strain hardening part of the curve can be expressed as

$$E' = E_{st} \exp\left(-\xi \frac{\varepsilon - \varepsilon_{st}}{\varepsilon_y} \right) \tag{5}$$

where E is the elastic modulus; ε_y is the yield strain; ε_{st} is the strain at the onset of strain hardening, taken as $10\varepsilon_y$; E_{st} is the initial strain hardening modulus taken as $E/40$ and E' is the assumed strain hardening modulus. The factor ξ is calibrated to reach the ultimate stress at a strain of 20%. The analysis is divided into two steps: firstly axial loading of the specimen, and secondly the application of transverse load until the peak load is reached and stability failure of the web occurs, leading to post-buckling behaviour. This last part of the behaviour is important when large rotations of the beam ends are expected, as tends to happen in fire conditions.

A comparison with experimental results [5] at ambient and elevate temperatures for transverse loading only and the finite element model described above shows a good correlation as illustrated in Fig. 5 below.

Good correlation between numerical and experimental results can be seen in the initial part, but when the load increases the model is weaker, and fails about 10% lower than the tests. This could be due to lower temperatures in the core of the tested section and therefore larger residual material strength. Also the temperature reduction factors account for the effects of thermal creep, which are not present in the steady-state experiments used, due to the testing speed. The creep effects are known to decrease the strength and stiffness of steel by about 8% to 9%. Furthermore, in the EC3-1.2 stress-strain curves no strain hardening effects are considered above 400°C but strain hardening has a significant influence on the capacity of the section,

because of the fairly large strains occurring directly under the transverse load and in the plastic hinges.

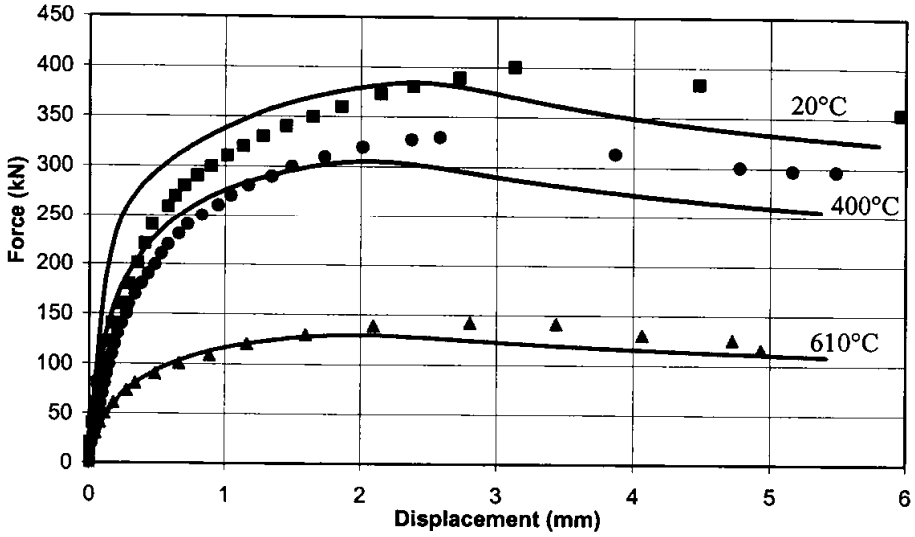

FIGURE 5 : Experimental and numerical results without axial load

The study was extended to bi-axial loading. A typical set of force – displacement curves is shown in Fig. 6 below.

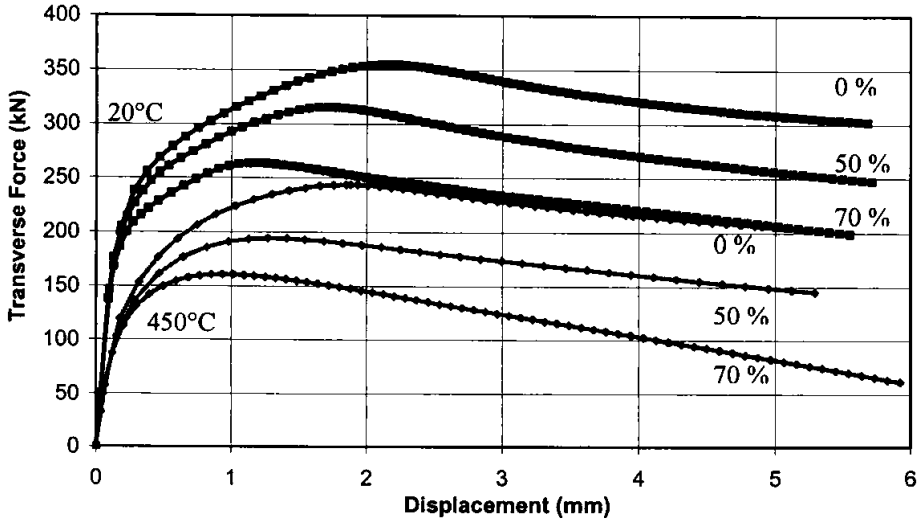

FIGURE 6 : Transverse force-displacement for UC 203x203x46 at 20°C and 450°C under axial loads 0% - 70% of yield.

From the force-displacement curves plotted in Fig. 6 a significant reduction of the capacity and the ductility of the compression zone is apparent in the presence of axial load. This reduction

increases as temperatures increase, due to the decrease of the proportional limit of the stress-strain curve and therefore reduced tangent modulus at low stress levels. Furthermore, the missing strain-hardening at temperatures above 400°C changes the post-peak behaviour of the column web. Whereas at ambient temperature, even for high axial load levels, the web behaviour recovers slightly due to membrane effects after the peak load, at elevated temperatures no membrane effects can be developed in the highly strained areas due to the lack of strain-hardening. Hence, under high axial loads the post peak behaviour decreases rapidly because of the second-order effects in the buckled column web introduced by the axial load. In Fig. 7 the interaction of the normalised peak loads (R/R_T) and the normalised axial forces (N/N_{pl}) are shown for all 45 analyses.

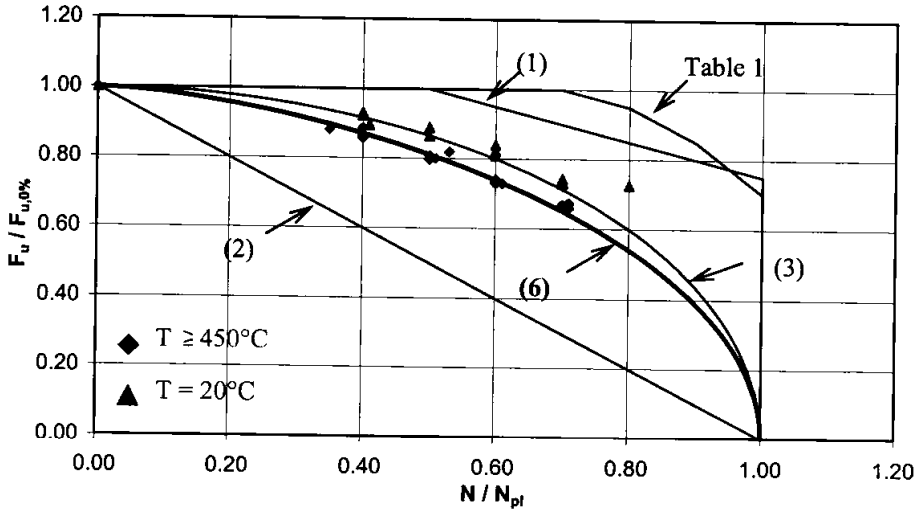

FIGURE 7 : Reduction of the peak load due to axial loads in the column

Details of the analyses are shown in the Appendix. For each section at each temperature the peak loads are normalised with respect to the peak load under zero axial load and the axial load to the yield load of the section using the yield stress at the relevant temperature.

It is remarkable that both the ambient- and elevated-temperature sets of results (T=20°C, T>450°C) show similar behaviour, which suggests that the change in the style of the stress-strain curve has a larger influence on the peak load reduction than the different temperatures. Furthermore, the different approaches for the reduction factors given in the literature are shown in Fig. 7 and it becomes quite clear that only equation (3) gives reasonable results for the ambient temperature cases, but at the higher temperatures which occur in a protected column exposed to fire a rather larger reduction factor should be used. Until an analytical equation has been developed the following approach can be used:

$$k_N = \sqrt{1-\left(\frac{\sigma_N}{k_{y,\theta} f_{y,w}}\right)^{1.55}} \qquad (6)$$

where σ_N is the longitudinal stress in the column web; $k_{y,t}$ is the temperature-dependent yield strength reduction factor given in EC3 and $f_{y,w}$ the yield stress of the column web.

Referring back to Fig. 6, the displacements associated with the peak load are reduced by the influence of the axial force in the column. To make this reduction more visible the displacements at peak load are normalised against those under zero axial load for each set of temperatures and section sizes. This reduction is shown in Fig. 8.

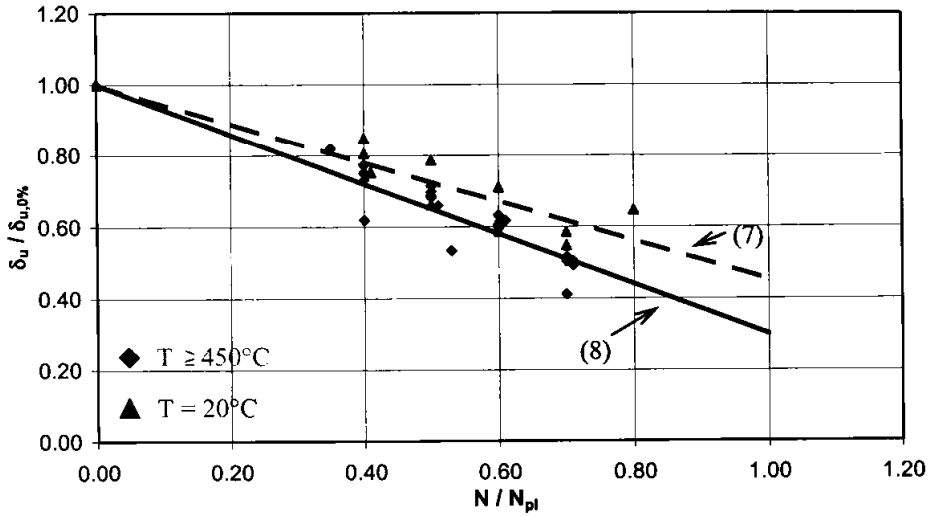

FIGURE 8 : Reduction of the peak displacement due to the presence of axial load

For this phenomenon no reduction factor has been published to date, but it is important to know this factor if the full force-displacement curve for the component is to be predicted. Linear equations based on a regression calculation can be proposed which represent the mean peak load reduction factor. The first, for ambient temperature behaviour, is

$$k_{N,\delta,20°C} = -0.55\frac{\sigma_N}{f_y} + 1 \qquad (7)$$

and for temperatures above 400°C,

$$k_{N,\delta,\geq 400°C} = -0.70\frac{\sigma_N}{f_y} + 1 \qquad (8)$$

Using the above reduction factors it is possible to extend the simplified approach for the compression zone to include the effect of axial load in the column. As an example the results from the numerical analysis of the UC 203x203x46 at 450°C and 650°C for axial load levels of 0%, 50% and 70% are shown in Fig. 9, together with analytical results based on the simplified method presented in [6].

In similar fashion to the comparison with experiments given in Fig. 5 the numerically calculated curves show weaker behaviour than the analytical approach, but in general a good correlation can be seen.

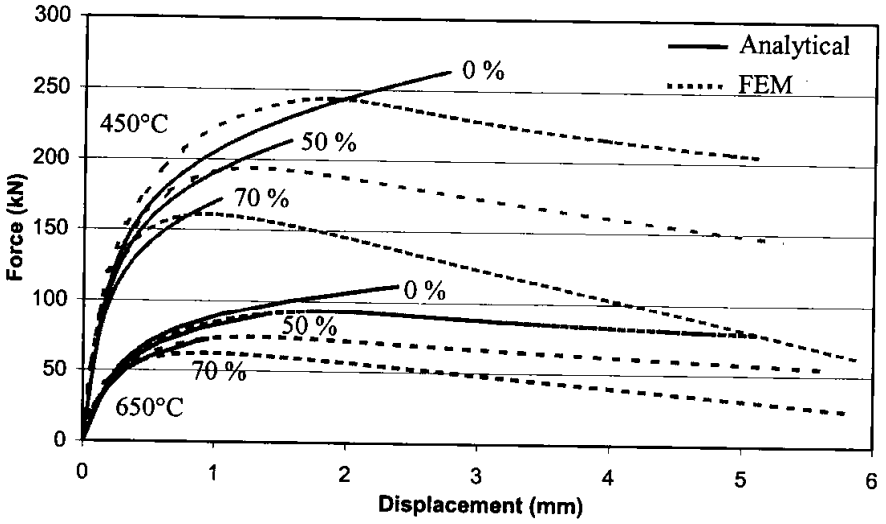

FIGURE 9 : Comparison of simplified prediction with FEM results for UC203x203x46.

EXPERIMENTAL STUDIES

An experimental study is due to start in April 2004 in order to validate the finite element analysis of the column web under bi-axial loading at elevated temperatures. A British universal column section (UC 152x152x37) is to be tested in a horizontal position. The experimental set-up consists of three major parts. A horizontal loading device, which includes a hydraulic jack attached via a pressure-controlled pump to a reaction frame, applies the axial force. The role of the pressure-control system is to keep the axial load constant as the specimen expands due to its increasing temperature (see Fig. 10a). An electrically-heated furnace box wraps around the column section, which protrudes through shaped holes in removable panels at both ends. The furnace is insulated with 50mm fibre-board and uses commercial electric heating elements, closely arranged around the specimen. The elements have a total power rating of 8kW. Each of the six elements can be controlled separately to achieve a uniform heating profile in the column section (see Fig. 10b). A vertical loading device (a displacement-controlled actuator attached to the reaction frame) applies the transverse compression to the section. To simulate the beam flanges in an internal joint this transverse load is introduced via steel plates of 20mm thickness with rounded edges. These plates can be moved out of the furnace to prevent them from becoming overheated (see Fig. 10c). To allow for the vertical movement of the centre-line of the specimen, which occurs when the transverse load is applied, roller blocks are mounted at the ends of the specimen. They allow frictionless movement even under an axial load of 400kN. The experimental procedure will consist of three main steps:

1. Load the column section axially.
2. Heat the column section up to the test temperature, maintaining its axial load.
3. Load the column section transversely until failure occurs in the column web.

Tests are planned at 20°C, 450°C, 550°C and 600°C with axial load ratios of 0.0, 0.2 and 0.3. Using the reduction factors for steel yield stress given in the EC3 Part 1.2, the axial load ratios for the different temperatures are shown in Table 2.

Temperature	Reduction Factor	LR 0.0	LR 0.2	LR 0.3
	$k_{y,\theta}$	$\sigma_N / (k_{y,\theta} * f_y)$	$\sigma_N / (k_{y,\theta} * f_y)$	$\sigma_N / (k_{y,\theta} * f_y)$
20°C	1.000	0.00	0.200	0.300
450°C	0.890	0.00	0.225	0.338
550°C	0.625	0.00	0.320	0.480
600°C	0.470	0.00	0.426	0.638

Table 2 : Summary of the planned tests

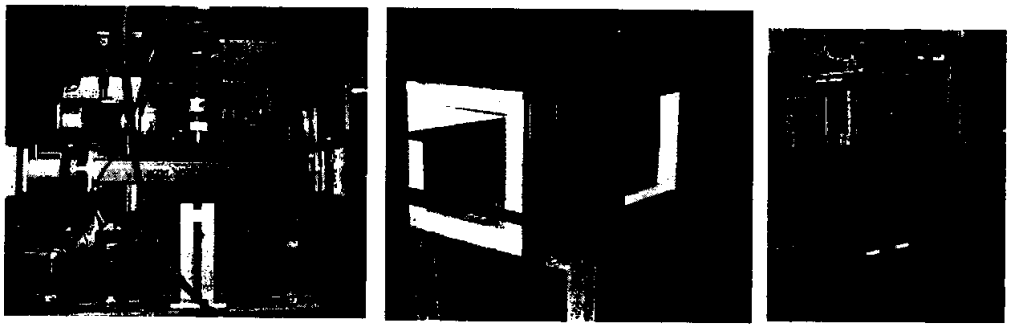

(a) (b) (c)

FIGURE 10 : (a) Experimental setup, (b) furnace, (c) load introduction system.

CONCLUSION

A finite element study has been performed in order to investigate the influence of the axial load in a column on its transverse compression resistance at elevated temperatures. The transverse resistance becomes important in an unstiffened beam-to-column connection if large rotations of the beam-ends in fire and thermal expansion introduce large compression forces into the column via the bottom beam flange.

From the numerical analyses a significant reduction of the ultimate transverse resistance and the displacement associated with this ultimate resistance could be seen. This is consistent with the experimental results at ambient temperatures found in the literature, but the present reduction factors for this effect are not sufficiently accurate. A new factor for the ultimate load at elevated temperatures has been developed, based on an existing approach and a large number of numerical calculations. A new reduction factor has been developed for the displacement of the ultimate load needed to be able to describe the full force-displacement curve of the compression zone in the column web. To further validate the new reduction factors a scries of high-temperature, biaxial loading experiments are planned, and the test setup is described briefly in this paper.

The compression zone in the column web is one of the major components needed to describe the full moment-rotation-thrust-temperature characteristics of steel and composite joints in fire. This knowledge will contribute to more accurate analysis of steel-framed structures in fire and thereby increase the safety and economy of structural design.

ACKNOWLEDGMENT

The authors gratefully acknowledge sponsorship of the first author by Buro Happold FEDRA Ltd, and support for the experimental work by Corus Group Ltd.

REFERENCES

[1] European Committee for Standardization, *"Eurocode 3: Design of steel structures, Part 1.8: Design of joints (Stage 49 draft)"*, Document prEN 1993-1-8, (2003).

[2] Kühnemund F., "*Zum rotationsnachweis nachgiebiger knoten im stahlbau*", Dissertation, Institut für Konstruktion und Entwurf Stahl-, Holz- und Verbundbau,Universität Stuttgart, (2003).

[3] European Committee for Standardization, *"EC 3: Design of steel structures, Part 1.2: Structural fire design (Stage 49 draft)"*, Document prEN 1993-1-2, (2003).

[4] Aribert, J.M., Lachal, A. and Moheissen, M., "*Modelling and experimental investigation of plastic resistance and local buckling of H or I steel sections submitted to concentrated or partially distributed loading*", Proc. IUTAM Symposium, Prague, (1990), pp.101-110.

[5] Spyrou, S., "*Development of a component based model of steel beam-to-column joints at elevated temperatures*", PhD Thesis, Department of Civil and Structural Engineering, University of Sheffield (2002).

[6] Block, F.M., Burgess, I.W., Davison, J.B., Plank, R., (2004), "*A Component approach to modelling steelwork connections in fire: behaviour of column webs in compression*", Proc. ASCE Structures Congress 2004, Nashville, Tennessee, (2004).

[7] Lagerqvist, O., Johansson, B., "Resistance of I-girders to concentrated loads", *J. Construct. Steel Research*, **39** (2), (1996), pp.87-119.

[8] Zoetemeijer, P., "*Influence of normal-, bending- and shear-stresses in the web of European rolled sections*", Report 6-75-18, Stevin Laboratory, Delft University of Technology, Netherlands, (1975).

[9] Ahmed B. and Nethercot D.A., "Effect of column axial load on composite connection behaviour", *Engineering Structures*, **20** (1-2), (1998), pp.113-128.

[10] Bailey, C.G. and Moore, D.B., "*The influence of local and global forces on column design*", Final Report, PII Contract No. CC1494, BRE, Garston, UK, (1999).

[11] Djubek, J. and Škaloud, M., "*Postbuckling behaviour of web plates in the new edition of Czechoslovak design specifications*" ,Proc. International Conference on Steel Plated Structures, Imperial College, London, (1976).

[12] Tryland T., Hopperstad O.S. and Langseth M., "Finite-element modelling of beams under concentrated loading", *Journal of Structural Engineering, ASCE*, **127** (2), (2001), pp.176-185.

[13] Zheng, Y., Usami, T. and Ge, H.B., "Ductility of thin-walled steel box stub-columns", *Journal of Structural Engineering, ASCE*, **126** (11), (2000), pp.1304-1311.

APPENDIX: Summary of analysed British column sections presented in Figs. 7 and 8:

UC Section	d / t	Temp. [°C]	Axial Load Level N / N_{pl}	Peak Load [kN]	Peak Load Reduction	Displ. at Peak Load [mm]	Displ. Reduction
203x203x46	22.30	20 C	0.00	354.89	1.00	2.17	1.00
			0.40	330.35	0.93	1.85	0.85
			0.50	315.58	0.89	1.71	0.79
			0.60	291.54	0.82	1.34	0.62
			0.70	263.54	0.74	1.19	0.55
		450 C	0.00	243.56	1.00	1.85	1.00
			0.40	209.01	0.86	1.43	0.77
			0.50	193.96	0.80	1.27	0.69
			0.60	177.67	0.73	1.17	0.63
			0.71	160.69	0.66	0.93	0.50
		650 C	0.00	92.97	1.00	1.84	1.00
			0.35	82.01	0.88	1.51	0.82
			0.50	74.17	0.80	1.26	0.68
			0.60	68.75	0.74	1.12	0.61
			0.71	62.56	0.67	0.91	0.49
152x152x37	15.50	20 C	0.00	345.84	1.00	3.06	1.00
			0.41	309.96	0.90	2.30	0.75
			0.50	299.12	0.86	2.02	0.66
			0.60	279.24	0.81	1.79	0.59
			0.70	252.16	0.73	1.79	0.58
		450 C	0.00	238.02	1.00	2.20	1.00
			0.40	206.32	0.87	1.61	0.73
			0.51	190.48	0.80	1.45	0.66
			0.60	175.16	0.74	1.31	0.60
			0.70	157.20	0.66	1.12	0.51
		550 C	0.00	165.75	1.00	2.15	1.00
			0.40	143.72	0.87	1.61	0.75
			0.50	133.92	0.81	1.50	0.70
			0.61	120.80	0.73	1.33	0.62
			0.70	109.64	0.66	1.11	0.52
		650 C	0.00	91.22	1.00	2.37	1.00
			0.40	78.84	0.86	1.84	0.77
			0.50	73.60	0.81	1.70	0.72
			0.60	67.56	0.74	1.43	0.60
			0.70	60.96	0.67	1.19	0.50
203x203x167	10.40	20 C	0.00	2117.56	1.00	10.29	1.00
			0.40	1955.08	0.92	8.29	0.81
			0.60	1778.94	0.84	7.31	0.71
			0.80	1536.58	0.73	6.65	0.65
		450 C	0.00	1341.85	1.00	10.65	1.00
			0.40	1189.47	0.89	6.59	0.62
			0.53	1099.03	0.82	5.68	0.53
			0.70	968.93	0.72	4.37	0.41
		650 C	0.00	519.99	1.00	10.06	1.00
			0.40	461.84	0.89	6.53	0.65

Effective thermal actions and thermal properties of timber members in natural fires

Jürgen König
Trätek – Swedish Institute for Wood Technology Research
Box 5609, SE-114 86, Stockholm, Sweden
juergen.koenig@tratek.se

ABSTRACT

For the thermal analysis of structural or non-structural timber members, using conventional simplified heat transfer models, thermal conductivity values of timber are normally calibrated to test results such that they implicitly take into account influences such as mass transport that are not included in the model. Various researchers and designers have used such effective thermal conductivity values, originally determined for standard fire exposure, to evaluate other fire scenarios such as natural fires. This paper discusses in qualitative terms some parameters that govern combustion of wood and their influence on effective conductivity values. Reviewing fire tests of timber slabs under natural fire conditions, it is explained why effective conductivity values, giving correct results for the ISO 834 standard fire scenario, should not be used in other fire scenarios. Therefore, the thermal properties of timber given in EN 1995-1-2 are limited to standard fire exposure. As shown by heat transfer calculations, the effective thermal conductivity of the char layer is strongly dependent on the charring rate and varies therefore during a natural fire scenario. It has also been shown that char oxidation during the decay phase in a natural fire has a significant influence on the temperature development in the timber member, since char surface temperatures exceed the gas temperature in the compartment or furnace. Using increased effective gas temperature as thermal action during the decay phase, and varying conductivity values for the char layer, fairly good agreement could be obtained regarding the temperature development in the timber member and the char depth.

KEYWORDS: *charring, char oxidation, conductivity, natural fires, temperature, thermal analysis, timber structures, wood*

INTRODUCTION

In design by calculation the load-bearing performance of steel and concrete structures exposed to fire is verified by performing a thermal analysis of structural parts and a subsequent structural analysis taking into account the thermo-mechanical material properties. In timber structures, the thermal analysis is normally replaced by determining the char depth and the structural analysis is carried out by replacing the cold strength and stiffness properties of the residual cross-section by reduced properties that are valid in the fire situation, see e.g. the Fire Part of Eurocode 5 (EN 1995-1-2). For advanced calculations, this code also contains thermal and thermo-mechanical properties of timber which may be applied in the standard fire scenario. In this paper, some of the background of thermal properties given in EN 1995-1-2 is given, and their limitations with regard to different fire scenarios.

In solids heat is transferred by conduction, while heat transfer in gases takes place by radiation and convection. In porous materials heat flux is governed by all three modes of heat transfer. Since wood and charcoal are porous, the temperature development is dependent on all three of them. The physics of heat transfer from a fire compartment into a wood slab forming a boundary of the compartment has been described in several sources, e.g. Kanury (1995), Parker (1995) and Drysdale (1997). For the stage after ignition, the different components of heat flux can be illustrated as shown in Figure 1. The border between wood and the char layer coincides fairly well with the position of the 300-degree isotherm while pyrolysis takes place at different depths (at different temperatures) and at different rates. Apart from conductive heat flux, convective heat flux takes place in the wood due to vaporization of water and its re-condensation in cooler zones, and in the char layer due to reverse flow of cooling pyrolysis gases. Due to the formation of fissures in the char layer, heat transfer is increased due to radiation and convection.

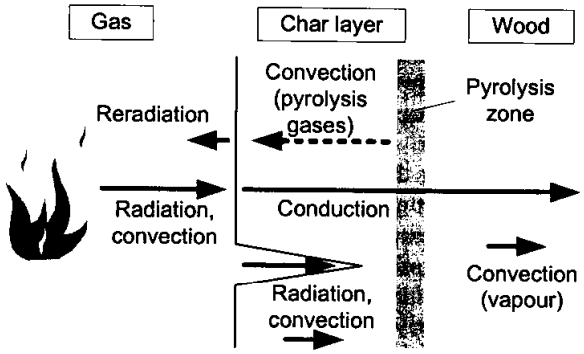

Figure 1 Heat flux components in fire-exposed semi-infinite wood slab

An rigorous analysis of the heat transfer into a wood slab in order to determine the temperature profile in the wood would require a model taking into account mass transport (see e.g. Fredlund,

1988). Unfortunately such models are not developed as easy to use design tools or not yet publicly available, and therefore analyses must be performed using conventional heat transfer models. These heat transfer models and computer codes normally take into account

- conduction in solids;
- radiation in the gas on the fire exposed and ambient side, and in voids;
- convection in the gas at borders between the solid material and the gas;
- the absorption of energy when water is vaporised by introducing a heat sink.

Conductivity values given in different sources vary considerably, see Figure 2 (König et al. 1999, Källsner et al. 2000). There are several reasons: Some represent physically correct values, obtained from direct measurements, while others may have been determined by calibration to the results of fire tests. The values by Fredlund (1988) were used in a model that included mass transport.

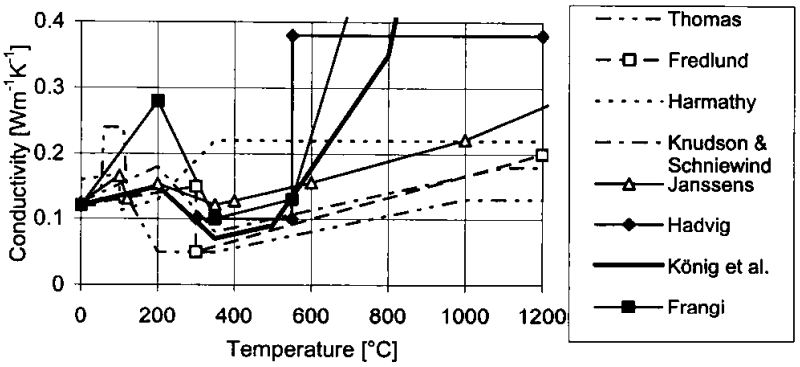

Figure 2 Conductivity vs. temperature of wood and the char layer

The effect of mass transport (e.g. vapour and pyrolysis gases) and the effect of fissures in the charcoal and surface recession of the char layer are often taken into account by applying effective conductivity values rather than the physically correct ones and are normally obtained by calibrating them to test results. When water is vaporised most of the vapour is transferred inwards towards cooler regions of the wood slab until it re-condenses. This energy transport can be modelled by assuming higher conductivity values for temperatures below vaporization temperature, that is about 100°C, and lower conductivity values in the following temperature interval up to about 350°C. This has been done by Thomas (1997), see Figure 2, and similarly by Clancy (2002). The advantage of this manipulation is that the delay of temperature increase beyond 100°C is described in a more realistic way. (This may have consequences when the mechanical resistance is determined, since the temperature around 100°C are significantly sensitive to strength and stiffness reduction of wood.) Apart from this deviation, for wood, i.e. for temperatures below 300°C, most conductivity values shown in Figure 2 are fairly close together. For temperatures greater than 300°C, that is for the char layer, the curves by Hadvig (1981), König et al. (1999) and Frangi (2001) deviate considerably from the others. König et al. (1999) modelled the formation of fissures in the charcoal, starting at about 500°C, and surface recession of the of the char layer by assuming rapidly increasing conductivity values above

500°C. The values by Hadvig (1981) shown in the graph are based on the assumption that the formation of cracks in the char layer takes place at a distance of 6 mm from the char line.

The heat capacity values given by König et al. (1999) were modified in order to fit together with density ratios given by Janssens (1994), see Figure 3, the product of heat capacity c and density ρ are, however, the same. Similarly as above, by modifying Janssens' relationship of density versus temperature, the recession of the surface of the char layer is modelled by assuming that the density of the char-layer decreases linearly to zero between 800 and 1200°C.

Other authors have modelled the effect of fissures and surface recession of the char layer in a similar way as done König et al., e.g. Povel (2002). Frangi also assumed a heat sink between 200 and 300°C in order to take into account the heat of combustion, similarly as done by Mehaffey et al. (1994). It is, however, highly disputed whether pyrolysis is endothermic or exothermic (Roberts, 1971); therefore it is neglected by most authors. The introduction of a heat sink to model an endothermic reaction would probably cause higher conductivity values than assumed by König.

From this discussion can be seen that the choice of thermal properties is strongly dependent on the model used and that there is an interdependence of the properties, mainly conduction and heat capacity: A change of one property can be compensated by another change of the other property.

The values by König et al. (1999), also included in the Fire Part of Eurocode 5 (EN-1995-1-2) for application to standard fire scenarios, should only be used when the conventional heat transfer model is applied, that is when mass transport is not explicitly taken into account. The restriction to standard fire scenarios will be explained below.

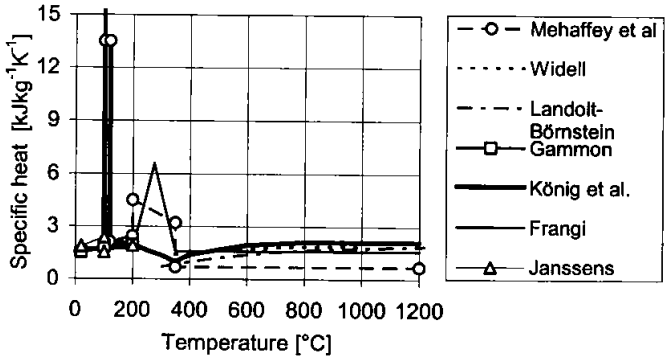

Figure 3 Specific heat values of wood

REVIEWING THE PARAMETRIC FIRE TESTS BY KÖNIG ET AL. (1999)

Apart from tests with standard fire exposure, König et al. (1999) also performed six fire tests of timber slabs exposed to natural fires, represented by different parametric fire curves. In three of these tests, C1 to C3, the fire curve corresponded to an opening factor of 0,04 $m^{0,5}$ and a fire

load density of 170 MJ/m^2 related to the total area of the enclosure. In three further tests, C4 to C6, during the heating phase the fire curves corresponded to opening factors of about 0,06 to 0,08. All tests were conducted using a a small-scale furnace. The objective of these tests was to verify the charring rates for parametric fire curves given in EN 1995-1-2 which were based on Hadvig (1981) and Toft Hansen et al. (1992). The charring rate during the heating phase is given as

$$\beta_{par} = k_{par}\,\beta_0 \tag{1}$$

where

β_0 is the charring rate for standard fire exposure;

k_{par} is a charring factor dependent on the opening factor O and the absorptivity b of the enclosure.

For the fixed value of the absorptivity given by

$$b = \sqrt{\rho c \lambda} = 1160 \text{ J/m}^2\text{s}^{0,5}\text{K} \tag{2}$$

where ρ is the density, c is the heat capacity and λ is the thermal conductivity of the enclosure, Figure 4 shows the relationship between the opening factor and k_{par}. In this case the opening factor O = 0,04 m^{0,5} corresponds to the heating conditions according to the ISO 834 standard fire curve. Correspondingly, for some opening factors, Figure 5 shows the char depth during the heating phase as a function of time.

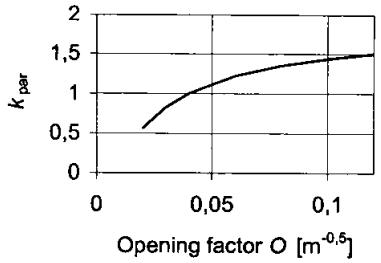

Figure 4 Effect of opening factor on charring factor

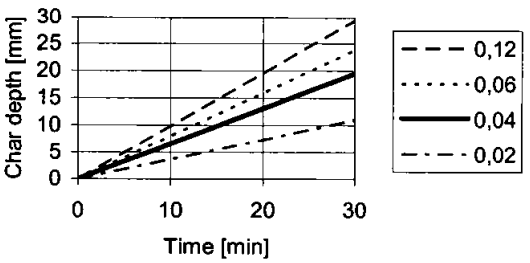

Figure 5 Effect of opening factor on char depth vs. time during heating phase according to EN 1995-1-1

Whereas the experimental results confirm the expressions adopted by EN 1995-1-2, it was seen that, performing heat transfer calculations, the calculated charring rate and char depth was

- *overpredicted during the heating phase for opening factors greater than 0,04*, i.e. for a temperature development that is faster than in the standard fire scenario;
- *underpredicted during the decay phase* when temperature is decreasing and the char depth is reaching its maximum value.

In the following sections, results of heat transfer calculations are presented, using the software TCD 5.0 that includes Super-Tempcalc. The advantage of this software is that a heat transfer

analysis can be subdivided into several steps, each of them with different thermal properties and different configurations of the structure. (For example, the latter option enables to model a sudden loss of a fire protection attached to a structural member.)

MODELLING OF HEATING PHASE

The graph of Figure 6 shows temperature histories recorded during the heating phase of test C4. The furnace was controlled with a plate thermocouple located 100 mm below the horizontally arranged timber plate. For comparison, the graph also shows the standard fire curve according to ISO 834. Thermocouples were attached to the surface of the timber and at depths of 6, 18, 30, 42 and 54 mm respectively (smooth lines).

Using the temperature of the plate thermocouple as input thermal action, temperature histories were calculated shown as broken lines. Assuming the thermal conductivity by König et al. (1999), also shown as curve A in Figure 7, the temperature rise at 18 and 30 mm was considerably overpredicted, see the broken lines of Figure 6. Also, the calculated char depth is overpredicted, see Figure 8.

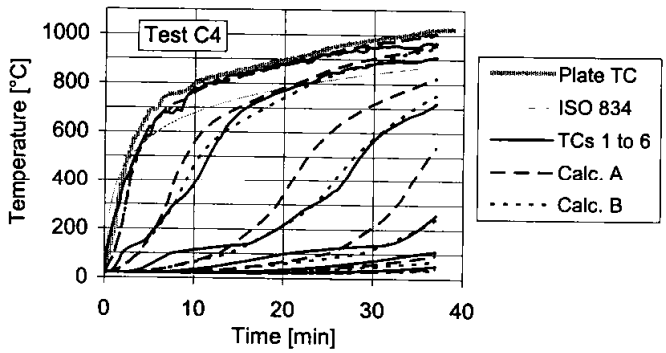

Figure 6 Temperature histories during heating phase of test C4 – Comparison of test results and calculations

Since the charring rate in the test is greater than the charring rate normally observed for standard fire exposure (which would give a char depth of about 20 mm after 30 minutes) the reverse flow of cooling pyrolysis gases must also be greater. Consequently, the effective conductivity of the char layer, where the reverse flow of cooling gases occurs, must be reduced. Therefore, on a trial and error basis, an alternative relationship B of conductivity and time was chosen with reduced conductivity values in the char layer (where this cooling gas flow occurs) and fitted to the test results. See the dotted lines in Figure 6 to 8.

Similar results (not shown here) were obtained for test C5. For test C6 with a higher gas temperature than in tests C4 and C5, relationship C of Figure 7, implying a further reduction of the effective conductivity of the char layer, gave reasonable agreement with the test results, see Figure 9 and 10.

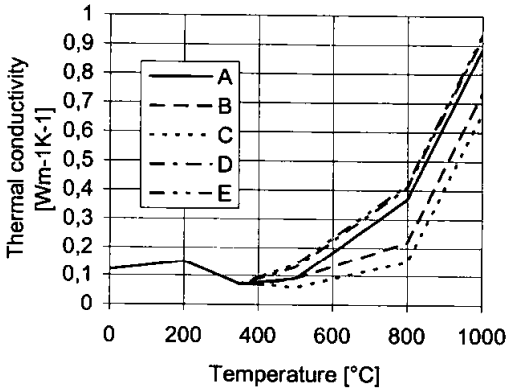

Figure 7 Thermal conductivity values used in the calculations

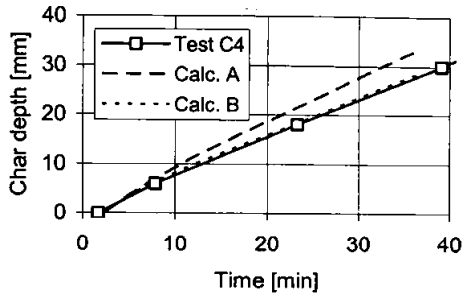

Figure 8 Char depth vs. time during heating phase of test C4 – Comparison of test results and calculations

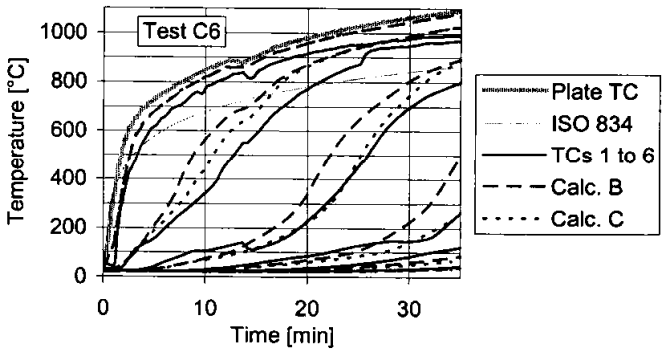

Figure 9 Temperature histories during heating phase of test C6 – Comparison of test results and calculations

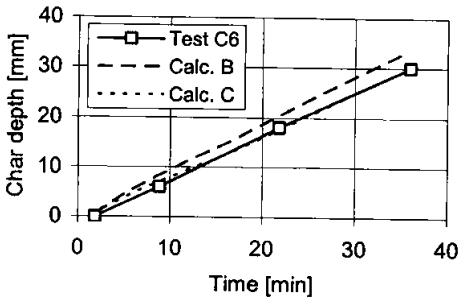

Figure 10 Char depth vs. time during heating phase of test C4 – Comparison of test results and calculations

Vice versa, for fire scenarios with slower heating than during a standard fire exposure, it can be expected that the effective conductivity values of the char layer must be increased, since there is less cooling by pyrolysis gases. In this case, the effective conductivity values valid for standard fire exposure would give non-conservative prediction of the char depth.

DECAY PHASE

As a consequence of what has been described above, it can be expected that the effective conductivity values of the char layer during the decay phase should increase as the charring rate decreases and finally becomes zero. This measure alone, however, is not sufficient to model heat transfer in a correct way. We will have a look at some typical test results from König et al. (1999) shown in Figure 11 and 12. Having passed the maximum gas temperature in the furnace, during the decay phase, the temperature of, in that order, thermocouples 1 to 4 increase above the gas temperature that was measured with the plate thermocouple. The same can be seen from the temperature profiles shown in Figure 12. The maximum temperature appears to be in the char layer close to its recessing surface and a temperature gradient exists in the gas layer close to the surface.

A reasonable explanation of the occurrence of higher temperatures in the char layer is that glowing combustion starts when increasingly becoming exposed to air (Beyer et al., 1995). Normally, during standard fire exposure, glowing oxidation has no major effect on surface temperature, since "it is unlikely that both glowing combustion of the char and gas-phase combustion can occur simultaneously in the same zone above the surface, since the flow of volatiles through the char will tend to exclude air from direct contact with the char. Therefore, in general, solid-phase char combustion tends to occur after volatization has largely ended" (Beyer et al., 1995). Char has a rather high heat of oxidation and is susceptible to rapid oxidation at moderate temperatures approximately above 400°C (Ohlemiller, 1995). This statement roughly agrees with Figure 13 showing that the maximum temperature in the char tends to reapproach the gas temperature in the furnace when it decreases below about 400°C. The existence of a temperature in the gas layer close to the char surface is possible since the conditions in the furnace are less turbulent during the decay phase than during the heating phase.

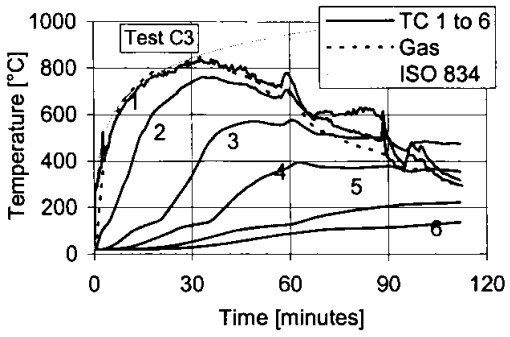

Figure 11 Recorded complete temperature histories for test C3

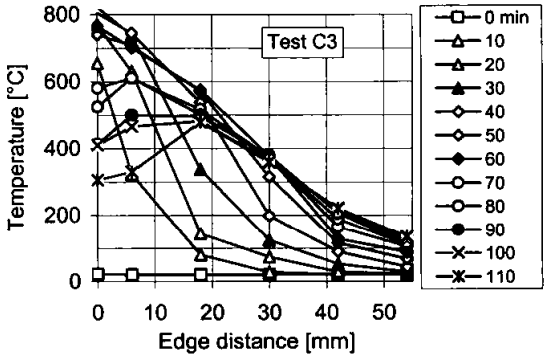

Figure 12 Temperature profiles at specified times

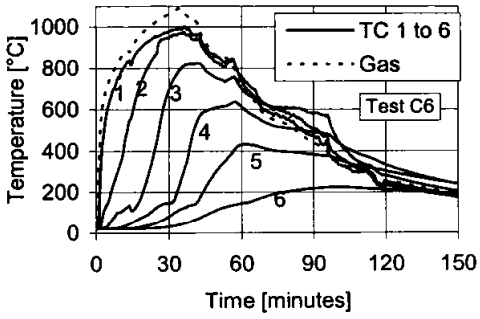

Figure 13 Recorded complete temperature histories for test C6

A heat transfer analysis was carried out, using the temperature recorded by the plate thermocouple as thermal action and the thermal conductivity values according to curve A in Figure 7, that is the same values as given by König et al. (1999) and EN 1995-1-2 (The heat capacity values from the same sources were used in all calculations referred to in this paper). The results show that, during the heating phase, the calculated temperature histories agree fairly well with the test results, while temperature reverses too early in the decay phase (Figure 14). Compared to the test results, the calculated final char depth is too small (Figure 15).

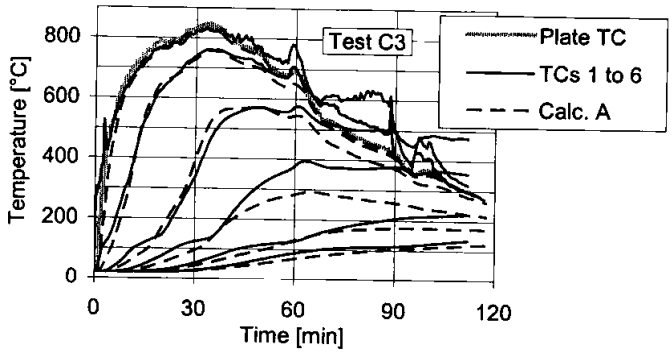

Figure 14 Temperature histories during heating and decay phase of test C3 – Test results and calculation with thermal action as recorded by plate TC

In the next step, during the decay phase, the thermal action fire curve was replaced by a linear curve ending with 400°C at 120 minutes, roughly approximating the maximum temperatures recorded by the thermocouples located at 0, 6, 18 and 30 mm depth. The predicted temperature histories and char depths agreed better with the test results as before (see Figure 15 and 16), however, they were still non-conservative.

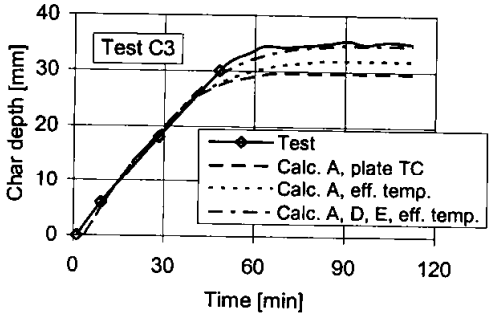

Figure 15 Char depth vs. time of test C4 – Test results and calculations

In order to reduce this discrepancy, in the following calculations increased conductivity values were used during the decay phase as proposed in the beginning of this section. A reasonably well fitted results were obtained using curve A for the interval 0 to 37 minutes, curve D for 37 to 45 minutes and curve E for 45 to 112 minutes, see Figure 15 and 17.

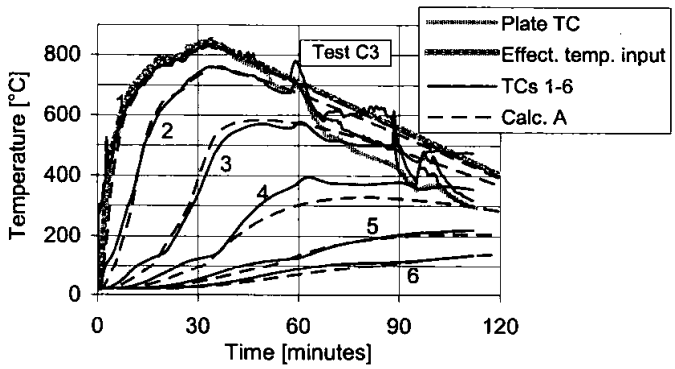

Figure 16 Temperature histories during heating and decay phase of test C3 – Test results and calculation with effective temperature taken as thermal action

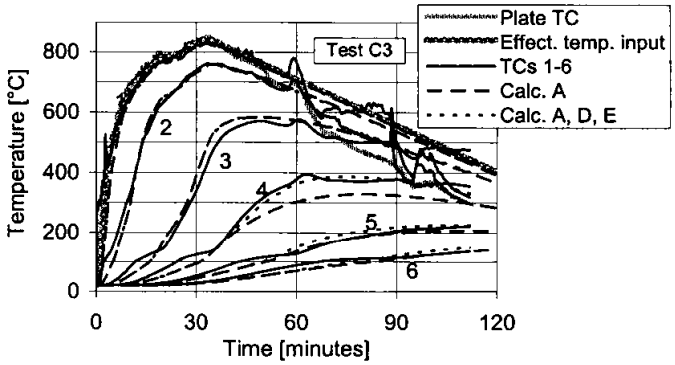

Figure 17 Temperature histories during heating and decay phase of test C3 – Comparison of test results and calculation with effective temperature taken as thermal action and increased conductivity values during decay phase

EFFECTS OF LININGS OR OTHER PROTECTION

EN 1995-1-2 accounts for the insulating effect of applied protection, e.g. gypsum plasterboard, by reducing the charring rate of timber behind the protection by a factor k_2. After the onset of charring, for gypsum plasterboard type F with thickness h_p, the reduction factor is given as

$$k_2 = 1 - 0{,}018\, h_p \qquad (3)$$

A lining consisting of a 15 mm thick gypsum plasterboard would reduce the charring rate by 27 %, two layers by 54 %. Since the production of cooling pyrolysis gases is reduced correspondingly, the effective thermal conductivity of the char layer should be increased. Alternatively, if the effective conductivity of the char layer is used as given by curve A, the effective conductivity of gypsum plasterboard should be increased for large temperatures. (This

might be the reason why effective conductivity values of gypsum plasterboard used by König et al. (2000) for temperature above 700°C are greater than those given by other sources).

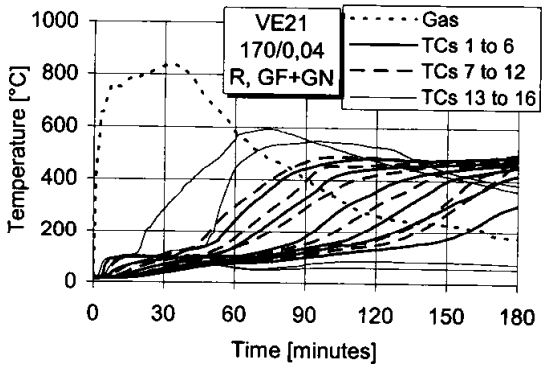

Figure 18 Temperature histories from fire test of timber frame wall assembly

Oxidation of char requires supply of oxygen to the char layer, see above. It should be expected that an applied protection would normally prevent this supply and the char layer would exhibit temperature above the gas temperature in the furnace or compartment during the decay phase. During fire tests in medium scale on timber frame elements, clad with gypsum plasterboard linings and rock or glass fibre filled cavities, however, the temperatures in the char layer behind the lining were considerably higher than the gas temperature (König et al. 1997), see Figure 18. (The fine lines to the left refer to thermocouples between the two layers of the lining and behind the inner layer respectively between the two studs of the wall element). This cannot be explained by retarded reverse heat flux during the decay phase since the temperature histories indicate that pyrolysis is continuously taking place. It is therefore most likely that some oxygen supply occurred, since the furnace exhibited underpressure. In reality, underpressure will only take place below the neutral layer of a fire compartment. These conditions would require to model a heat source in the char layer.

CONCLUSIONS

Due to the complex nature of heat transfer in wood and char coal, including phenomena like the formation of fissures in the char layer and the internal convection due to pyrolysis gases and vaporized water, it is necessary to use effective rather than physically correct thermal properties when simplified models are used that do not explicitly take into account mass transport. For timber structures, this need appears to a considerably greater extend than for concrete structures where moisture transport plays a role. The formation of fissures in the char layer due to char contraction has a great influence on the effective conductivity of the char layer.

It has been shown that effective thermal properties that have been verified for standard fire exposure would give incorrect results when applied to other fire scenarios such as parametric fire curves for natural fires. Due to convective cooling by reverse flow of pyrolysis gases the heat flux through the char layer into the wood is delayed. Since this delay is dependent on the rate of charring, the effective conductivity is a function of the charring rate; thus it is also a function of the rate of increase or decrease of temperature.

Char oxidation may occur during the decay phase in natural fires giving rise to char surface temperatures that are considerably above the gas temperature in the furnace or fire compartment. It has been shown that, by assuming effective conductivity values and modified thermal actions

using an effective gas temperature in the compartment, good agreement can be obtained between the results from calculations and fire tests.

The present limitation of the use of effective thermal properties should be overcome by deriving them from analytical models that take into account the phenomena described above. Since, for the time being, no such model exists, as an alternative, extensive series of fire tests with various fire scenarios need to be performed. Such fire tests should also be a prerequisite for the validation of models that take into account the relevant parameters governing combustion of wood.

ACKNOWLEDGEMENT

The investigation described in this paper was funded by Vinnova – Swedish Agency for Innovation Systems.

REFERENCES

Beyler, C.L. and Hirschler, M.M., 1995, Thermal decomposition of polymers. The SFPE Handbook of Fire Protection Engineering, 2nd edition

Clancy, P., 2002, A parametric study on the time-to-failure of wood framed walls. Fire Technology, 38, 243-269

Drysdale, D. D., 1997, Chemistry and physics of fire. National Fire Protection Association, Quincy, Mass.

EN 1995-1-2:2004 Eurocode 5: Design of timber structures – Part 1-2: General – Structural fire design.

Frangi, A., 2001, Brandverhalten von Holz-Beton-Verbunddecken. Dissertation, Eidgenössische Technische Hochschule Zürich

Fredlund, B., 1988, A model for heat and mass transfer in timber structures during fire. Lund University, Lund

Hadvig, S., 1981, Charring of wood in building fires. Technical University of Denmark, Lyngby

Janssens, M., 1994, Thermo-physical properties for wood pyrolysis models. Pacific Timber Engineering Conference Gold Coast, Australia

Källsner, B. and König, J., 2000, Thermal and mechanical properties of timber and some other materials used in light timber frame construction. Proceedings of CIB W18, Meeting 33, Delft, Paper 33-16-3

Kanury, A. M., 1995, Flaming ignition of solid fuels. The SFPE Handbook of Fire Protection Engineering, 2nd edition

König, J. and Walleij, L., 1999, One-dimensional charring of timber exposed to standard and parametric fires in initially protected and non-protected fire situations. Trätek – Swedish Institute for Wood Technology Research, Report No. I 9908029

König, J., Norén, J., Bolonius Olsen, F. and Toft Hansen, F., Timber frame assemblies exposed to standard and parametric fires – Part 1: Fire tests

Mehaffey, J., R., Cuerrier, P., Carisse, G., 1994, A model for predicting heat transfer through gypsum board/wood stud walls exposed to fire. Fire and materials, Vol. 18

Ohlemiller, T.J., 1995, Smouldering combustion. The SFPE Handbook of Fire Protection Engineering, 2nd edition

Parker, W. J., 1992, Wood materials. In Barbrauskas, V. and Grayson, S. J. (ed.), Heat release in fires. Elsevier Applied Science, London and New York

Povel, D., 2002, Tragfähigkeit von Holzverbindungen mit stabförmigen Verbindungsmitteln im Brandfall. Dissertation, Technische Universität Berlin

Thomas, G. C., 1997, Fire resistance of light timber framed walls and floors. University of Canterbury, Christchurch, Fire Research Report 97/7

Toft Hansen, F. and Bolonius Olesen, F., 1992. Full-scale tests on loaded glulam beams exposed to natural fires. Department of Building Technology and Struct. Engineering, Aalborg University, Aalborg, Denmark

FIRE PERFORMANCE OF LAMINATED VENEER LUMBER (LVL) WITH GLUED-IN STEEL ROD CONNECTIONS

Stuart HARRIS, Warren LANE, Andy BUCHANAN and Peter MOSS
Department of Civil Engineering, University of Canterbury, Christchurch, New Zealand

ABSTRACT

This paper describes an investigation into the fire performance of laminated veneer lumber (LVL) made from radiata pine, with glued-in steel rod connections.

To determine charring rates, cone calorimeter tests were carried out on samples of LVL with a number of grain orientations, each for a range of constant heat flux exposures. Full size load-bearing fire resistance tests were carried out on large size LVL beams (with no connections) in a 3 m x 4 m full size furnace, following the ISO 834 curve. Charring rates were found to be similar to solid wood or glulam.

To determine connection performance, an experimental investigation was carried out on the axial tensile strength of connections that utilised a threaded steel rod bonded into the timber using two epoxy resins and a composite adhesive. Some specimens were tested at a constant elevated temperature while similar specimens were tested in fire conditions under constant load. The three adhesives gave different connection strengths at ambient temperatures and showed different strength losses at elevated temperatures.

Design recommendations are given in the paper.

KEYWORDS: *fire resistance, fire test, charring, fire performance, ignition, laminated veneer lumber, LVL, epoxy, connections*

INTRODUCTION

Fire is one of the most unpredictable and dangerous accidents that may occur in our environment, especially in residential buildings. Fire development and behaviour and the effects of fire on structural members are very complex because of the large number of variables involved.

Ignition is one of the essential fire properties of a material and must always be considered in any assessment of fire hazard. The ignition of wood is more complex than for many other materials, especially because a layer of char is formed. The time to ignition depends on the species, moisture content, inherent variability of wood as a natural material, and the grain orientation of the specimen when exposed to the incident heat flux. In the case of laminated veneer lumber (LVL), the inherent variability of the timber may be a lesser factor because the raw material is carefully selected.

Once ignition has occurred, a layer of char is formed as the wood burns. A structural wood member will lose load capacity as the wood is converted to charcoal which has no strength. The thickening char layer protects the remaining wood, resulting in a predictable rate of charring below the surface. The rate of development of this charred layer determines how long the member can continue to carry load before the strength of the remaining unburned wood material is exceeded. A thin layer of heat-affected wood below the char layer will have reduced strength and stiffness.

To determine connection performance, an experimental investigation was carried out on the axial tensile strength of connections that utilised a threaded steel rod bonded into the timber using two epoxy resins and a composite adhesive. Some specimens were tested at a constant elevated temperature while similar specimens were tested in fire conditions under constant load. The three adhesives gave different connection strengths at ambient temperatures and showed different strength losses at elevated temperatures.

Design recommendations are given in the paper.

TEST MATERIAL

The tested LVL was made in New Zealand by Carter Holt Harvey Ltd using veneers 3 mm thick, glued into panels of up to 105 mm thickness. The average measured density and moisture content for the material used in each series of tests is shown in Table 1.

	Density kg/m^3	Moisture content %	Dry density kg/m^3
Ignition & instrumented	607	13.7	556
Pilot tests	604	12.0	540
Loaded test	608	12.4	541

Table 1: Density and moisture contents of samples tested.

IGNITION TESTS

Ignition tests were carried out at five different levels of heat flux and two main grain orientations, with three replications of each test. The grain orientations were on the exterior veneer face (face grain) and on the edges of the cut veneers parallel to the grain of the veneers (edge grain) (see Figure 1). The results of these tests are shown in Figures 2 and 3 for the face grain and 3 for the edge grain where the inverse of the square root of the temperature has been plotted against the incident heat flux, together with the line of best fit. Two methods were used to estimate the ignition properties of the LVL. The first method is that of Mikkola & Wichman [1] and the second one is by Delichatsios, Panagiotou & Kiley [2]. These methods were recommended by Ngu [3] as having the best correlations based on his testing of the ignition properties of New Zealand timbers. The resulting values for the surface ignition temperature (T_{ig}) and the thermal inertia (kρc) of the LVL samples, along with the estimate of the critical heat flux (q_{cr}) are shown in Table 2.

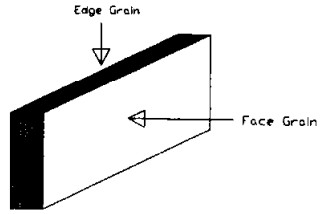

FIGURE 1 LVL Grain Orientation

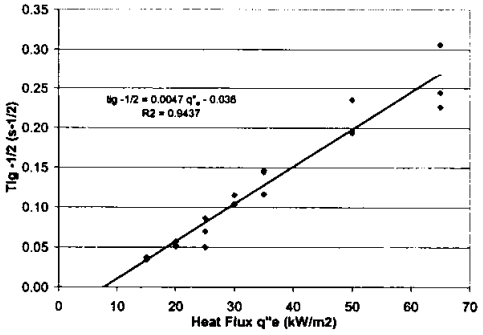

FIGURE 2 Ignition data LVL – Face Grain.

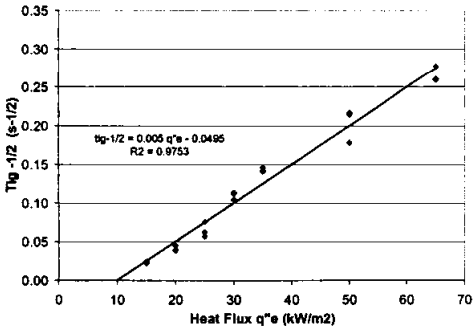

FIGURE 3 Ignition data LVL – Edge Grain.

		Face grain		Edge grain	
		MW [1]	DPK [2]	MW [1]	DPK [2]
Critical heat flux	q_{cr} (kW/m^2)	7.66	11.97	9.90	15.47
Surface ignition temperature	T_{ig} (°C)	251	341	294	380
Thermal inertia	kρc (kW/m2)^{2}s	1.080	0.558	0.678	0.393

Table 2: Estimated ignition properties, MW – Mikkola & Wichman [1], DPK – Delichatsios, Panagiotou & Kiley [2]

The critical heat flux, q''_{cr}, for the Mikkola & Wichman [1] correlation is obtained as the intercept of the best-fit regression line (see Figs 2 & 3) on the q''_e axis whereas for the Delichatsios, Panagiotou & Kiley [2] correlation q"cr is obtained as the intercept on the q''_e axis divided by 0.64. The ignition temperature can be estimated by solving the equation

$$\varepsilon \dot{q}''_{cr} = h_c\left(T_{ig} - T_\infty\right) + \varepsilon\sigma\left(T_{ig}^4 - T_\infty^4\right)$$

where hc = convective heat transfer coefficient

ϵ = emmissivity or absorptivity of the surface, and

σ = Stefan Boltzmann coefficient (= 5.67 x 10^{-11} kW/m^{2}K^4)

The thermal inertia, kρc, is determined from the slope of the regression line as

$$slope = \frac{2}{\sqrt{\pi k\rho c}\left(T_{ig} - T_\infty\right)} \quad \text{which can be rearranged to give} \quad k\rho c = \frac{4}{\pi}\left[\frac{1}{slope\left(T_{ig} - T_\infty\right)}\right]^2$$

CHARRING TESTS

Charring tests were carried out at three different scales; small blocks of LVL in the cone calorimeter, unloaded LVL beams in a pilot scale furnace, and a full-size loaded LVL beam in a large furnace.

Cone calorimeter tests

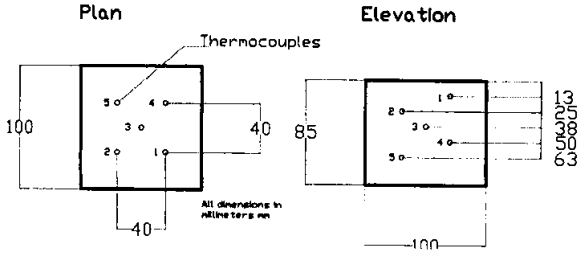

FIGURE 4 Layout and depth of thermocouples

Instrumented tests were carried out using the cone calorimeter to determine the char depths with time. Eighteen samples of LVL measuring 100 mm square and 85 mm deep were instrumented using thermocouples placed in the central region of the blocks and at depths of 13, 25, 38, 50 and 63 mm from the face as shown in Figure 4. These samples were exposed to a constant heat flux of 35, 50 or 65 kW/m^2. The char depths were determined by using the thermocouples to locate the 300°C isotherm which characterises the char front within the samples. From the results of these tests, the time for each thermocouple to reach 300°C was interpolated for each thermocouple depth and the results averaged. Figure 5 shows the plot of char depth against time for each grain orientation and each heat flux.

Eighteen additional un-instrumented LVL blocks of the same dimensions were exposed to the same heat fluxes for specific periods of time; 20, 40 & 60 minutes. At the end of the test time, the blocks were immediately removed from the heat source, the char removed, and remaining solid LVL measured and recorded. The un-instrumented results for each of the heat fluxes and

the different grain orientations have been included in Figure 5. It can be seen that very good correlations were obtained between the instrumented and the un-instrumented test results.

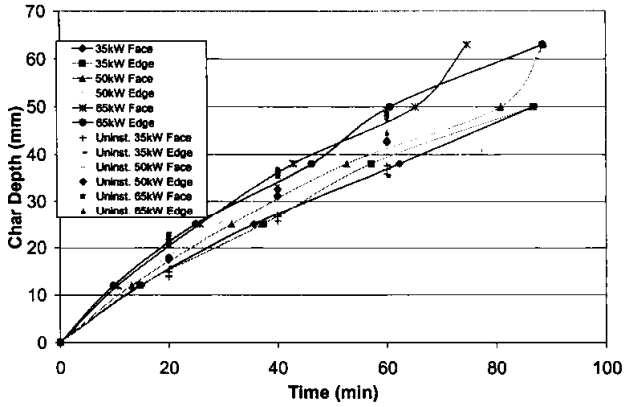

FIGURE 5 Instrumented & un-instrumented char depth results

For each of the 18 un-instrumented tests, the cumulative charring rate was calculated, and the average for each heat flux, including both grain orientations, was plotted against time as shown in Figure 6.

Pilot furnace tests

Three tests on instrumented LVL beams exposed to the standard ISO 834 design fire were carried out using the pilot furnace at the BRANZ Fire Research facility. In the first two tests, the beams were 105 mm x 300mm deep and 2200 mm long. In the third test, two 66 mm thick by 360 mm beams were glued together using resorcinol adhesive prior to being instrumented, to give a beam size 132 mm x 360 mm deep. The beams were instrumented at two sections along the beam with 12 thermocouples installed at depths of 18 mm and 36 mm as shown in Figure 7. The instrumented sections were at the 1/3rd points in tests 1 and 2, and at one 1/3rd point and the centre for test 3. The thermocouples at the corners were affected by fire exposure on two faces whereas all other thermocouples essentially had single face exposure.

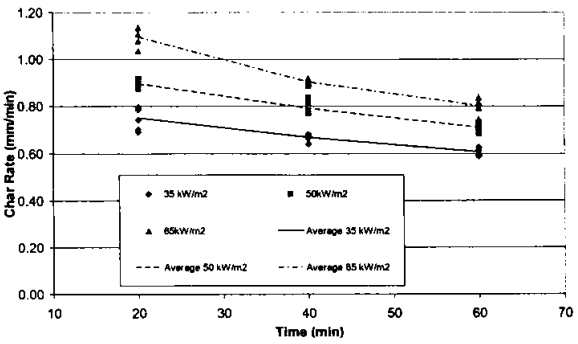

FIGURE 6 LVL Char Rate from un-instrumented cone calorimeter tests

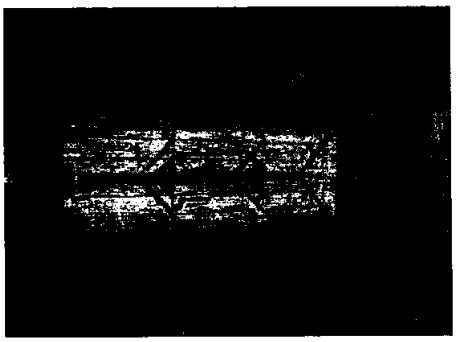

FIGURE 7 Instrumented Section LVL beam Pilot Tests

The results from the tests in the pilot furnace are shown in Figure 8 where they are compared with the results from the cone calorimeter tests. The current design charring rate of $\beta = 0.65$

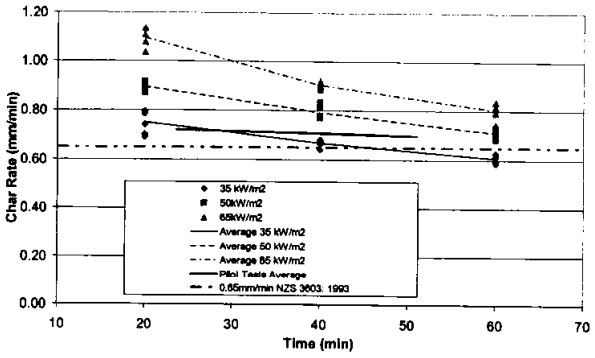

FIGURE 8 LVL char rate from the pilot furnace tests and the un-instrumented cone calorimeter tests compared with the NZS 3603 [4] charring rate.

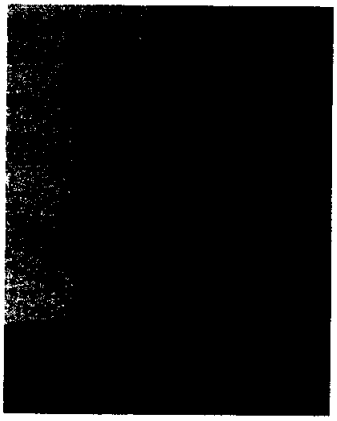

FIGURE 9 Beam cross-sections before and after testing in the pilot furnace.

mm/min from NZS 3603 [4] is also shown in the Figure. It can be seen from Figure 8 that the results from the pilot tests using the ISO 834 standard fire compare reasonably well with the results from the cone calorimeter using a heat flux of 35 kW/m^2. A typical beam cross-section after the fire test is compared with the original section in Figure 9.

The average char rate obtained from the 3 pilot tests varied from $\beta = 0.72$ mm/min at 18mm depth to $\beta = 0.70$ mm/min at 36 mm depth. The char rate of 0.72 mm/min was used to predict the behaviour of the load test in the full scale furnace.

From the pilot test results the time lag at each thermocouple between recording 100°C and 300°C was evaluated. This was used with the cumulative charring rate for that particular thermocouple to calculate the thickness of LVL at a temperature over 100°C. This layer of material is likely to have reduced mechanical properties because of the elevated temperatures. The estimated thickness of the temperature-affected material varied from 6 to 13 mm, with an average thickness of 9 mm. This information is useful because some design methods require an estimate of the thickness of zero-strength heated wood below the char layer [5]. The Australian timber code [6] states that a zero-strength layer thickness of 7.5 mm should be used, which is consistent with the findings of this study, recognising that not all of the wood between 100°C and 300°C will have zero strength.

Load-bearing tests

The 105 x 300 mm LVL beam that was used for this test is shown in Figure 10 prior to being loaded and exposed to the standard ISO 834 design fire, in the full-scale furnace at the BRANZ Fire Research facility.

The beam was subjected to an ambient temperature bending test to obtain a value for the Modulus of Elasticity (E). From the E value and by interpolation from the manufacturer's data [7] a value for the mean bending strength (f_b) was estimated.

The following properties were used for design of the 105 x 300 mm LVL beam:

Modulus of elasticity	E	=	11.2	GPa
Mean bending strength	f_b	=	55.6	MPa
Ultimate section capacity	ϕM_n	=	87.5	kN.m
Bending moment in test	M	=	34.1	kN.m

The beam was simply supported over a span of 4.4 metres and subjected to a central point load of 30kN applied by means of a hand-operated hydraulic jack. The load was kept approximately constant during the test and the mid-span deflection of the beam was recorded. Figure 11 shows the beam after the fire test, while Figure 12 shows the plot of applied load and central deflection.

FIGURE 10 LVL beam before the fire test

FIGURE 11 LVL beam after the fire test

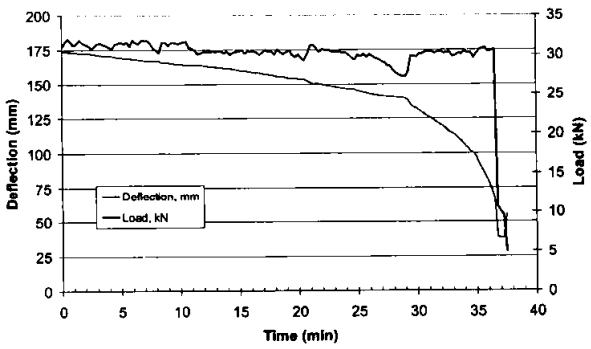

FIGURE 12 Load and deflection plots

It was observed through the observation ports of the furnace that charring of the surface did not begin until 3 or 4 minutes into the test. This delay in the onset of charring is not considered in most design methods which assume a constant rate of charring from the time of flashover [5].

DISCUSSION

Based on a charring rate of 0.72 mm/min. from the cone calorimeter and pilot furnace tests, the loaded beam was expected to fail after approximately 38 minutes. It can be seen from Figure 12 that the beam actually failed at about 37 minutes after the start of the fire. Measurements of the remaining cross-section approximately 7 minutes after the test finished confirmed that the rate of charring for the section was similar to the pilot tests.

Considering the above findings and observations the following two options for fire design of LVL can be considered:

- Design using the char rate β = 0.72 mm/min (found experimentally in this study) to calculate a reduced cross section which can be used with normal temperature properties (characteristic bending stress and modulus of elasticity) with no zero-strength layer of LVL below the char line.
- Design using the char rate β = 0.65 mm/min (complying with NZS 3603 [4]) to calculate a reduced cross section which can be used with normal temperature properties, with an allowance for a 7 mm to 9 mm zero-strength layer of LVL below the char line.

CONNECTION TESTS

Two different epoxy resins and one hybrid adhesive were used in the connection tests. One was the West System epoxy resin, designed for boat building purposes, used previously in several research programmes and in glulam construction for the Sydney Olympic Games. Another was the RE500 epoxy system supplied by the Hilti company of Germany, while the third was the HY150 hybrid adhesive also supplied by Hilti. This latter adhesive is a hybrid adhesive of urethane methacrylate and cement [8]. This hybrid adhesive is designed for use in concrete applications and the adhesion to timber was not expected to be as good as for the epoxies, but it was expected to have better fire resistance.

Cold connection tests

These tests were carried out to compare the performance of the different adhesives under normal operating temperatures. As previous tests had only used the West System epoxy it was necessary to test whether the alternative adhesives would give the necessary performance at ambient temperatures prior to evaluating their strength at elevated temperatures.

The samples used for this testing were LVL with a 105 x 105 mm cross-section and a length of 900 mm. All of the samples had the grain running in the longitudinal direction of the samples. A 20mm diameter hole was bored to a depth of 300mm into both ends of the samples with an auger bit. High strength (f_y = 680MPa) threaded steel rods were grouted into these holes using one of the three adhesives. Both ends of each specimen were grouted with the same adhesive.

After allowing the specimens to cure fully they were loaded to failure in tension, using an Instron testing machine. From these tests it was evident that both of the epoxy resins had similar performance, in terms of both failure modes and failure loads. With the hybrid HY150 adhesive system the behaviour was very different to the epoxies, with significantly lower ultimate strengths. Failures for the HY150 specimens occurred consistently at the glue/wood interface, with insignificant wood being attached to the glue after failure. This failure mode is in direct contrast to that of the epoxies where the failures were within the wood, with significant amounts of timber being removed with the rod.

As the failure of the HY150 sample did not occur within the wood there is also concern that apart from the lower strength, it may also have poorer durability and lead to premature failure under fluctuating moisture conditions.

Heated connection tests

For these tests, the specimens were placed in a large oven, heated to temperatures of 50, 75 or 100°C and left overnight to ensure a uniform temperature throughout. Immediately prior to testing, each specimen was removed from the oven and placed in the testing apparatus and tested to failure.

The loss of strength with increased temperature is shown in Figure 13.

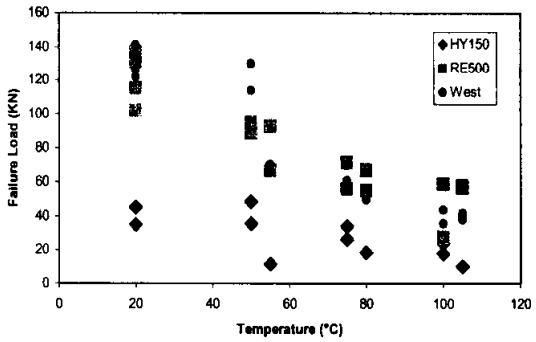

FIGURE 13 Comparison of adhesives at elevated temperatures

It can be seen that at 100°C the epoxy grouted samples have only approximately one third of their cold strength remaining. The hybrid HY150 samples also lost strength, although at a lesser rate than the epoxy grouted specimens.

At the higher temperatures the failure modes for the epoxy altered from being a timber failure (Figure 15) to being a failure within the epoxy (Figure 14). This mode of failure was evidenced in the 75°C and 100°C tests, but not at 50°C, where behaviour was consistent with that at ambient temperatures.

FIGURE 14 Failure of epoxy resin

FIGURE 15 Wood failure

Cooled connection tests

Consultants using epoxy grouted bars in designs are concerned as to whether the connection will regain its strength following a fire. In a moderate fire heavy timber members will often survive with only a small degree of charring. However, if the connections to these members will not regain their strength following a fire then the connections and possibly the timber members will have to be replaced.

In these tests, the specimens were heated to 75 or 100°C overnight, then removed from the oven and allowed to cool overnight before being tested at ambient temperatures.

These samples all showed the same behaviour as was seen from the original specimens tested at ambient temperatures. Failures for the epoxy samples all occurred within the wood, indicating that the bond between the wood and the adhesive was stronger than the timber itself, as seen in the cold tests. Whether the samples were heated to 75°C or 100°C made no difference to the strength recovery. Figures 16 through 18 compare the cooled strength of the samples to the strengths recorded during the oven tests for each of the adhesives. The distribution of the results from the cooled tests is clearly within the limits for the initial tests at ambient temperature.

For the hybrid HY150 samples the failure modes at all temperatures were the same, with failures occurring at the adhesive and timber interface. Strengths for these samples were back up to their normal strengths at ambient temperatures, similar to the behaviour of the epoxy resins.

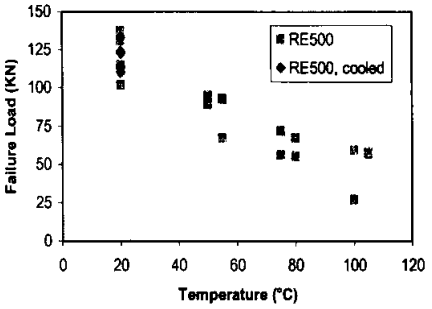

FIGURE 16 RE500 Tests

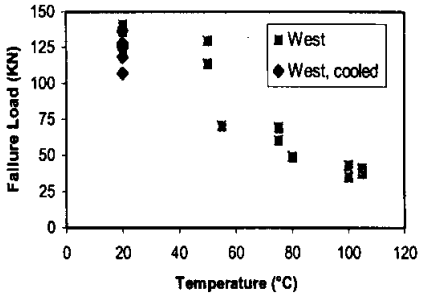

FIGURE 17 West System Tests

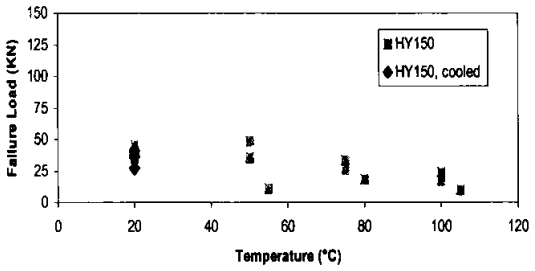

FIGURE 18 HY150 tests

Furnace load tests

A special furnace was designed to fit around the specimen while it was mounted in the testing frame. Two sizes of LVL, 105 x 105 mm and 63 x 63 mm, were tested under a constant load of approximately 20% of the predicted failure load, based on the previous tests. This 20% is estimated to be the load which the connection would be expected to carry during a design fire. This is based on the fire loads being roughly 30% of the gravity design loads and the design strength of the connection being roughly 70% of the average cold strength.

The furnace was heated by means of an electric element, with a constant current, which caused the LVL to ignite and char. The time taken to cause failure of the loaded connection was measured. Upon failure of the specimens they were removed from the furnace and immediately cooled to prevent further charring.

To calculate the predicted fire resistance of the connections, the failed specimens had the char layer scraped away to expose the residual cross section. From the dimensions of the residual cross section and the time of exposure, a rate of char can be calculated. This rate of char can then be compared to the results shown in Figure 8 to predict an equivalent time of exposure to the ISO standard fire which was used in the pilot furnace tests. Char rates found in the

connection tests are shown in Figure 19, it can be seen from these that they are significantly lower than the average 0.72mm/min found in the pilot furnace tests, under the ISO standard fire.

By dividing the char depths measured from the connection test specimens by the charring rate of 0.72 mm/min measured under the ISO standard fire a time of equivalent exposure and failure time can be found. This time is a prediction of the fire resistance of the connection and the conversion between the two can be seen in Figure 20.

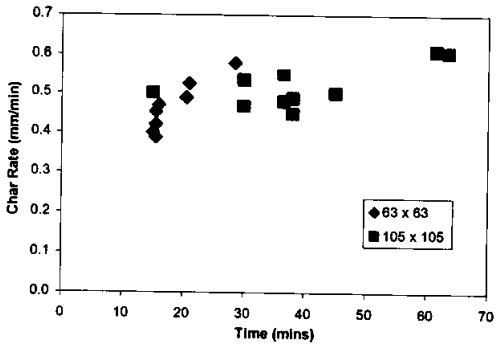

FIGURE 19 Char rates from connection tests

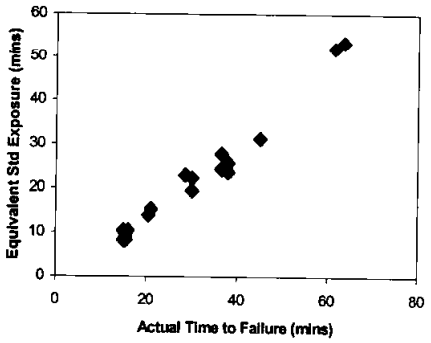

FIGURE 20 Expected time to failure in standard FRR test compared with results of connection tests.

DISCUSSION

In the furnace tests the protruding end of the steel rod was insulated to prevent heat being conducted up the steel bar and into the epoxy. If this heat transfer was not prevented then the epoxy would have heated up much quicker and failed sooner, because steel conducts heat at a much greater rate than wood. Where the connection between the rods is by way of an unprotected steel hub or connection plate [9], then the heat is likely to transfer through the steel components of the assembly into the timber much more quickly than the rates described here.

Although the fire performance of the epoxy grouted rods is poor, it should not be ruled out as a design option. The information in this paper makes it possible to design LVL structures with glued-in rods for fire resistance, provided that the expected loads at the time of the fire are considerably less than the design load in ambient conditions. Under the New Zealand Building Act and other national codes, single storey buildings under single ownershipand remote from property boundaries would typically not be required to have any fire resistance [10] which would allow these materials to be used in buildings such as portal frame warehouses, swimming complexes and public halls.

While the HY150 hybrid adhesive was seen to maintain its strength under fire exposure, particularly in the furnace tests, it is not considered to be a worthwhile substitute for epoxy resin as it has poor cold strength and the lack of adhesion to the timber makes its strength less consistent and also raises questions of its durability.

CONCLUSIONS

A series of ignition and charring tests was carried out on laminated veneer lumber (LVL) manufactured from radiata pine. The results were similar to those previously found for solid timber of the same species.

More investigations should be carried out to determine the effects of the delay in the onset of charring under exposure to post-flashover fire conditions, and also on the thickness and properties of the "zero-strength layer" below the char line.

A simple method for predicting the fire performance of radiata pine LVL exposed to post-flashover fires is to use the experimentally found char rate $\beta = 0.72$ mm/min to determine a reduced cross-section, and design using normal temperature properties without considering a heat-affected layer of wood below the char line.

For epoxy resins, considerable strength loss is observed once the temperature within the resin exceeds 50°C. This strength loss continues at higher temperatures, with the residual strength in the epoxy being reduced to around 30% of its cold strength at 100°C. For the hybrid HY150 adhesive the strength loss is less, but its poor adhesion to timber makes it unsuitable as a replacement for epoxy resin in this application.

With both the epoxy resins and the hybrid adhesive the strength losses were found to be recoverable upon cooling provided that the connection did not slip while it was heated. This means that structures fitted with these connections can be reused after a fire if the connection has not failed and there is sufficient unburnt timber remaining.

REFERENCES

[1] Mikkola, E. and Wichman I.S., On the Thermal Ignition of Combustible Materials., *Fire and Materials*, Vol. 14, 87-96, 1989.

[2] Delichatsios, M.A., Panagiotou, T.H. and Kiley, F., The Use of Time to Ignition Data for Characterizing the Thermal Inertia and the Minimum (Critical) Heat Flux for Ignition or Pyrolysis., *Combustion and Flame*, Vol. 84, 323-332, 1991.

[3] Ngu, Chu Kan, *Ignition Properties of New Zealand Timber*, Fire Engineering Research Report 2001/5, University of Canterbury, Christchurch, New Zealand, 1997.

[4] NZS 3603:1993, *Code of Practice for Timber Design*, Standards Association of New Zealand, 1993

[5] Buchanan, A.H., *Structural Design for Fire Safety*. John Wiley & Sons, Chichester, U.K, 2001.

[6] *Timber Structures, Part 4: Fire Resistance of Structural Timber Members*. AS 1720.4 - 1990. Standards Association of Australia, 1990.

[7] *LVL Properties Evaluation Documents*, CHH internal quality control data. Carter Holt Harvey Ltd, New Zealand.

[8] *HY150 Material Safety Data Sheet,* Hilti, 2000

[9] Thelandersson, S. and Larsen, H.J., (editors), *Timber Engineering*. John Wiley & Sons, Chichester, U.K, 2003.

[10] *Acceptable Solutions to the New Zealand Building Code, C/AS1*, Building Industry Authority, New Zealand, 2001.

DETERMINATION OF THERMAL PROPERTIES OF CONCRETE AND WOOD AT ELEVATED TEMPERATURE WITH TRANSIENT PLANE SOURCE

Bijan ADL-ZARRABI, Lars BOSTRÖM, Ulf WICKSTRÖM
SP Fire Technology, Box 857, SE-501 15 Borås, Sweden
bijan.adl-zarrabi@sp.se, lars.bostrom@sp.se, ulf.wickstrom@sp.se

ABSTRACT

Since full-scale fire testing of structural elements often is expensive it is beneficial to estimate the fire resistance by calculations. A first step is then to calculate the temperature in the fire-exposed structure before performing a fire test. The accuracy of such a calculation depends on the accuracy of the assumed material properties. Unfortunately, for many materials there is little published information on the material properties at elevated temperature.

The Thermal Plane Source (TPS) method is shown to be very promising for determination of thermal properties at room temperature as well as temperatures up to 700 °C. It has been used in the study for determining thermal properties of wood (spruce) and concrete. Thermal conductivity (λ) and thermal diffusivity (α) were determined simultaneously.

The measured thermal properties have been compared to values found in literature. The paper will also present results where calculations based on measured values compared with real fire tests measurements. The results are very encouraging showing that the TPS-method can very well be used for determination of thermal properties at elevated temperature.

KEYWORDS: *Thermal properties, thermal conductivity, thermal diffusivity, heat capacity, specific heat capacity, wood, particle board, concrete, transient plane source.*

INTRODUCTION

Thermal calculations can be needed in many different applications such as drying of wood or design of structures exposed to fire. In order to make valid predictions, reliable data of the physical and the mechanical properties of the material are required at elevated temperatures. There are several methods available for the determination of the thermal properties at ambient conditions but at elevated temperatures only a few methods can be applied. Furthermore, wood is an orthotropic material and thus the method must be capable to handle the anisotropy. The purpose of this paper is to introduce a new measuring technique, Transient Plane Source (TPS), for measuring of thermal properties of wood and concrete. The TPS methodology enables measurements of thermal conductivity and thermal diffusivity simultaneously at ambient as well as elevated temperatures. The can as a mater of fact be used for great variety of materials, e.g. metals and even liquids.

TRANSIENT PLANE SOURCE

Gustafson et. al have described the principal of using the TPS method [1, 2]. It is a transient technique for determining thermal conductivity and thermal diffusivity of materials. A flat source (sensor) is located between two specimen halves and acts as a heater as well as a detector of temperature increase. The flat plane source is insulated between two layers of Kapton or Mica. The thickness of the insulation is about 25 μm. The sensor insulated by Kapton can be used when measurements are made up to 200 °C and the Mica insulated sensor can be used for temperatures up to about 700 °C. The technique is in itself transient since it measures the temperature response when a predefined effect is applied to the heater. The sample must, however, have a uniform temperature before the measurement are made.

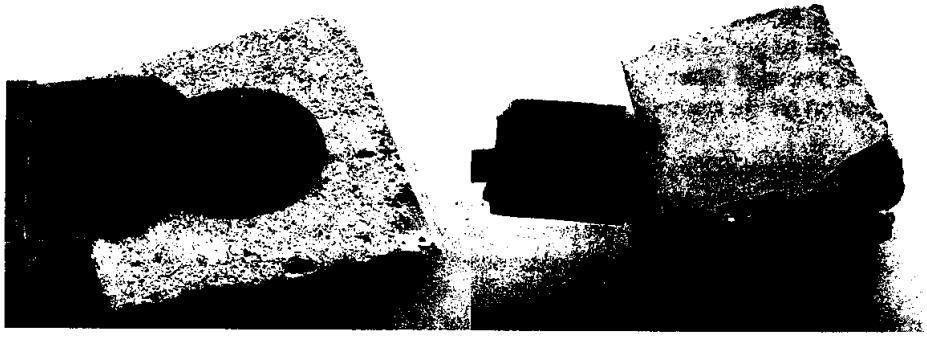

Figure 1. The TPS sensor is located between two specimen halves of concrete.

By using the measured temperature increase in the sample and the effect applied to the heater it is possible to solve the partial differential equation of heat transfer by using iterative methods and the thermal conductivity and thermal diffusivity can be obtained simultaneously. Furthermore, anisotropy can be handled by this method.

Thermal conductivities between 0.005-500 W/mK can be measured by using different sensors, level of power and time periods of transient measurements.

THERMAL PROPERTIES OF WOOD

Literature survey

Wood is an anisotropic cellular material with varying material properties. Due to the orthotropic nature of wood the determination of the thermal properties is complex. The thermal conductivity of wood in the radial direction is about 5 to 10 % greater than tangential direction and the conductivity in longitude direction is about 2.25-2.75 times the conductivity across the grain [3, 4]. Measured specific heat capacity given in literature of different wood species varies in the range of 1.0-3.0 kJ/kgK. The specific heat capacity of cellulose is about 1.55 kJ/kgK [3, 4, 5].

Furthermore, since wood is a hygroscopic material it will always contain more or less water. The amount of the water has a profound influence on almost all properties of wood, which also is the case for the thermal properties. Thus it is of great importance that the determined properties are given together with the actual moisture content. Also the temperature affects the thermal properties. Kollmann and Cote suggested equations (1) to (4) for calculation of the influence of temperature, moisture and density on the thermal properties of wood [3].

$$c_d = 1.114 + 0.0046 \cdot T \qquad (1)$$

$$c_w = (4.19u + c_d)/(1+u) \qquad (2)$$

$$\lambda = 0.000195 \cdot \rho + 0.025 \qquad (3)$$

$$\lambda_2 = \lambda_1(1 - 0.015(u_1 - u_2)) \qquad (4)$$

c_d is the specific heat capacity of dry wood in kJ/kgK and c_w is the specific heat capacity of wet wood. λ is the thermal conductivity in W/mK and ρ is the density in the range 200-800 kg/m^3. T [°C] is the temperature and finally u is moisture content by mass.

Eurocode 5, part 1-2, give informative values for the thermal properties at elevated temperatures [6]. These values do not consider different species, density, moisture content or the orthotropic behavior. Hence, the values given must be used with care as they may in practice vary considerably.

Test specimens

Thermal properties of Norway spruce (*Picea abies*) have been measured at different temperatures up to 150 °C. Two pieces of the material is needed for the measurement since the sensor is placed between these two pieces. In order to investigate anisotropic behavior five specimens (ten specimens halves) were prepared. The size of the specimens was 60x60x30 mm (length, width and thickness). The dry density was 485 kg/m^3. All specimens were taken from same piece of timber. The density was measured on one specimen only.

Measurements on anisotropic materials

The TPS has different toolboxes for measurements of the thermal properties. For the measurements on spruce the biaxial anisotropic toolbox has been used. In this toolbox the properties of

the material in one plane are assumed to be isotropic. In order to use this toolbox the specific heat capacity of the material must be known. Thus two separate measurements must be made for anisotropic materials, one for determination of the specific heat capacity, and one for determination of conductivity.

Volumetric specific heat capacity of wood is determined with TPS by using a special sensor. The sample is, during the measurement, kept inside a thermally insulated holder or enclosure made of a material with high thermal conductivity. The holder is exposed to a constant output of power from a sensor, which is permanently attached to the holder. During the heating the temperature is continuously recorded by following the resistance of the sensor.

Measurement results - Volumetric specific heat capacity

The volumetric specific heat capacity was measured with the special sensor for measuring specific heat capacity. It was determined on both a dried sample and on a sample with a moisture content of u = 9.5 %. The volumetric specific heat capacity was determined to 0.52 MJ/m^3K for the dry sample and to 0.74 MJ/m^3K for the sample with moisture content u = 9.5 %.

Measurement results - Thermal conductivity and thermal diffusivity

Conductivity and diffusivity were measured by using two different measuring set-ups. In the first set-up, specimens were prepared so that the surface of specimen that should be in connection with the sensor was cut in different orientations of the wood specimen. Three combinations of the contact surface were applied.

I. The contact surface is in the radial - tangential plane
II. The contact surface is in the radial - longitudinal plane
III. The contact surface is in the tangential - longitudinal plane

In the second set-up conductivity and diffusivity were measured by assuming that the difference of the thermal properties in tangential and radial direction are negligible. Thus, in these measurements wood is assumed to be an orthotropic material with two principal directions, the longitudinal direction (fiber direction) and the cross fiber direction. The anisotropic toolbox in TPS was used for determination of thermal properties. Since this toolbox require the specific heat capacity (χ) as input the measured values χ_{wet} = 0.74 MJ/m^3K and χ_{dry} = 0.52 MJ/m^3K were used.

The results of these measurements are presented in tables 1 and 2. The orientation of the sensor is according to these results essential for performing a correct measurement. The TPS method can handle orthotropic materials by placing the sensor in the radial - tangential plane of the specimen. The two other cases do not generate correct values.

Table 1. Thermal conductivity and thermal diffusivity of a wood with different orientation.

Orientation of sensor	Conductivity [W/mK]		Diffusivity [mm^2/s]	
	∥	⊥	∥	⊥
I	0.71	0.091	0.963	0.124
II	0.263	0.165	0.355	0.222
III	0.249	0.165	0.336	0.223

Table 2. Thermal properties at different temperatures as mean values of three to five measurements for each specimen.

Temperature [°C]	Conductivity [W/mK]		Diffusivity [mm^2/s]		Specific heat used as input [MJ/m^3K]
	∥	⊥	∥	⊥	
20	0.559	0.107	0.756	0.145	0.74
110	0.524	0.115	0.572	0.126	0.92
150	0.565	0.115	0.518	0.106	1.09

Comparison of results with literature - Volumetric specific heat

Volumetric specific heat can be calculated according to equations (1) and (2). The measured results and calculated results as well as data from the Wood Handbook [4] are presented in table 3.

Table 3. Specific heat of dry wood and wood with moisture content u = 9.5 %.

	Specific heat (dry) [MJ/m^3K]	Specific heat (wet) [MJ/m^3K]
Present study	0.52	0.74
Kollmann and Cote [3]	0.59	0.74
Wood Handbook [4]	0.55	0.69

Measurements on spruce are shown as well as the relation given by Kollmann and Cote [3]. The comparison indicates that the TPS method is a reliable method for determination of specific heat of the wood and wood based materials.

Comparison of results with literature - Thermal conductivity

Table 4 show a comparison on measurements made on two specimens with values found in literature. Both conductivity and diffusivity is higher in the longitudinal direction compared with Kollmann and Cote [3]. In the perpendicular direction the measured values of the conductivity coincide well with the literature, while in the other directions the values differ considerably.

Table 4. Comparison of thermal conductivity and thermal diffusivity of two wood specimens and values found in literature at 20 °C.

	Conductivity [W/mK]		**Diffusivity [mm²/s]**	
	∥	⊥	∥	⊥
Specimen A	0.559	0.107	0.756	0.145
Specimen B	0.495	0.103	0.668	0.140
Kollmann and Cote [3]	0.261	0.110	0.35*	0.149*
Wood Handbook [4]	-	0.108	-	-

* Calculated values

THERMAL PROPERTIES OF CONCRETE

Concrete is a heterogeneous material with material properties that can vary within a large range depending on concrete quality, age, moisture content etc. Also the thermal properties of concrete may vary strongly depending on recipe and different type of constituents. Thus, in order to be able to make accurate temperature calculations and predictions it is essential to determine the thermal properties of appropriate concrete qualities i.e. thermal properties.

Thermal conductivity, thermal diffusivity and specific heat capacity, have been measured with the TPS method at elevated temperatures. The specific heat capacity of concrete has also been measured by Modulate Differential Scanning Calorimeter (MDSC) in order to compare to the results.

Specimens and temperature levels

Specimens of a self-compacting concrete with polypropylene fibers were prepared from cubes with the dimensions 150 x 150 x 150 mm^3. These cubes were cast at the same time as the casting of large concrete elements that later were fire tested. The recipe of the concrete is presented in table 5. Further more, specimens of cement paste with a water/cement ratio 0.41 were prepared in order to measure thermal properties of pure cement paste.

The size of the specimens to be used for the TPS measurements was 70 x 70 x 25 mm^3. According to the manual for the TPS the width, length and thickness of the samples should be at least 60 x 60 x 20 mm^3. The specimens were dried before being tested. Thermal properties of the concrete were measured at six temperature levels, 20, 100, 200, 300, 500 and 600 °C.

When measuring the specific heat by MDSC the concrete must be in powder form. Hence samples of the concrete were moulded. Specific heat of the concrete powder was measured at a number of temperature levels from 20 °C up to 480 °C.

Table 5. Concrete mixture.

Dry materials (kg/m^3)		
Cement	Slite (CEM I)	380.76
Limestone filler	Limus 25	119.24
Fine gravel	0-8 Sätertorp	899.96
Coarse gravel	8-16 Sätertorp	721.90
Plasticizer*	CemFlux Prefab	5.73
Plasticizer	(% of C+F)	1.15%
Fibres	Fibrin 18μm	1.0
Water/moisture (kg/m^3)		
Water		149.69
Dilution water		10.02
Moisture in material		37.54
w/c-ratio		0.518

* Plasticizers are given as weight in diluted form, as delivered. The moisture is included in "Moisture in material" in the table.

Measurement results - Specific heat

Specific heat of two specimen of the concrete were measured with TPS at elevated temperature and the results were compared with the results obtained by (MDSC).

The results presented in figure 2 and table 6 show that the measured values by TPS-method are in good agreement with MDSC method. However, the measured value of sample (II) by TPS deviates strongly from the other measurements. A possible reason for this could be the heterogeneity of concrete. In the other words sample (II) was not representative sample of the concrete for TPS measurements and measured value of sample (II) presents specific heat of the cement paste or the aggregate. In order to investigate this possibility specific heat of the cement paste were measured by TPS. The result of the measurement is compared to the specific heat of sample (II). The cement paste was prepared with 0.41 water-cement ratio.

Table 6. Specific heat measured with TPS and MDSC.

Temperature	TPS (I)	TPS (II)	MDSC (I)	MDSC (II)
90	1.02	1.20	1.04	0.96
110	1.05	1.28	1.05	0.99
200	1.08	1.37	1.14	1.09
300	1.13	1.40	1.21	1.18
400	-	-	1.28	1.26
480	-	-	1.32	1.29
500	1.23	1.77	-	-
600	1.44	1.96	-	-

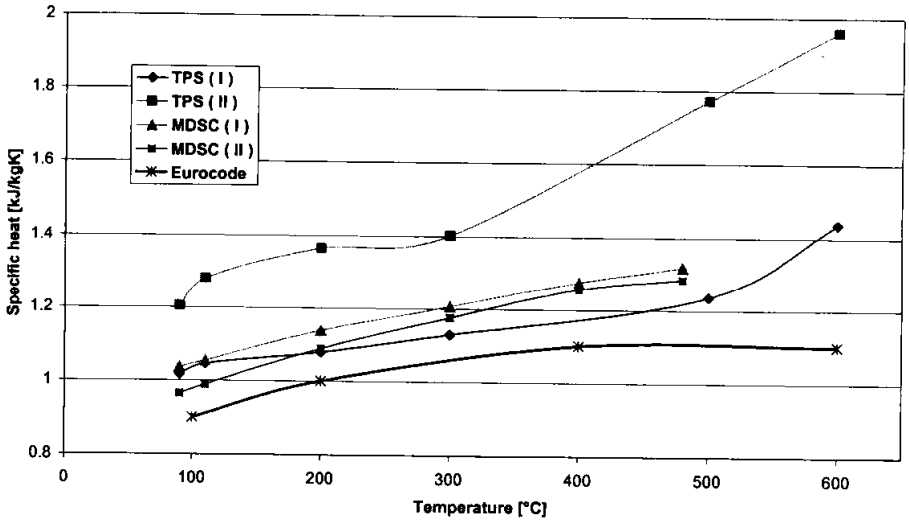

Figure 2. Specific heat measured with TPS and MDSC as well as values fromn by Eurocode.

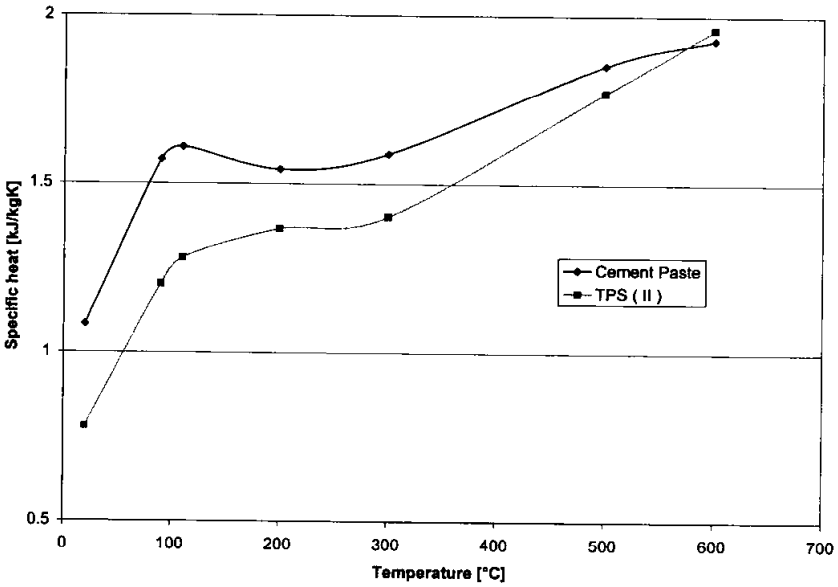

Figure 3. Specific heat of cement paste and specific heat of sample (II) measured by TPS.

The results presented in figure 3 shows that the measured specific heat of sample (II) by TPS is very close to specific heat of the cement paste. Thus, the results of this sample are excluded concerning further analyses.

Measurement results - Thermal conductivity

Thermal properties, thermal conductivity and thermal diffusivity, of the concrete and the cement paste were measured at six temperature levels, 20, 100, 200, 300, 500 and 600 °C by using TPS method. They were even determined under cooling from 600 to 20 °C. The measured thermal conductivities and the corresponding values for thermal conductivity given in Eurocodes [9] are presented in figure 4 and 5.

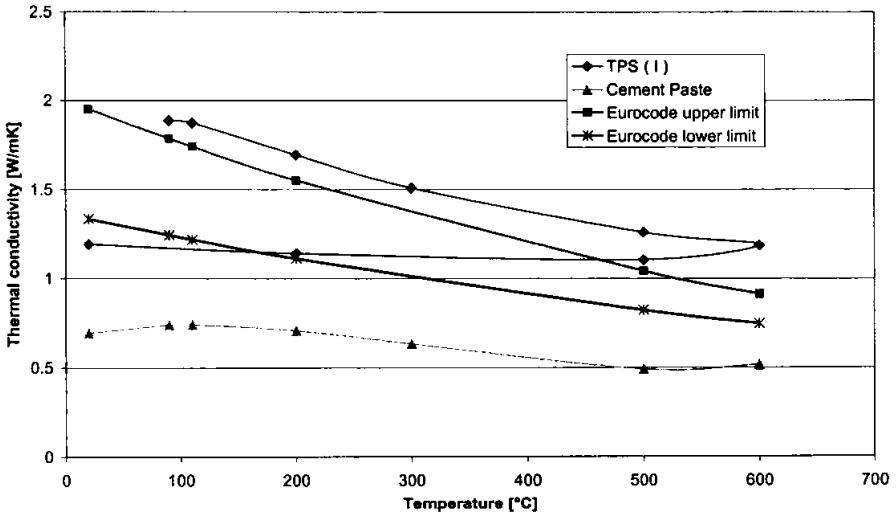

Figure 4. Thermal conductivity of concrete and cement paste measured by TPS method.

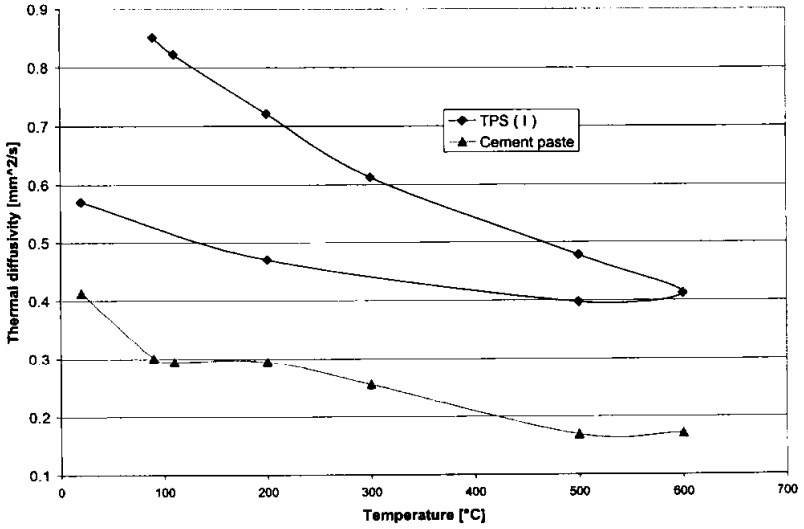

Figure 5. Thermal diffusivity of concrete and cement paste measured by TPS method.

Comparison of results with literature

The type of cement and aggregates has a large influence on the thermal properties. Water-cement ratio is another important parameter that has large influence on the thermal properties. Thus, it is difficult to compare the results of these measurements with the results presented in literature. Anyhow, the thermal conductivity of the cement paste and the concrete is compared with reported data, see tables 7 and 8.

Table 7. Comparison of the measured thermal conductivity of the cement paste and reported data.

	20 °C	100°C	200°C	500°C	600°C
TPS, Cement paste, w/c=0.41	0.7	0.7	0.7	0.5	0.5
Haramathy[10], Cement paste w/c=0.33	0.7	0.7	0.7	0.5	0.5

Normally higher water-cement ratio in cement paste leads to lower thermal conductivity. Thus, the measured thermal conductivity by TPS should be slightly lower than Haramathy[10].

Table 8. Comparison of the measured thermal conductivity and thermal diffusivity of the concrete and reported data.

Thermal conductivity [W/mK]					
	20°C	100°C	200°C	500°C	600°C
TPS, w/c=0.52	1.88	1.69	1.51	1.25	1.18
Harada[11], w/c=0.6	1.64	1.61	1.42	1.17	1.06
Thermal diffusivity [mm^2/s]					
	20°C	100°C	200°C	500°C	600°C
TPS, w/c=0.52	0.84	0.72	0.61	0.48	0.41
Harada[11], w/c=0.6	0.77	0.64	0.53	0.36	0.33

Measure thermal conductivities in this study are higher than the reference [11]. It can depend on the water/cement ratio 0.52 of the concrete in this study that is lower than the concrete in [11]. Lower cement ratio gives lower porosity that means the air, which has a low thermal conductivity, replaces by cement paste or aggregates, which has higher thermal conductivity than air. Thus, lower porosity gives higher thermal conductivity.

Temperature distribution over cross section of the concrete plate

Fire test was performed on a concrete plate 200 mm thick, 1200 mm (width) and 1800 mm (length). Standard time-temperature curve was used. The temperature distribution over cross section of the concrete plate was measured during the fire test at various depths using thermocouples. The corresponding temperatures were calculated with the finite element codes TASEF [12]. The measured thermal properties by TPS were used as input. The results of the measurements and calculations are presented in figure 6. In order to eliminate the inaccurate surface condition (boundary condition) in calculation the measured temperature by first thermocouple (about 10 mm in the concrete from the exposed side) was used as the reference point

(boundary condition) in calculations. Calculations are carried out for two-moisture content (u) namely 4.8 % and 0 %.

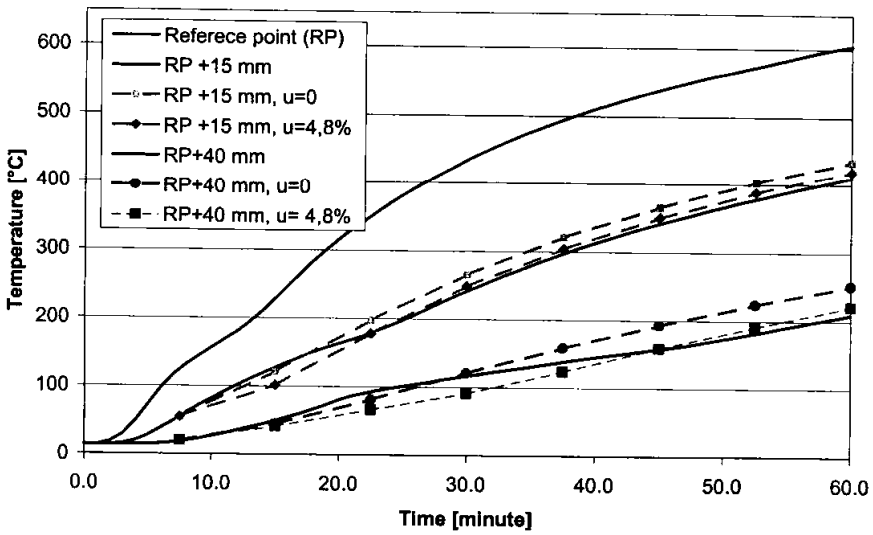

Figure 6. Measured and calculated temperature of the concrete plate at 25 and 50 mm depth from exposed side.

CONCLUSIONS

The TPS method is a fast, cost effective method for measurement of the thermal properties of materials. The method can handle measurements on anisotropic materials at temperatures up to 700 °C. The objective with the present study was to see if the method is applicable to wood and concrete, and to see whether there are any limitations. From the present study can the following conclusions be drawn:

Measurements on wood

- Thermal conductivity, diffusivity and specific heat can be measured with TPS on wood and wood based materials.
- For anisotropic materials such as wood must a toolbox for anisotropic materials be used which means that the specific heat must be determined separately.
- The measured values are of the same magnitude as the ones found in literature.
- The measured conductivity and diffusivity for wood in the radial - tangential plane is almost equal to the values found in literature.
- The measured conductivity and diffusivity for wood in the longitudinal direction is higher compared to the values found in literature.

- The measured effect of temperature on the thermal properties where approximately the same as shown in literature.

Measurements on concrete

- Thermal conductivity, diffusivity and specific heat of concrete can be measured with TPS method.
- In order to obtain more accurate measurements, larger samples, than used in this study, (larger TPS-sensors) should be used.
- Measured thermal properties of the concrete in this study are in good agreement with the values on thermal properties found in literature.
- The comparison between the measured temperatures in a concrete plate exposed to fire and the corresponding calculated temperatures show a very good agreement.

REFERENCES

[1] Gustafsson, S.E. & Long, T., "Transient Plane Source (TPS) Technique for Measuring Thermal Properties of Building Materials," *Fire and Material,* Vol. 19, 1995, pp. 43-49.

[2] Gustafsson, S.E., "Transient Plane Source (TPS) Technique for Thermal Conductivity and Thermal Diffusivity Measurements of Solid Materials," *Rev. Sci. Instrum, 62(3),1991, pp 797-804.*

[3] Franz F.P. Kollman, Wilfred A.Cote, "Principles of Wood science and Technology",1968

[4] Forest Products Laboratory, Wood handbook: Wood as an engineering material. Gen. Tech. Rep. FPL-GTR-113. Madison, WI: U.S. Department of Agriculture, Forest Service, Forest Products Laboratory, 1999.

[5] Frank P. Incropera, Fundamentals of Heat and Mass Transfer, John Wiely&Sons, 1981

[6] Eurocode 5 - Design of Timber Structures, Part 1-2, General Rules-Structural Fire Design, Version 8, Annex B(informative) Thermal and Mechanical properties, 2001

[7] Detail Summary of a Result from NIST Building Materials Database, Version 1.0, Summary for ID 1833

[8] Lars Boström, Innovative self-compacting concrete-Development of test methodology for determination of fore spalling, SP report 2004:06, Sweden 2004

[9] Eurocode 2 - Design of Concrete Structures, Part 1-2, General Rules-Structural Fire Design.

[10] T Z Haramathy, Fire Safety Design & Concrete,1993

[11] Flynn, D.R., "Response of High performance Concrete to Fire Condition, Review of Thermal Property, Data and Measurement Technique," *NIST GCR 99-767.*

[12] Ulf Wickström, TASEF User's Manual, Swedish National Testing and Research Institute, Sweden 1989

MODELLING THE FIRE BEHAVIOUR OF FRP-STRENGTHENED REINFORCED CONCRETE COLUMNS

Luke BISBY
Dept. Of Civil Eng., Queen's Univ., Kingston, ON, Canada
bisby@civil.queensu.ca

Venkatesh KODUR
Fire Risk Management, Bldg. M-59, National Research Council, Ottawa, ON, Canada
venkatesh.kodur@nrc-cnrc.gc.ca

Mark GREEN
Dept. Of Civil Eng., Queen's Univ., Kingston, ON, Canada
greenm@civil.queensu.ca

ABSTRACT

Rehabilitation and strengthening of reinforced concrete (RC) structures have changed significantly in recent years, due in large part to the introduction of fibre-reinforced polymers (FRP) as economical and effective infrastructure materials. FRPs are currently gaining acceptance in a wide range of civil engineering applications, including the external flexural repair of RC beams and slabs, and axial strengthening and ductility enhancement of RC columns, both of which can be achieved by bonding FRP plates and sheets to the exterior of the members. To date, the use of FRP materials for repair of RC structures has been limited primarily to bridge and transportation structures, while relatively few large scale applications have been conducted in buildings.

One major factor preventing the widespread use of FRP materials in buildings, where fire resistance criteria must satisfied, is the lack of information available on the fire performance of FRP materials in general, and on the overall behaviour of FRP-strengthened concrete members during fire. Since FRP materials are sensitive to the effects of elevated temperatures, there are a number of significant concerns that must be considered with respect to the fire performance of

FRP-strengthened members. These concerns include strength and stiffness degradation at high temperature, and loss of bond. To address these concerns, an ongoing collaborative research project is being conducted by researchers at Queen's University, Canada, and the National Research Council of Canada in conjunction with various industrial partners, to study the effects of fire on concrete slabs, beams, and columns strengthened with externally-bonded FRP materials.

This paper presents details and results of a numerical model developed to simulate both the heat transfer behaviour and load-carrying capacity of FRP-wrapped and insulated RC columns in fire. The model that has been developed is unique in that it accounts for the variation in thermal and mechanical properties of the columns' constituent materials with temperature, including FRP. In addition, the model accounts for the confining effect of a circumferential FRP wrap on the stress-strain characteristics of the concrete. The model's predictions are compared against results from full-scale fire tests and are shown to agree satisfactorily.

KEYWORDS: *fire resistance, fibre reinforced polymers, columns, reinforced concrete, strengthening, numerical modelling.*

INTRODUCTION

Fibre reinforced polymers (FRPs) have, in the last fifteen years or so, become increasingly popular as materials for externally-bonded repair systems for deteriorated or under-strength reinforced concrete (RC) members. One application for which FRPs have shown significant promise, and have indeed been used in hundreds of field applications around the world, is as external confining reinforcement for RC columns [1]. In this application, unidirectional FRP materials consisting of either glass or carbon fibres and an epoxy polymer adhesive/matrix are bonded, generally in the circumferential direction, to the surface of an existing concrete member. Research has shown that FRP wraps are effective at increasing both the strength and ductility of RC columns. The mechanisms of FRP confinement and the various factors influencing design of FRP-wrapped concrete members are now relatively well-understood [1], and design guidelines are currently available for their use in many countries [2, 3, 4, 5].

However, with new and innovative structural systems come a host of associated factors that require investigation. For FRP, one primary concern is that exposure to high temperatures, as would be expected during a building fire, could lead to failure of the FRP repair system and premature collapse of the strengthened member. Indeed, recently published research gap analyses on the use of FRP in structural applications have identified fire performance as a critical factor requiring study before FRP can be used with confidence in strengthening applications in buildings [6, 7].

To address concerns associated with the fire performance of FRP repair systems for concrete, a comprehensive collaborative research program is currently underway at the National Research Council of Canada in conjunction with Queen's University, the Networks of Centres of Excellence on Intelligent Sensing for Innovative Structures (ISIS Canada), and industry partners Fyfe Co., San Diego, CA and Watson Bowman Acme Corp., Cleveland, OH. As part of this study, full-scale fire tests have been conducted on loaded FRP-wrapped and insulated circular

RC columns, and numerical models have been developed to simulate their behaviour in fire. This paper presents details of the numerical models that have been developed to date, and verifies these models against test data obtained during the current research program as well as data available in the literature.

BACKGROUND

It is now well recognized that both the strength and ductility of concrete compressive members can be greatly enhanced using transverse FRP wraps [1]. The observed increases in strength and ductility can be attributed to the fact that the FRP wrap generates a confining pressure on the dilating concrete core when the column is subjected to compressive load. This places the concrete in a state of triaxial stress and increases both the ultimate strength and strain of the concrete by reducing shear stresses and controlling crack initiation. It is evident that these increases in strength and ductility depend primarily on the mechanical properties of the FRP wrap, which may be severely degraded at a high temperature. Figure 1 shows typical axial compressive stress-strain behaviour for circular concrete columns incorporating steel-reinforcing spirals or FRP wraps.

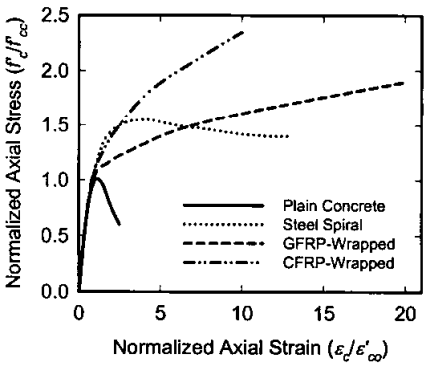

FIGURE 1 : Typical effects of FRP confinement on circular reinforced concrete columns [8].

The mechanical and bond properties of FRP materials deteriorate rapidly above their polymer matrices' glass transition temperature (T_g). Thus, the structural performance of FRP-wrapped columns during fire needs to be studied before these strengthening systems can be used with confidence in buildings. Few studies investigating the fire performance of FRP-strengthened concrete members exist in the literature. A series of full-scale fire tests have been conducted in Europe to investigate the fire performance of flexurally FRP-strengthened and insulated concrete beams and slabs [9] and have demonstrated the sensitivity of FRP strengthening systems to temperatures greater than their matrix T_g. However, no research has yet been reported studying performance of FRP-wrapped concrete columns at a high temperature.

FIRE ENDURANCE

The fire endurance of RC columns has traditionally been defined in terms of their load-carrying capacity during exposure to a standard fire. In North America, the standard fire is defined by ASTM E119 [10] or CAN/ULC S101 [11]. Columns are required to carry their full unfactored service load for the required fire duration, which is generally between two and five hours,

depending on the type of building and its use and occupancy. Thus, the fire endurance of FRP-wrapped columns is considered herein to be defined in terms of the columns' ability to carry their service load during fire, regardless of whether the FRP has exceeded its matrix T_g. It is important to note that there are a number of environmental fire hazards associated with combustion of FRP materials that must be considered when these materials are considered for use in buildings, although these are not discussed in detail here.

MODELS

Full-scale fire tests are relatively time consuming and costly to perform, and while the current study includes fire tests on insulated FRP-wrapped RC columns, it was desired to develop numerical models that could be verified based on the test results and subsequently used to conduct parametric studies to investigate the effects of a number of column parameters on member behaviour in fire. Once validated, the models can also be used to provide design guidance to engineers wishing to implement FRP strengthening applications in buildings.

The numerical models that have been developed are similar in methodology to those developed previously by researchers at the National Research Council of Canada [12]. They consist of a coupled heat transfer/strain equilibrium analysis which can approximate both the axial crushing and/or buckling strength of unwrapped, FRP-wrapped, and insulated FRP-wrapped circular concrete columns during exposure to the standard fire. The models are unique in that they have been extended to include the effects of both the FRP wraps and supplemental insulation on heat transfer, and in that they account for the effects of the variable confining pressure applied by an FRP wrap on the crushing or buckling strength of a concrete column during fire.

Heat transfer model

The heat transfer model has been developed using a finite difference methodology in which the column is divided into a series of ring elements, as shown schematically in Figure 2. For each ring element an energy balance is formulated, leading to a series of equations that describe a relatively straightforward one-dimensional explicit finite difference analysis. The boundary condition at the surface of the column is treated by assuming that heat transfer is due to radiation only, an assumption which has been used successfully in the past [12]. The equations have been derived in a similar fashion as has been presented previously [12] and the details are omitted here.

The effect of moisture in the concrete on the heat transfer within the member is accounted for by assuming that evaporation begins in a ring element when its temperature reaches 100°C, and that all heat subsequently supplied to the element is used for dehydration until all of the moisture has evaporated. Thus the temperature in an element remains constant at 100°C until all the water has evaporated. The analysis does not currently account for movement of moisture within the pore structure of the cement paste, nor does it consider the potential for thermally-induced pore pressure build-up or spalling. The member is assumed to be infinitely long, and the effects of

reinforcing steel on the heat transfer within the member are assumed to be negligible. The analysis accounts for the variation in thermal properties of all materials involved with temperature, using relationships discussed in detail below.

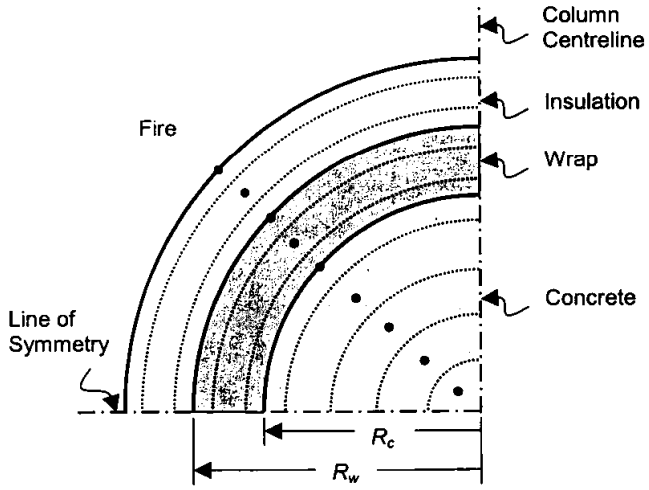

FIGURE 2 : Idealized discretization of insulated FRP-wrapped column for heat-transfer analysis.

The column is assumed initially to be at room temperature. The heat transfer equations are then used to step forward through time and to determine the spatial and temporal temperature distribution in the column, at any location, based on the thermal properties and temperatures of the adjacent elements at the previous time step. In this manner, the complete temperature history throughout the column can be obtained.

Load capacity model

The load capacity of an FRP-wrapped column during exposure to fire depends on the stress-strain behaviour of the concrete in the cross-section, which in turn depends on the temperature of the concrete at that particular location and time and on the lateral confining pressure applied by the FRP wrap. However, the confinement pressure depends also on the temperature of the wrap (temperature strongly influences the wrap's mechanical properties) and on the lateral dilation of the concrete. Thus, an iterative analysis is required.

The load capacity of the column during fire is calculated both for the axial crushing strength and the buckling strength. The buckling strength, which generally governs for members that are likely to be encountered in practice, is calculated using a procedure similar to that suggested by Lie and Celikkol [12] for conventionally-reinforced concrete columns, wherein the column

cross-section is divided into a series of annular elements, as shown in Figure 3. Neither the FRP wrap nor the insulation is assumed to provide any direct contribution to the axial strength of the column. However, the effect of the confinement provided by the FRP is included in the analysis using an iterative confinement model.

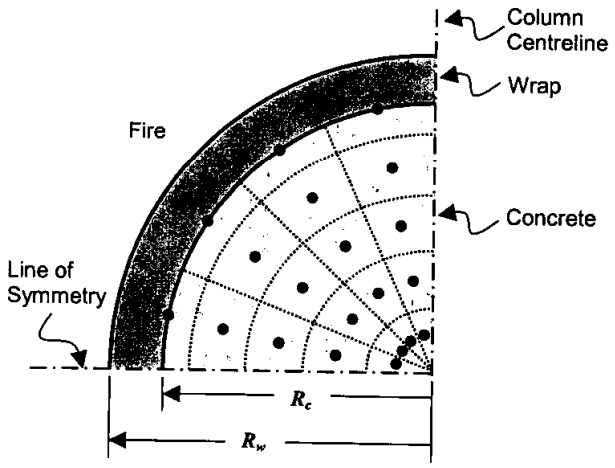

FIGURE 3 : Idealized discretization of an insulated FRP-wrapped column for buckling strength analysis.

For each element in the column's cross-section, the temperature, stress, and strain are assumed to be represented by those at the centroid of the element. The axial strain that causes stress in any element is equal to the sum of the free thermal strain, the bending strain, and the column's average axial strain, since all elements are subjected to both axial and flexural loads (in the buckling analysis). Once the strain in each element is determined, its stress-strain characteristics at its current temperature, determined using an iterative Spolestra and Monti [8] confinement routine in combination with concrete thermomechanical subroutines suggested by Lie [13] for unconfined concrete, can be used to determine the element's stress. In this manner the elemental force due to each element or reinforcing bar under some axial compressive load can be obtained.

The curvature of the column is assumed to vary linearly from the inflection points to mid-height, as shown in Fig. 4, so for any assumed curvature the mid-height deflection of the column can be calculated (refer to Fig. 4). At each instant in time, the overall axial strain in the column is varied until the internal moment at mid-height is equal to the external moment due to the product of applied load and mid-height lateral deflection.

To facilitate the numerical analysis, an initial eccentricity of the axial load must be assumed. In the current study, this eccentricity has been assumed as $e_o = 15 + 0.03d$ (mm), where d is the column diameter, in accordance with the minimum eccentricity recommended by ACI 318 [14] for conventional RC columns.

By repeating the above procedure for increasing curvatures, load-deflection plots can be obtained for a range of times during exposure to fire. From these plots, the maximum load capacity of the column can determined, and a plot of load capacity versus fire exposure time can be developed (Fig. 9, for example). The above model can also be used to predict the axial deformation of circular FRP-wrapped RC columns during fire, as well as their pure axial (crushing) strength. A flowchart showing the overall program logic is shown in Figure 5, and a complete discussion of the load capacity analysis is given by Bisby [15].

FRP Confinement Model

A unique aspect of the numerical model described herein is that it accounts for the effects of FRP confinement on the strength of FRP-wrapped RC columns exposed to fire. The confinement effect is incorporated into the analysis using a modified version of an iterative confinement procedure developed by Spolestra and Monti [8].

During fire, the mechanical properties of the concrete in the column and the FRP wrap, both required as inputs for the Spolestra and Monti confinement routine, are reduced. In addition, the concrete's properties are non-uniform over the column cross-section due to thermal gradients. Thus, an extension of the confinement model was developed to account for the damaging effects of fire on the properties of both the concrete and the FRP.

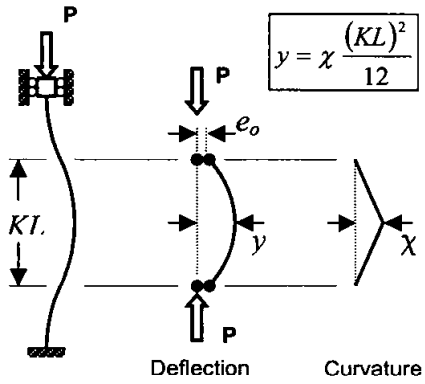

FIGURE 4 : Assumed variation in curvature for buckling analysis.

With the overall axial strain in the concrete assumed, and the temperatures throughout the cross-section known, the maximum unconfined concrete stress and strain for each ring of the column, and the modulus and ultimate tensile strength of the wrap (based on its average temperature) are obtained from thermomechanical subroutines. These mechanical properties are used as inputs for the Spolestra and Monti model, and the overall confining pressure is determined. Once the confining pressure is known, it can be used to modify the stress-strain characteristics of the concrete in each ring of the column, also using the Spolestra and Monti confinement routine, as required for the buckling analysis discussed previously.

The confinement model, as implemented in the current analysis, assumes a constant confining pressure at all points over the column's cross-section. Tests have indicated that, for columns subjected to both axial and flexural loads, a bonded FRP wrap actually provides a higher level of confinement in the compressive flexural regions of the column. The assumption of a constant confining pressure is thus conservative.

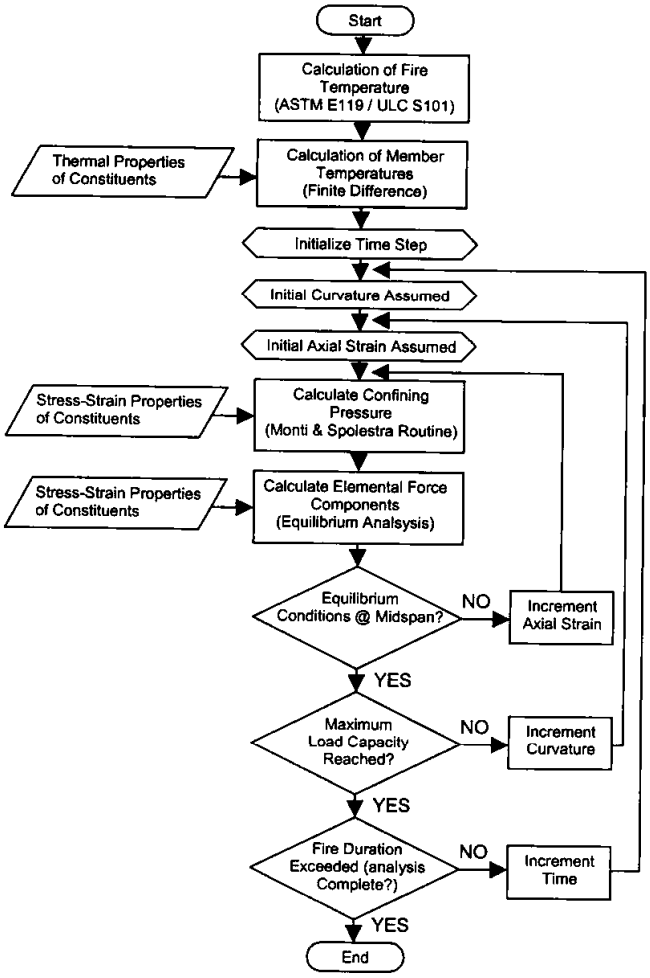

FIGURE 5 : Flowchart showing the overall program logic for buckling strength analysis.

MATERIAL PROPERTIES AT ELEVATED TEMPERATURE

For the above models to provide accurate predictions of the heat transfer within, and the load capacity of insulated FRP-wrapped concrete columns, a detailed knowledge of the variation in both the thermal and mechanical properties of the constituent materials with temperature is required. For concrete and steel, thermal and mechanical behaviour at a high temperature have been studied extensively in the literature. For the purposes of the current analyses, the variation in thermal and mechanical properties of steel and concrete with temperature has been assumed based on mathematical relationships suggested by Lie [13].

In contrast to steel and concrete, the thermal and mechanical properties of FRP materials at a high temperature have not been extensively studied, particularly for FRPs used in infrastructure applications. In the current analysis, the thermal properties of FRPs have been assumed to vary as suggested by previous researchers [16], who performed tests on a specific carbon/epoxy FRP that has been used in aerospace applications. The resulting assumed variation in thermal properties of FRP is shown in Figure 6.

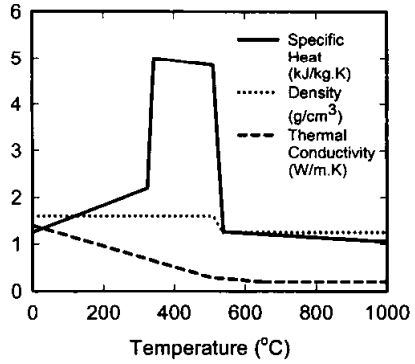

FIGURE 6 : Assumed variation in thermal properties of FRP with temperature [16].

The variation in mechanical properties of FRPs with increasing temperature is also poorly understood, and, because of the enormous variety of FRP materials currently available in industry, it is difficult to arrive at generalizations with respect to their high temperature behaviour. For the purposes of the current analysis, a series of semi-empirical analytical relationships were derived based on least-squares regression analysis of high temperature tensile strength data reported in the literature. These data were obtained from tests conducted on a variety of carbon and glass FRP materials, and in many cases the specific composition and properties of the FRPs remains unknown. The analytical relationships assume that the behaviour can be described by sigmoid functions, as suggested by previous authors [17]. The resulting assumed variation in strength and stiffness of carbon and glass FRP materials are given in Figure 7, where significant scatter is evident in the data. Tensile tests at high temperature on the specific FRP materials used in the current study will be required to more confidently validate the numerical models. In addition, the current analysis makes no attempt to specifically account for deterioration of the FRP-concrete bond at high temperature, which is likely severe at temperatures above T_g.

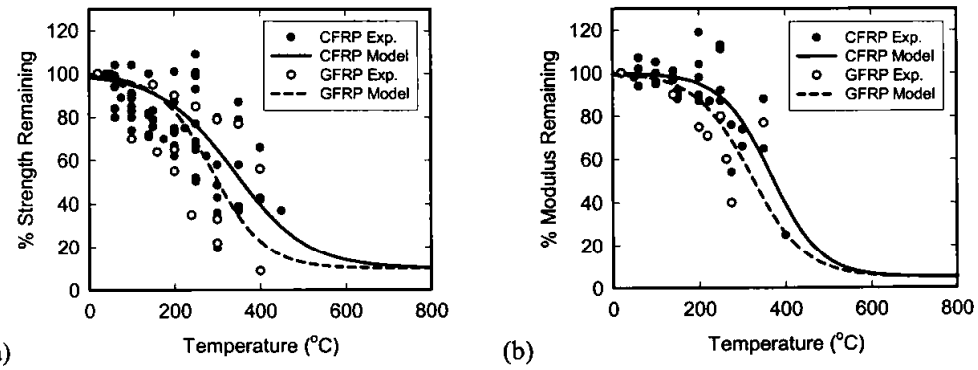

FIGURE 7 : Assumed variation in (a) strength and (b) stiffness of FRP with temperature (based on semi-empirical regression analysis performed by Bisby [15]).

No.	Source	Diam. (mm)	Principal steel reinf.	f'_c (MPa)	f_y (MPa)	FRP wrap[1]	Fire insulation[2]
1	Lie & Celikkol, 1992	356	6 Ø 20mm	42	414	--	--
2	Lie & Celikkol, 1992	356	6 Ø 20mm	42	414	--	--
3	Franssen & Dotreppe, 2003	300	6 Ø 12mm	60	500	--	--
4	Franssen & Dotreppe, 2003	300	6 Ø 12mm	60	500	--	--
5	Franssen & Dotreppe, 2003	300	6 Ø 20mm	60	500	--	--
6	Franssen & Dotreppe, 2003	300	6 Ø 20mm	60	500	--	--
7	Bisby, 2003	400	8 Ø 20mm	39	456	1-layer	32 mm
8	Bisby, 2003	400	8 Ø 20mm	40	456	1-layer	57 mm

[1]Proprietary Tyfo® SCH system carbon/epoxy FRP produced by Fyfe Co. LLC, San Diego, CA
[2]Proprietary Tyfo® EI/VG insulation produced by Fyfe Co. LLC, San Diego, CA.

Table 1 : selected details of columns used to verify the numerical models.

MODEL VERIFICATION

The models described above have been verified against data available in the literature [12, 18] and against data obtained from full-scale tests conducted by the authors [15]. Table 1 shows selected details of eight fire-tested concrete columns that have been used to verify the models. Tests available in the literature (columns 1 through 6 in Table 1) consisted of full-scale fire tests on conventionally-reinforced concrete columns without insulation or FRP wraps. The authors have recently conducted two full-scale fire tests on insulated FRP-wrapped concrete columns (columns 7 and 8 in Table 1), the complete details of which will be published elsewhere.

Temperatures

Figure 8a shows experimental and predicted temperatures in the concrete at various depths as a function of fire exposure time for columns 1 and 2 of Table 1. At a depth of 25 mm there is generally good agreement between the experimental and predicted temperatures, although the model tends to under-predict temperatures within the first hour of fire exposure. At depths of 64 and 178 mm the experimental curves are characterized by rapid increases in temperature followed by regions of relatively constant temperature. This behaviour is more pronounced at greater depths and has been attributed by previous authors [12, 13] to thermally-induced moisture migration in the concrete which is not accounted for in the model. Hence, the numerical model tends to under-predict concrete temperatures early in the fire exposure, with closer agreement demonstrated later in the exposure. The reader will recognize that the late-stage temperatures are those that play an important role in determining the fire endurance of the columns, and hence the initial discrepancy is not of major concern.

Figure 8b shows experimental and predicted temperatures in the concrete at various depths as a function of fire exposure time for column 8 of Table 1; a carbon FRP-wrapped RC column with 57 mm of the Tyfo® EI/VG sprayed cementitious insulation system applied to the exterior of

the wrap. Again, the model predictions agree reasonably well with the experimental data, and the model accurately captures the overall trends observed in the test data. However, the model does not precisely capture the 100°C temperature plateau observed in the test data at the level of the FRP wrap. This can be explained by considering that the model does not explicitly account for the evaporation of moisture from the insulation at 100°C, nor does it account for moisture movement within the insulation. The model accounts for moisture evaporation in the insulation by artificially increasing the specific heat of the insulation elements at temperatures near 100°C. While capturing the 100°C plateau is not critical for calculating the *structural* fire endurance of the FRP-wrapped columns, it could become important if fire endurance is defined in terms of the matrix T_g, since T_g is close to 100°C for many currently available FRPs. Further work is thus required to allow more accurate modelling of heat transfer within the insulation and to obtain more accurate predictions at temperatures near 100°C.

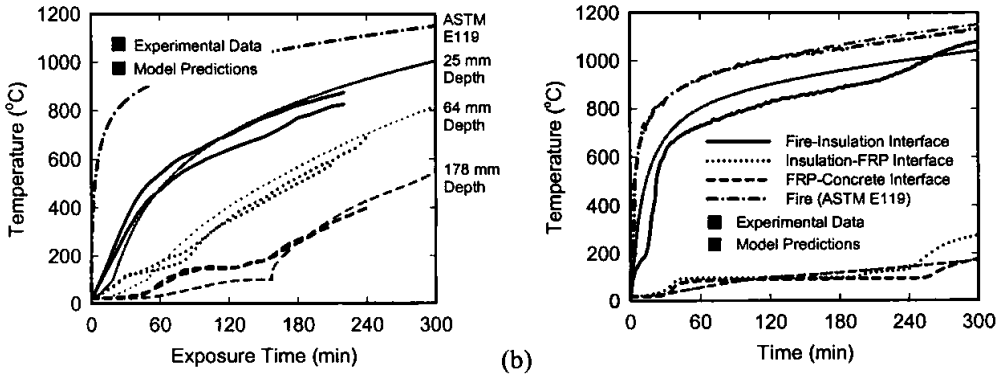

FIGURE 8 : Predicted and observed temperatures at various locations during fire tests by (a) Lie and Celikkol [12] and (b) Bisby [15].

Load capacity

Figure 9 shows the predicted buckling strength of columns 7 and 8 (insulated FRP-wrapped columns) as a function of fire exposure. Also included in Figure 9 are predicted fire endurance curves for equivalent columns in the unwrapped and wrapped *but uninsulated* conditions. Fire endurances (failure loads) observed during fire testing of columns 7 and 8 have been included as points in Figure 9.

Good agreement is evident between the model predictions and experimentally observed fire endurances for the insulated FRP-wrapped

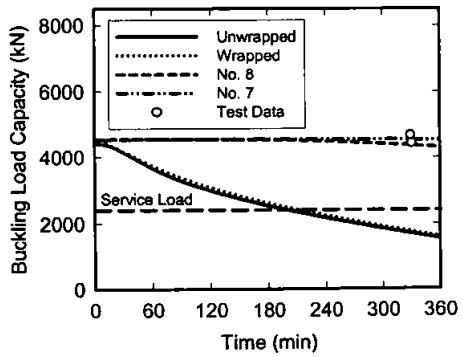

FIGURE 9 : Predicted and observed concentric axial load capacity during fire tests performed by Bisby [15].

columns. However, with only two data points it is not possible to conclusively verify the model's predictions. More tests are planned during 2004 to provide additional validation data. However, credence is given to the model's predictive abilities by comparing the predictions of the model with fire test data available for conventional RC columns. Table 2 gives a comparison of predicted and observed fire endurances for all eight of the columns listed in Table 1. It is evident that the model satisfactorily predicts the fire endurance of circular RC columns, and that it appears slightly conservative (from 3% to 16%).

No.	Source	Test load (kN)	FR_{test} (min)	FR_{model} (min)	$\frac{FR_{model}}{FR_{test}}$
1	Lie & Celikkol, 1992	1431	220	209	0.95
2	Lie & Celikkol, 1992	1431	245	209	0.85
3	Franssen & Dotreppe, 2003	1260	156	152	0.97
4	Franssen & Dotreppe, 2003	1770	131	119	0.91
5	Franssen & Dotreppe, 2003	1450	187	146	0.78
6	Franssen & Dotreppe, 2003	1900	163	120	0.74
7	Bisby, 2003	2515	> 300	> 300	--
8	Bisby, 2003	2515	> 300	> 300	--

Table 2 : predicted and observed fire endurances.

FRP-WRAPPED COLUMNS IN FIRE: MODEL PREDICTIONS

Referring to Figure 9, the predicted initial (room temperature) strength of the unwrapped RC column is slightly less than that predicted for the FRP-wrapped columns due to the confining effect of the wrap. It is interesting to note that the predicted initial strength increase due to FRP wrapping is relatively small (only about 4%). This can be explained by considering that Figure 9 presents the predicted *buckling strength* of the columns, and FRP confinement cannot be expected to significantly increase the elastic modulus of the concrete. Hence, the room temperature buckling strength of the columns is increased only slightly by FRP wrapping.

Figure 9 also suggests that an RC column with insulation but without FRP would presumably perform similarly to an FRP-wrapped *and* insulated column during fire, since the structural effectiveness of the FRP is predicted to be lost during fire exposure, even for well-insulated columns, and because FRP wrapping does not significantly increase the columns' buckling strength. However, it is important to recognize that columns are not wrapped with FRP for increased fire endurance, but rather for greater axial load capacity or for seismic upgrade. In these cases, the analysis presented herein suggests that fire protection is required to ensure that the overall structural member has sufficient capacity to carry the increased expected *service* load at the elevated temperatures experienced during fire. The insulation is not required specifically to protect the FRP wrap.

Axial Deformation

Figure 10a shows the measured and predicted axial deformation of columns 1 and 2 (unwrapped columns) as a function of fire exposure time under an applied compressive load of 1431 kN. During the first two hours of exposure, the predicted deformation is generally slightly greater than that observed in tests. This could be due to the short term creep of the concrete or to the seating effects not accounted for in the model, both of which would tend to decrease the observed deformation. However, both the maximum deformation and the point of failure are predicted reasonably well by the model. The greatest difference between predicted and measured axial deformation is in the order of 1.5 mm, which is satisfactory in comparison to the overall elongation of the columns ($\approx$7.5 mm). Axial deformation of the members is influenced by a number of factors, including thermal expansion, load effects, short-term thermally induced creep, and bending, some of which cannot be completely accounted for by the model. Nonetheless, the model adequately predicts the overall magnitude of elongation when compared against test data.

Figure 10b shows the measured and predicted axial deformations of columns 7 and 8 (insulated FRP-wrapped columns) as a function of fire exposure time under an applied axial load of 2515 kN. The model over-predicts the expansion of both columns for the full length of fire exposure. Nonetheless, the largest difference between predicted and measured axial deformation is in the order of 1.5 mm, which is small in comparison to the overall length of the columns. Given the extremely small magnitude of the deformations, both predicted and observed, it is difficult to state conclusively whether the model is an adequate predictor of axial elongation for insulated FRP-wrapped columns.

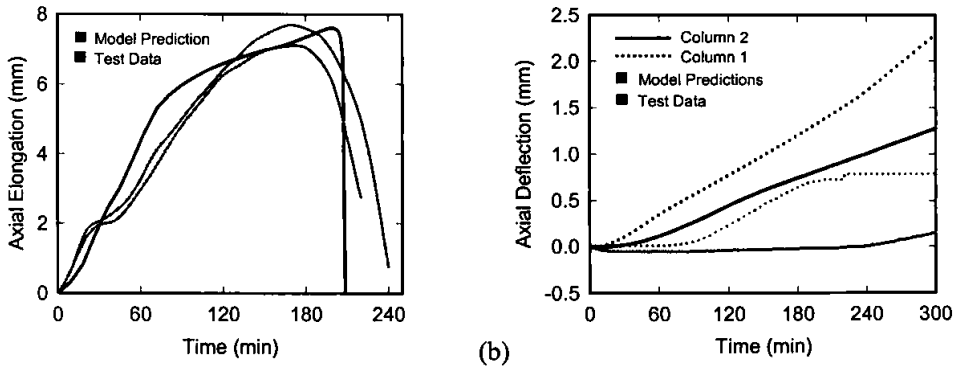

FIGURE 10 : Predicted and observed column deformations during fire tests by (a) Lie and Celikkol [12] and (b) Bisby [15].

CONCLUSIONS

In this paper, a numerical model was described that can be used to predict the behaviour of circular insulated and FRP-confined RC columns to exposure to a standard fire. The model has been verified against data from fire endurance tests on RC columns available in the literature and from tests on insulated FRP-wrapped columns performed by the authors. The model agrees reasonably well with experimental results.

With respect to the fire performance of FRP-wrapped columns, the model suggests that it will likely be very difficult, within the practical range of insulation thicknesses, to maintain the confining effectiveness of an FRP wrap during fire. If fire endurance is defined in terms of the load-carrying capacity of the column, as it should be according to current North American fire endurance guidelines, then the FRP wrap should likely be considered ineffective during fire. However, supplemental insulation applied to the exterior of the wrap is capable of dramatically improving the structural fire endurance of the overall column. Thus, satisfactory fire endurance of FRP-wrapped RC columns can be ensured by providing supplemental fire insulation and limiting the allowable strength increases due to FRP wrapping, as discussed above.

REFERENCES

[1] Bisby, L.A., Dent, A.J.S, & Green, M.F. *A comparison of models for FRP-confined concrete*, Accepted, Journal of Composites for Construction, American Society of Civil Engineers, New York, USA, 9 pp. (2004).

[2] ISIS Canada, *Design Manual No. 4*, Intelligent Sensing for Innovative Structures, Winnipeg, Canada, 2001.

[3] CAN/CSA, *CSA-S806-02: Design and construction of building components with fibre-reinforced polymers*, Canadian Standards Association, Ottawa, Canada, 2002.

[4] ACI, *ACI 440.2R-02,* American Concrete Institute, Farmington Hills, USA, 2002.

[5] The Concrete Society, *Technical Report 55: Design guidance for strengthening concrete structures using fibre-composite materials*, The Society, London, UK, Crowthorne, 2000.

[6] Karbhari, V., Chin, J., Hunston, D., Benmokrane, B., Juska, T., Morgan, R., Lesko, J.J., Sorathia, U., & Reynaud, U., *Durability gap analysis for fibre-reinforced polymer composites in civil infrastructure*, Journal of Composites for Construction, 7, N° 3, American Society of Civil Engineers, New York, USA, pp. 238-247 (2003).

[7] Harries, K., Porter, M., & Busel, J., *FRP materials and concrete - research needs*, Concrete International, 25, N° 10, American Concrete Institute, pp. 69-74 (2003).

[8] Spolestra, M., & Monti, G., *FRP-confined concrete model*, Journal of Composites for Construction, 3, N° 3, American Society of Civil Engineers, New York, USA, pp. 143–150 (1999).

[9] Blontrock, H., Taerwe, L., & Vandevelde, P., *Fire testing of concrete slabs strengthened with fibre composite laminates*, FRPRCS-5, Thomas Telford Ltd, London, pp. 547-556 (2001).

[10] ASTM, *Test Method E119-01,* American Society for Testing and Materials, West Conshohocken, USA, 21 pp., 2001.

[11] CAN/ULC, *CAN/ULC-S101-M89,* Underwriters' Laboratories Canada, Scarborough, Canada, 49 pp., 1989.
[12] Lie, T.T. & Celikkol, B., *Method to calculate the fire resistance of circular reinforced concrete columns*, ACI Materials Journal, 88, N° 1, American Concrete Institute, Farmington Hills, USA, pp. 84-91 (1991).
[13] Lie, T., *Structural Fire Protection*, American Society of Civil Engineers, New York, USA, 241 pp., 1992.
[14] ACI, *ACI 318-95: Building code requirements for structural concrete*, American Concrete Institute, Farmington Hills, USA, 1995.
[15] Bisby, L., *Fire behaviour of fibre-reinforced polymer reinforced or confined concrete*, Ph.D. Thesis, Department of Civil Engineering, Queen's University, Kingston, Canada, 371 pp., 2003.
[16] Griffis, C.A., Masmura, R.A., & Chang, C.I. *Thermal response of graphite epoxy composite subjected to rapid heating*, Environmental Effects on Composite Materials, V. 2, Technomic, Lancaster, USA, pp. 245-260, 1984.
[17] Dimitrienko, Y.I., *Thermomechanics of composites under high temperatures.* Klewer Academic Publishers, London, UK, 347 pp., 1999.
[18] Franssen, J.-M. & Dotreppe, J.-C., *Fire tests and calculation methods for circular concrete columns*, Fire Technology, Klewer Academic Publishers, London, UK, 39, pp. 89-97 (2003).

ACKNOWLEDGEMENTS

The authors are members of the Intelligent Sensing for Innovative Structures Network (ISIS Canada) and wish to acknowledge the support of the Networks of Centres of Excellence Program of the Government of Canada and the Natural Sciences and Engineering Research Council of Canada. The authors would also like to acknowledge the financial contributions of the National Research Council of Canada and Queen's University, Canada.